

Model reduction techniques for simulating complex flow processes

Vom Stuttgart Research Centre for Simulation Technology
und der Fakultät Bau- und Umweltingenieurwissenschaften
der Universität Stuttgart genehmigte Habilitationsschrift

vorgelegt von
Dr. rer. nat. Tobias Köppl
aus
Regensburg

Hauptberichter: Prof. Dr.-Ing. Rainer Helmig
1. Mitberichter: Prof. Dr. rer. nat. Christian Rohde
2. Mitberichter: Prof. Dr. Inga Berre
3. Mitberichter: Prof. Dr. Luca Formaggia

Tag der mündlichen Prüfung: 23. Juli 2020

Institut für Wasser- und Umweltsystemmodellierung
Lehrstuhl für Hydromechanik und Hydrosystemmodellierung
2020

Danksagung

Die vorliegende Habilitationsschrift entstand in den Jahren 2014 bis 2018 im Rahmen einer PostDoc Stelle, welche an der Universität Stuttgart durch das Forschungsnetzwerk SimTech (Simulation Technology) finanziert wurde. Neben der Mittel für Reiseausgaben und sonstiger Posten, möchte ich mich stellvertretend beim Direktorium des Forschungsnetzwerkes SimTech bedanken, dass ich mich sowohl in der Forschung als auch in der Lehre betätigen durfte und dadurch wertvolle Erfahrungen sammeln konnte.

Des Weiteren möchte ich mich bei verschiedenen Menschen bedanken, die meinen Lebensweg in den letzten Jahren sowohl im wissenschaftlichen als auch im privaten Bereich geprägt haben. Hinsichtlich des wissenschaftlichen Bereichs, gilt mein größter Dank meinem Mentor Herrn Prof. Dr. Rainer Helmig. Er hat mir die Möglichkeit verschafft die eben erwähnte PostDoc Stelle anzutreten zu dürfen. Darüber hinaus konnte ich mit seiner Hilfe gute Kontakte zu verschiedenen Arbeitsgruppen knüpfen und auf diese Weise mein Wissen in den verschiedensten Bereichen des wissenschaftlichen Rechnens vertiefen. Seine Hilfestellungen in Lehre und Forschung waren für mich ein großer Gewinn und haben wesentlich dazu beigetragen die vorliegende Arbeit erfolgreich abschließen zu können. Die tägliche Zusammenarbeit mit ihm war aufgrund seiner positiven und motivierenden Arbeitseinstellung äußerst angenehm. Außerdem danke ich allen weiteren Mitgliedern der Lehr- und Forschungseinheit LH2 (Lehrstuhl für Hydromechanik und Hydrosystemmodellierung am Institut für Wasser- und Umweltsystemmodellierung, Universität Stuttgart), der ich in den letzten vier Jahren angehört habe, für die gute Zusammenarbeit. Besonders möchte ich an dieser Stelle das Sekretariat bestehend aus Frau Prudence Lawday und Frau Stefanie Siegert sowie die Systemadministratoren Frau Michelle Hartnick und Herrn David Werner und die stellvertretenden Arbeitsgruppenleiter Prof. Dr. Holger Class und Prof. Dr. Bernd Flemisch hervorheben. Jedem Einzelnen von Ihnen möchte ich für zahlreiche Hilfestellungen während meiner Zeit am LH2 danken.

Darüber hinaus gilt mein Dank auch allen Koautoren, die zu den Publikationen welche in dieser Habilitationsschrift enthalten sind, einen Beitrag geleistet haben. Zunächst, möchte ich mich bei meinen ehemaligen LH2-Kollegen Dr. Martin Schneider und Dr. Timo Koch bedanken. Aus dem weiteren Umfeld der Universität Stuttgart und SimTech danke ich Prof. Dr. Haasdonk und Dr. Gabriele Santin (Fakultät für Mathematik) sowie Prof. Dr. Hilfer und Dr. Rouven Steinle (Institut für Computerphysik) für die gute Zusammenarbeit. Ein wesentlicher Bestandteil dieser Arbeit ist das Ergebnis einer engen Zusammenarbeit mit dem Lehrstuhl Numerische Mathematik an der TU München. Insbesondere danke ich meiner Doktormutter Prof. Dr. Barbara Wohlmuth sowohl für ihren fachlichen Rat als auch für die Möglichkeit diese Arbeit in ihrer Arbeitsgruppe fertigstellen zu können. Des Weiteren bedanke ich mich bei Prof. Dr. Rainer Callies für viele gute Ratschläge, sowie bei Dr. Ettore Vidotto und MSc. Daniel Drzisga für die gemeinsame Arbeit an den verschiedensten Projekten.

Außerdem möchte ich noch meine internationalen Partner dankend erwähnen. Dies sind im Einzelnen: Prof. Dr. Paolo Zunino (MOX, Politecnico Mailand), Prof. Dr. Cornelis Johannes van Duijn, Dr. Koondanibha Mitra (Fakultät für Mathematik, TU Eindhoven),

Herr Prof. Dr. Sorin Pop (Fakultät für Mathematik, Universität Hasselt), sowie Herr Dr. Mikhail Fedoseyev (CPC, Gubkin Universität Moskau).

Schließlich danke ich meiner Familie und meinen Freunden, die mich zu allen Zeiten unterstützt haben. Dabei denke ich vor allem an meine Ehefrau Katrin und meine Eltern. Die täglichen Gespräche und die gemeinsame Zeit mit ihnen gaben mir die Möglichkeit auch einmal Abstand vom Arbeitsleben zu gewinnen und neue Kräfte sammeln zu können.

Garching im August 2020

Tobias Köppl

Acknowledgments

This habilitation thesis was written between 2014 and 2018 as part of a postdoctoral position funded by the SimTech (Simulation Technology) research network at the University of Stuttgart. In addition to the funds for travel expenses etc., I would like to thank the board of directors of the SimTech research network for the opportunity to do both research and teaching and gain valuable experiences. Furthermore, I would like to thank various people who have shaped my life in recent years, both in the scientific and private field. Regarding the scientific field, I want to thank my mentor Prof. Dr. Rainer Helmig. He made it possible for me to receive the PostDoc position I just mentioned. Furthermore, with his help, I was able to establish valuable contacts to various research groups and thus deepen my knowledge in various areas of scientific computing. His assistance in teaching and research was a great benefit for me and contributed significantly to the successful completion of this thesis. The daily cooperation with him was extremely pleasant due to his positive and motivating work attitude. In addition, I would like to thank all the other members of the teaching and research unit LH2 (Chair for Hydromechanics and Modelling of Hydrosystems at the Department of Hydromechanics and Modelling of Hydrosystems, University of Stuttgart), which I belonged to the last four years. At this point I would especially like to mention the secretariat consisting of Mrs. Prudence Lawday and Mrs. Stefanie Siegert as well as the system administrators Mrs. Michelle Hartnick and Mr. David Werner and the deputy research group leaders Prof. Dr. Holger Class and Prof. Dr. Bernd Flemisch. I would like to thank everyone of them for their help during my time at the LH2.

Next, I would like to thank all co-authors who contributed to the publications contained in this habilitation thesis. First of all, I thank my former LH2 colleagues Dr. Martin Schneider and Dr. Timo Koch. Further, I would like to thank Prof. Dr. Haasdonk and Dr. Gabriele Santin (Department of Mathematics) as well as Prof. Dr. Hilfer and Dr. Rouven Steinle (Institute of Computer Physics) for their excellent cooperation. An essential part of this thesis is the result of a close cooperation with the Chair of Numerical Mathematics at the University of Technology Munich. In particular, I would like to thank my doctoral supervisor Prof. Dr. Barbara Wohlmuth for her scientific advice as well as for the opportunity to complete this thesis in her research group. Moreover, I would also like to thank Prof. Dr. Rainer Callies for many valuable advice, as well as Dr. Ettore Vidotto and MSc. Daniel Drzisga for working together on various projects. In addition to that, I am thanking also my international partners. These are in detail: Prof. Dr. Paolo Zunino (MOX, Politecnico Milan), Prof. Dr. Cornelis Johannes van Duijn, Dr. Koondanibha Mitra (Department of Mathematics, TU Eindhoven), Prof. Dr. Sorin Pop (Department of Mathematics, University of Hasselt) and Dr. Mikhail Fedoseyev (CPC, Gubkin University of Moscow).

Finally, I thank my family and friends who have supported me at all times. In particular, I am thinking of my wife Katrin and my parents. The daily conversations and the time I spent together with them gave me the opportunity to gain new strength.

Garching, August 2020

Tobias Köppl

Contents

Danksagung	iii
Acknowledgments	v
Deutsche Zusammenfassung	ix
Summary	xix
1 Introduction	3
Introduction	3
1.1 Why do we require model reduction techniques for simulating flow processes?	3
1.2 Basic modelling approaches	10
1.2.1 Model reduction techniques for macroscale networks	10
1.2.2 Model reduction techniques for fine scale structures	29
1.3 Structure of the thesis	38
1.3.1 Part I: Simulation of flow processes in macroscale networks	38
1.3.2 Part II: Simulation of blood flow in microvascular networks	43
1.3.3 Part III: Simulation of fluid injection into porous media	49
I Simulation of flow processes in macroscale networks	55
2 Numerical modeling of compensation mechanisms for peripheral arterial stenoses	59
3 Numerical modelling of a peripheral arterial stenosis	73
4 Simulation of surge reduction systems using dimensionally reduced models	99
4.1 Introduction and motivation	99
4.2 Technical details	100
4.3 Modelling a pipeline with a pumping station and a SRS	101
4.3.1 Modelling oil transport within a pipeline	101
4.3.2 0D model for a SRS	104
4.3.3 0D model for a pumping station	105
4.3.4 Numerical methods	106
4.4 Simulation results	107
4.4.1 Change of pressure and velocity distribution in case of a shutdown .	108
4.4.2 Comparison of simulation results and measurements	112
4.5 Concluding remarks	114

II	Simulation of blood flow in microvascular networks	117
5	A local error estimate for the Poisson equation with a line source term	121
6	Elliptic problems with inclusions	131
7	Hybrid models for microvascular networks	161
III	Simulation of fluid injection into porous media	191
8	Stable propagation of saturation overshoots	195
9	Fronts in two-phase porous flow problems	217
10	Concluding remarks	263

Deutsche Zusammenfassung

Die Modellierung und Simulation von Strömungsprozessen in technischen, geologischen und biologischen Systemen stellt Forscher aus dem Bereich der Ingenieurwissenschaften, Mathematik, Physik und Informatik vor große Herausforderungen. Dies liegt zum einen darin begründet, dass die mathematischen Gleichungen oftmals nichtlinear sind. Des Weiteren genügt es für interessante Anwendungsfälle nicht nur ein einzelnes mathematisches Modell oder eine bestimmte numerische Methode zu verwenden. Um eine realistische Beschreibung der jeweiligen Problemstellung zu ermöglichen, ist es oftmals von Nöten verschiedenartige Modelle miteinander zu koppeln oder neben den reinen Strömungsvorgängen weitere physikalische Prozesse mit in Betracht zu ziehen. Hinsichtlich der Aufbereitung, Visualisierung und Verwaltung der Simulationsdaten steht man häufig vor dem Problem, dass große Datenmengen anfallen, welche nicht mehr auf gewöhnlichen Rechnern gespeichert werden können oder lange Simulationszeiten verursachen können. Diese Beobachtungen motivieren den Einsatz von Modellreduktionstechniken, welche darauf abzielen komplexe mathematische Modelle durch vereinfachte Modelle zu ersetzen. In dieser Habilitationsschrift werden verschiedene Modellreduktionstechniken präsentiert, die eine effiziente Beschreibung von Strömungsprozessen erlauben ohne an Genauigkeit bezüglich physikalischer Größen, welche für das jeweilige Anwendungsgebiet interessant sind, einzubüßen. Insgesamt lassen sich die betrachteten Modellreduktionstechniken in vier Kategorien einteilen: Dimensionsreduzierte Modellierung, Homogenisierungsmethoden, Gebietszerlegungsmethoden und datenbasiertes Lernen. Um deren Einsatzmöglichkeiten im Zusammenhang mit Strömungsprozessen darlegen zu können, betrachten wir in der vorliegenden Arbeit vier verschiedene Strömungsprozesse, die in der Medizin, Energieversorgung und Umweltwissenschaften eine wichtige Rolle spielen. Dies sind im Einzelnen: Blutströmung in großen Arterien und mikrovaskularen Systemen, Öltransport in Rohrleitungen sowie die Injektion von Flüssigkeiten in poröse Medien. Bei genauerer Betrachtung lassen sich unter den aufgezählten Strömungsprozessen verschiedene Größenskalen und Strömungseigenschaften identifizieren. Während die Strömungen in den großen Arterien und Rohrleitungssystemen höhere Reynoldszahlen aufweisen und sich durch großskalige Hohlräume bewegen, beobachtet man bei Strömungen in mikrovaskularen Netzwerken und porösen Medien kleine Reynoldszahlen und kleinskalige Hohlräume. Im Falle der großen Arterien und Röhrensysteme haben die Gefäße und die Röhren Durchmesser im Bereich von Zentimetern und Metern. Im Gegensatz dazu weisen Gefäße in einem mikrovaskularen Netzwerk Durchmesser im Bereich von Mikrometern auf. Poren und Porenhäse in einem Gestein oder Gewebe weisen sogar noch kleinere Abmessungen auf. Diese Unterschiede motivieren die Behandlung der Strömungsprozesse in verschiedenen Teilen, die sich an den Eigenschaften der jeweiligen Anwendung orientieren. Insgesamt ergeben sich für die Habilitationsschrift die drei folgenden Teile:

- *Teil I: Simulation von Strömungsprozessen in makroskaligen Netzwerken*
- *Teil II: Simulation von Blutströmung in mikrovaskularen Netzwerken*
- *Teil III: Simulation von Flüssigkeitsinjektionen in poröse Medien*

Die ersten beiden Teile sind in drei Kapitel untergliedert, während der letzte Teil zwei weitere Kapitel beinhaltet. Jedes der insgesamt acht Kapitel basiert auf bereits veröffentlichten, eingereichten oder zur Veröffentlichung genehmigten Arbeiten. Mit Ausnahme von Kapitel 4 wurden die eingereichten oder veröffentlichten PDF-Dokumente der einzelnen Publikationen in die Habilitationsschrift eingebunden. Die Tatsache, dass die Publikation aus Kapitel 4 nicht im Original eingebunden werden konnte, liegt in den Copyright Bestimmungen des zugehörigen Verlags begründet. Aufgrund der Bestimmungen der Zeitschrift, erstreckt sich das Copyright des Autors nur auf die Abbildungen und Tabellen dieser Publikation. Insgesamt ergibt sich die folgende Gliederung:

- *Teil I: Simulation von Strömungsprozessen in makroskaligen Netzwerken*
 - Kapitel 2: Numerische Modellierung von Kompensationsmechanismen für periphere arterielle Stenosen
 - Kapitel 3: Numerische Modellierung einer peripheren arteriellen Stenose unter Benutzung dimensionsreduzierter Modelle und maschinellem Lernen
 - Kapitel 4: Simulation von Überspannungsreduktionssystemen unter Benutzung dimensionsreduzierter Modelle
- *Teil II: Simulation von Blutströmung in mikrovaskulären Netzwerken*
 - Kapitel 5: Lokale Fehlerabschätzung für die Poissongleichung mit einem Linienquellterm
 - Kapitel 6: Mathematische Modellierung, Analyse und numerische Lösung von elliptischen Gleichungen zweiter Ordnung mit kleinen Einschlüssen
 - Kapitel 7: Hybride Modelle zur Simulation von Blutströmungen in mikrovaskulären Netzwerken.
- *Teil III: Simulation von Flüssigkeitsinjektionen in poröse Medien*
 - Kapitel 8: Stabile Ausbreitung von Sättigungsüberschüssen für eine zweiphasige Strömung in porösen Medien.
 - Kapitel 9: Sättigungsfronten in zweiphasigen Strömungen durch poröse Medien: Effekte von Hysterese und dynamischem Kapillardruck

Im ersten Kapitel wird ein Modell zur Simulation einer peripheren arteriellen Stenose vorgestellt d.h. einer Stenose die sich weit weg vom Zentrum des Körpers befindet. Insbesondere betrachten wir eine Stenose in einer der Hauptarterien des rechten unteren Beins. Zur Vereinfachung dieser Problemstellung wird die Blutströmung in den 55 Hauptarterien des menschlichen Körpers mit eindimensionalen (1D) Strömungsmodellen simuliert. Die Randbedingungen sowie der Einfluss der Stenose werden durch gewöhnliche Differentialgleichungen beschrieben. Da diese Modelle nur eine Zeitvariable aber keine Raumvariable besitzen, bezeichnet man sie auch als 0D Modelle. Dieses vereinfachte 1D-0D gekoppelte

Strömungsmodell wird um Modelle für zwei Ausgleichsmechanismen erweitert. Dazu betrachten wir die metabolische Regulierung durch Arteriolen und die Arteriogenese. Sinkt die Sauerstoffkonzentration in einem Teil des Gewebes, das durch das betroffene Gefäß versorgt ab, so beobachtet man, dass sich die Querschnittsflächen der Arteriolen, die zwischen den großen Arterien und dem Kapillarbett liegen, vergrößern. Dies bedeutet, dass sich der Strömungswiderstand der Arteriolen verringert, was dazu führt, dass der Blutfluss in die betroffene Region erleichtert wird. Die Größe der Querschnittsflächen wird über Muskeln reguliert, die die Gefäßwände der Arteriolen umgeben. Arteriogenese beschreibt einen Mechanismus, der ebenfalls eine Vergrößerung der Querschnittsflächen von Gefäßen beschreibt. Diese Gefäße haben ähnliche Abmessungen wie Arteriolen, befinden sich aber typischerweise zwischen zwei größeren Arterien und bilden Querverbindungen zwischen zwei größeren Arterien. Diese Querverbindungen können die Blutströmung um eine Verengung herumleiten. Die verstärkte Strömung durch diese Gefäße ruft eine erhöhte Schubspannung an den Gefäßwänden hervor. Die Zellen an den Gefäßinnenwänden werden dadurch aktiviert und leiten ein Signal an die Muskulatur im Inneren der Gefäßwand weiter, welche sich daraufhin entspannt und dadurch die Querschnittsfläche des Gefäßes erhöht. Messungen zeigen, dass sich die Querschnittsflächen um das 2.5-fache vergrößern können, was eine erhebliche Absenkung des Strömungswiderstands bedeutet. Das Ziel dieses Kapitels besteht nun darin die Effizienz der beiden Ausgleichsmechanismen mittels verschiedener Simulationen zu beurteilen. Dadurch lassen sich die beiden Ausgleichsmechanismen auch getrennt betrachten, was in einem Tierversuch in der Regel nicht möglich ist. Eine getrennte Simulation der beiden Mechanismen ergibt Aufschlüsse darüber, wie groß der Beitrag eines einzelnen Mechanismus zur Wiederherstellung des Blutflusses ist. Es lässt sich beispielsweise ermitteln, wie viele Querverbindungen notwendig sind, um eine bestmögliche Kompensation des reduzierten Blutflusses zu erzielen. Zur numerischen Simulation benutzen wir für die hyperbolischen 1D Strömungsmodelle die Methode der Charakteristiken. Dies ist auf den ersten Blick überraschend, da dieses Verfahren nur von erster Ordnung in Raum und Zeit ist. Andererseits lässt sich beweisen, dass dieses Verfahren unbedingt stabil ist, obwohl es explizit ist. Diese Eigenschaft macht das Verfahren sehr attraktiv, da man nicht dazu gezwungen wird winzige Zeitschritte ausführen zu müssen. Die niedrige Approximationsordnung, welche zu großen Dissipations- und Dispersionsfehlern führen kann, wird in Kauf genommen, da das Problem nur eine einzelne Raumdimension besitzt. Denn ein feines Gitter in einer einzelnen Raumdimension erzeugt einen beherrschbaren numerischen Aufwand. Außerdem ist die Charakteristiken-Methode keiner klassischen CFL-Bedingung unterworfen, welche uns bei einer feinen Ortsdiskretisierung zu winzigen Zeitschritten zwingen kann. Für die Zeitdiskretisierung wählen wir Zeitschritte, die hinreichend klein sind, um die schnelle konvektionsdominierte Strömung in den großen Arterien genau genug beschreiben zu können, was dazu führt, dass sich auch der Diskretisierungsfehler in der Zeit in Grenzen hält.

Um gesicherte Aussagen hinsichtlich dieser Problemstellung treffen zu können, ist es erforderlich eine ausreichende Menge an Simulationsdaten zu erzeugen. Dazu ist es notwendig den Verengungsgrad der Stenose viele Male zu variieren, was zu langen Simulationszeiten führt. Zur Verkürzung der Simulationszeiten wird zunächst eine Abbildung konstruiert, die einem bestimmten Stenosegrad eine abgetastete Blutdruck- oder Flußratenkurve in der Umgebung der Stenose zuweist. Insgesamt ergibt sich sowohl für den Druck als auch die Flußrate ein Vektor bestehend aus $q \in \mathbb{N}$ abgetasteten Werten. Unter der Annahme, dass sich der Stenosegrad nur zwischen 0 und 1 bewegt, wobei der Stenosegrad 0 einem gesunden Gefäß entspricht und der Stenosegrad 1 einen vollständigen Gefäßverschluß repräsentiert,

ergibt sich eine Abbildung vom Einheitsintervall in den vektorwertigen Raum \mathbb{R}^q . Im zweiten Kapitel des ersten Teils beschäftigen wir uns damit diese Abbildung möglichst genau und effizient durch ein Ersatzmodell zu beschreiben. Das Ersatzmodell hat dabei die Gestalt einer Linearkombination von Kernfunktionen. Eine Kernfunktion besitzt zwei Variablen und gegebenenfalls weitere Parameter, die ihre genaue Form bestimmen. Außerdem ist sie symmetrisch bezüglich ihrer Variablen und positiv, weshalb sich durch derartige Funktionen auch ein Skalarprodukt induzieren lässt. Ein klassisches Beispiel für eine Kernfunktion ist die Gaußfunktion. Die Koeffizienten dieser Linearkombination und die Parameter, welche die Form der Kernfunktionen bestimmen, werden durch Greedy Algorithmen und unter der Verwendung von Simulationsdaten ermittelt. Dabei wird für jede Komponente eine eigene Linearkombination von Kernfunktionen bestimmt. In jedem Schritt des Greedy Algorithmus wird ein regularisiertes Ausgleichsproblem gelöst, dessen Systemmatrix symmetrisch und positiv definit ist, da die Einträge der Matrix durch Auswertungen der Kernfunktionen bestimmt sind. Daraus folgt sofort, dass jedes Ausgleichsproblem wohlgestellt ist, was die Verwendung von Kernfunktionen nachträglich rechtfertigt. Für die numerische Simulation verwenden wir wie schon im vorherigen Kapitel die Methode der Charakteristiken.

Im letzten Kapitel des ersten Teils benutzen wir wie in den beiden ersten Kapiteln 1D-0D gekoppelte Strömungsmodelle zur Simulation von Öltransport in Rohrleitungen. Im Gegensatz zu den 1D Blutströmungsmodellen sind die 1D Modelle für das Röhrensystem linear in den Unbekannten, da die Wechselwirkung zwischen der starren Röhrenwand und der Strömung vernachlässigt werden kann. Diese Wechselwirkungen können im Falle von Blutströmungen in großen Arterien mit ihren stark deformierbaren Gefäßwänden nicht vernachlässigt werden. Die 0D Modelle beschreiben in diesem Zusammenhang den Einfluss von Pumpen und Sicherheitssystemen. Mit Hilfe des modifizierten 1D-0D Strömungsmodells werden das Geschwindigkeits- und Druckfeld in einem Teilstück einer Ölpipeline berechnet, welche Ölfelder im Nordosten des Kaspischen Meeres und einen Hafen am Schwarzen Meer verbindet. Durch Simulationen sollen Erkenntnisse über die Wirkungsweise der Sicherheitssysteme gewonnen werden. Insbesondere untersuchen wir die Auswirkungen auf die Strömung, wenn sich eine Versorgungsklappe am Ende des Röhrensystems schließt oder eine Pumpe ausgeschaltet wird. Beide Szenarien sind für die Praxis von großer Bedeutung. Das Schließen einer Versorgungsklappe findet jeweils am Ende eines Abfüllungsprozesses statt, d.h. wenn beispielsweise mehrere Öltanker mit einer neuen Ölladung bestückt werden, muss die Versorgungsklappe mehrmals geöffnet und geschlossen werden. Das Herunterfahren einer Pumpe ist meistens zu Wartungszwecken, Reparaturarbeiten oder bei Unfällen notwendig. In beiden Fällen beobachtet man dynamische Druckänderungen in den Rohrleitungen, welche zur Entstehung von Druckwellen mit erhöhter Amplitude führen können. In der Fachsprache bezeichnet man dieses Phänomen als Druckstoß, Wasserhammer oder auch Druckschlag (engl. *pressure surge*). Dies bewirkt, dass die Wände der Rohre Risse bekommen können oder Nähte und Verschraubungen beschädigt werden. Beides kann zu einem Verlust von größeren Ölmengen führen. Neben der wirtschaftlichen Verluste können sich auch massive Umweltschäden ergeben. Obwohl die Gefahren, die im Zusammenhang mit einem Druckstoß stehen schon seit der römischen Antike bekannt sind, ergeben sich immer wieder Schäden durch Druckstöße. So kam es beispielsweise im Jahre 2009 in Hamburg zu einem Stromausfall, der auch einige Pumpen in verschiedenen Wasserwerken betraf. Der abrupte Ausfall der Pumpen erzeugte mehrere Druckstöße, welche das Leitungssystem stark belasteten. Nachdem die Pumpen wieder gestartet werden konnten, ergaben sich aufgrund der Vorbelastungen mehrere Rohrbrüche. Die Auswirkungen

gen einer heruntergefahrenen Pumpe sind ebenfalls Gegenstand des vorliegenden Kapitels. Dabei betrachten wir Druckkurven, welche sich durch das Abschalten einer Pumpstation bei Astrakhan ergeben. Astrakhan liegt im südlichen Russland in der Nähe des Kaspischen Meeres. Diese Pumpstation ist neben der reinen Pumpvorrichtung auch noch mit einer Rückschlagklappe und einem speziellen Überdruckschutzsystem versehen. Die Messungen der Druckkurven sind nahe der Pumpe während des Abschaltvorgangs stromaufwärts und stromabwärts bezüglich der Transportrichtung erhoben worden. In diesem Kapitel sind wir nun der Frage nachgegangen, ob sich diese Druckkurven auch durch eine vereinfachte Modellierung der Pumpe sowie des Überdruckschutzsystems mit gewöhnlichen Differentialgleichungssystemen beschreiben lassen. Das Überdruckschutzsystem besteht neben einer Notfallklappe, die an die Rohrleitung angeschlossen ist noch aus einer Serie von Gasakkumulatoren, welche durch den Gegendruck des Gases eine stetige und kontrollierte Öffnung der Notfallklappe ermöglichen. Dies ist ein wesentlicher Unterschied zu den herkömmlichen Notfallklappen, welche sich schlagartig öffnen, falls der Innendruck im Rohr einen gewissen Schwellenwert überschritten hat. Im Gegensatz dazu kann mit Hilfe einer Notfallklappe, die mit Gasakkumulatoren gekoppelt ist, der Druckanstieg in einer Ölpipeline effektiver kontrolliert werden. Durch eine Kontrolle des Druckanstiegs kann der Betreiber einer Ölpipeline verhindern, dass sich die Auffangbecken, die an die Notfallklappen angeschlossen sind, nicht zu schnell füllen. Dies gibt dem Betreiber die Zeit den Innendruck in einer Pipeline durch weitere Maßnahmen, wie zum Beispiel durch die Öffnung weiterer Notfallklappen, zu senken. Die Motivation dimensionsreduzierte 1D-0D gekoppelte Strömungsmodelle für derartige Prozesse in Erwägung zu ziehen, liegt darin begründet, dass man die Auswirkungen von Druckstößen in der gesamten Pipeline und nicht nur lokal studieren möchte. Eine dreidimensionale Vernetzung eines gesamten Leitungssystems mit Pumpen und Überdruckschutzsystemen sprengt die Möglichkeiten von Standardcomputern und erfordert lange Rechenzeiten. Wie in den vorherigen Kapiteln verwenden wir die Methode der Charakteristiken für die 1D Strömungsmodelle. Neben der Charakteristiken-Methode benutzen wir ein stabilisiertes DG-Verfahren kombiniert mit einem expliziten Runge-Kutta-Verfahren dritter Ordnung. Beide Methoden werden miteinander hinsichtlich ihrer Genauigkeit und Effizienz verglichen. Es stellt sich dabei heraus, dass das DG-Verfahren trotz der höheren Ordnung keine genauere Approximation der Messdaten als die Methode der Charakteristiken erzeugt. Außerdem zeigt sich, dass sich bei der DG-Diskretisierung eine strengere CFL-Bedingung als bei der Methode der Charakteristiken ergibt. Damit ist die Methode der Charakteristiken auch in diesem Fall effizienter.

Der zweite Teil dieser Arbeit beschäftigt sich mit der dimensionsreduzierten Modellierung von Blutströmung in mikrovaskularen Netzwerken. Da bereits kleine Gewebelöcher mit einem Volumen von 1.0 mm^3 bis 2.0 mm^3 tausende Gefäße mit Durchmessern im Bereich von einigen Mikrometern enthalten, besteht eine Möglichkeit die Komplexität dieser Problemstellung zu verringern darin mikrovaskuläre Netzwerke vereinfacht durch eindimensionale graphenartige Strukturen zu beschreiben. Die Blutströmung innerhalb des Netzwerks wird durch die Poiseuille Gleichung beschrieben. Im umliegenden porösen Gewebe wird die Strömung mit Hilfe der Darcy Gleichung modelliert. Zur Kopplung der beiden Strömungsprozessen betrachten wir das Starlingsche Filtrationsgesetz und bestimmen damit die Form der Quellterme sowohl für die Poiseuille Gleichung, welche die Strömung im vaskulären System bestimmt, als auch für die Darcy Gleichung, die für das Gewebe zuständig ist. Um Massenerhaltung zu garantieren, besitzen die Quellterme ein unterschiedliches Vorzeichen. Dadurch ergibt sich eine Kopplung der beiden Differentialgleichungen über ihre Quellterme, wobei der Quellterm der Darcy Gleichung ein Dirac-

maßaufweist, das auf die 1D Graphenstruktur des Netzwerks konzentriert ist. Insgesamt ergibt sich auf diese Art und Weise ein 3D-1D gekoppeltes Strömungsmodell.

Um die mathematische Struktur derartiger Modelle zu verstehen, betrachten wir in Kapitel 5 ein mathematisches Modellproblem. Dabei verzichten wir zunächst auf die Kopplung und betrachten in Anlehnung an die Darcy Gleichung ein Poissonproblem mit Linienquellterm. Für dieses Modellproblem analysieren wir das lokale Konvergenzverhalten der linearen Galerkin Finite Elemente Methode, d.h. wir schätzen den Diskretisierungsfehler dieser Methode in einem gewissen Abstand zu der Linie numerisch und analytisch ab. Die Motivation, nur das lokale Konvergenzverhalten zu studieren, liegt darin begründet, dass die nähere Umgebung um die Linienquellen durch das vaskuläre Netzwerk bedeckt ist. Damit ist die Lösung an diesen Orten zur Beschreibung des Druck- und Geschwindigkeitsfelds im Gewebe von geringem Interesse. Dies bedeutet wiederum, dass man nur lokal eine gute Qualität der numerischen Lösung für das Poissonproblem sicherstellen muss. Dadurch könnte es vermieden werden, die Singularität, welche entlang der Linie entsteht genau approximieren zu müssen.

Es zeigt sich, dass die Finite Elemente Methode lokal optimal konvergiert, obwohl ein quasi-uniformes Gitter verwendet wird. Andererseits erkennt man eine lange Präasymptotik, was dazu führt, dass das Gitter bereits sehr fein sein muss, damit dieses Verfahren optimal konvergiert. Bei genauerer Betrachtung der numerischen Simulationsergebnisse erkennt man außerdem, dass der präasymptotische Bereich genau dann endet, wenn die Gitterweite in der Größenordnung des Radius des ausgeschnitten Zylinders liegt. Ruft man sich in Erinnerung, dass die Radien von mikrovaskulären Netzwerken klein sind gegenüber den Abmessungen des Gesamtgebietes, lässt sich daraus schließen, dass diese Kopplungsstrategie nur dann eine genaue Beschreibung der Druckverteilung im Gewebe liefert, wenn das Gitter sehr fein ist. Damit wäre der Vorteil, der sich durch die Modellreduktion ergibt, wieder verspielt.

Daher wenden wir uns in Kapitel 6 der Entwicklung eines neuen Kopplungskonzepts zu, welches nicht auf einem Linienquellterm beruht. Die Idee des neuen Kopplungskonzepts besteht darin den Quellterm der Darcygleichung nicht auf die Mittelachse der einzelnen Gefäße zu konzentrieren, sondern auf deren Gefäßwände, da dort auch der eigentliche Austausch mit dem umliegenden Gewebe stattfindet. Weitere Analysen zeigen, dass sich entlang der Gefäßwände keine Singularitäten mehr bilden, sondern nur noch Knicke auftreten. Dies bedeutet, dass die Lösung des 3D Problems nun eine höhere Regularität besitzt, was auch das Konvergenzverhalten numerischer Lösungsverfahren verbessert. Im Gegensatz zum Linienquellterm beobachtet man nun auch eine Konvergenz in der H^1 -norm. Ein weiterer wichtiger Aspekt dieses Kapitels besteht darin, dass die Konstruktion dieses Kopplungskonzepts Möglichkeiten aufzeigt, den Modellierungsfehler, der durch Modellreduktionen entsteht, in Abhängigkeit des Gefäßradius abzuschätzen. Der Modellierungsfehler lässt sich wiederum in zwei Teile aufspalten. Zum einen ergibt sich ein Fehler durch die Übertragung des 3D Problems, welches sich eigentlich nur auf das Gewebe beziehen sollte, auf das gesamte Volumen, welches von dem Gewebe und dem mikrovaskulären Netzwerk eingenommen wird. Der zweite Fehler besteht darin, dass zur Bestimmung des Flusses über die Gefäßwand keine punktweise Berechnung stattfindet. Stattdessen wird der Druck im Gewebe auf der Gefäßoberfläche gemittelt und mit dem Druck im Gefäß verglichen. Dadurch wird die Flußberechnung stark vereinfacht. Für beide Fehlerquellen lassen sich im Rahmen eines zweidimensionalen Modellproblems Fehlerschranken in Abhängigkeit der Modellparameter, insbesondere des Radius herleiten. Es zeigt sich dabei, dass der Modellierungsfehler mit kleiner werdenden Radius abnimmt. Dies ist für dieses Anwendungsgebiet

von großer Wichtigkeit, da die Gefäßradien eines mikrovaskularen Netzwerks im Vergleich zur Größe des Simulationsgebietes klein sind.

Mit Hilfe der Modellreduktionstechniken, welche in den ersten beiden Kapiteln des zweiten Teils der Arbeit analysiert wurden, lassen sich vaskuläre Systeme in kleineren Gewebsblöcken effizient simulieren. Um aber Blutströmungen in größeren Teilen eines Organs simulieren zu können, benötigen wir weitere Modellreduktionstechniken. Ein Grund dafür ist, dass sich größere mikrovaskuläre Systeme nur sehr schwer aus Bilddaten rekonstruieren lassen. Des Weiteren übersteigen die Dimensionen der Gleichungssysteme, welche sich aus den numerischen Diskretisierungsverfahren ergeben, schnell die Leistungsfähigkeit von durchschnittlichen Computersystemen. Um nicht jede einzelne Kapillare explizit mit einem 1D Modell behandeln zu müssen, gehen wir dazu über, nur die Arteriolen und Venolen in einem mikrovaskularen Netzwerk mit 1D Strömungsmodellen zu behandeln. Das dichte Kapillarnetz hingegen wird homogenisiert und mit Parametern für poröse Medien wie Permeabilitätstensoren und Porositäten charakterisiert. Dabei stellt sich die Frage wie groß die REVs (Representative Elementary Volume) zu wählen sind, damit die jeweiligen Permeabilitätstensoren und Porositäten das homogenisierte Kapillarnetz sinnvoll beschreiben. Wählt man das REV zu klein oder zu groß, so zeigt bei der Homogenisierung klassischer poröser Medien wie Gestein oder Sand, dass die Permeabilitäten und Porositäten stark oszillieren und damit nicht repräsentativ sind. Aus diesem Grund führen wir basierend auf einem Datensatz, der uns von Prof. Dr. Bruno Weber und Prof. Dr. Patrick Jenny (ETH Zürich) zur Verfügung gestellt wurde, einen Test zur Bestimmung der REV Größe durch. Der vorliegende Datensatz beschreibt einen Teil der zerebralen Mikrozirkulation einer Ratte und füllt einen Quader mit den Dimensionen $1.0 \text{ mm} \times 1.0 \text{ mm} \times 2.0 \text{ mm}$. In einem ersten Schritt wird basierend auf einem bestimmten Schwellenwert bezüglich des Gefäßradius das Kapillarnetz von den Arteriolen und den Venolen getrennt. Als nächstes positionieren wir in der Mitte des Gebiets ein kleines REV in Form eines Quaders mit den Abmessungen $12.0 \mu\text{m} \times 12.0 \mu\text{m} \times 24.0 \mu\text{m}$ und verlängern die Kanten dieses REVs in jedem Schritt um $4.0 \mu\text{m}$ in x - und y -Richtung und um $8.0 \mu\text{m}$ in z -Richtung. Für die jeweiligen REVs werden für das in dem REV enthaltene Kapillarnetz die Porosität und die Permeabilitäten in den drei Raumrichtungen berechnet. Zur Bestimmung der Permeabilitäten legen wir in die jeweilige Raumrichtung einen Druckgradienten an und setzen an den übrigen Rändern des Quaders no-flow Randbedingungen. Danach wird der Volumenfluß durch das Kapillarnetz berechnet und mit Hilfe des Darcygesetzes die Permeabilität bestimmt. Es stellt sich heraus, dass sich die Parameter des porösen Mediums ab einer Kantenlänge von $600.0 \mu\text{m}$ in x - oder y -Richtung stabilisieren. Dies würde aber bedeuten, dass für den vorliegenden Datensatz nur ein einziges REV verwendet werden könnte. Damit aber Heterogenitäten im Kapillarnetz abgebildet werden können, verwenden wir für jede Raumrichtung jeweils 2 REVs. Betrachtet man die vorherigen Ergebnisse, so erkennt man, dass bei einer Kantenlänge von $500.0 \mu\text{m}$ die Permeabilitäten auch nur schwach oszillieren.

Insgesamt ergibt sich durch die Homogenisierung ein neues 3D Kontinuum, welches mit einem anderen 3D Kontinuum für das Gewebe gekoppelt ist (dualer Kontinuumsansatz). Berücksichtigt man noch die Kopplung des porösen 3D Kontinuums für das Kapillarnetz mit den Arteriolen und Venolen, so erhält man ein gekoppeltes 3D-3D-1D Modell. Zur Validierung dieses neuen Ansatzes, vergleichen wir die Simulationsergebnisse mit denen des 3D-1D Modells aus den vorherigen Kapiteln. Es zeigt sich, dass eine geeignete Kalibrierung bestimmter Modellparameter eine gute Übereinstimmung zwischen Massenflüssen erzeugt, wobei diese Parameter für jeden Datensatz neu bestimmt werden müssen. Zur Berechnung der Drücke in den Blutgefäßen und dem Gewebe verwenden wir die Finite Vol-

umen Methode, da sie lokal massenerhaltend sind und relativ einfach zu implementieren ist. Die Freiheitsgrade für die Finite Volumen Methode zur Diskretisierung der 3D Probleme liegen dabei auf den Zellmittelpunkten der Kontrollvolumina, welche die Form von einfachen Würfeln haben. Da außerdem der Permeabilitätstensor für die verschiedenen 3D Kontinua diagonal ist, genügt es den Fluß über die Grenzen der Kontrollvolumina mit einer einfachen Zwei-Punkt Approximation zu berechnen. Im Falle des vaskularen Netzwerks, das durch eine graphenartige Struktur beschrieben wird, approximieren wir die Druckwerte an den Knoten des Netzwerks und wählen ein Kontrollvolumen symmetrisch um die Knoten. Bezüglich der Ränder des Kontrollvolumens bilanzieren wir wiederum die Flüße. An den Rändern, welche mit den Gefäßquerschnitten übereinstimmen, verwenden wir wiederum eine Zwei-Punkt Approximation. Hinsichtlich der Ränder, welche mit den Gefäßwänden übereinstimmen, werden zunächst die gemittelten 3D Drücke berechnet und danach mit Hilfe des 1D Drucks im Kontrollvolumen eine Zwei-Punkt Approximation des Flußes.

Im letzten Teil dieser Arbeit, beschäftigen wir uns mit der mathematischen Modellierung von Flüssigkeitsinjektionen in poröse Medien. Betrachten wir Messungen, die sich bei der Injektion von Wasser in trockene Sandsäulen ergeben, so stellt sich heraus, dass die Wassersättigungsprofile, welche man an verschiedenen Tiefen der Sandsäule aufzeichnet, nicht monoton sind. Außerdem erkennt man, dass sich in geringeren Tiefen zunächst kleinere Sättigungsüberschüsse bilden. Mit zunehmender Tiefe vergrößern sich diese Überschüsse und bilden eine plateauartige Form. Dies erscheint auf den ersten Blick überraschend, da nur am Eingang der Sandsäule Wasser injiziert wird und über die Wände der Sandsäule kein Wasser zugeführt wird. Unter diesen Bedingungen lässt sich das eben beschriebene Phänomen nicht mit Standardgleichungen der porösen Medientheorie erklären.

Aus diesem Grund erweitert man die herkömmlichen Modelle um eine weitere gewöhnliche Differentialgleichung, die die Entstehung eines Sättigungsüberschusses modelliert. Diese Differentialgleichung enthält einen Parameter τ , der zur Kontrolle des Sättigungsüberschuss dient. Daher bezeichnet man in der Fachsprache diese Zusatzgleichung auch als τ -Term. Außerdem benutzt man bezüglich des Kapillardrucks und der relativen Permeabilitäten Hysterese Modelle, um den Wechsel zwischen Bewässerung und Austrocknung zu simulieren, welcher entscheidend für die Bildung von Plateaus ist. Denn der Wechsel zwischen den beiden Kurven ruft eine unterschiedliche Ausbreitungsgeschwindigkeit der beiden Fronten an einem Sättigungsüberschuss hervor.

Das Hauptaugenmerk der beiden letzten Kapitel ist es nun zu bestimmen, welche Sättigungsprofile sich durch die vorgegebenen Modelle beschreiben lassen. Dazu gehen wir in Kapitel 8 der Frage nach, wie sich ein vorgegebenes Sättigungsplateau durch ein poröses Medium bewegt. Dabei ist es insbesondere von Interesse, ob das Plateau stabil bleibt, sich vergrößert oder verschwindet und sich auf einem anderen Niveau neu bildet. Zur Abschätzung der Geschwindigkeiten der Sättigungsfronten benutzen wir Rankine-Hugoniot Bedingungen. Damit lässt sich entscheiden, wie sich ein vorgegebenes Sättigungsplateau qualitativ verhält. Unsere analytischen Vorhersagen, spiegeln sich in numerischen Simulationen wieder. Die numerischen Simulationen beruhen auf einer Finiten Volumen Methode für die Ortsdiskretisierung und dem impliziten Eulerverfahren für die Zeitintegration, d.h. wir verwenden ein voll-implizites Verfahren. Die nichtlinearen Gleichungssysteme, welche sich daraus ergeben, werden durch ein gedämpftes Newtonverfahren gelöst. Damit das Newtonverfahren auch bei einem Wechsel zwischen den Bewässerungs- und den Trocknungskurven konvergent ist, berechnen wir im Falle eines Wechsels glatte Übergänge in Form von kubischen Splinekurven.

Im letzten Kapitel der vorliegenden Arbeit wird das Modell aus dem vorherigen Kapitel um die Differentialgleichung, welche für die Entstehung der Sättigungsüberschüsse verantwortlich ist, erweitert. Der Übergang zwischen den Trocknungs- und Bewässerungskurven wird durch Sprünge, d.h. gerade Linien, beschrieben. In der Fachliteratur wird diese Art der Übergangsmodellierung auch als play-type Hysterese bezeichnet.

Zur Analyse dieses Modells transformieren wir das Differentialgleichungssystem auf ein reines System gewöhnlicher Differentialgleichungen und benutzen Analysetechniken für gewöhnliche Differentialgleichungssysteme. Dadurch lassen sich interessante Einblicke in die Struktur der zugehörigen Lösungen gewinnen, beispielsweise welche Gleichgewichtspunkte das Differentialgleichungssystem besitzt und welche Eigenschaften diese Gleichgewichtspunkte besitzen. Berechnet man die Eigenwerte der Jakobimatrix, welche sich aus der rechten Seite des Differentialgleichungssystems herleiten lässt, so kann man anhand der Eigenwerte entscheiden, ob ein Gleichgewichtspunkt ein Attraktor oder ein Repeller ist. Bei genauerer Betrachtung stellt man fest, dass die Eigenwerte auch von τ abhängen. Dies bedeutet, dass der Charakter der Gleichgewichtspunkte stark von τ abhängt. Damit lassen sich auch Kriterien ableiten für welche Werte von τ ein bestimmter Gleichgewichtspunkt ein Attraktor oder ein Repeller ist. Lassen sich beispielsweise ein Gleichgewichtspunkt auf einer Bewässerungskurve mit einem Gleichgewichtspunkt (Attraktor) auf der Trocknungskurve durch einen Orbit verbinden, so bedeutet dies, dass sich ein Sättigungsüberschuss bildet. Landet man hingegen nur auf einem Attraktor der Bewässerungskurve, so ergibt sich kein Überschuss. Abhängig von einem gegebenen Parametersatz weiß man damit, wie τ zu wählen ist, so dass sich eine Lösung mit einem Sättigungsüberschuss ergibt. Mit der Kenntnis der Gleichgewichtspunkte und der Eigenschaften der Lösungskurven erhält man somit ein genaues Bild darüber, welche Sättigungsprofile sich für einen vorgegebenen Parametersatz ergeben.

Die theoretischen Ergebnisse werden sowohl durch numerische Simulationen als auch durch Messungen aus anderen Publikationen wieder. Im Gegensatz zum vorherigen Kapitel verwenden wir kein vollimplizites Verfahren sondern ein IMPES artiges Verfahren. In jedem Zeitschritt lösen wir ein nichtlineares elliptisches Randwertproblem für den Fluiddruck durch eine Finite Volumen Methode, wobei das zugehörige nichtlineare Gleichungssystem durch ein L -Schema gelöst wird.

Das L -Schema ist ein iteratives Lösungsverfahren, welches in jedem Iterationsschritt ein lineares Gleichungssystem löst, das dadurch entsteht, dass in die nichtlinearen Terme die Lösung aus der vorherigen Iteration eingesetzt wird, wohingegen die linearen Terme die Lösung aus dem aktuellen Iterationsschritt beinhalten. Der Name L -schema rührt von der Tatsache her, dass zu den ursprünglichen Gleichungen ein linearer Term mit einem Parameter $L > 0$ hinzugefügt wird. Durch eine geschickte Wahl dieses Parameters lässt sich eine schnelle Konvergenz dieses iterativen Verfahrens erzwingen. Der große Vorteil des L -Schemas gegenüber dem Newtonverfahren besteht darin, dass für das L -schema keine Jakobimatrix berechnet werden muss. Dadurch vermeidet man einerseits eine weitere Fehlerquelle, die sich durch eine numerische Approximation der Jakobimatrix ergibt oder andererseits den Aufwand, der sich im Rahmen einer analytischen Berechnung ergibt. Darüber hinaus ist zu erwarten, dass aufgrund der sprunghaften Übergänge zwischen Trocknungs- und Bewässerungskurve das Newtonverfahren nicht konvergiert oder nur dann konvergiert, falls der Zeitschritt sehr klein gewählt wird und als Startlösung die Lösung aus dem letzten Zeitschritt verwendet wird. Am Ende des Zeitschritts wird durch einen expliziten Eulerschritt eine neue Sättigung berechnet. Dazu verwenden wir den Druck und die Sättigung aus dem vorherigen Zeitschritt.

Bevor wir nun in den nachfolgenden Kapiteln die einzelnen Veröffentlichungen präsentieren, werden in einem einleitenden Kapitel die Modellreduktionstechniken, welche in den jeweiligen Veröffentlichungen verwendet werden, näher erläutert. Darüber hinaus wird aufgezeigt, wie die verschiedenen Teile und Kapitel inhaltlich zusammenhängen und welche innovativen Aspekte beleuchtet wurden.

Summary

Modelling and simulation of flow processes in technical, geological and biological systems poses great challenges for researchers from the fields of engineering sciences, mathematics, physics and computer science. One reason for this is that the mathematical equations are often non-linear. Furthermore, it is not sufficient to use a single mathematical model or a specific numerical method for interesting applications. In order to enable a realistic description of the respective problem, it is often necessary to couple different flow models with each other or to consider further physical processes besides the pure flow processes. Regarding the processing, visualisation and administration of the simulation data, one often faces the problem that large amounts of data accumulate, which can no longer be stored on ordinary computers or can cause long simulation times.

These observations motivate the use of model reduction techniques replacing complex mathematical models with simplified models. In this habilitation thesis, different model reduction techniques are presented that allow an efficient description of flow processes without accuracy loss with respect to physical quantities that are interesting for a certain field of application. Altogether, the model reduction techniques considered in this thesis can be divided into four categories: Dimension-reduced modelling, homogenisation methods, domain decomposition methods, and data based learning. In order to be able to demonstrate their possible applications in context of flow processes, we consider four different flow processes that play an important role in medicine, energy supply and environmental sciences. These are in detail: Blood flow in large arteries and microvascular systems, oil transport in pipelines and the injection of fluids into porous media. On closer examination, these flow processes can be associated with different length scales and flow properties. While flows in the large arteries and piping systems show higher Reynolds numbers and move through large scale cavities, small Reynolds numbers and small scale cavities are observed in microvascular networks and porous media. In the case of large arteries and tube systems, the vessels or tubes have diameters in the range of centimeters or meters. In contrast, vessels in a microvascular network have diameters in the range of micrometers. Pores and pore necks in a rock or tissue have similar or even smaller dimensions.

These differences motivate the treatment of the flow processes in different parts, which are oriented on the properties of the respective application. Altogether, we obtain the following three parts for the submitted habilitation thesis:

- *Part I: Simulation of flow processes in macroscale networks*
- *Part II: Simulation of blood flow in microvascular networks*
- *Part III: Simulation of fluid injection into porous media*

The first two parts are divided into three chapters, while the last part contains two further chapters. Each of the eight chapters is based on accepted publications. Except of Chapter 4, the submitted or published PDF documents of the individual publications have been incorporated into the habilitation thesis. The fact that the publication from Chapter 4 could not be integrated into the thesis is due to the copyright regulations of the associated

publishing house. Following the guidelines of the journal, the author is only allowed to use the illustrations and tables of this publication.

In the first chapter we present a model for the simulation of a peripheral arterial stenosis, i.e. a stenosis that is located far away from the center of the body, e.g. the heart. In particular, we consider a stenosis in one of the main arteries of the right lower leg. To simplify this problem, blood flow within the 55 main arteries of the human body are simulated with one-dimensional (1D) flow models. The boundary conditions and the influence of the stenosis are described by ordinary differential equations (ODEs). Since these models have only one time variable but no space variable, they are also called 0D models. This simplified 1D-0D coupled flow model is extended by models for two mechanisms to compensate the reduced blood flow. As compensation mechanisms we consider metabolic regulation by arterioles and arteriogenesis, i.e. the enlargement of small vessels between two main arteries. The aim of this chapter is to assess the efficiency of the two balancing mechanisms by means of a series of simulations.

In order to be able to make reliable statements regarding this problem, it is necessary to generate a sufficient amount of simulation data. Therefore it is necessary to vary the degree of stenosis many times, which leads to long simulation times. In order to shorten the simulation time, in a first step a mapping is constructed which assigns a certain degree of stenosis to a sampled blood pressure or flow rate curve in the vicinity of the stenosis. In the second chapter of the first part, we deal with describing this mapping as precisely and efficiently as possible using a surrogate model. The surrogate model has the form of a linear combination of Gaussian kernels. The coefficients of this linear combination and the parameters of the Gaussian kernels are determined by Greedy algorithms applied to simulation data.

In the last chapter of the first part, we use as in the first two chapters 1D-0D coupled flow models to simulate oil transport in pipeline systems. In contrast to the 1D blood flow models, the 1D models for the pipeline system are linear in their unknowns, since the interaction between the rigid tube wall and the flow can be neglected. These interactions cannot be neglected in the case of blood flow through large arteries with deformable vascular walls. The 0D models describe the influence of pumps and safety systems. By means of this modified 1D-0D flow model we calculate the velocity and pressure field in a section of an oil pipeline connecting oil fields in the north-east of the Caspian Sea with a port at the Black Sea. Numerical simulations are performed to provide insights into the mode of operation of the safety systems.

The second part of this thesis deals with dimensionally reduced modelling of blood flow in microvascular networks. Since even small tissue blocks with a volume of 1.0 mm^3 to 2.0 mm^3 contain thousands of vessels with diameters in the range of a few micrometers, it is necessary to reduce the complexity of this problem by modelling microvascular networks in a simplified way by one-dimensional graph-like structures. Blood flow within the network is described by the Poiseuille equation. In the surrounding porous tissue, flow is governed by the Darcy equation. For the coupling of the two flow processes we consider Starling's filtration law and use it to determine the shape of the source terms both for the Poiseuille equation and for the Darcy equation. In order to guarantee mass conservation, the source terms have a different sign. This results in a coupling of the two differential equations by their source terms, where the source term of the Darcy equation exhibits a Dirac measure concentrated on the 1D graph structure of the network. Such type of flow model is called 3D-1D coupled flow model.

To understand the mathematical structure of such models, we consider a mathematical

model problem in Chapter 5. For this purpose, we neglect the coupling and consider a pure Poisson problem with a line source term. With respect to this, the local convergence behaviour of the linear Galerkin finite element method is analysed, i.e. we estimate the discretisation error at a certain distance from the line. The motivation to study only the local convergence behaviour is due to the fact that the vicinity around the line sources is covered by the vascular network.

It reveals that the finite element method converges locally in an optimal way, although a quasi-uniform grid is used. On the other hand, there is a long preasymptotic range, which leads to the fact that the grid must be very fine such that this method converges optimally. The reason for this is a singularity along the line. These observations motivate the development of a new coupling concept that is not based on a line source term. Therefore, in Chapter 6, we turn to the development of a new coupling concept. The idea of the new coupling concept is to concentrate the source term of the Darcy equation not on the central axis of the individual vessels, but on their vessel walls, since the actual exchange with the surrounding tissue takes place there. Further analyses show that there are no more singularities along the vessel walls, but only kinks. This means that the solution of the 3D problem now has a higher regularity, which also improves the convergence behaviour of numerical solution methods. Another important aspect of this chapter is that the construction of this coupling concept offers possibilities to estimate the modelling error caused by model reductions as a function of the vessel radius. It is shown in this context that the modelling error decreases with decreasing radius. This is important for this application since the vessel radii of a microvascular network are usually small compared to the domain size.

Using the model reduction techniques analysed in the first two chapters of the second part of this thesis, vascular systems in smaller tissue blocks can be efficiently simulated. In order to simulate blood flow in larger parts of an organ, however, we need further model reduction techniques. One reason for this is that larger microvascular systems are very difficult to reconstruct from image data. Furthermore, the dimensions of the equation systems resulting from the numerical discretisation methods quickly exceed the performance of average computer systems. In order to avoid modelling every single capillary explicitly by a 1D model, we model only the arterioles and venules in a microvascular network by 1D flow models. The dense capillary network is homogenised and characterised with parameters for porous media such as a permeability tensor and porosity. The homogenisation results in a new 3D continuum which is coupled with another 3D continuum for the tissue (dual continuum approach). If one considers also the coupling of the porous 3D continuum for the capillary bed with the arterioles and venules, a coupled 3D-3D-1D model is obtained. To validate this new approach, we compare the simulation results with those produced by the 3D-1D model from the previous chapters. It shows that a suitable calibration of certain model parameters produces a good agreement between mass flows and averaged pressures, where these parameters must be determined once again for a new data set.

In the last part of this thesis, we consider the injection of fluids into porous media. In particular, we study the phenomenon that after the injection, non-monotonous saturation profiles with respect to the injected fluid occur, which after travelling a certain flow path form a plateau-like saturation profile. These observations are of particular interest from the perspective of mathematical modelling, since these saturation profiles cannot be explained by the usual flow models for porous media.

For this reason, these models are extended by a further ODE, which models the formation of a saturation overshoot. In addition to that, hysteresis models are used for the capillary

pressure and the relative permeabilities to simulate the change between imbibition and drainage, which is crucial for the formation of plateaus. The main focus of the last two chapters is to determine which saturation profiles can be described by the given models. In Chapter 8, we examine how a given saturation plateau moves through a porous medium. In particular, it is of interest whether the plateau remains stable, enlarges or disappears and is formed once again at a different level. To estimate the velocities of the saturation fronts, we use Rankine-Hugoniot conditions. This allows us to decide how a given saturation plateau behaves qualitatively. Our analytical predictions agree with numerical simulations.

In the last chapter of this thesis, the model from the previous chapter is extended by the differential equation modelling the formation of saturation overshoots. For the analysis of this model, we transform the differential equation system into a system of ordinary differential equations and use analysis techniques for ordinary differential equation systems. By this, interesting insights into the structure of the corresponding solutions can be obtained, e.g. what are the equilibrium points of the differential equation system and what are the properties of these equilibrium points. Having the knowledge on the equilibrium points and the properties of the solution curves at hand, one gets an exact picture on saturation profiles resulting from a given parameter set. The theoretical considerations are reflected in the numerical simulations.

Before we present the different publications in the following chapters, the model reduction techniques used in the respective publications are explained in more detail in an introductory chapter. Furthermore, it is shown how the different parts and chapters are connected in terms of content and which innovative aspects have been considered.

1 Introduction

The introductory chapter of the submitted thesis is divided into three parts: In the first part we describe four flow processes from different application areas which are examined in the further parts of this thesis. In particular, it is discussed why the application of model reduction methods is desirable or almost unavoidable in context of these flow processes. The middle part of the introductory chapter deals with the description of the considered simplification techniques. At the end of the introduction, a detailed overview on the structure of the thesis is given. In a first step, we motivate the rough classification of the publications that have been included into this thesis. Then the respective publications are described in more detail. Thereby, we are guided by the following questions: First: What are the novel modelling aspects? Second: Which numerical methods have been used to solve the underlying mathematical equations? Third: Which issues of practical relevance have been considered in the respective publication?

1.1 Why do we require model reduction techniques for simulating flow processes?

Flow processes are omnipresent in our everyday lives. Both in technical and biological systems, flows of different kind are essential components [49]. In this work, we investigate four different flow processes, which play an important role in different subfields of medicine, biomedical engineering, pipeline engineering and geology (see e.g. Table 1.1). In order to

(FP 1) *Flows through large arteries in a human cardiovascular system.*

(FP 2) *Flows within microvascular networks.*

(FP 3) *Fluid transport in pipelines.*

(FP 4) *Injection of fluids into a porous medium.*

Table 1.1: List of flow processes that are considered in this thesis.

quantify the flow properties within natural or technical systems, great efforts have been made since the early beginnings of engineering and natural sciences to design theoretical models allowing us to predict flow patterns. Thereby, it turns out that the arising models have the shape of partial differential equations (PDEs) like the Navier-Stokes equations [51], ordinary differential equations (ODEs), algebraic equations or a combination of them. Quite often, one can observe that flow models for complex applications exhibit strong nonlinearities [56, 80]. Furthermore, if several model equations are involved, they are usually coupled in a complex way [82]. Due to that, it is in general not possible to provide analytical solutions for the flow processes under consideration. This motivates the usage of computer based methods. However, despite of an enormous increase of computational power and the

development of advanced solution algorithms for PDEs, ODEs and algebraic equations, it is still a huge challenge to compute an accurate solution in an acceptable time.

In application fields requiring solution data in almost real-time, it is of great importance to provide accurate numerical solutions of flow equations by standard computers without making an excessive use of means from high performance computing.

FP 1: Flows through large arteries in a human cardiovascular system

A fast and reliable simulation of (FP 1) from the above list, would support physiologists to improve their diagnosis methods and tools in a non-invasive way, since it is not necessary to cut through the skin or blood vessels of patients or animals. Therefore both the risk of infections and treatment time could be decreased.

A widespread disease, which occurs typically in arteries is atherosclerosis, i.e., the accumulation of plaque clogging the lumen of arteries (see Figure 1.1). Due to this disease, blood flow through arteries can be decreased, drastically. It may even happen that a sufficient supply of organ tissue is endangered [24, 37, 64, 85, 92, 124, 153]. The most dangerous stenosis types are stenoses in the coronary arteries, in the branching between the outer and inner carotid arteries as well as the leg arteries. This motivates the development of therapy options for this disease and an exact analysis of this disease. Common treatment options to alleviate or completely eliminate the consequences of arteriogenesis include the removal of deposits, the insertion of stents, the placement of bypasses or the stimulation of the body's own compensatory mechanisms. Intact coronary arteries are essential for maintaining the pumping power of the heart as they supply the heart muscle with oxygen-rich blood. It is therefore of great interest to determine the narrowing degree, at which a coronary stenosis endangers an adequate supply of the heart muscle. If an exact reconstruction of the corresponding vessels is available, a flow simulation could be used to find out whether a stenosis restricts blood flow in a critical way. However, the use of computer-aided methods is not limited to this. It would also be possible to test the impact of bypasses and stents before surgery. If it is, e.g., possible to vary the number and form of bypasses in a computer model and to be able to observe the effect of these measures on blood flow after a short time, an operation could be planned more effectively. A stenosis in one of the carotid arteries is critical, since the carotid arteries are the main supply channels for brain tissue. Due to the fact that the brain requires about 20 percent of the total amount of oxygen in the blood [3, 4, 32], an unrestricted blood supply of the brain is of great importance. In order to maintain the cerebral blood circulation, there is a circular blood vessel system called Circle of Willis having the ability to replace the missing blood volume by means of supply channels, linking the main arteries and the Circle of Willis (CoW) (see Figure 1.2) [4]. However, the conductivity of the Circle of Willis is limited and therefore just a certain amount of the missing blood volume can be compensated. In addition to that, not every human exhibits a complete CoW (see Figure 1.3). Using numerical simulations, it can be determined whether the reduced blood flow caused by a carotid stenosis of a certain degree can be compensated [85]. By this a vascular surgeon can prioritise the treatments of patients suffering from this vascular illness. If a severe stenosis has to be removed, it can be necessary to occlude the affected carotid artery. For the planning of a surgery, it is of great interest, how an occlusion of a carotid artery influences the blood circulation and the blood supply of organs in particular the brain and the heart muscle. This can provide information, e.g., on how long a carotid artery

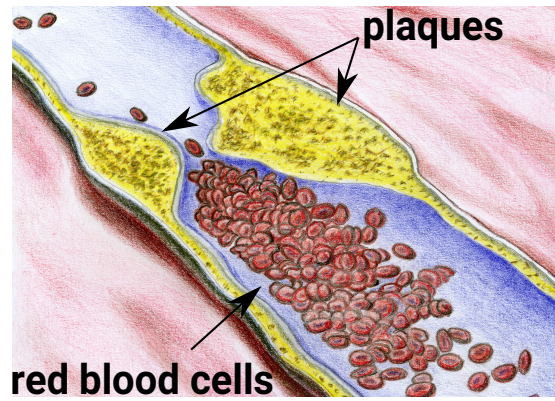


Figure 1.1: This figure shows a stenosis of higher degree in a blood vessel. Due to the plaques which have formed at the vessel walls, only little red blood cells can pass through the affected blood vessel. Therefore not enough oxygen is transported to the tissue cells.

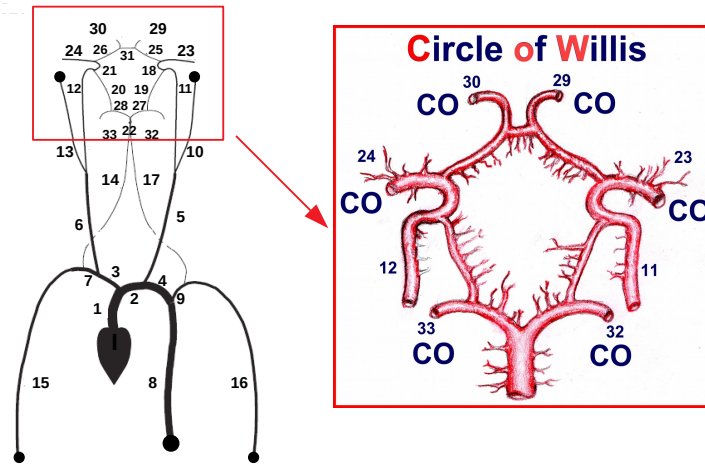
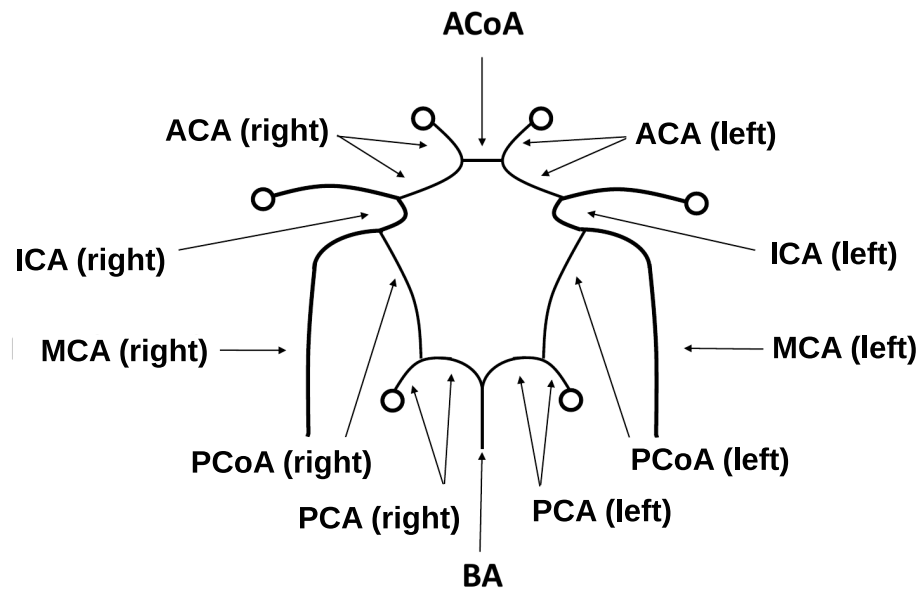


Figure 1.2: In the figure one can see the most important arteries, which are branching out of the heart into the arms, the head and the lower part of the body. Vessel 5 and 6 represent the left and right carotid arteries, while the indices 14 and 17 label the left and right vertebral arteries. The CoW inflows consist of the basilar artery (Vessel 22) and the left and right inner carotid arteries (Vessels 11 and 12). The CoW has six outlets, which supply the brain tissue with blood. The outlets are marked by the label CO (Cerebral Outflow).

can be occluded without causing health damage to the affected patient. By the help of a computer-aided model, such data could be collected without any danger for the patient or a test person. However, it is necessary to keep the simulation time as short as possible in order not to prolong the planning process unnecessarily. A reduction of the simulation time can be achieved, among other things, by using simplified computer models, which are derived by model reduction techniques. In case of a stenosis occurring in a lower leg artery, which can often be found in vessels of a smoker, one is faced with similar problems. On the one hand, one wants to determine to what extent natural balancing mechanisms



Complete Circle of Willis (CoW), Frequency: 49%

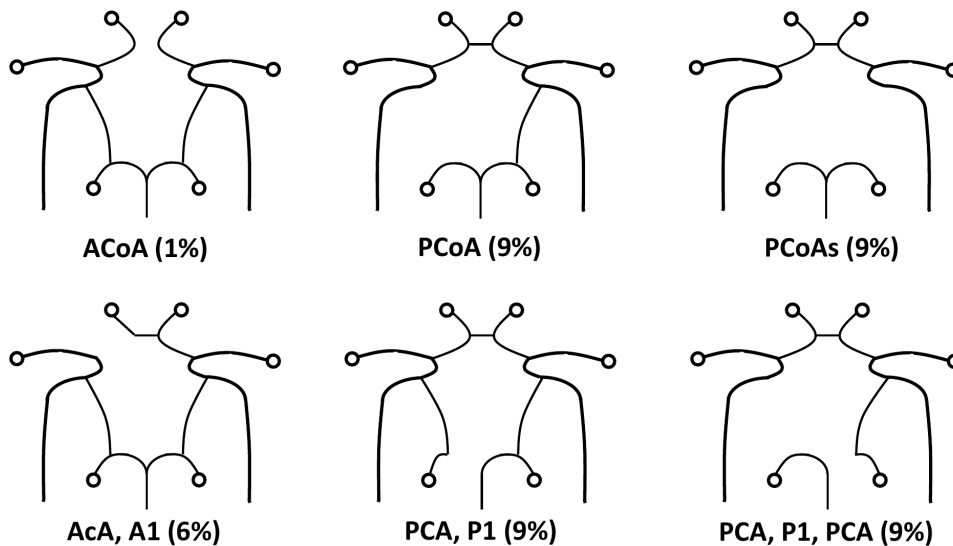


Figure 1.3: Complete Circle of Willis and its components: BA: Basilar artery, PCA: posterior cerebral artery, MCA: middle cerebral artery, ACA: Cerebral front artery, PCoA: Rear communicating artery, ACoA: Communicating front artery, ICA: Internal carotid artery (top). Malformations of the Circle of Willies and their frequency. The abbreviations below the individual illustrations indicate the missing vessels (bottom).

can restore the reduced blood flow caused by a lower leg stenosis. There are, e.g., small connecting arteries between the larger leg arteries [120], having the ability to enlarge their cross section areas to some extent, such that blood volume can be conducted around the stenosis. This is of great importance, since the oxygen supply of tissue far away

from the heart is very sensitive to a reduced blood flow. A stenosis located in an artery far away from the heart is also called peripheral stenosis. On the other hand, standard diagnosis tools and treatment methods for this illness are still improvable. As it has been described in the case of the coronary stenoses and the carotid stenoses model reduction techniques for computational models offer a possibility to enhance these standard methods.

FP 2: Flows within microvascular networks

Another flow process that belongs to a medical field of application is blood flow in microvascular networks (FP 2) (see Table 1.1). Contrary to (FP 1), we are in this case at a complete different level of the cardiovascular tree. While the larger arteries transport blood volume to the organs, the microvascular networks have the function to make the exchange of oxygen, nutrients, metabolites etc. between the vascular system and the tissue cells possible. Since these networks consist of vessels having lengths or diameters on the scale of micrometers, they are referred to as microvascular networks. Being able to simulate flow within both the microvascular networks and the surrounding tissue, opens the possibility to investigate many interesting issues from biology or medicine without the need to set up expensive and risky experiments.

One of the most important issues is the development of strategies to combat cancer, since according to the world health organization (WHO) cancer is the most important cause of death and morbidity in Europe after cardiovascular diseases.

Well known cancer therapies are chemotherapy, radiation and hyperthermia [94]. During chemotherapy, therapeutic agents are injected into the patient's blood and transported through the vascular tree to the tumor cells. The therapeutic agents have the function of killing the tumor cells directly or to prevent the vascularisation of tumor tissue, such that the tumor cells can not be supplied by oxygen and nutrients. This is crucial to prevent a severe cancer illness, since the vascularisation of a tumor enables its proliferation. In order to ensure the efficiency of the chemotherapy and to keep the side effects low, the dosage of the therapeutic agents has to be chosen carefully. Using numerical simulations, which yield a realistic concentration distribution in the cancerous tissue region, an appropriate dosage of the therapeutic agents, can be determined. Therefore, the simulation has to be performed several times. This motivates the application of well tailored model reduction techniques decreasing the simulation time while keeping a sufficient precision for the quantities of interest. The main challenges in this context are simulating blood flow through a dense microvascular network containing thousands of blood vessels. In Figure 1.4, one can see an example for a microvascular network that is taken from the cortex of a rat brain and is contained in a $1.0 \text{ mm} \times 1.0 \text{ mm} \times 2.0 \text{ mm}$ tissue block. A full three-dimensional (3D) model meshing such a complex structure introduces many degrees of freedom into the discrete model, such that the numerical treatment of the corresponding flow problem becomes expensive, i.e., the simulation time is relatively long. A further complexity that occurs in the addressed problem, is that flow in the vascular system has to be coupled with flow in the surrounding tissue. Besides cells and fibers, a block of tissue consists of an interstitial space filled with a mixture of water and different substances. From a computational point of view it is very expensive to resolve every pore by a fine 3D mesh to determine the flow field and concentrations of medications numerically. Due to that we require simplified models for the simulation of flow and transport in tissue.

When hyperthermia is applied, cancer tissue is subjected to high temperature for some time, such that the cancer cells are dying step by step. Contrary to chemotherapy,

it is possible to localise the heating causing minimal damage to the healthy tissue. This can be achieved by injection of small particles and heating them by means of radiation concentrated on the cancerous part. For an efficient removal of the cancer cells, it is necessary to produce a homogeneous temperature distribution within the affected tissue block [99]. In order to achieve this, a series of tests is required similar to chemotherapy, to determine an appropriate concentration of particles. Moreover it is necessary to choose types of particles emitting a sufficient amount of energy that is equally distributed in space. Model reduction techniques can help to decrease the computational costs such that a decision making for hyperthermia is possible in an acceptable time.

FP 3: Fluid transport in pipelines

In addition to the flow processes (FP 1) and (FP 2), which play an important role in biomechanics and physiology, we also consider in this thesis flow processes in technical and geological systems. Important technical systems for our daily life are e.g. pipeline systems for the transport of energy carriers such as oil or gas, but also of important supply goods such as water (see (FP 3), Table 1.1). In order to ensure the safe transport of liquid goods such as oil, gas or water, a robust pipe system and powerful pumps are needed, as well as advanced safety systems such as relief valves and security tanks. Unfortunately, the transport security could be endangered by different phenomena, like corrosion of the vessel walls. Another issue that is relevant for pipeline engineers is the formation of water hammers after the shutdown of a pump. Thereby, one observes that the decrease of the inner pipeline pressure due to the shutdown of a pump, introduces an upstream and a downstream travelling wave with respect to the location of the pump, which might exceed the pressure under standard conditions, significantly [151]. A similar behaviour occurs, when the oil loading of a tanker or a truck stops instantaneously [137]. If the vessel wall is weakened due to some exterior influence, it is likely that the overpressure causes a crack in the vessel wall such that fluid can flow out of the pipeline system. The fluid volume that is lost due to the leakage, combined with the need to stop the fluid transport through the affected pipeline system can cause an enormous economical harm. In case of oil leakage, oil may enter the sea or soil surrounding the pipeline, depending where the pipeline system is located. As a consequence the environment and drinking water may be polluted leading to severe health and environmental problems. A standard remedy, to prevent the rupture of vessel walls is to make the vessel walls thicker. However, for a pipeline system covering huge distances, a minimal enlargement of the vessel walls makes it necessary to invest additional money into the required material. A further difficulty arising in this context is that enlarging the vessel thickness adds additional weight to the pipeline system. As a result, more effort has to be put in the construction of holder systems fixing the position of the single tubes, since they have to carry more weight. Typically, such pipeline systems extend over hundreds of kilometers, transporting water or oil from their source locations to the consumer, factories or loading stations for ships and trucks [65]. Due to that a detailed simulation of flow through a larger pipeline system is computationally too demanding for standard computers. However, in order to be able to design efficient pumping and security systems, it is crucial to study their effect not only locally, but also globally. A complex 3D meshing resolving the details of the technical devices and pipelines, would cause a huge amount of data, which is difficult to handle on standard computers. Furthermore, it is quite often not necessary to resolve the whole pipeline system to compute a pressure average across the section area of the tube. Should it be necessary

to resolve the turbulences in the flow as part of a specific issue, only a small part of the pipeline could be resolved by a 3D model, while the rest of the pipeline is described in a simplified way. These aspects motivate the usage of simplified models for pipeline systems.

FP 4: Injection of fluids into a porous medium

A further flow process occurring both in the context of technical and geological systems is the injection of fluids into a porous medium. Classical examples for (FP 4) are flows through filter systems or the infiltration of ink into paper [39]. Over the past eight years, this flow process has gained great importance, especially within the framework of the German energy industry (Energiewende). In view of the nuclear accident at Fukushima in March 2011, greater efforts are being made to steadily increase the market share of wind and solar energy in the production of electrical energy with the aim of reducing the market share of fossil fuels and nuclear energy. The goals associated with the promotion of renewable energy sources are the reduction of CO₂ emissions and the containment of the dangers of nuclear energy production such as the storage of nuclear waste and reactor accidents. The renunciation of established energy production technologies, however, creates other difficulties that are mainly related to the volatility of wind and solar energy.

There are various possibilities to store energy. It can be stored in thermal, chemical or mechanical form using technical as well as geological systems (e.g. the subsurface). Concerning thermal energy, one can exploit the nature of chemical reactions. Thermochemical heat storage systems are charged based on endothermal reactions and discharged by means of exothermal reactions. Calcium oxide e.g. reacts exothermically in presence of water to calcium hydroxide. Due to its environmental compatibility, Calcium oxide is of great interest for this purpose [125]. Simulating the injection of a hot fluid into calcium oxide, we are faced with the issue to model an injection process of a fluid into a porous structure. Since calcium oxide exhibits a crystalline structure, it can be considered as a porous medium. Typically, thermochemical heat storage systems are used for small scale energy storage. Energy storage on a larger scale is usually provided by underground energy storage systems [15]. For these storage systems, mechanical storage is based on compressed air energy storage. Chemical storage in underground systems uses hydrogen and synthetic natural gas and thermal storage is realised by underground thermal energy storage. In order to improve the understanding of complex and coupled flow processes through porous soil and rock layers in the subsurface, efficient and consistent numerical models are needed. As in the case of tissue, resolving each pore in the respective porous medium, a 3D simulation can not be performed due to limited computational resources. Numerical models resolving each pore are often applied to simulate thin interfaces between e.g. a free flow zone and a porous medium [145], however, they are not considered for huge 3D domains. For these reasons, a reduction of model complexity and thus computational costs is required. This can be achieved, among other things, by describing the porous medium by averaged quantities [14, 73]. By this, it is possible to simulate flows through larger systems with porous structures. A further difficulty arising in context of this flow problem, is that despite of a constant injection rate and no external source, overshoots in the saturation profile of the injected fluid can be observed in experiments [57]. This phenomenon can not be explained by standard equations, which motivates the development of additional model equations. However, even in context of this modelling approach one is confronted with the difficulty of constructing a model which describes on the one hand the flow problem with sufficient accuracy and on the other hand in a simplified way. This is crucial in order to prevent

a loss of all the advantages provided by the other model reduction techniques for porous media flow.

1.2 Basic modelling approaches

In the publications that are presented in this thesis, different modelling approaches are discussed with the aim to reduce the overall computational complexity. In details, the considered model reduction techniques will involve:

- *Dimension reduced modelling:* This technique is used to derive models for blood flow within vascular and pipeline systems. Thereby, one-dimensional (1D) or zero-dimensional (0D) formulations of 3D flow equations are considered to decrease the complexity of the flow models.
- *Homogenisation methods:* These methods are considered for approximating complex fine scale structures such as capillary networks, tissue and other porous structures. The key idea is to avoid a detailed resolution of individual pores or capillaries. Instead, such fine scale structures are turned into a less complex continuum based model.
- *Domain decomposition techniques:* These techniques are based on the "divide and conquer" principle, i.e. a complex problem is decomposed into several sub-problems, which are modelled, separately. Afterwards the different sub-models are again combined to obtain a model for the whole issue. In the following parts of the submitted thesis, we will use this idea e.g. to simulate flows through microvascular networks and tissue. Thereby, the microvascular network is separated from the surrounding tissue and different flow models are assigned to the network and the surrounding tissue. A complete model is then obtained by deriving suitable coupling conditions between the two flow problems.
- *Data based learning:* This concept is used to design simple surrogate models for parameterised problems. The resulting surrogate model should be representative and its evaluation should be cheaper as the evaluation of a complex standard model in terms of computational costs. As a data source yielding the required training data, experiments as well as simulations results could be considered. In our application fields, we consider flow through a stenosis, where the parameter is given by the degree of the stenosis.

The rest of this section is dedicated to the issue, how these different modelling approaches are used to simplify the simulation of the flow processes listed in Table 1.1.

1.2.1 Model reduction techniques for macroscale networks

In a first step we draw our attention to blood flow problems. When deriving a reduced model for blood flow one has to recall the basic structure of a human cardiovascular system.

In the center of a human cardiovascular system is the heart connecting two subcirculations. One subcirculation is the systemic circulation supplying the organs with oxygenated blood and transporting deoxygenated blood back to the heart. The other subcirculation is called pulmonary circulation, in which deoxygenated blood is turned into oxygenated blood and transported back to the heart. Each subsystem, the systemic circulation as well as the pulmonary circulation can be further subdivided into larger arteries, smaller arteries and arterioles, capillary bed, venules and smaller veins and finally the larger veins.

Table 1.2: Vessel properties within the systemic circulation [56, Chapter 1]

Vessle type	Thickness (vessel wall) [mm]	Blood volume [%]	Re	Wo
Aorta	2.0	2.0	4000.0	10.5
Large arteries	1.0	5.0	2500.0	7.7
Small arteries	1.0	5.0	100.0	1.4
Arterioles	0.03	5.0	0.5	0.014
Capillaries	0.001	5.0	0.003	0.007
Venules	0.003	25.0	0.5	0.014
Large veins	0.5	50.0	1600.0	5.6

All the vessel types forming the subcirculations have their specific features and functions. The heart pumps blood in discrete pulses into the large arteries of both circulations. This results in a convection dominated, pulsatile and in some parts turbulent flow. In order to quantify the pulsation and turbulence in a certain blood vessel, the Womersley number Wo and the Reynolds number Re are used [56]. The Womersley number is a dimensionless number that contains the frequency ω of the pulse and the viscosity of a fluid:

$$Wo = D \sqrt{\frac{\omega \rho}{\eta}},$$

where ρ is the density of blood, D is the diameter of the vessel, and η is the viscosity of blood. The dimensionless Reynolds number Re , which quantifies the degree of turbulence of flow, is calculated for blood vessels with a diameter of D as follows:

$$Re = \frac{\rho DU}{\eta}.$$

U is the average velocity of the flow. According to Table 1.2, there are high Reynolds numbers in the large arteries, whereas low Reynolds numbers can be measured in the small arterioles and capillaries. The same behaviour can be observed for the Womersley numbers. This means that there is fast, turbulent and pulsatile flow in the large arteries, while flow in the small arterioles, venules and capillaries is almost stationary, laminar and not pulsatile.

Besides the different flow types, the blood vessel types exhibit further differences. The diameter and lengths of the larger arteries are in size of centimeters. Contrary to that the small arterioles have lengths and diameters of some micrometers [32], which means that the human cardiovascular system includes several orders of magnitude with respect to lengths and diameters. Concerning the vessel walls of large arteries, it can be shown that they are highly deformable and impermeable. The vessel walls of arterioles are also not permeable,

but they do not deform remarkably since they are wrapped with smooth muscles to control the blood flow. In case of the capillaries, the vessel walls are very thin and exhibit only a single cell layer. Furthermore they have gaps such that exchange processes between the vascular system and the organ tissues can take place. This shows that the interaction with the environment is different for each vessel type. It is obvious that an appropriate modelling of these interactions is crucial to obtain realistic simulation results.

Taking all the different features of the respective vascular level into account, we consider first a separation of three different scales, since each scale in the cardiovascular system requires a specific type of modelling. Thereby, three different scales are identified in the vascular system, these are: Macroscale networks, mesoscale networks and microscale or microvascular networks (see Figure 1.4). A macroscale network consists of larger venes or arteries covering space dimensions in the order of meters in width and length. A mesoscale network is composed of middle sized to small arteries (veins) or larger arterioles (venules) exhibiting a few bifurcations. The third scale, contains typically dense networks, whose vessel diameters are in the order of micrometers and which fill volumes of a few cubic millimeters. Since the flow processes (FP 1) and (FP 2) occur in macroscale and microscale networks, they are objectives of Part I (macroscale networks) and Part II (microvascular networks).

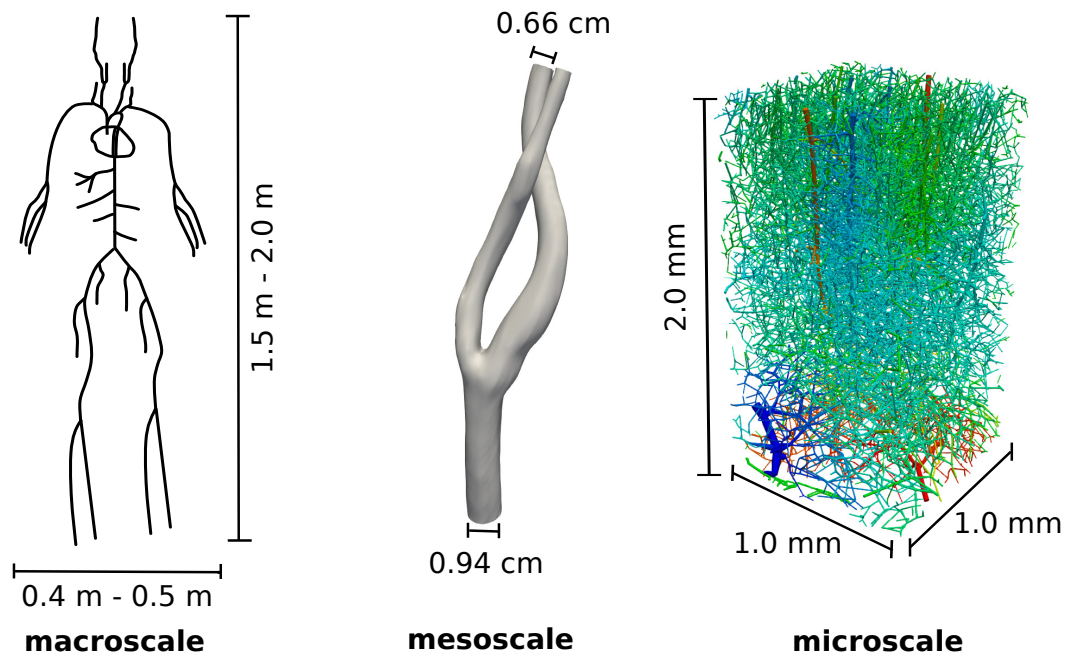


Figure 1.4: Representation of different vascular systems on the level of the **macroscale**, **mesoscale** and **microscale**. **Left:** Vascular system consisting of the 55 largest arteries branching out of the heart [134]. Vascular systems of this type connect the heart to the individual organs and therefore have a height of 1.5 m – 2.0 m and a width of about 0.5 m. **Middle:** Bifurcation in the right carotid artery. The main vessel has an average diameter of 0.94 cm, while the branches have an average diameter of 0.94 cm [134]. **Right:** Capillary network with penetrating arterioles (red) and outgoing venules (blue) in a tissue block of dimension: 1 mm × 1 mm × 2 mm [115].

Open loop 1D-0D coupled model for blood flow in the large arteries

Examples for macroscale vessel networks, which have been used to demonstrate the performance of blood flow models [134], can be seen in Figure 1.2 and 1.4. Both vessel networks, are part of the systemic arterial network branching out of the heart. Figure 1.4 (left) shows the basic arterial system of the systemic circulation consisting of the 55 main arteries, which allows us to simulate the rough distribution of blood volume into the different parts of the body. The other network shown in Figure 1.2 comprises 33 main arteries and includes the basic structure of the Circle of Willis. This network is of high interest for investigating issues arising in the context of a carotid stenosis and difficulties in blood supply of brain tissue. In order to derive a model for blood flow within a network of this kind, it is considered isolated from the rest of the cardiovascular system in a first step. Applying the principles of the *domain decomposition method*, the considered arterial network is then split into its single vessels (see Figure 1.5).

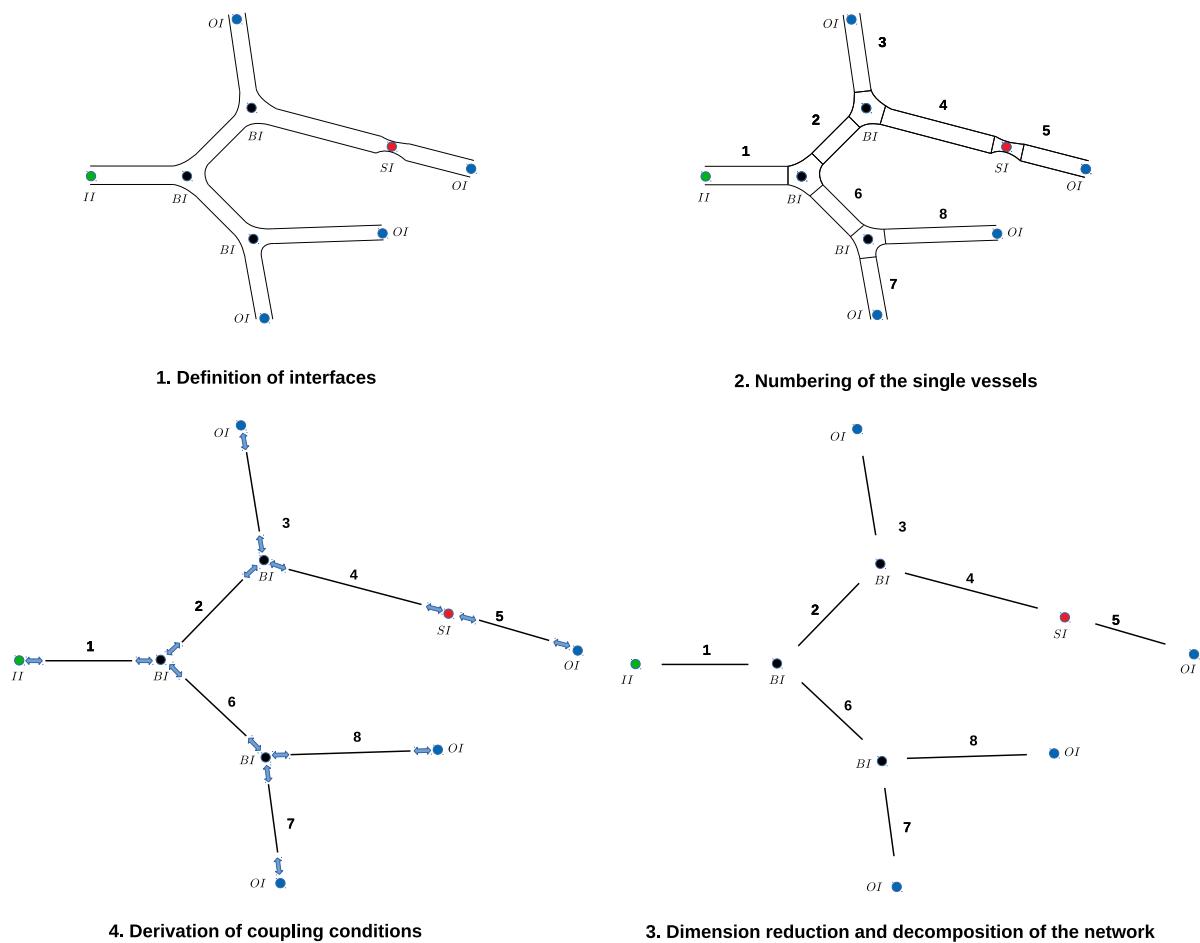


Figure 1.5: Domain decomposition method and dimension reduction applied to a small blood vessel network.

Modelling blood flow in a single vessel

For each of the vessels, we determine an appropriate flow model. Thereby, we use *dimension reduced models* to simulate flow through a single vessel, which are derived from the incompressible 3D Navier-Stokes equations [109]:

$$\rho \frac{\partial \mathbf{u}}{\partial t} + \rho (\mathbf{u} \cdot \nabla) \mathbf{u} + \nabla P - \eta \Delta \mathbf{u} = \mathbf{f}, \text{ in } \Omega(t), t > 0, \quad (1.1a)$$

$$\operatorname{div}(\mathbf{u}) = 0, \text{ in } \Omega(t), t > 0. \quad (1.1b)$$

$\Omega(t) \subset \mathbb{R}^3$ is a compliant vessel of length $l > 0$ and $R(z, t) > 0$ is a function describing the radius of the vessel. It results from a transformation of a curved vessel geometry in space to a cylindrical vessel, whose main axis is aligned with the z -axis of a Cartesian coordinate system (see Figure 1.6):

$$\Omega(t) = \{ (r, \theta, z) \in \mathbb{R}^3 \mid 0 \leq z \leq l, 0 \leq r \leq R(z, t), 0 \leq \theta < 2\pi \}.$$

In (1.1a) and (1.1b) the solution variables \mathbf{u} and P represent the 3D velocity and pressure field in the considered vessel. ρ and η denote the density and the viscosity of the fluid.

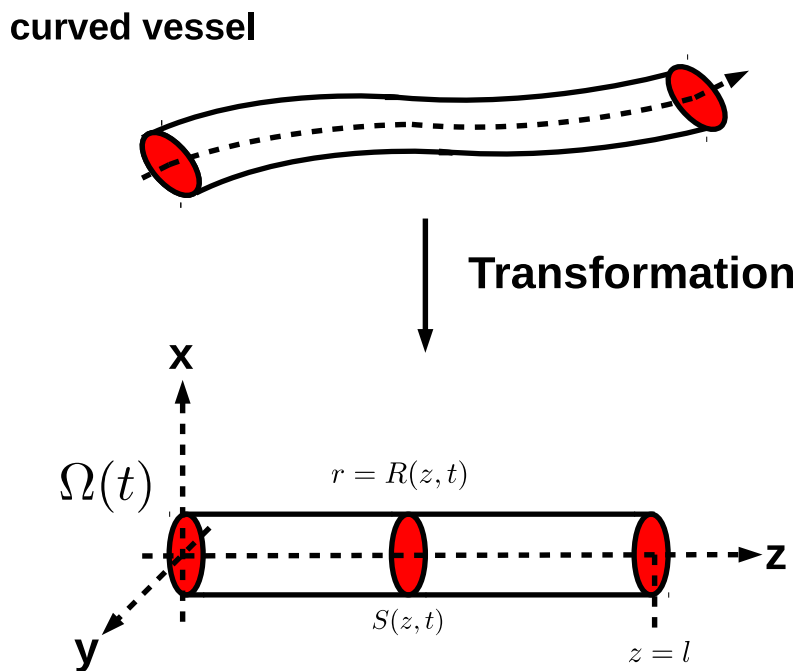


Figure 1.6: Transformation of a curved vessel to a simplified compliant vessel. The surface of the compliant vessel is described by a function $R(z, t)$ along the z -axis.

Since we assume that blood is incompressible and due to the fact that blood in larger vessels can be considered as Newtonian [108], ρ and η are taken to be constant. The source term \mathbf{f} incorporates external body forces like gravity. However, in the remainder of this

thesis, we neglect the influence of external forces for simplicity i.e., we set: $\mathbf{f} \equiv \mathbf{0}$. A further simplification of (1.1a) and (1.1b) is achieved by introducing new solution variables in 1D. Mathematically, they can be expressed as integrals with respect to a section area $S(z, t)$ that is located at the place z and time t :

$$A(z, t) = \int_{S(z,t)} dS, \quad Q(z, t) = \int_{S(z,t)} \mathbf{u} dS, \quad p(z, t) = \frac{1}{A} \int_{S(z,t)} P dS.$$

The new solution variables A , Q and p stand for the section area A , the flow rate Q and the 1D pressure p , respectively. For the velocity field \mathbf{u} we assume that it has the following shape:

$$\mathbf{u}(r, \theta, z, t) = \mathbf{u}_z(z, t) \cdot \frac{\gamma + 2}{\gamma} \left[1 - \left(\frac{r}{R(z, t)} \right)^\gamma \right], \quad (1.2)$$

where $\mathbf{u}_z(z, t)$ is the z -component of the velocity field \mathbf{u} . Integrating (1.1a) and (1.1b) on both sides over $S(z, t)$, we obtain [11, 22, 75]:

$$\frac{\partial A}{\partial t} + \frac{\partial Q}{\partial z} = 0, \quad z \in (0, l), \quad t > 0, \quad (1.3a)$$

$$\frac{\partial Q}{\partial t} + \frac{\partial}{\partial z} \left(\frac{Q^2}{A} \right) + \frac{A}{\rho} \frac{\partial p}{\partial z} = -K_r \frac{Q}{A}, \quad z \in (0, l), \quad t > 0. \quad (1.3b)$$

K_r is a resistance parameter containing the dynamic viscosity η of blood [129]:

$$K_r = 2(\gamma + 2) \frac{\pi \eta}{\rho}.$$

Choosing $\gamma = 2$, we obtain a resistance parameter corresponding to a parabolic Poiseuille flow profile. However, setting $\gamma = 9$, the profile in (1.2) is almost constant in the middle of the blood vessel and decays rapidly to zero in the vicinity of the boundary. According to [4] the latter choice of γ describes realistic flow profiles. Therefore, we use $\gamma = 9$ in the remainder of this thesis.

In order to close the PDE-system (1.3a) and (1.3b), an algebraic relationship is used, which can be derived similar to the Young-Laplace equation [101, 136]:

$$p(z, t) = G_0 \left(\sqrt{\frac{A}{A_0}} - 1 \right), \quad G_0 = \frac{\sqrt{\pi} \cdot h_0 \cdot E}{(1 - \nu^2) \cdot \sqrt{A_0}}, \quad (1.4)$$

where E is the Young modulus, A_0 stands for the section area at rest, h_0 is the vessel thickness and ν is the Poisson ratio. Due to the fact that biological tissue is practically incompressible, ν is chosen as: $\nu = 0.5$. Equation (1.4) can be considered as a simple FSI-model relating the section area of the blood vessel to the blood pressure p . Thereby, it is assumed that the vessel wall is instantaneously in equilibrium with the forces acting on it. Effects like wall inertia and viscoelasticity could be incorporated by means of a differential pressure law [33, 98, 138] involving the time derivative of the section area A . However, this would increase the complexity of the mathematical structure. Furthermore, in [53] the influence of a viscoelastic term in the 1D FSI-model has been investigated. The authors came to the conclusion that the influence of viscoelasticity is neglectable and that a FSI-model like (1.4) is sufficient to simulate realistic pressure and velocity curves in larger arteries. Finally, neglecting the viscoelasticity, maintains the strict hyperbolicity

of the above PDE system [1] so that efficient solvers for hyperbolic PDE-systems can be applied. Due to its hyperbolicity, the system (1.3a)-(1.3b), can be locally transformed into characteristic variables W_1 and W_2 , with new source terms S_{W_1} and S_{W_2} (see [22, 28, 84, 83]):

$$\frac{\partial W_1}{\partial t} + \lambda_1 \frac{\partial W_1}{\partial z} = S_{W_1}, \quad (1.5a)$$

$$\frac{\partial W_2}{\partial t} + \lambda_2 \frac{\partial W_2}{\partial z} = S_{W_2}. \quad (1.5b)$$

λ_1 and λ_2 are the eigenvalues of the Jacobi matrix corresponding the flux function \mathbf{F} of the hyperbolic system:

$$\mathbf{F}(A, Q) = \begin{pmatrix} Q \\ \frac{Q^2}{A} + \frac{A^{\frac{3}{2}}}{\rho\sqrt{A_0}} \end{pmatrix}.$$

Since we can assume for the considered application that $\lambda_1 = v - c < 0$ and $\lambda_2 = v + c > 0$ holds [55], the characteristic variables W_1 and W_2 can be considered as waves moving into opposite direction, where W_1 is moving into negative space direction and W_2 is moving into positive space direction. The variables v and c denote the flow velocity and the characteristic wave speed of a certain vessel. They are defined by:

$$v(A, Q) = \frac{Q}{A} \quad \text{and} \quad c(A) = 4\sqrt{\frac{G_0}{2\rho}} \left(\frac{A}{A_0}\right)^{\frac{1}{4}}.$$

After some calculations, it can be shown that the primary variables A and Q and the characteristic variables W_1 and W_2 are related to each other by the following algebraic equations:

$$W_1 = -\frac{Q}{A} + 4\sqrt{\frac{G_0}{2\rho}} \left(\left(\frac{A}{A_0}\right)^{\frac{1}{4}} - 1 \right) = -v + 4 \cdot (c(A) - c(A_0)), \quad (1.6a)$$

$$W_2 = \frac{Q}{A} + 4\sqrt{\frac{G_0}{2\rho}} \left(\left(\frac{A}{A_0}\right)^{\frac{1}{4}} - 1 \right) = v + 4 \cdot (c(A) - c(A_0)). \quad (1.6b)$$

Extrapolating the outgoing characteristic variables at the boundaries of the considered vessel and using (1.6a) and (1.6b) allows us to prescribe boundary data in a mathematical consistent way. The handling of boundary conditions will be discussed in detail at the end of this subsection. Before turning to that issue, we show how the PDE-system (1.3a) and (1.3b) can be further simplified.

If one is not interested in resolving the pulse waves in space, it is meaningful to reduce (1.3a) and (1.3b) to a system of ordinary differential equations (ODEs). Due to the fact that the spatial dependency is dropped, this type of model is referred to as *0D-model*. As a first step towards a 0D-model, we introduce spatially averaged units:

$$\hat{Q} = \frac{\rho}{l} \int_0^l Q(z) dz, \quad \hat{p} = \frac{1}{l} \int_0^l p(z) dz \quad \text{and} \quad \hat{A} = \frac{1}{l} \int_0^l A(z) dz \quad (1.7)$$

Integrating the 1D continuity equation (1.3a) over the interval $[0, l]$, it follows by means of (1.7):

$$l \frac{d\hat{A}}{dt} + Q_{out} - Q_{in} = 0, \quad \text{where } Q_{out} = Q(l, t) \quad \text{and} \quad Q_{in} = Q(0, t).$$

Concerning the 1D momentum equation (1.3b), we further assume [56, Chapter 10.2]:

- The contribution of the convective term $\frac{\partial}{\partial z} (Q^2/A)$ is neglected.
- The variation of A with respect to z is small compared to that of p and Q .

Considering Table 1.2, the first assumption is suitable for simulating blood flow in smaller vessels, in which the Reynolds numbers and flow velocities are slow compared to the larger vessels. The second assumption can be justified, if the average is carried out over small vessels. Following this assumption, we set $A \approx A_0$ in the 1D momentum equation (1.3b). After integrating this equation, we obtain:

$$\frac{\rho l}{A_0} \frac{d\hat{Q}}{dt} + p_{out} - p_{in} = -\frac{\rho K_r l}{A_0^2} \hat{Q}, \text{ where } p_{out} = p(l, t) \text{ and } p_{in} = p(0, t).$$

Exploiting the second assumption, it can be shown that:

$$l \frac{d\hat{p}}{dt} = \frac{l G_0}{2A_0} \frac{d\hat{A}}{dt}.$$

Finally, we have:

$$C \frac{dp_{in}}{dt} + Q_{out} - Q_{in} = 0, \tag{1.8a}$$

$$L \frac{dQ_{out}}{dt} + p_{out} - p_{in} = -RQ_{out}, \tag{1.8b}$$

where the following approximations have been used:

$$\hat{p} \approx p_{in} \text{ and } \hat{Q} \approx Q_{out}.$$

In [50], it has been shown that choosing the solution variables in this way and providing p_{out} and Q_{in} by means of boundary data, the ODE system (1.8a) and (1.8b) is well posed. ODEs of this type are also used to model electrical circuits. In the electric network analogy, Q corresponds to the current and p to voltage. The physical significance of the parameters R , C and L can be described as follows (see also Figure 1.7):

- *Compliance:* This parameter is given by $C = \frac{2lA_0}{G_0}$ in (1.8a). It quantifies the capacity for blood volume in a certain vessel and can therefore be compared to a capacitor in an electric circuit.
- *Inductance:* The parameter $L = \frac{\rho l}{A_0}$ is a weighting factor for the inertia term in (1.8a). It is comparable to the inductivity of a coil, since an increased density of the fluid increases the inertia of the flow system. Due to that the effective flow resistance is also increased.
- *Resistance:* The parameter $R = \frac{\rho K_r l}{A_0^2}$ in (1.8b) represents the flow resistance caused by the blood viscosity. In an electric network this parameter would correspond to an ohmic resistance. Transferring Ohm's law into the hydraulic world, it reads as follows: $R = \frac{\Delta p}{Q}$, where Δp denotes the pressure drop across the resistance.

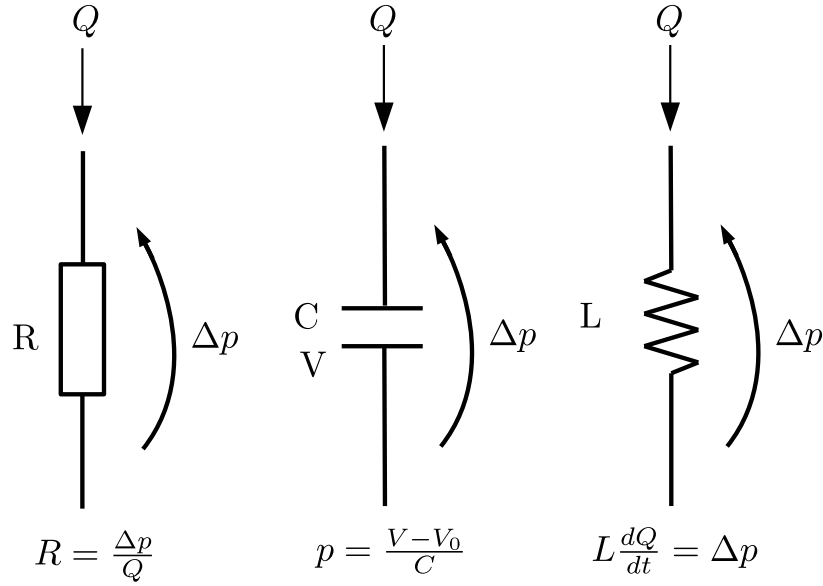


Figure 1.7: Analogy between electrical and hydraulic units.

An alternative computation of the pressure is given by an algebraic relationship between the blood volume V contained in the blood vessel and the averaged inner pressure p_{in} :

$$V - V_0 = C \cdot p_{in}, \quad (1.9)$$

which can be derived just as the Young-Laplace equation. The parameter V_0 is called dead volume and corresponds to the reference pressure $p_{in} = 0$. By this (1.8a) and (1.8b) can be represented as follows:

$$\frac{dV}{dt} + Q_{out} - Q_{in} = 0, \quad (1.10a)$$

$$L \frac{dQ_{out}}{dt} + p_{out} - p_{in} = -RQ_{out}. \quad (1.10b)$$

Modelling of boundary conditions

After describing dimension reduced flow models for single blood vessels, the last step in the domain decomposition approach is to connect the flow models for the single arteries. Besides the interior interfaces, there are also interfaces at the outer boundaries of the network, connecting the considered network with the rest of the cardiovascular system (see Figure 1.8). With respect to the inner interfaces, we consider bifurcations or junctions (*BI*) as well as stenotic areas (*SI*) separating an affected blood vessel into two parts. At the bifurcations, six unknowns regarding the pressure and flow rate variables have to be determined for each timepoint. Three flow conditions at a bifurcation or junction are given by mass conservation and total pressure continuity. Next, we label the vessels at a bifurcation by *I*, *II* and *III*. Thereby, *I* represents the mother vessel, while *II* and *III* stand for the branches. By this the flow conditions read as follows:

$$Q_I = Q_{II} + Q_{III},$$

$$p_{t,I} = p_{t,II} = p_{t,III}, \quad p_{t,i} = \frac{\rho}{2} \left(\frac{Q_i}{A_i} \right)^2 + p(A_i),$$

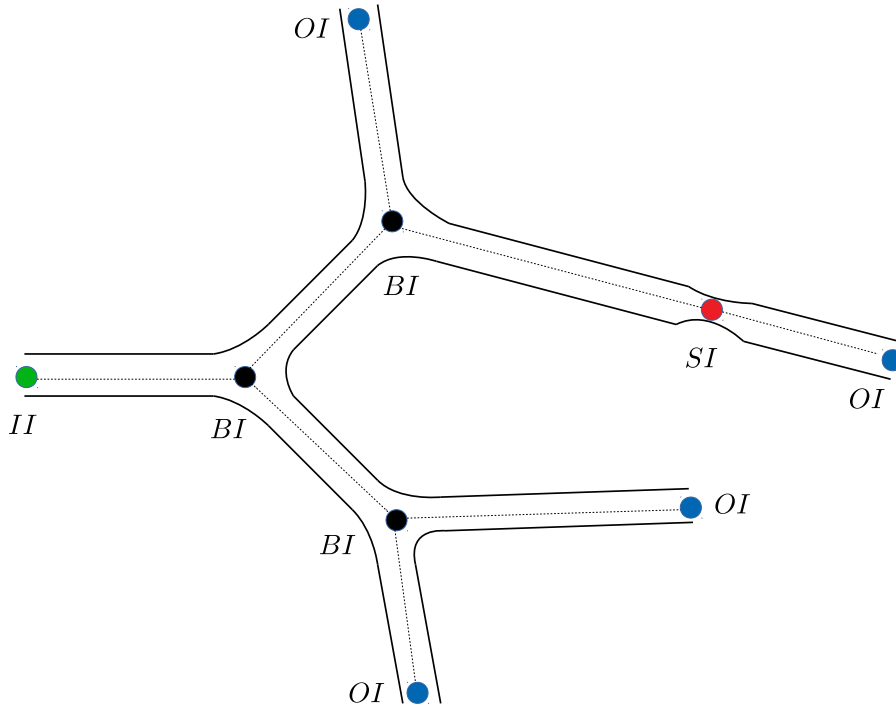


Figure 1.8: This figure shows a portion of an arterial network with several bifurcations and a stenosis as inner interfaces. At the boundaries there are inflow and outflow boundaries, linking the network to the rest of the cardiovascular system.

where $p(A_i)$ is given by (1.4). The remaining equations are obtained by extrapolating the outgoing characteristic waves and using (1.6a) and (1.6b). This is possible, since we know that each of the 1D problems governing the blood flow in each vessel is strictly hyperbolic. Therefore, at each boundary there is exactly one characteristic wave entering and leaving the domain. For further information, we refer to: [1, 55].

In order to simulate the influence of a stenosis, we first separate the affected artery in three parts i.e. we apply again the decomposition method. Here, we consider separately the stenotic area as well as the left and the right part of the artery with respect to the stenosis. Next, the stenotic part is lumped to a node. This simplification is justified by the fact that the length l_s of the stenotic part is usually not very large. Using the following ODE [124, 134, 153], we compute for each time point the flow rate Q_s through the stenosis:

$$\frac{K_u \cdot \rho \cdot l_s}{A_{0,s}} \frac{dQ_s}{dt} = \Delta p_s - \frac{K_v \cdot \eta \cdot l_s}{A_{0,s} \cdot D_s} Q_s - \frac{K_t \cdot \rho}{2A_{0,s}^2} \left(\frac{A_{0,s}}{A_s} - 1 \right)^2 Q_s |Q_s|. \quad (1.12)$$

$A_{0,s}$ and $A_s = (1 - R_s) \cdot A_{0,s}$ refer to the section areas of the healthy and stenotic segments, while D_0 and D_s denote the corresponding diameters [92]. The degree of stenosis is represented by a parameter

$$R_s \in (0, 1), \quad (1.13)$$

where $R_s = 0$ corresponds to the healthy state and $R_s = 1$ stands for the case of a completely occluded blood vessel. For convenience, it is assumed that both vessel parts have the same section area $A_{0,i}$ as well as the same elasticity parameters. Δp_s is the pressure drop across the stenosis. The second term on the right hand side of (1.12) quantifies the

viscous effects within the stenosis. Furthermore, compared to the 0D-model (1.8a), there is a third term on the right hand side accounting for the energy loss due to the formation of vortices. The remaining parameters are empirical coefficients, which are given by [92]:

$$K_v = 32.0 \cdot (0.83 \cdot l_s + 1.64 \cdot D_s) \cdot \left(\frac{A_{0,s}}{A_s} \right)^2 \frac{1}{D_s}, \quad K_t = 1.52 \quad \text{and} \quad K_u = 1.2.$$

For each time point the flow rate Q_s is prescribed at the boundaries of the adjacent vessel parts. Just as in the case of the bifurcation, we have at each vessel boundary an outgoing characteristic variable, which can be extrapolated based on the solution data at the boundary or at some point from the interior of each vessel. All in all, we obtain a dimension reduced *1D-0D coupled model* to simulate the influence of a stenosis in a simplified way.

With respect to the outer interfaces, we distinguish between inflow (*II*) and outflow interfaces (*OI*). Typically, we consider for the macroscale networks in this thesis only a single inflow boundary that is adjacent to the outlet of the left heart chamber or the inlet of the aorta. In order to emulate the influence of the heart, one can prescribe an appropriate pressure profile or flow rate profile [4]. Another possibility is to consider dimensional reduced models for the heart [54, 92] providing a pressure or flow rate boundary condition. Combined with an extrapolation of the outgoing variable at the inlet of the aorta, boundary data for both solution variables can be determined. At the outflow boundaries, we consider simplified models accounting for the resistance and storage capacities of the blood vessels that are not part of the 1D arterial network. In this context, there are two approaches how to model the omitted parts of the cardiovascular system. The first one is called *open loop model*, while the other one is referred to as *closed loop model*.

Using the open loop model, we do not simulate blood flow through the whole cardiovascular system as the term suggests, but we focus ourselves on the 1D arterial system. In Figure 1.10, a blood vessel network consisting of the 55 main arteries can be seen. To be able to simulate realistic pressure and flow rate curves within the considered network, appropriate model equations are required at the outlets of the terminal vessels as well as at the only inlet, which is identical to the inlet of the aorta. For this purpose, it is required to prescribe at the inlet of the aorta a boundary condition that emulates the heart beats. Quite often a half sine wave is considered for the flow rate variable Q , where the corresponding wave length is adapted to the heart's ejection phase. Besides, the amplitude of the sine wave has to be determined in such a way that about 5.0 to 6.0 liter of blood volume are flowing per minute through the inlet of the aorta [4, 5]. Another way would be to construct a simplified model for the left heart chamber, simulating the inner pressure and the volume flux through the aortic valve. Thereby, the filling process of the left chamber has to be modelled in a simplified way, since the pulmonary circulation is omitted. Together with the extrapolated outgoing characteristic variable W_1 and (1.6a) the missing solution variable can be determined. Concerning the terminal vessels, we assume that their main axes are parameterised such that W_2 is the outgoing characteristic variable, which can be extrapolated at the outflow boundaries of the terminal vessels. The influence of the omitted systemic vascular system is accounted for by means of a three-element R_1CR_2 -Windkessel model. Thereby, we use as before an analogy from electrical science. Here, the parameter C stands for the storage capacity of the arterial vessels and capillaries that are connected to a certain 1D terminal vessel. For these vessels we compute an averaged pressure p_c and a blood volume V_c . The blood volume V_c is determined by two flow rates Q_{in} and Q_{out} . Q_{in} represents the flux from the terminal vessel into the omitted arterial vessels and capillaries,

while Q_{out} quantifies the flux from these vessels into the venous system. This yields the following ODE:

$$\frac{dV_c}{dt} = Q_{in} - Q_{out}.$$

Using an equation analogous to (1.9):

$$V_c - V_{0,c} = C \cdot p_c,$$

we can rewrite the above equation as follows:

$$C \frac{dp_c}{dt} = Q_{in} - Q_{out}.$$

By means of the ohmic law in hydraulic units, the fluxes Q_{in} and Q_{out} can be represented by (see Figure 1.7 and 1.9):

$$Q_{in} = \frac{p(A) - p_c}{R_1} \text{ and } Q_{out} = \frac{p_c - p_v}{R_2}.$$

p_v denotes an average venous pressure and $p(A)$ is the pressure at the outlet of the considered terminal vessel. Combining the last two equations, we obtain:

$$C \frac{d}{dt} (p - R_1 Q_{in}) = Q_{in} - \frac{p_c - p_v}{R_2}$$

and after some calculations, it follows:

$$p - p_v + CR_2 \frac{dp}{dt} = (R_1 + R_2) Q_{in} + CR_1 R_2 \frac{dQ_{in}}{dt}. \quad (1.14)$$

Integrating (1.14) and using the outgoing characteristic W_2 , we can prescribe boundary conditions accounting for the influence of the omitted systemic vessels. Concerning a possible choice of the parameters $R = R_1 + R_2$ and C , we refer to [134]. A possible relationship between R_1 and R_2 is reported in [25]. The reason, why this type of model is called *Windkessel*-model, can be explained by means of the term *Windkessel*-effect. The *Windkessel*-effect is a mechanism damping the large difference between the systolic and diastolic pressure and ensuring a continuous blood supply of the organs. A crucial factor for this is the elasticity of the arterial walls (especially the aorta). Thanks to this vessel property, a significant volume of blood can be stored in the respective vessels. In order to transport blood volume to the organs, the muscles in the arterial vessel walls contract and push blood volume towards the tissue cells. The muscles are supported by the elastic vessel walls, exerting counter-pressure on the stored blood volume. This leads to a continuous blood supply of the organ tissue.

The name of this mechanism stems from the first fire engines, in which a large air chamber (*Windkessel*) had been installed. In the cardiovascular system, the heart corresponds to the pump, while the air chamber corresponds to the arteries with elastic vessel walls. The air chamber located between the pump and the syringe offers the possibility to store water during the pumping process. As the air chamber fills with water, the air in the air chamber is compressed, causing a counter-pressure on the inflowing water. This results in a continuous and weakly pulsating water flow through the syringe of the pump. Due to their deformable vessel walls, the arteries of the systemic circulatory system are comparable to

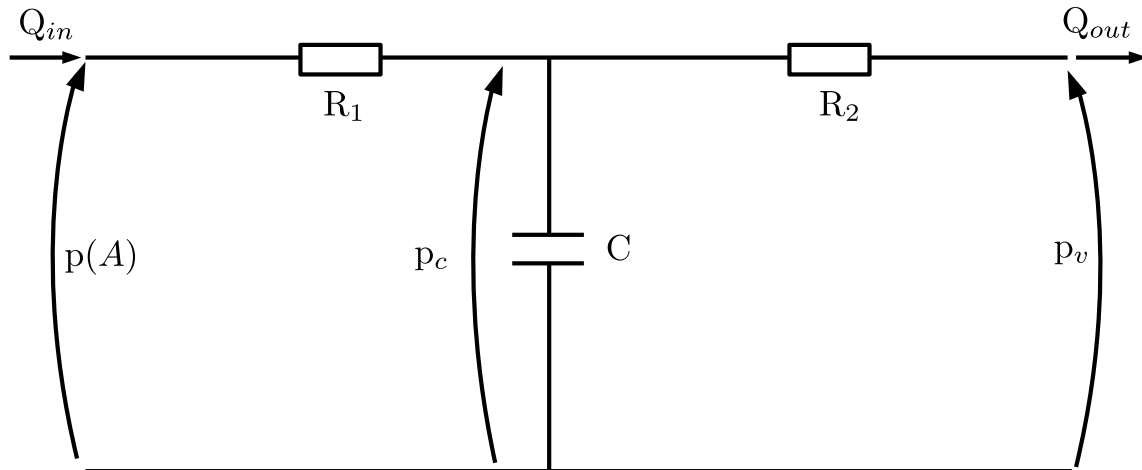


Figure 1.9: Electric module representing the three-element Windkessel-model attached to a 1D terminal artery. The resistance R_1 represents the hydraulic resistance of the arteries and capillaries and C their capacity. R_2 quantifies the hydraulic resistance of the corresponding veins. $p(A)$ is the pressure at the outlet of the 1D artery, while p_c and p_v denote the pressures in the omitted arterial vessels and veins, respectively.

an air chamber, as they can store fluid volume like the air vessel. The contraction of muscles and tension in the elastic arterial walls correspond to the counter-pressure compressed air exerts on the water in the air chamber (Windkessel).

In case of the closed loop model, the whole cardiovascular system is modelled, where flow in the macroscale network consisting of larger arteries is modelled by the 1D flow model, while the rest of the cardiovascular system is modelled by means of 0D-models having the same shape as the 0D-model given by (1.10a) and (1.10b). In Figure 1.11, the rest of the cardiovascular system is decomposed into different compartments. Here, we consider compartments for the vascular systems in the upper and lower body, the four heart cavities, the pulmonary circulation as well as the two largest veins of the systemic circulation. Certainly, this decomposition is just one of many possible decompositions. In particular, the compartment for the upper and lower compartment can be further subdivided, e.g. one could design a compartment for the main organs in the systemic circulation [91]. For each of these compartments one can estimate values for the hydraulic resistance R , the inductance L and the capacity C [92, 103]. By means of (1.10a) and (1.10b), we compute for each compartment an averaged blood pressure and at its outlets an averaged flow rate. Please note that the equations for the heart cavities have to be adapted since its outlets are equipped with valves (see Chapter 3). The compartments for the upper and lower body are connected to the outlets of the 1D arterial network (thick-framed numbers) by three element R_1CR_2 -Windkessel models.

Similarly to the closed loop model, the resistance values incorporate the flow resistances of the arterial vessels, which are subsequent to a terminal 1D artery. The difference between the two modelling approaches is that the mentioned parameters characterise the omitted

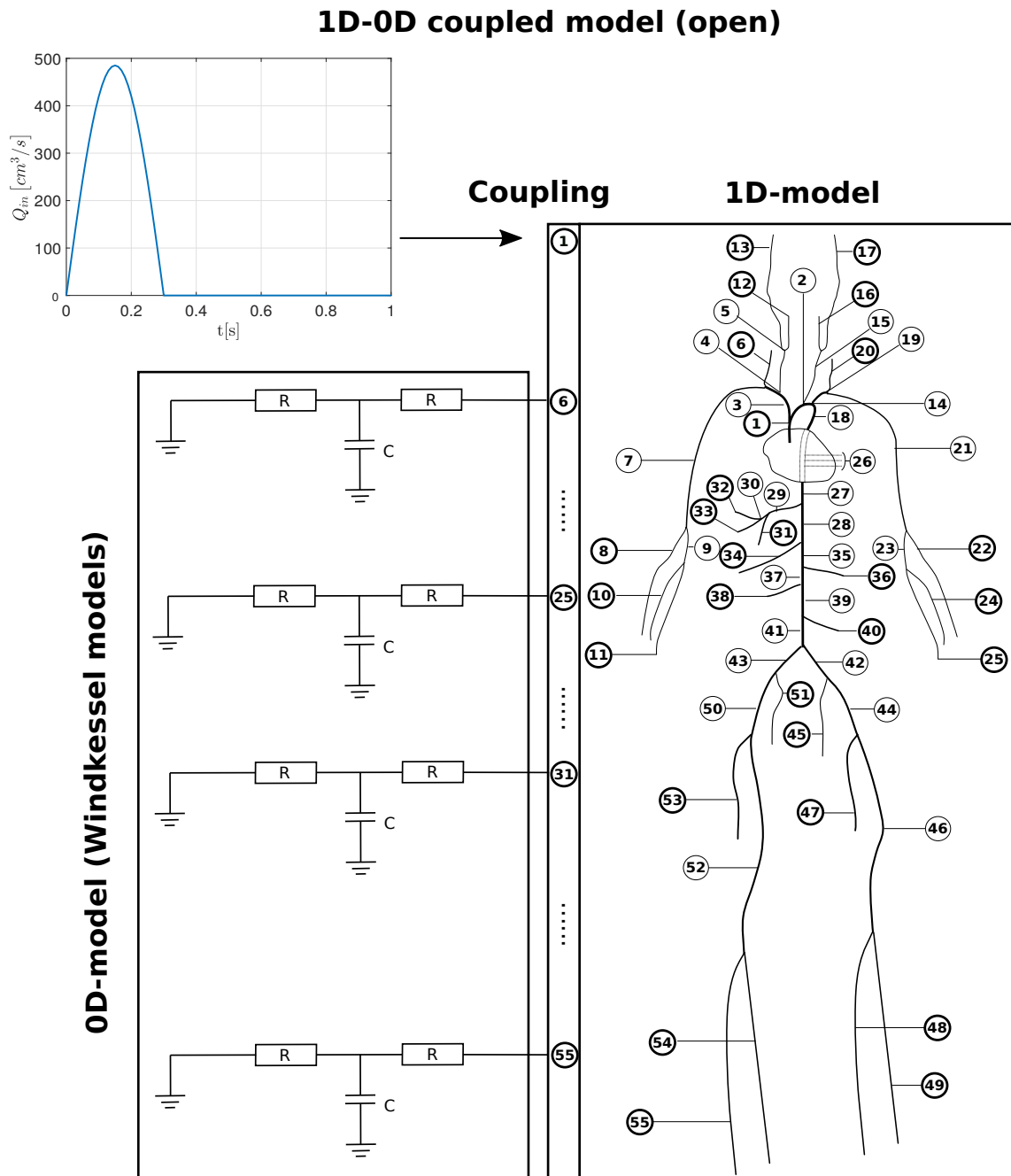


Figure 1.10: Example of an **open** 1D-0D coupled model. The larger arteries of the systemic circulation are described by means of 1D-models, while the rest of the cardiovascular system is described by means of 0D-models. To take the Windkessel effect into account, the 1D-arteries with thick-framed numbers are coupled with three-element RCR-models. Contrary to the closed model, the 0D-models attached to the outflow boundaries are not linked to the rest of the cardiovascular system. Therefore, blood volume has to be refilled at the inlet of the aorta. Overall, this modelling approach results in an **open** blood circulation.

vessels contained neither in the upper nor in the lower body compartment. Summarising, this approach results again in a 1D-0D coupled model for flow in the considered network. A

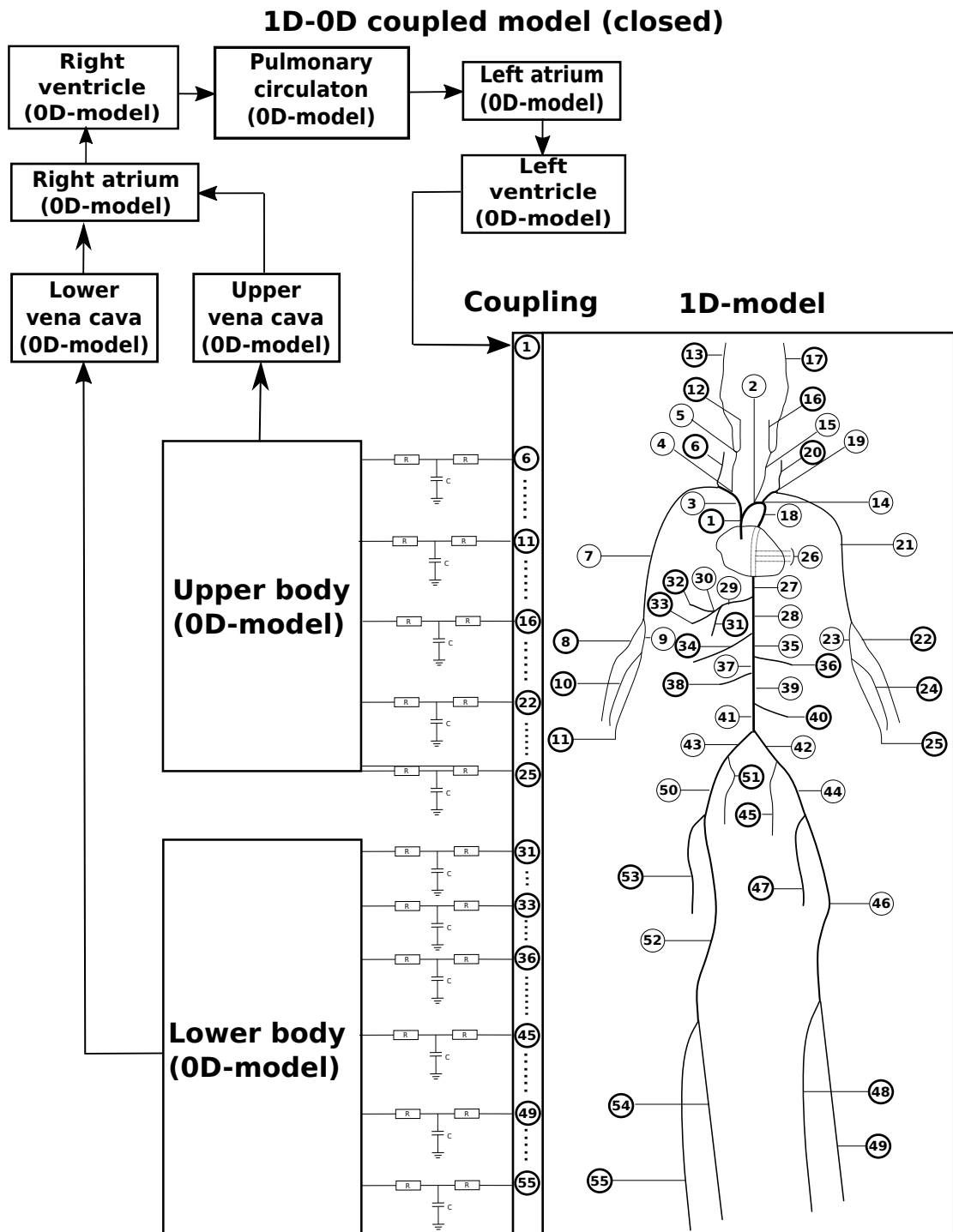


Figure 1.11: Example of a **closed** 1D-0D coupled model. The larger arteries of the systemic circulation are described by means of 1D-models, while the rest of the cardiovascular system is described by means of 0D-models. To take the Windkessel effect into account, the 1D-arteries with thick-framed numbers are coupled with three-element RCR-models. The remaining part of the cardiovascular system is also described by 0D-models and coupled to the inlet of the aorta. Overall, this modelling approach results in a **closed** blood circulation.

suitable choice of the mentioned model parameters can be found in [92] and the references therein. In Part I of the submitted thesis dealing with macroscale networks, we use in context with blood flow modelling in networks of large arteries open loop models. Since, we do not investigate blood flow in the pulmonary circulation, an open loop model is sufficient for the issues investigated in the respective chapters.

A 1D-0D coupled model for flow in pipelines

Besides blood vessel networks, a model pipeline equipped with a pump and a surge reduction system (SRS) preventing the pipeline from rupture, has been investigated. In a few hundred meters distance of a pump a SRS is installed dividing the pipeline into three parts. At the inlet of the upstream pipeline a fixed pressure value p_{in} and at the outlet of the downstream pipeline a fixed pressure value p_{out} is prescribed. The modelling concept is similar to the one applied to the macroscale arterial networks i.e. we use a domain decomposition approach and dimension reduced models for the pipeline as well as the pump and the SRS. Doing so, we decompose the model pipeline into five single components: Upstream tube, downstream tube, SRS, pump and finally a short tube linking the SRS and the pump. In a next step the SRS and the pumping station are lumped and modelled by 0D-models. As in the case of a stenosis or the R_1CR_2 -Windkessel model, they have the shape of ODE systems. Using the principles of mass and momentum conservation combined with averaging techniques, one obtains for each tube a 1D flow model in form of a PDE, involving the solution variable p representing the inner pressure and v denoting the fluid velocity. The PDE-system reads as follows [93, Section 1.3 and 1.4]:

$$\frac{\partial p}{\partial t} + \rho c^2 \frac{\partial v}{\partial x} = 0, \quad x \in (0, l), \quad t > 0, \quad (1.15a)$$

$$\frac{\partial v}{\partial t} + \frac{1}{\rho} \frac{\partial p}{\partial x} = -\lambda(Re, \varepsilon) \frac{1}{d} \frac{v|v|}{2\rho} - g \sin \alpha, \quad x \in (0, l), \quad t > 0. \quad (1.15b)$$

The constant c is the characteristic wave speed of the system, it depends on the diameter of the pipeline, the modulus of elasticity of the pipeline wall and the oil as well as on the thickness of the pipeline wall and the oil density. ρ and g denote the fluid density and the gravity constant, respectively. Viscous forces are accounted for by the first summand in the source term of (1.15b), where d is the internal diameter of the pipeline. The skin friction coefficient λ is given by [58]:

$$\lambda(Re, \varepsilon) = 0.11 \left(\varepsilon + \frac{68}{Re} \right)^{\frac{1}{4}}.$$

In this formula ε is a relative roughness coefficient and $Re = \frac{v \cdot d}{\nu}$ is the Reynolds number for pipe flow relating the convective term $v \cdot d$ and the fluid viscosity ν . To integrate the gravity force into the model, the expression $-g \sin \alpha$ is added to the source term of the momentum equation (1.15b), where α denotes the tilt angle of the considered tube. On closer examination, it can be observed that this PDE-system is a hyperbolic PDE of first order such as the 1D blood flow model given by (1.3a) and (1.3b). The major differences between the two models consist in the structure of the flux function. While the flux function of the blood flow model is non-linear, we have in case of the pipeline flow model a flux function depending linearly on the solution variables. As a consequence, the linearisation

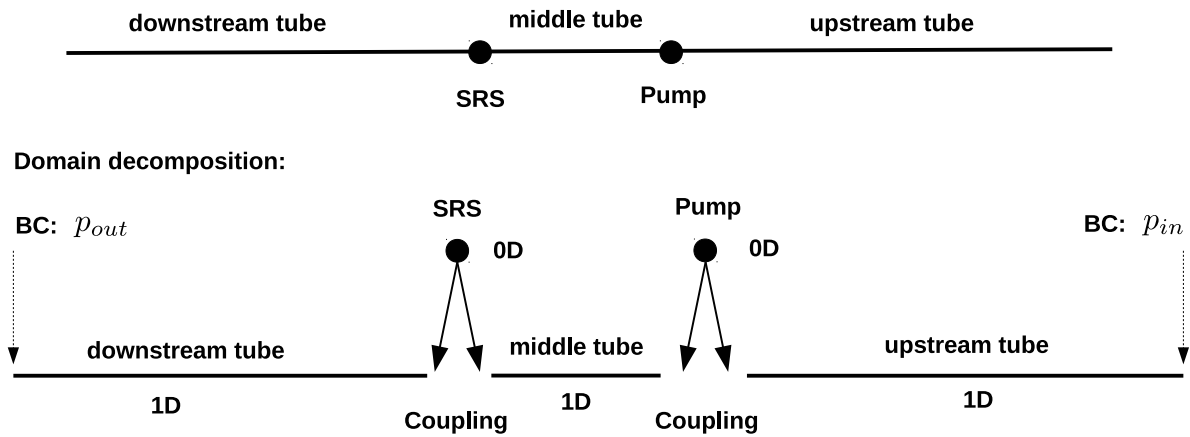


Figure 1.12: Domain decomposition method and dimension reduced modelling applied to a simple model pipeline. The model pipeline is decomposed into three tubes: Upstream tube, middle tube and downstream tube. In each tube flow is modelled by 1D equations. The SRS and the pumping station contained in the model pipeline are lumped and modelled by 0D-models (ODE-systems). At the inlets and outlets of the three tubes, we prescribe fixed pressure values p_{in} and p_{out} or we couple the 1D flow models with the adjacent 0D-models. This results in a 1D-0D flow model for the considered pipeline.

of the flux function is not necessary. Consequently, there is a linear relationship between the characteristic and the primary variables:

$$W_1 = p - \rho \cdot c \cdot v \quad \text{and} \quad W_2 = p + \rho \cdot c \cdot v.$$

Another aspect in which the two models differ is the FSI-model for coupling the flow and the deformation of the tube walls. In contrast to the elastic vessel walls of the arteries, the tube walls, which are made of steel, are hardly deformable. For this reason, the derivation of (1.15a) and (1.15b) is based on the assumption that the diameters of the tubes are almost constant. This means that a non-linear relationship between the cross-sectional area and the internal pressure like (1.4) is no longer required. Based on this simplifying assumption, we obtain a linear flow function in (1.15a) and (1.15b). As in the 1D blood flow model, we use an extrapolation of the outgoing characteristic variables combined with given pressure values or solutions of the 0D-models to compute appropriate boundary conditions at the corresponding interfaces. By this, we obtain similar to the previous subsection a 1D-0D coupled model simulating the influence of a pump and a SRS on flows in a pipeline system. For more detailed information, we refer to Chapter 4 (Part I) of this thesis and the references therein.

Data based modelling of blood flow in the vicinity of a stenosis

Simulating the influence of a stenosis on the peripheral blood circulation, i.e., the blood flow far away from the heart, we reconsider the arterial network depicted in Figure 1.10 and place a stenosis in Vessel 54 located in the lower right leg. By this, we split Vessel 54 into two new vessels that are numbered by 54 and 56 (see Figure 1.13). Within the vessels i , $i \in \{52, 54, 55, 56\}$ that are adjacent to the stenosis, we compute for one heart

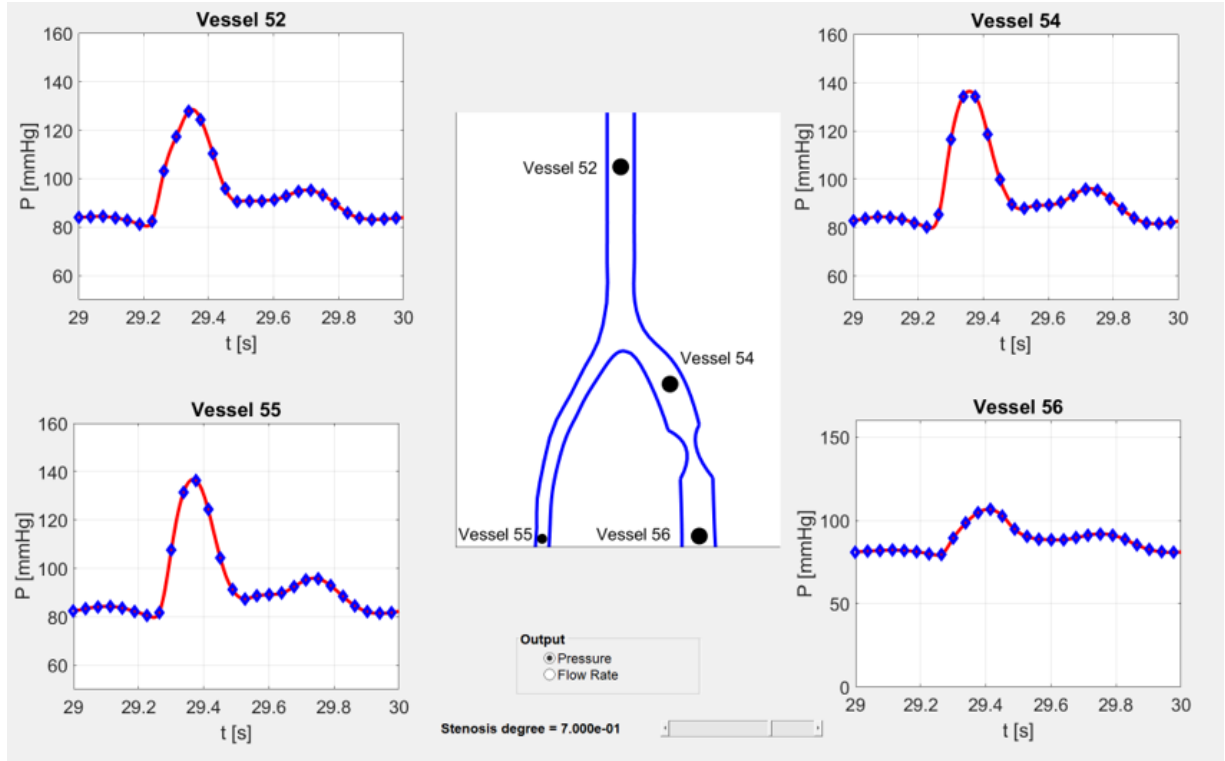


Figure 1.13: Pressure curves during one heart beat reported in the vicinity of a stenosis of degree $R_s \in (0, 1)$. From each curve $i \in \{52, 54, 55, 56\}$, we take q samples (blue diamonds) in order to construct a mapping $f_{i,P} : (0, 1) \rightarrow \mathbb{R}^q$, $R_s \mapsto f_{i,P}(R_s)$ that can be approximated by a surrogate model.

beat (about 1.0 s) at fixed places pressure and flow rate curves. In order to compute these curves, the 1D-0D model from the previous subsection is used. Recalling the 0D flow model for the stenosis (1.12), we note that one of the main parameters is the stenosis degree $R_s \in (0, 1)$. For a well-founded investigation of the influence of stenosis on the surrounding blood vessels, it is necessary to vary this parameter several times and to study the changes on the pressure and flow rate curves. Thereby, it is possible to investigate, which stenosis degrees have a relevant impact on the considered hemodynamic curves. A standard way to do this, would be to restart the simulations for every stenosis parameter R_s and to report for each simulation the data of interest. An alternative way consists in simulating the pressure and flow rate curves for some $R_s \in (0, 1)$. After each simulation, we store q samples of each pressure and flow rate curve with respect to the considered heart beat. By means of these data one can easily produce a dense output for the whole heart beat using interpolation polynomials of higher order. Since the samples for each vessel i can be associated with a certain R_s , we can design for both pressure (P) and flow rate (Q) a function $f_{i,n}$, $n \in \{P, Q\}$, mapping the stenosis degree to the corresponding sample:

$$f_{i,n} : (0, 1) \rightarrow \mathbb{R}^q, R_s \mapsto f_{i,n}(R_s).$$

The idea to reduce the computational complexity of the whole issue is to compute a surrogate function $\hat{f}_{i,n}$, whose evaluation is cheap. In a first step towards this goal, it is assumed that $\hat{f}_{i,n}$ can be represented as a linear combination of $N \in \mathbb{N}$ kernel functions K_k . Denoting the corresponding coefficients by $\alpha_{k,l}$, we have for the l -th component of the image

vector related to \hat{f}_i :

$$\hat{f}_{i,n}(R_s)(l) = \sum_{k=1}^N \alpha_{k,l} \cdot K_k(R_s, R_{s,i}), \quad i \in \{52, 54, 55, 56\}, \quad l \in \{1, \dots, q\}. \quad (1.16)$$

In this context, a function $K : (0, 1) \times (0, 1) \rightarrow \mathbb{R}$ is considered as a strictly positive kernel on $(0, 1)$, if it is symmetric and for any $N \in \mathbb{N}$ and any set of pairwise distinct points

$$S_N := \{R_{s,1}, \dots, R_{s,N}\} \subset (0, 1),$$

the $N \times N$ kernel matrix $A_{K,S_N} := (K(R_{s,k}, R_{s,j}))_{k,j=1}^N$ is positive definite. An example for a strictly positive definite kernel is the Gaussian kernel function

$$K(x, y) := \exp(-\varepsilon^2 \|x - y\|_2^2),$$

where ε is a tunable parameter. In order to determine the coefficients $\alpha_{k,l}$, we use the simulated data as training data. From (1.16), we obtain for each component l interpolation conditions by inserting the values from S_N and replacing $\hat{f}_{i,n}(R_s)(l)$ by the corresponding value from the simulated data set. By this, a linear system of equations is obtained for the computation of the coefficients $\alpha_{k,l}$.

Since the kernel function is chosen to be strictly positive definite, the matrix A_{K,S_N} is symmetric and positive definite for any S_N . Therefore, the resulting linear system of equations exhibits a unique solution. In other terms, the model satisfying the interpolation conditions (1.16) is uniquely defined for arbitrary pairwise distinct data points S_N .

However, despite the fact that the kernel method can deal with arbitrary pairwise distinct inputs S_N , the resulting surrogate model is required to be fast to evaluate. It is clear that the computational costs related to the evaluation of the surrogate model for a new stenosis degree R_s is essentially related to the number N of elements in the sum. For this reason, it is desirable to determine a sparse expansion, i.e., a linear combination in which most of the coefficients $\alpha_{k,l}$ are equal to zero. A sparse structure can be obtained by selecting a small subset $S_m \subset S_N$ of the data points, and computing the surrogate. An optimal selection of these points is a combinatorial problem, which is too expensive with respect to the computational effort. Instead, we employ greedy methods (see [135] for a general treatment, and [31, 116] for the case of kernel approximation). These methods select a sequence of data points starting with the empty set $S_0 := \emptyset$. At iteration $m \geq 1$ the set

$$S_m = S_{m-1} \cup \{R_{s,m}\}$$

is updated by adding a suitable selected point $R_{s,m} \in S_N \setminus S_{m-1}$. The selection of $R_{s,m}$ is based on the Vectorial Kernel Orthogonal Greedy Algorithm (VKOGA, [149]). Thereby, the greedy algorithm chooses the new value $R_{s,m}$, such that the residual vector

$$r_{i,n}^{(m)}(f)(R_s) = f_{i,n}(R_s) - \hat{f}_{i,n}^{(m)}(R_s)$$

is minimised in a suitable norm, where $\hat{f}_{i,n}^{(m)}$ denotes the surrogate model resulting from the m -th iteration. For further information, we refer to Chapter 3 in Part I and the references therein.

1.2.2 Model reduction techniques for fine scale structures

In the previous subsection, we have discussed model reduction techniques for flows in networks consisting of large arteries and pipeline systems (see (FP 1) and (FP 3)). These flow processes exhibit larger Reynolds numbers and convection dominated flow, which are modelled by 1D hyperbolic PDE-systems. Considering Table 1.1, it remains to present model reduction techniques for flows in microvascular networks (FP 2) and injections in porous media (FP 4). Contrary to (FP 1) and (FP 3), we observe for these flow processes small Reynolds numbers. A further difference is that in the case of (FP 1) and (FP 3) the fluid is not moving through a system of large cavities, but through networks of small pores or small capillaries. Taking the differences into account, it becomes obvious that for (FP 2) and (FP 4) totally different modelling approaches are required. In the following, we discuss the fundamentals of simplified models for blood flow in microvascular networks and injection of fluids into porous media.

A 3D-1D coupled model for blood flow in microvascular networks

As a first step towards a model for blood flow in microvascular networks and surrounding tissue, we recall briefly the most important properties of fluid and flow within such systems. Concerning the fluid filling the space inbetween the tissue cells (interstitial space), it is assumed that this fluid consists mostly of water. Since water is an incompressible and Newtonian fluid, a constant density and viscosity can be considered for the tissue fluid. This holds only partially for blood in microvascular networks.

Blood is composed of blood plasma, which can be compared to the interstitial fluid and blood cells, which can be classified as red blood cells, white blood cells and blood platelets. In particular, red blood cells determine the flow behaviour of blood, since they are the most frequent ones. Furthermore their diameter exceeds the diameter of the capillaries and small arterioles. Therefore they have to deform so that they can be transported through a microvascular network. As a consequence the viscosity of the fluid is strongly dependent on the vessel diameter, which means that it can not be considered as a Newtonian fluid. In order to determine the corresponding viscosity parameter μ_{bl} , we use the following function depending on the vessel diameter D [107]:

$$\mu_{bl}(D) = \mu_p \left(1 + (\mu_{0.45} - 1) \frac{(1-H)^C - 1}{(1-0.45)^C - 1} \cdot \left(\frac{D}{D-1.1} \right)^2 \right) \cdot \left(\frac{D}{D-1.1} \right)^2. \quad (1.17)$$

The viscosity of the blood plasma is denoted by μ_p , and H stands for the discharge hematocrit which is defined by the ratio between the volume of the red blood cells and the total blood volume. The apparent viscosity $\mu_{0.45}$ for a discharge hematocrit of 0.45 is calculated by:

$$\mu_{0.45} = 6.0 \exp(-0.085 \cdot D) + 3.2 - 2.44 \exp(-0.06 \cdot D^{0.645})$$

and C is a coefficient determining the influence of H on μ_{bl} :

$$C = (0.8 + \exp(-0.075 \cdot D)) \left(-1 + \frac{1}{1 + 10^{-11} D^{12}} \right) + \frac{1}{1 + 10^{-11} D^{12}}.$$

The density of blood might also vary locally, since the blood cells are not equally distributed within the microvascular network [106]. However, in the publications of Part II, we will neglect this effect and consider the blood density as constant.

According to Table 1.2, Reynolds and Womersley numbers in microvascular networks are smaller than one. This means that on this vascular level and within the tissue almost stationary and no pulsatile flow can be observed. Instead, mass exchange with the surrounding tissue has to be taken into account, since the vessel walls of the capillaries exhibit gaps in their vessel walls such that oxygen and nutrients can be transported to the tissue cells and that waste can be removed from the interstitial space.

To design a model for this flow problem, we use again the domain decomposition method. In this case, we separate the vascular system from the surrounding tissue and derive different models for them. Afterwards, coupling concepts have to be determined in order to obtain a consistent and representative global solution (see Figure 1.14).

For the microvascular network, we apply a similar model reduction approach as for the larger arteries, i.e., we split the network into its single vessels and derive a dimensional reduced model for each vessel. In a second step, the single vessels are connected by means of coupling conditions yielding a complete model for the network flow. In [102] it has been shown that the Navier Stokes equations for flow in a microvascular network can be simplified to a 1D Poiseuille type equation, which is defined on the main axis of the corresponding vessel. For simplicity, it can be assumed that each vessel can be represented by a straight edge in space, such that the network can be considered as a dense graph-like structure in space (see Figure 1.4). Assuming that the network consists of N vessels, we obtain for the i -th vessel, $i \in \{1, \dots, N\}$ the following 1D PDE [105]:

$$-\frac{\partial}{\partial s} \left(\rho_{\text{bl}} \pi R_i^2 \frac{K_{v,i}}{\mu_{\text{bl}}} \frac{\partial p_i^v}{\partial s} \right) = S_{vt,i}, \quad s \in [0, 1] \quad (1.18)$$

In (1.18) p_i^v indicates the pressure within the i -th vessel and s is the curve parameter of the mapping describing the main axis of the corresponding vessel:

$$\Lambda_i : [0, 1] \rightarrow \mathbb{R}^3, s \mapsto \Lambda_i(s).$$

R_i is the vessel radius, which is assumed to be constant on each edge. The viscosity parameter is governed by the vessel radius or diameter as it is shown in (1.17). ρ_{bl} is the density of blood, which is taken to be constant. Finally, $K_{v,i}$ is a parameter representing the permeability of the i -th vessel and is given by: $K_{v,i} = R_i^2/8$.

The exchange process with the surrounding tissue matrix is incorporated in the source term S_{vt} . In order to model flow from the interstitial space into the vascular system and vice versa, Starling's filtration law is considered [89, 130]. This physical law describes the mass flux through the surface area of a permeable membrane. As driving forces for this flow process, the pressure difference across the membrane as well as the difference of osmotic pressures are considered. Using the notation from above, the flux $F_{p,i}$ through the vessel surface

$$S_i = 2\pi \cdot R_i \|\Lambda_i\|_2,$$

with a permeability $L_{p,i}$ is given by:

$$F_{p,i} = S_i \cdot L_{p,i} \cdot \rho_{\text{int}} \cdot (\Delta p_i + (\pi_p - \pi_{\text{int}})).$$

Thereby, π_p and π_{int} denote the osmotic pressures. For simplicity, we consider them as constants. The pressure difference between the fluids in the vascular system and the interstitial space is given by Δp_i . Since we have essentially an exchange of interstitial fluid, its density ρ_{int} has to occur in Starling's filtration law.

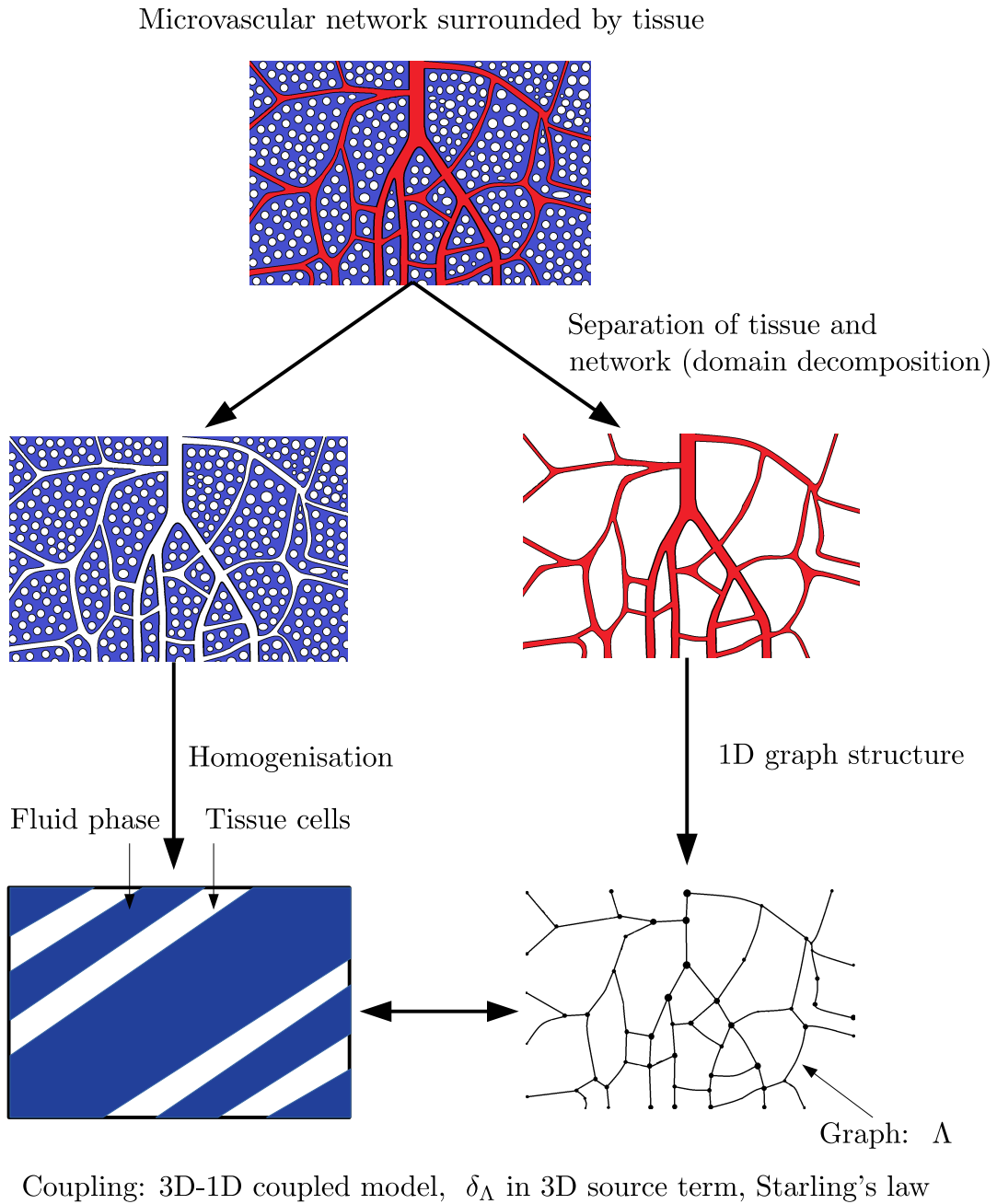


Figure 1.14: Outline of the 3D-1D modelling approach for microvascular networks in tissue.

Due to fact that $S_{vt,i}$ describes the mass flux per vessel length it is necessary to divide $F_{p,i}$ by the length of the vessel i.e. $\|\Lambda_i\|_2$, which yields for a curve parameter $s \in [0, 1]$:

$$S_{vt,i}(s) = 2\pi \cdot R_i \cdot L_{p,i} \cdot \rho_{\text{int}} \cdot \left(\overline{p_i^t}(s) - p_i^v(s) + (\pi_p - \pi_{\text{int}}) \right). \quad (1.19)$$

Please note that in (1.19), we have replaced Δp_i for each parameter by the difference between the blood pressure p_i and an averaged pressure of the interstitial fluid within the

tissue p_t , where the averaged pressure with respect to p_t is given as follows:

$$\overline{p}_i^t(s) = \frac{1}{2\pi R_i} \int_0^{2\pi} p^t(\Lambda_i(s) + R_i \mathbf{n}_{\Lambda_i}(s, \theta)) R_i d\theta,$$

where the vector $\mathbf{n}_{\Lambda_i}(s, \theta)$ indicates a normal vector perpendicular to the midaxis of the i -the vessel and depending on an angle θ , such that the set $\{\mathbf{n}_{\Lambda_i}(s, \theta) \mid \theta \in [0, 2\pi)\}$ describes a unit circle around $\Lambda_i(s)$ and perpendicular to the midaxis of the i -the vessel. All in all we obtain for flow in a single vessel:

$$-\frac{\partial}{\partial s} \left(\rho_{\text{bl}} \pi R_i^2 \frac{K_{v,i}}{\mu_{\text{bl}}} \frac{\partial p_i^v}{\partial s} \right) = 2\pi \cdot R_i \cdot L_{p,i} \cdot \rho_{\text{int}} \cdot \left(\overline{p}_i^t(s) - p_i^v(s) + (\pi_p - \pi_{\text{int}}) \right).$$

To obtain a complete flow model for the microvascular network, we enforce at the bifurcations pressure continuity and mass conservation. Depending on the given data, fixed pressures or fluxes are prescribed at the inflow and outflow boundaries. Contrary to the hyperbolic system that is used for the larger arteries, this is possible without further investigations, since the 1D flow problems for the microvascular network are of elliptic type. As it is known from standard literature, elliptic problems are well posed for pure Dirichlet boundary conditions or mixed boundary conditions.

It remains to design a model for the tissue flow. For this purpose, we consider the tissue cells and the interstitial space as a homogeneous porous medium i.e. we assume that the tissue block containing the microvascular network exhibits a constant porosity and permeability K_t . A definition of the terms porosity and permeability in context with porous media can be found in [73, Chapter 2]. Since it is further assumed that the extracellular space is filled with a homogeneous fluid, we use a single phase flow model for porous media to determine the tissue pressure p_t . The domain containing both the tissue matrix Ω_t and the vascular system Ω_v is denoted by

$$\Omega = \Omega_t \cup \Omega_v \subset \mathbb{R}^3.$$

Actually, the flow model for porous media would have to be defined on Ω_t . However, due to the fact that the vascular flow model is composed of 1D flow models and that the blood vessels of microvascular networks are small compared to the dimensions of the whole domain, Ω is identified with Ω_t : $\Omega_t \approx \Omega$. This means that we define on Ω a *single continuum model* governing the *single phase flow process* in the tissue block. A standard flow model describing the velocity field for such a flow process is the well-known Darcy law [73]. Combined with a mass balance equation, the underlying PDE reads as follows:

$$-\nabla \cdot \left(\rho_{\text{int}} \frac{K_t}{\mu_{\text{int}}} \nabla p_t \right) = S_{tv}.$$

Here, the source term S_{tv} models the exchange between the tissue matrix and the microvascular system. Deriving this source term, we use a concept that has been intensively studied in [29, 30]. The fundamental idea of this modelling approach is to define a source term that is concentrated on the midaxes of the vessels forming the microvascular network. Therefore, we define the 1D graph Λ describing the location of the 1D network in space:

$$\Lambda = \bigcup_{i=1}^N \Lambda_i \subset \Omega.$$

As Λ is a 1D structure in a 3D space it has zero measure in Ω . As a consequence, one requires Dirac measures with respect to Λ in S_{tv} to define it in a consistent way. In order to guarantee the mass conservation, we reuse the source terms of the 1D flow problems with the opposite sign:

$$S_{tv} = \underbrace{2\pi \cdot R \cdot L_p \cdot \rho_{\text{int}} \cdot (p^v - \bar{p}^t - (\pi_p - \pi_{\text{int}}))}_{=ex_{tv}} \delta_\Lambda,$$

where

$$ex_{tv} |_{\Lambda_i} = 2\pi \cdot R_i \cdot L_{p,i} \cdot \rho_{\text{int}} \cdot (p_i^v - \bar{p}_i^t - (\pi_p - \pi_{\text{int}})).$$

Finally, this results by means of (1.18) in the following 3D-1D flow model for a microvascular network:

$$-\frac{\partial}{\partial s} \left(\rho_{\text{bl}} \pi R^2 \frac{K_v}{\mu_{\text{bl}}} \frac{\partial p^v}{\partial s} \right) = 2\pi \cdot R \cdot L_p \cdot \rho_{\text{int}} \cdot (\bar{p}^t - p^v + (\pi_p - \pi_{\text{int}})), \quad (1.20a)$$

$$-\nabla \cdot \left(\rho_{\text{int}} \frac{K_t}{\mu_{\text{int}}} \nabla p_t \right) = 2\pi \cdot R \cdot L_p \cdot \rho_{\text{int}} \cdot (p^v - \bar{p}^t - (\pi_p - \pi_{\text{int}})) \delta_\Lambda. \quad (1.20b)$$

A 3D-3D-1D coupled model for blood flow in microvascular networks

The 3D-1D coupled model from the previous subsection can be simplified by introducing a further continuum arising from the homogenisation of discrete microstructures. Within the 3D-1D coupled model the interstitial space as well as the tissue cells have been described in an averaged sense by the permeability parameter K_t and a porosity. To model the flow in this porous media system, Darcy's law has been applied. This concept can be further applied to the fine scale components of the microvascular network. For this purpose, we choose a threshold R_T with respect to the radii of the blood vessels. Usually, it is chosen such that it marks the limit between the arterioles or venules and the capillary bed. Based on R_T the microvascular system is divided such that the vessels whose radii are larger than R_T are classified as *large vessels*. All the other vessels are assigned to the *capillary bed* (see Chapter 7). Flow within the network formed by the larger vessels is modelled by means of (1.20a). Assuming that the exchange processes between the vascular system and the tissue take only place within the capillary bed, we set for the larger vessels: $L_p = 0$ (see Figure 1.15).

In a next step, the discrete capillary bed is turned into a homogenised continuum just as the porous tissue structure. The goal is to use a Darcy flow model for the capillary bed as for the tissue, while preserving the information on the main flow channels via the 1D flow models. As in the case of the interstitial flow, we consider a *single phase flow model* for the homogenised capillary bed. The corresponding solution variable is the capillary pressure p^{cap} and the Darcy flow model is given by:

$$-\nabla \cdot \left(\frac{K_{\text{up}}}{\mu_{\text{bl}}^{\text{up}}} \nabla p^{\text{cap}} \right) = q_t^{\text{cap}} + q_v^{\text{cap}}. \quad (1.21)$$

Considering (1.21), it is necessary to determine a permeability K_{up} for the homogenised medium as well as a viscosity $\mu_{\text{bl}}^{\text{up}}$ to set up the left hand side of Darcy's equation. Contrary to the tissue matrix we can not assume that the permeability is given by a constant, since the capillary bed exhibits a hierarchical structure. Due to that the permeability

varies locally in Ω . This means that a tensor has to be computed for the permeability function of the capillary bed. For simplicity, we restrict ourselves to a diagonal tensor accounting for anisotropies in the three space dimensions. Following the standard porous media theory [14, 73], we subdivide the tissue block Ω containing the capillary bed into N_{REV} *representative elementary volumes* (REVs) having the shape of a rectangular blocks. For each REV $j \in \{1, \dots, N_{\text{REV}}\}$, we determine a permeability tensor $K_{up}^{(j)}$ as well as an

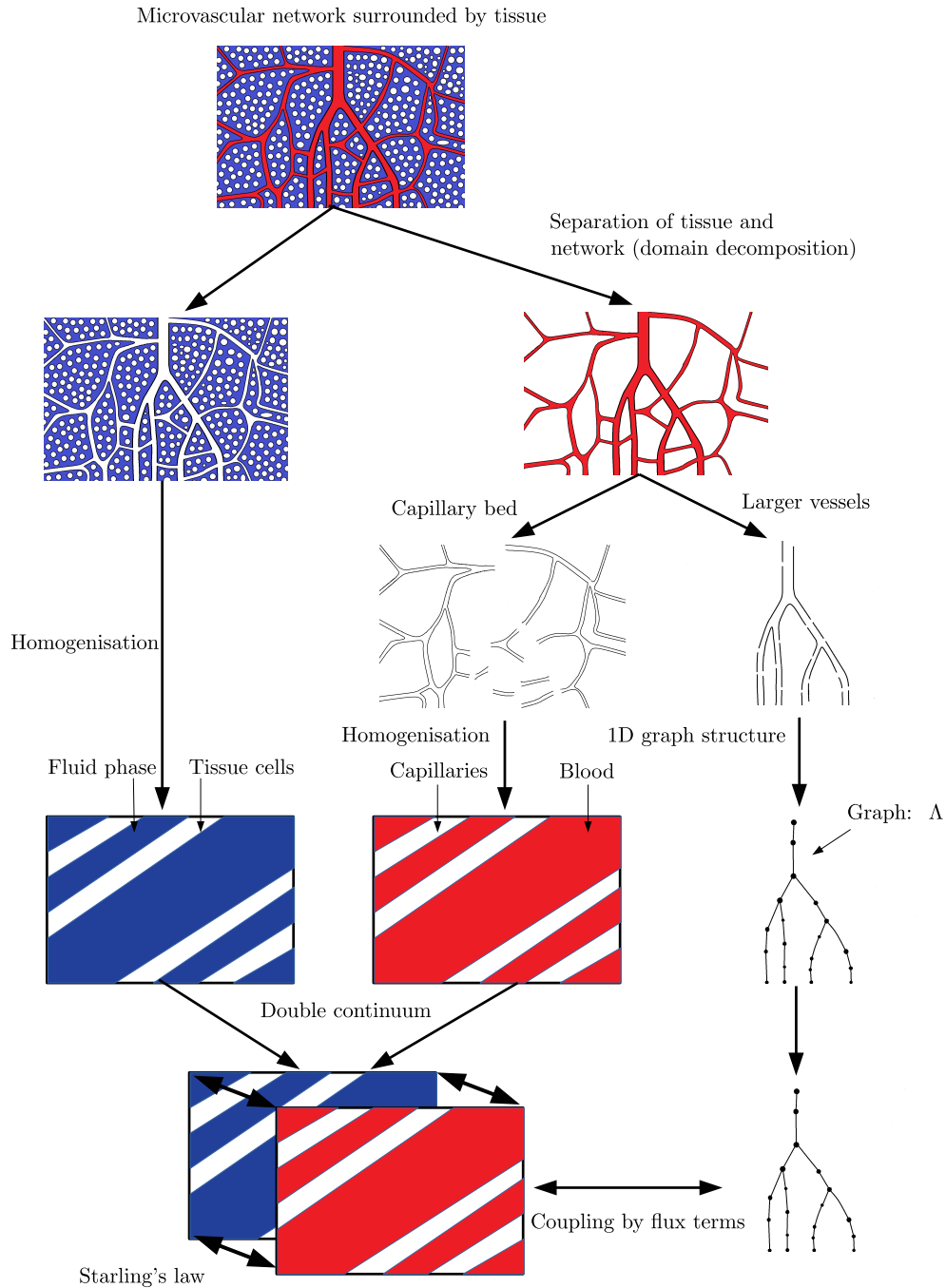


Figure 1.15: Outline of the hybrid 3D-3D-1D modelling approach for microvascular networks in tissue.

averaged viscosity $\mu_{bl,j}^{\text{up}}$. The averaged viscosity is computed as a simple arithmetic mean of the viscosity for all the capillaries contained in REV j . In order to determine the viscosity for the single vessels, we use (1.17). For the computation of the diagonal entries of $K_{up}^{(j)}$ a pressure gradient is applied at the facets of the REVs that are perpendicular to the corresponding coordinate axes. On the remaining facets no-flow boundary conditions are set. Next we compute the flux through one of the facets at which the pressure gradient is applied. By means of this flux, the pressure gradient and the corresponding edge length, the permeability value in the considered space direction can be calculated. For further information, we refer to [115]. The determination of the source terms connecting the capillary bed with the tissue matrix (q_t^{cap}) and the larger vessels of the microvascular network (q_v^{cap}) is outlined in detail in Chapter 7.

Hysteresis models for fluid injection into porous media

In the previous subsection, we discussed modelling approaches for flow processes in tissue. Thereby, we have assumed that the interstitial space in the tissue matrix is filled with a homogeneous fluid. As a consequence, it has been sufficient to consider a *single-phase flow model*. Creating a model for fluid injections into a porous medium, it is required that besides a fluid, i.e., a wetting phase and a non-wetting phase like air have to be taken into account. This is due to the fact that an injection of a fluid into a porous medium is only meaningful, if the pores of the porous medium are not fully saturated with the fluid. Therefore, we assume that this flow process can be considered as a *two-phase flow process* (see Figure 1.16). To each REV, averaged quantities are assigned as phase pressures and phase saturations. The saturations are fractions of the volumes of the phases within the REV and the volume of the REV. Moreover, there are parameters characterising the porous medium like the porosity ϕ and the absolute permeability K , where the porosity ϕ is defined as the fraction of pore volume contained in a REV and the volume of the REV itself. In order to describe the REV based quantities in a comprehensive manner, a mass balance equation and momentum balance equation for each phase is required.

According to [13, 73] the mass balance equations for the phases read in the absence of source terms as follows:

$$\phi \frac{\partial (\rho_\alpha S_\alpha)}{\partial t} + \nabla \cdot (\rho_\alpha v_\alpha) = 0, \quad \alpha \in \{w, n\}, \quad (1.22)$$

where $\alpha = n$ denotes the non-wetting phase and $\alpha = w$ the wetting phase. S_α and ρ_α are the saturations and densities of the phases. The momentum balance equations governing the phase-velocities v_α are given by Darcy's law [13, 73]:

$$v_\alpha = -\frac{k_{r\alpha}}{\mu_\alpha} K (\nabla p_\alpha - \rho_\alpha g \hat{e}_g), \quad \alpha \in \{w, n\}. \quad (1.23)$$

In (1.23) K is the absolute permeability of the porous medium, μ_α the viscosity and $k_{r\alpha}$ the relative permeability of each phase. Moreover, p_α , g and \hat{e}_g are the phase pressure, the gravitational acceleration and the unit vector along gravity, respectively.

Obviously, the system (1.22)-(1.23) is not closed, since there are more unknowns than equations. Therefore, one needs to make assumptions. Assuming incompressibility yields that ρ_α are constant. Moreover, due to the fact that we consider a two-phase flow system, it holds:

$$S_w + S_n = 1. \quad (1.24)$$

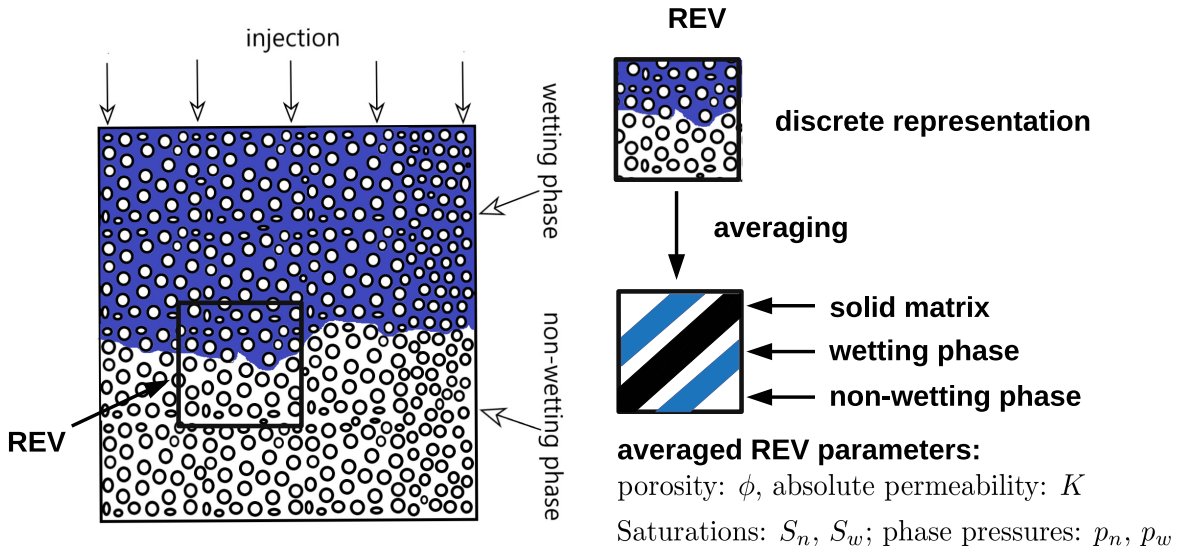


Figure 1.16: Injection of a fluid (wetting phase) into a porous medium filled with air (non-wetting phase). The fluid is considered as a wetting phase, while the air represents a non-wetting phase. On the right hand side the averaged quantities with respect to a REV are listed.

The relative permeabilities are given by constitutive laws relating S_w to a dimensionless value between 0 and 1 [13, 73]:

$$k_{r\alpha} : [0, 1] \rightarrow [0, 1], \quad S_w \mapsto k_{r\alpha}(S_w), \quad \alpha \in \{n, w\}, \quad (1.25)$$

where the most widespread model curves are given by the *van Genuchten* or *Brooks-Corey* model. At the interfaces between the wetting and non-wetting phase, it can be noted that there is a pressure jump between the phase pressures p_w and p_n . In order to quantify this pressure difference a further variable is introduced and indicated as capillary pressure p_c :

$$p_c(S_w) = p_n - p_w. \quad (1.26)$$

As the relative permeabilities, p_c can be modelled by a *van Genuchten* or *Brooks-Corey* curve relating the capillary pressure and the saturation of the wetting phase:

$$p_c : (0, 1] \rightarrow \mathbb{R}^+, \quad S_w \mapsto p_c(S_w). \quad (1.27)$$

Summarising equations (1.22)-(1.27), we obtain a closed model for a two-phase flow process in a homogeneous porous medium. In the different chapters of Part III, we model the injection of water into a narrow sand column of height H (see Figure 1.17). Due to the fact that a narrow column and a homogeneous porous medium is considered, it is assumed that the water saturation is almost constant across the section area of the sand column. Therefore, only 1D versions of (1.22) and (1.23) are investigated. Simulating injection processes like the one depicted in Figure 1.17, it can be observed that the flow process in the porous matrix is governed by imbibition and drainage processes. Experimental studies reveal that the relationships for the relative permeabilities k_{rw} and k_{rn} as well as for p_c exhibit a different behaviour during imbibition and drainage [97, 155]. Thereby,

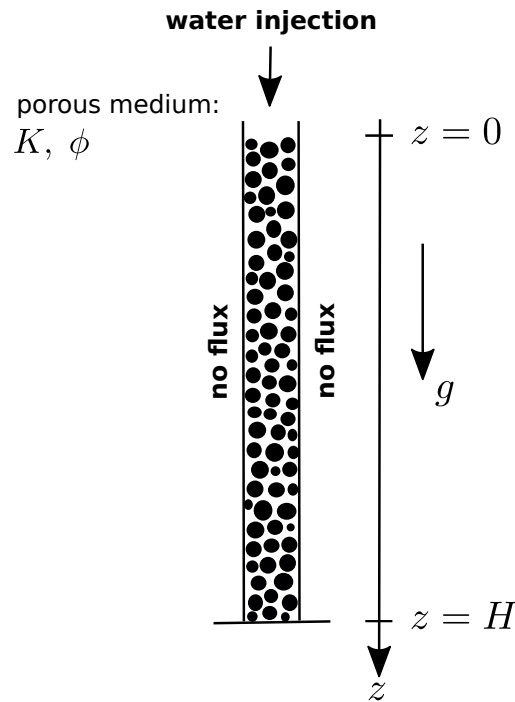


Figure 1.17: Setup of an infiltration experiment. At the inlet of a column having the height H water is injected by a constant rate. The main axis of the column is orientated such that it is aligned with the gravity vector.

it can be observed that both drainage and imbibition processes can be described by *van Genuchten* or *Brooks-Corey* curves. However, different curve parameters have to be used for the corresponding processes. In technical language these curves are referred to as main drainage or main imbibition curves. A change from an imbibition to a drainage process or vice versa is accomplished by moving from one main curve to the other. If the time derivative of the water saturation is changing its sign, the relative permeability or capillary pressure follows a curve linking the main curves, which is known as scanning curve. Depending on the setting and the fluid moving through the porous medium these linking curves can have steep gradients or a rather smooth course (see Figure 1.18). Based on these experimental results one can conclude that a useful two-phase flow model for injection processes has to incorporate a hysteresis model for the relative permeabilities and the capillary pressure, since the course of the scanning curves suggest that a change between drainage and imbibition processes occurs usually with a slight delay. Similar phenomena can also be observed in context of many different fields of physics. A very prominent one is magnetism [17].

In this thesis, we consider only flow processes with steep scanning curves. There are essentially two ways to integrate a steep scanning curve into the two-phase flow equations (1.22) and (1.23): One way is based on approximating the scanning curve by constant saturation lines (see Figure 1.18). This type of numerical model is referred to as play-type hysteresis model in the literature [16, 38]. It has been investigated analytically [23, 114, 123, 140] and a physical basis for this approach has been provided in [16, 121]. It can be extended to account for smooth scanning curves by considering additional terms modelling horizontal redistribution [38]. The second possibility consists in computing splines between

the main drainage and imbibition curves ensuring a smooth transition between the two processes. This is crucial if a Newton solver is used to solve the non-linear systems of equations arising in the context of an implicit time stepping scheme.

Another phenomenon that can be observed in experiments is the formation of saturation overshoots if the injection rate is large enough. The surprising thing about this is that despite there are no external sources and the injection rate or other boundary conditions are constant, non-monotone saturation profiles can be observed. According to the theory of PDEs [40, 122, 142], this cannot be explained by a second order PDE-system such as (1.22) and (1.23). Based on thermodynamic considerations a dynamic capillary model has been proposed in [71]. Thereby, the standard relationship (1.27) is extended by a term involving the time derivative of the wetting saturation and a parameter τ . Therefore, it is indicated by "τ-term". Taking also hysteresis effects into account, we obtain:

$$p_n - p_w = p_c(S_w) = \frac{1}{2}(p_c^{(i)}(S_w) + p_c^{(d)}(S_w)) - \frac{1}{2}(p_c^{(d)}(S_w) - p_c^{(i)}(S_w)) \cdot \text{sign}\left(\frac{\partial S_w}{\partial t}\right) - \tau \frac{\partial S_w}{\partial t}, \quad (1.28)$$

where $p_c^{(i)}$ and $p_c^{(d)}$ denote the main drainage and imbibition curves for the capillary pressure. The dynamic capillary term has been measured experimentally [21, 81] and it has been successfully used to explain overshoots [26, 96, 114, 123, 141, 139, 140].

1.3 Structure of the thesis

After discussing the main features of the model reduction techniques applied in this thesis, we will now turn in this last section of the introduction to the different publications presented in this thesis. In particular, it is outlined which novel aspects concerning mathematical modelling and analysis have been investigated. In addition to that, we will have a brief look on the numerical methods used to solve the mathematical model equations. The submitted thesis is roughly subdivided into three larger parts: In the first part, we summarise all the publications dealing with modelling and simulation of blood flow in larger arteries and pipeline systems, while the second part of the thesis is concerned with blood flow in microvascular networks. Finally, in the third part, we are focused on hysteresis models for fluid injections into porous media.

1.3.1 Part I: Simulation of flow processes in macroscale networks

The first part of this thesis comprises three chapters, where the first two chapters are focused on simulating blood flow through networks in large arteries. For this purpose, the arterial network consisting of the 55 main arteries in Figure 1.10 is used to illustrate our findings. Data on lengths, diameters, wall thicknesses and section areas can be found e.g. in [126][Tab. 1]. The third publication is dedicated to the simulation of flow through pipeline systems equipped with pumping stations and surge reduction systems (SRS). As we outlined in Section 1.2.1 flow processes both in large arterial networks and pipelines can be simulated in an efficient way by means of 1D-0D coupled flow models. Thereby, flow in single arteries and pipeline parts have been modelled on the basis of 1D hyperbolic PDE-systems. This results from the fact that both flow systems are on a macroscale level within their area of application and that both flow processes exhibit higher Reynolds numbers. For these reasons these publications are put together in Part I dealing with flow processes in macroscale networks.

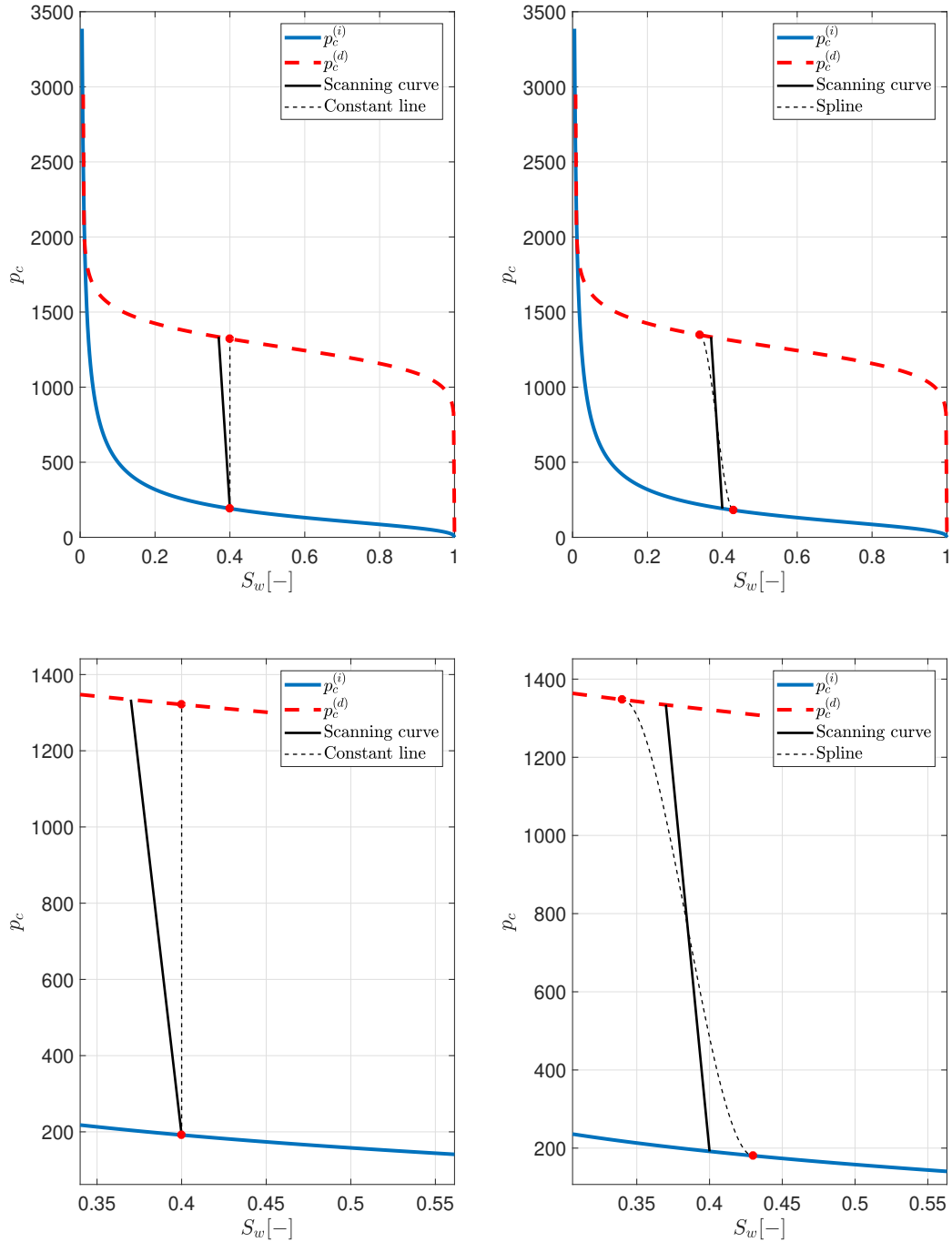


Figure 1.18: This figure shows a simple scanning curve with a steep gradient between the two main curves for the capillary pressures in case of a switch from imbibition to drainage. On the left hand side the scanning curve is approximated by a constant line (play-type hysteresis model), while on the right hand side a cubic spline is constructed around the scanning curve to ensure a smooth transition between the two curves.

In Chapter 2, the impact of a stenosis in the right lower leg is investigated. Besides the simulation of the pure influence of a stenosis on hemodynamics, we have considered

two endogenous compensation mechanisms to balance out the reduced blood flow caused by a stenosis. One of these compensation mechanisms is called metabolic regulation. It is based on estimating the average oxygen concentration in the tissue that is supplied by a terminal 1D artery. If it is below a certain threshold, we decrease the resistance value R_1 in (1.14), otherwise it is kept constant or increased. A similar model has been studied in [3]. The difference between our modelling approach and the model presented in [3] is that the driving force for adapting the resistance is based on carbon dioxide and not on oxygen. A change of R_1 corresponds to shrinking or widening of the arterioles by means of the smooth muscles that are wrapped around the vessel walls. In order to include this mechanism into our flow model, we add further ODEs to (1.14) governing the averaged oxygen concentration and an activation variable for the resistance R_1 .

As a second compensation mechanism we study arteriogenesis, i.e., the growth of pre-existing shunts between two main arteries. In Chapter 2, the two main arteries in the lower right leg are considered. A widening of these shunts allows to partially redirect the blood volume around the stenosis located in one of the leg arteries. To the knowledge of the authors this compensation mechanism has not been modelled in the way as it is described in Chapter 2. As a flow model for the shunts, we chose a simple Poiseuille flow model and use a growth function measured in the context of rat experiments [117, 120] to adapt the section areas of the shunts. A Poiseuille flow model is applicable, since the shunts have dimensions of arterioles and do not allow for fast and pulsatile flow. Moreover, the section area of the shunts can not be considered as constant. However, for the 1D hyperbolic blood flow model (1.3a) and (1.3b), we assumed that A_0 is constant. On closer examination they are typically smaller in the middle as on the inlets and outlets. Therefore, we approximate the radial profile by small and piecewise constant units and apply to each unit a Poiseuille flow model. The section areas of these units are adapted according to the growth function from [120, Table 1].

Using this computational model, we investigate the impact of both compensation mechanisms, separately. Thereby, it has been revealed that including only one of these mechanisms is not sufficient for a complete compensation if the stenosis blocks the entire section area. This is still true, if the number of shunts is steadily increased. Only a combination of both compensation mechanisms and at least five shunts are required to restore the reduced blood flow.

Concerning the numerical discretisation, we are faced with several difficulties, since the two compensation mechanisms are related to different time scales. While the metabolic regulation is adapting the resistances of the arterioles within minutes, the growth of arterial shunts exceeds over weeks. This means that we have to consider two different time scales. In order to account for the different time scales, two different time steps Δt_{ma} and Δt_{mi} are introduced for the slow and the fast compensation mechanism, respectively. After exerting a macro time step and updating the arteriogenesis model, we perform several micro time steps using the enhanced 0D outflow model until the pressure and flow rate curves become periodic again. Since we are only interested to what extend the reduced blood flow can be compensated, it is admissible to simulate both processes, sequentially. As a time stepping scheme for the 1D PDEs, we consider an explicit scheme. Due to the fact that we have to simulate fast and convection dominated flow it is necessary to use small time steps in order to be able to represent the pressure and flow rate waves with a sufficient accuracy. On the other hand the choice of the time step size can be severely restricted by the CFL-condition of a standard explicit time stepping scheme. Therefore, we have considered the numerical method of characteristics (NMC) presented in [1]. It is shown in Theorem 1

of this publication that the NMC is of first order in space and time, which might cause large dissipation and dispersion errors. This can be prevented by a dense mesh in space causing a low computational effort, since we are discretising a 1D flow problem. The time steps resolving the pressure and flow rate curves are usually small enough to keep the discretisation errors low. However, we are not forced to exert tiny timesteps since it is proven in [1, Proposition 2] that the NMC is unconditionally stable even for CFL numbers greater than one. In particular this property makes the NMC attractive for simulation problems involving large simulation periods.

The next chapter is essentially concerned with the same setting. Contrary to Chapter 2 the stenosis is modelled by the ODE (1.12). Moreover no compensation mechanisms are considered in this case. Apart from these aspects the 1D-0D blood flow model is the same as in the previous chapter. For the numerical discretisation we use again the NMC, where in this chapter further details on the NMC are provided like the most important derivation steps of this method. Thereby, we put a special emphasis on the grid nodes near the boundaries. Using sufficiently large time steps, it may happen that characteristic curves passing through grid nodes near the boundaries are leaving the computational domain within a certain time step. This means that regarding these curves no spatial values from the old time step can be determined for the time stepping scheme. Therefore, we compute within each time step for the affected grid nodes the time points at which the characteristic curves are crossing the boundary. Afterwards, we use the boundary conditions for the old and the new time step to interpolate the corresponding characteristic boundary values at the respective time points. These values are then used as substitute values within the NMC. It is obvious that the computation of the substitute values has to be handled with care. Since this issue has not been considered in [1] we have discussed this aspect in Chapter 3.

However, the main focus of this chapter is the combination of dimensional reduced blood flow models with data based surrogate modelling. Besides classical model reduction techniques like homogenisation or dimension reduced modelling, data based modelling has become a further important approach to decrease the complexity of a simulation problem. In particular for parameterised problems, in which one or several parameters are varied many times, this model reduction technique offers the possibility to save computation time by creating a surrogate model which can be evaluated at low costs. In context of blood flow modelling the Reduced basis (RB) method has been used many times in the recent years [95, 111, 112]. The basic idea of the RB-method is to solve in an offline phase the parameterised PDEs for a few parameters (see e.g. [18, 25, 67]). In a second step the corresponding solutions, which are denoted as snapshots are used to design a basis of a low-dimensional space. Projecting the PDE into this space results in a low-dimensional problem. The corresponding reduced system is solved in a so-called online phase, in which solutions for several parameters can be computed, efficiently. Concerning blood flow modelling these parameters determine usually the shape of a bifurcation, a stenosis, a bypass or an inflow profile [110, Chap. 8], [111, 112]. In this chapter, we have investigated the performance of a different type of data based modelling approach, which is referred to as Kernel method [48, 66, 68, 119, 148]. Contrary to the RB method, the surrogate model is in this case represented by a linear combination of kernel functions like the Gaussian or the Wendland kernel [147, 150]. The coefficients in the linear combination and the parameters for the kernel functions are obtained from a training and validation process which is performed in an offline phase [69] (see last part of Section 1.2.1).

The influence of a stenosis on the peripheral blood flow is simulated, varying the parameter $R_s \in (0, 1)$ in the ODE (1.12). In order to obtain a realistic surrogate model it is

necessary to run several simulations. Since it is sufficient to compute in the vicinity of the stenosis averaged pressure and flow rate curves to demonstrate the impact of the stenosis, the 1D-0D blood flow model instead of a complex 3D blood flow model can be used. As a consequence, it is possible to generate more training data within the same time range as in the case of a complex 3D model. We have been able to show by means of numerical simulations that by providing an increasing amount of training data, the model reduction errors for both the pressure and flow rate curves are monotonously decreasing. Analysing the model reduction error with respect to $R_s \in (0, 1)$, it turns out that for $R_s \rightarrow 1$, which corresponds to the case of a full occlusion, the relative errors attain their largest values. Furthermore, we have demonstrated that an inverse problem can be solved by means of this surrogate model. Given some pressure and flow rate curves it is possible to recover the corresponding stenosis degrees accurately, in particular if $R_s > 0.6$ holds. This is even true, if some noise is added to the pressure and flow rate curves.

In the final chapter of Part I, we consider the simulation of a pipeline system with an integrated pump and a surge reduction system (SRS). As it has been described in Section 1.2.1 a 1D-0D coupled model similar to the one considered in the previous chapters has been used for this purpose. Thereby, the 1D model is used to simulate flow in the pipeline vessels. For the pump and the SRS, 0D models in the form of ODE systems are used. The 1D model has again the form of a hyperbolic PDE-system of first order, however its flux function is linear in its unknowns contrary to the 1D blood flow model. Therefore it is easier to handle as the blood flow model. Using the dimensional reduced model we have studied the impact of hydraulic wave shocks [72, 78], which typically occur when a valve is closed or when pumps are started or stopped [137, 151]. It has been revealed that a hydraulic wave shocks causes an overpressure within the pipeline, which might lead to the rupture of the pipeline wall. For this reason a pipeline has to be equipped with overpressure protection systems. Typical protection systems are relief valves [10, 47], gas accumulators or air chambers [133]. Relief valves are forced to open when pressure in the pipe exceeds a pre-set value allowing oil to flow from the main pipeline to the relief tank, while gas accumulators are used to reduce the increase of pressure.

In this chapter, an advanced type of protection system called SRS (surge reduction system) [93] is examined. A SRS combines relief valves and gas accumulators. However, contrary to a pure pressure relief valve, maintaining a constant pressure value in the pipe, a SRS is used to control the steepness of a pressure wave front. This is achieved by using a specifically constructed pilot operated relief valve with its control pipe connected to a gas accumulator. The gas accumulator dumps the rate of change of pressure difference on the sides of the relief valve, thus the valve is linked with the pressure change rate in the main pipe rather than to the pressure absolute value. An operation of a SRS resembles the operation of a gas accumulator reducing the speed of pressure increase. At the same time, a gas accumulator usually consists of a large vessel filled with pressurised gas, whereas a SRS uses significantly smaller gas vessels in order to control the pressure wave gradient. A new aspect related to other works [9, 93] in this field, is the comparison of simulation data and field data taken upstream and downstream of a pumping station with a SRS. This pumping station is part of a pipeline connecting a marine terminal located on the shore of the Black Sea with a production site at the Caspian Sea.

For the numerical discretisation of the PDE systems, two different discretisation methods are tested: The first method is a combination of a stabilised discontinuous Galerkin (DG) method in space and an explicit, third order and strong-stability-preserving Runge-Kutta scheme in time [63, 88] (SSP-scheme), where we denote the degree of the polynomial basis

by p . The other solution method is the numerical method of characteristics [59, 151]. Studying both a higher order method (DG-method) and a robust lower order method, it is intended to show, to what extent the usage of a higher order method pays off in terms of accuracy and computational effort for the respective PDE-systems. Our numerical results reveal that both methods can emulate the field data with a sufficient accuracy. Thereby, we have used the same number of grid nodes for the method of characteristics as degrees of freedom for the DG-method. Denoting the number of elements for the DG-method by N_h , the number of degrees of freedom is given by: $(p + 1) \times N_h$. However, the numerical method of characteristics proved to be much more efficient as the DG-method due to the fact that the SSP scheme exhibits a CFL-condition that is very restrictive related to the admissible time step size.

1.3.2 Part II: Simulation of blood flow in microvascular networks

This part consists again of three different chapters. While the first two chapters contain mathematical analysis of issues arising in the context of models for blood flow in microvascular networks, the third chapter presents new modelling ideas for blood flow in microvascular networks.

Related to the 3D-1D coupled blood flow model given by (1.20a) and (1.20b), one can formulate an elliptic model problem [28, Chapter 5]. Doing so, the solution variables p_t and p_v are renamed by u_{3D} and u_{1D} , respectively. Neglecting the osmotic pressures, introducing new constants K_{1D} and K_{3D} for the permeabilities, setting $\rho_{\text{int}} = 1$ and defining

$$\beta = 2\pi RL_p,$$

we obtain the following 3D-1D elliptic model problem:

$$-\frac{\partial}{\partial s} \left(K_{1D} \frac{\partial u_{1D}}{\partial s} \right) = \beta (\bar{u}_{3D} - u_{1D}) \quad \text{on } \Lambda, \quad (1.29a)$$

$$-\nabla \cdot (K_{3D} \nabla u_{3D}) = \beta (u_{1D} - \bar{u}_{3D}) \delta_{\Lambda} \quad \text{in } \Omega. \quad (1.29b)$$

$\Omega \subset \mathbb{R}^3$ is a bounded, open and convex domain with a piecewise smooth boundary and $\Lambda \subset \Omega$ is a C^2 -curve. As the source term of (1.29b) contains a Dirac measure concentrated on a 1D curve, the 3D solution u_{3D} exhibits a singularity along the curve Λ [29]. This raises different issues in the context of mathematical analysis as well as numerical discretisation. It can be revealed that $u_{3D} \in L^2(\Omega)$. However, it can be shown that $u_{3D} \notin H^1(\Omega)$. Therefore, non-standard Sobolev spaces are required to show existence and uniqueness of solutions. In [28, Chapter 4], it is demonstrated how weighted Sobolev spaces $H_{\alpha}^1(\Omega)$ can be used to tackle this issue. For $-1 < \alpha < 1$, these spaces are defined as follows:

$$H_{\alpha}^1(\Omega) = \left\{ u \in L_{\alpha}^2(\Omega) \mid d^{\alpha} \nabla u \in [L^2(\Omega)]^3 \right\} \quad \text{and} \quad L_{\alpha}^2(\Omega) = \left\{ u : \Omega \rightarrow \mathbb{R} \mid d^{\alpha} u \in L^2(\Omega) \right\},$$

where $d(x)$ represents the distance function for an arbitrary point $x \in \Omega$ to the curve Λ . Considering literature on convergence theory for standard finite elements [19, 70], it becomes obvious that the reduced regularity of u_{3D} deteriorates the convergence behaviour of this numerical solution technique. A way to circumvent this drawback is to use locally refined meshes (graded meshes) around Λ . By this, the huge gradients in the vicinity of Λ can be resolved in a more accurate way. In case of a Poisson problem with a source term

concentrated on a straight line Λ , which can also be considered as a 2D Poisson problem with a point source (see Figure 1.19), it is possible to show a quasi optimal convergence order with respect to the L^2 -norm [8] and an optimal convergence order for weighted Sobolev spaces [29]. Another way to deal with the singularity is to split the solution in a singular component and a smooth part. Thereby, the singular component accounts for the Dirac source term, whereas the smooth part incorporates boundary conditions and possible smooth correction terms. If an explicit representation of the singular part is known (e.g. for a straight line or piecewise straight lines), the elliptic differential operator can be applied to it in a weak sense and integrated into the right hand side. It remains to solve a standard elliptic PDE with a source term in $L^2(\Omega)$ [60]. In the first chapter of Part II, we investigate the local convergence behaviour of standard finite element methods on domains excluding a cylinder around the singularity, where only quasi-uniform meshes are used to discretise the domain Ω . This is motivated by the fact that the 3D solution u_{3D} in (1.29a) and (1.29b) is of higher interest in a domain excluding cylinders of radius R around Λ , since the space is occupied by the vascular system there. Therefore, u_{3D} or in real applications the tissue pressure p_t is of little interest there. The reason, why we are interested in quasi-uniform meshes is that we want to avoid an expensive adaptive meshing if a complex network structure is used. For this purpose, we examine in Chapter 5 the following elliptic model problem with a line source term (Dirac measure concentrated on a C^2 -curve):

$$-\Delta u = \delta_\Lambda \text{ in } \Omega, \quad u = 0 \text{ on } \partial\Omega. \quad (1.30)$$

The local L^2 -error e_h related to (1.30) is measured on the domain Ω excluding a cylinder Z_R around Λ :

$$e_h = \|u - u_h\|_{L^2(\Omega \setminus Z_R)}, \quad Z_R = \{x \in \Omega \mid d(x) < R\},$$

where u_h represents the linear finite element approximation. Related to the error e_h , we show that bounding e_h can be reduced to estimating the pointwise finite element error on Λ for a dual problem derived from (1.30). In order to estimate the $L^\infty(\Lambda)$ -error for the dual problem a further auxiliary problem is introduced. This auxiliary problem has the form of a Poisson equation with a Dirac right hand side concentrated on a point $x \in \Lambda$. After deriving a weak formulation of this auxiliary problem, the finite element error of the dual problem can be used as a test function. By this, we obtain an equation for the dual error at $x \in \Lambda$. Finally, an optimal upper bound of the left hand side of this equation can be derived using estimates presented in [86, 118]. The theoretical findings are supported by numerical simulations. Thereby, we observe that the pre-asymptotic range grows as the radius R of the cylinder Z_R is decreasing. If the meshsize of the uniform discretisation mesh is below R , an optimal convergence of second order can be observed.

The reduced regularity and convergence order of finite element methods applied to (1.29b), motivate the development of an alternative coupling concept. Deriving the 3D-1D coupled model (1.20a) and (1.20b), the pressure in the vascular system is first averaged across the section area of the vessels and then concentrated on the midaxes of the corresponding vessels. Therefore a line source term occurs in the in the right hand side of (1.20b) and (1.29b).

In Chapter 6 we demonstrate how the usage of a line source term within the 3D problem can be circumvented. The new coupling concept, that is investigated in this chapter is based on the observation that the exchange process between the vascular system and the surrounding tissue matrix occurs across the vessel surface. For this reason, it is reasonable to concentrate the source term in (1.20b) or (1.29b) on the vessel surfaces. In order to

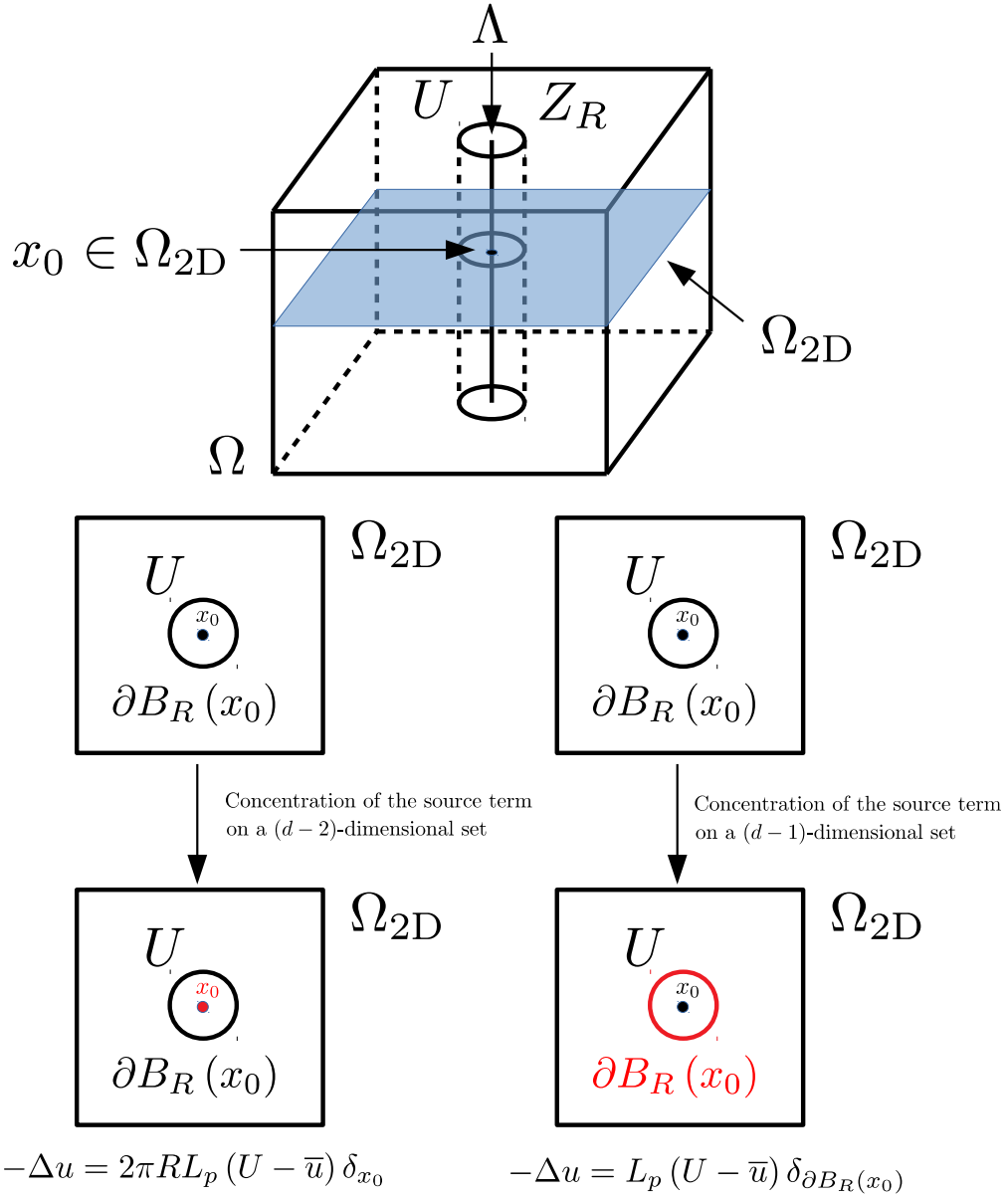


Figure 1.19: Derivation of a 2D model problem from a 3D problem with a straight line Λ . There are two possibilities for coupling the lower dimensional model having a solution U with the higher dimensional model. One is to restrict the source term on a line Λ or a point x_0 . Another one is to concentrate the source term on the surface of a cylinder Z_R or a circle line $\partial B_R(x_0)$.

simplify the analysis of this new coupling concept, we assume that Λ is a single straight line and that the solution u_{1D} of (1.29a) is constant on Λ and equal to U (see Figure 1.19). Fixing a 2D slice Ω_{2D} perpendicular to Λ , it can be shown that (1.29b) can be reduced to the following 2D model problem [28]:

$$-\Delta u = 2\pi R L_p (U - \bar{u}) \delta_{x_0} \text{ in } \Omega_{2D}, \quad u = 0 \text{ on } \partial\Omega_{2D}, \quad (1.31)$$

where $K_{3D} \equiv I$ and $x_0 \in \Omega_{2D} \subset \mathbb{R}^2$ marks the location of the straight line within the 2D slice Ω_{2D} . Applying the new coupling idea, the source term is not concentrated on the

midaxis Λ or the point x_0 , but on the circle line $\partial B_R(x_0) \subset \Omega_{2D}$. By this, (1.31) can be reformulated as follows:

$$-\Delta u = L_p (U - \bar{u}) \delta_{\partial B_R(x_0)} \text{ in } \Omega_{2D}, \quad u = 0 \text{ on } \partial\Omega_{2D}. \quad (1.32)$$

Another way to derive model problem (1.32) is to consider in a first step the following elliptic problem:

$$\begin{aligned} -\Delta u_{\text{ref}} &= 0 \text{ in } \Omega_p = \Omega_{2D} \setminus B_R(x_0), \\ u_{\text{ref}} &= 0 \text{ on } \partial\Omega_{2D}, \quad -\nabla u_{\text{ref}} \cdot \mathbf{n} = L_p (U - u) \text{ on } \partial\Omega_p \setminus \partial\Omega_{2D}, \end{aligned} \quad (1.33)$$

where the vector \mathbf{n} denotes the outer normal on $\partial\Omega_p$ and Ω_p stands for the porous tissue matrix excluding the vascular system. (1.33) can be considered as a reference problem, representing the standard coupling concept between a 3D vascular system and the tissue matrix Ω_p . Contrary to the previous coupling concepts, the tissue matrix is not identified with the whole domain Ω or Ω_{2D} . Moreover the coupling between the vascular system and the tissue matrix is based on a Neumann boundary condition, while in (1.31) or (1.32) the coupling is based on source terms and averaged quantities. A weak formulation of (1.33) is given by:

$$(\nabla u_{\text{ref}}, \nabla v)_{\Omega_p} + L_p (u_{\text{ref}}, v)_{\partial B_R(x_0)} = L_p \cdot U \cdot \int_{\partial B_R(x_0)} v \, dS, \quad \forall v \in V(\Omega_p). \quad (1.34)$$

Please note that in the above equation, the standard notation for the L^2 -inner product is used. The function space $V(\Omega_p)$ is defined as follows:

$$V(\Omega_p) = \{v \in H^1(\Omega_p) \mid v|_{\partial\Omega_{2D}} = 0\}.$$

The idea to further simplify the weak formulation (1.34) is based on splitting u_{ref} and the test functions v on $\partial B_R(x_0)$ into their mean values and fluctuations:

$$w|_{\partial B_R(x_0)} = \bar{w} + \tilde{w}, \quad w \in \{u_{\text{ref}}, v\}.$$

By this and (1.34), we obtain:

$$(u_{\text{ref}}, v)_{\partial B_R(x_0)} = \int_{\partial B_R(x_0)} u_{\text{ref}} v \, dS = 2\pi R \bar{u}_{\text{ref}} \bar{v} + \int_{\partial B_R(x_0)} \tilde{u}_{\text{ref}} \tilde{v} \, dS.$$

Taking into account that the crosssection areas of blood vessels in microvascular networks are small, we make two basic modelling assumptions:

1. The domain Ω_p can be identified with the entire domain Ω_{2D} .
2. The product of the fluctuations is small: $\int_{\partial B_R(x_0)} \tilde{u}_{\text{ref}} \tilde{v} \, dS \approx 0$.

Based on these assumptions, the following variational problem can be formulated: Find $u_{\text{red}} \in H_0^1(\Omega_{2D})$ such that:

$$(\nabla u_{\text{red}}, \nabla v)_{\Omega_{2D}} + 2\pi R \cdot L_p \cdot \bar{u}_{\text{red}} \cdot \bar{v} = 2\pi R \cdot L_p \cdot U \cdot \bar{v}, \quad \forall v \in H_0^1(\Omega_{2D}). \quad (1.35)$$

On closer examination, it is revealed that (1.35) is a weak formulation of (1.32). This means that the reduced problem (1.32) can be derived from the reference problem (1.33)

by considering the assumptions from above. Concerning the well posedness of (1.35), we have shown that this variational problem exhibits a unique solution in $H_0^1(\Omega_{2D})$. Moreover it can be proved that

$$u_{\text{red}} \in H_0^1(\Omega_{2D}) \cap H^{\frac{3}{2}-\epsilon}(\Omega_{2D}), \quad \epsilon > 0,$$

which implies that the weak formulation of (1.32) exhibits a higher regularity as the weak formulation corresponding to problem (1.31). Due to the point source term, the weak solution of (1.31) is not even contained in $H_0^1(\Omega_{2D})$. This is in accordance with the fact that a Dirac measure concentrated on a manifold of co-dimension 1, like a circle $\partial B_R(x_0) \subset \Omega_{2D}$, induces less roughness into a solution as a Dirac measure concentrated on a manifold of co-dimension 2 like $x_0 \in \Omega_{2D}$ or $\Lambda \subset \Omega$ [62].

Besides issues concerning well posedness and regularity of solutions, it is of high interest, to estimate the modelling errors caused by the modelling assumptions 1 and 2. For this purpose, we study the error $e = u_{\text{ref}} - u_{\text{red}}|_{\Omega_p}$ on Ω_p . According to the modelling assumptions 1 and 2, the total error e can be decomposed into two error components which can be estimated separately. We show that it holds for the modelling error e :

$$\|e\|_{H^1(\Omega_p)} \leq C_1 U L_p \cdot R |\ln R|^{\frac{1}{2}} + C_2 U L_p^2 \cdot R^2 |\ln R|^{\frac{1}{2}},$$

where the constants C_1 and C_2 are independent of R , L_p and U . Thereby, the first summand quantifies the error caused by modelling assumption 1, while the second summand represents an upper bound for the error arising due to modelling assumption 2. Considering the upper bound for the H^1 -norm of error e , it can be concluded that the modelling error e is small, if the radius R is small, which is a further attractive feature of this coupling concept. This observation is supported by a numerical test.

A further issue that is discussed in Chapter 6 is the numerical discretisation of elliptic problems like (1.32). Considering the structure of corresponding solutions, it is revealed that they do not exhibit singularities like the solutions of (1.31), but kinks are visible along the circle lines $\partial B_R(x_0)$. Due to that, we have shown that a standard finite element method converges both in the H^1 -norm and L^2 -norm. However, the convergence rates for standard quasi-uniform meshes are still sub-optimal i.e. around 1.0 for the L^2 -norm and 0.5 for the H^1 -norm. Optimal convergence orders can be obtained using again graded meshes i.e. locally refined meshes or quasi-uniform triangulations in which the edges of the triangles that are intersected by $\partial B_R(x_0)$ form a linear interpolant of $\partial B_R(x_0)$ [90].

Chapter 6 is concluded by solving a 3D-1D coupled model problem based on the geometry of a small microvascular network. Thereby, the 1D problem and the 3D problem are coupled by means of the new coupling concept that has been investigated in the previous sections of the chapter.

Considering the microvascular network in Figure 1.4 it can be observed that even a small tissue block of 2.0 mm^3 contains a huge number of capillaries and some arterioles. If one is interested in simulating larger parts of an organ even a 1D resolution of the whole vascular system would cause an enormous amount of data. Furthermore, it can be observed quite often that a reconstruction of microvascular networks from image data exhibits many segmentation errors, such that even a 1D graphlike network can not be composed. In such cases, it is necessary to use instead of the fully-discrete 3D-1D coupled flow models, a 3D-3D-1D coupled flow model (see Section 1.2.2). Using the 3D-3D-1D modelling approach, besides the tissue also the fine scale parts of the microvasculature are converted into a porous structure (dual continuum model), while flow processes within the larger vessels are still modelled by 1D Poiseuille type equations.

In Chapter 7, this modelling approach is outlined in detail. As a first step, we describe how the permeability tensor for the finescale network parts are computed. In this context we have decided to restrict ourselves to diagonal tensors, since according to [41], the off-diagonal entries of the resulting tensors are on average two orders of magnitude smaller than the diagonal terms [41, Table 2]. Next we explain, how pressure boundary conditions for the homogenised capillary structure can be computed from the given data. The most important part of this section is concentrated on the issue how to connect the different compartments of the 3D-3D-1D model. Contrary to existing works in this field [105, 128] we do not place point sources at the outlets or inlets of the 1D vessels, but we compute the fluxes between the larger vessels and the capillary bed by means of pressure differences, weighted by an averaged permeability of the blood flow paths in the capillary bed and divided by the length of these blood flow paths. However, the permeabilities and lengths of these blood flow paths are hard to determine from the given data. Therefore a weighting parameter is introduced, which can be used to calibrate the ratio of these parameters such that the total mass fluxes provided by the fully-discrete 3D-1D flow model can be reproduced. For the double-continuum approach modelling flow in the homogenised capillary bed and tissue, Starling's law is used, however, contrary to the fully-discrete 3D-1D model, it is incorporated into the model based on volume source terms. The numerical solution is obtained by means of cell-centered finite volumes for the 3D equations and a simple box method (or vascular graph model) [115]. The reason for this is that these methods are locally mass conservative and robust, if they are applied to segmented image data.

The section containing the numerical tests, begins with a justification of the choice of the threshold R_T separating the capillary bed from the larger vessels. It can be observed that $R_T = 7.0 \mu\text{m}$ is a reasonable choice for separating the different scales that can be detected in the given microvascular network (see [115]). On closer examination this threshold marks essentially the limit between arterioles and the capillary bed (see [42, Table 1]). Afterwards, it has been determined how the size of a REV for the capillary bed has to be chosen, such that the averaged porous media parameters like the porosity and the permeabilities are representative. It turns out that the $1 \text{ mm} \times 1 \text{ mm} \times 2 \text{ mm}$ cube containing the network should be decomposed into 8 cubes having the dimensions $0.5 \text{ mm} \times 0.5 \text{ mm} \times 1 \text{ mm}$. In the further subsections, we have investigated the how well the mass fluxes into and out of the system can be determined by means of the 3D-3D-1D coupled model. Thereby, we demonstrate that there is an optimal choice for the parameter controlling the fluxes between the larger vessels and the homogenised capillary bed, such that the mass fluxes into the large vessels can be approximated in an accurate way. However, it turns out that the choice of this parameter is very sensitive with respect to the pressure boundary conditions of the larger vessels. This means that the addressed parameter has to be calibrated even if the boundary conditions are changing, which is a certain drawback of the proposed model. The pressures averaged with respect to the REVs differ at most 22 % from the fully-discrete model. Despite of these deviations and the fact that a free parameter has to be calibrated, the new 3D-3D-1D approach can reduce the complexity and several uncertainties. This might open up the possibility to simulate larger parts of an organ in an efficient way, in particular if besides the pure flow problem transient transport problems have to be simulated or parameter estimations have to be performed.

1.3.3 Part III: Simulation of fluid injection into porous media

The last two chapters of this thesis are concerned with the analysis of 1D two-phase flow equations modelling fluid injections into porous media. As it has been pointed out in the last part of Subsection 1.2.2, there are different phenomena occurring in the context of fluid injections into porous media. Considering experimental data (see Chapter 8 and 9), it can be seen that the saturation profiles of the wetting phase form overshoots, which expand to plateaus as the fluid front moves deeper into the porous medium. Having the modelling techniques described in Subsection 1.2.2 at hand we want to investigate by analytical and computational means, what type of saturation profiles can be produced by these modelling techniques.

In the first chapter of Part III, we focus on analysing the shape of a given saturation plateau. Our goal is to find out, under which conditions such a plateau restores its given shape and which parameters have to be chosen such that the length of the plateau is enlarged or enshrunked. In particular, the latter case is of high interest, since it is not clear a priori, what happens after a plateau vanishes. A new plateau could be formed or a simple shock could remain. The formation process of an overshoot is not subject of this chapter, which means that the τ -term (1.28) is not considered in this chapter. Investigating the stability of saturation plateaus two different types of models are considered. For the first model, we have assumed that the sum of both phase velocities v_n and v_w is equal to a constant total velocity v in space:

$$v(t) = v_n(z, t) + v_w(z, t), \quad z \in (0, L), \quad t > 0, \quad (1.36)$$

where L indicates the length of the interval $[0, L]$ our 1D two-phase flow models are defined on. This assumption is particularly useful for experiments, in which a pump injects a fluid with a constant total velocity v into the porous medium. In this case v is known and can be controlled experimentally. A plateau is generated by means of transient Dirichlet boundary conditions at the inlet $z = 0$:

$$S_w(z = 0, t) = \begin{cases} S_w^P, & t \leq 500 \text{ s}, \\ S_w^{in}, & t > 500 \text{ s}. \end{cases} \quad (1.37)$$

In (1.37) S_w^P marks the top level of the plateau. The saturation on the left hand side of the plateau is given by S_w^{in} and on the right hand side it is denoted by S_w^{out} . S_w^{out} is identical to the initial condition for S_w .

Based on (1.36), the two-phase flow equations (1.22) and (1.23) can be simplified to a *fractional flow equation*. The name of this PDE is motivated by the fact that it contains only the saturation variable S_w for the wetting phase and no variable of the non-wetting phase:

$$\frac{\partial S_w}{\partial t} + \frac{v(t)}{\phi} \frac{\partial}{\partial z} \left[f(S_w) - D(S_w) \frac{\partial S_w}{\partial z} \right] = 0. \quad (1.38)$$

The function f in (1.38) is called *fractional flow function* and is defined by:

$$f(S_w) = \frac{1 + k_{rn}(S_w) \frac{\rho_w g K}{v \mu_n} \left(1 - \frac{\rho_n}{\rho_w} \right)}{1 + \frac{\mu_w}{\mu_n} \frac{k_{rn}(S_w)}{k_{rw}(S_w)}},$$

while the second function D represents the diffusion function of the system:

$$D(S_w) = -\frac{k_{rw}(S_w) \frac{K}{v\mu_w} p'_c(S_w)}{1 + \frac{\mu_n}{\mu_w} \frac{k_{rw}(S_w)}{k_{rn}(S_w)}}.$$

Provided that the total velocity v is given, we obtain:

$$\frac{\partial p_n}{\partial z} = \frac{\lambda_w}{\lambda_{to}} \left(\frac{\partial p_c(S_w)}{\partial z} + \rho_w g \right) + \frac{\lambda_n}{\lambda_{to}} \rho_n g - \frac{v(t)}{\lambda_{to} K},$$

where the mobilities λ_α are defined as follows:

$$\lambda_\alpha = \frac{k_{r\alpha}}{\mu_\alpha}, \quad \alpha \in \{w, n\} \quad \text{and} \quad \lambda_{to} = \lambda_w + \lambda_n.$$

As a second model, we consider the 1D versions of (1.22) and (1.23). In order to obtain comparable results, we have chosen for $z = L$ a Neumann boundary condition incorporating the total velocity v into the standard two-phase flow model:

$$\left. \frac{\partial}{\partial z} p_n(z, t) \right|_{z=L} = \frac{g}{\lambda_{to}} \left(\lambda_w \rho_w + \lambda_n \rho_n - \frac{v}{gK} \right), \quad t > 0.$$

Within both models the transition between the main imbibition and drainage curves is computed by means of cubic splines in order to ensure a smooth transition between the two processes.

In order to analyse the stability of a saturation plateau generated by (1.37), we observe in a first step that such a plateau can be considered as a composition of a imbibition wave determining the first front and a drainage wave representing the second front. Next the velocities of both fronts are estimated. Thereby, we assume that the diffusive term is dominated by the convective term:

$$D \frac{\partial S_w}{\partial z} \ll f, \tag{1.39}$$

which means that (1.38) can be regarded as a Buckley-Leverett-type equation. The basic idea to analyse the stability of saturation overshoots is to approximate the travelling wave profile with piecewise constant functions [74]. By this, the approximated profile can be considered as a superposition of two Buckley-Leverett shock fronts [74]. At the imbibition and drainage discontinuities the Rankine-Hugoniot condition [46, Section 3.4.1] allows us to estimate the velocity of imbibition and drainage front [74, Section 4.2]. The stability of the overshoot region is preserved if the velocities of the imbibition and drainage front are equal. Otherwise, the overshoot region grows or shrinks.

For a computational analysis we use in case of the fractional flow formulation (1.38) the open source CFD-software OpenFOAM [79, 146]. Thereby, a constant total velocity v is assumed and only equation (1.38) is solved by numerical means. The implementation of the numerical solution scheme is based on an explicit discretisation scheme for the convective part, which is described by the flow function f . For the diffusive part, which is governed by the function D an implicit discretisation scheme is considered [74, Section 5.2]. For the solution of the non-linear systems of equations arising in each time step, a Newton solver is

used. Due to that the scanning curves between the main imbibition and drainage curves are approximated by cubic splines. By this, a smooth transition is ensured and the convergence of the Newton solver is not deteriorated.

The numerical solution of the second model is carried out by means of the software package DuMuX [144], where the abbreviation DuMuX stands for the term DUNE for Multi-Phase, Component, Scale, Physics, ...}. This software package is a free and open-source simulator for flow and transport processes in porous media [52] based on the modular PDE-toolbox DUNE (Distributed and Unified Numerics Environment, [12]). The discretisation method implemented in DuMuX uses the Implicit Euler method for the time integration. For the spatial discretisation the standard cell-centered Finite Volume method is considered in case of both models.

In the section on numerical tests, the inlet saturation S_w^{in} is varied resulting in different shapes and propagation speeds for the saturation plateaus. Doing so, we can identify isolated values for which the plateaus remain stable. For all the other choices of S_w^{in} the plateau is growing or enshrinking. Comparing the analytical and numerical predictions, it can be noticed that they coincide very well. Even the formation of a second plateau after the original plateau has been vanished, can be predicted by both analysis tools. The numerical results produced by the fractional flow model and the pressure saturation formulation are also close together, which means that both models yield the same predictions on the qualitative behaviour of the saturation plateaus.

In the second chapter of Part III, we use as in the first chapter the fractional flow formulation to study the behaviour of water saturation fronts for two phase flow in a homogeneous porous medium. The only difference is that the transition between the main drainage and imbibition curves is described by means of a play-type hysteresis model, approximating the scanning curves as constant saturation lines. Moreover, we replace the transient boundary condition (1.37) by a constant Dirichlet value. In order to generate the saturation overshoots, the τ -term expansion (1.28) is combined with a PDE similar to the fractional flow formulation (1.38).

All in all, we obtain a mathematical model in the following dimensionless form:

$$\frac{\partial S}{\partial t} + \frac{\partial}{\partial z} \left(F(S, p) + N_c h(S, p) \frac{\partial p}{\partial z} \right) = 0 \text{ with } F = f + N_g h, \quad (1.40a)$$

$$\frac{\partial S}{\partial t} = \frac{1}{\tau} \mathcal{F}(S, p) := \frac{1}{\tau} \begin{cases} p_c^{(d)}(S) - p & \text{if } p > p_c^{(d)}(S), \\ 0 & \text{if } p \in [p_c^{(i)}(S), p_c^{(d)}(S)], \\ p_c^{(i)}(S) - p & \text{if } p < p_c^{(i)}(S), \end{cases} \quad (1.40b)$$

where the saturation S_w is now denoted by S and p_c has been replaced by p . The fractional flow function F and the diffusion function h include all the relative permeabilities and capillary pressure functions. N_g and N_c are dimensionless numbers which are referred to as gravity and capillary numbers. As the names suggest, they incorporate besides some other parameters the gravity constant as well as a reference pressure for the capillary pressure.

Analysing this mathematical model, we do not drop the condition (1.39), but we consider the solution of (1.40a) as a viscous approximation of the hyperbolic Buckley-Leverett equation with gravity. Thereby the velocities of the saturation fronts are not estimated by a Rankine-Hugoniot condition. In this case, we transfer the model to an ODE-system. For this purpose, we assume that (1.40a) is defined on \mathbb{R} with respect to the spatial variable z .

Next the following transformation of coordinates is performed:

$$S(z, t) = S(\xi), \quad p(z, t) = p(\xi), \quad \text{with } \xi = ct - z.$$

$c \in \mathbb{R}$ indicates a wave-speed. This type of transformation is called travelling wave formulation, where we demand that the following holds:

$$\begin{cases} \lim_{\xi \rightarrow -\infty} S(\xi) = S_B, & \lim_{\xi \rightarrow \infty} S(\xi) = S_T, \\ \lim_{\xi \rightarrow -\infty} p'(\xi) = \lim_{\xi \rightarrow \infty} p'(\xi) = 0. \end{cases} \quad (1.41)$$

In (1.41), S_B corresponds to the initial saturation and S_T to the injected saturation. Performing some calculations we obtain the following ODE-system (dynamical system):

$$(TW) \begin{cases} S' = \frac{1}{c\tau} \mathcal{F}(S, p), & (1.42a) \\ p' = \mathcal{G}(S, p), & (1.42b) \end{cases}$$

where

$$\mathcal{G}(S, p) := \frac{1}{h(S, p)} (F(S, p) - \ell(S)) \quad \text{with } \ell(S) = F(S_B, p_B) + c(S - S_B). \quad (1.43)$$

p_B is the initial pressure. The remainder of Chapter 9 is concerned with the analysis of the dynamical system (1.42a)-(1.42b). In particular, we identify equilibrium points of this system and study the local behaviour in the vicinity of these points. A further important issue that has been investigated is the identification of orbits or curves connecting the equilibrium points. By this, one can study, which types of solutions can be represented by the model at hand. Concerning the functions F and h , two different scenarios are investigated separately:

- **Scenario A:** No hysteresis in the permeabilities is considered and F is monoton.
- **Scenario B:** Hysteresis is considered both for the permeabilities and the capillary pressure.

For each scenario, entropy solutions of the corresponding Riemann problems are presented. Moreover it is shown, how the parameter τ and S_T have to be chosen such that an overshoot occurs and a plateau can be formed. Our theoretical findings are supported by means of numerical tests in the last sections of this chapter.

Part I

Simulation of flow processes in macroscale networks

The first part of this thesis consists of three chapters that are based on different journal articles. Every article is concerned with 1D-0D coupled models for flow problems in pipeline systems or in arterial blood vessel systems that are part of the macrocirculation. The basis of the 1D-0D modelling concept is based on a domain decomposition approach. Thereby, the pipeline or the blood vessel network is decomposed into its different tubes or blood vessels. Flow processes within a single tube or a blood vessel are modelled by 1D hyperbolic PDE systems. The term 0D-model indicates that e.g. the influence of the heart and the omitted microcirculation as well as pumps and overpressure protection systems are modelled by ODE systems i.e. by models, which exhibit a time variable but no space variable. At the corresponding interfaces, the 1D PDEs and the ODE systems (0D models) are coupled with each other to obtain a global solution in which the influences of the heart beats, omitted vessels, pumps or overpressure protection systems are contained.

Chapter 2:

Numerical modeling of compensation mechanisms for peripheral arterial stenoses

In the first chapter of Part I, we use the 1D-0D coupled blood flow model for macroscale arterial networks (see Subsection 1.2.1), to simulate the influence of a stenosis in the lower right leg. A stenosis having this feature, is called peripheral stenosis, since it is located far away from the center of the body. A peripheral stenosis is a typical vascular disease that is caused by smoking or bad diet. As the heart and the peripheral circulation, the stenosis is modelled by a 0D model. For our simulations, we use an arterial network whose data are published e.g. in [134]. In order to compensate the reduced blood flow caused by the stenosis, the human body exhibits different compensation mechanisms. As examples, we consider in Chapter 2 arteriogenesis and metabolic regulation. Arteriogenesis refers to the growth of collateral vessels redirecting blood flow around the stenosis, while metabolic regulation denotes the adjustment of the flow resistances of the peripheral blood vessels. We show, how the standard 1D-0D coupled model can be enhanced such that these compensation mechanisms can be integrated into the model. By means of this model, it is investigated whether the reduced blood flow can be compensated for a certain degree of stenosis. Thereby, we test both compensation mechanisms isolated from each other and combined with each other. It turns out that only a combination of both compensation mechanisms can restore the blood flow of a healthy blood vessel.

Chapter 3:

Numerical modelling of a peripheral arterial stenosis using dimensionally reduced models and machine learning techniques

The following chapter is concerned with the same issue that has been investigated in Chapter 2. However, contrary to the previous chapter, we do not consider any compensation mechanisms, but we simulate the pure influence of a stenosis with a certain degree. Therefore, pressure and flow rate curves over one heart beat are

reported at some places in the neighbourhood of the stenosis. Recalling the numerical effort that has been arising when many different stenosis degrees are considered, we decided to create a surrogate model mapping a stenosis degree to the curves reported around the stenosis. Thereby, the evaluation of the surrogate model should be very cheap such that the computational effort can be decreased remarkably. The goal is, to facilitate the performance of a parameter study like the one in Chapter 2. In order to construct such a surrogate model, we use a linear combination of kernel functions. The coefficients of this linear combination are determined by means of a Greedy algorithm and a huge amount of training data, which are produced by simulations. It is demonstrated that providing an increasing amount of training data, the error between the surrogate model and the exact simulations is decreasing monotonously. Finally, we use the surrogate model to solve inverse problems. Having some pressure and flow rate curves at hand, the surrogate model enables us to compute the degree of stenosis corresponding to these curves in a very efficient way.

Chapter 4:

Simulation of surge reduction systems using dimensionally reduced models

In the final chapter of Part I, we apply a 1D-0D modelling concept, to simulate the performance of overpressure protection systems for oil pipelines. In contrast to Chapter 1 and 2, the 1D hyperbolic PDE system is linear in its solution variables, since the interaction between flow and the deformation of the pipeline wall can be linearised. This is due to the fact that the walls consist of robust steel, which deforms only little in operation. Using ODE systems, we describe the influences of a pump and safety systems and use the resulting solutions to provide boundary conditions for the 1D subproblems. There are several overpressure protection systems like relief valves opening if a certain pressure threshold in the pipeline is exceeded. In Chapter 4, a more advanced protection system is investigated. It is referred to as surge reduction system (SRS), since its relief valves open based on a pressure difference between the pipeline pressure and the pressure in a gas accumulator attached to the relief valve. By this, not only the pipeline pressure is controlled, but also its surge within the pipeline system. This is crucial since a slow increase of pressure implies a slow filling of an auxiliary tank that is attached to a relief valve. This provides more time for a pipeline operator to react and use eventually other means to decrease the pressure within the pipeline. Our numerical tests demonstrate the importance of a SRS. In addition to that, we compare our numerical results to some field data.

2 Numerical modeling of compensation mechanisms for peripheral arterial stenoses

Bibliographic note: The content of this chapter is based on the following original article: D. Driszga, T. Köppl, R. Helmig and B. Wohlmuth (2016): Numerical modeling of compensation mechanisms for peripheral arterial stenoses. *Computers in Biology and Medicine*, 70, pages: 190-201, with courtesy of Elsevier.



Numerical modeling of compensation mechanisms for peripheral arterial stenoses



D. Drzisga^{a,*}, T. Köppl^{b,*}, U. Pohl^{c,1,2}, R. Helmig^b, B. Wohlmuth^a

^a Institute for Numerical Mathematics, Technische Universität München, Boltzmannstr. 3, D-85748 Garching b. München, Germany

^b Department of Hydromechanics and Modelling of Hydrosystems, University of Stuttgart, Pfaffenwaldring 61, D-70569 Stuttgart, Germany

^c Walter-Brendel-Centre of Exp. Medicine, Ludwig-Maximilians-Universität, Marchionistr. 27, D-81377 München, Germany

ARTICLE INFO

Article history:

Received 20 October 2015

Accepted 14 January 2016

Keywords:

Reduced model

Peripheral stenosis

Arteriogenesis

Metabolic regulation

Numerical method of characteristics

ABSTRACT

The goal of this paper is to develop a numerical model for physiological mechanisms that help to compensate reduced blood flow caused by a peripheral arterial stenosis. Thereby we restrict ourselves to the following compensation mechanisms: Metabolic regulation and arteriogenesis, i.e., growth of pre-existing collateral arteries. Our model is based on dimensionally reduced differential equations to simulate large time periods with low computational cost. As a test scenario, we consider a stenosis located in the right posterior tibial artery of a human. We study its impact on blood supply for different narrowing degrees by the help of numerical simulations. Moreover, the efficiency of the above compensation mechanisms is examined. Our results reveal that even a complete occlusion of this artery exhibiting a cross-section area of 0.442 cm² can be compensated at rest, if metabolic regulation is combined with collateral arteries whose total cross-section area accounts for 8.14% of the occluded artery.

© 2016 Elsevier Ltd. All rights reserved.

1. Introduction

Mathematical models have become more and more important in many applications from medicine and biology [1,6,9,10,12,25,40]. Since these techniques are non-invasive, known physiological processes in the human body can be applied to clinical problems and used to predict the outcome with no risk for a patient. In this work, we are concerned with the simulation of blood flow from the heart through the arterial vessel system to the peripheral arteries, e.g., arteries in arms or legs. In particular, the impact of a stenosis in a peripheral artery on blood supply of distal organs is investigated.

A stenosis is an abnormal narrowing in a blood vessel caused by plaque made up of fat, cholesterol, calcium and other substances or, acutely, by a thrombus [23,36,43]. Due to pressure drops and reduced oxygen supply, caused by a peripheral stenosis, ischemia in distal tissue can result. In severe cases, it may be necessary to perform amputations, e.g., of legs or arms.

As a response to arterial occlusion, the human vascular system exhibits some compensation mechanisms helping to restore the reduced blood flow. Here, we focus on two different compensation mechanisms: metabolic regulation and arteriogenesis.

Metabolic regulation adjusts the resistance of the arterioles supplying the surrounding tissue domain in cases of elevated oxygen demands or hypoxia [33]. Depending on the metabolic demand of the tissue, the resistances of the corresponding arterioles are decreased or increased. This is achieved by muscles wrapped around the walls of the arterioles, which can reduce or enlarge the diameter of the corresponding vessels. This is a short term regulatory process which occurs within seconds.

Arteriogenesis indicates the growth and remodeling of pre-existent small vessels into physiologically relevant arteries. Usually, these vessels are interarterial connections which are present in almost all organs (see Figs. 1 and 2). In medical literature they are often referred to as collateral vessels. If an artery is partially or completely occluded their diameters can be enlarged significantly (up to 2.5 times). Thus, they can function as additional blood transport routes often preventing or limiting necrosis. Measurements in mice reveal that this process endures about 3 weeks [34,35].

Comparing both compensation mechanisms, it becomes obvious that they exhibit different time scales. For metabolic regulation and arterial blood flow it is important to resolve every heart beat, while in case of arteriogenesis, almost no change of the

* Corresponding authors.

E-mail addresses: drzisga@ma.tum.de (D. Drzisga), tobias.koeppel@iws.uni-stuttgart.de (T. Köppl), upohl@lmu.de (U. Pohl), rainer.helmig@iws.uni-stuttgart.de (R. Helmig), wohlmuth@ma.tum.de (B. Wohlmuth).

¹ DZHK (German Centre of Cardiovascular Research), partner site Munich Heart Alliance.

² Munich Cluster for Systems Neurology (SyNergy).

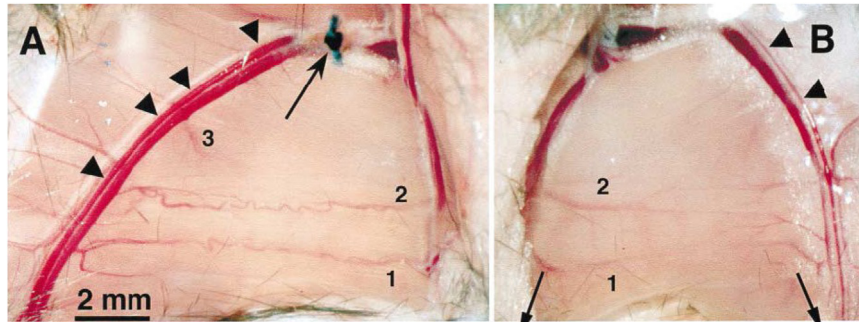


Fig. 1. Growth of three collateral vessels (numbered by 1–3) between two femoral arteries of a mouse. The right femoral artery is artificially occluded (black arrow labels a clamp; left). Femoral arteries from the non-occluded side of the same mouse (right) [35, Fig. 1].

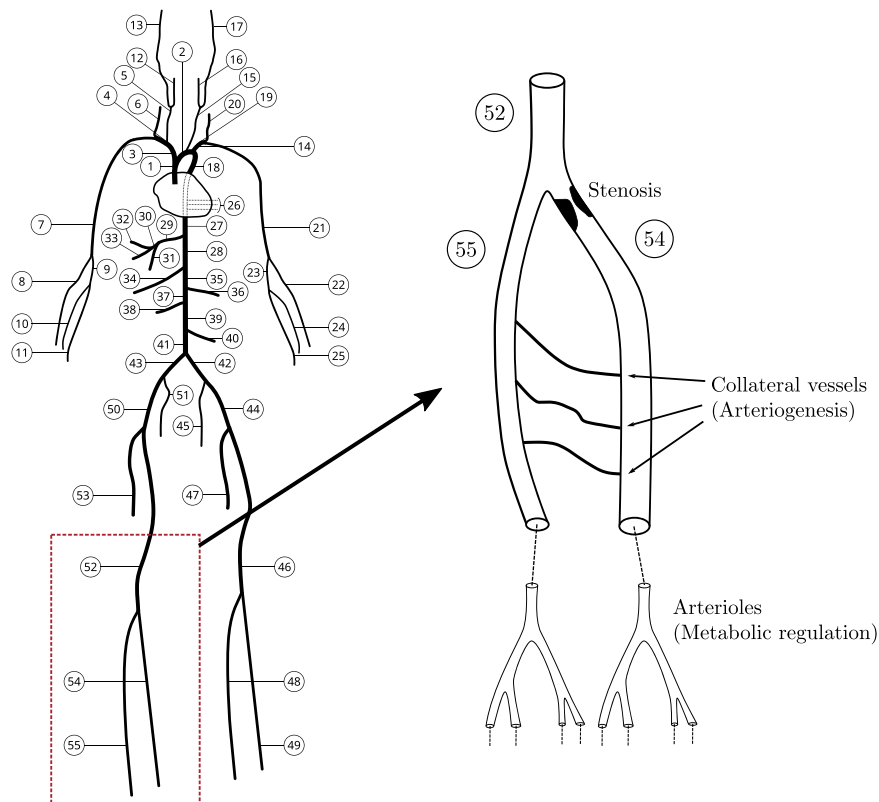


Fig. 2. Arterial vessel system consisting of the 55 main arteries [41,42] (left). In Vessel 54 we put a stenosis and study the effect on blood flow. In particular, we want to investigate, if the compensation mechanisms (metabolic regulation and arteriogenesis) can help to restore the reduced blood supply (right).

collateral vessels can be observed within the same time period. In order to couple the different processes, we design a time stepping scheme using macro time steps for the arteriogenesis and micro time steps for the fast processes. The simulation of metabolic regulation and arterial blood flow is based on dimensionally reduced, i.e., one-dimensional (1D) and zero-dimensional (0D) models, which can be derived by means of 1D mass and momentum balance equations [3,5,14,15,21,27]. The choice of these models is motivated by the intention to keep the computational costs low and to obtain simulation results faster. Besides the fact that the computational effort related to 1D models is low, some recent publications [17,30] reveal that quantities of interest, e.g., pressure and flow waveforms, can be computed with small deviations to numerical data obtained from 3D models.

We investigate numerically whether the previously described mechanisms can compensate a certain degree of stenosis. To do so, we consider an arterial network consisting of the 55 main arteries

(see Fig. 2). The effect of a peripheral arterial stenosis is studied by placing a stenosis of different degrees in the right posterior tibial artery (Vessel 54).

The rest of the paper is structured as follows: In Section 2, we present the mathematical models for arterial blood flow, stenoses and the compensation mechanisms. Section 3 contains our simulation results and a short comment on the efficiency of the considered compensation mechanisms.

2. Mathematical modeling

In this section, numerical models for arterial blood flow, the stenosis and the compensation mechanisms are presented. Moreover, we discuss the used numerical methods and the time stepping scheme.

2.1. Blood flow in a single vessel

The basis of our model is formed by a domain decomposition technique [13,15,29], i.e., in a first step we split the network (see Fig. 2) into its single vessels and assign a decoupled submodel to each vessel. Next, we interconnect the independent subsystems by suitable interface conditions. It is assumed that the arteries can be considered as simple compliant tubes.

Within a single vessel V_i , $i \in \{1, \dots, 55\}$, having the length l_i and the initial section area $A_{0,i}$, blood flow is governed by a 1D non-linear system of transport equations [4,5]:

$$\frac{\partial A_i}{\partial t} + \frac{\partial Q_i}{\partial z} = \phi_i, \quad z \in (0, l_i), \quad t > 0, \quad (1a)$$

$$\frac{\partial Q_i}{\partial t} + \frac{\partial}{\partial z} \left(\frac{Q_i^2}{A_i} \right) + \frac{A_i}{\rho} \frac{\partial p_i}{\partial z} = -K_r \frac{Q_i}{A_i}, \quad z \in (0, l_i), \quad t > 0, \quad (1b)$$

where A_i , Q_i and p_i denote the section area, average volumetric flux and pressure of the i -th vessel, respectively. ρ is the blood density. By z and t , we denote the space and time variable. The constant K_r is the friction force per unit length: $K_r = 22\pi\eta/\rho$, where η is the blood viscosity. The modeling assumptions leading to this choice of K_r are specified in [5]. The 1D Eqs. in (1a) and (1b) result from a cross section averaging of mass and momentum which is reasonable for medium-sized to large arteries [7].

A possible way to close this system is to provide an algebraic relation linking p_i and A_i :

$$p_i(z, t) = G_{0,i} \left(\sqrt{\frac{A_i}{A_{0,i}}} - 1 \right), \quad G_{0,i} = \frac{\sqrt{\pi} \cdot h_{0,i} \cdot E_i}{(1-\nu^2) \cdot \sqrt{A_{0,i}}}, \quad (2)$$

where E_i is the Young modulus, $h_{0,i}$ the thickness and ν the Poisson ratio of the vessel wall. Due to the fact that biological tissue is practically incompressible, ν is chosen as follows: $\nu = 0.5$. Eq. (2) assumes that the vessel wall is instantaneously in equilibrium with the forces acting on it. Effects like wall inertia and viscoelasticity could be incorporated using a differential pressure law, see, e.g., [15,19].

ϕ_i in (1a) is a term accounting for loss of blood volume across the vessel wall. This term is equal to zero for almost all vessels V_i except for the ones which are linked by the collateral vessels, i.e., in our case $i \in \{54, 55\}$ (see Fig. 2). In these cases the blood transfer between the vessels V_{54} and V_{55} is simulated by a suitable source or sink term (see Section 2.4).

Computing the characteristics of system (1a), (1b) and (2) shows that changes in A_i and Q_i are propagated by $W_{1,i}$ and $W_{2,i}$:

$$W_{1,i} = -\frac{Q_i}{A_i} + 4\sqrt{\frac{G_{0,i}}{2\rho}} \left(\left(\frac{A_i}{A_{0,i}} \right)^{\frac{1}{4}} - 1 \right) = -v_i + 4(c(A_i) - c(A_{0,i})), \quad (3a)$$

$$W_{2,i} = +\frac{Q_i}{A_i} + 4\sqrt{\frac{G_{0,i}}{2\rho}} \left(\left(\frac{A_i}{A_{0,i}} \right)^{\frac{1}{4}} - 1 \right) = +v_i + 4(c(A_i) - c(A_{0,i})). \quad (3b)$$

Under physiological conditions, it holds [14]:

$$v_i = \frac{Q_i}{A_i} \ll \sqrt{\frac{G_{0,i}}{2\rho}} \sqrt{\frac{A_i}{A_{0,i}}} = c(A_i). \quad (4)$$

Based on (4), one can show that $W_{1,i}$ is a backward and $W_{2,i}$ a forward traveling wave [7] [10, Chapter 2]. This insight is crucial for a consistent coupling of the submodels to obtain a global solution.

2.2. Incorporation of interface conditions

The hyperbolic system of transport equations provided by (1a), (1b) and (2) has to be equipped with suitable interface conditions at the endpoints $z=0$ and $z=l_i$.

At the inlet of the aorta (Vessel 1), we prescribe a periodical flow rate Q_{in} having a period of 1 s:

$$Q_{in}(t) = \begin{cases} 485 \frac{\text{cm}^3}{\text{s}} \cdot \sin\left(\frac{\pi}{T_s} \cdot t\right) & \text{for } 0 \leq t \leq T_s \\ 0 \frac{\text{cm}^3}{\text{s}} & \text{for } T_s < t \leq 1.0 \text{ s.} \end{cases} \quad (5)$$

T_s determines the duration of the systole. In this work, we choose it as follows: $T_s = 0.3$ s. Setting Q_{in} to zero in $(T_s, 1.0 \text{ s})$ results in a total reflector, simulating the closure of the aortic valve during the diastole [4]. Combined with the outgoing characteristic (3a), the equation for Q_{in} yields the required interface data for every time step.

Interface conditions for systems linked at a bifurcation can be derived by the principles of mass conservation and continuity of the total pressure. The total pressure for Vessel i is defined by:

$$p_{t,i} = \frac{1}{2\rho} \left(\frac{Q_i}{A_i} \right)^2 + p(A_i).$$

Indexing the vessels at a bifurcation by $\{I, II, III\} \subset \{1, \dots, 55\}$ as shown in Fig. 3, we have at a time t :

$$Q_I(l_I, t) = Q_{II}(0, t) + Q_{III}(0, t),$$

$$p_{t,I}(l_I, t) = p_{t,II}(0, t), \quad p_{t,I}(l_I, t) = p_{t,III}(0, t).$$

The remaining equations are obtained by the characteristics entering the bifurcation. Due to (4) there are three characteristics leaving the vessels into the bifurcation. This results in a non-linear algebraic system of equations for six unknowns. For more detailed information concerning the coupling conditions at a bifurcation, we refer to [15, Chapter 11][22,38].

At the outlets of the terminal vessels, we require again two equations in order to be able to compute the interface data. The first one is obtained by interpolating the outgoing characteristic (3b) at $z=l_i$. The second one is given by a three element $(R_{1,i}, C_i, R_{2,i})$ windkessel model incorporating the resistance $R_{2,i}$ and the compliance C_i of the omitted vessels:

$$p_{i,l} + R_{2,i} C_i \frac{dp_{i,l}}{dt} = p_v + (R_{1,i} + R_{2,i}) Q_{i,l} + R_{1,i} R_{2,i} C_i \frac{dQ_{i,l}}{dt}, \quad (6)$$

where $p_{i,l} = p(A_i)$ and $Q_{i,l}$ denote the pressure and flow rate at the outlet $z=l_i$ of a terminal vessel V_i , respectively. p_v is an averaged pressure in the venous system. In this paper, we set: $p_v = 5$ mmHg according to [20]. This ODE (0D-model) can be derived using averaging techniques and the principles of electricity, where the pressure corresponds to voltage, the flow rate to current, the resistances to Ohm's resistances and the compliance to the capacity of a capacitor [4]. A detailed description how to couple this 0D-model and the corresponding 1D-model in the terminal vessel can be found in the following articles: [5,26]. Since we have a 1D-0D coupling at the outflow boundaries, this model for arterial blood flow is often referred to as a *multi-dimensional or multi-scale model* [5].

2.3. Simplified stenosis model

In order to simulate the influence of a stenosis, the affected artery (Vessel 54) is split into three parts: The proximal part V_p , the stenotic part V_s and the distal part V_d (see Fig. 4):

$$V_{54} = V_p \cup V_s \cup V_d.$$

Next we assign to V_p and V_d the 1D-model given by: (1a), (1b) and (2). Due to the fact that the length of a stenotic domain is usually not very large, we neglect V_s . In our model, pressure drops and reduced flow caused by a stenosis are accounted for by prescribing algebraic interface conditions at the outlet of V_p and the inlet of V_d .

The corresponding equations are written in terms of characteristic variables and a reflection coefficient $R_t \in [0, 1]$. $R_t=0$ corresponds to the healthy state and $R_t=1$ simulates a complete occlusion. We propose the following interface conditions:

$$W_{1,V_p} = R_t \cdot W_{2,V_p} + (1 - R_t) \cdot W_{1,V_d}, \tag{7a}$$

$$W_{2,V_d} = R_t \cdot W_{1,V_d} + (1 - R_t) \cdot W_{2,V_p}. \tag{7b}$$

The idea behind this approach is that the characteristic waves traveling through the stenosis are damped by the factor $1 - R_t$ and reflected by the factor R_t [28].

W_{2,V_p} and W_{1,V_d} can be computed by the data at the corresponding interfaces, since they are leaving the vessels. Combining (7a) and (7b) with Eqs. (3a) and (3b) for the outgoing characteristic variables W_{2,V_p} and W_{1,V_d} , yields two non-linear systems of equations for the required interface data.

A more complex model simulating a stenosis can be found in [21,25,36,39,43]. It is given by an ODE and links the 1D-models adjacent to a stenosis by a 1D-0D-coupling. However, our numerical tests revealed that this model is less stable with respect to the time step size used in a numerical discretization scheme. Furthermore it is not possible to simulate a complete occlusion. If the area of a stenosis is equal to zero, we would have to exert a division by zero in this model. For these reasons, we have decided to use the simplified stenosis model described in this subsection.

2.4. Blood flow through collateral vessels and arteriogenesis

Let us denote the total number of collateral vessels between the tibial arteries 54 and 55 by N_{col} . In order to establish a flow model for the j -th collateral vessel of length l_j , $j \in \{1, \dots, N_{col}\}$, we first reconsider Fig. 1 and discuss some properties of these vessels.

According to [35] they have the size of arterioles. Though this may also be partly the cause in humans, measurements in the human heart yield collateral vessels in a diameter range of

0.031 cm to 0.136 cm [32]. Assuming growth rates up to a factor 2–3, we choose here starting radii of 0.03 cm to 0.04 cm. The average radii of the posterior and anterior tibial arteries have the size of 0.375 cm and 0.197 cm, respectively [41].

Considering Fig. 1, which has been taken from [35, Fig. 1], we observe that the collateral vessels have larger radii at their inlets and outlets than in the middle. For convenience, we assume that the radius r_{mj} in the middle is approximately half as large as the radius r_{bj} at an endpoint and that the radii at both endpoints are equal. In the following r_{bj} is set to 0.04 cm for all $j \in \{1, \dots, N_{col}\}$. To model the specific shape of the collateral vessels, these values are interpolated by a second order polynomial:

$$r_j(z) = \frac{2 \cdot z}{l_j^2} \cdot (z - l_j) \cdot r_{bj} + r_{bj},$$

yielding a profile for the radius of the considered vessel (see Fig. 5).

We choose the Hagen–Poiseuille model to compute blood flow through the collateral vessels because of the fact that in smaller arteries less pulsatile blood flow is observed [24]. Since we have pulsative blood flow of higher amplitudes in the main arteries, a different flow model for the collateral vessels has to be considered. In order to account for the variable vessel profile, we subdivide the interval $[0, l_j]$ equally in N_j elements. Each element has the length $\Delta z_j = l_j/N_j$ and the k -th element $k \in \{1, \dots, N_j\}$ is given by $\Omega_{j,k} = ((k-1)\Delta z_j, k\Delta z_j)$. On $\Omega_{j,k}$ the profile for r_j is approximated by a constant. Denoting the interpolant by \tilde{r}_j , we set (see Fig. 5):

$$\tilde{r}_j|_{\Omega_{j,k}} = r_j\left(\frac{(2k-1)\Delta z_j}{2}\right) =: \tilde{r}_{j,k}. \tag{8}$$

Within each element, we compute a flow rate $q_j \left[\frac{\text{cm}^3}{\text{s}}\right]$ and

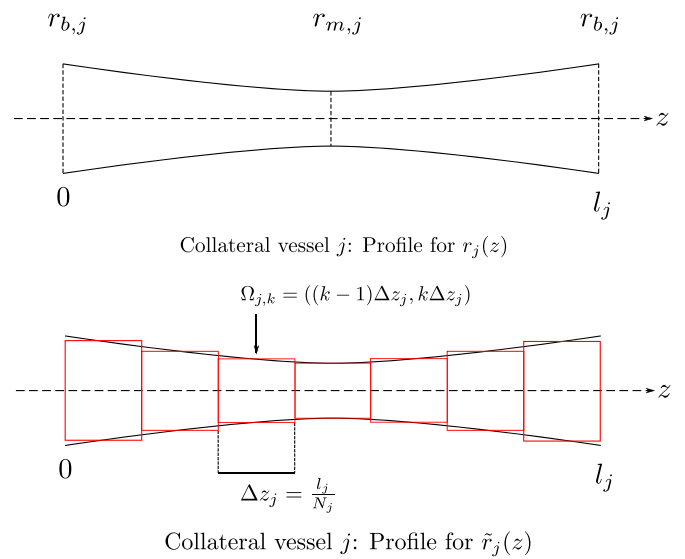


Fig. 5. Parabolic profile for the radius r_j of the j -th collateral vessel (top). Uniform subdivision of $[0, l_j]$ in elements $\Omega_{j,k}$. r_j is approximated on each $\Omega_{j,k}$ by a constant. The new profile is denoted by \tilde{r}_j (bottom).

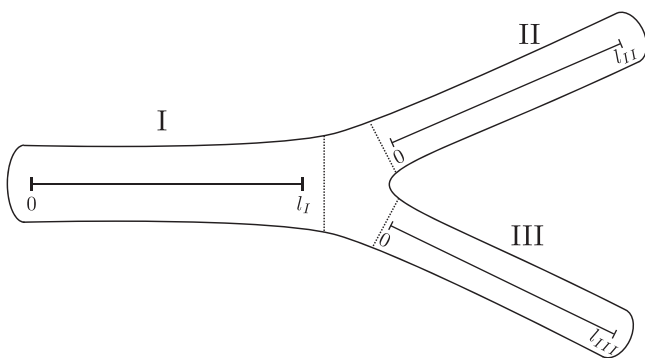


Fig. 3. 1D vessels at a bifurcation interface.

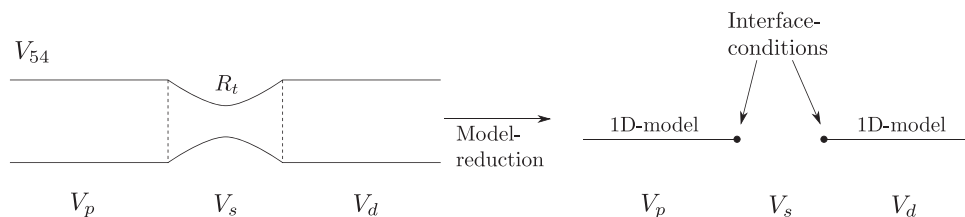


Fig. 4. Vessel V_{54} which contains a stenotic segment V_s is split into a proximal part V_p and a distal part V_d (left). Blood flow through the vessels adjacent to the stenosis is governed by a 1D-model, whereas the stenosis is incorporated into the model by algebraic interface conditions (right).

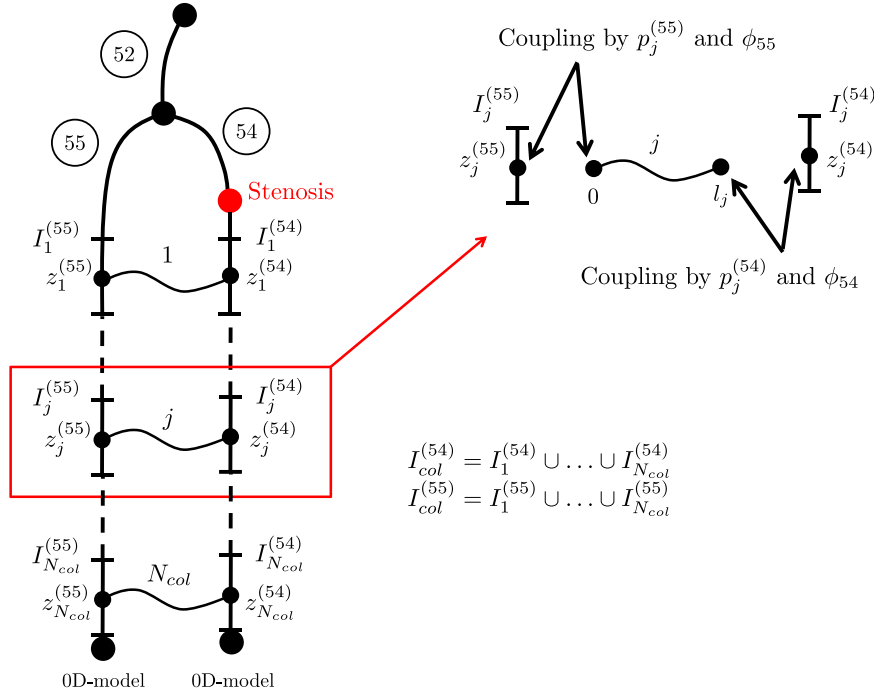


Fig. 6. The collateral vessels are contained in the intervals $I_{col}^{(54)} \subseteq [0, l_{54}]$ and $I_{col}^{(55)} \subseteq [0, l_{55}]$. Each of these intervals is decomposed into N_{col} disjoint intervals $I_j^{(i)}$, where its centers $z_j^{(i)}$ are equal to the connection points of the collateral vessels. We place the inlets of the collateral vessels on Vessel 55 and its outlets on Vessel 54. The models for the collateral vessels and the tibial vessels are coupled by the source terms ϕ_i and the averaged pressures $p_j^{(i)}$, $i \in \{54, 55\}$, $j \in \{1, \dots, N_{col}\}$. At the outlets of the tibial vessels, 0D-models are attached to account for the influence of the omitted vessels.

pressures $p_{j,k}$ [Pa] by the Hagen–Poiseuille law:

$$q_j = -\frac{\pi \cdot \tilde{r}_{j,k}^4}{8 \cdot \eta \cdot \Delta z_j} \Delta p_{j,k} = -\frac{\pi \cdot \tilde{r}_{j,k}^4}{8 \cdot \eta \cdot \Delta z_j} (p_{j,k} - p_{j,k-1}), \quad k = 2, \dots, N_j.$$

In order to close this system, we require for the pressure two additional values $p_j^{(54)}$ and $p_j^{(55)}$ which are provided by the 1D models governing the flow in the tibial arteries (Vessel 54 and 55):

$$q_j = -\frac{\pi \cdot \tilde{r}_{j,1}^4}{8 \cdot \eta \cdot \Delta z_j} (p_{j,1} - p_j^{(55)}), \quad q_j = -\frac{\pi \cdot \tilde{r}_{j,N_j}^4}{8 \cdot \eta \cdot \Delta z_j} (p_j^{(54)} - p_{j,N_j}).$$

For the computation of the pressures $p_j^{(54)}$ and $p_j^{(55)}$, we assume that the 1D models for the tibial vessels are defined on the intervals $[0, l_{54}]$ and $[0, l_{55}]$. The points at which the tibial arteries are connected with the j -th collateral vessel are denoted by: $z_j^{(54)} \in I_{col}^{(54)}$ and $z_j^{(55)} \in I_{col}^{(55)}$.

$I_{col}^{(54)} \subseteq [0, l_{54}]$ and $I_{col}^{(55)} \subseteq [0, l_{55}]$ are intervals containing all the points where Vessel 54 and 55 are connected with the collateral vessels. Each of these intervals is decomposed into N_{col} intervals (see Fig. 6):

$$I_{col}^{(i)} = I_1^{(i)} \cup \dots \cup I_{N_{col}}^{(i)}, \quad i \in \{54, 55\}.$$

The centers of the intervals $I_j^{(i)}$ are identified with the connection points $z_j^{(i)}$. Moreover, we require that these intervals fulfill the following assumptions:

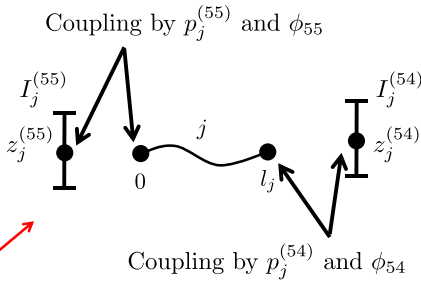
$$[z_j^{(55)} - \tilde{r}_{j,1}, z_j^{(55)} + \tilde{r}_{j,1}] \subseteq I_j^{(55)}, \quad [z_j^{(54)} - \tilde{r}_{j,N_j}, z_j^{(54)} + \tilde{r}_{j,N_j}] \subseteq I_j^{(54)}.$$

Having this notation at hand, we compute the boundary pressures for the j -th collateral vessel by the following averages:

$$p_j^{(54)} = \frac{1}{2 \cdot \tilde{r}_{j,N_j}} \int_{z_j^{(54)} - \tilde{r}_{j,N_j}}^{z_j^{(54)} + \tilde{r}_{j,N_j}} p_{54}(z) dz, \quad p_j^{(55)} = \frac{1}{2 \cdot \tilde{r}_{j,1}} \int_{z_j^{(55)} - \tilde{r}_{j,1}}^{z_j^{(55)} + \tilde{r}_{j,1}} p_{55}(z) dz,$$

where p_{54} and p_{55} are provided by (2).

As already mentioned in Section 2.1, the 1D models in the tibial arteries are coupled by means of their source terms with the



$$I_{col}^{(54)} = I_1^{(54)} \cup \dots \cup I_{N_{col}}^{(54)}$$

$$I_{col}^{(55)} = I_1^{(55)} \cup \dots \cup I_{N_{col}}^{(55)}$$

collateral vessels. In order to simulate a loss or gain of blood volume across the vessel walls, we have to specify the terms ϕ_{54} and ϕ_{55} in (1a). ϕ_{54} and ϕ_{55} are defined as piecewise constant functions in space, where these functions are constant on the intervals $I_j^{(i)}$, $i \in \{54, 55\}$.

Division of the flow rate q_j by the diameters of the j -th collateral vessels yields the corresponding function values on the intervals $I_j^{(i)}$. These values having the unit $(\frac{\text{cm}^3}{\text{s}})$ are measures for the blood volume leaving or entering the tibial vessels per second through the inlets or outlets of the collateral vessels. Without loss of generality, the inlets ($z=0$) of the collateral vessels are placed on Vessel 55 and their outlets ($z=l_j$) on Vessel 54. Provided that $q_j \geq 0$ holds, ϕ_{55} has to act as a sink and ϕ_{54} as a source term. Due to that, we have to take the negative value in the case of ϕ_{55} (see Fig. 6):

$$\phi_{54}(z, t) = \begin{cases} \frac{1}{2 \cdot \tilde{r}_{j,N_j}} q_j(t), & z \in I_j^{(54)}, j \in \{1, \dots, N_{col}\}, \\ 0, & z \in [0, l_{54}] \setminus I_{col}^{(54)}, \end{cases}$$

$$\phi_{55}(z, t) = \begin{cases} -\frac{1}{2 \cdot \tilde{r}_{j,1}} q_j(t), & z \in I_j^{(55)}, j \in \{1, \dots, N_{col}\}, \\ 0, & z \in [0, l_{55}] \setminus I_{col}^{(55)}. \end{cases}$$

Arteriogenesis, i.e., the enlargement of the collateral vessels, is simulated by making the piecewise constant profiles \tilde{r}_j time-dependent. Therefore, we attach to each segment $\Omega_{j,k}$ a suitable growth function for the corresponding radius $\tilde{r}_{j,k}$ (see (8)):

$$\tilde{r}_{j,k} : [0, \infty) \rightarrow \mathbb{R}^+, \quad t \mapsto \tilde{r}_{j,k}(t), \quad (9)$$

A function type that is frequently used to model a growth process is the generalized logistic function [31]:

$$\tilde{r}_{j,k}(t) = \tilde{r}_{j,k} \cdot \left(O + \frac{D}{(1 + Ke^{-B(t-M)})^\xi} \right). \quad (10)$$

Table 1
List of different parameters occurring in our numerical model.

Physical parameter	Sign	Value	Unit
Blood density	ρ	1.028	g/cm ³
Blood viscosity	η	4.500	mPa s
Total tissue dry weight	M	10.0	kgdw
Oxygen concentration in blood	C_{O_2}	8.75	$\mu\text{mol}/\text{cm}^3$
Average oxygen concentration in tissue	$\overline{C_tO_2}$	6.5	mmol/kgdw
Proportional gain	G_r	2.000	kgdw/mmol

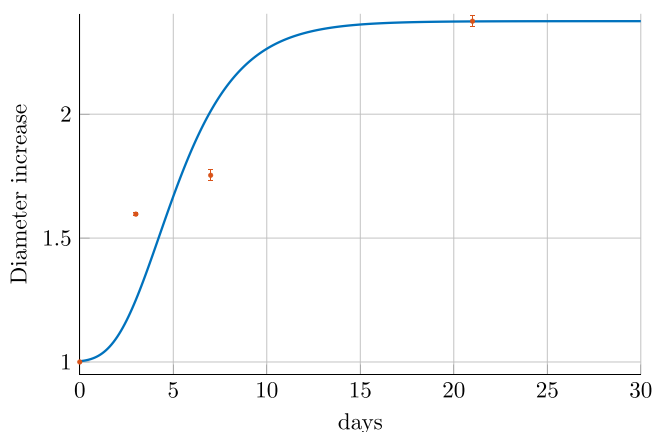


Fig. 7. Increase in diameter of growing collateral arteries obtained from [35, Table 1]. The data points are fitted by a generalized logistic growth function.

$\tilde{r}_{j,k}$ is the radius for $t=0$. In order to determine the parameters O, D, K, B, M and ξ in (10), we fit the generalized logistic function with data describing the growth of collateral arteries in mice. Considering Table 1 in [35], one can find measurements with respect to the diameters of the growing collateral arteries.

These data are recorded for the initial state (0 days) and after 3, 7 and 21 days using 4 different groups of mice. For a certain group (C57Bl/6), we observe that the diameters of the collateral vessels are magnified by a factor of 1.59 after 3 days, 1.75 after 7 days and 2.3754 after 21 days. We compute by the help of the curve fitting application from MATLAB the following parameters:

$$O = 1.000, \quad D = 1.375, \quad B = 4.969 \cdot 10^{-6}, \quad M = -7.96 \cdot 10^5, \\ K = 1.000 \quad \text{and} \quad \xi = 322.997. \quad (11)$$

The diameter increase and the fitted normalized curve $\tilde{r}_{j,k}(t)/\tilde{r}_{j,k}$ are depicted in Fig. 7. Combining (9)–(11) a growth model for the collateral arteries is obtained. We point out that one is not restricted to this growth function. If measurements with respect to the growth of collateral arteries are available, one can use these data.

2.5. Terminal vessels and metabolic regulation

The haemodynamic effect of vessels located beyond the 1D main arteries is accounted for using lumped parameter or OD models (see (6)). These models exhibit three parameters $R_{1,i}$, C_i and $R_{2,i}$ for each terminal vessel $i \in I_{Ter}$. By $I_{Ter} \subset \{1, \dots, 55\}$, we define the index set of the terminal vessels. The total resistances $R_{t,i} = R_{1,i} + R_{2,i}$ and compliances C_i are listed in [39, Table 2]. For the computation of $R_{1,i}$, the authors of [5] recommend to use the characteristic impedance $Z_i = \rho \cdot c(A_{0,i})/A_{0,i}$ of the i -th terminal vessel to avoid non-physical reflections. Due to the stenosis in Vessel 54 (right posterior tibial artery) blood flow will be decreased in its distal part and increased in the neighboring Vessel 55 (right anterior tibial artery).

In order to prevent an oversupply at the outlet of Vessel 55, the arterioles located beyond that outlet have to increase their resistances, while the arterioles beyond the neighboring outlet have to decrease their resistances to compensate the reduced blood supply, at least partially.

Within our model, we adjust the resistances $R_{2,i}$ to incorporate this mechanism. A possible way to control $R_{2,i}$ is based on the concentration of carbon dioxide in the affected tissue [3]. Here, we couple $R_{2,i}$, similar to [21, Section 24], with the oxygen concentration $(C_tO_2)_i$ in the tissue. This type of controlling the arterial blood flow is called metabolic regulation. The governing equation for the tissue concentration $(C_tO_2)_i$ in millimoles per kilogram of dry weight $\left[\frac{\text{mmol}}{\text{kgdw}}\right]$ is given by:

$$M_i \frac{d}{dt} (C_tO_2)_i = Q_i(t)(C_{O_2} - \sigma \cdot (C_tO_2)_i(t)) - v_i((C_tO_2)_i, t). \quad (12)$$

M_i denotes the dry weight of the tissue volume, which is perfused by vessel V_i . We assume that the total tissue dry weight

$$M = \sum_{i \in I_{Ter}} M_i$$

is given by: $M = 10$ kgdw [10, Chapter 2, Section 2.5]. The individual masses M_i are distributed according to the flow behavior for fixed resistances $R_{2,i}$. After blood flow has become periodic in our simulations for the healthy state ($R_t = 0$), we determine how much blood volume has left the vessel system within one heart beat. Then we compute the percentage of blood volume leaving the terminal vessel V_i . Finally, the masses M_i are determined such that they have the same percentage with respect to the total mass M . Q_i is the flow rate at the outlet of the terminal vessel V_i . The variable σ denotes the partition coefficient and v_i models the metabolic rate of consumption of oxygen. $C_{O_2} = 8.75 \frac{\mu\text{mol}}{\text{cm}^3}$ is the mean oxygen concentration in blood.

ODE (12) has been taken from [10, Chapter 2, Section 2.5], its right hand side consists of three terms. The first term quantifies the amount of oxygen supplying the corresponding tissue, the second term accounts for the amount of oxygen extraction from the blood under normal conditions. Finally, the third term simulates the metabolic demand of the corresponding tissue.

A possible choice for the consumption rate is the Michaelis-Menten law given by [18, Chapter 10]:

$$v_i((C_tO_2)_i, t) = V_{\max,i}(t) \cdot \frac{(C_tO_2)_i(t)}{\overline{C_tO_2} + (C_tO_2)_i(t)},$$

where $\overline{C_tO_2} = 6.5 \frac{\text{mmol}}{\text{kgdw}}$ is the average oxygen concentration in tissue, and $V_{\max,i} = 2 \cdot K_{0,i}$ is the average consumption rate. $K_{0,i} = 0.18 \cdot \frac{M_i \text{ mmol}}{M \text{ s}}$ denotes the consumption rate of oxygen at rest [10, Chapter 2, Section 2.5]. The partition coefficient σ is determined such that the following balance equation holds:

$$Q_{0,i} \cdot (C_{O_2} - \sigma \cdot \overline{C_tO_2}) - K_{0,i} = 0,$$

where $Q_{0,i}$ is the mean flow rate within vessel V_i .

In the previous subsection, we used a logistic function to model arteriogenesis. The time-dependent resistances $R_{2,i}(t), t \geq 0$ are again described by a logistic function [19,21]:

$$R_{2,i}(t) = \frac{R_L + R_U e^{A_{r,i}(t) - \hat{C}}}{1 + e^{A_{r,i}(t) - \hat{C}}}, \quad \hat{C} = -\log \left[\frac{R_{2,i}^{(sp)} - R_L}{R_U - R_{2,i}^{(sp)}} \right]. \quad (13)$$

$R_{2,i}^{(sp)}$ is the set point of the outflow resistances $R_{2,i}(t)$. It is computed from $R_{1,i} = Z_i$ and the total resistance $R_{t,i} = R_{1,i} + R_{2,i}^{(sp)}$ with data from [39, Table 2]. R_U and R_L are the upper and lower bounds for $R_{2,i}(t), t \geq 0$, respectively. Following [3], we choose them as $R_U = 1.30 \cdot R_{2,i}^{(sp)}$ and $R_L = 0.74 \cdot R_{2,i}^{(sp)}$. Regarding the choice of \hat{C} one has to note that it ensures the equality $R_{2,i} = R_{2,i}^{(sp)}$, if $A_{r,i} = 0$ holds. $A_{r,i}$ represents an activation function for $R_{2,i}$. Based on ODE (9) in

[3], we propose the following ODE for $A_{r,i}$:

$$\frac{dA_{r,i}}{dt} = rhs_{A_{r,i}}, \quad (14)$$

where the right hand side $rhs_{A_{r,i}}$ is determined by Algorithm 1.

Algorithm 1. Choice of $rhs_{A_{r,i}}$.

```

if  $|R_{2,i} - R_L| < TOL$  then
  if  $(C_t O_2)_i - \overline{C_t O_2} > 0 \wedge \frac{d}{dt}(C_t O_2)_i > 0$  then
     $rhs_{A_{r,i}} = G_r \cdot ((C_t O_2)_i - \overline{C_t O_2})$ 
  else
     $rhs_{A_{r,i}} = 0$ 
  end if
else if  $|R_{2,i} - R_U| < TOL$  then
  if  $(C_t O_2)_i - \overline{C_t O_2} < 0 \wedge \frac{d}{dt}(C_t O_2)_i < 0$  then
     $rhs_{A_{r,i}} = G_r \cdot ((C_t O_2)_i - \overline{C_t O_2})$ 
  else
     $rhs_{A_{r,i}} = 0$ 
  end if
else
   $rhs_{A_{r,i}} = G_r \cdot ((C_t O_2)_i - \overline{C_t O_2})$ 
end if

```

The constant $TOL > 0$ denotes a certain tolerance which is set to 0.5. $G_r = 2.0$ is a suitable proportional gain [3,21]. We enhanced ODE (9) in [3] by introducing the distinction of cases in Algorithm 1. Simulating effects arising from arteriogenesis without the proposed distinction, we have observed that the activation values $A_{r,i}(t)$ can become very small or large. This results in a delayed change of the resistances and excessive fluctuations of the oxygen concentrations $(C_t O_2)_i$. Motivated by this fact, we prevent $A_{r,i}$ from growing or falling by setting its time derivative to zero. This is done, if $R_{2,i}$ is close to its extreme values R_U and R_L and if the tissue concentration $(C_t O_2)_i$ is decreasing or increasing in certain cases. Solving (12) and (14) and inserting the results of (14) into (13) yield a complete model for metabolic regulation.

2.6. Numerical solution scheme

For the numerical treatment of the 1D model (1a), (1b) and (2), we use the numerical method of characteristics (NMC). This discretization method has been analyzed in [2] where it has been shown that the NMC is convergent of first order in space and time, even for CFL-numbers that are greater than one. Due to this attractive property, we are able to choose quite large time steps which is desirable in the context of the presented model, since it requires the simulation of many heart beats.

According to Fig. 7, one can see that a long simulation period of about 3 weeks has to be treated. Simulating the growth of the collateral arteries by (10) and (11), it becomes obvious that during a single heart beat almost no change in the profiles of the collateral arteries can be identified. Consequently, there is no need in resolving every heart beat within 3 weeks and we choose for the growth of the collateral vessels a macro time step size Δt_{ma} . For the simulation of a single heart beat a micro time step size $\Delta t_{mi} < \Delta t_{ma}$ is used. By means of these definitions our time stepping scheme is designed as follows: At first we perform a macro time step Δt_{ma} from a discrete point in time t_n , $n \in \mathbb{N}$ to $t_n + \Delta t_{ma}$. Then the growth function (10) is evaluated at $t = t_n + \Delta t_{ma}$ and the profiles of the collateral vessels are adapted.

Resulting from this, the flow behavior in our vessel system is changed and we simulate using the time step size Δt_{mi} several

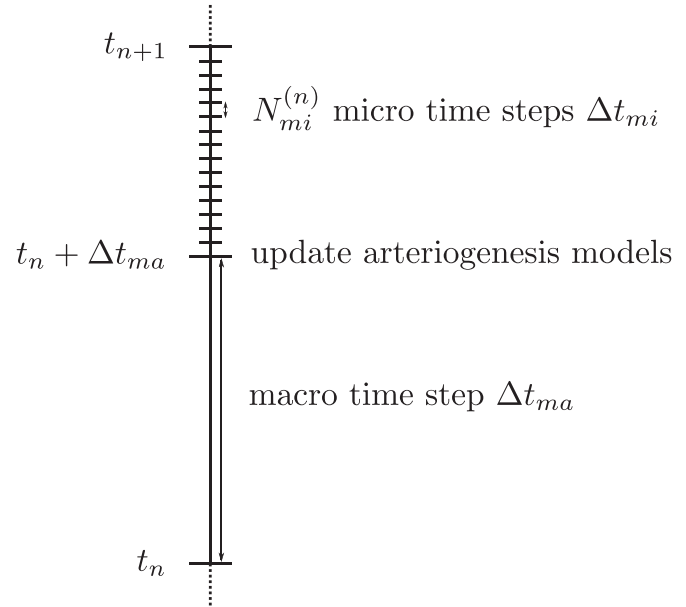


Fig. 8. Illustration of the time stepping scheme used for the simulation of the arteriogenesis.

heart beats until the flow rate, pressure and concentration values become periodic again. Exerting $N_{mi}^{(n)}$ micro steps, we arrive at $t_{n+1} = t_n + \Delta t_{ma} + N_{mi}^{(n)} \cdot \Delta t_{mi}$. Typically, several hundred heart beats are required (see Fig. 8). This procedure is repeated until the end of our simulation period (t_{end}) is reached. In our simulations, we have chosen $\Delta t_{ma} = 6$ h and $\Delta t_{mi} = 7.5 \times 10^{-4}$ s. As shown in [2, Remark 5], the NMC is stable even for CFL numbers greater than one. Thus we do not have a time step size restriction with respect to the discretization of the transport equations. The interface conditions between vessel segments, however, require the solution of non-linear equations by the help of Newton's method. Numerical tests reveal that the micro time step size $\Delta t_{mi} = 7.5 \times 10^{-4}$ s yields convergence of the Newton solver and numerical stability of the discretization. This means that we have to simulate several thousands of heart beats in total.

3. Simulation results

By means of the numerical model presented in the previous section, we simulate in this section the impact on arterial blood flow of a stenosis located in Vessel V_{54} .

Of considerable interest is the question which conductivity of the collateral vessels is required to achieve an almost complete compensation of the reduced blood supply depending on the reflection parameter $R_r \in [0, 1]$ of the stenosis. This depends of course on the original size, growth ability and number of collateral vessels. These data are difficult to obtain in humans and assumptions have to be made which may influence any considerations about the necessary number of vessels. The advantage of this modeling approach is that different parameters can be considered which allows a better adaption of animal data to the human situation.

3.1. Physiological data

The complete data for the 1D models (1a), (1b) and (2) such as the different lengths l_i , section areas $A_{0,i}$ and elasticity parameters β_i can be found in [37, Table I], $i \in \{1, \dots, 55\}$. Having β_i and $A_{0,i}$ at hand, the elasticity parameters $G_{0,i}$ in (2) can be calculated as follows: $G_{0,i} = \beta_i \cdot \sqrt{A_{0,i}}$. Note that these data represent the arterial

geometry and elasticity of a healthy young adult. For the three element windkessel model (see Section 2.5 and (6)), we use the values presented in [39, Table 2]. All vessel segments are discretized with a spatial length of 0.5 cm. The remaining fluid parameters and the parameters determining the regulation model are summarized in Table 1. The stenosis is placed 10 cm away from the inlet of V_{54} . Furthermore, we assume that each collateral vessel has a length of 5 cm. The radial profile of the j -th collateral vessel is approximated by $N_j = 10$ elements. We initially set $A_i(z, 0) = A_{0,i}$ and $Q_i(z, 0) = 0$ in the corresponding vessels. Pulsatile blood flow is simulated by prescribing (5) at the inlet of the aorta (Vessel 1, Fig. 2).

Using fixed terminal resistances, we compute by the 1D–0D coupled model several heart beats until the numerical solution becomes periodic. For the considered network this takes about 20 heart beats. Afterwards the regulation mechanism is switched on and we simulate the arterial system until the curves for Q_i , p_i and the oxygen concentrations $(C_i O_2)_i$ become periodic again. Next, the stenosis is activated by smoothly increasing the reflection parameter from 0 to $R_t \in [0, 1]$ during a time period of 60 s). Finally, arteriogenesis is activated (see Section 2.4) and simulated by the time stepping scheme described in Section 2.6. The simulation is terminated after a time span of 3 weeks is covered.

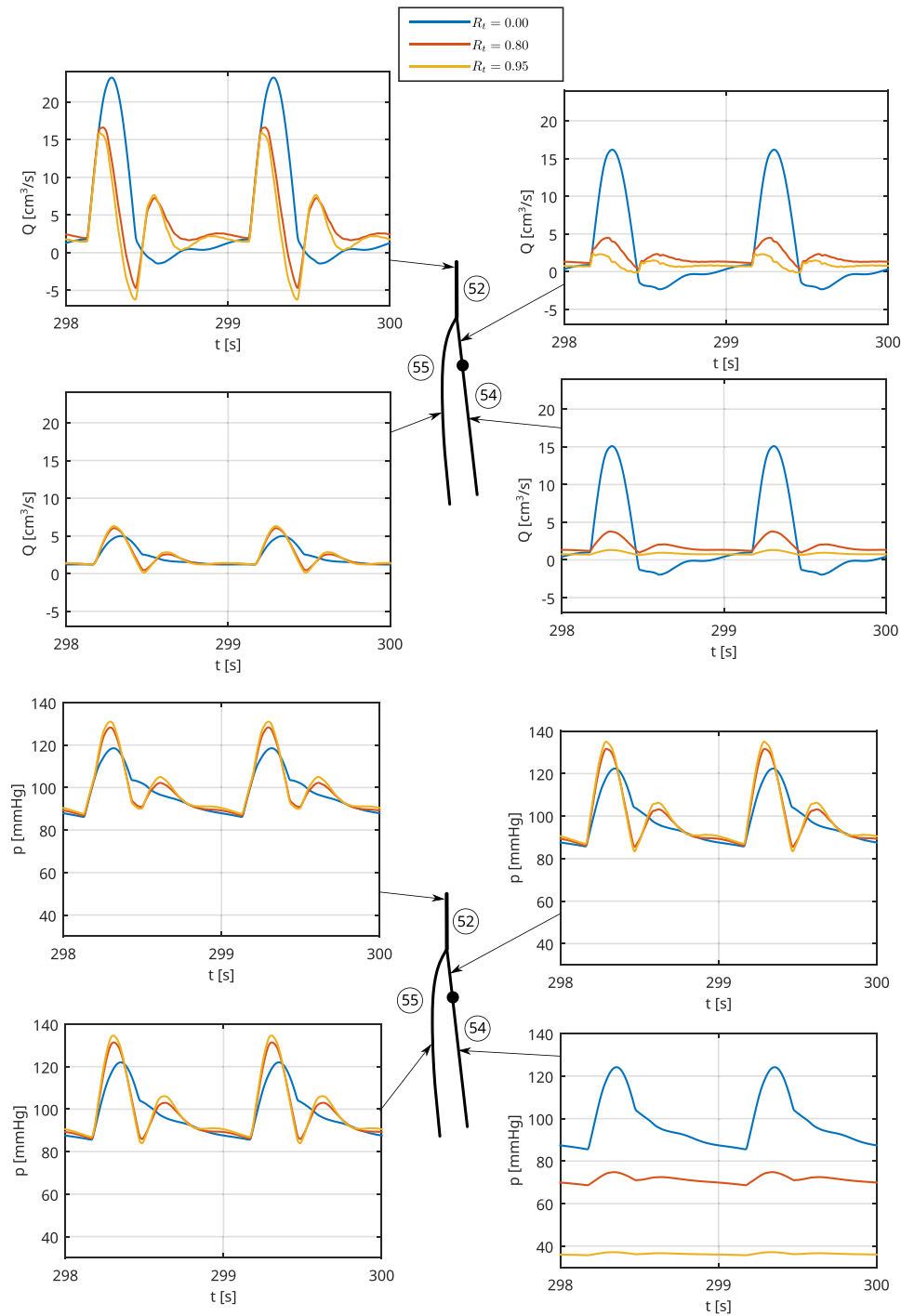


Fig. 9. Flow rates Q (top) and pressures p (bottom) reported at some locations in the vicinity of the stenosis placed in the tibial vessel 54, where $R_t \in \{0.00, 0.80, 0.95\}$. The data are shown for the time interval [298 s, 300 s] before metabolic regulation and arteriogenesis are activated.

Table 2
Pressure drops and conservation rates at a stenosis for some reflection parameters R_t .

R_t (%)	Δp (mmHg)	p_{cons}^s (%)
0	0.00	100.00
5	2.52	97.95
10	5.10	95.86
15	7.73	93.74
20	10.41	91.60
25	13.14	89.43
30	15.93	87.24
35	18.78	85.01
40	21.72	82.74
45	24.78	80.39
50	28.01	77.95
55	31.46	75.35
60	35.23	72.55
65	39.47	69.42
70	44.35	65.86
75	50.10	61.70
80	57.16	56.62
85	66.25	50.10
90	78.87	41.09
95	98.15	27.42
100	132.02	3.65

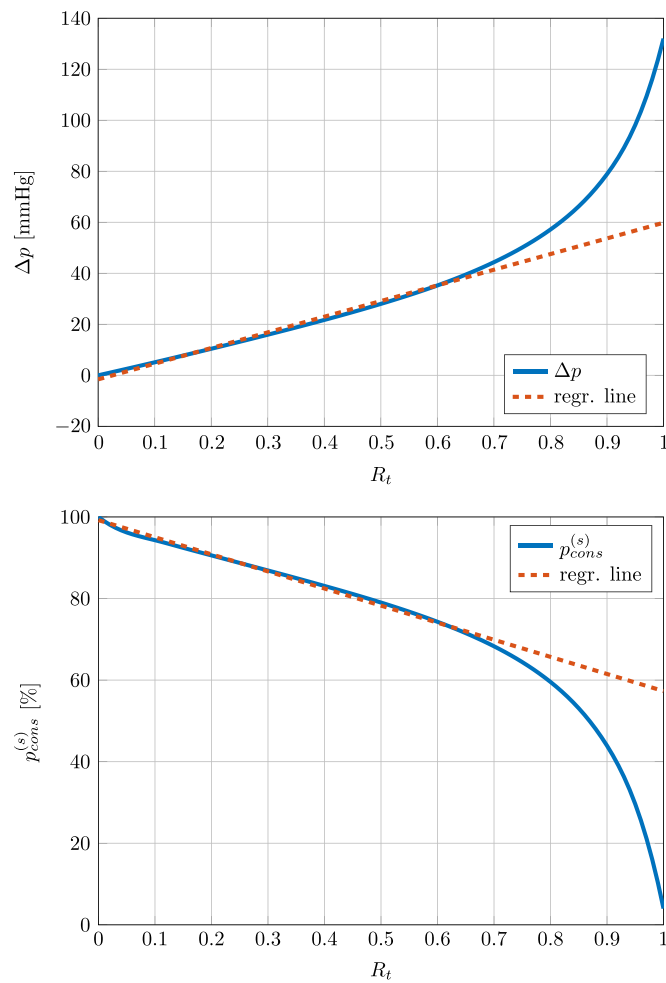


Fig. 10. Visualization of pressure drops and conservation rates at a stenosis for some reflection parameters R_t . The regression lines suggest a linear behavior for $R_t < 0.7$.

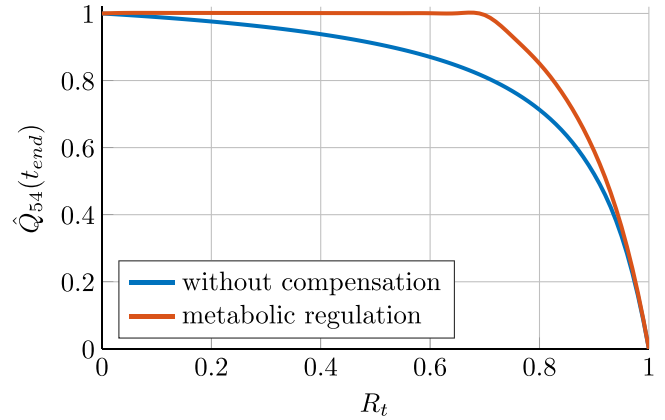


Fig. 11. Recovery rates depending on R_t with and without metabolic regulation.

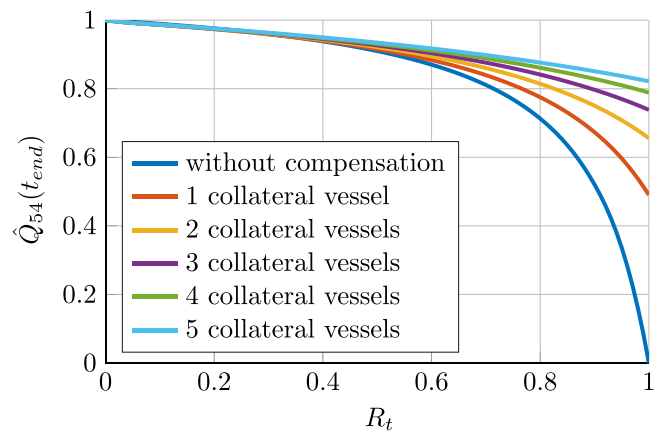


Fig. 12. Recovery rates depending on R_t for arteriogenesis with different numbers of collateral vessels.

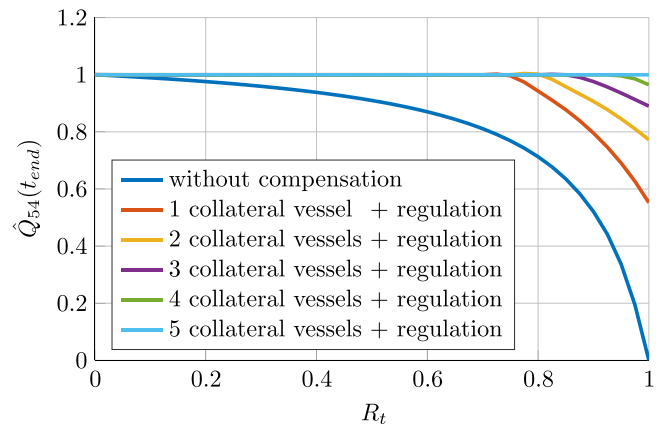


Fig. 13. Recovery rates depending on R_t for arteriogenesis combined with metabolic regulation.

3.2. Numerical results and discussion

The pressure and flow rate values in the healthy state ($R_t=0.0$) are within a reasonable range (see Fig. 9). Blood pressure ranges from 83 mmHg to 121 mmHg which is in accordance with [11]. Moreover, the curves exhibit the typical shape of pressure and flow rate curves in a peripheral artery. This justifies the usage of 1D models for arterial blood flow in order to analyze the effects of compensation mechanisms.

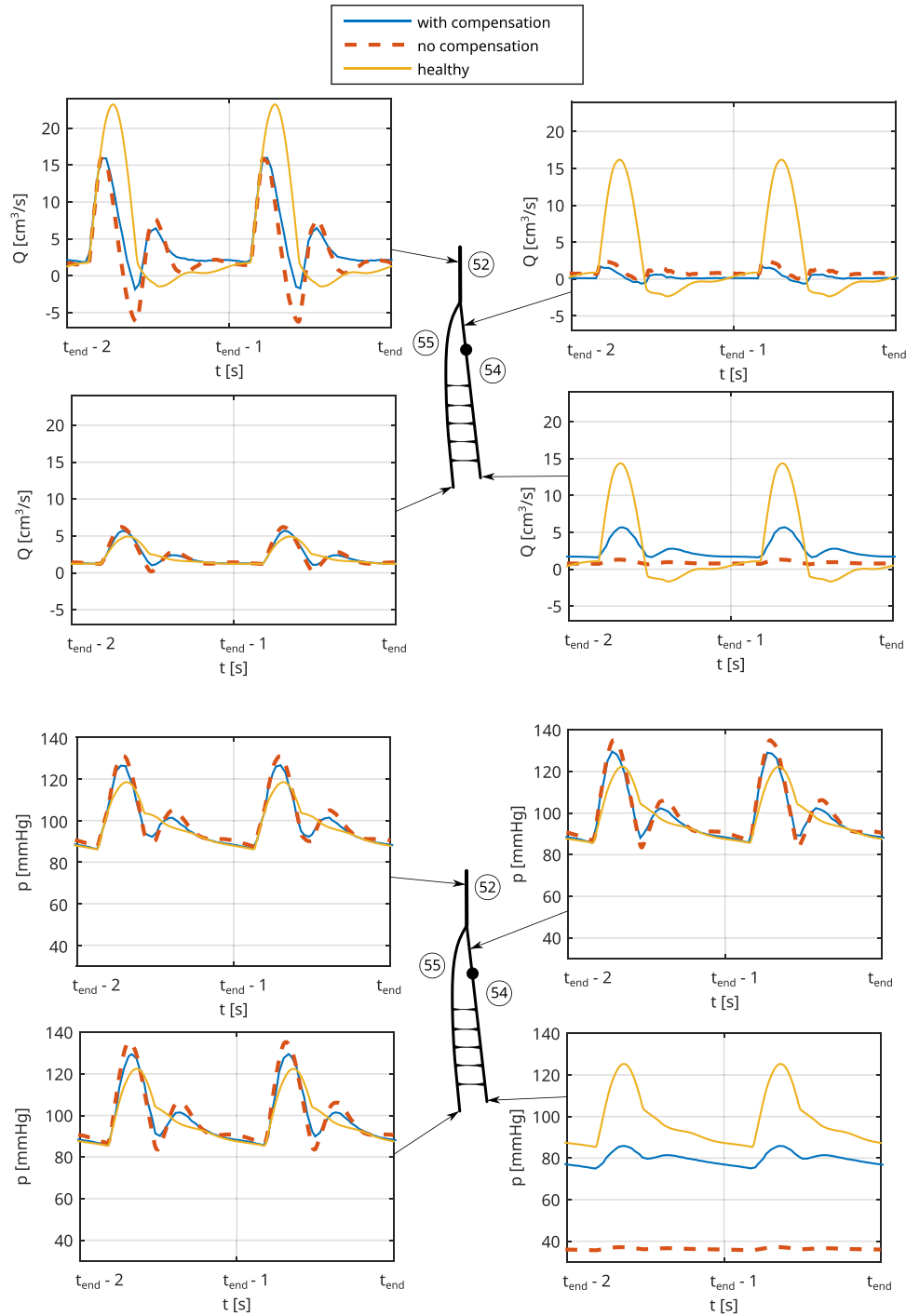


Fig. 14. Flow rates Q (top) and pressures p (bottom) reported at some locations in the vicinity of the stenosis with $R_t=0.95$ placed in the tibial Vessel 54. The data are shown in the last two seconds of the simulations for different scenarios.

At first we demonstrate the impact of the stenosis by comparing the maximal systolic pressure values at the inlet and the outlet of the stenosis within the time interval $[120\text{ s}, 121\text{ s}]$. We denote these values by $p_{max}^{(i)}$, $i \in \{in, out\}$. Using these data, we compute the absolute pressure drops Δp and conservation rates $p_{cons}^{(s)}$ as follows:

$$\Delta p = \left| p_{max}^{(in)} - p_{max}^{(out)} \right| \quad \text{and} \quad p_{cons}^{(s)} = 1 - \frac{\Delta p}{p_{max}^{(in)}}$$

The corresponding simulation results are listed in Table 2. We observe a non-linear relation between the reflection parameter R_t and the conservation rates. In Fig. 10, it can be seen that the

conservation rates decrease severely for higher values of R_t . If R_t is smaller than 0.7, we have a slow and almost linear decline of the conservation rates and pressure drops. Thus, we define a stenosis with $R_t \geq 0.7$ as critical.

The influence of a stenosis on the adjacent vessels is illustrated in Fig. 9. Not surprisingly, pressure and flow rate drop severely in the distal part of Vessel 54, whereas in Vessel 55 both the flow rate and the systolic pressure are slightly increased as R_t grows. Due to reflections at the stenosis, the flow rate in Vessel 52 is reduced and the pressure is significantly increased. This increases peak wall tension which in an already weakened artery could add to the risk of aneurysm formation.

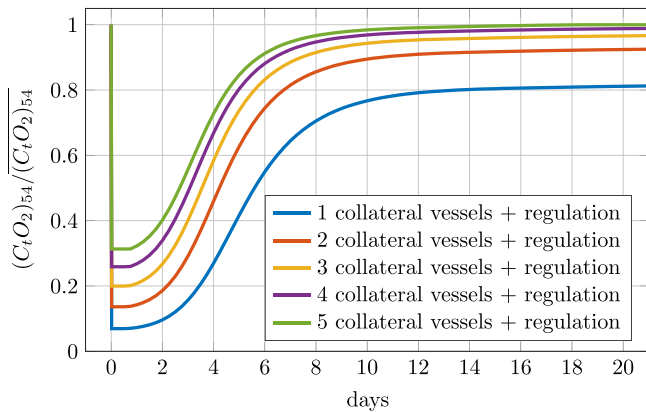


Fig. 15. Ratios between $(C_t O_2)_{54}$ and the mean oxygen concentration $\overline{(C_t O_2)}_{54}$ in a period of 21 days.

Next, we want to examine the efficiency of the compensation mechanisms. Therefore, we define the recovery rate \hat{Q}_{54} for the mass flux at the outlet of Vessel 54 by averaging the flow rate over the last simulated minute and comparing it to the mean flow rate $Q_{0.54}$:

$$\hat{Q}_{54}(t_{end}) = \frac{1}{60 \text{ s} \cdot Q_{0.54}} \int_{t_{end}-60 \text{ s}}^{t_{end}} Q_{54}(\tau, l_{54}) d\tau.$$

Fig. 11 shows the recovery rates depending on R_t for two cases. In the first case, no compensation mechanism is considered whereas in the second case only metabolic regulation is used at the outlets of V_{54} and V_{55} . It can be observed that the reduced flow can be completely compensated for $R_t < 0.7$ in contrast to the case where no compensation mechanism is used. For $R_t \geq 0.7$, metabolic regulation cannot recover the complete blood flow anymore. However, we observe that the recovery rates are still higher compared to the case without compensation mechanism.

In Fig. 12, one can see the recovery rates depending on R_t if only arteriogenesis is applied as a compensation mechanism. A complete recovery is not possible regardless of the number of collateral vessels. For a complete occlusion, i.e., $R_t = 1$, blood supply can be partially restored. As expected, the recovery rates increase with a growing number of collateral vessels.

Finally, we combine both compensation mechanisms and present the resulting recovery rates in Fig. 13. The effects of both mechanisms in the vicinity of the stenosis are illustrated in Fig. 14. In this scenario, a single collateral vessel allows a complete recovery up to a stenosis degree of $R_t = 0.75$. A complete compensation for all reflection parameters is achieved if five collateral vessels exist. Summing the cross-sectional areas of the collateral vessels at their centers results in a total cross-sectional area of 0.036 cm^2 which accounts for 8.14% of the occluded vessel's area.

In addition to that, we record the oxygen concentration $(C_t O_2)_{54}$ for every macro time step in the case of a complete occlusion. In Fig. 15, the ratios between $(C_t O_2)_{54}$ and the mean oxygen concentration $\overline{(C_t O_2)}_{54}$ are depicted. The results are in agreement with the recovery rates of the flow rate. The curve for five collateral vessels is similar to the measurements in [35, Fig. 6B]. This figure shows a comparison of haemoglobin oxygen saturations in healthy and artificially occluded feet of mice. Even though the topic of compensation mechanisms for stenoses is actively studied [8,16], experimental data of humans concerning the issue of this work are still missing mainly because in humans we usually observe endpoints rather than the development of compensatory structural adaption mechanisms. Therefore, only measurements obtained from mice are considered.

4. Final remarks

In this paper, we have simulated the influence of a peripheral arterial stenosis on blood supply of distal tissue. Furthermore, we have modeled two mechanisms that help to restore the reduced blood flow, i.e., metabolic regulation and arteriogenesis. The presented model is based on dimensionally reduced differential equations and algebraic coupling equations. It has been revealed that reduced blood supply caused by a critical stenosis can only be recovered if both compensation mechanisms are combined and a sufficient growth and number of collateral vessels is present. It should be mentioned however, that in large animal experiments incomplete compensation was reported and that the muscle oxygen consumption rates refer only to the resting state of the muscles, allowing structural maintenance and basic function. However, the collateral growth calculated here would not allow us to compensate for the consumption during muscle exercise. In order to balance the missing blood supply caused by a stenosis of lower degree it is sufficient to take only metabolic regulation into consideration. The existing model can be enhanced by incorporating further compensation mechanisms, e.g., angiogenesis or a more complex model for arteriogenesis.

Conflict of interest statement

There is no conflict of interest associated with this work.

Acknowledgments

Funding: This work was partially supported by the DFG (WO671/11-1), DZHK Munich Heart Alliance (Z 1 60 1 0 02 1100), SyNergy – the Munich Cluster for Systems Neurology (EXC1010), and Cluster of Excellence in Simulation Technology (EXC 310/2) at the University of Stuttgart. We would also like to thank Elsevier for the permission to reuse Figs. 1 and 4 from [35].

Ethical approval: There is nothing to declare.

References

- [1] S. Acosta, D.J. Penny, C.G. Rusin, An effective model of blood flow in capillary beds, *Microvasc. Res.* 100 (2015) 40–47.
- [2] S. Acosta, C. Puelz, B. Riviere, D.J. Penny, C.G. Rusin, Numerical method of characteristics for one-dimensional blood flow, *J. Comput. Phys.* 294 (2015) 96–109.
- [3] J. Alastruey, S. Moore, K. Parker, T. David, J. Peiró, S. Sherwin, Reduced modelling of blood flow in the cerebral circulation: coupling 1-d, 0-d and cerebral auto-regulation models, *Int. J. Numer. Methods Fluids* 56 (8) (2008) 1061–1067.
- [4] J. Alastruey, K. Parker, J. Peiro, S. Byrdc, S. Sherwin, Modelling the circle of Willis to assess the effects of anatomical variations and occlusions on cerebral flows, *J. Biomech.* 40 (2007) 1794–1805.
- [5] J. Alastruey, K. Parker, J. Peiro, S. Sherwin, Lumped parameter outflow models for 1-D blood flow simulations: effect on pulse waves and parameter estimation, *Commun. Comput. Phys.* 4 (2008) 317–336.
- [6] K. Baber, Coupling free flow and flow in porous media in biological and technical applications: from a simple to a complex interface description, University of Stuttgart, 2014. ISBN: 978-3-942036-40-5.
- [7] S. Canic, E. Kim, Mathematical analysis of quasilinear effects in a hyperbolic model blood flow through compliant axi-symmetric vessels, *Math. Methods Appl. Sci.* 26 (2003) 1161–1186.
- [8] M. Carvalho, A. Oliveira, E. Azevedo, A.J. Bastos-Leite, Intracranial arterial stenosis, *J. Stroke Cerebrovasc. Dis.* 23 (4) (2014) 599–609.
- [9] L. Cattaneo, P. Zunino, Computational models for fluid exchange between microcirculation and tissue interstitium, *Netw. Heterog. Media* 9 (2014) 135–159.
- [10] C. D'Angelo, Multi scale modelling of metabolism and transport phenomena in living tissues (Ph.D. thesis), EPFL, Lausanne, 2007.
- [11] A. Despopoulos, S. Silbermagl, Color atlas of physiology, Thieme, 2003.

- [12] K. Erbertseder, J. Reichold, B. Flemisch, P. Jenny, R. Helmig, A coupled discrete/continuum model for describing cancer-therapeutic transport in the lung, *PLoS One* 7 (3) (2012) e31966.
- [13] L. Formaggia, D. Lamponi, A. Quarteroni, One-dimensional models for blood flow in arteries, *J. Eng. Math.* 47 (3–4) (2003) 251–276.
- [14] L. Formaggia, F. Nobile, A. Quarteroni, A one-dimensional model for blood flow: application to vascular prosthesis, in: I. Babuška, T. Miyoshi, P.G. Ciarlet (Eds.), *Mathematical Modeling and Numerical Simulation in Continuum Mechanics. Lecture Notes in Computational Science and Engineering*, vol. 19, Springer-Verlag, Berlin, 2002, pp. 137–153.
- [15] L. Formaggia, A. Quarteroni, A. Veneziani, *Cardiovascular Mathematics-Modelling and Simulation of the Circulatory System*, Springer-Verlag, Italia, Milano, 2009.
- [16] B.H. Grimard, J.M. Larson, et al., Aortic stenosis: diagnosis and treatment, *Am. Fam. Physician* 78 (6) (2008) 717–724.
- [17] L. Grinberg, E. Cheever, T. Anor, J.R. Madsen, G. Karniadakis, Modeling blood flow circulation in intracranial arterial networks: a comparative 3D/1D simulation study, *Ann. Biomed. Eng.* 39 (1) (2011) 297–309.
- [18] M. Hacker, I. Messer, S.W. S, K. Bachmann, *Pharmacology: Principles and Practice*, Academic Press, Burlington, San Diego, London, 2009.
- [19] J. Alastruey, T. Passerini, L. Formaggia, J. Peiro, Physical determining factors of the arterial pulse waveform: theoretical analysis and calculation using the 1-D formulation, *J. Eng. Math.* 77 (1) (2012) 19–37.
- [20] M.E. Klingensmith, et al., *The Washington Manual of Surgery*, Lippincott Williams & Wilkins, Philadelphia, 2008, Table 30-1.
- [21] T. Köppl, M. Schneider, U. Pohl, B. Wohlmuth, The influence of an unilateral carotid artery stenosis on brain oxygenation, *Med. Eng. Phys.* 36 (7) (2014) 905–914.
- [22] T. Köppl, B. Wohlmuth, R. Helmig, Reduced one-dimensional modelling and numerical simulation for mass transport in fluids, *Int. J. Numer. Method Fluids* 72 (2) (2013) 135–156.
- [23] E. Lakatta, Age-associated cardiovascular changes in health: impact on cardiovascular disease in older persons, *Heart Fail. Rev.* 7 (2002) 29–49.
- [24] J.J. Lee, K. Tymi, A.H. Menkis, R.J. Novick, F. McKenzie, Evaluation of pulsatile and nonpulsatile flow in capillaries of goat skeletal muscle using intravital microscopy, *Microvasc. Res.* 48 (3) (1994) 316–327.
- [25] F. Liang, S. Takagi, R. Himeno, H. Liu, Multi-scale modeling of the human cardiovascular system with applications to aortic valvular and arterial stenoses, *Med. Biol. Eng. Comput.* 47 (2009) 743–755.
- [26] E. Marchandise, M. Willemet, V. Lacroix, A numerical hemodynamic tool for predictive vascular surgery, *Med. Eng. Phys.* 31 (1) (2009) 131–144.
- [27] J. Murillo, P. Garcia-Navarro, A Roe type energy balanced solver for 1D arterial blood flow and transport, *Comput. Fluids* 117 (2015) 149–167.
- [28] J.P. Mynard, P. Nithiarasu, A 1D arterial blood flow model incorporating ventricular pressure, aortic valve and regional coronary flow using the locally conservative Galerkin (LCG) method, *Commun. Numer. Methods Eng.* 24 (2008) 367–417.
- [29] A. Quarteroni, A. Valli, *Domain Decomposition Methods for Partial Differential Equations*, Numerical Mathematics and Scientific Computation, The Clarendon Press and Oxford University Press, Oxford, 1999.
- [30] P. Reymond, P. Crosetto, S. Deparis, A. Quarteroni, N. Stergiopoulos, Physiological simulation of blood flow in the aorta: comparison of hemodynamic indices as predicted by 3-D fsi, 3-D rigid wall and 1-D models, *Med. Eng. Phys.* 35 (6) (2013) 784–791.
- [31] F. Richards, A flexible growth function for empirical use, *J. Exp. Botany* 10 (2) (1959) 290–301.
- [32] J. Rockstroh, B.G. Brown, Coronary collateral size, flow capacity, and growth estimates from the angiogram in patients with obstructive coronary disease, *Circulation* 105 (2) (2002) 168–173.
- [33] I. Sarelius, U. Pohl, Control of muscle blood flow during exercise: local factors and integrative mechanisms, *Acta Physiol.* 199 (4) (2010) 349–365.
- [34] W. Schaper, *The Collateral Circulation of the Heart*, vol. 1, North-Holland Pub. Co., Amsterdam, 1971.
- [35] D. Scholtz, et al., Contribution of arteriogenesis and angiogenesis to post-occlusive hindlimb perfusion in mice, *J. Mol. Cell. Cardiol.* 34 (2002) 775–787.
- [36] B. Seeley, D. Young, Effect of geometry on pressure losses across models of arterial stenoses, *J. Biomech.* 9 (1976) 439–448.
- [37] S. Sherwin, L. Formaggia, J. Peiro, V. Franke, Computational modelling of 1D blood flow with variable mechanical properties and its application to the simulation of wave propagation in the human arterial system, *Int. J. Numer. Methods Fluids* 43 (2003) 673–700.
- [38] S. Sherwin, V. Franke, J. Peiro, K. Parker, One-dimensional modelling of a vascular network in space-time variables, *J. Eng. Maths.* 47 (2003) 217–250.
- [39] N. Stergiopoulos, D. Young, T. Rogge, Computer simulation of arterial flow with applications to arterial and aortic stenoses, *J. Biomech.* 25 (1992) 1477–1488.
- [40] Q. Sun, G. Wu, Coupled finite difference and boundary element methods for fluid flow through a vessel with multibranches in tumours, *Int. J. Numer. Methods Biomed. Eng.* 29 (3) (2013) 309–331.
- [41] J. Wang, K. Parker, Wave propagation in a model of the arterial circulation, *J. Biomech.* 37 (2004) 457–470.
- [42] N. Westerhof, F. Bosman, C. de Vries, A. Noordergraaf, Computer simulation of arterial flow with applications to arterial and aortic stenoses, *J. Biomech.* 2 (1969) 121–143.
- [43] D. Young, F. Tsai, Flow characteristics in models of arterial stenoses II, *J. Biomech.* 6 (1973) 547–559.

3 Numerical modelling of a peripheral arterial stenosis using dimensionally reduced models and machine learning techniques

Bibliographic note: The content of this chapter is based on the following original article: T. Köppl, G. Santin, R. Helmig and B. Haasdonk (2018): Numerical modelling of a peripheral arterial stenosis using dimensionally reduced models and machine learning techniques. International Journal for Numerical Methods in Biomedical Engineering, pages: e3095, with courtesy of Wiley.

Numerical modelling of a peripheral arterial stenosis using dimensionally reduced models and kernel methods

Tobias Koeppel¹  | Gabriele Santin² | Bernard Haasdonk² | Rainer Helmig¹

¹Department of Hydromechanics and Modelling of Hydrosystems, University of Stuttgart, Pfaffenwaldring 61, D-70569 Stuttgart, Germany

²Institute of Applied Analysis and Numerical Simulation, University of Stuttgart, Pfaffenwaldring 57, D-70569 Stuttgart, Germany

Correspondence

Tobias Koeppel, Department of Hydromechanics and Modelling of Hydrosystems, University of Stuttgart, Pfaffenwaldring 61, D-70569 Stuttgart, Germany.
Email: tobias.koeppel@iws.uni-stuttgart.de

Funding information

German Research Foundation (DFG), Grant/Award Number: EXC 310/2

Abstract

In this work, we consider 2 kinds of model reduction techniques to simulate blood flow through the largest systemic arteries, where a stenosis is located in a peripheral artery, i.e., in an artery that is located far away from the heart. For our simulations, we place the stenosis in one of the tibial arteries belonging to the right lower leg (right posterior tibial artery). The model reduction techniques that are used are on the one hand dimensionally reduced models (1-D and 0-D models, the so-called mixed-dimension model) and on the other hand surrogate models produced by kernel methods. Both methods are combined in such a way that the mixed-dimension models yield training data for the surrogate model, where the surrogate model is parametrised by the degree of narrowing of the peripheral stenosis. By means of a well-trained surrogate model, we show that simulation data can be reproduced with a satisfactory accuracy and that parameter optimisation or state estimation problems can be solved in a very efficient way. Furthermore, it is demonstrated that a surrogate model enables us to present after a very short simulation time the impact of a varying degree of stenosis on blood flow, obtaining a speedup of several orders over the full model.

KEYWORDS

blood flow simulations, dimensionally reduced models, kernel surrogate models, mixed-dimension models, peripheral stenosis, real-time simulations

1 | INTRODUCTION

During the recent decades, the interest in numerical simulation of blood flow has been growing continuously. Main reasons for this development are the increase of computational power, the design of efficient numerical algorithms, and the improvement of imaging techniques combined with elaborated reconstruction techniques yielding data on the geometry of interesting objects as well as important modelling parameters like densities of a fluid or tissue.¹⁻³ The motivation for putting more and more effort into these developments has been evoked by the fact that computational tools enable clinical doctors and physiologists to obtain some insight into cardiovascular diseases in a non-invasive way. By this, the risk of infections and other dangers can be remarkably reduced. Using numerical models, it is, e.g., possible to make predictions on how a stenosis affects the blood supply of organs; in particular, one wants to find out to what extent a vessel can be occluded without reducing the blood flow significantly. In this context, it is also of great interest whether blood vessel systems like the circle of Willis^{4,5} or small interarterial connections^{6,7} can help to restore the reduced blood flow. Furthermore, the simulation of fundamental regulation mechanisms like vasodilation, arteriogenesis, and angiogenesis helps to

understand how the impact of an occlusion on blood flow can be reduced.⁸⁻¹⁰ Further important application areas are the stability analysis of an implanted stent or an aneurysm. Thereby, it is crucial to compute realistic pressure values, mass fluxes, and wall shear stresses in an efficient way such that these data can be evaluated as fast as possible.

However, the simulation of flow through a cardiovascular system is a very complex matter. Since it is composed of a huge number of different vessels that are connected in a very complex way, it is usually not possible to resolve large parts of the cardiovascular systems due to an enormous demand for computational power and data volume. In addition to that, there are many different kinds of vessels covering a large range of radii, wall thicknesses, and lengths.^{2, chap.1, table 1.1, table 1.2} The vessel walls of arteries are, eg, much thicker than those of veins, due to the fact that they have to transport blood at high pressure. As the heart acts like a periodic pump, blood flow in the larger arteries and veins having an elastic vessel wall is pulsatile and exhibits high Reynolds numbers.^{2, chap. 1, table 1.7} This requires the usage of fluid-structure interaction algorithms and discretisation techniques for convection-dominated flows.¹⁴⁻¹⁷ Contrary to that, flows in small vessels with respect to diameter or length^{2, chap. 1, table 1.7} exhibit small Reynolds numbers. Moreover, the walls of such vessels are not significantly deformed, and therefore, they can be modelled as quasirigid tubes. Vessels having these properties can be typically classified as arterioles, venules, or capillaries. Taking all these facts into account, it becomes obvious that to this part of the cardiovascular system, totally different models and methods have to be applied.^{18, chap. 6.2,19,20}

Due to the variety of different vessel geometries and types of flows, it is unavoidable to consider a coupling of different kinds of models such that realistic blood flow simulations within the entire or within a part of the cardiovascular system can be performed. To reduce the complexity of the numerical model, mixed-dimension models have been introduced.²¹⁻²⁸ Thereby, subnetworks of larger vessels are modelled by three-dimensional or one-dimensional (1-D) PDEs in space. At the inlets and outlets of these networks, the corresponding models are coupled with 1-D PDEs or zero-dimensional (0-D) models (systems of ODEs) incorporating, e.g., the Windkessel effect of the omitted vessels and the pumping of the heart.²⁹⁻³¹ An alternative to these open-loop models for arterial or venous subnetworks of the systemic circulation are closed-loop models linking the inlets and the outlets of a subnetwork by a sequence of 0-D models for the organs, pulmonary circulation, and the heart.³²⁻³⁴

Besides the usage of dimensionally reduced or multiscale models, a further method of reducing the complexity of blood flow simulations has been established in the recent years.³⁵⁻³⁷ This approach is called Reduced Basis method (RB method) and is based on the idea to solve in an offline-phase parameterised PDEs for a few parameters (see, e.g., Haasdonk³⁸). These so-called solution snapshots are then used as basis of a low-dimensional space, and projecting the PDE to this space results in a low-dimensional problem. This reduced system can be solved in a so-called online phase, where solutions for multiple parameters can be efficiently computed. Within relevant biomedical application areas, these parameters determine usually the shape of a bifurcation, a stenosis, a bypass, or an inflow profile.^{39, chap. 8,36,37}

In this paper, we want to investigate the performance of a different type of surrogate model obtained via machine learning techniques and in particular with kernel methods.⁴⁰⁻⁴⁴ Contrary to the RB method, the surrogate model is in this case represented by a linear combination of kernel functions like the Gaussian or the Wendland kernel.^{45,46} The coefficients in the linear combination and the parameters for the kernel functions are obtained from a training and validation process, which is performed in an offline or training phase.⁴⁷ These methods have the advantage of constructing non-linear, data-dependent surrogates that can reach significant degrees of accuracy, while not needing an excessively large amount of data, as for different machine learning techniques.

Using this method, we want to simulate the impact of a stenosis on blood flow; in particular, we consider a peripheral arterial stenosis. This type of stenosis is of high interest for physiologists, since peripheral arteries supply organs that are located far away from the heart. It is obvious that peripheral organs and tissues are affected by a potential risk of under-supply and, therefore, an occlusion of peripheral arteries is extremely critical. For our simulations, we place a stenosis in the right tibial artery located in the lower right leg (see Figure 1) and study the pressure and flow rate curves, i.e., the evolution of the 2 quantities at different points over a complete heartbeat, in the vicinity of this stenosis.

We use for the blood flow simulations a 1-D-0-D coupled model, where we assign a 1-D flow model to the 55 main arteries of the systemic circulation.^{8,18,21,48} At the outlets of this network, 0-D models are attached to the 1-D models to incorporate the influence of the omitted vessels. The stenosis is modelled by a 0-D model consisting of an ODE.^{27,49,50} Using the dimensionally reduced model, we can produce realistic pressure and flow rate curves in a fast way.

Although this model is already both accurate and relatively fast, it is still too slow and hence not suitable for real-time simulation or parameter estimation. To overcome this problem, we train a kernel-based surrogate model that predicts, depending on the degree of stenosis, a pressure or flow rate curve. The surrogate is trained in a data-dependent way by computing pressure and flow rate curves for different degrees of stenosis, which are used as training data for the kernel method to construct an accurate surrogate model. The intention of this modelling approach is that a combination of

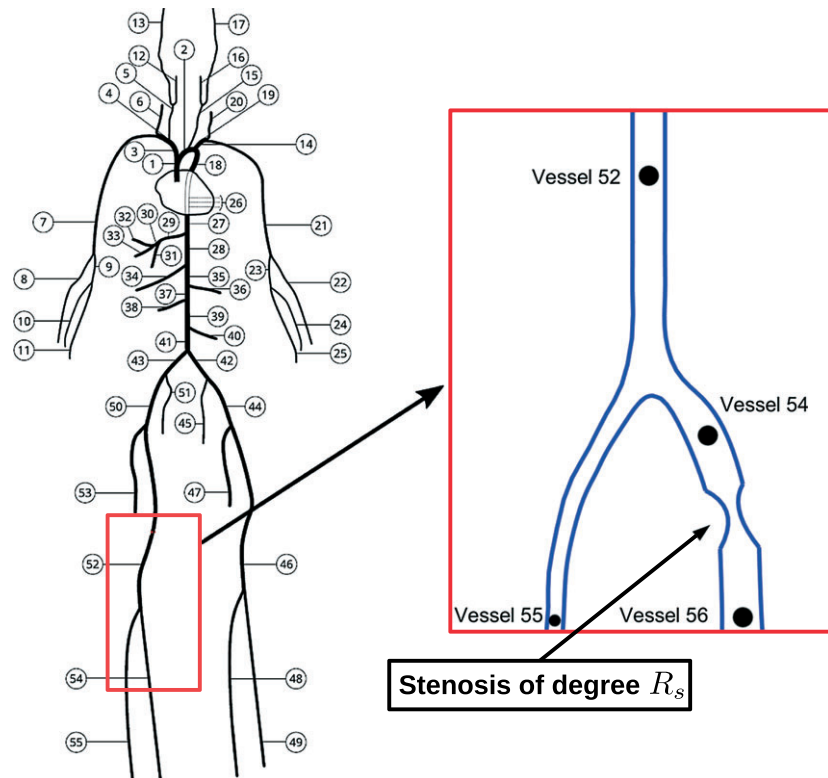


FIGURE 1 This figure shows an arterial network consisting of the 55 main arteries of the systemic circulation.^{11–13} In vessel 54 (right anterior tibial artery), we put a stenosis and study the effect on blood flow. The stenosis splits vessel 54 into 2 parts. The proximal part is again labelled with the index 54, while the distal part receives the index 56. At the places of the black dots that are located at the outlet of vessel 52, at the inlets of vessels 54 and 55 as well as at the inlet of vessel 56, we report over one heartbeat pressure and flow rate curves. Samples of these curves serve as training data for the kernel methods creating a surrogate model, which maps the degree of stenosis $R_s \in [0, 1]$ to the samples of the corresponding curves

dimensionally reduced models and kernel methods allows us to simulate the impact of a stenosis for an arbitrary degree of narrowing in a very short time. Simulation techniques of this kind might support clinical doctors and researchers with some important information after a relative short time, such that their diagnostic process can be optimised.

This combination of techniques is relatively new, and the results presented in this paper demonstrate its effectiveness. Moreover, although we concentrate here on the prediction of pressure and flow rate curves, the same technique can be easily adapted to construct surrogates of other relevant quantities of the blood flow simulation.

We remark that the present approach has potentially different advantages over the RB method. Indeed, the RB method typically requires the computation of several time snapshots in the offline phase to simulate the time evolution and also requires a time integration, with mostly the same time step used in the full model, during the online phase. On the other hand, kernel-based surrogates only require the time evolution of the quantities of interest in the desired time interval as training data, and in the online phase, they can directly predict it for a new parameter, without the need of any time integrations. Moreover, it is well known that the RB method may perform poorly when applied to transport problems, especially in the presence of moving structures or discontinuities evolution. This behaviour is reflected in a slowly decreasing Kolmogorov width, as it is discussed, e.g., in Haasdonk.^{38, example 3.4}

The remainder of our work is structured as follows: In Section 2, we outline all the details of the 1-D–0-D coupled model and the model for the stenosis. In addition to that, some comments on the numerical methods are presented. The first subsection of the following Section 3 contains some information on the fundamentals of kernel methods. This first part presents results that are mainly already discussed in the cited literature. Nevertheless, since we aim to address researcher of both the blood flow and machine learning communities, we include it to provide a clearer explanation for the interested reader, which may be acquainted on only one of the 2 fields. The second and third subsections describe how kernel methods can be used to compute flow variables in dependence of the degree of stenosis. By means of the models and methods from Sections 2 and 3, we perform in Section 4 some numerical tests illustrating the accuracy of

the surrogate kernel model. Moreover, it is shown how the surrogate kernel model can be used to solve a state estimation problem. The paper is concluded by Section 5, in which we summarise the main results and make some comments on possible future work.

2 | SIMULATION OF ARTERIAL BLOOD FLOW BY DIMENSIONALLY REDUCED MODELS

Simulating blood flow from the heart to the arms and legs, we consider the arterial network, presented in literature.¹¹⁻¹³ This network consists of the 55 main arteries including the aorta, the carotid arteries, the subclavian arteries, and the tibial arteries (see Figure 1). Our modelling approach for simulating blood flow through this network is based on the idea to decompose in a first step the network into its single vessels. In the next step, a simplified 1-D flow model is assigned to each vessel. Finally, the single models have to be coupled at the different interfaces, to obtain global solutions for the flow variables.

The following subsections present the basic principles of the 1-D model and the coupling conditions at bifurcations as well as at the stenosis. Furthermore, we make some comments on the numerical methods that are used to compute a suitable solution. At the inlet of the aorta (vessel 1, Figure 1 left), we try to emulate the heartbeats by a suitable boundary condition. To account for the Windkessel effect of the omitted vessels, the 1-D flow models associated with the terminal vessels are coupled with ODE systems (0-D models), which are derived from electrical science.²¹ Usually, the term Windkessel effect is related to the ability of large deformable vessels to store a certain amount of blood volume such that a continuous supply of organs and tissue can be ensured. However, also, many of the vessels that are not depicted in Figure 1 exhibit this feature to some extent. Furthermore, the arterioles located beyond the outlets of this network can impose some resistance on blood flow.^{8,10} These features have to be integrated into the outflow models to be able to simulate realistic pressure and flow rate curves.

2.1 | Modelling of blood flow through a single vessel

Let us suppose that the Navier-Stokes equations are defined on cylindrical domains of length $l_i \in \mathbb{R}$, $i \in \{1, \dots, 55\}$ and that their main axis are aligned with the z -coordinate. Modelling the viscous forces, we assume that the blood in large and medium-sized arteries can be treated as an incompressible Newtonian fluid, since blood viscosity is almost constant within large and middle-sized vessels.⁵¹ The boundaries of the computational domain change in time due to the elasticity of the arterial vessels walls and the pulsatile flow. Thereby, it is assumed that the vessel displaces only in the radial direction and that the flow is symmetric with respect to the main axis of the vessel.^{23,52} In addition to that, we postulate that the z -component \mathbf{u}_z of the velocity field \mathbf{u} is dominant with respect to the other components. Taking all these assumptions into account and integrating the Navier-Stokes equations across a section area $S(z, t)$ perpendicular to the z -axis at the place $z \in (0, l_i)$ and a time $t > 0$, one obtains the following system of PDEs^{29,53,54}:

$$\frac{\partial A_i}{\partial t} + \frac{\partial Q_i}{\partial z} = 0, \quad z \in (0, l_i), \quad t > 0, \quad (1)$$

$$\frac{\partial Q_i}{\partial t} + \frac{\partial}{\partial z} \left(\frac{Q_i^2}{A_i} \right) + \frac{A_i}{\rho} \frac{\partial p_i}{\partial z} = -K_r \frac{Q_i}{A_i}, \quad z \in (0, l_i), \quad t > 0. \quad (2)$$

The unknowns of this system A_i , Q_i , and p_i denote the section area of vessel V_i , the flow rate, and the averaged pressure within this vessel. Mathematically, these quantities are defined by the following integrals:

$$A_i(z, t) = \int_{S(z,t)} dS, \quad Q_i(z, t) = \int_{S(z,t)} \mathbf{u}_z dS, \quad p_i(z, t) = \frac{1}{A_i} \int_{S(z,t)} P_i dS,$$

where P_i is the three-dimensional pressure field. Please note that (1) is the 1-D version of the mass conservation equation, while (2) represents the 1-D version of the momentum equations. ρ stands for the density of blood. K_r is a resistance parameter containing the dynamic viscosity η of blood⁵⁵: $K_r = 22\pi\eta/\rho$. The PDE system (1)-(2) is closed by means of an algebraic equation, which can be derived from the Young-Laplace equation³¹:

$$p_i(z, t) = G_{0,i} \left(\sqrt{\frac{A_i}{A_{0,i}}} - 1 \right), \quad G_{0,i} = \frac{\sqrt{\pi} \cdot h_{0,i} \cdot E_i}{(1 - \nu^2) \cdot \sqrt{A_{0,i}}}, \quad (3)$$

where E_i is the Young modulus, $A_{0,i}$ stands for the section area at rest, $h_{0,i}$ is the vessel thickness, and ν is the Poisson ratio. Due to the fact that biological tissue is practically incompressible, ν is chosen as follows: $\nu = 0.5$. Equation 3 assumes that the vessel wall is instantaneously in equilibrium with the forces acting on it. Effects like wall inertia and viscoelasticity could be incorporated using a differential pressure law.^{34,56,57} However, neglecting the viscoelasticity maintains the strict hyperbolicity of the above PDE system.⁵⁸ Therefore, the interaction between the blood flow and the elastic vessel walls (3) is accounted for by using (3). Assuming that $G_{0,i}$ and $A_{0,i}$ are constant, the PDE system (1)-(3) can be represented in a compact form:

$$\frac{\partial \mathbf{U}_i}{\partial t} + \frac{\partial \mathbf{F}_i}{\partial z}(\mathbf{U}_i) = \mathbf{S}_i(\mathbf{U}_i), \quad z \in (0, l_i), \quad t > 0. \quad (4)$$

For $\mathbf{U}_i = (A_i, Q_i)^T$, the flux function \mathbf{F}_i and the source function \mathbf{S}_i are given by

$$\mathbf{F}_i(\mathbf{U}_i) = \left(\begin{array}{c} Q_i \\ \frac{Q_i^2}{A_i} + \frac{A_i^{\frac{3}{2}}}{\rho \sqrt{A_{0,i}}} \end{array} \right) \text{ and } \mathbf{S}_i(\mathbf{U}_i) = \left(\begin{array}{c} 0 \\ -K_{r,i} \frac{Q_i}{A_i} \end{array} \right).$$

This system may be written in a quasilinear form:

$$\frac{\partial \mathbf{U}_i}{\partial t} + \nabla_{\mathbf{U}_i} \mathbf{F}_i \frac{\partial \mathbf{U}_i}{\partial z} = \mathbf{S}_i(\mathbf{U}_i), \quad z \in (0, l_i), \quad t > 0,$$

where $\nabla_{\mathbf{U}_i} \mathbf{F}_i$ is the 2×2 Jacobian matrix of the flux function \mathbf{F}_i , having the eigenvalues $\lambda_{i,1}$ and $\lambda_{i,2}$. Denoting by $v_i = Q_i/A_i$ the fluid velocity and $v_{c,i}(A_i)$ the characteristic wave velocity of vessel V_i , it can be shown that $\lambda_{i,1} = v_i - v_{c,i}$ and $\lambda_{i,2} = v_i + v_{c,i}$. Under physiological conditions, it can be observed that⁵⁹

$$v_i = \frac{Q_i}{A_i} \ll \sqrt{\frac{G_{0,i}}{2\rho} \sqrt{\frac{A_i}{A_{0,i}}}} = v_{c,i}(A_i). \quad (5)$$

Therefore, it holds for the eigenvalues: $\lambda_{i,1} < 0$ and $\lambda_{i,2} > 0$, and the above PDE system is hyperbolic. Exploiting the fact that the Jacobian matrix $\nabla_{\mathbf{U}_i} \mathbf{F}_i$ is diagonalisable, there is an invertible matrix L_i such that it can be decomposed as follows: $\nabla_{\mathbf{U}_i} \mathbf{F}_i = L_i^{-1} \Lambda_i L_i$, where Λ_i is a diagonal matrix that has the eigenvalues $\lambda_{i,1}$ and $\lambda_{i,2}$ on its diagonal. By this, the PDE system (4) can be written in its characteristic variables $\mathbf{W}_i = (W_{1,i}, W_{2,i})^T$:

$$\frac{\partial \mathbf{W}_i}{\partial t} + \Lambda_i \frac{\partial \mathbf{W}_i}{\partial z} = L_i \mathbf{S}_i(\mathbf{W}_i), \quad z \in (0, l_i), \quad t > 0. \quad (6)$$

The characteristic variables \mathbf{W}_i and L_i are related by the following equation:

$$\frac{\partial \mathbf{W}_i}{\partial \mathbf{U}_i} = L_i, \quad \mathbf{W}_i(\mathbf{U}_i) = \begin{pmatrix} 0 \\ 0 \end{pmatrix} \text{ for } \mathbf{U}_i = \begin{pmatrix} A_{0,i} \\ 0 \end{pmatrix}. \quad (7)$$

An integration of (7) yields that the characteristic variables $W_{1,i}$ and $W_{2,i}$ can be expressed by the primary variables A_i and Q_i as follows:

$$W_{1,i} = -\frac{Q_i}{A_i} + 4\sqrt{\frac{G_{0,i}}{2\rho}} \left(\left(\frac{A_i}{A_{0,i}} \right)^{\frac{1}{4}} - 1 \right) = -v_i + 4 \cdot (v_{c,i}(A_i) - v_{c,i}(A_{0,i})), \quad (8)$$

$$W_{2,i} = \frac{Q_i}{A_i} + 4\sqrt{\frac{G_{0,i}}{2\rho}} \left(\left(\frac{A_i}{A_{0,i}} \right)^{\frac{1}{4}} - 1 \right) = v_i + 4 \cdot (v_{c,i}(A_i) - v_{c,i}(A_{0,i})). \quad (9)$$

Based on condition (5) and the signs of $\lambda_{1,i}$ and $\lambda_{2,i}$, one can prove that $W_{1,i}$ is a backward and $W_{2,i}$ is a forward travelling wave.^{29,18, chap. 2} Furthermore, it can be shown that $W_{1,i}$ and $W_{2,i}$ are moving on characteristic curves $c_{j,i}$ defined by 2 ODEs:

$$\frac{dc_{j,i}}{dt}(t) = \lambda_j(c_{j,i}(t), t), \quad j \in \{1, 2\}. \quad (10)$$

These insights are crucial for a consistent coupling of the submodels at the different interfaces, since it reveals that at each inlet and outlet of a vessel, exactly one coupling or boundary condition has to be imposed. The other condition is obtained from the outgoing characteristic variable. At the inlet $z = 0$, the variable $W_{1,i}$ is leaving the computational domain, whereas at $z = l_i$, the variable $W_{2,i}$ is the outgoing characteristic variable.

2.2 | Numerical solution techniques

According to standard literature,⁶⁰ the main difficulties that arise in terms of numerical treatment of hyperbolic PDEs are to minimise dissipation and dispersion errors, in order to avoid an excessive loss of mass and a phase shift for the travelling waves. A standard remedy for these problems is to apply higher-order discretisation methods in both space and time¹³ such that the numerical solution is as accurate as possible. However, higher-order discretisation methods tend to create oscillations in the vicinity of steep gradients or sharp corners, which can be removed by some additional postprocessing.^{48,61,62} Moreover, time stepping methods of higher-order require small time steps to be able to resolve the dynamics of a fast and convection-dominated flow and to fulfil a CFL condition, if they are explicit.

Considering all these features, we use in this work the numerical method of characteristics (NMC), which is explicit and of low approximation order (first order in space and time^{58, theorem 1}), leading to large dissipation and dispersion errors. This drawback can be circumvented by using a fine grid in space and sufficiently small time steps. Since we deal in this work with 1-D problems, a fine grid in space is affordable with respect to computational effort. On the other hand, a fine grid might force an explicit method to exert very small time steps. However, for the NMC, it can be proven that its time step size is not restricted by a condition of CFL type.⁵⁸ This means that the NMC can use a fine grid in space and time step sizes that are small enough to capture the convection-dominated blood flow and large enough to have an acceptable number of time steps.

Let us suppose now that the interval $[0, l_i]$ for vessel V_i is discretised by a grid having a mesh size Δz_i and grid nodes $z_{i,k} = k \cdot \Delta z_i \in [0, l_i]$, $k \in \{0, \dots, N_{h,i}\}$. Here, $N_{h,i}$ is the index of the last grid node. In a time step $[t_n, t_n + \Delta t]$, the NMC iterates over all the grid nodes. At each grid node $z_{i,k}$, there are 2 characteristic curves $c_{1,i}^{(k)}$ and $c_{2,i}^{(k)}$ for $W_{1,i}$ and $W_{2,i}$ (see Figure 2). Both curves are linearised in $z_{i,k}$ and $t_{n+1} = t_n + \Delta t$. In the next step, the resulting tangents are traced back to the previous time point t_n , where the corresponding intersection points are denoted by $g_{1,i}^{(k)}$ and $g_{2,i}^{(k)}$, respectively (see Figure 2). This procedure is equivalent to solving for every $z_{i,k}$ the final value problem,^{58, equation 10} which can be derived from (10):

$$\frac{dc_{j,i}(z_i, t_{n+1}, t)}{dt} = \lambda_j(c_{j,i}(z_i, t_{n+1}, t), t), \quad c_{j,i}(z_i, t_{n+1}, t_{n+1}) = z_{i,k}, \quad j \in \{1, 2\}.$$

Setting $c_{j,i}(z_i, t_{n+1}, t_n) = g_{j,i}^{(k)}$, we have by a first-order approximation:

$$\begin{aligned} c_{j,i}(z_i, t_{n+1}, t_{n+1}) - c_{j,i}(z_i, t_{n+1}, t_n) &= \int_{t_n}^{t_{n+1}} \lambda_j(c_{j,i}(z_i, t_{n+1}, t), t) dt, \\ z_{i,k} - g_{j,i}^{(k)}(t_n) &= \int_{t_n}^{t_{n+1}} \lambda_j(c_{j,i}(z_i, t_{n+1}, t), t) dt \\ &\approx \Delta t \lambda_j(c_{j,i}(z_i, t_{n+1}, t_n), t_n) = \Delta t \lambda_j(g_{j,i}^{(k)}(t_n), t_n). \end{aligned}$$

Restricting the PDE system (6) to the characteristic curves $c_{j,i}^{(k)}$, we have to solve the following ODEs in order to determine approximations for $W_{1,i}$ and $W_{2,i}$:

$$\frac{d}{dt} \mathbf{W}_{j,i}(c_{j,i}^{(k)}(t), t) = L_i \mathbf{S}_i(\mathbf{W}_{j,i}(c_{j,i}^{(k)}(t), t)). \quad (11)$$

An explicit first-order discretisation of (11) yields the following extrapolation formula for $\mathbf{W}_{j,i}$ at $c_{j,i}^{(k)}(t_{n+1}) = z_{i,k}$:

$$\mathbf{W}_{j,i}(z_{i,k}, t_{n+1}) = \mathbf{W}_{j,i}(g_{j,i}^{(k)}(t_n), t_n) + \Delta t \cdot L_i \mathbf{S}_i(\mathbf{W}_{j,i}(g_{j,i}^{(k)}(t_n), t_n)). \quad (12)$$

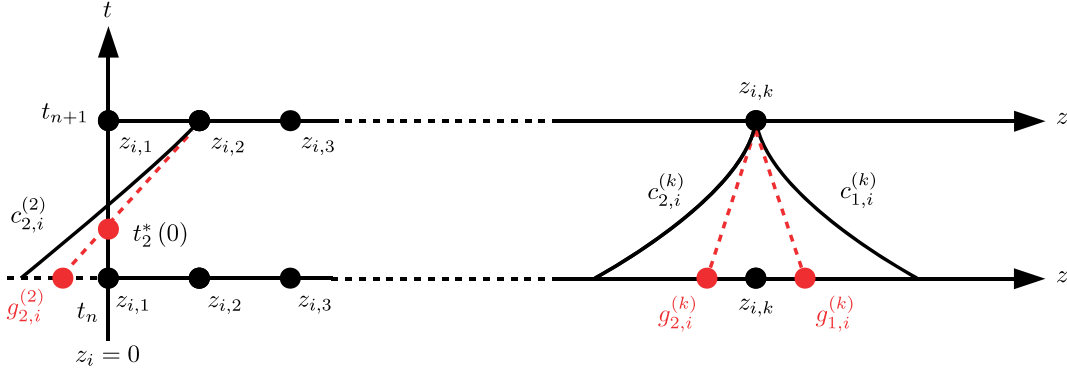


FIGURE 2 Linearisation of the characteristic curves $c_{j,i}^{(k)}$ for grid nodes $z_{i,k}$ in the vicinity of the boundary and in the inner of the computational domain

At the old time step t_n , the values $\mathbf{W}_{j,i} \left(g_{j,i}^{(k)}(t_n), t_n \right)$ can be interpolated using the precomputed values at the grid nodes $z_{i,k}$. For large time steps, it may happen that $g_{j,i}^{(k)}(t_n) \notin [0, l_i]$ (see Figure 2). In these cases, the values $\mathbf{W}_{j,i} \left(g_{j,i}^{(k)}(t_n), t_n \right)$ cannot be interpolated from the spatial values. Therefore, we require a temporal interpolation at a time point at which the linearised characteristic curves leave the computational domain. At the boundaries $z_i = 0$ and $z_i = l_i$, these time points $\{t_k^*(0), t_k^*(l_i)\} \subset [t_n, t_{n+1}]$ can be computed by

$$t_k^*(0) = t_n - \Delta t \frac{g_{2,i}^{(k)}}{z_{i,k} - g_{2,i}^{(k)}} \quad \text{and} \quad t_k^*(l_i) = t_n + \Delta t \frac{l_i - g_{1,i}^{(k)}}{z_{i,k} - g_{1,i}^{(k)}}.$$

After computing the ingoing characteristic variables $\mathbf{W}_{2,i}(0, t_{n+1})$ and $\mathbf{W}_{1,i}(l_i, t_{n+1})$ for the new time step by means of an external model (see Sections 2.3-2.6), we use a linear interpolation to provide a surrogate value for the missing characteristic variable:

$$\begin{aligned} \mathbf{W}_{2,i}(0, t_k^*(0)) &= \frac{t_{n+1} - t_k^*(0)}{\Delta t} \mathbf{W}_{2,i}(0, t_n) + \frac{t_k^*(0) - t_n}{\Delta t} \mathbf{W}_{2,i}(0, t_{n+1}), \\ \mathbf{W}_{1,i}(l_i, t_k^*(l_i)) &= \frac{t_{n+1} - t_k^*(l_i)}{\Delta t} \mathbf{W}_{1,i}(l_i, t_n) + \frac{t_k^*(l_i) - t_n}{\Delta t} \mathbf{W}_{1,i}(l_i, t_{n+1}). \end{aligned} \quad (13)$$

2.3 | Modelling of heartbeats

At the inlet of the aorta, we couple the corresponding 1-D model with a lumped parameter model (0-D model) for the left ventricle of the heart. By means of this model and the outgoing characteristic variable $W_{1,1}$, the missing ingoing variable $W_{2,1}$ can be determined. To compute the pressure P_{LV} in the left ventricle, we consider the following elastance model^{23,33}:

$$P_{LV}(t) = E(t)(V(t) - V_0) + S(t)Q_{LV}(t), \quad \frac{dV}{dt} = -Q_{LV}(t), \quad (14)$$

where V is the volume of the left ventricle and Q_{LV} is the flow rate from the left ventricle into the aorta. V_0 is the dead volume of the left ventricle, and S denotes the viscoelasticity coefficient of the cardiac wall. For simplicity, we assume that S depends linearly on P_{LV} : $S(t) = 5.0 \cdot 10^{-4} \cdot P_{LV}(t)$. The time-dependent elasticity parameter E is given by³³

$$E(t) = E \cdot e_v(t) + E, \quad e_v(t) = \begin{cases} 0.5 \left(1.0 - \cos \left(\frac{\pi t}{T_{vcp}} \right) \right), & 0 \leq t \leq T_{vcp}, \\ 0.5 \left(1.0 - \cos \left(\frac{\pi(t - T_{vcp})}{T_{vrp}} \right) \right), & T_{vcp} \leq t \leq T_{vcp} + T_{vrp}, \\ 0.0, & T_{vcp} + T_{vrp} < t \leq T. \end{cases}$$

T represents the length of the heart cycle. E_{\max} and E_{\min} are the maximal and minimal elasticity parameters, while T_{vcp} and T_{vrp} refer to the durations of the ventricular contraction and relaxation. The flow rate Q_{LV} through the aortic valve is governed by the Bernoulli law⁶³ incorporating the viscous resistance and inertia of blood:

$$L \frac{dQ_{LV}}{dt} = \Delta P_v(t) - R \cdot Q_{LV}(t) - B \cdot Q_{LV}(t) \cdot |Q_{LV}(t)|. \quad (15)$$

The parameters R , B , and L quantify the viscous effects, flow separation, and inertial effects. Finally, the pressure drop $\Delta P_v(t)$ is computed as follows: $\Delta P_v(t) = P_{LV}(t) - p_1(0, t)$, $t > 0$, where $p_1(0, t)$ is the pressure at the root of the aorta.

During the systolic phase of the heart cycle, it holds: $\Delta P_v(t) > 0$, and we use (14) to (15) to compute $Q_{LV}(t)$. This value serves as a Dirichlet boundary value at $z_1 = 0$ for the 1-D model in vessel V_1 . Based on $Q_{LV}(t)$, Equations (8) and (9), and an approximation of $W_{1,1}(0, t)$ by (12), the ingoing variable $W_{2,1}(0, t)$ can be determined.

Within the diastolic phase of the heart cycle, $p_1(0, t)$ begins to exceed the pressure in the left ventricle $P_{LV}(t)$. As a result, the aortic valve is closing, and we have no flux or a very little flux between the left ventricle and the aorta and, therefore, we set $Q_{LV}(t) = 0$. Since we simulate only the left ventricle without taking into account the filling process by the left atrium, we reactivate the model at the begin of every heart cycle.²³ Thereby, at the end of each heart cycle, the volume of the left ventricle is set to its maximal value: $V(k \cdot T) = V_{\max}$, $k \in \mathbb{N}$.

2.4 | Modelling of bifurcations

To decrease the flow velocity and to cover the whole body with blood vessels, the arterial system exhibits several levels of branchings. Therefore, it is very important to simulate blood flow through a bifurcation as exact as possible. Bifurcations and their mathematical modelling have been the subject of many publications.^{48,64-67} Coupling conditions for systems linked at a bifurcation can be derived by the principles of mass conservation and continuity of the total pressure. The total pressure for vessel V_i is defined by

$$p_{t,i} = \frac{\rho}{2} \left(\frac{Q_i}{A_i} \right)^2 + p(A_i).$$

Indexing the vessels at a bifurcation by V_i , $i \in \{I, II, III\} \subset \{1, \dots, 55\}$, we obtain the following 3 coupling conditions:

$$Q_I = Q_{II} + Q_{III} \quad \text{and} \quad p_{t,I} = p_{t,II}, \quad p_{t,I} = p_{t,III}. \quad (16)$$

The remaining equations are obtained by the characteristics entering the bifurcation (see Figure 3). According to Section 2.1, we have at each bifurcation 3 characteristics moving from the vessels into the bifurcation. The outgoing characteristic variables can be determined by tracing back the corresponding characteristic curves (see Section 2.2 and Equations (12) and (13)). Using the characteristic variables and inserting (8) and (9) into (16), we obtain a non-linear system of equations for the 3 unknown ingoing characteristic variables $W_{1,I}$, $W_{2,II}$, and $W_{2,III}$.

2.5 | Modelling of the peripheral circulation

At the outlet of a terminal vessel V_i , the reflections of the pulse waves at the subsequent vessels have to be incorporated to simulate a realistic pressure decay. For this purpose, we assign to each terminal vessel a reflection parameter $R_{p,i} =$

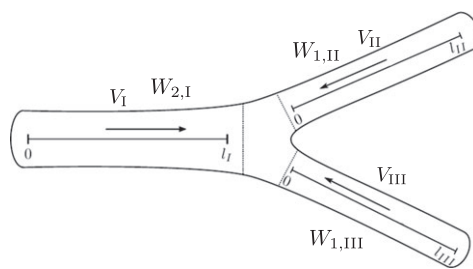


FIGURE 3 Decomposition of a bifurcation into 3 independent vessels V_I , V_{II} , and V_{III} . Orientating the axes of the vessels as in the figure, the characteristic variables $W_{2,I}$, $W_{1,II}$, and $W_{1,III}$ are leaving the corresponding vessels. These variables can be determined by values from the inside of the vessels, and combined with the coupling conditions (16), we have a system of equations yielding the boundary values for V_I , V_{II} , and V_{III}

$R_{1,i} + R_{2,i}$, where $R_{1,i}$ is the resistance parameter of V_i and $R_{2,i}$ is the equivalent resistance parameter for all the vessels, which are connected to V_i but not contained in the 1-D network. A third parameter C_i quantifies the compliance of the omitted vessels, and therefore, it is a measure for the ability of these vessels to store a certain blood volume. These parameters form a triple $(R_{1,i}, C_i, R_{2,i})$ that is referred to as a *3-element Windkessel* model in literature.^{21,2, chap. 10} To describe the dynamics of a Windkessel model, the following ODE has been derived using averaging techniques and an analogy from electrical science^{4,21,25}:

$$p_{i,t} + R_{2,i}C_i \frac{dp_{i,t}}{dt} = p_v + (R_{1,i} + R_{2,i}) Q_{i,t} + R_{1,i}R_{2,i}C_i \frac{dQ_{i,t}}{dt}. \quad (17)$$

$p_{i,t} = p(A_i)$ and $Q_{i,t}$ denote the pressure and flow rate at the outlet $z = l_i$ of a terminal vessel V_i , respectively. p_v is an averaged pressure in the venous system. Combining (17) with (3), (8), and (9) yields an equation depending on the characteristic variables. By means of this equation and the given outgoing characteristic variable $W_{2,i}$, the missing ingoing characteristic variable $W_{1,i}$ can be computed, by solving for each time point of interest a non-linear equation. Having $W_{1,i}$ and $W_{2,i}$ at $z = l_i$ and for a time point $t > 0$ at hand, the boundary values $A_i(l_i, t)$ and $Q_i(l_i, t)$ can be computed for each $t > 0$ using (8) and (9). Further information on the derivation of lumped parameter models for the peripheral circulation can be found in Olufsen and Nadim.⁶⁸

2.6 | Modelling the influence of a stenosis on blood flow

A blood vessel V_i containing a stenosis is split into 3 parts: A proximal part $V_{i,p}$, the stenosis itself, and a distal part $V_{i,d}$. In the next step, we assign to $V_{i,p}$ and $V_{i,d}$ the 1-D blood flow model from Section 2.1, while the part of V_i that is covered by the stenosis is lumped to a node (see Figure 4).

The degree of stenosis is represented by a parameter $R_s \in [0, 1]$, where $R_s = 0$ corresponds to the healthy state and $R_s = 1$ stands for the case of a completely occluded blood vessel. For convenience, it is assumed that both vessel parts have the same section area $A_{0,i}$ as well as the same elasticity parameters. The lengths of $V_{i,p}$ and $V_{i,d}$ are denoted by $l_{i,p}$ and $l_{i,d}$. At the boundaries $z_{i,p} = l_{i,p}$ and $z_{i,d} = 0$ that are adjacent to the stenosis, 2 characteristic variables $W_{2,i,p}$ and $W_{1,i,d}$ are moving towards the stenosis (see Figure 4 and Section 2.1). Using these characteristic variables and an appropriate 0-D model, we have enough equations to compute the boundary conditions for the two 1-D models. Modelling the stenosis, we consider an ODE containing several parameters of physical relevance to couple both parts of the affected vessels. According to previous studies,^{49,50,69} the flow rate Q_s through a stenosis and the pressure drop $\Delta p_s(t) = p_{i,d}(0, t) - p_{i,p}(l_{i,p}, t)$ across a stenosis are related to each other by the following ODE:

$$\frac{K_u \cdot \rho \cdot l_s}{A_{0,s}} \frac{dQ_s}{dt} = \Delta p_s - \frac{K_v \cdot \eta \cdot l_s}{A_{0,s} \cdot D_s} Q_s - \frac{K_t \cdot \rho}{2A_{0,s}^2} \left(\frac{A_{0,s}}{A_s} - 1 \right)^2 Q_s |Q_s|. \quad (18)$$

$A_{0,s}$ and $A_s = (1 - R_s) \cdot A_{0,s}$ refer to the section areas of the normal and stenotic segments, while D_0 and D_s denote the corresponding diameters.³³ l_s is the length of the stenosis. The remaining parameters are empirical coefficients, which are given by³³:

$$K_v = 32.0 \cdot (0.83 \cdot l_s + 1.64 \cdot D_s) \cdot \left(\frac{A_{0,s}}{A_s} \right)^2 \frac{1}{D_s}, \quad K_t = 1.52 \text{ and } K_u = 1.2.$$

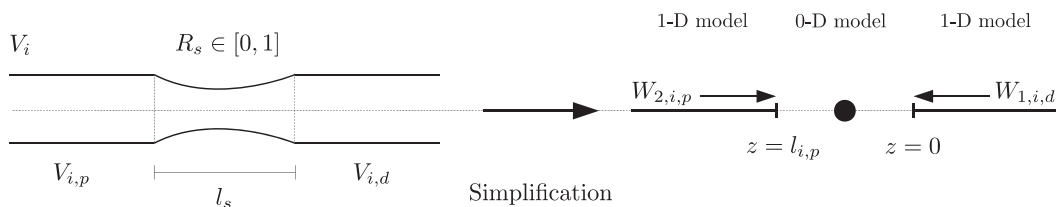


FIGURE 4 Decomposition of a blood vessel V_i into a proximal part $V_{i,p}$ and a distal part $V_{i,d}$. The stenosis having a degree of stenosis $R_s \in [0, 1]$ is lumped to a node and modelled by a 0-D model. To provide boundary conditions at $z = l_{i,p}$ and $z = 0$ for the 1-D models accounting for the influence of the stenosis, the outgoing characteristics $W_{2,i,p}$ and $W_{1,i,d}$ are combined with the coupling conditions of the 0-D model

Solving (18), we use the solution value Q_s for each time point as a boundary condition at $z_{i,p} = l_{i,p}$ and $z_{i,d} = 0$. Together with the extrapolated characteristic variables $W_{2,i,p}$ and $W_{1,i,d}$ as well as (8) and (9), we have a system of equations for the boundary conditions adjacent to the stenosis. In the case of a full occlusion, i.e., $R_s = 1$, we multiply (18) by A_s^2 . Considering the limit $A_s \rightarrow 0$, we obtain an algebraic equation that gives $Q_s = 0$. This is equivalent to a full reflection of the ingoing characteristics $W_{2,i,p}(l_{i,p}, t)$ and $W_{1,i,d}(0, t), t > 0$.

3 | KERNEL-BASED SURROGATE MODELS

In this section, we introduce kernel methods for surrogate modelling. First, we present the general ideas of kernel methods applied to the approximation of an arbitrary continuous function $f : \Omega \subset \mathbb{R}^d \rightarrow \mathbb{R}^q$, where Ω is a given input parameter domain and d, q are the input and output dimensions, which can be potentially large (e.g., the present setting will lead to $q = 400$). Then we concentrate on the present field of application and discuss how this general method can be used to produce cheap surrogates of the full model described in the previous sections.

Our goal is to construct a surrogate function $\hat{f} : \Omega \rightarrow \mathbb{R}^q$ such that $\hat{f} \approx f$ on Ω , while the evaluation of \hat{f} for any input value is considerably cheaper than evaluating f for the same input. This approximation is produced in a data-dependent fashion, i.e., a finite set of snapshots, obtained with the full simulation, is used to train the model to provide a good prediction of the exact result for any possible input in Ω . The computationally demanding construction of the snapshots is performed only once and in an offline phase, while the online computation of the prediction for a new input parameter uses the cheap surrogate model.

3.1 | Basic concepts of kernel methods

We introduce here only the basic tools needed for our analysis. For an extensive treatment of kernel-based approximation methods, we refer to the monographs,^{40,44,70} while a detailed discussion of kernel-based sparse surrogate models can be found in Haasdonk and Santin.⁴⁷ Nevertheless, we recall that this technique has several advantages over other approximation methods, namely, it allows for large input and output dimensions, it works with scattered data, it allows fast and sparse solutions through greedy methods, and it has a notable flexibility related to the choice of the particular kernel.

As recalled before, we aim at the reconstruction of a function $f : \Omega \rightarrow \mathbb{R}^q$, $\Omega \subset \mathbb{R}^d$. We assume to have a dataset given by $N \in \mathbb{N}$ pairwise distinct inputs, ie, a set $X_N := \{x_1, \dots, x_N\} \subset \Omega$ of N points in Ω (the data points) and corresponding function evaluations $F_N := \{f(x_i), x_i \in X_N\} \subset \mathbb{R}^q$ (the data values).

The construction of \hat{f} makes use of a positive definite kernel K on Ω . We recall that a function $K : \Omega \times \Omega \rightarrow \mathbb{R}$ is a strictly positive kernel on Ω if it is symmetric and, for any $N \in \mathbb{N}$ and any set of pairwise distinct points $X_N := \{x_1, \dots, x_N\} \subset \Omega$, the $N \times N$ kernel matrix $A_{K, X_N} := (K(x_i, x_j))_{i,j=1}^N$ is positive definite. Many strictly positive definite kernels are known in explicit form, and notable examples are, e.g., the Gaussian $K(x, y) := \exp(-\varepsilon^2 \|x - y\|_2^2)$ (where ε is a tunable parameter) and the Wendland kernels,⁴⁵ which are radial and compactly supported kernels of piecewise polynomial type and of finite smoothness. Given a kernel K , the surrogate model $\hat{f} : \Omega \rightarrow \mathbb{R}^q$ is constructed via the ansatz

$$\hat{f}(x) := \sum_{j=1}^N \alpha_j K(x, x_j), \quad x \in \Omega, \quad (19)$$

with unknown coefficient vectors $\alpha_j \in \mathbb{R}^q$. The coefficients are obtained by the vectorial interpolation conditions

$$\hat{f}(x_i) = f(x_i), \quad 1 \leq i \leq N, \quad (20)$$

i.e., the surrogate model \hat{f} is required to predict the same value of the full model f when computed on each of the data points contained in the dataset. Putting together the ansatz (19) and the interpolation conditions (20), one obtains the set of equations

$$\hat{f}(x_i) = \sum_{j=1}^N \alpha_j K(x_i, x_j) = f(x_i), \quad 1 \leq i \leq N,$$

which can be formulated as a linear system $A_{K, X_N} \alpha = b$ with

$$A_{K, X_N} := [K(x_i, x_j)]_{i,j=1}^N \in \mathbb{R}^{N \times N}, \quad \alpha := \begin{bmatrix} \vdots \\ \alpha_j^T \\ \vdots \end{bmatrix} \in \mathbb{R}^{N \times q}, \quad b := \begin{bmatrix} \vdots \\ f(x_i)^T \\ \vdots \end{bmatrix} \in \mathbb{R}^{N \times q}. \quad (21)$$

Since the kernel is chosen to be strictly positive definite, the matrix A_{K,X_N} is positive definite for any X_N ; thus, the above linear system possesses a unique solution $\alpha \in \mathbb{R}^{N \times q}$. In other terms, the model (19) satisfying interpolation conditions (20) is uniquely defined for arbitrary pairwise distinct data points X_N and data values F_N .

This interpolation scheme can be generalised by introducing a regularisation term, which reduces possible oscillations in the surrogate at the price of a nonexact interpolation of the data. We remark that in principle, this does not reduce the accuracy, since a parameter $\lambda \geq 0$ can be used to tune the influence of the regularisation term, and a zero value can be used when no regularisation is needed.

To explain this in details, we first recall that, associated with a strictly positive definite kernel, there is a uniquely defined Hilbert space $\mathcal{H}_K(\Omega)$ of functions from Ω to \mathbb{R}^q . For the sake of simplicity, we discuss the case $q = 1$, i.e., scalar-valued functions, while the generalisation to vectorial functions will be sketched at the end of this section. The space $\mathcal{H}_K(\Omega)$ contains in particular all the functions of the form (19), and their squared norm can be computed as $\|\hat{f}\|_{\mathcal{H}_K(\Omega)}^2 = \alpha^T A_{K,X_N} \alpha$. This means that a surrogate with small $\mathcal{H}_K(\Omega)$ -norm is defined by coefficients α with small magnitude.

With these tools, and again for $q = 1$ and a regularisation parameter $\lambda \geq 0$, a different surrogate can be defined as the solution of the optimisation problem

$$\min_{\hat{f} \in \mathcal{H}_K(\Omega)} \sum_{i=1}^N (f(x_i) - \hat{f}(x_i))^2 + \lambda \|\hat{f}\|_{\mathcal{H}_K(\Omega)}^2 = \min_{\alpha \in \mathbb{R}^N} \|A_{K,X_N} \alpha - b\|_2^2 + \lambda \alpha^T A_{K,X_N} \alpha, \quad (22)$$

which is a regularised version of the interpolation conditions (20), where exact interpolation is replaced by square error minimisation, and the surrogate is requested to have a small norm. When a strictly positive definite kernel is used, the representer theorem⁷¹ guarantees that the problem (22) has a unique solution, that this solution is of the form (19), and that the coefficients α are defined as the solutions of the linear system

$$(A_{K,X_N} + \lambda I) \alpha = b,$$

where I is the $N \times N$ identity matrix and where now α and b are column vectors. It is now clear that pure interpolation can be obtained by letting $\lambda = 0$ although a positive λ improves the conditioning of the linear system, reducing possible oscillations in the solution.

These Hilbert spaces, the corresponding error analysis, and the formulation of the regularised interpolant can be extended to the case of vector-valued functions $f : \Omega \rightarrow \mathbb{R}^q$ just by applying the same theory to each of the q components. The fundamental point here, to have an effective method to be used in surrogate modelling, is to avoid having q different surrogates, one for each component. This would result in q independent sets of centres, hence many kernel evaluations to compute a point value $\hat{f}(x)$. To reduce the overall number of centres, one can make the further assumption that a common set of centres is used for all components. From the point of view of the actual computation of the interpolant, this is precisely equivalent to the solution of the linear system (21), where in the regularised case also the term λI is included. We remark that more sophisticated approaches are possible to treat vector-valued functions, but the approach presented in this work yields already satisfactory results.

3.2 | Sparse approximation

So far, we have shown that kernel interpolation is well defined for arbitrary data and that the corresponding interpolant has certain approximation properties. Although the method can deal with arbitrary pairwise distinct inputs X_N , the resulting surrogate model \hat{f} is required to be fast to evaluate. From formula (19), it is clear that the computational cost of the evaluation of $\hat{f}(x)$ on a new input parameter $x \in \Omega$ is essentially related to the number N of elements in the sum. It is thus desirable to find a sparse expansion of the form (19), i.e., one where most of the coefficient vectors α_j are zero. This sparsity structure can be obtained by selecting a small subset $X_n \subset X_N$ of the data points and computing the corresponding surrogate.

An optimal selection of these points is a combinatorial problem, which is too expensive with respect to the computational effort. Instead, we use greedy methods (see Temlyakov⁷² for a general treatment and De Marchi et al⁷³ and Schaback and Wendland⁷⁴ for the case of kernel approximation). Such methods select a sequence of data points starting with the empty set $X_0 := \emptyset$, and, at iteration $n \geq 1$, they update the set as $X_n := X_{n-1} \cup \{x_n\}$ by adding a suitable selected point $x_n \in X_N \setminus X_{n-1}$. The selection of x_n is done here with the f -vectorial kernel orthogonal greedy algorithm (f -VKOGA⁷⁵), which works as follows. At each iteration, a partial surrogate can be constructed as

$$\hat{f}_n(x) = \sum_{j=1}^n \alpha_j K(x, x_j), \quad (A_{K, X_n} + \lambda I)\alpha = b_{X_n},$$

where A_{K, X_n} , b_{X_n} are the matrix and vector of (21) restricted to the points X_n . To evaluate the quality of the partial surrogate, one can check the residual vector

$$r_n(f)(x) := f(x) - \hat{f}_n(x),$$

for all $x \in X_N \setminus X_n$. The f -VKOGA takes precisely $x_n := \max_{x \in X_N \setminus X_{n-1}} \|r_n(x)\|_2$, ie, it includes in the model the data point where the error is currently largest. By checking the size of the residual, one can stop the iteration with $\hat{f}_n \approx \hat{f}$, while potentially $n \ll N$, ie, the new surrogate model is much cheaper to evaluate, but it retains the same accuracy of \hat{f} . More precisely, it has been proven that, under smoothness assumptions on the target function f , the VKOGA algorithm, with the f - or similar selection strategies, can attain algebraic or even spectral convergence rates.^{75,76}

Finally, we remark that the partial surrogates can be efficiently updated when adding a new point, i.e., \hat{f}_n can be obtained from \hat{f}_{n-1} by computing only a new coefficient in the expansion, while the already computed ones are not modified. We point to the paper⁴⁷ for a more in-depth explanation of this efficient computational process.

Observe that this greedy method results in the selection of a small subspace $V_n := \text{span}\{K(\cdot, x_i), x_i \in X_n\}$, and \hat{f}_n is computed as the projection, thus best approximation, of f into V_n . The selection of the points X_n via the f -greedy selection strategy makes use of the values of f on all the points X_N . In this sense, the procedure is similar to a least square approximation, where a small set of points is used to generate an accordingly small approximation space. Nevertheless, it is not clear in the least square setting how these few points should be selected, whereas the present approach allows an incremental selection of points and an efficient update of the approximant, which can be stopped when a tolerance criterion is reached. Moreover, by solving (22), we are indeed constructing an approximant that minimises a least squares accuracy term combined with a regularisation term.

3.3 | Simulating blood flow in the vicinity of a peripheral stenosis by means of kernel methods

Coming back to the blood flow simulation, we define in details the target functions f , which will be approximated by the kernel method. These functions will represent the maps from an input stenosis degree $R_s \in [0, 1]$ to the resulting pressure or flow rate curve for different vessels, as computed by the full simulation of Section 2.2. The definition of f is described in the following.

Since the numerical simulation is expected to have a transient phase before reaching an almost-periodic behaviour, the system is first simulated with the method of Section 2.2 in the time interval $[T_0 := 0\text{s}, T_1 := 20\text{s}]$ for the healthy state $R_s = 0$. The state reached at time T_1 is then used as initial value for the subsequent simulations. At the time T_1 , the stenosis is activated with a degree $R_s \in [0, 1]$ and the system is simulated until $T_2 = 30$ seconds for various values of R_s .

From this set of simulations for different values of R_s , we keep the pressure and flow rate curves of the last heartbeat, i.e., in the time interval $[29\text{s}, 30\text{s}]$. This means that for each point in the spatial grid, we have the time evolution of the pressure and flow rate, which are represented as a q -dimensional vector for each space point, where q depends on the actual time discretisation step.

To study the effect of the stenosis, we concentrate on the vessels number $N_v \in \{52, 54, 55, 56\}$, which are the ones surrounding the stenosis (see Figure 1), and for each of those, we select a reference space point. Putting all together, for each of the 4 vessels, we have one reference point located in the middle of these vessels. For each point, we have the q -dimensional time discretisation of the pressure and flow rate curve in the time interval $[29\text{s}, 30\text{s}]$. The maps from an input stenosis degree to these vectors define functions $f_{N_v}^P : [0, 1] \rightarrow \mathbb{R}^q$ (for the pressure) and $f_{N_v}^F : [0, 1] \rightarrow \mathbb{R}^q$ (for the flow rate).

Figures 5 and 6 show examples of pressure and flow rate curves, for both healthy state and $R_s \approx 0.7$. It can be observed that in the case $R_s \approx 0.7$, the flow rate in vessels 54 and 56 is remarkably reduced, while the flow rate in vessel 55 is slightly enlarged. The pressures in vessels 52, 54, and 55 are increased, which may lead to the formation of an aneurysm, if the vessel walls are weakened in this region. Concerning the healthy state $R_s = 0$, one has to note that the pressure values are within a physiological reasonable range, i.e., 79 mmHg for the diastolic pressure and 130 mmHg for the systolic pressure. Similar pressure curves have also been published in other works.^{21,33}

With respect to the general setting introduced in the previous section, we have here $d := 1, q = 400, \Omega := [0, 1]$. We can then train a kernel model for each of the 8 functions (corresponding to pressure and flow rate for each of the 4

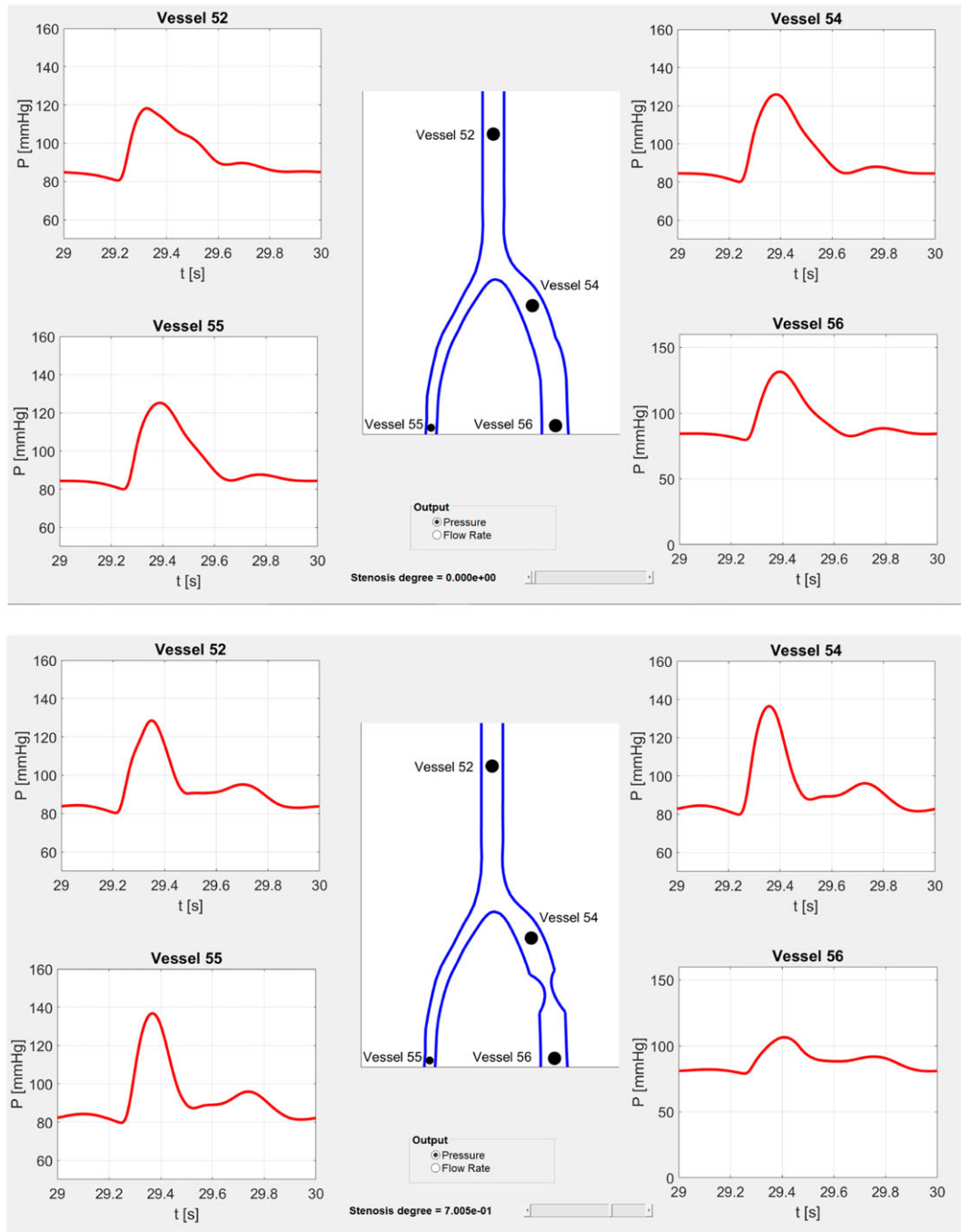


FIGURE 5 Pressure curves around the stenosis for the healthy state (top) and a degree of stenosis $R_s \approx 0.7$ (bottom). The curves are reported at the black dots for $t \in [29 \text{ s}, 30 \text{ s}]$

vessels) using snapshot-based datasets. In particular, the data points $X_N \subset [0, 1]$ are a set of N pairwise distinct stenosis degrees, and $F_N \subset \mathbb{R}^q$ is the set of snapshots obtained by the full model run on the input parameters X_N .

Those models can then be used to predict the output of the simulation for an input stenosis not present in the dataset. For example, for a given value $R_s \in [0, 1]$, the evaluation $\hat{f}_{N_v}^P(R_s)$ is a q -dimensional vector that approximates the pressure curve in the time interval $[29\text{s}, 30\text{s}]$ in vessel N_v with stenosis degree R_s . We remark that this setting can be easily modified to approximate different aspects of the full simulation, although the present ones yield interesting insights into the behaviour of the system.

Before we present the numerical tests, 2 remarks on the data are in order. First, the current time step produces 400 samples per second, which means that we have $q = 400$, i.e., we are approximating functions $[0, 1] \rightarrow \mathbb{R}^{400}$. Second, the data obtained with $R_s = 0$ are removed from the datasets and replaced with the one with $R_s = 10^{-6}$, since the ODE

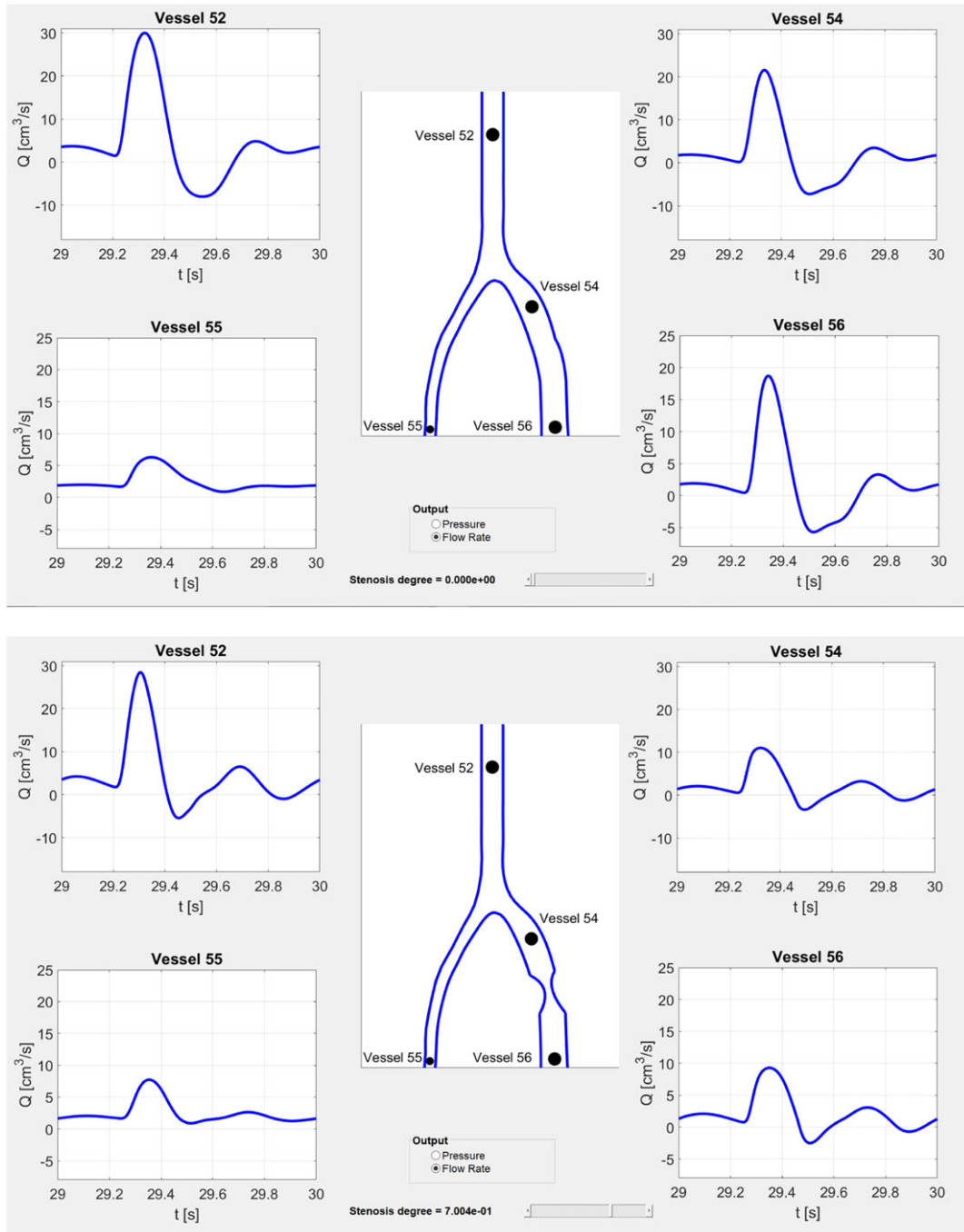


FIGURE 6 Flow rate curves around the stenosis for the healthy state (top) and a degree of stenosis $R_s \approx 0.7$ (bottom). The curves are reported at the black dots for $t \in [29 \text{ s}, 30 \text{ s}]$

model (18) is meaningful only for a strictly positive value of the stenosis degree, while the quadratic term vanishes for $R_s = 0$, thus leading to a different model. This restriction is not relevant from an application point of view, since the a value $R_s = 10^{-6}$ can be considered to effectively represent the healthy state.

In the training of each model, the parameters ε and λ are chosen within a range of possible values by k -fold cross-validation. This means that the training data are randomly permuted and divided into k disjoint subsets of approximately the same size and, for each pair (ε, λ) of possible parameters, a model is trained on the union of $k - 1$ subsets and tested on the remaining one. This operation is repeated k times changing in all possible ways the $k - 1$ sets used for training. The average of the error obtained by these k tests is assigned as the error score of the parameter pair, and the best pair (ε, λ) is chosen as the one yielding the smallest error score. The actual model is then trained on the whole training set using these parameters. In more details, we use here 10-fold cross-validation and test 20 logarithmic equally

spaced values $\varepsilon \in [10^{-2}, 50]$ and 15 logarithmic equally spaced values $\lambda \in [10^{-16}, 10^{-2}]$. The error measure to sort the parameters is the maximum absolute error.

4 | NUMERICAL TESTS

This section is concerned with the training of the surrogate models and analyses them under different perspectives. We train different surrogates using different training sets of increasing size to analyse the number of full model runs needed to have an accurate surrogate. They are obtained each with N equally spaced stenosis degrees in $[10^{-6}, 1]$, with $N = \{5, 10, 20, 40, 80, 160, 320, 640\}$.

A further dataset of $N = 1000$ equally spaced stenosis degrees is used as a test set, i.e., the surrogates computed with the various training datasets are evaluated on this set of input stenosis degrees, and the results are compared with the full model computations. We remark that the values of this test set are not contained in the training sets (except for $R_s = 10^{-6}$ and $R_s = 1$), so the results are reliable assessments of the models' accuracy. For every value $(R_s)_i$ in the test set, we consider the absolute and relative errors

$$e_A^{(i)} := \|f((R_s)_i) - \hat{f}((R_s)_i)\|_2, \quad e_R^{(i)} := \frac{\|f((R_s)_i) - \hat{f}((R_s)_i)\|_2}{\|f((R_s)_i)\|_2},$$

and, to measure the overall error over the test set, we compute both the maximum absolute and relative errors, i.e.,

$$E_A := \max_{1 \leq i \leq 1000} e_A^{(i)}, \quad E_R := \max_{1 \leq i \leq 1000} e_R^{(i)}.$$

We use the Gaussian kernel, and the f -VKOGA is stopped using a tolerance $5 \cdot 10^{-8}$ on the regularised *Power Function*, which controls the model stability.⁴⁷

4.1 | Simulation parameters

Before we study the performance of the numerical model, we summarise the simulation parameters in this subsection. For the 1-D arterial network, the data from Sherwin et al^{13, Table 1} have been used. In this table, the different lengths l_i , section areas $A_{0,i}$, and elasticity parameters β_i can be found. By means of β_i and $A_{0,i}$, the elasticity parameters $G_{0,i}$ in (3) can be calculated as follows: $G_{0,i} = \beta_i \cdot \sqrt{A_{0,i}}$. Please note that vessel 54 from the original dataset is split into a new vessel 54 of length $l_{54} = 10.0$ cm, the stenosis of length $l_s = 1.0$ cm, and an additional vessel 56 of length $l_{56} = 21.2$ cm (see Figures 1 and 4). The resistances $R_{p,i} = R_{1,i} + R_{2,i}$ and capacities C_i occurring in (17) are listed in Stergiopoulos et al,^{69, Table 2} where the resistance $R_{1,i}$ is determined by the characteristic impedance $Z_i = \rho \cdot c(A_{0,i}) / A_{0,i}$.²¹ For $t = 0$, we set $A_i(z, 0) = A_{0,i}$, $Q_i(z, 0) = 0$ and $p_i(z, 0) = 0$ in the corresponding vessels. The parameters for the left ventricle model are listed in Table 1. To solve the ODEs occurring in Section 2, we use an explicit discretisation scheme of first order.

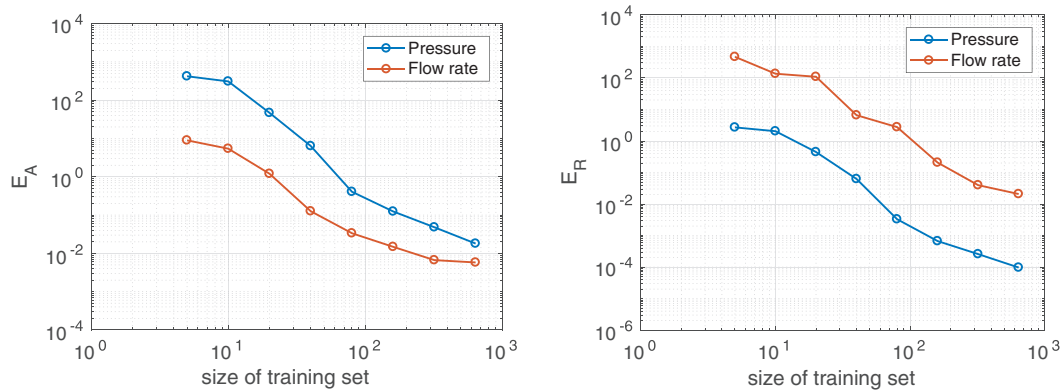
TABLE 1 List of the different parameters for the model of the left ventricle^{23, section 4.33, Table 2}

Physical Parameter	Sign	Value	Unit
Dead volume left ventricle	V_0	10.00	cm ³
Maximal volume	V_{\max}	130.00	cm ³
Duration of heart cycle	T	1.00	s
Duration of ventricular contraction	T_{vep}	0.30	s
Duration of ventricular relaxation	T_{vvp}	0.15	s
Maximal elastance	E_{\max}	2.75	mm Hg/cm ³
Minimal elastance	E_{\min}	0.08	mm Hg/cm ³
Viscous resistance	R	$3.0 \cdot 10^{-3}$	mm Hg · s/cm ³
Separation coefficient	B	$2.5 \cdot 10^{-5}$	mm Hg · s ² /cm ⁶
Inductance coefficient	L	$5.0 \cdot 10^{-4}$	mm Hg · s ² /cm ³

TABLE 2 Accuracy of the surrogates for pressure and flow rate for vessels 52, 54, and 55^a

N	Vessel 52		Vessel 54		Vessel 55	
	E_A	E_R	E_A	E_R	E_A	E_R
Pressure						
10	$5.76 \cdot 10^0$	$3.01 \cdot 10^{-3}$	$7.35 \cdot 10^0$	$3.80 \cdot 10^{-3}$	$7.41 \cdot 10^0$	$3.85 \cdot 10^{-3}$
40	$1.15 \cdot 10^0$	$6.00 \cdot 10^{-4}$	$1.50 \cdot 10^0$	$7.75 \cdot 10^{-4}$	$1.51 \cdot 10^0$	$7.85 \cdot 10^{-4}$
160	$9.53 \cdot 10^{-1}$	$4.97 \cdot 10^{-4}$	$1.23 \cdot 10^0$	$6.35 \cdot 10^{-4}$	$1.25 \cdot 10^0$	$6.47 \cdot 10^{-4}$
640	$2.95 \cdot 10^{-1}$	$1.54 \cdot 10^{-4}$	$2.98 \cdot 10^{-1}$	$1.54 \cdot 10^{-4}$	$3.01 \cdot 10^{-1}$	$1.56 \cdot 10^{-4}$
Flow rate						
10	$6.05 \cdot 10^0$	$3.35 \cdot 10^{-2}$	$5.48 \cdot 10^0$	$2.51 \cdot 10^{-1}$	$8.33 \cdot 10^{-1}$	$1.20 \cdot 10^{-2}$
40	$7.72 \cdot 10^{-1}$	$4.28 \cdot 10^{-3}$	$5.23 \cdot 10^{-1}$	$2.41 \cdot 10^{-2}$	$1.84 \cdot 10^{-1}$	$2.64 \cdot 10^{-3}$
160	$6.35 \cdot 10^{-1}$	$3.52 \cdot 10^{-3}$	$4.08 \cdot 10^{-1}$	$1.88 \cdot 10^{-2}$	$1.41 \cdot 10^{-1}$	$2.03 \cdot 10^{-3}$
640	$1.73 \cdot 10^{-1}$	$9.61 \cdot 10^{-4}$	$7.70 \cdot 10^{-2}$	$3.55 \cdot 10^{-3}$	$3.02 \cdot 10^{-2}$	$4.34 \cdot 10^{-4}$

^aThe table shows the absolute (E_A) and relative (E_R) errors obtained with datasets of increasing size N .

**FIGURE 7** Absolute (left) and relative (right) errors obtained by kernel surrogates with an increasing training set, for both the pressure (blue curves) and flow rate (red curves)

4.2 | Accuracy of the surrogate models

We start by describing in detail the results obtained for vessel 56, i.e., for the functions f_{56}^P and f_{56}^F . Figure 7 shows the absolute and relative errors E^A (left) and E^R (right) for the 2 functions. For both the pressure and flow rate, it is clear that an increase in the dataset size, hence in the number of full model runs, produces significantly more accurate models. The actual magnitude in the absolute errors is different between pressure and flow rate, due to a different magnitude of the output quantities. Nevertheless, the relative errors demonstrate that the pressure curves are better approximated by the kernel models by about 2 orders of magnitude, for each dataset size. In any case, the models exhibit a converging behaviour towards the full model. Moreover, it should be noted that already a relatively small dataset of $N = 160$ stenosis degrees produces good results in both cases. For a better understanding of the error behaviour, we report in Figure 8 the pointwise absolute and relative errors $e_A^{(i)}$, $e_R^{(i)}$ for pressure (left) and flow rate (right) in the case $N = 640$. Observe that the errors are in all cases very oscillating, since each point in the plots represents one value of $e_A^{(i)}$ (or $e_R^{(i)}$) for a different value of $(R_s)_i$, i.e., it is the 2-norm of the 400-dimensional vector $f((R_s)_i) - \hat{f}((R_s)_i)$. Thus, the small oscillations for a single parameter of the surrogate around the exact solution are amplified into the values depicted in the figures.

It is worth noticing that in both cases, the magnitude of the exact quantity is decreasing for R_s close to one; thus, the relative error is magnified for high stenosis degrees. This effect is particularly evident for the flow rate, where the kernel model has a better absolute accuracy for $R_s \approx 1$, but a significantly worse relative accuracy.

We remark that this causes the worse relative error for the flow rate observed in Figure 7. Indeed, the relative error E_R for a given size of the training set is computed as the maximum of the relative error $e_R^{(i)}$ for all the values $(R_s)_i$ in the test set. Thus, E_R is dominated by the relative error obtained in the region $R_s \approx 1$, which is large due to the small magnitude

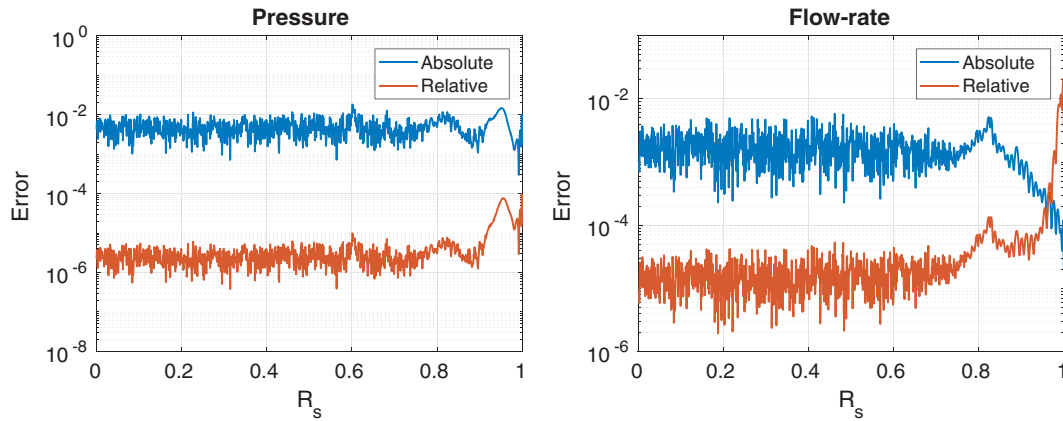


FIGURE 8 Pointwise absolute (blue) and relative (red) errors obtained by the kernel models with $N = 640$ training points for the prediction of the pressure (left) and flow rate (right)

of the flow rate computed by the full model. A different error measure, e.g., the average relative error, would result in a different error decay in Figure 7.

Similar results have been obtained for the other 3 vessels. The results are reported in Table 2. It is relevant to notice that for these vessels, the effect of the stenosis is much less visible. Indeed, the relative error for the flow rate is not significantly worse than the one of the pressure, since the flow does not completely vanish for increasing stenosis degrees. This effect is more evident for vessels 52 and 55, which are not directly connected with the stenosis.

To further measure the accuracy of the surrogate, we compare a relevant blood flow index obtained with the full model and with the surrogate. We consider the pulsatility index PI , which is a commonly used diagnostic index and has the advantage of being measurable in a non-invasive way (see, e.g., Stergiopoulos et al⁶⁹). For a given stenosis degree R_s , in vessel N_v , it is computed as

$$PI^P(R_s) := \frac{\max(f_{N_v}^P(R_s)) - \min(f_{N_v}^P(R_s))}{\text{mean}(f_{N_v}^P(R_s))}, \quad PI^F(R_s) := \frac{\max(f_{N_v}^F(R_s)) - \min(f_{N_v}^F(R_s))}{\text{mean}(f_{N_v}^F(R_s))},$$

for the pressure and flow rate, respectively. It measures the difference between the systolic and diastolic pressures (or flow rate) divided by its average value. This index can be computed in the same way also for the surrogate using the same formula with the full model replaced with the data-based prediction. Figure 9 reports the logarithmic error between the exact and the predicted values of PI^P (left) and PI^F (right) in vessel 56, for all values of R_s in the test set and for the surrogate obtained with $N = 640$. The results demonstrate the accuracy of the approximate model also in capturing a physically relevant quantity, and this is obtained by data accuracy only, ie, no constraint is imposed to the surrogate to match the desired values of the PI index of the full model. The simulation results that are provided in Figure 9 show a similar curve progression as in Stergiopoulos et al.⁶⁹, figure 3 or figure 6. For small stenosis degrees, the normalised PI indices with respect to $R_s = 0$, ie, the health state, are almost one. As the stenosis degree increases (see Figures 5 and 6), it can be observed that in particular, the systolic pressures and flow rates are damped significantly. As a consequence, the PI indices are decreasing monotonously. Up to a stenosis degree of $R_s = 0.5$, the gradient of the curve is rather low, while for a severe stenosis $R_s > 0.5$, the gradient of the PI curve is very high.

4.3 | Efficiency of the surrogate models

It is now of interest to investigate the online efficiency of the surrogates, that is, the time needed to evaluate the models on a new input stenosis. To understand the timing results, we remark that the evaluation of the full model for a given stenosis degree R_s takes around $t_{full} = 200$ seconds, only for the simulation of the time interval [29s, 30s], i.e., without considering the transient phase. We remark that the present MATLAB implementation can be significantly optimised for speed, and a smaller execution time can be expected using a compiled language.

Since the f -VKOGA constructs the surrogate selecting only a relevant subset of the full dataset, we look at the actual number of points that is selected for the various datasets and output quantities. Figure 10 (left) reports this number of points, as obtained in the approximation of f_{56}^P, f_{56}^F as discussed in the previous section. It is interesting to observe that

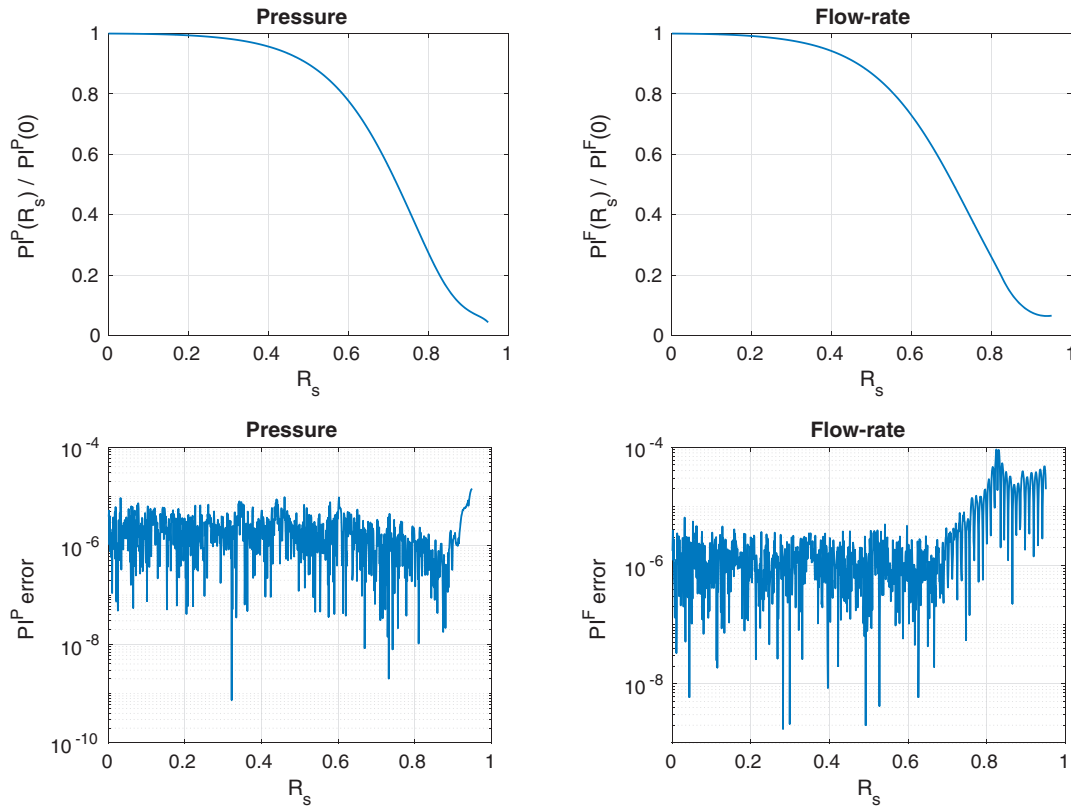


FIGURE 9 Absolute error between the pulsatility index (PI) computed with the full model and the one computed with the surrogate for the pressure (top, left) and flow rate (top, right). The results at the bottom line are obtained by a kernel model with $N = 640$

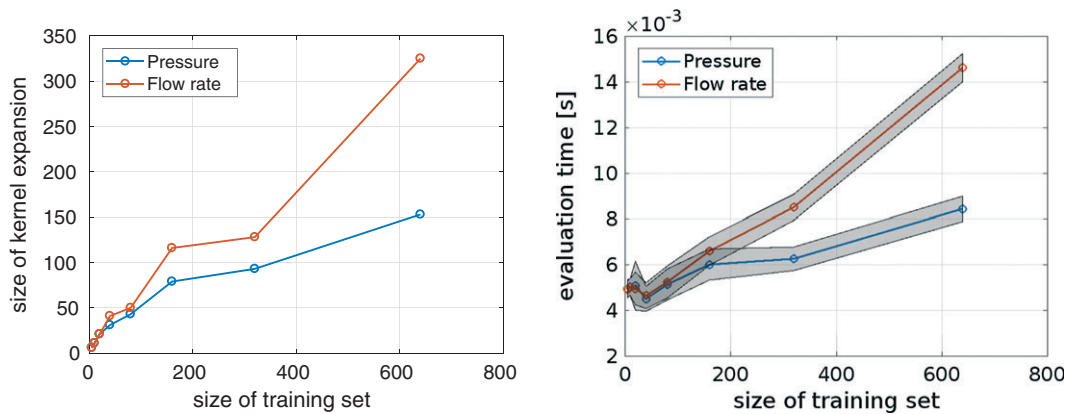


FIGURE 10 Number of points selected by the f -vectorial kernel orthogonal greedy algorithm (left) and runtime to evaluate the surrogates on 1000 inputs (right), for vessel 56 and for datasets of increasing sizes

the number of points increases as the dataset increases, but the number is well below the total number of points. This means that the surrogates are faster than a nonsparse kernel expansion. Moreover, the flow rate requires the selection of more points, which confirms that this output quantity is more difficult to predict. To assess the actual efficiency of the models, in Figure 10 (right), we report the runtime required to evaluate each model on the 1000 test stenosis degrees. The evaluation is repeated 100 times, and the figure shows the mean and standard deviation over the 100 experiments. As expected, the evaluation times are related to the sparsity of the models.

In all cases, the evaluation of the surrogates on 1000 inputs takes on average less than $1.5 \cdot 10^{-2}$ seconds, ie, for the largest (hence slowest) model, we can estimate an evaluation time per stenosis degree to $t_{surrogate} = 1.5 \cdot 10^{-5}$ seconds. Compared with $t_{full} = 2 \cdot 10^2$ seconds, this still gives a speedup factor of about 10^6 in the worst case.

4.4 | Solving a state estimation problem by means of kernel methods

To demonstrate the use of the surrogate model, we use it to solve a state estimation problem that would be infeasible by using the full model. Namely, for a given pressure or flow rate curve in a time interval, we want to predict as accurately as possible the stenosis degree that corresponds to a given curve. We assume to collect the measurements into a vector $y \in \mathbb{R}^q$, which is given by the model output for a fixed, but unknown input stenosis degree R^* , plus some additive noise, i.e.,

$$y := f(R^*) + \eta v,$$

where $\eta \geq 0$ is a noise level and v is a random vector. In the following experiments, v is drawn from the uniform distribution in $(0, 1)$. We aim at detecting the value R^* from y only. Doing so, we define a cost function $J(R_s)$ measuring the squared distance between the measurements and the model prediction for a given stenosis degree R_s , i.e.,

$$J(R_s) := \frac{1}{2\|y_j\|_2^2} \sum_{j=1}^q (y_j - \tilde{f}_j(R_s))^2, \quad (23)$$

and consider the solution \tilde{R}^* of the optimisation problem

$$\tilde{R}^* = \min_{R_s \in [0,1]} J(R_s).$$

Observe that, when the noise term ηv is vanishing and the model prediction is exact, the unique minimiser is the exact solution, ie, $\tilde{R}^* = R^*$.

In principle, it would be possible to formulate the cost function (23) also in terms of the full model f . Nevertheless, this is infeasible in practice, since multiple evaluations of f are required to compute a minimiser. The use of the cheap surrogate

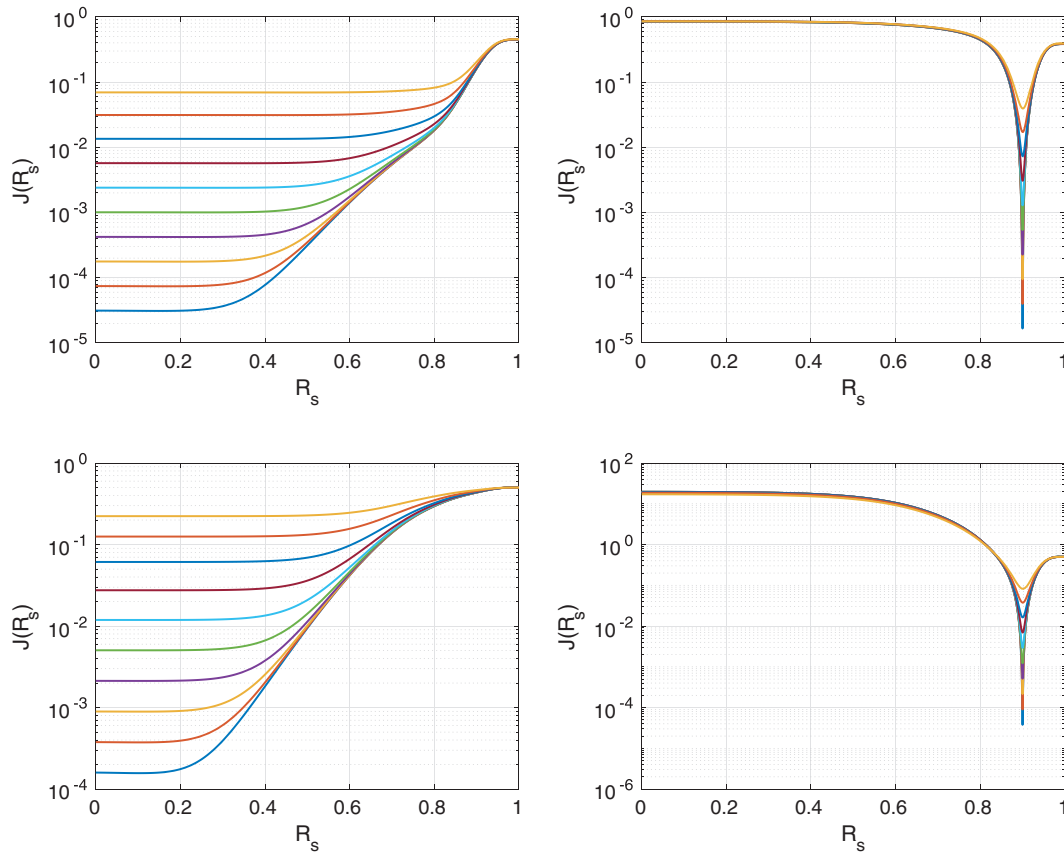


FIGURE 11 Cost functions J for $R^* = 0.1$ (left) and $R^* = 0.9$ (right) for the pressure curve (top line) and the flow rate (bottom line), for vessel 56 and using the surrogate based on the dataset of $N = 160$ full model runs. The various curves correspond to increasing noise levels in the target value y

model, instead, allows a real-time estimation of R^* . Moreover, since the kernel is differentiable the cost function is also differentiable, thus, the use of gradient-based methods is possible. In particular, we have

$$\frac{d}{dR_s} J(R_s) = \frac{1}{\|y_j\|_2^2} \sum_{j=1}^q (y_j - \tilde{f}_j(R_s)) \frac{d}{dR_s} f_j(R_s),$$

with

$$\frac{d}{dR_s} f_j(R_s) = \frac{d}{dR_s} \left(\sum_{i=1}^N \alpha_{ij} K(R_s, R_i) \right) = \sum_{i=1}^N \alpha_{ij} \frac{d}{dR_s} K(R_s, R_i),$$

and the R_s derivative of the kernel can be explicitly computed, since the kernel itself is known in closed form. In other terms, both the cost function J and its derivative can be computed efficiently by means of the surrogate, and they both only involve the evaluation of matrix-vector products.

We proceed to some experiments for vessel 56 and the surrogate models obtained with the dataset of $N = 160$ full model runs. In Figure 11, we plot the cost function J for $R_s \in [0, 1]$ and $R^* = 0.1$ (left) and $R^* = 0.9$ (right) for the pressure (top) and flow rate (bottom). The results are reported for increasing noise levels η , obtained as 10 logarithmically spaced values in $[0.01, 0.5]$. It is clear that the surrogate provides a reliable prediction when the stenosis degree is large, also in the presence of noise, since the cost function has a unique minimiser. Instead, for small target stenosis degrees, the cost function is flat, so we should expect a less accurate prediction.

The values of \tilde{R}^* can then be computed with any constrained optimisation solver, and we use here the MATLAB built-in `fmincon`, which uses an active set search procedure. The noisy input y for $\eta = 0.1$, as well as the resulting estimated curves, is depicted in Figure 12, for both $R^* = 0.1$ and 0.9 and both pressure and flow rate. The estimated values \tilde{R}^* are reported in Table 3.

At a first look, the results could seem somehow surprising, since the estimation is much better for large stenosis degrees, i.e., in the cases where the surrogates are less accurate. Nevertheless, the exact values of the pressure and the flow rate indeed are less variable for small R_s , so for the estimator, it is more difficult to discriminate between different values.

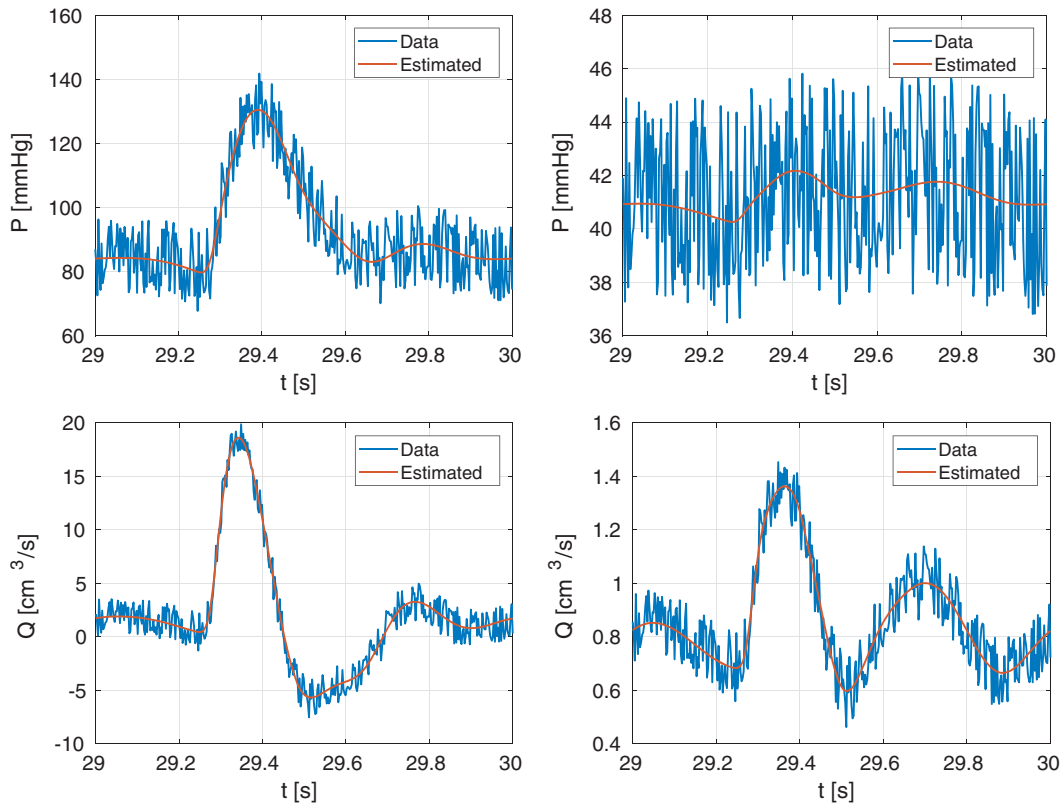


FIGURE 12 Noisy data and estimated curves for $R^* = 0.1$ (left) and $R^* = 0.9$ (right) for the pressure curve (top line) and the flow rate (bottom line) (vessel 56). The surrogate model is based on the dataset of $N = 160$ full model runs

TABLE 3 Results of the parameter identification problem for the pressure and flow rate curves with $R^* = 0.1$ and $R^* = 0.9^a$

R^*	Pressure		Flow rate	
	\bar{R}^*	Error	\bar{R}^*	Error
0.1	$3.11 \cdot 10^{-1}$	$2.11 \cdot 10^{-1}$	$1.37 \cdot 10^{-1}$	$3.71 \cdot 10^{-2}$
0.9	$9.00 \cdot 10^{-1}$	$1.67 \cdot 10^{-4}$	$9.00 \cdot 10^{-1}$	$1.83 \cdot 10^{-4}$

^aThe table reports the estimated values \bar{R}^* and the errors with respect to the exact state.

5 | CONCLUSION AND FURTHER WORK

In this paper, we have simulated blood flow in the 55 main arteries of the systemic circulation. For this purpose, 1-D blood flow models have been considered. At the outlets of the main arteries, 0-D lumped parameter models have been coupled with the corresponding 1-D models to include the Windkessel effect of the omitted vessels, while at the inlet of the aorta (vessel 1), a lumped parameter model for the left ventricle has been coupled with the 1-D model for the aorta. Furthermore, the impact of a stenosis in a tibial artery has been simulated by an ODE depending on the degree of the stenosis. To be able to obtain insight into the flow behaviour in the vicinity of the stenosis for an arbitrary degree of stenosis without starting the simulation for every degree of stenosis again, the output data are provided by a surrogate model based on kernel methods. It has been demonstrated that the error between the surrogate kernel model and the exact simulation result is decreasing as more and more training data are included into the surrogate model. In addition to that, the efficiency of the kernel method has been investigated. The surrogate kernel model has been used to solve a parameter and state estimation problem: For a given pressure or flow rate curve in the vicinity of the stenosis, the corresponding degree of stenosis is estimated, and the kernel-based surrogate yields also a prediction of the state. This is a step towards real-time estimation and decision in patient-specific treatments.

Future work may be concerned with simulating the whole circulation by means of a closed-loop model. This means that besides the left ventricle, also the remaining chambers of the heart as well as the pulmonary circulation and the venous part of the systemic circulation have to be modelled.³³ A further aspect that could be investigated would be to include besides the stenosis degree more parameters of interest. Two possible parameters would be the peripheral resistances of vessels 55 and 56. In Section 2.5, we denoted them by $R_{2,55}$ and $R_{2,56}$. Varying these parameters, one could simulate the effect of vasodilation, i.e., the enlargement of arterioles due to a reduced blood supply of tissue. In this context, it is of great interest how these resistances have to be adapted such that for a given degree of stenosis, a maximal blood flow rate distal to the stenosis can be restored.

Moreover, the cost function for the state estimation problem in Section 4.4 could be improved such that the estimates for low stenosis degrees are more accurate.

In more general terms, other aspects of model- and data-driven surrogate modelling could be investigated. For instance, the same kernel-based technique has been recently applied to uncertainty quantification.⁷⁷ In the present setting, this could lead to the fast assessment of the impact of uncertainty on the model output, e.g., in a setting where the stenosis degree or other possible input quantities are not exactly measured.

ACKNOWLEDGEMENTS

The authors would like to thank the German Research Foundation (DFG) for the financial support of the project within the Cluster of Excellence in Simulation Technology (EXC 310/2) at the University of Stuttgart.

ORCID

Tobias Koeppl  <http://orcid.org/0000-0003-3548-2807>

REFERENCES

1. Ambrosi D, Quarteroni A, Rozza G. *Modeling of Physiological Flows*, Vol. 5. Mailand, Italy: Springer Science & Business Media; 2012.
2. Formaggia L, Quarteroni A, Veneziani A. *Cardiovascular mathematics: Modeling and Simulation of the Circulatory System*, Vol. 1. Mailand, Italy: Springer Science & Business Media; 2010.

3. Quarteroni A, Tuveri M, Veneziani A. Computational vascular fluid dynamics: problems, models and methods. *Comput Vis Sci*. 2000;2(4):163-197.
4. Alastruey J, Parker K, Peiró J, Byrd S, Sherwin S. Modelling the circle of Willis to assess the effects of anatomical variations and occlusions on cerebral flows. *J Biotechnol*. 2007;40(8):1794-1805.
5. Ryu J, Hu X, Shadden S. A coupled lumped-parameter and distributed network model for cerebral pulse-wave hemodynamics. *J Biomed Eng*. 2015;137(10):101009.
6. Schaper W, Piek J, Munoz-Chapuli R, Wolf C, Ito W, et al. Collateral circulation of the heart. *Angiogenesis and Cardiovascular Disease*. 1999:159-198.
7. Scholz D, Ziegelhoeffer T, Helisch A, et al. Contribution of arteriogenesis and angiogenesis to postocclusive hindlimb perfusion in mice. *J Mol Cell Cardiol*. 2002;34(7):775-787.
8. Alastruey J, Moore S, Parker K, David T, Peiró J, Sherwin S. Reduced modelling of blood flow in the cerebral circulation: coupling 1-D, 0-D and cerebral auto-regulation models. *Int J Numer Methods Fluids*. 2008;56(8):1061.
9. Drzisga D, Köppl T, Pohl U, Helmig R, Wohlmuth B. Numerical modeling of compensation mechanisms for peripheral arterial stenoses. *Comput Biol Med*. 2016;70:190-201.
10. Köppl T, Schneider M, Pohl U, Wohlmuth B. The influence of an unilateral carotid artery stenosis on brain oxygenation. *Med Eng Phys*. 2014;36(7):905-914.
11. Wang J, Parker K. Wave propagation in a model of the arterial circulation. *J Biomech*. 2004;37(4):457-470.
12. Westerhof N, Bosman F, De Vries C, Noordergraaf A. Analog studies of the human systemic arterial tree. *J Biomech*. 1969;2(2):121IN1135IN3137IN5139-134136138143.
13. Sherwin S, Formaggia L, Peiro J, Franke V. Computational modelling of 1D blood flow with variable mechanical properties and its application to the simulation of wave propagation in the human arterial system. *Int J Numer Methods Fluids*. 2003;43(6-7):673-700.
14. Bazilevs Y, Gohean J, Hughes T, Moser R, Zhang Y. Patient-specific isogeometric fluid-structure interaction analysis of thoracic aortic blood flow due to implantation of the Jarvik 200 left ventricular assist device. *Comput Methods Appl Mech Eng*. 2009;198(45):3534-3550.
15. Colciago C, DeParis S, Quarteroni A. Comparisons between reduced order models and full 3D models for fluid-structure interaction problems in haemodynamics. *J Comput Appl Math*. 2014;265:120-138.
16. Crosetto P, Reymond P, DeParis S, Kontaxakis D, Stergiopoulos N, Quarteroni A. Fluid-structure interaction simulation of aortic blood flow. *Comput Fluids*. 2011;43(1):46-57.
17. Torii R, Oshima M, Kobayashi T, Takagi K, Tezduyar T. Fluid-structure interaction modeling of blood flow and cerebral aneurysm: significance of artery and aneurysm shapes. *Comput Methods Appl Mech Eng*. 2009;198(45):3613-3621.
18. D'Angelo C. Multiscale modelling of metabolism and transport phenomena in living tissues. *Ph.D. Thesis: École Polytechnique Fédérale de Lausanne*; 2007.
19. Notaro D, Cattaneo L, Formaggia L, Scotti A, Zunino P. A mixed finite element method for modeling the fluid exchange between microcirculation and tissue interstitium. In: *Advance in Discretization Methods*. Cham: Springer; 2016:3-25.
20. Reichold J, Stampanoni M, Keller A, Buck A, Jenny P, Weber B. Vascular graph model to simulate the cerebral blood flow in realistic vascular networks. *J Cereb Blood Flow Metab*. 2009;29(8):1429-1443.
21. Alastruey J, Parker K, Peiró J, Sherwin S. Lumped parameter outflow models for 1-D blood flow simulations: effect on pulse waves and parameter estimation. *Commun Comput Phys*. 2008;4(2):317-336.
22. Alastruey J, Passerini T, Formaggia L, Peiró J. Physical determining factors of the arterial pulse waveform: theoretical analysis and calculation using the 1-D formulation. *J Eng Math*. 2012:1-19.
23. Formaggia L, Lamponi D, Tuveri M, Veneziani A. Numerical modeling of 1D arterial networks coupled with a lumped parameters description of the heart. *Comput Methods Biomech Biomed Engin*. 2006;9(5):273-288.
24. Malossi A, Blanco P, Crosetto P, DeParis S, Quarteroni A. Implicit coupling of one-dimensional and three-dimensional blood flow models with compliant vessels. *Multiscale Model Simul*. 2013;11(2):474-506.
25. Marchandise E, Willemet M, Lacroix V. A numerical hemodynamic tool for predictive vascular surgery. *Med Eng Phys*. 2009;31(1):131-144.
26. Marsden A, Esmaily-Moghadam M. Multiscale modeling of cardiovascular flows for clinical decision support. *Appl Mech Rev*. 2015;67(3):030804.
27. Mynard J, Nithiarasu P. A 1D arterial blood flow model incorporating ventricular pressure, aortic valve and regional coronary flow using the locally conservative galerkin (LCG) method. *Int J Numer Methods Biomed Eng*. 2008;24(5):367-417.
28. Passerini T, Luca M, Formaggia L, Quarteroni A, Veneziani A. A 3D/1D geometrical multiscale model of cerebral vasculature. *J Eng Math*. 2009;64(4):319-330.
29. Čanić S, Kim E. Mathematical analysis of the quasilinear effects in a hyperbolic model blood flow through compliant axi-symmetric vessels. *Math Methods Appl Sci*. 2003;26(14):1161-1186.
30. Ismail M, Wall W, Gee M. Adjoint-based inverse analysis of windkessel parameters for patient-specific vascular models. *J Comput Phys*. 2013;244:113-130.
31. Olufsen M. Structured tree outflow condition for blood flow in larger systemic arteries. *Am J Phys Heart Circ Phys*. 1999;276(1):H257-H268.
32. Liang F, Hao L. A closed-loop lumped parameter computational model for human cardiovascular system. *JSME Int J Ser C Mech Syst Mach Elem Manuf*. 2005;48(4):484-493.
33. Liang F, Takagi S, Himeno R, Liu H. Multi-scale modeling of the human cardiovascular system with applications to aortic valvular and arterial stenoses. *Med Biol Eng Comput*. 2009;47(7):743-755.

34. Mynard J, Smolich J. One-dimensional haemodynamic modeling and wave dynamics in the entire adult circulation. *Ann Biomed Eng.* 2015;43(6):1443-1460.
35. Manzoni A, Quarteroni A, Rozza G. Model reduction techniques for fast blood flow simulation in parametrized geometries. *Int J Numer Methods Biomed Eng.* 2012;28(6-7):604-625.
36. Quarteroni A, Rozza G. Optimal control and shape optimization of aorto-coronary bypass anastomoses. *Math Models Methods Appl Sci.* 2003;13(12):1801-1823.
37. Quarteroni A, Rozza G. *Reduced Order Methods for Modeling and Computational Reduction*, Vol. 9. Cham: Springer; 2014.
38. Haasdonk B. Reduced basis methods for parametrized PDEs—a tutorial introduction for stationary and instationary problems. In: Benner P, Cohen A, Ohlberger M, Willcox K, eds. *Model Reduction and Approximation: Theory and Algorithms*. Philadelphia: SIAM; 2017:65-136.
39. Quarteroni A, Manzoni A, Negri F. *Reduced Basis Methods for Partial Differential Equations: An Introduction*, Vol. 92. Cham, Heidelberg, New York, Dordrecht, London: Springer; 2015.
40. Fasshauer G, McCourt M. *Kernel-Based Approximation Methods using MATLAB*, Interdisciplinary Mathematical Sciences, vol. 19. Hackensack, NJ: World Scientific Publishing Co. Pte. Ltd.; 2015.
41. Haasdonk B. Transformation knowledge in pattern analysis with kernel methods. *Ph.D. Thesis*: Albert-Ludwigs-Universität Freiburg; 2005.
42. Haasdonk B, Burkhardt H. Invariant kernel functions for pattern analysis and machine learning. *Mach Learn.* 2007;68(1):35-61.
43. Schölkopf B, Smola AJ. *Learning with Kernels*. Cambridge: MIT Press; 2002.
44. Wendland H. *Scattered Data Approximation*, Cambridge Monographs on Applied and Computational Mathematics, vol. 17. Cambridge: Cambridge University Press; 2005.
45. Wendland H. Piecewise polynomial, positive definite and compactly supported radial functions of minimal degree. *Adv Comput Math.* 1995;4(1):389-396.
46. Wirtz D, Karajan N, Haasdonk B. Surrogate modeling of multiscale models using kernel methods. *Int J Numer Methods Eng.* 2015;101(1):1-28.
47. Haasdonk B, Santin G. Greedy kernel approximation for sparse surrogate modeling. In: Keiper W, Milde A, Volkwein S eds. *Reduced-Order Modeling (ROM) for Simulation and Optimization: Powerful Algorithms as Key Enablers for Scientific Computing*. Springer International Publishing; 2018:21-45. https://doi.org/10.1007/978-3-319-75319-5_2
48. Köppl T, Wohlmuth B, Helmig R. Reduced one-dimensional modelling and numerical simulation for mass transport in fluids. *Int J Numer Methods Fluids.* 2013;72(2):135-156.
49. Seeley B, Young D. Effect of geometry on pressure losses across models of arterial stenoses. *J Biomech.* 1976;9(7):439-448.
50. Young D, Tsai F. Flow characteristics in models of arterial stenoses—ii. Unsteady flow. *J Biomech.* 1973;6(5):547-559.
51. Pries A, Neuhaus D, Gaetgens P. Blood viscosity in tube flow: dependence on diameter and hematocrit. *Am J Phys Heart Circ Phys.* 1992;263(6):H1770-H1778.
52. Quarteroni A, Formaggia L. Mathematical modelling and numerical simulation of the cardiovascular system. *Handb Numer Anal.* 2004;12:3-127.
53. Hughes T, Lubliner J. On the one-dimensional theory of blood flow in the larger vessels. *Math Biosci.* 1973;18(1-2):161-170.
54. Barnard A, Hunt W, Timlake W, Varley E. A theory of fluid flow in compliant tubes. *Biophys J.* 1966;6(6):717-724.
55. Smith N, Pullan A, Hunter P. An anatomically based model of transient coronary blood flow in the heart. *SIAM J Appl Math.* 2002;62(3):990-1018.
56. DeVault K, Gremaud P, Novak V, Olufsen M, Vernieres G, Zhao P. Blood flow in the circle of Willis: modeling and calibration. *Multiscale Model Simul.* 2008;7(2):888-909.
57. Valdez-Jasso D, Haider M, Banks H, et al. Analysis of viscoelastic wall properties in ovine arteries. *IEEE Trans Biomed Eng.* 2009;56(2):210-219.
58. Acosta S, Puelz C, Riviere B, Daniel J., Rusin C. Numerical method of characteristics for one-dimensional blood flow. *J Comput Phys.* 2015;294:96-109.
59. Formaggia L, Nobile F, Quarteroni A. A one dimensional model for blood flow: application to vascular prosthesis. In: *Mathematical Modeling and Numerical Simulation in Continuum Mechanics*. Springer; 2002; Berlin, Heidelberg:137-153.
60. Quarteroni A, Sacco R, Saleri F. *Numerical Mathematics*, Vol. 37. Hiedelberg, Germany: Springer Science & Business Media; 2010.
61. Gottlieb S, Shu C, Tadmor E. Strong stability-preserving high-order time discretization methods. *SIAM Rev.* 2001;43(1):89-112.
62. Krivodonova L. Limiters for high-order discontinuous Galerkin methods. *J Comput Phys.* 2007;226(1):879-896.
63. Sun Y, Beshara M, Lucariello R, Chiaramida S. A comprehensive model for right-left heart interaction under the influence of pericardium and baroreflex. *Am J Phys Heart Circ Phys.* 1997;272(3):H1499-H1515.
64. Carson J, Van Loon R. An implicit solver for 1D arterial network models. *Int J Numer Methods Biomed Eng.* 2017;33(7):e2837.
65. Formaggia L, Lamponi D, Quarteroni A. One-dimensional models for blood flow in arteries. *J Eng Math.* 2003;47(3-4):251-276.
66. Holden H, Risebro N. Riemann problems with a kink. *SIAM J Math Anal.* 1999;30(3):497-515.
67. Smith F, Ovenden N, Franke P, Doorly D. What happens to pressure when a flow enters a side branch? *J Fluid Mech.* 2003;479:231-258.
68. Olufsen M, Nadim A. On deriving lumped models for blood flow and pressure in the systemic arteries. *Math Biosci Eng.* 2004;1(1):61-80.
69. Stergiopoulos N, Young D, Rogge T. Computer simulation of arterial flow with applications to arterial and aortic stenoses. *J Biomech.* 1992;25(12):1477-1488.

70. Fasshauer G. *Meshfree Approximation Methods with MATLAB*, Interdisciplinary Mathematical Sciences, vol. 6. Hackensack, NJ: World Scientific Publishing Co. Pte. Ltd.; 2007.
71. Schölkopf B, Herbrich R, Smola A. *A Generalized Representer Theorem*. Berlin, Heidelberg: Springer; 2001;416-426.
72. Temlyakov V. Greedy approximation. *Acta Numer*. 2008;17:235-409.
73. De Marchi S, Schaback R, Wendland H. Near-optimal data-independent point locations for radial basis function interpolation. *Adv Comput Math*. 2005;23(3):317-330.
74. Schaback R, Wendland H. Adaptive greedy techniques for approximate solution of large RBF systems. *Numer Algorithms*. 2000;24(3):239-254.
75. Wirtz D, Haasdonk B. A vectorial kernel orthogonal greedy algorithm. *Dolomites Res Notes Approx*. 2013;6:83-100. Proceedings of DWCAA12.
76. Santin G, Haasdonk B. Convergence rate of the data-independent P-greedy algorithm in kernel-based approximation. *Dolomites Res Notes Approx*. 2017;10:68-78.
77. Köppel M, Franzelin F, Kröker I, et al. Comparison of data-driven uncertainty quantification methods for a carbon dioxide storage benchmark scenario. ArXiv preprint Nr. 1802.03064; 2017.

SUPPORTING INFORMATION

Additional supporting information may be found online in the Supporting Information section at the end of the article.

How to cite this article: Koepl T, Santin G, Haasdonk B, Helmig R. Numerical modelling of a peripheral arterial stenosis using dimensionally reduced models and kernel methods. *Int J Numer Meth Biomed Engng*. 2018;e3095. <https://doi.org/10.1002/cnm.3095>

4 Simulation of surge reduction systems using dimensionally reduced models

Bibliographic note: The content of this chapter is based on the following original article: T. Köppl, M. Fedoseyev and R. Helmig (2018): Simulation of surge reduction systems using dimensionally reduced models. *Journal of Hydraulic Engineering*, 45(1), 04018079, the illustrations and tables contained in this article are reused with courtesy of ASCE.

The focus of this chapter is to study transient flow processes in an oil pipeline caused by a sudden stoppage of a pumping station combined with an overpressure protection system. Our numerical investigation is based on a dimensional reduced model, where a 1D system of PDEs is considered to simulate flow in the pipeline. The pumping units, valves and overpressure protection systems, are modelled by algebraic systems of equations and ODEs (0D models). Our simulation results demonstrate the efficiency of overpressure protection systems. Finally, they are compared to some measurements.

4.1 Introduction and motivation

To facilitate a secure transport of oil or gas in a pipeline, it is important that pipeline walls are stable and have no leakages. However, during operation a rupture of pipelines may occur because of several reasons [9, 43, 76]. One reason for ruptures in pipeline walls are hydraulic wave shocks [78, 72], occurring when a valve is closing or when a pump is started or stopped [137, 151]. For this reason, pipelines exhibit protection systems. One of the simplest protection systems is a union of relief valves that opens when pressure in the pipeline exceeds a certain threshold allowing oil to leave the main pipeline into a relief tank [10, 47]. Another pressure-control device in a pipeline is an air vessel [133]. In this chapter, we study another type of protection system called surge reduction system (SRS) [93]. Contrary to a pressure relief valve whose purpose is to maintain a constant pressure value in the pipeline, a SRS is used to control the steepness of a surge wave front. This is implemented using a relief valve with a control pipe linked to a gas accumulator. The gas accumulator has the function to dump the rate of change of pressure difference on the sides of the relief valve piston, thus making the valve to react rather to the pressure change rate in the main pipe and not to the pressure absolute value. Since a complex 3D model for this technical system would cause a high computational effort [151], a dimensional reduced model is used for this system. Thereby a 1D hyperbolic PDE system is considered to compute pressure and velocity values in a pipeline system [93]. At the places, where the pump and SRS are installed, the adjacent 1D models for the pipeline are coupled by algebraic equations and ODEs. By this the influence of the pumping station and the SRS on pipeline flow can be accounted for. However, this type of modelling approach is not limited to oil pipelines, it has already been applied successfully in many application areas such as blood flow simulations [87] and hydropower systems [143]. For the numerical treatment of the corresponding PDE systems, we consider two different discretisation techniques:

The first technique is a stabilised DG-method in space combined with a third order SSP Runge-Kutta scheme in time [88, 63]. A further technique that is considered is the method of a characteristics (MOC) [59, 151]. Considering both a higher order numerical method (DG-method) and a lower order numerical method (MOC), we want to study, to what extent the usage of a higher order method pays off concerning accuracy and computational effort. Using the simplified model two scenarios are investigated, where in the first scenario a pump without a SRS is simulated. The simulation results from this first scenario are compared to the simulation results of a second scenario, in which a pump with a SRS is simulated. By this, the significance of a SRS for maintaining the stability of pipeline walls can be demonstrated. A further new aspect related to other works [9, 93] in this field, is the comparison of simulation data with field data taken upstream and downstream of a pump with a SRS. The pump is part of a pipeline transporting oil from an oil field in Kazakhstan to a marine terminal on the shore of the Black Sea. The rest of this chapter is structured as follows: In Section 4.2, we explain the technical details of a SRS and a pump. The next Section 4.3 presents a 1D-0D modelling concept for a pipeline combined with a pumping station and a SRS, using a domain decomposition approach. In the last Section 4.4 the simulation results are summarised and discussed.

4.2 Technical details

A pipeline system is a combination of a long pipe with pumping stations (PS), installed almost every 100 km. The pumps add potential energy to the fluid and therefore they help to overcome energy losses due to friction and turbulence. A pump is a very complex facility, fulfilling besides pumping the following tasks: Filtering, storage, gathering, control of chemical composition of the fluid within the pipeline. The technical system under consideration exhibits pumps with downstream non-return valves and overpressure protection systems (see Figure 4.1). Auxiliary facilities, that do not have any significant influence on flow processes in the main pipeline, are excluded from the further considerations. It consists of a PS located between two other PS upstream and downstream of pipeline. A PS is composed of a protection system and centrifugal pumps with a non-return valve (NRV). Typically 3-phase electric motors are used to drive centrifugal pumps; the design of the motors implies rotation of the shaft only in a predetermined direction. Changing the direction of flow within a pipeline may force opposite rotation of the shaft, which can damage the motor. Preventing this, a NRV restricting a back flow in the pipe is added downstream of the pumping units. Upstream of the pump, a protection system is installed. In this chapter, we study a special kind of protection system, which is referred to as surge reduction system (SRS). An outline of a SRS is shown in Figure 4.2 a). It is connected to the pipeline by two branch pipes. The first pipe connects the main pipeline with a relief valve, whereas the other pipe connects the main pipeline with a gas accumulator by a control valve. Contamination of the control valve orifice is prevented, replacing oil with ethylene glycol in an auxiliary tank. Ethylene glycol flow into the gas accumulator is regulated by the control valve having a variable discharge coefficient. Pressurised gas in the accumulator controls the opening pressure of the pilot-operated relief valve. An example for a SRS with its main mechanical components is presented in Figure 4.2 b).

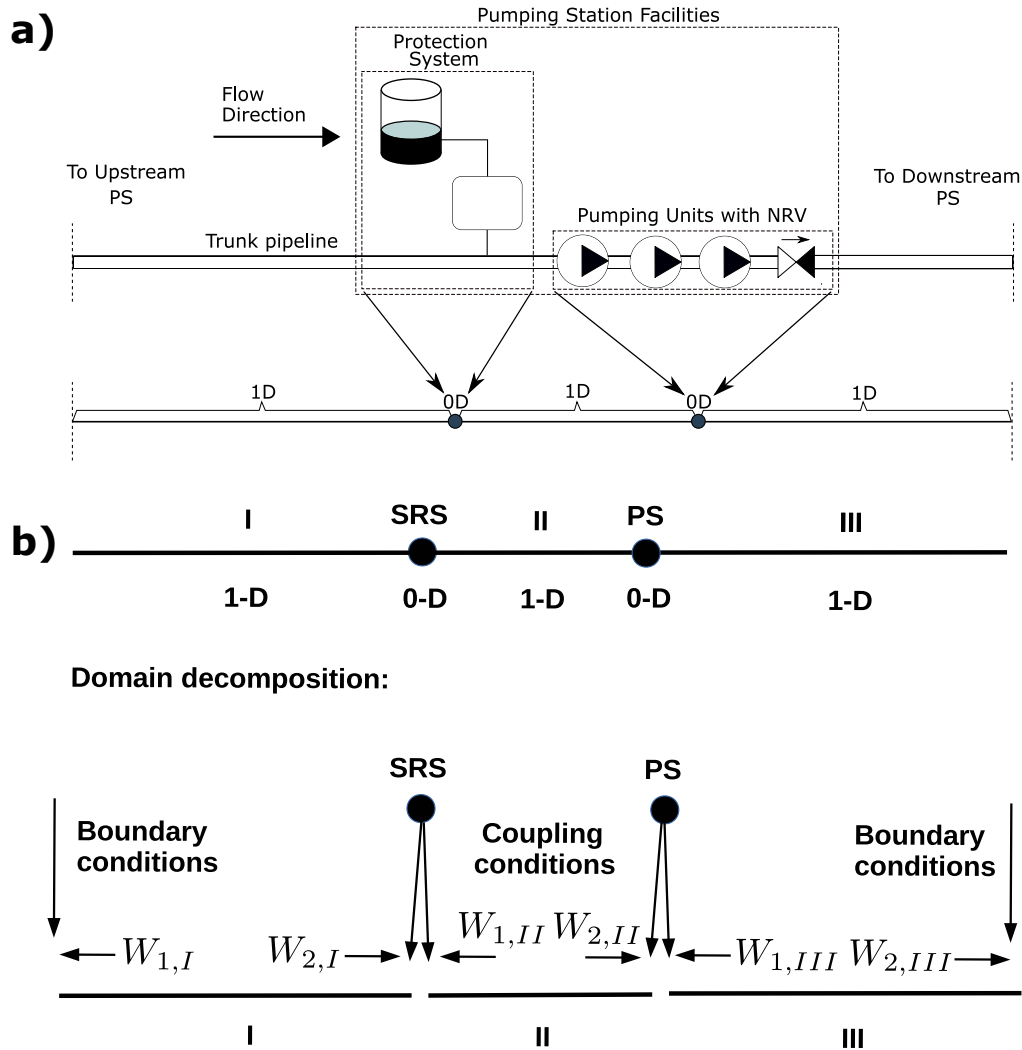


Figure 4.1: Technical setup that is investigated in this chapter. Upstream of a pump equipped with a non return valve (NRV), a protection system is installed to prevent overpressure (a). Dimensional reduced model for the SRS, the PS and the main pipeline (b).

4.3 Modelling a pipeline with a pumping station and a SRS

The transformation of the technical system into a mathematical model is depicted in Figure 4.1 a): The pipeline is considered as a 1D line, while the pumping station, the NRV and the SRS are lumped. In the following subsections, we discuss how the different components of the technical system from the previous section are modelled by a 1D-0D approach. Moreover, we show how the different parts can be linked with each other such that pressure and velocity curves in the whole pipeline can be simulated.

4.3.1 Modelling oil transport within a pipeline

First, the 1D pipeline is separated into three different parts (see Figure 4.1 b)), where each part has a certain length l_j , $j \in \{I, II, III\}$. It is assumed that oil can be considered as a weakly compressible fluid. The pipelines are modelled as impermeable tubes and the deformations of the vessel wall are assumed to be small. Therefore, no FSI has to be

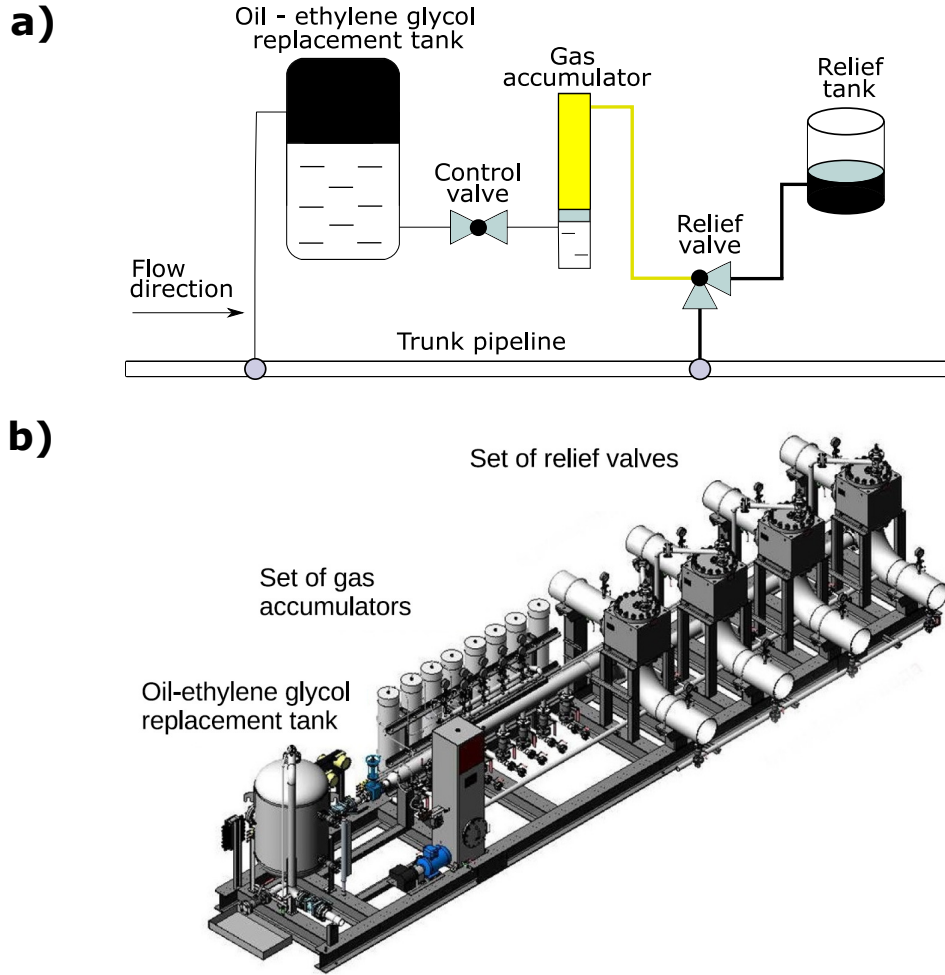


Figure 4.2: Design scheme (a) and visualisation (b) of a surge reduction system (SRS) (Image (b) with courtesy of IMS Industries, LLC, <http://www.imsholding.ru>).

considered. By means of mass and momentum conservation, a system of PDEs for the fluid pressure and velocity in the j -th part can be determined [2, 59, 93]:

$$\frac{\partial p_j}{\partial t} + \rho c_j^2 \frac{\partial v_j}{\partial x_j} = 0, \quad x_j \in (0, l_j), \quad t > 0, \quad (4.1a)$$

$$\frac{\partial v_j}{\partial t} + \frac{1}{\rho} \frac{\partial p_j}{\partial x_j} = -\lambda_j (Re_j, \varepsilon_j) \frac{1}{d_j} \frac{v_j |v_j|}{2\rho} - g \sin \alpha_j, \quad x_j \in (0, l_j), \quad t > 0, \quad (4.1b)$$

x_j [m] and t [s] are space and time variables. $p_j(x_j, t)$ [Pa] and $v_j(x_j, t)$ [m/s] represent pressure and velocity at the place x_j and time t . c_j [m/s] denotes the wave speed of the system, depending on the diameter d_j [m] of the main pipeline, the modulus of elasticity of the main pipeline wall, the oil density ρ [kg/m³] and finally on the thickness of the main pipeline wall. g [m/s²] represents the gravity constant. Viscous forces are incorporated by the source term of (4.1b). The friction coefficient λ_i [-] occurring in this source term is given by Altschul's formula [58]:

$$\lambda_j (Re_j, \varepsilon_j) = 0.11 \left(\varepsilon_j + \frac{68}{Re_j} \right)^{\frac{1}{4}}.$$

Here, $\varepsilon_j [-]$ denotes a relative roughness coefficient and $Re_j = \frac{v_j \cdot d_j}{\nu}$ stands for the Reynolds number. Integrating the gravity force into the model, the expression $-g \sin \alpha_j$ is added to the momentum equation (4.1b), where α_j is the tilt angle of the pipeline in part j . (4.1a) and (4.1b) can be rewritten as follows:

$$\frac{\partial \mathbf{U}_j}{\partial t} + \frac{\partial \mathbf{F}_j}{\partial x_j}(\mathbf{U}_j) = \mathbf{S}_j(\mathbf{U}_j), \quad x_j \in (0, l_j), \quad t > 0. \quad (4.2)$$

\mathbf{U}_j in (4.2) is given by

$$\mathbf{U}_j = (p_j, v_j)^T,$$

the flux function \mathbf{F}_j and the source function \mathbf{S}_j read as follows:

$$\mathbf{F}_j(\mathbf{U}_j) = \begin{pmatrix} \rho \cdot c_j^2 \cdot v_j \\ \frac{1}{\rho} \cdot p_j \end{pmatrix} \quad \text{and} \quad \mathbf{S}_j(\mathbf{U}_j) = \begin{pmatrix} 0 \\ -\lambda_j (Re_j, \varepsilon_j) \frac{v_j |v_j|}{2\rho d_j} - g \sin \alpha_j \end{pmatrix}.$$

Since \mathbf{F}_j can be represented as follows:

$$\mathbf{F}_j(\mathbf{U}_j) = \mathbf{H}_j \cdot \mathbf{U}_j := \begin{pmatrix} 0 & \rho \cdot c_j^2 \\ \frac{1}{\rho} & 0 \end{pmatrix} \cdot \begin{pmatrix} p_j \\ v_j \end{pmatrix},$$

the Jacobian matrix of \mathbf{F}_j is given by the matrix \mathbf{H}_j . The eigenvalues μ_{ji} , $i \in \{1, 2\}$ of \mathbf{H}_j are given by:

$$\mu_{j1} = -c_j \quad \text{and} \quad \mu_{j2} = c_j.$$

This implies that there is exactly one positive and exactly one negative eigenvalue. Due to that, the PDE system (4.2) is hyperbolic and can be reformulated as follows:

$$\frac{\partial \mathbf{W}_j}{\partial t} + \Lambda_j \frac{\partial \mathbf{W}_j}{\partial x_j} = L_j \mathbf{S}_j(\mathbf{W}_j), \quad x_j \in (0, l_j), \quad t > 0, \quad (4.3)$$

where $\mathbf{W}_j = (W_{1,j}, W_{2,j})^T$ and the other parameters are defined as follows:

$$\Lambda_j = \begin{pmatrix} -c_j & 0 \\ 0 & c_j \end{pmatrix}, \quad \mathbf{W}_j = L_j \mathbf{U}_j, \quad L_j = \begin{pmatrix} 1 & -\rho c_j \\ 1 & \rho c_j \end{pmatrix}, \quad \mathbf{H}_j = L_j^{-1} \Lambda_j L_j. \quad (4.4)$$

The characteristic variables \mathbf{W}_j can be interpreted as waves moving in opposite directions. This is of great importance determining suitable boundary conditions for the subsystems, since it reveals that at each boundary only one condition for the ingoing characteristic variables has to be provided. The outgoing characteristics (see Figure 4.1 b)) are computed by reducing the PDE system (4.3) to a system of ODEs. Thereby, the characteristic waves are restricted to space-time curves

$$(x_{i,j}(t), t), \quad j \in \{\text{I}, \text{II}, \text{III}\}, \quad i \in \{1, 2\}$$

and the PDE system (4.1a), (4.1b) is reduced to the following ODEs:

$$\begin{aligned} \frac{dW_{1,j}}{dt}(x_{1,j}(t), t) &= -\Phi_j(v_j), \quad \frac{dx_{1,j}}{dt} = -c_j, \\ \frac{dW_{2,j}}{dt}(x_{2,j}(t), t) &= \Phi_j(v_j), \quad \frac{dx_{2,j}}{dt} = c_j, \quad t > 0, \end{aligned}$$

where

$$\Phi_j(v_j) = \rho c_j \left(-\lambda_j (Re_j, \varepsilon_j) \frac{v_j |v_j|}{2\rho d_j} - g \sin \alpha_j \right).$$

The dynamical system from above can now be used to approximate the outgoing characteristic variables within a numerical algorithm. This procedure is illustrated by means of $W_{2,I}$. Doing so, we consider a time step $[t - \Delta t, t]$. Using this notation, we have for the space-time curve:

$$x_{2,I}(t) = x_{2,I}(t - \Delta t) + c_1 \Delta t.$$

Choosing $x_{2,I}(t) = l_I$, we have:

$$x_{2,I}(t - \Delta t) = l_I - c_1 \Delta t$$

and a first order approximation of $W_{2,I}$, yields the following formula:

$$W_{2,I}(l_I, t) = W_{2,I}(l_I - c_1 \Delta t, t - \Delta t) + \Delta t \cdot \Phi_I(v_I(l_I - c_1 \Delta t, t - \Delta t)), \quad (4.5)$$

assuming that $W_{2,I}$ and v_I can be interpolated at

$$x_I = l_I - c_1 \Delta t \text{ and } t = t - \Delta t.$$

Similarly, the other outgoing characteristic variables can be computed. In order to determine the ingoing characteristic variables further boundary conditions are required, accounting for a prescribed inflow pressure or velocity as well as the impact of a SRS or a PS. Another possibility to compute $W_{2,I}(l_I, t)$ is to use a time integrator of higher order. Using an explicit time integrator for solving (4.1a) and (4.1b) an extrapolation as (4.5) is not required. Due to the fact that for an explicit time integrator the solution variables from the previous time step $t = t - \Delta t$ are known, the values for pressure and velocity can be directly obtained at $x_I = l_I$. By this, the outgoing characteristic $W_{2,I}(l_I, t - \Delta t)$ can be determined. Using both characteristic variables, a transformation to the primary variables \mathbf{U}_j , is equivalent to multiplying the inverse matrix of L_j with \mathbf{W}_j :

$$\mathbf{U}_j = L_j^{-1} \mathbf{W}_j.$$

In the remainder of this section, we show how the coupling conditions for a SRS and a PS can be derived.

4.3.2 0D model for a SRS

At $x_I = l_I$ and $x_{II} = 0$, we require at each time point $t > 0$ four conditions to set up a well-posed problem within the parts of the main pipeline. Two conditions can be derived based on pressure continuity and mass conservation. With respect to the mass conservation it has to be taken into account that if the relief valve is partially or completely open, there is some mass flux from the pipeline system into the SRS. Indicating the flowrate through the inlet piping of the SRS by q_{sr} [m^3/h], the following coupling conditions are obtained:

$$p_I(l_I, t) = p_{II}(0, t) = p_{sr}(t), \quad \frac{d_I^2 \pi}{4} v_I(l_I, t) - \frac{d_{II}^2 \pi}{4} v_{II}(0, t) = q_{sr}(t). \quad (4.6)$$

By means of the pressure difference $p_{\text{sr}}(t) - p_{\text{out}}$ between the inlet and outlet piping of the relief valve, q_{sr} can be determined by [77, 93]:

$$q_{\text{sr}}(t) = \frac{K_{rv}(\Delta p)}{3600} \sqrt{\frac{p_{\text{sr}}(t) - p_{\text{out}}}{\rho} \cdot \frac{\rho_w}{\Delta p_{Kv}}}, K_{rv}(\Delta p) = \begin{cases} 0, & \text{if } \Delta p \leq \Delta p_1, \\ K_{rv}^* \frac{\Delta p - \Delta p_1}{\Delta p_2 - \Delta p_1}, & \text{if } \Delta p_1 < \Delta p \leq \Delta p_2, \\ K_{rv}^*, & \text{if } \Delta p_2 < \Delta p. \end{cases} \quad (4.7)$$

K_{rv} [m^3/h] represents the discharge coefficient of the relief valve, ρ_w [kg/m^3] denotes the density of water and Δp_{Kv} [Pa] the static pressure loss. The pressure p_{out} is the static pressure of oil in a relief tank. In case of an initially empty tank it can be approximated by the atmospheric pressure p_{atm} . Please note that the discharge coefficient K_{rv} is depending on the pressure drop Δp between the main pipeline and the pressure in the gas accumulator:

$$\Delta p(t) = p_{\text{sr}}(t) - p_{\text{gas}}(t).$$

Δp_1 is the pressure drop at which the pressure relief valve starts opening, whereas Δp_2 is the pressure drop at which the valve is fully opened. This means that: $K_{rv} = K_{rv}^*$, if the valve is fully open. If the valve is opening, the discharge coefficient depends linearly on the pressure drop. p_{gas} in the gas accumulator is governed by the volume flow q_{cv} [m^3/h] of ethylene glycol through the control valve into the gas accumulator. It can be regulated, varying the control valve discharge coefficient K_{cv} [m^3/h]. Assuming that the process of gas compression in the accumulator is isothermal, pressure and volume of gas V_{gas}^t are expressed as follows [77, 93]:

$$\frac{dV_{\text{gas}}^t}{dt} = -q_{cv} = -K_{cv} \cdot \sqrt{\frac{|\Delta p|}{\rho_e} \cdot \frac{\rho_w}{\Delta p_{Kv}} \cdot \text{sign}(\Delta p)}, \quad p_{\text{gas}} \cdot V_{\text{gas}}^t = p_0 \cdot V_0. \quad (4.8)$$

ρ_e [kg/m^3] denotes the density of ethylene glycol, p_0 [Pa] and V_0 [m^3] represent a reference pressure and the volume of gas in the gas accumulator. To close the system, we use the characteristic variables of the adjacent PDE systems that are travelling towards the considered interface. According to (4.4) and Figure 4.1 b) the characteristic variables $W_{2,\text{I}}$ and $W_{1,\text{II}}$ are leaving I and II. Using some values from the inside of these subdomains at a previous time point these characteristics can be interpolated tracing back the characteristic curves for these variables (see (4.5)). Using the outgoing characteristics $W_{2,\text{I}}$, $W_{1,\text{II}}$ and (4.6), we have a system of equations governing all the boundary conditions at this interface:

$$W_{2,\text{I}}(l_{\text{I}}, t) = p_{\text{I}}(l_{\text{I}}, t) + \rho \cdot c_{\text{I}} \cdot v_{\text{I}}(l_{\text{I}}, t), \quad W_{1,\text{II}}(0, t) = p_{\text{II}}(0, t) - \rho \cdot c_{\text{II}} \cdot v_{\text{II}}(0, t). \quad (4.9)$$

4.3.3 0D model for a pumping station

Deriving coupling equations at the interfaces adjacent to the pump, we use the same techniques as in the previous subsection. Two coupling equations are obtained by conservation equations for momentum and mass flux. The remaining equations are related to the characteristic variables travelling towards this interface. Pumps use centrifugal pumps to add energy to the oil transport. Therefore, the pressure downstream of the pump is increased causing a pressure jump at the point where the pumping station is located. Due to the fact that there is no remarkable loss or gain of oil within a pump, we require the continuity of the flux at $x_{\text{II}} = l_{\text{II}}$ and $x_{\text{III}} = 0$. This yields the following coupling equations at II and III:

$$p_{\text{III}}(0, t) = p_{\text{II}}(l_{\text{II}}, t) + \rho \cdot g \cdot H(q_p(t)), \quad q_p(t) = \frac{d_{\text{II}}^2 \pi}{4} v_{\text{II}}(l_{\text{II}}, t) = \frac{d_{\text{III}}^2 \pi}{4} v_{\text{III}}(0, t). \quad (4.10)$$

Assuming that the flowrate through the pump q_p [m³/h] is positive, it holds that: $q_p(t) > 0$. H [m] denotes the total dynamic head of the pumping unit, quantifying the power of a pump depending on the flowrate q_p . In our modelling approach, we use the following relation to compute the total dynamic head [93]:

$$H(q_p) = A \cdot \bar{\omega}^2 - B \cdot \bar{\omega} \cdot q_p - C \cdot q_p^2.$$

A , B and C are given positive coefficients depending on the design of the pump. $\bar{\omega}$ is the relation between the current rotational speed of the rotors and its maximal value. For $\bar{\omega} = 1$ a pump is operating at full rotational speed. According to the characteristic analysis, it can be observed that $W_{2,II}$ and $W_{1,III}$ are the outgoing variables. For the pump, the outgoing characteristics can be extrapolated from the inside of the intervalls $[0, l_{II}]$ and $[0, l_{III}]$ (see Subsection 4.3.1). The missing coupling conditions are given by:

$$W_{2,II}(l_{II}, t) = p_{II}(l_{II}, t) + \rho \cdot c_{II} \cdot v_{II}(l_{II}, t), \quad W_{1,III}(0, t) = p_{III}(0, t) - \rho \cdot c_{III} \cdot v_{III}(0, t). \quad (4.11)$$

Combining (4.10) and (4.11) we obtain an equation system that can be used to incorporate the pump and to establish a well-posed problem. For $q_p(t) \leq 0$ the NRV has to prevent any flow through the pump. Incorporating this property into the model, the equations for mass and momentum conservation (4.10) are governed by coupling equations simulating a full reflection. This is accomplished by setting the ingoing characteristic variables to the values of the outgoing characteristic variables:

$$W_{1,II}(l_{II}, t) = W_{2,II}(l_{II}, t) \quad \text{and} \quad W_{2,III}(0, t) = W_{1,III}(0, t). \quad (4.12)$$

Using (4.11) and (4.12), we can simulate flow in the vicinity of the pumping station, if the NRV is closed.

4.3.4 Numerical methods

The mathematical models developed in the previous section, exhibit strong nonlinearities in the coupling equations as well as in the source term of (4.1b). Therefore, it is difficult to determine an analytical solution in a general case and numerical solution schemes are required. The main difficulties occurring in the context of solving hyperbolic PDE-systems numerically are to suppress the artificial damping of the solution and dispersion errors caused by the discretisation [113, Chapter 13]. To tackle these difficulties, we apply a DG-method of third order for the spatial discretisation and a Runge-Kutta method of third order for the time integration. On the other hand, numerical schemes of higher order tend to create unphysical oscillations in the vicinity of steep gradients or shocks. In the application area that is investigated in this work, there are shocks in the solutions if the pumping station is shut down or a valve is closing. Therefore, it is of great importance to choose a solution method damping numerical oscillations. In order to remove numerical oscillations, we use the adaptive slope-limiter technique. Thereby the slopes of the numerical solution are damped by a suitable coefficient such that wiggles are removed, while smooth extrema [88] are not damped. To preserve a non-oscillatory solution in a certain time step a 3-stage SSP-scheme (Strong-Stability-Preserving) is considered. A SSP-scheme is a special kind of Runge-Kutta scheme [63], which does not enlarge existing oscillations. Therefore, a time stepping scheme of this class of solvers stabilises the solution. A drawback of this method is that it exhibits a time step restriction due to a CFL-condition, which is more severe

than the time step restriction for the Explicit-Euler method. Therefore, we considered another numerical technique, whose CFL-condition is milder. Due to the fact that the MOC is a robust method for hyperbolic PDEs [59, 151], we select this method to compute a numerical reference solution. The disadvantage is that it is just of first order both in space and time. For this reason, dissipation and dispersion errors are significantly larger than in case of the DG-method. In the following, we will test which feature of the both methods is more significant for the numerical discretisation of the model. To quantify the time step restriction, we define the Courant numbers of the DG-method and the MOC as follows:

$$CN_{DG} = \max_{j \in \{I, II, III\}} \frac{\Delta t_{DG} \cdot c_j}{\Delta x_{DG}}, \quad CN_{MOC} = \max_{j \in \{I, II, III\}} \frac{\Delta t_{MOC} \cdot c_j}{\Delta x_{MOC}}, \quad (4.13)$$

where Δt_k , $k \in \{DG, MOC\}$ are the time step sizes for both methods. In the case of the DG-method Δx_{DG} refers to the length of a finite element, while Δx_{MOC} indicates the distance between two grid nodes at which the MOC approximates the solution variables. For each discretisation method, we consider a uniform grid in space. c_j is the characteristic wave speed of the j -th part (see Equation (4.1a) and (4.1b)).

4.4 Simulation results

Based on the numerical model developed in the previous sections two different scenarios are studied. The first scenario illustrates the significance of a SRS. For this purpose, flow in a pipeline without a SRS is simulated. Instead of a SRS, we use at the same interface coupling conditions simulating a transition of pressure and velocity waves. In addition to the two characteristic variables that can be extrapolated, the two remaining coupling conditions are given by:

$$W_{2,II}(0, t) = W_{2,I}(l_I, t) \quad \text{and} \quad W_{1,I}(l_I, t) = W_{1,II}(0, t).$$

Additionally, a second simulation is performed considering a SRS 200 m upstream of



Figure 4.3: Oil pipeline linking Tengiz in Kazakhstan and a marine terminal at the Black Sea. Field data are taken in the vicinity of the pump at Astrakhan (Map with courtesy of IMS Industries, LLC, <http://www.imsholding.ru>).

the pump. Validating the numerical model, the simulation results are compared to field

measurements. These measurements are reported for a pipeline of the Caspian Pipeline Consortium (CPC). CPC is a large international oil transportation project operating on a more than 1500 km long pipeline system. The main objective of this project is to transfer crude oil from some oil fields in Kazakhstan to a marine terminal located in Novorossiysk, Russia (see map in Figure 4.3). In the vicinity of the PS Astrakhan pressure curves have been reported, during and after a stoppage with a duration of 90 s. In both scenarios, gravity forces are neglected, which means that we set $\alpha_i = 0$, $i \in \{I, II, III\}$ in (4.2). At $x_I = 0$ and $x_{III} = l_{III}$ constant Dirichlet conditions for the pressures are chosen. They are denoted by p_I^{in} and p_{III}^{out} . Using p_I^{in} and p_{III}^{out} combined with the variables $W_{1,I}(0, t)$ and $W_{2,III}(l_{III}, t)$, the other characteristics are given by:

$$W_{2,I}(0, t) = 2 \cdot p_I^{\text{in}} - W_{1,I}(0, t) \quad \text{and} \quad W_{1,III}(l_{III}, t) = 2 \cdot p_{III}^{\text{out}} - W_{2,III}(l_{III}, t).$$

The simulation time t_{end} has been chosen such that reflected shock waves caused by the shutdown of the pump reach the pumping station. The parameters ν , ρ_e and ρ_w as well as the static pressure loss Δp_{Kv} , we use for both scenarios, are given by:

$$\nu = 1.5 \cdot 10^{-5} \text{ m}^2/\text{s}, \quad \rho_e = 1110 \text{ kg/m}^3, \quad \rho_w = 1000 \text{ kg/m}^3 \quad \text{and} \quad \Delta p_{Kv} = 10^5 \text{ Pa}.$$

The initial condition for the pressure, is given by a piecewise linear function;

$$p(x, 0) = \begin{cases} p_I^{\text{in}} + \frac{p_I^{\text{out}} - p_I^{\text{in}}}{l_I} x_I, & \text{for } x_I \in [0, l_I], \quad x = x_I, \\ p_{II}^{\text{in}} + \frac{p_{II}^{\text{out}} - p_{II}^{\text{in}}}{l_{II}} x_{II}, & \text{for } x_{II} \in [0, l_{II}], \quad x = l_I + x_{II}, \\ p_{III}^{\text{in}} + \frac{p_{III}^{\text{out}} - p_{III}^{\text{in}}}{l_{III}} x_{III}, & \text{for } x_{III} \in [0, l_{III}], \quad x = l_I + l_{II} + x_{III}. \end{cases} \quad (4.14)$$

$x \in [0, l_I + l_{II} + l_{III}]$ denotes the global coordinate of the pipeline. p_I^{out} , p_{II}^{in} , p_{II}^{out} and p_{III}^{in} are the pressures at the inner interfaces for $t = 0$. The initial condition for the velocity is represented by a piecewise constant function:

$$v(x, 0) = \begin{cases} v_I^{(0)}, & \text{for } x_I \in [0, l_I], \quad x = x_I, \\ v_{II}^{(0)}, & \text{for } x_{II} \in [0, l_{II}], \quad x = l_I + x_{II}, \\ v_{III}^{(0)}, & \text{for } x_{III} \in [0, l_{III}], \quad x = l_I + l_{II} + x_{III}. \end{cases} \quad (4.15)$$

4.4.1 Change of pressure and velocity distribution in case of a shutdown

Figure 4.4 a) shows the initial condition (4.14) for the pressure of the first scenario, while the pressure parameters for (4.14) are presented in Table 4.1 and Table 4.3. The parameters for the initial velocity (4.15) area listed in the same table, together with most of the other model parameters. With respect to the discharge coefficient K_{cv} , different values are selected, to study the damping effect of a SRS:

$$K_{cv} \in \{5.0 \text{ m}^3/\text{h}, 8.0 \text{ m}^3/\text{h}, 12.0 \text{ m}^3/\text{h}, 20.0 \text{ m}^3/\text{h}, 50.0 \text{ m}^3/\text{h}\}.$$

$\bar{\omega}$ is determined by a time dependent function decaying linearly from 1.0 to 0.0 for $t \in [0, t_*]$. For our considerations, we set: $t_* = 5$ s and for the density of oil we set: $\rho = 900.0 \text{ kg/m}^3$. In this subsection only the simulation results obtained by the DG-method are presented, where we use quadratic Legendre polynomials in space. The discretisation parameters are given

Table 4.1: Parameters for the first scenario

	I	II	III
Inlet pressures p_i^{in} [MPa]	3.0	0.69924	4.35
Outlet pressures p_i^{out} [MPa]	0.69924	0.68996	2.20
Initial velocities $v_i^{(0)}$ [m/s]	2.5	2.5	2.5
Diameters d_i [m/s]	1.0	1.0	1.0
Lengths l_i [m]	$4.98 \cdot 10^4$	$2.0 \cdot 10^2$	$5.0 \cdot 10^4$
Relative roughnesses ϵ_i [-]	$0.1 \cdot 10^{-3}$	$0.1 \cdot 10^{-3}$	$0.1 \cdot 10^{-3}$
Wave velocities c_i [m/s]	$1.0 \cdot 10^3$	$1.0 \cdot 10^3$	$1.0 \cdot 10^3$
Fluid densities ρ_i [kg/m ³]	800	800	800
Fluid viscosities ν_i [m ² /s]	$1.5 \cdot 10^{-5}$	$1.5 \cdot 10^{-5}$	$1.5 \cdot 10^{-5}$

Table 4.2: Parameters for the second scenario

	I	II	III
Inlet pressures p_i^{in} [MPa]	3.33	1.14044	4.36
Outlet pressures p_i^{out} [MPa]	1.14044	1.13605	2.16
Initial velocities $v_i^{(0)}$ [m/s]	1.504	1.504	1.504
Diameters d_i [m/s]	1.0	1.0	1.0
Lengths l_i [m]	$9.98 \cdot 10^4$	$2.0 \cdot 10^2$	$1.0 \cdot 10^5$
Relative roughnesses ϵ_i [-]	$0.1 \cdot 10^{-3}$	$0.1 \cdot 10^{-3}$	$0.1 \cdot 10^{-3}$
Wave velocities c_i [m/s]	$1.0 \cdot 10^3$	$1.0 \cdot 10^3$	$1.0 \cdot 10^3$
Fluid densities ρ_i [kg/m ³]	800	800	800
Fluid viscosities ν_i [m ² /s]	$1.5 \cdot 10^{-5}$	$1.5 \cdot 10^{-5}$	$1.5 \cdot 10^{-5}$

by: $\Delta x_{DG} = 50.0$ m and $\Delta t_{DG} = 0.025$ s. In Figure 4.4 a), we can see that the stoppage of a pump causes the creation of two pressure waves: A high-pressure wave travelling through the upstream pipeline and a low-pressure wave travelling downstream. This graph shows that during the process the surge pressure is added to the static line pressure. As it can be observed, it clearly exceeds the initial conditions for the pressure and an allowed pressure level possibly damaging the pipeline wall.

If a SRS with a discharge coefficient $K_{cv} = 12.0$ m³/h is located upstream of the pump, the pressure shock wave travelling upstream is damped remarkably (see Figure 4.4 b)). Observing the pressure curves for $t = 45$ s at $x = 1.0 \cdot 10^4$ m, we note that the pressure exceeds even the inlet pressure $p_I^{in} = 3.0$ MPa, if no SRS is added. Otherwise, the upstream pressure curve for $t = 45$ s is remarkably lower than the inlet pressure. In Figure 4.4 b) the maximal pressure of the corresponding upstream curve is around 2.75 MPa at $x = 3.10 \cdot 10^4$ m. Therefore the propagation of high-pressure waves through the pipeline can be damped and by this a rupture of the pipeline wall could be prevented. However, the SRS also increases an amplitude of a discharge wave generated in the downstream pipe leading to a higher risk of column separation. In Figure 4.4 c) and d), the velocity distribution along the pipeline at different time points can be seen. As for the pressure, a propagation of shock waves can be seen. Contrary to the pressure curves the velocity curves for the same simulation are symmetric to an axis located at the pump. Due to the

Table 4.3: Parameters for the relief valves and pumping equipment

	First scenario	Second scenario
Relief valve discharge coeff. K_{rv}^* [m^3/h]	$5.0 \cdot 10^3$	$5.0 \cdot 10^3$
Relief valve set pressure Δp_1 [Pa]	$55.0 \cdot 10^3$	$1.0 \cdot 10^5$
Relief valve full opening pressure Δp_2 [Pa]	$178 \cdot 10^3$	$1.25 \cdot 10^5$
Gas accumulator initial pressure p_0 [Pa]	$9.0 \cdot 10^5$	$1.2 \cdot 10^5$
Gas accumulator initial volume V_0 [m^3]	0.448	0.448
Atmospheric pressure p_{atm} [Pa]	$1.0 \cdot 10^5$	$1.0 \cdot 10^5$
Pump characteristic coeff. A [m]	435	512
Pump characteristic coeff. B [h/m^2]	0.0	$1.423 \cdot 10^{-2}$
Pump characteristic coeff. C [h^2/m^5]	0.0	$2.0 \cdot 10^{-6}$

fact that the slopes of the pressure curves in the vicinity of the pump are smaller than the slopes of the initial condition, the flow velocity decreases in the same region to a lower and almost constant velocity distribution. This can be seen exemplarily at the velocity curve for $t = 45.0$ s in Figure 4.4 c). Adding a SRS to the pipeline, one can see in Figure 4.4 d) a jump in the velocity curve, where the SRS is installed, which means that the oil flow is partially redirected from the pipeline through the relief valves into a relief tank. An important parameter controlling the damping of high pressure waves, is the discharge coefficient K_{cv} of the control valve linking the replacement tank and the gas accumulator. It has to be carefully chosen, since it can not be changed during operation. Considering all engineering difficulties arising during production of the system elements, the only way to change the system working parameters in an easy way, is to vary a discharge coefficient of the control valve K_{cv} by opening/closing the control valve. In some rare occasions, the SRS producer decides to change the equipment by installing a second gas accumulator in parallel to the existing one. This causes a doubling of gas volume having the same effect on a pressure wave as a reduction of K_{cv} . However, the installation of a further gas accumulator can only be performed during the production of a SRS, so that the user is still left with being able to change K_{cv} . Thus it is important to determine suitable values for K_{cv} by a numerical simulation, before the SRS is used. Considering (4.8), the ethylene glycol flux from the replacement tank into the accumulator (see Figure 4.2) is influenced besides a pressure difference also by K_{cv} . Choosing $K_{cv} = 0$ there is no flow from the replacement tank into the accumulator. In this case the SRS is equal to a simple relief valve opening, if a certain pressure threshold is exceeded (4.7). The drawback of this protection system is that an overflow of the relief tank may happen, if the pressure in the main pipeline is not decreasing early enough. This means that a device is needed to control the discharge coefficient of a relief valve. Varying K_{cv} , it can be observed for a low discharge coefficient that a low pressure gradient with respect to time can be produced (see Figure 4.5). On the other hand, choosing a higher discharge coefficient ($K_{cv} \in \{20 \text{ m}^3/\text{h}, 50 \text{ m}^3/\text{h}\}$) we see that the pressure curves are similar to the setting in which no SRS is considered (red curve in Figure 4.5). If no SRS is installed, the pressure gradient is much higher as for a low discharge coefficient K_{cv} . Comparing the pressure curves we conclude that by a carefully chosen parameter K_{cv} the high pressure wave can be damped sufficiently, allowing us to maintain safe operation of the pipeline. Moreover a fast opening of a relief valve can be prevented and a fast overflow of the attached tank does not take place. In case of the relief

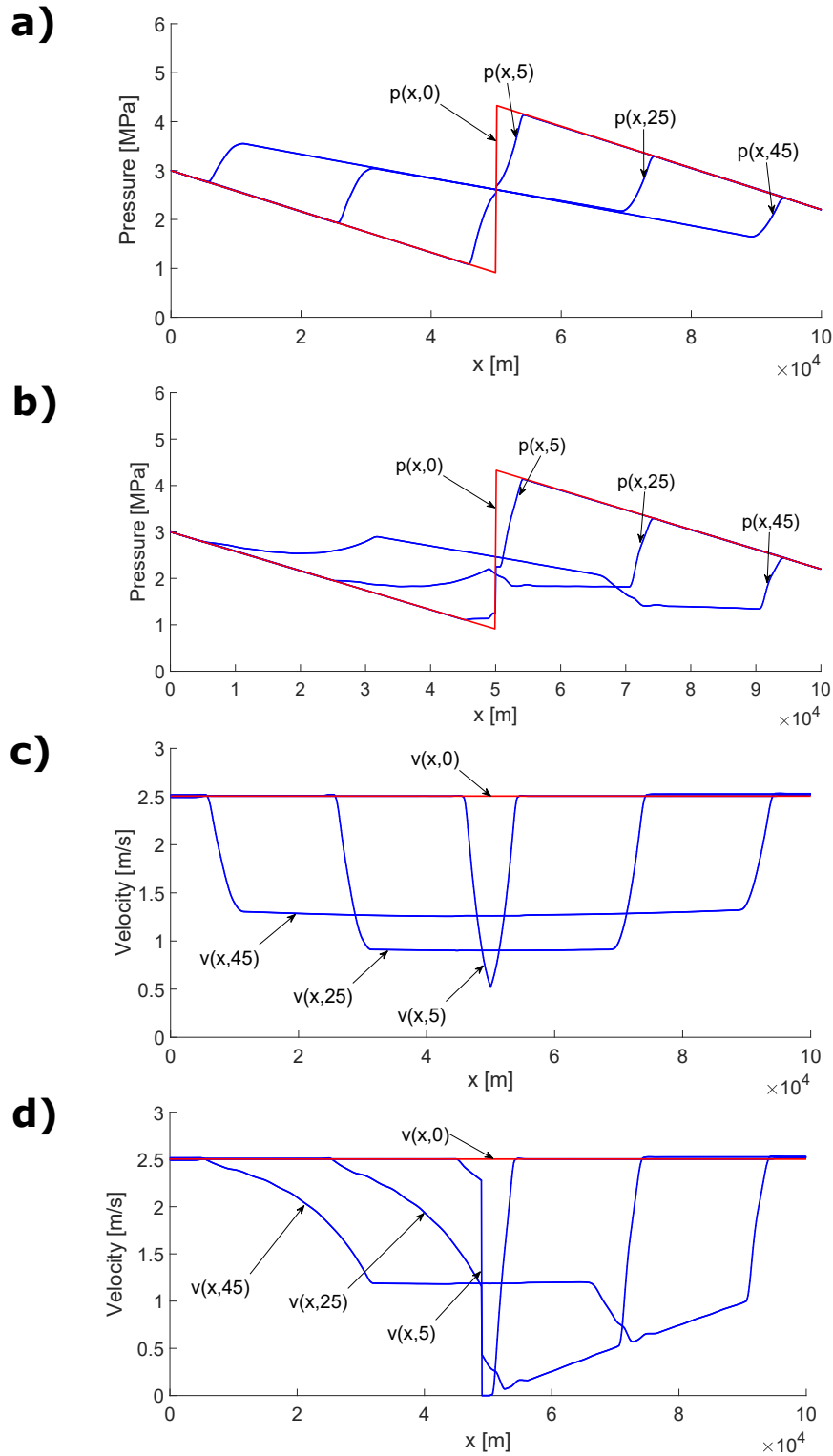


Figure 4.4: Pressure shock waves for different time points (5.0 s, ..., 45.0 s) after the shutdown of a pump. In (a), the pump is *not* combined with a SRS, whereas in (b), the pump *is* combined with a SRS. Figures (c) and (d) show the velocity shock waves for different time points (5.0 s, ..., 45.0 s) after the shutdown of a pump. In (c) the pump is *not* combined with a SRS, whereas in (d), the pump *is* combined with a SRS.

valve opening within a short time period, it can happen that the tank is filling too fast. This can prevent a pipeline operator from decreasing the pressure in another way, which means that this measure enables a pipeline operator to react accordingly to an emergency and perform additional measures (like the stoppage of an upstream pump or the closure of a pressure control valve generating a discharge wave) to prevent a rupture of a pipeline wall. Thus a SRS does not mainly control the maximum amplitude of a pressure wave like conventional relief valves, but it is used to regulate the rate of change of pressure with respect to time.

4.4.2 Comparison of simulation results and measurements

To reproduce the field measurements taken after a stoppage of the pump at Astrakhan, we study essentially the same scenario investigated in the previous subsection, but with different values for the model parameters (see Table 4.2 and Table 4.3). The initial conditions for the pressure and velocity, are again given by functions like (4.14) and (4.15). Further the function for the relative angular velocity is adopted from the previous scenario. The discharge coefficient, for this scenario is given by $K_{cv} = 5.2 \text{ m}^3/\text{h}$ and $\rho = 800 \text{ kg/m}^3$. As we can see in Figure 4.5 b), the pressures based on measurements and DG-simulations coincide very well. The numerical results do not leave the confidence interval of pressure measurement units (green shaded area) up to $t = 65 \text{ s}$. After that, the measurements differ only slightly. However, the course of the corresponding curves is similar. Measuring the difference between the measurements and simulation we compute a discrete L^2 -norm of the absolute difference and the measurements. Using these data, a relative error is computed. For a function f and discrete time points t_k the L^2 -norm it is given by:

$$\|f\|_{L^2} = \sqrt{\frac{1}{N_m} \sum_{k=1}^{N_m} f^2(t_k)}.$$

N_m is the number of measurement points. By this formula, the relative errors $E_{rel}^{(i)}$, $i \in \{\text{up}, \text{do}\}$ between the upstream and downstream measurements and simulations are given by:

$$E_{rel}^{(i)} = \frac{\|p_m^{(i)} - p_s^{(i)}\|_{L^2}}{\|p_m^{(i)}\|_{L^2}}.$$

$p_m^{(i)}$ and $p_s^{(i)}$, $i \in \{\text{up}, \text{do}\}$ indicate the measured and simulated pressure curves upstream and downstream of the pump. For $N_m = 1801$ measurement points and the DG-method, it can be seen that both the relative error upstream and downstream are below 5 % (see Table 4.4). These numbers and the graphs in Figure 4.5 b), suggest that measurements can be emulated by the 1D-0D model. Next, we compare the results obtained by the DG-method with the results that are obtained solving the same setup by means of the MOC. The simulation results produced by the two different methods are shown in Figure 4.5 c), while the comparison of the relative errors is reported in Table 4.4. For the DG-method, we use 200 elements and quadratic Legendre polynomials, which is equal to 600 degrees of freedom. To have the same number of degrees of freedom in space, we used for the MOC 600 grid nodes in space. However, testing both methods based on these space discretisations, it can be observed that for the DG-method a time step size of $\Delta t_{DG} = 0.005 \text{ s}$ has to be

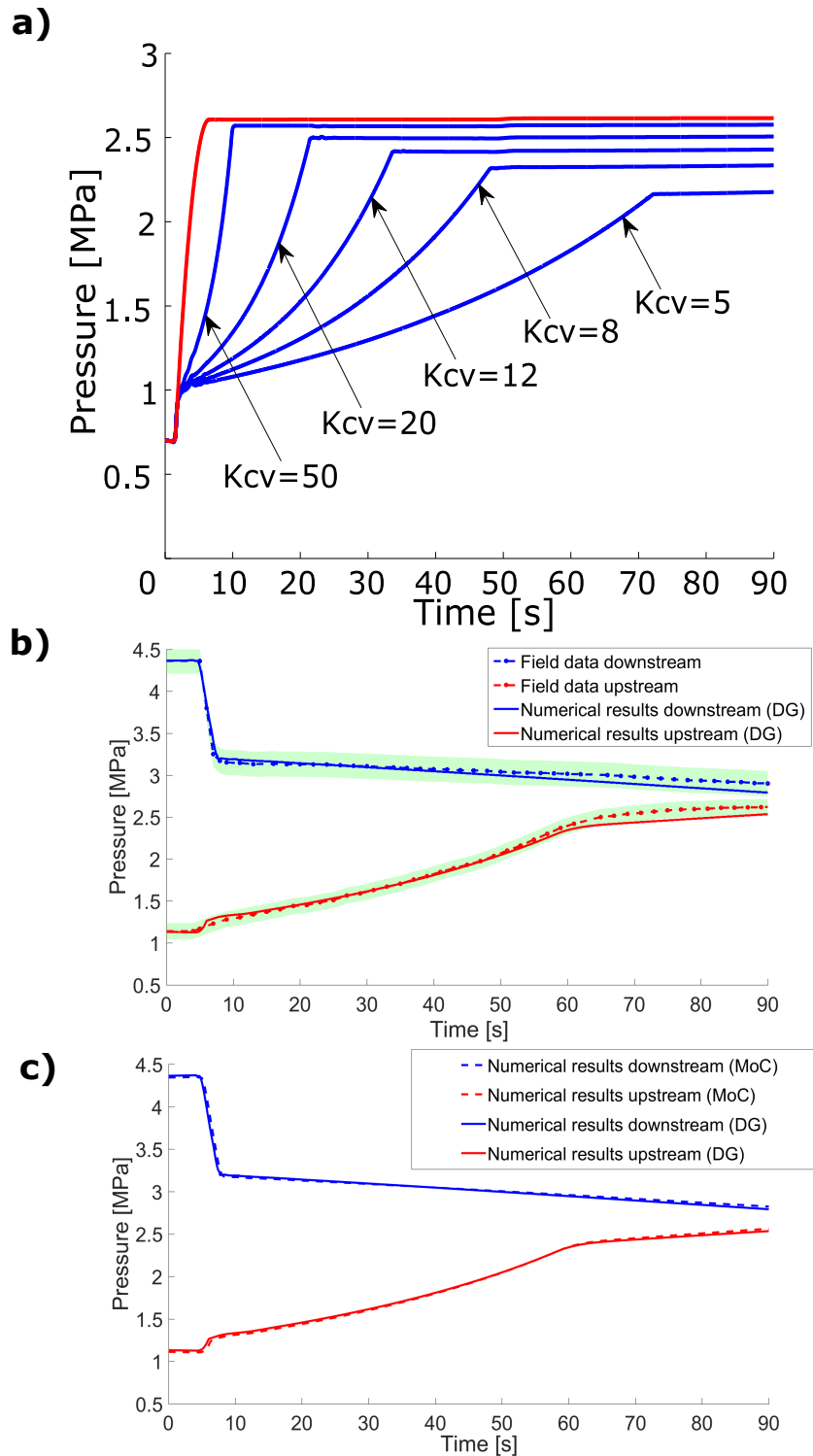


Figure 4.5: Change of pressure over time in the pipeline upstream of the SRS (a). Comparison of field measurements and numerical simulation results upstream and downstream of a PS located at Astrakhan (b). Comparison of the simulation results produced by the DG-method and the MOC (c).

selected in order to provide stable results. This yields a Courant number of $CN_{DG} = 0.005$ (see (4.13)). The largest time step size for the MOC method is given by $\Delta t_{MOC} \approx 0.333$ s, which means that the Courant number for the MOC-method is given by $CN_{MOC} \approx 1.0$.

Investigating the simulation results shows that both methods provide comparable results but the simulations performed with the MOC is much faster than the calculation of the same setup using the DG-method. This might be due to the slope limiter deteriorating the accuracy of the DG-method. Summarising, we can conclude that for this problem the DG-method does not provide more accurate results as the MOC and that it is not that efficient as the MOC.

Table 4.4: Relative errors for the field case

Numerical Method	$E_{rel}^{(up)}$	$E_{rel}^{(down)}$
Discontinuous Galerkin (200 elements, polynomials of 2nd order)	4.7 %	5.0 %
Method of Characteristics (600 nodes)	3.2 %	4.7 %

4.5 Concluding remarks

In this chapter, a numerical model for transport processes in pipelines with a PS and a SRS is presented. Our model decreases the complexity of the issue by means of dimensionally reduced models and a domain decomposition method. Thereby, flow in the main pipeline is simulated by a 1D system of transport equations, while the PS and the SRS are simulated by systems of ODEs (0D models). At the places where the PS and the SRS are located, the main pipeline is decomposed. In order to couple the different pipeline parts again, the ODE-systems yield for each time coupling values at the interfaces. For the numerical treatment, we have considered a DG-method and the MOC, where the MOC proved to be as accurate as the DG-method. However, it is much more efficient as the DG-method. By means of this model, we have shown that a shock wave, that is initiated by the stoppage of a PS, can be sufficiently damped by a SRS and a rupture of the pipeline may be prevented. Additionally, we have reproduced field measurements taken upstream and downstream of a PS, which demonstrates the efficiency of our model. Future work in this field may focus on further validating the dimensionally reduced model, for example, by comparing the reduced model with 3D models. Concerning the discretisation methods, one could apply a stable time integrator for the DG-method with a less restrictive CFL-condition. Besides, a more sophisticated limiter method for the DG-discretisation in space could be investigated. Finally, more advanced relief systems, which do not enlarge the amplitude of the downstream wave should be designed and modeled.

Acknowledgements

This work was supported by the Cluster of Excellence in Simulation Technology (EXC 310/2) and the German Academic Exchange Service (DAAD). We thank IMS Industries, LLC for providing Figure 4.2 b) and Figure 4.3 (<http://www.imsholding.ru/>). Finally, we thank Dr. Nikolay Arbuzov (arbuzov@imsholding.ru) for providing the field data.

Part II

Simulation of blood flow in microvascular networks

As the first two chapters of Part I, the second part of the submitted thesis is concerned with modelling and simulating of blood flow. However, contrary to the first part we consider blood vessel networks on a different scale. While in Chapter 2 and 3 large blood vessel networks on the macroscale level are considered, the following chapters study blood vessel networks on a microscale level. Typically, these networks fill volumes of a few cubic meters and have diameters of a few micrometers. Therefore networks on this vascular level are called microvascular networks. Moreover, blood flow at this level is slow and not pulsatile, which means that inertia terms and interactions with the vessel walls can be neglected. In addition to that, exchange processes with flow in surrounding tissue have to be included into the model. Taking these features into account, we simulate blood flow in microvascular networks by means of Poiseuille type equations with suitable source terms. Since microvascular blood vessels can be considered as small inclusions within the tissue, microvascular networks are represented as 1D graphlike structures. The surrounding tissue can be regarded as a composition of the cellular matrix and an interstitial space filled with some fluid, where the interstitial space is regarded as a combination of pores and pore throats. Due to that, flow within tissue is modelled as flow within a 3D isotropic porous medium. The exchange processes with the vascular system is accounted for by Dirac source term combined with Starling's law, where the Dirac measure is concentrated on the 1D graph describing the network. Part II consists as the previous part of three chapters. These three chapters contain a conference proceeding and two journal articles. The first two publications investigate theoretical aspects related to this 3D-1D coupling approach. In the final publication of this part, a further model reduction technique for simulating blood flow in microvascular systems is presented.

Chapter 5:

A local error estimate for the Poisson equation with a line source term

In Chapter 5, we study the local convergence behaviour of a standard finite element method for a Poisson problem with a line source term, i.e., we cut out a cylinder of a certain radius around the line and investigate the convergence with respect to the L^2 -norm on the rest of the domain. This is motivated by the fact that the Darcy equation with a Dirac source term concentrated on a line is an elliptic PDE with a pure line source term, if the coupling terms are neglected. It turns out that a standard linear finite element method converges with an optimal rate after a preasymptotic range. On the contrary, the L^2 -error converges poorly on the whole domain. This is due to the fact that line source terms introduce singularities along the line. However, the preasymptotic range for the local L^2 -error ends, if the meshsize is below the radius of the omitted cylinder. Recalling the fact that micro vessels have small radii, it becomes obvious that the 3D mesh has to be very fine, to obtain an optimal convergence rate.

Chapter 6:

Mathematical modeling, analysis and numerical approximation of second-order elliptic problems with inclusions

Motivated by the results of Chapter 5, we develop in the following chapter an

alternative coupling concept avoiding the formation of singularities. For this purpose, the Dirac measure is not concentrated on the centerline of the vascular network but on the surface of the vessel walls. This means that the Dirac measure is concentrated on a manifold with co-dimension 1. The exchange term is again governed by Starling's law. As a result, the pressure solution in the tissue exhibits only kinks but no singularities. Based on a 2D model problem that can be derived from a 3D problem with a single straight cylinder, we show that the model reduction error between the simplified model and a full-dimensional model is decreasing as the radius of the vessel is decreasing. This implies that for vessels with small radii related to the dimensions of the whole domain a small modelling error can be expected. Obviously, this feature is characteristic for a typical microvascular network. Finally, we investigate the global convergence behaviour of a standard linear finite element method with respect to the L^2 -norm and H^1 -norm. Due to the reduced regularity, this numerical method converges suboptimal if quasi-uniform meshes are used. However, compared to the standard 3D-1D coupling concept the convergence behaviour is improved.

Chapter 7:

Hybrid models for simulating blood flow in microvascular networks

Considering the key results of the previous chapters, one can conclude that the new coupling concept presented in Chapter 6 has many advantages compared to the standard 3D-1D coupling approach [30], which is based on line source terms. Applying the new coupling concept to a very dense and large microvascular network, it turns out that still a fine mesh has to be used to compute the mass exchange and the pressure field in an accurate way. In addition to that the system matrix arising from the numerical treatment of the new coupling approach is usually denser as the system matrix corresponding to the standard 3D-1D coupling approach. Further, both coupling algorithms considered so far require an accurate description of the vascular system. However, due to reconstruction errors from image data, it is quite often not possible to describe microvascular networks with a sufficient accuracy. These observations motivate a further simplification step. Doing so, only the larger vessels of a microvascular network are described by 1D graphlike structures, while the finescale components of the network are homogenised and considered as a 3D porous medium. Since this modelling approach results in a coupling of the 3D porous continuum for the homogenised network with the 3D porous continuum for the tissue, such a modelling approach is referred to as 3D-3D-1D coupled double-continuum approach. In order to illustrate the efficiency of this hybrid model, it is compared to the 3D-1D coupled model from Chapter 6.

5 A local error estimate for the Poisson equation with a line source term

Bibliographic note: The content of this chapter is based on the following original article: T. Köppl, E. Vidotto and B. Wohlmuth (2016): A local error estimate for the Poisson equation with a line source term. Numerical Mathematics and Advanced Applications, ENUMATH 2015, pages: 421-429, with courtesy of Springer (Cham).

A local error estimate for the Poisson equation with a line source term

Tobias Köppl, Ettore Vidotto, and Barbara Wohlmuth

Abstract. In this paper, we show a local a priori error estimate for the Poisson equation in three space dimensions (3D), where the source term is a Dirac measure concentrated on a line. This type of problem can be found in many application areas. In medical engineering, e.g., blood flow in capillaries and tissue can be modeled by coupling Poiseuille's and Darcy's law using a line source term. Due to the singularity induced by the line source term, finite element solutions converge suboptimal in classical norms. However, quite often the error at the singularity is either dominated by model errors (e.g. in dimension reduced settings) or is not the quantity of interest (e.g. in optimal control problems). Therefore we are interested in local error estimates, i.e., we consider in space a L^2 -norm on a fixed subdomain excluding a neighborhood of the line, where the Dirac measure is concentrated. It is shown that linear finite elements converge optimal up to a log-factor in such a norm. The theoretical considerations are confirmed by some numerical tests.

1 Introduction

Our model problem is defined on an open, convex and polyhedral domain $\Omega \subset \mathbb{R}^3$. Within Ω we consider a C^2 -curve Γ , having the following properties:

$$\Gamma \subset \Omega, \quad |\Gamma| \leq C < \infty \quad \text{and} \quad \text{dist}(\Gamma, \partial\Omega) \geq c > 0, \quad (1)$$

where $C, c > 0$ are fixed constants and dist denotes the Euclidean distance. Using these definitions, the model problem reads as:

$$\begin{cases} -\Delta u = \delta_\Gamma & \text{in } \Omega, \\ u = 0 & \text{on } \partial\Omega, \end{cases} \quad (2)$$

where δ_Γ is the Dirac measure concentrated on the curve Γ . Considering a more general Poisson problem with a source term that is given by a real and

T. Köppl
Institut für Wasser- und Umweltsystemmodellierung, Universität Stuttgart, D-70569 Stuttgart, Germany
e-mail: tobias.koepl@iws.uni-stuttgart.de

E. Vidotto · B. Wohlmuth
Institute for Numerical Mathematics, Technische Universität München, D-85748 Garching b. München, Germany
e-mail: vidotto@ma.tum.de; wohlmuth@ma.tum.de

regular Borel measure, one can show existence and uniqueness of a weak solution [7, Thm. 1]. Moreover it can be proved that it belongs to the space $W_0^{1,p}(\Omega)$ for $p \in [1, 3/2)$ and that linear finite element solutions have a reduced convergence order of $1/2$ with respect to the standard L^2 -norm.

For the case of a Dirac measure concentrated on a C^2 -curve fulfilling the conditions (1), the authors of [9] proved that the weak solution of (2) is in $W_0^{1,p}(\Omega)$ for $p \in [1, 2)$ (see [9, Thm. 2.1, Case (ii)]) and that linear finite elements converge with first order in the standard L^2 -norm.

In [2], the authors have performed some numerical tests to investigate the convergence behavior of an elliptic 3D-1D coupled problem arising in the context of blood flow simulations [3,4]. Thereby, a 1D problem is defined on a straight line in 3D and is embedded into the 3D problem by a Dirac source term concentrated on this line. The L^2 -error of the 3D problem has not been computed on Ω , but on a subdomain $\Omega \setminus \tilde{Z}_R$, where \tilde{Z}_R is a cylinder of radius R around this line. It has been observed that the local L^2 -convergence behavior of linear finite elements is optimal up to a log-factor.

Motivated by these numerical results, we prove a quasi-optimal convergence behavior with respect to a local L^2 -norm. For this purpose, we define a domain Z_R covering a certain neighborhood of the curve Γ :

$$Z_R := \{x \in \Omega : \text{dist}(x, \Gamma) < R\},$$

where $0 < R < \text{dist}(\Gamma, \partial\Omega)$ is a fixed constant. The rest of this paper is organized as follows: In Section 2, we formulate the main result, which is a quasi-optimal bound of the L^2 -error on $\Omega \setminus Z_R$ and give an outline of the proof. A key ingredient for this proof is an auxiliary result, which is proved in Section 3. Finally in Section 4, we illustrate our theoretical result by some numerical tests.

2 Main result

The weak formulation of problem (2) reads as follows: Find $u \in W_0^{1,p}(\Omega)$ for $p \in [1, 2)$ such that

$$(\nabla u, \nabla \varphi) = \int_{\Gamma} \varphi \, d\Gamma \quad \forall \varphi \in W_0^{1,q}(\Omega), \quad (3)$$

where (\cdot, \cdot) denotes the duality pairing of $L^p(\Omega)$ and $L^q(\Omega)$, and $q > 2$ satisfies $1/p + 1/q = 1$. The right-hand side of the weak problem (3) is well-defined, since for $q > 3$ the embedding $W^{1,q}(\Omega) \hookrightarrow C(\Omega)$ is continuous (see, e.g., [1, Thm. 4.12]).

In order to solve (3), we introduce a family of quasi-uniform simplicial triangulations $\mathcal{T}_h = \{\tau\}$ of Ω , where h_τ is the diameter of the element τ . Furthermore, let $h := \max_{\tau \in \mathcal{T}_h} h_\tau$ be the meshsize. Our finite element space is then defined by standard conforming linear finite elements:

$$V_h := \{\varphi_h \in H_0^1(\Omega) : \varphi_h|_\tau \in \mathbb{P}_1(\tau), \forall \tau \in \mathcal{T}_h\}, \quad (4)$$

where $\mathbb{P}_1(\tau)$ denotes the space of linear polynomials on the element τ . Due to $V_h \subset W_0^{1,q}(\Omega) \subset W_0^{1,p}(\Omega)$, the following discrete version of (3) is well-defined: Find $u_h \in V_h$ such that

$$(\nabla u_h, \nabla \varphi_h) = \int_{\Gamma} \varphi_h d\Gamma \quad \forall \varphi_h \in V_h. \quad (5)$$

In order to derive an upper bound for the finite element error, we use a standard duality argument and define the corresponding dual problem as follows:

$$\begin{cases} -\Delta w = e\chi_{\Omega \setminus Z_R} & \text{in } \Omega, \\ w = 0 & \text{on } \partial\Omega, \end{cases} \quad (6)$$

where $\chi_{\Omega \setminus Z_R}$ is the characteristic function of $\Omega \setminus Z_R$ and $e := u - u_h$. Since Ω is convex and $e\chi_{\Omega \setminus Z_R} \in L^2(\Omega)$, it holds that $w \in H^2(\Omega) \cap H_0^1(\Omega)$ (see [8, Chap. 8]).

From now on, we fix $p = 7/5$. The choice is somehow arbitrary, but guarantees that $H^2(\Omega) \subset W^{1,q}(\Omega)$ for $q = 7/2$. Moreover, we have $w \in W^{1,\frac{7}{2}}(\Omega)$. A weak formulation of (6) is given by:

$$(\nabla w, \nabla \varphi) = (e\chi_{\Omega \setminus Z_R}, \varphi), \quad \forall \varphi \in W^{1,\frac{7}{2}}(\Omega) \quad (7)$$

and it is well defined. The corresponding finite element approximation $w_h \in V_h$ satisfies the following equality:

$$(\nabla w_h, \nabla \varphi_h) = (e\chi_{\Omega \setminus Z_R}, \varphi_h), \quad \forall \varphi_h \in V_h. \quad (8)$$

For the proof of our main result, a pointwise error estimate for the finite element error $w - w_h$ is required. Such an estimate is presented in the following lemma.

Lemma 1. *Let $w \in H_0^1(\Omega) \cap H^2(\Omega)$ be the solution of problem (6) and let $w_h \in V_h$ be its finite element approximation given by (8). Then for a $x_0 \in \Gamma$, the following pointwise error estimate holds*

$$|(w - w_h)(x_0)| \lesssim h^2 |\ln h| \|w\|_{H^2(\Omega)}. \quad (9)$$

We use the notation \lesssim for $\leq C$, with a generic constant C independent of h . The proof of this lemma is presented in the next section. Comparing this result with the standard L^∞ -estimate [5, Thm. 22.7], we have on the right-hand side of (9) the norm $\|w\|_{H^2(\Omega)}$ and not the stronger norm $\|w\|_{W^{2,\infty}(\Omega)}$. This is a consequence of the H^2 -regularity of w and the fact that w is harmonic in Z_R . By means of this lemma, one can prove the following theorem, which is the main result of our paper.

Theorem 2. *Let $u \in W^{1,p}(\Omega)$ for $p \in [1, 2)$ be the weak solution of (2) and let $u_h \in V_h$ be its finite element approximation. Then it holds the following quasi-optimal estimate for the local error:*

$$\|u - u_h\|_{L^2(\Omega \setminus Z_R)} \lesssim h^2 |\ln h|. \quad (10)$$

Proof. Using the Galerkin orthogonality, properties (1) of Γ , Lemma 1 and H^2 -regularity of w , we obtain:

$$\begin{aligned} \|e\|_{L^2(\Omega \setminus Z_R)}^2 &= (e\chi_{\Omega \setminus Z_R}, u - u_h) = (\nabla w, \nabla(u - u_h)) \\ &= (\nabla(w - w_h), \nabla(u - u_h)) = (\nabla u, \nabla(w - w_h)) \\ &= \int_{\Gamma} (w - w_h) d\Gamma \leq \int_{\Gamma} |w - w_h| d\Gamma \leq |\Gamma| \max_{x \in \Gamma} |(w - w_h)(x)| \\ &\lesssim h^2 |\ln h| \|w\|_{H^2(\Omega)} \lesssim h^2 |\ln h| \|e\|_{L^2(\Omega \setminus Z_R)}. \end{aligned}$$

3 Proof of Lemma 1

Let $x_0 \in \Gamma$ be fixed. We denote a ball of radius r around x_0 by B_r and assume $h < r/4$. Moreover, we demand $B_{r+2h} \subset B_{2r} \subset Z_R$. In order to study the finite element error of the dual problem within B_r , a smooth cut-off function η is introduced. Besides $\eta \in C^\infty(\Omega)$, this function is supposed to satisfy:

$$\begin{cases} \eta(x) = 1, & \text{if } x \in B_r, \\ \eta(x) = 0, & \text{if } x \in \Omega \setminus B_{2r}, \\ 0 \leq \eta(x) \leq 1, & \text{if } x \in B_{2r} \setminus B_r. \end{cases}$$

By the help of this cut-off function, an auxiliary Dirac problem is introduced, where the Dirac measure is concentrated at $x_0 \in \Gamma$:

$$\begin{cases} -\Delta z = \alpha(\delta_{x_0} + f_0) & \text{in } \Omega, \\ z = 0 & \text{on } \partial\Omega, \end{cases} \quad (11)$$

with $\alpha := \text{sgn}((w - w_h)(x_0))$. The function f_0 is defined as follows:

$$f_0(x) := \begin{cases} -2\nabla\eta \cdot \nabla G_{x_0} - G_{x_0} \Delta\eta & \text{if } x \in B_{2r} \setminus B_r \\ 0 & \text{if } x \notin B_{2r} \setminus B_r \end{cases}$$

and $G_{x_0}(x) := \frac{1}{4\pi} \frac{1}{|x - x_0|}$ denotes Green's function in 3D with respect to x_0 for $x \neq x_0$. This choice of f_0 leads to the following solution of the Dirac problem (11):

$$z = \alpha \cdot \eta \cdot G_{x_0}.$$

A straightforward computation shows that $z \notin H^1(\Omega)$, but $z \in W_0^{1,p}(\Omega)$ for $p \in [1, 3/2)$. The weak formulation of (11) reads now: Find $z \in W_0^{1, \frac{7}{5}}(\Omega)$ such that:

$$(\nabla z, \nabla \varphi) = \alpha \left(\int_{\Omega} f_0 \varphi d\Omega + \varphi(x_0) \right), \quad \forall \varphi \in W_0^{1, \frac{7}{5}}(\Omega). \quad (12)$$

The discrete version of (12) is given by:

$$(\nabla z_h, \nabla \varphi_h) = \alpha \left(\int_{\Omega} f_0 \varphi_h d\Omega + \varphi_h(x_0) \right), \forall \varphi_h \in V_h. \quad (13)$$

Setting $\varphi = w - w_h$, we obtain by (12):

$$(\nabla z, \nabla(w - w_h)) = (f_0, \alpha(w - w_h)) + |(w - w_h)(x_0)|.$$

This yields:

$$|(w - w_h)(x_0)| = (\nabla z, \nabla(w - w_h)) - (f_0, \alpha(w - w_h)). \quad (14)$$

Using the Hölder inequality, $f_0 \in L^2(\Omega)$, $w \in H^2(\Omega)$ and standard finite element estimates, one obtains obviously:

$$\int_{\Omega} \alpha(w - w_h) f_0 d\Omega \leq \|f_0\|_{L^2(\Omega)} \cdot \|w - w_h\|_{L^2(\Omega)} \lesssim h^2.$$

Inserting this bound in (14) and using the Galerkin orthogonality, it follows:

$$|(w - w_h)(x_0)| \lesssim h^2 + (\nabla(z - z_h), \nabla(w - w_h)).$$

It remains to estimate the second term on the right-hand side. For this purpose, we consider an interpolation operator $S_h : W^{n,p}(\Omega) \rightarrow V_h$ of Scott-Zhang type [11], due to its stability properties. By Galerkin orthogonality, we have:

$$|(w - w_h)(x_0)| \lesssim h^2 + (\nabla(z - z_h), \nabla(w - S_h w)).$$

Splitting the domain Ω into B_r and $\Omega \setminus B_r$ and applying the Hölder inequality yields:

$$\begin{aligned} |(w - w_h)(x_0)| &\lesssim h^2 + \|\nabla(z - z_h)\|_{L^2(\Omega \setminus B_r)} \|\nabla(w - S_h w)\|_{L^2(\Omega \setminus B_r)} \\ &\quad + \|\nabla(z - z_h)\|_{L^1(B_r)} \|\nabla(w - S_h w)\|_{L^\infty(B_r)}. \end{aligned} \quad (15)$$

Next, we have to bound the four error terms occurring on the right-hand side of (15). The estimates for these error terms are provided in the following.

For the second term $\|\nabla(w - S_h w)\|_{L^2(\Omega \setminus B_r)}$, a standard estimate (see, e.g. [11, Thm 4.1]) and the H^2 -regularity of w , yields:

$$\|\nabla(w - S_h w)\|_{L^2(\Omega \setminus B_r)} \lesssim h \|w\|_{H^2(\Omega)}, \quad (16)$$

Next we estimate the interpolation error $\|\nabla(w - S_h w)\|_{L^\infty(B_r)}$ using some results about the interior regularity of w .

Lemma 3. *Let w be the solution of (7) and let us assume that $B_{r+2h} \subset B_{2r} \subset Z_R$ and $4h < r$ holds. Then we have on B_r :*

$$\|\nabla(w - S_h w)\|_{L^\infty(B_r)} \lesssim h \|w\|_{H^2(\Omega)}. \quad (17)$$

Proof. Using the approximation properties of S_h and the Sobolev embedding $W^{4,2}(B_{r+2h}) \hookrightarrow W^{2,\infty}(B_{r+2h})$ [1, Thm. 4.12], one obtains:

$$\|\nabla(w - S_h w)\|_{L^\infty(B_r)} \lesssim h \|w\|_{W^{2,\infty}(B_{r+2h})} \lesssim h \|w\|_{W^{4,2}(B_{r+2h})}.$$

Interior regularity [8, Thm. 8.10], H^2 -regularity of w and the fact that w is harmonic in Z_R (and in particular in B_{2r}), yield:

$$\|w\|_{W^{4,2}(B_{r+2h})} \lesssim \|w\|_{W^{1,2}(B_{2r})} \lesssim \|w\|_{H^2(\Omega)},$$

which completes the proof.

Finally, we have to derive suitable bounds for the error terms involving the finite element error $z - z_h$. Since z is the weak solution of a homogeneous Poisson problem whose source term consists of a L^2 -function and a pointwise Dirac measure, we can use the results derived in [10].

Lemma 4. *Let $z \in H^2(\Omega \setminus B_r) \cap W_0^{1,p}(\Omega)$ for $p \in [1, 3/2)$ be defined by (12) and let $z_h \in V_h$ be its finite element approximation defined by (13). Then the following two bounds are valid:*

$$\|\nabla(z - z_h)\|_{L^2(\Omega \setminus B_r)} \lesssim h + \|z - z_h\|_{L^2(\Omega \setminus B_{r-2h})}. \quad (18)$$

and

$$\|\nabla(z - z_h)\|_{L^1(B_r)} \lesssim h |\ln h|. \quad (19)$$

Proof. The proof of this lemma is a direct consequence of [10, Lemma 3.6] and [10, Lemma 3.10].

Combining equation (16) and Lemmas 3 and 4, we find

$$|(w - w_h)(x_0)| \lesssim h^2 |\ln h| \|w\|_{H^2(\Omega)} + h \|z - z_h\|_{L^2(\Omega \setminus B_{r-2h})} \|w\|_{H^2(\Omega)}.$$

Using [10, Thm. 2.1] for the term $\|z - z_h\|_{L^2(\Omega \setminus B_{r-2h})}$ and the H^2 -regularity of w , it finally follows

$$|(w - w_h)(x_0)| \lesssim h^2 |\ln h| \|w\|_{H^2(\Omega)}. \quad (20)$$

4 Numerical experiments

In this section, we illustrate the theoretical estimate (10) by numerical examples. For this purpose, we choose the unit cube as our computational domain, i.e., $\Omega = (0, 1)^3$. By the help of the curves:

$$\begin{aligned} \Gamma_1 &: [0, 1] \rightarrow \overline{\Omega}, & \Gamma_1(s) &= (0.5, 0.5, s), \\ \Gamma_2 &: [0, 1] \rightarrow \Omega, & \Gamma_2(s) &= 0.5(1 + 0.06 \cos(2\pi s), 1 + 0.06 \sin(2\pi s), s + 0.5), \end{aligned}$$

we define two different Poisson problems, setting in (2) Γ to Γ_1 or Γ_2 .

In the first case, we modify the homogeneous boundary condition in (2), such that the exact solution of the considered Poisson problem is given by:

$$u(x) = -\frac{1}{2\pi} \log |x - \Gamma_1(x_3)|.$$

In the second case, we keep the homogeneous boundary condition. However, for this problem no analytical solution is available. Therefore, we precompute a numerical reference solution on a fine mesh and determine the finite element errors by comparing numerical solutions on coarser meshes to the reference solution. The numerical results (see Figure 1) are obtained by means of a linear finite element solver implemented in DUNE [6].

According to Theorem 2, we report the local L^2 -error on $\Omega \setminus Z_R$ for different radii $R \in \{0, 0.0625, 0.125, 0.25\}$. The approximation errors and convergence rates for the different refinement levels ℓ are listed in Table 1 and 2. It can be seen that for $R = 0$ the finite element scheme converges only with first order, as predicted by [9, Lemma 3.3]. In the remaining cases second order convergence can be observed, if $h < R$ holds. This is in agreement with estimate (10) in Theorem 2.

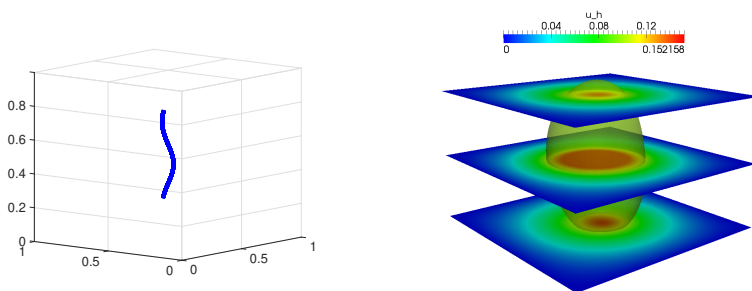


Fig. 1. The figure shows the position of Γ_2 within the unit cube (left) and a contour plot for $u_h = 0.1$ together with three different slices at $x_3 = 0.2, 0.5, 0.8$ (right).

Table 1. L^2 -error on $\Omega \setminus Z_R$ for $\Gamma = \Gamma_1$.

ℓ	Dof	$R = 0$	Rate	$R = 0.0625$	Rate	$R = 0.125$	Rate	$R = 0.25$	Rate
2	125	1.0461e-2	/	1.0461e-2	/	1.0461e-2	/	4.3424e-3	/
3	729	5.4648e-3	0.94	5.4648e-3	0.94	2.5806e-3	2.02	1.4692e-3	1.56
4	4913	2.7741e-3	0.98	1.3369e-3	2.03	8.0692e-4	1.68	2.3815e-4	2.63
5	35937	1.3968e-3	0.99	4.1809e-4	1.68	1.4183e-4	2.51	5.7466e-5	2.05
6	274625	7.0077e-4	1.00	7.4890e-5	2.48	3.4535e-5	2.04	1.4533e-5	1.98
7	2146689	3.5097e-4	1.00	1.8260e-5	2.04	8.7158e-6	1.99	3.6356e-6	2.00

Table 2. Discrete L^2 -error on $\Omega \setminus Z_R$ for $\Gamma = \Gamma_2$.

ℓ	Dof	$R = 0$	Rate	$R = 0.0625$	Rate	$R = 0.125$	Rate	$R = 0.25$	Rate
2	125	9.9816e-3	/	5.7708e-3	/	4.1503e-3	/	2.8019e-3	/
3	729	6.5546e-3	0.61	2.6437e-3	1.13	1.5200e-3	1.45	6.3984e-4	2.13
4	4913	4.6708e-3	0.49	1.1080e-3	1.25	3.9200e-4	1.96	1.5896e-4	2.01
5	35937	1.8626e-3	1.33	2.8450e-4	1.96	1.0354e-4	1.92	3.9731e-5	2.00
6	274625	7.7970e-4	1.26	5.6445e-5	2.33	2.1513e-5	2.27	8.2663e-6	2.26

References

1. R. Adams, and J. Fournier, *Sobolev spaces*. Vol. 140. Academic press, 2003.
2. L. Cattaneo, and P. Zunino, *Numerical Investigation of Convergence Rates for the FEM Approximation of 3D-1D Coupled Problems*. Numerical Mathematics and Advanced Applications-ENUMATH 2013. Springer International Publishing, 2015. 727-734.
3. L. Cattaneo, and P. Zunino, *A computational model of drug delivery through microcirculation to compare different tumor treatments*. International journal for numerical methods in biomedical engineering. Wiley Online Library (2014): 1347-1371.
4. C. D'Angelo, and P. Zunino, *Multiscale models of drug delivery by thin implantable devices*. Applied and Industrial Mathematics in Italy III, Ser. Adv. Math. Appl. Sci. World Scientific (2009): 298-310.
5. P. Ciarlet, *Basic error estimates for elliptic problems*. Handbook of numerical analysis 2 (1991): 17-351.
6. P. Bastian et al, *A generic grid interface for parallel and adaptive scientific computing. Part I: abstract framework*. Computing 82.2-3 (2008): 103-119.
7. E. Casas, *L^2 estimates for the finite element method for the Dirichlet problem with singular data*. Numerische Mathematik 47.4 (1985): 627-632.
8. D. Gilbarg, and N. Trudinger, *Elliptic partial differential equations of second order*. springer, 2015.
9. W. Gong, G. Wang, and N. Yan, *Approximations of Elliptic Optimal Control Problems with Controls Acting on a Lower Dimensional Manifold*. SIAM Journal on Control and Optimization 52.3 (2014): 2008-2035.
10. T. Köppl, and B. Wohlmuth, *Optimal a priori error estimates for an elliptic problem with Dirac right-hand side*. SIAM Journal on Numerical Analysis 52.4 (2014): 1753-1769.
11. R. Scott, and S. Zhang, *Finite element interpolation of nonsmooth functions satisfying boundary conditions*. Mathematics of Computation 54.190 (1990): 483-493.

6 Mathematical modeling, analysis and numerical approximation of second-order elliptic problems with inclusions

Bibliographic note: The content of this chapter is based on the following original article: T. Köppl, E. Vidotto, B. Wohlmuth and Paolo Zunino (2018): Mathematical modeling, analysis and numerical approximation of second-order elliptic problems with inclusions. *Mathematical Models and Methods in Applied Sciences* 28(05), pages: 953-978, with courtesy of World Scientific.

Mathematical modeling, analysis and numerical approximation of second-order elliptic problems with inclusions

Tobias Köppl

*Department of Hydromechanics and Modelling of Hydrosystems,
University of Stuttgart, Pfaffenwaldring 61, 70569 Stuttgart, Germany
tobias.koepl@iws.uni-stuttgart.de*

Ettore Vidotto* and Barbara Wohlmuth†

*Lehrstuhl für Numerische Mathematik, Technical University of Munich,
Boltzmannstraße 3, 85748 Garching, Germany
*ettore.vidotto@ma.tum.de
†barbara.wohlmuth@ma.tum.de*

Paolo Zunino‡

*MOX, Department of Mathematics, Politecnico di Milano,
Piazza Leonardo da Vinci 32, 20133 Milano, Italy
paolo.zunino@polimi.it*

Received 22 May 2017

Revised 20 December 2017

Accepted 13 January 2018

Published 16 March 2018

Communicated by C. Canuto

Many biological and geological systems can be modeled as porous media with small inclusions. Vascularized tissue, roots embedded in soil or fractured rocks are examples of such systems. In these applications, tissue, soil or rocks are considered to be porous media, while blood vessels, roots or fractures form small inclusions. To model flow processes in thin inclusions, one-dimensional (1D) models of Darcy- or Poiseuille type have been used, whereas Darcy-equations of higher dimension have been considered for the flow processes within the porous matrix. A coupling between flow in the porous matrix and the inclusions can be achieved by setting suitable source terms for the corresponding models, where the source term of the higher-dimensional model is concentrated on the center lines of the inclusions. In this paper, we investigate an alternative coupling scheme. Here, the source term lives on the boundary of the inclusions. By doing so, we lift the dimension by one and thus increase the regularity of the solution. We show that this model can be derived from a full-dimensional model and the occurring modeling errors are estimated. Furthermore, we prove the well-posedness of the variational formulation and discuss the convergence behavior of standard finite element methods with respect to this model. Our theoretical results are confirmed by numerical tests. Finally,

‡Corresponding author

we demonstrate how the new coupling concept can be used to simulate stationary flow through a capillary network embedded in a biological tissue.

Keywords: Elliptic problems; small inclusions; model reduction; finite element approximation.

AMS Subject Classification: 78M34, 65N30, 65N12, 65N15

1. Introduction

In this work, we address a special type of second-order elliptic equation, which can be considered a model problem for diffusion processes in porous media with small inclusions. To define this problem, a two-dimensional, open, bounded and convex domain $\Omega \subset \mathbb{R}^2$ is considered. Moreover, we assume that Ω is a polygonal domain. Within Ω there are $N \in \mathbb{N}$ open balls $B_i \subset \Omega$. By B_i , we denote a ball around a center $x_i \in \Omega$ having the radius R_i . For a given constant $C > 0$ it holds:

$$\text{dist}(\partial\Omega, B_j) > C, \quad \text{dist}(B_i, B_j) > C, \quad i \neq j, \quad i, j \in \{1, \dots, N\},$$

where

$$\text{dist}(M, B_j) = \min\{\|x - y\|_2 \mid x \in \overline{M}, y \in \overline{B_j}\}, \quad M \in \{\partial\Omega, B_i\}.$$

For notational convenience, we split the domain Ω in two parts, Ω_f, Ω_p :

$$\Omega_p = \Omega \setminus \overline{\Omega}_f, \quad \text{where } \Omega_f = \bigcup_{i=1}^N B_i. \quad (1.1)$$

In the applications discussed in more detail later on, Ω_f represents the collection of channels and fractures, while Ω_p is the surrounding porous material. Having this notation at hand, our model problem reads as follows:

$$-\Delta u_{\text{ref}} = f \text{ in } \Omega_p, \quad -\nabla u_{\text{ref}} \cdot n_i = \kappa_i(U_i - u_{\text{ref}}) \text{ on } \partial B_i, \quad u_{\text{ref}} = 0 \text{ on } \partial\Omega. \quad (1.2)$$

The source term $f \in L^2(\Omega_p)$ represents a body force or external source and sink terms, while $\kappa_i(U_i - u_{\text{ref}})$ is modeling a flux through the interface Γ_i from the inclusions into the porous medium or vice versa. More precisely, $\kappa_i \in \mathbb{R}$, $\kappa_i > 0$ plays the role of a permeability, $U_i \in \mathbb{R}$, $U_i > 0$ is a given intensity of the inclusion Ω_i , and n_i denotes the outward unit normal vector of ∂B_i . In Sec. 7, we will also consider the case where U_i are functions that obey partial differential equations coupled with problem (1.2). For applications with many small inclusions, model (1.2) is computationally unfeasible, because of the excessive computational cost that would arise using a computational mesh that conforms to all inclusions. Therefore, we present in this work a simplified form of problem (1.2), which considerably reduces the cost of numerical simulations. The reduced model we propose consists of the following equations for the unknown u_{red} :

$$-\Delta u_{\text{red}} = \mathcal{F} + \sum_{i=1}^N \kappa_i (U_i - \overline{u}_{\text{red}}^{(i)}) \delta_{\partial B_i} \text{ in } \Omega, \quad u_{\text{red}} = 0 \text{ on } \partial\Omega, \quad (1.3)$$

where $\delta_{\partial B_i}$ stands for a Dirac measure laying on ∂B_i and the expression $\bar{u}_{\text{red}}^{(i)}$ abbreviates the mean value of u_{red} on ∂B_i :

$$\bar{u}_{\text{red}}^{(i)} = \frac{1}{2\pi R_i} \int_{\partial B_i} u_{\text{red}} dS. \quad (1.4)$$

The fluctuations $\tilde{u}_{\text{red}}^{(i)}$ of u_{red} on ∂B_i are defined by:

$$\tilde{u}_{\text{red}}^{(i)} = u_{\text{red}}|_{\partial B_i} - \bar{u}_{\text{red}}^{(i)}. \quad (1.5)$$

The source term $\mathcal{F} \in L^2(\Omega)$ is an extension of the source term f in (1.2), where we claim that \mathcal{F} coincides with f on Ω_p :

$$\mathcal{F}(x) = \begin{cases} f(x), & \text{for } x \in \Omega_p, \\ f_i(x), & \text{for } x \in B_i. \end{cases} \quad (1.6)$$

In addition to that, it may hold that \mathcal{F} exhibits no jumps at the interfaces ∂B_i and that for a constant $C_f > 0$:

$$\|f_i\|_{L^2(B_i)} \leq C_f \|f\|_{L^2(\Omega_p)}, \quad \forall i \in \{1, \dots, N\}. \quad (1.7)$$

In cases where U_i are the solutions of partial differential equations derived from model reduction techniques, thus defined on lower-dimensional manifolds or sets (2D, 1D, 0D), this gives rise to coupled systems of PDEs defined on embedded domains with heterogeneous dimensionality.^{5,7,14,26} Such PDE systems are often classified into PDE systems with co-dimension 1, i.e. 3D-2D or 2D-1D coupled PDEs, and PDEs with co-dimension 2, i.e. 3D-1D or 2D-0D coupled problems.

The numerical analysis and discretization of these types of problems have been investigated in several publications.^{6,17,22} For the numerical treatment of interface problems with co-dimension 1, XFEM methods have proved to be very effective.^{10,33} In the case of co-dimension 2, the solution of the higher-dimensional problem exhibits singularities along the manifolds representing the inclusions. When the lower-dimensional problems are represented as a distribution of Dirac source terms embedded into the higher-dimensional space, the reduced regularity deteriorates the convergence of numerical methods and optimal convergence rates can only be recovered using graded meshes or local error norms.^{2,6,19,20}

In this paper, we investigate by means of the model problem (1.3) a different way of coupling partial differential equations with heterogeneous dimensionality. The fundamental difference between the coupling term in (1.3) and the existing coupling concepts is that the inclusion is not represented by a single line or point in space. In the source term of (1.3) the Dirac measure is concentrated on the physical boundary of the inclusions. Therefore, a dimensional gap of two in the coupling term is avoided and the corresponding solution is smoother. At the same time, the averaging technique applied to the interface conditions makes it possible to couple the bulk problem with sub-problems defined on manifolds of co-dimension 2. This formulation allows for a more natural mathematical analysis of the model, numerical discretization and error analysis of the resulting approximation schemes.

In this work, we thoroughly analyze a prototype version of the problem, addressing point-wise inclusions embedded into a two-dimensional domain. We point out that for the 3D-1D setting, the analysis can be worked out in a similar way for special cases such as one isolated inclusion on a straight line. However, since the embedding results are dimension dependent and since the choice of the boundary condition influences the regularity of the solution, we do not work out the 3D-1D case in detail. More complex situations such as networks of inclusions, possibly showing bifurcations and curvilinear branches, require much more care. In case of curvilinear inclusions one has to use local finite covering arguments and in case of bifurcations possible new singular terms may appear.

The coupling of three-dimensional continua with embedded 1D inclusions, of which the proposed model represents a template, arises in applications of great importance such as microcirculation, flow through perforated media and the study of reinforced materials.

Flow and transport simulations in complex vascular networks are becoming a popular approach to study the physiology of tumors and to design new treatments.^{12,25,36} This new trend is motivated by the need to incorporate accurate physical models of flow, biochemical transport and mechanical interactions within a realistic geometrical description of the vasculature, which in turn enables the comparison of simulations with imaging data captured at the microscale by means of intravital microscopy techniques.^{3,4,18,21,38} We also point out that a similar approach is being used for simulating the interaction of plant roots with soil.³²

This new approach for solving PDEs in domains with inclusions is also of interest in many other fields such as in the design of cooling systems for electronics (for designing pulsating heat pipes for space applications) in neuroscience (to study the impact of cerebrospinal fluid clearance on chronic mental disease and dementia) and in the simulation of floods (through the interaction of the hydraulic network with the surrounding territory).

The remaining parts of this work are organized as follows: In Sec. 2, we summarize some trace inequalities which are required for the mathematical analysis in the following sections. Section 3 presents the model derivation and the weak formulation of (1.3). Moreover, the existence and uniqueness of the weak solution is shown and its regularity is discussed. Section 4 characterizes the modeling error. In Sec. 5, we consider the numerical discretization by the finite element method and study its convergence. Our theoretical results are confirmed by numerical tests, which are presented in Sec. 6. Finally, in Sec. 7, the new coupling concept is used to address a relevant application, i.e. the perfusion of vascularized biological tissues.

2. Trace Inequalities

In this section, we discuss two trace inequalities that are key ingredients for our mathematical analysis. The first trace inequality allows us to bound the mean value

$\bar{v}^{(i)}$ (see (1.4)) of a function $v \in H_0^1(\Omega)$ with respect to the boundary of a ball B_i , while the second trace inequality is an inequality of Steklov-type providing an upper bound for traces of functions v , whose averages vanish on ∂B_i :

$$\int_{\partial B_i} v \, dS = 0.$$

In order to prove the well-posedness of our model problem (Sec. 3) and to derive suitable upper bounds for the modeling error (Sec. 4), it is crucial to know how the arising constants depend on the radii R_i of the circular inclusions B_i . Therefore, we investigate these constants in more details.

Lemma 2.1. *Let $B_i \subset \Omega$ be a ball with a sufficiently small radius R_i . Then it holds for the mean value $\bar{v}^{(i)}$ of $v \in H_0^1(\Omega)$:*

$$\bar{v}^{(i)} \leq C |\ln R_i|^{\frac{1}{2}} \|\nabla v\|_{L^2(\Omega)},$$

where the constant $C > 0$ is independent of R_i .

Proof. According to Remark 1 of Ref. 1, it holds for B_i :

$$\bar{v}^{(i)} \leq \frac{1}{2\pi R_i} \left(\frac{2}{R_i} \int_{B_i} |v| \, dx + \int_{B_i} |\nabla v| \, dx \right).$$

Applying the Hölder inequality to both summands, we have:

$$\begin{aligned} \bar{v}^{(i)} &\leq \frac{1}{\pi R_i^2} (\pi R_i^2)^{\frac{1}{q}} \|v\|_{L^p(B_i)} + \frac{\sqrt{\pi R_i^2}}{2\pi R_i} \|\nabla v\|_{L^2(B_i)}, \\ &\leq (\pi R_i^2)^{-\frac{1}{p}} \|v\|_{L^p(B_i)} + \frac{\sqrt{\pi R_i^2}}{2\pi R_i} \|\nabla v\|_{L^2(B_i)}. \end{aligned}$$

For the parameters p and q such that $1/p + 1/q = 1$, while the L^1 -norm in the second summand is estimated by a product of L^2 -norms. The choice $p = |\ln R_i| \geq 2$ and $q = \frac{|\ln R_i|}{|\ln R_i| - 1}$ yields:

$$\begin{aligned} \bar{v}^{(i)} &\leq \pi^{-\frac{1}{|\ln R_i|}} R_i^{-\frac{2}{|\ln R_i|}} \|v\|_{L^p(B_i)} + \frac{\sqrt{\pi R_i^2}}{2\pi R_i} \|\nabla v\|_{L^2(B_i)} \\ &\leq \exp(2) \|v\|_{L^p(\Omega)} + \frac{1}{2\sqrt{\pi}} \|\nabla v\|_{L^2(\Omega)}. \end{aligned}$$

According to a Sobolev inequality (see Eq. (6.20) in Ref. 39), there exists a constant $C > 0$ independent of R_i such that for $v \in H_0^1(\Omega)$ it holds true:

$$\|v\|_{L^p(\Omega)} \leq C p^{\frac{1}{2}} \|\nabla v\|_{L^2(\Omega)}. \quad (2.1)$$

Therefore, we have

$$\bar{v}^{(i)} \leq C (|\ln R_i|^{\frac{1}{2}} \|\nabla v\|_{L^2(\Omega)} + \|\nabla v\|_{L^2(\Omega)}),$$

with a constant $C > 0$ independent of R_i . \square

Next, we derive by means of the Steklov inequality a trace inequality for the fluctuation $\tilde{v}^{(i)}$ with respect to a ball B_i (see (1.5)).

Lemma 2.2. *Let $B_i \subset \mathbb{R}^2$ be a ball with a sufficiently small radius R_i and $v \in H_0^1(\Omega)$. Then we have:*

$$\|v\|_{L^2(\partial B_i)} \leq C \sqrt{R_i |\ln R_i|} \|\nabla v\|_{L^2(\Omega)},$$

where $C > 0$ is a constant independent of R_i .

Proof. Observing that $\int_{\partial B_i} \tilde{v}^{(i)} dS = 0$, we find in terms of Sec. 3 in Ref. 16 and Sec. 5 in Ref. 23 that

$$\|\tilde{v}^{(i)}\|_{L^2(\partial B_i)} \leq \sqrt{R_i} \|\nabla v\|_{L^2(B_i)}. \quad (2.2)$$

Using the orthogonal decomposition of v , we obtain:

$$\|v\|_{L^2(\partial B_i)}^2 = \|\bar{v}^{(i)} + \tilde{v}^{(i)}\|_{L^2(\partial B_i)}^2 = 2\pi R_i (\bar{v}^{(i)})^2 + \|\tilde{v}^{(i)}\|_{L^2(\partial B_i)}^2.$$

In order to bound the first term, we apply Lemma 2.1 and the second term is bounded by (2.2). \square

3. Model Derivation and Analysis

Let us start with the variational formulation of reference problem (1.2). It consists of finding $u_{\text{ref}} \in V(\Omega_p)$ such that

$$(\nabla u_{\text{ref}}, \nabla v)_{\Omega_p} + \sum_{i=1}^N \kappa_i (u_{\text{ref}}, v)_{\partial B_i} = (f, v)_{\Omega_p} + \sum_{i=1}^N \kappa_i U_i \int_{\partial B_i} v dS, \quad \forall v \in V(\Omega_p), \quad (3.1)$$

where we have adopted the standard notation for the L^2 -inner product. The function space $V(\Omega_p)$ is defined as follows:

$$V(\Omega_p) = \{v \in H^1(\Omega_p) | v|_{\partial\Omega} = 0\}.$$

Using (1.4) and (1.5), the interface terms can be written as:

$$(u, v)_{\partial B_i} = \int_{\partial B_i} u v dS = 2\pi R_i \bar{u}^{(i)} \bar{v}^{(i)} + \int_{\partial B_i} \tilde{u}^{(i)} \tilde{v}^{(i)} dS. \quad (3.2)$$

We derive a simplified model (also named here as *reduced model*) on the basis of the following assumptions, which rely on the fact that the inclusions are small:

- (A1) we identify the domain Ω_p with the entire Ω ;
- (A2) we assume that the residual term in (3.2) is small, namely

$$\int_{\partial B_i} \tilde{u}^{(i)} \tilde{v}^{(i)} dS \simeq 0.$$

In Sec. 4, we will define the error components associated with each of these assumptions, and we will analyze their magnitude in terms of the parameters of the problem. We replace (3.1) with a surrogate problem: Find $u_{\text{red}} \in H_0^1(\Omega)$ such that

$$(\nabla u_{\text{red}}, \nabla v)_\Omega + 2\pi \sum_{i=1}^N R_i \kappa_i \bar{u}_{\text{red}}^{(i)} \bar{v}^{(i)} = (\mathcal{F}, v)_\Omega + 2\pi \sum_{i=1}^N R_i \kappa_i U_i \bar{v}^{(i)}, \quad \forall v \in H_0^1(\Omega). \quad (3.3)$$

Problem (3.3) is equivalent to finding $u_{\text{red}} \in H_0^1(\Omega)$ such that:

$$a(u_{\text{red}}, v) = L(v), \quad \forall v \in H_0^1(\Omega), \quad (3.4)$$

where the bilinear form $a(\cdot, \cdot) : H_0^1(\Omega) \times H_0^1(\Omega) \rightarrow \mathbb{R}$ is given by:

$$a(u, v) = (\nabla u, \nabla v)_\Omega + 2\pi \sum_{i=1}^N R_i \kappa_i \bar{u}^{(i)} \bar{v}^{(i)}. \quad (3.5)$$

The linear form L is defined as follows:

$$L : H_0^1(\Omega) \rightarrow \mathbb{R}, \quad L(v) = (\mathcal{F}, v)_\Omega + 2\pi \sum_{i=1}^N R_i \kappa_i U_i \bar{v}^{(i)}. \quad (3.6)$$

Obviously, (3.4) is the weak formulation of the reduced problem (1.3). For the variational problem (3.4), one can prove the following result on the well-posedness.

Theorem 3.1. *Let the requirements of Lemma 2.1 be fulfilled. Then problem (3.4) has a unique solution*

$$u_{\text{red}} \in H_0^1(\Omega) \cap H^{\frac{3}{2}-\epsilon}(\Omega), \quad \forall \epsilon > 0.$$

Furthermore, it holds the following stability estimate:

$$\|u_{\text{red}}\|_{H_0^1(\Omega)} \leq C \left(\|\mathcal{F}\|_{L^2(\Omega)} + \sum_{i=1}^N \kappa_i R_i |\ln R_i|^{\frac{1}{2}} U_i \right).$$

Proof. The variational problem (3.4) can be analyzed by means of the Lax–Milgram Lemma. We begin by proving that the symmetric bilinear form (3.5) is continuous and coercive. The coercivity is a direct consequence of the Poincaré inequality. More precisely for any $v \in H_0^1(\Omega)$ there exists a positive constant C_P independent of R_i and κ_i , such that:

$$a(v, v) \geq (\nabla v, \nabla v)_\Omega \geq (1 + C_P^2)^{-1} \|v\|_{H_0^1(\Omega)}^2.$$

By means of Lemma 2.1, we have

$$2\pi R_i \bar{u}^{(i)} \bar{v}^{(i)} \leq 2\pi R_i C |\ln R_i| \|u\|_{H_0^1(\Omega)} \|v\|_{H_0^1(\Omega)}. \quad (3.7)$$

Then, using (3.7), we obtain the continuity of the bilinear form:

$$a(u, v) \leq \left(1 + 2\pi C \sum_{i=1}^N \kappa_i R_i |\ln R_i| \right) \|u\|_{H_0^1(\Omega)} \|v\|_{H_0^1(\Omega)}.$$

The boundedness of the linear form (3.6) then remains to be proven. According to Lemma 2.1, we have:

$$2\pi R_i \bar{v}^{(i)} \leq 2\pi R_i C |\ln R_i|^{\frac{1}{2}} \|\nabla v\|_{L^2(\Omega)} \leq 2\pi R_i C |\ln R_i|^{\frac{1}{2}} \|v\|_{H_0^1(\Omega)}.$$

All in all, it follows that there is a unique solution $u_{\text{red}} \in H_0^1(\Omega)$. Due to the presence of Dirac source terms in (1.3) no H^2 -regularity can be recovered and the question arises as to which interspace \tilde{V} with $H^2(\Omega) \subset \tilde{V} \subset H_0^1(\Omega)$ the solution u_{red} belongs. Since the right-hand side in (1.3) is in $H^{-\frac{1}{2}-\epsilon}(\Omega)$, $\forall \epsilon > 0$ it can be shown, analogous to Case (iii) in Theorem 2.1 of Ref. 15, that $u_{\text{red}} \in H^{\frac{3}{2}-\epsilon}(\Omega)$, $\forall \epsilon > 0$. Testing (3.4) with $v = u_{\text{red}}$, using the coercivity of the bilinear form a , the continuity result of the linear form L and the Cauchy–Schwarz inequality the above stability estimate can be derived. \square

4. Analysis of the Modeling Error

We aim to analyze the error arising from assumptions (A1) and (A2) at the basis of the reduced model (3.3). Let us denote by u_{int} the solution of the problem obtained after the intermediate step (A1), that is

$$(\nabla u_{\text{int}}, \nabla v)_{\Omega} + \sum_{i=1}^N \kappa_i (u_{\text{int}}, v)_{\partial B_i} = (\mathcal{F}, v)_{\Omega} + \sum_{i=1}^N \kappa_i U_i \int_{\partial B_i} v \, dS, \quad \forall v \in H_0^1(\Omega). \quad (4.1)$$

Proceeding as in Theorem 4.12 in Ref. 37 and Theorem 3.1, one can prove that problems (3.1) and (4.1) admit unique solutions $u_{\text{ref}} \in V(\Omega_p)$, and $u_{\text{int}} \in H_0^1(\Omega)$, respectively. We define the modeling error as $e := u_{\text{ref}} - u_{\text{red}}|_{\Omega_p}$, and we naturally decompose it as the error related to assumption (A1), that is $e_1 := u_{\text{ref}} - u_{\text{int}}|_{\Omega_p}$ and the one associated to (A2), namely $e_2 := u_{\text{int}} - u_{\text{red}}$. The two parts of the error are analyzed separately, and we show that the following inequality holds true:

$$\begin{aligned} \|e\|_{H^1(\Omega_p)} &\leq \|e_1\|_{H^1(\Omega_p)} + \|e_2\|_{H^1(\Omega)} \\ &\leq C_1 \left[\|\mathcal{F}\|_{L^2(\Omega)} \sum_{i=1}^N R_i |\ln R_i|^{\frac{1}{2}} (1 + \kappa_i) + \sum_{i=1}^N U_i \kappa_i R_i |\ln R_i|^{\frac{1}{2}} \right] \\ &\quad + C_2 \left[\|\mathcal{F}\|_{L^2(\Omega)} \sum_{i=1}^N \kappa_i R_i + \sum_{i,j=1}^N \kappa_i \kappa_j R_i R_j |\ln R_j|^{\frac{1}{2}} U_j \right], \end{aligned} \quad (4.2)$$

where the constants C_1 and C_2 are independent of R_i , κ_i and U_i , $\forall i \in \{1, \dots, N\}$. Equation (4.2) informs us of the structure of the modeling error. The first two terms on the right-hand side relate to the modeling assumption (A1) concerning extension of the physical domain Ω_p to the whole domain Ω . This component of the error scales quasi-linearly with the size of the inclusions. The third and fourth components on the right-hand side quantify the error of replacing the solution on

the interfaces with its average and relate to the modeling assumption (A2). Since a modeling error for one interface affects all the other interfaces, not surprisingly the fourth term is proportional to $\sum_{i,j=1}^N R_i R_j$, up to a log-term.

4.1. Analysis of the modeling error related to assumption (A1)

In this subsection, we derive an upper bound depending on the parameters which occur in our model problem for the modeling error corresponding to assumption (A1). As a first step we define an elliptic auxiliary problem:

$$-\Delta u_f = \mathcal{F} \text{ in } \Omega, \quad u_f = 0 \text{ on } \partial\Omega.$$

Having the weak formulation:

$$(\nabla u_f, \nabla v)_\Omega = (\mathcal{F}, v)_\Omega, \quad \forall v \in H_0^1(\Omega). \quad (4.3)$$

By means of the solution u_f , we decompose the solutions of (3.1) and (4.1) as follows:

$$u_{\text{ref}} = w_{\text{ref}} + u_f|_{\Omega_p} \quad \text{and} \quad u_{\text{int}} = w_{\text{int}} + u_f. \quad (4.4)$$

Next, we introduce two extension operators

$$E_{\text{sa}} : V(\Omega_p) \rightarrow H_0^1(\Omega) \quad \text{and} \quad E_{\text{st}} : H^2(\Omega) \rightarrow H_0^2(\hat{\Omega})$$

presented in Sec. 2.1 in Ref. 31 and Theorem 7.25 in Ref. 13, respectively. Here, $\hat{\Omega}$ is an open and bounded set with $\Omega \Subset \hat{\Omega} \subset \mathbb{R}^2$. In order to derive a stability estimate for w_{ref} , we exploit the following properties of E_{sa} and E_{st} :

- (P1) Let $v \in V(\Omega_p)$ then it holds: $E_{\text{sa}} v|_{\Omega_p} = v$ and $\overline{E_{\text{sa}} v}^{(i)} = \bar{v}^{(i)}$.
- (P2) According to the proofs of Lemma 2.2, Theorem 2.2, Example 2.1 in Ref. 31, there is a constant $C_{\text{sa}} > 0$ independent of R_i , such that:

$$\|\nabla E_{\text{sa}} v\|_{L^2(\Omega)} \leq C_{\text{sa}} \|\nabla v\|_{L^2(\Omega_p)} \quad \text{for } v \in V(\Omega_p).$$

- (P3) For $v \in H^2(\Omega)$, there is a constant $C_{\text{st}} > 0$, such that:

$$\|E_{\text{st}} v\|_{H^2(\hat{\Omega})} \leq C_{\text{st}} \|v\|_{H^2(\Omega)} \quad \text{and} \quad E_{\text{st}} v|_\Omega = v.$$

For $v = w_{\text{ref}} \in V(\Omega_p)$ in (3.1), using the decomposition in (4.4) we obtain:

$$\begin{aligned} \|\nabla w_{\text{ref}}\|_{L^2(\Omega_p)}^2 &\leq (\mathcal{F}, E_{\text{sa}} w_{\text{ref}})_\Omega - (\nabla u_f, \nabla E_{\text{sa}} w_{\text{ref}})_\Omega - \sum_{i=1}^N (f_i, E_{\text{sa}} w_{\text{ref}})_{B_i} \\ &\quad + \sum_{i=1}^N (\nabla u_f, \nabla E_{\text{sa}} w_{\text{ref}})_{B_i} - \sum_{i=1}^N \kappa_i (u_f, w_{\text{ref}})_{\partial B_i} \\ &\quad + \sum_{i=1}^N U_i \kappa_i \int_{\partial B_i} w_{\text{ref}} \, dS. \end{aligned}$$

Testing (4.3) with $v = E_{\text{sa}} w_{\text{ref}} \in H_0^1(\Omega)$, we have:

$$(\mathcal{F}, E_{\text{sa}} w_{\text{ref}})_\Omega - (\nabla u_f, \nabla E_{\text{sa}} w_{\text{ref}})_\Omega = 0$$

and by (P1) and the Hölder inequality, it follows:

$$\begin{aligned} \|\nabla w_{\text{ref}}\|_{L^2(\Omega_p)}^2 &\leq \sum_{i=1}^N \|f_i\|_{L^2(B_i)} \|E_{\text{sa}} w_{\text{ref}}\|_{L^2(B_i)} + \sum_{i=1}^N \|\nabla u_f\|_{L^2(B_i)} \|\nabla E_{\text{sa}} w_{\text{ref}}\|_{L^2(B_i)} \\ &\quad + \sum_{i=1}^N \kappa_i \|u_f\|_{L^2(\partial B_i)} \|w_{\text{ref}}\|_{L^2(\partial B_i)} + 2\pi \sum_{i=1}^N U_i \kappa_i R_i \cdot \bar{w}_{\text{ref}}^{(i)}. \end{aligned}$$

In order to bound the first summand, we consider once again the Hölder inequality with the parameters r and s fulfilling the condition $1/r + 1/s = 1$. By means of this, one can show that:

$$\|E_{\text{sa}} w_{\text{ref}}\|_{L^2(B_i)} \leq C R_i^{\frac{1}{r}} \|E_{\text{sa}} w_{\text{ref}}\|_{L^{2s}(B_i)}. \quad (4.5)$$

Setting $s = p/2$ and using (2.1), we obtain:

$$\|E_{\text{sa}} w_{\text{ref}}\|_{L^2(B_i)} \leq C R_i^{1-\frac{2}{p}} p^{\frac{1}{2}} \|\nabla E_{\text{sa}} w_{\text{ref}}\|_{L^2(\Omega)}. \quad (4.6)$$

Then, it follows for $p = |\ln R_i|$ together with (1.7) and (P2):

$$\sum_{i=1}^N \|f_i\|_{L^2(B_i)} \|E_{\text{sa}} w_{\text{ref}}\|_{L^2(B_i)} \leq C \|\mathcal{F}\|_{L^2(\Omega)} \|\nabla w_{\text{ref}}\|_{L^2(\Omega_p)} \sum_{i=1}^N R_i |\ln R_i|^{\frac{1}{2}}. \quad (4.7)$$

Analogously to (4.5) and (4.6) one can show that:

$$\|\nabla u_f\|_{L^2(B_i)} \leq C R_i^{1-\frac{2}{p}} \|\nabla u_f\|_{L^p(B_i)}.$$

Based on (2.1), (P3) and the H^2 -regularity of u_f , we obtain:

$$\begin{aligned} \|\nabla u_f\|_{L^p(B_i)} &\leq \left(\sum_{i=1}^2 \|\partial_{x_i} E_{\text{st}} u_f\|_{L^p(\hat{\Omega})}^p \right)^{1/p} \leq C p^{\frac{1}{2}} \left(\sum_{i=1}^2 \|\nabla(\partial_{x_i} E_{\text{st}} u_f)\|_{L^2(\hat{\Omega})}^p \right)^{1/p} \\ &\leq C p^{\frac{1}{2}} \|E_{\text{st}} u_f\|_{H^2(\hat{\Omega})} \leq C p^{\frac{1}{2}} \|u_f\|_{H^2(\Omega)} \leq C p^{\frac{1}{2}} \|\mathcal{F}\|_{L^2(\Omega)}. \end{aligned}$$

Choosing $p = |\ln R_i|$ the following estimate for the second summand results in:

$$\sum_{i=1}^N \|\nabla u_f\|_{L^2(B_i)} \|\nabla E_{\text{sa}} w_{\text{ref}}\|_{L^2(B_i)} \leq C \|\mathcal{F}\|_{L^2(\Omega)} \|\nabla w_{\text{ref}}\|_{L^2(\Omega_p)} \sum_{i=1}^N R_i |\ln R_i|^{\frac{1}{2}}. \quad (4.8)$$

Applying Lemma 2.2, (P1) and (P2) to the third summand and considering the H^2 -regularity of u_f together with a standard Sobolev embedding, we have:

$$\sum_{i=1}^N \kappa_i \|u_f\|_{L^2(\partial B_i)} \|w_{\text{ref}}\|_{L^2(\partial B_i)} \leq C \|\mathcal{F}\|_{L^2(\Omega)} \|\nabla w_{\text{ref}}\|_{L^2(\Omega_p)} \sum_{i=1}^N \kappa_i R_i |\ln R_i|^{\frac{1}{2}}. \quad (4.9)$$

The bound for the last summand follows directly from Lemma 2.1 and (P1):

$$2\pi \sum_{i=1}^N U_i \kappa_i R_i \cdot \bar{w}_{\text{ref}}^{(i)} \leq C \|\nabla w_{\text{ref}}\|_{L^2(\Omega_p)} \sum_{i=1}^N U_i \kappa_i R_i |\ln R_i|^{\frac{1}{2}}. \quad (4.10)$$

Summarizing (4.7)–(4.10), we finally have:

$$\|\nabla w_{\text{ref}}\|_{L^2(\Omega_p)} \leq C \left[\|\mathcal{F}\|_{L^2(\Omega)} \sum_{i=1}^N R_i |\ln R_i|^{\frac{1}{2}} (1 + \kappa_i) + \sum_{i=1}^N U_i \kappa_i R_i |\ln R_i|^{\frac{1}{2}} \right]. \quad (4.11)$$

As a next step, we derive a stability estimate for the function w_{int} . In this process, (4.1) is tested with $v = w_{\text{int}} \in H_0^1(\Omega)$. Inserting the decomposition of u_{int} (see (4.4)) into (4.1), it follows that

$$\begin{aligned} \|\nabla w_{\text{int}}\|_{L^2(\Omega)}^2 &\leq (\mathcal{F}, w_{\text{int}})_{\Omega} - (\nabla u_{\text{f}}, \nabla w_{\text{int}})_{\Omega} - \sum_{i=1}^N \kappa_i (u_{\text{f}}, w_{\text{int}})_{L^2(\partial B_i)} \\ &\quad + 2\pi \sum_{i=1}^N U_i \kappa_i R_i \cdot \bar{w}_{\text{int}}^{(i)}. \end{aligned}$$

By means of the techniques which have been used to derive the stability estimate for w_{ref} one can prove that:

$$\|\nabla w_{\text{int}}\|_{L^2(\Omega)} \leq C \left[\|\mathcal{F}\|_{L^2(\Omega)} \sum_{i=1}^N \kappa_i R_i |\ln R_i|^{\frac{1}{2}} + \sum_{i=1}^N U_i \kappa_i R_i |\ln R_i|^{\frac{1}{2}} \right]. \quad (4.12)$$

Based on (4.11) and (4.12) an upper bound for the error component e_1 can be derived:

$$\begin{aligned} \|e_1\|_{H^1(\Omega_p)} &= \|w_{\text{ref}} - w_{\text{int}}\|_{H^1(\Omega_p)} \leq \|w_{\text{ref}}\|_{H^1(\Omega_p)} + \|w_{\text{int}}\|_{H_0^1(\Omega)} \\ &\leq \|E_{\text{sa}} w_{\text{ref}}\|_{H_0^1(\Omega)} + \|w_{\text{int}}\|_{H_0^1(\Omega)} \leq C (\|\nabla w_{\text{ref}}\|_{L^2(\Omega_p)} + \|\nabla w_{\text{int}}\|_{L^2(\Omega)}) \\ &\leq C_1 \left[\|\mathcal{F}\|_{L^2(\Omega)} \sum_{i=1}^N R_i |\ln R_i|^{\frac{1}{2}} (1 + \kappa_i) + \sum_{i=1}^N U_i \kappa_i R_i |\ln R_i|^{\frac{1}{2}} \right]. \end{aligned}$$

4.2. Analysis of the modeling error related to assumption (A2)

Here, we aim to derive an upper bound for e_2 , in terms of the data and the geometrical configuration of the inclusions. By subtracting problem (3.3) from (4.1) and rearranging the terms, we obtain the following equation:

$$(\nabla(u_{\text{int}} - u_{\text{red}}), \nabla v)_{\Omega} + \sum_{i=1}^N \kappa_i (u_{\text{int}} - u_{\text{red}}, v)_{\partial B_i} + \sum_{i=1}^N \kappa_i (u_{\text{red}} - \bar{u}_{\text{red}}^{(i)}, v)_{\partial B_i} = 0,$$

$$\forall v \in H_0^1(\Omega).$$

Recalling that $\tilde{u}_{\text{red}}^{(i)} = u_{\text{red}} - \bar{u}_{\text{red}}^{(i)}$ and choosing $v = e_2 = u_{\text{int}} - u_{\text{red}} \in H_0^1(\Omega)$ it follows:

$$\|\nabla e_2\|_{L^2(\Omega)}^2 \leq \sum_{i=1}^N \kappa_i (-\tilde{u}_{\text{red}}^{(i)}, e_2)_{\partial B_i} \leq \sum_{i=1}^N \kappa_i \|\tilde{u}_{\text{red}}^{(i)}\|_{L^2(\partial B_i)} \|e_2 - \bar{e}_2^{(i)}\|_{L^2(\partial B_i)}.$$

This intermediate result is coherent with assumption (A2), because it shows that if the fluctuations on the interfaces ∂B_i are small, then the modeling error is small too. Now by Eq. (2.2) and the stability estimate in Theorem 3.1, we have:

$$\begin{aligned} \|\nabla e_2\|_{L^2(\Omega)}^2 &\leq \sum_{i=1}^N \kappa_i R_i \|\nabla u_{\text{red}}\|_{L^2(\Omega)} \|\nabla e_2\|_{L^2(\Omega)} \\ &\leq C_2 \left[\|\mathcal{F}\|_{L^2(\Omega)} \sum_{i=1}^N \kappa_i R_i + \sum_{i,j=1}^N \kappa_i \kappa_j R_i R_j |\ln R_j|^{\frac{1}{2}} U_j \right] \|\nabla e_2\|_{L^2(\Omega)}. \end{aligned}$$

By means of Poincaré's inequality, the result reported in inequality (4.2) is proved.

5. Numerical Approximation

In this section, we study the convergence behavior of a standard finite element discretization applied to the variational problem (3.4). Let \mathcal{T}_h be a family of quasi-uniform triangular meshes which partitions the computational domain Ω . By h , we denote the characteristic mesh size of the grid. As a finite element space $V_h \subset H_0^1(\Omega)$ piecewise linear finite elements are considered:

$$V_h = \{v \in C(\bar{\Omega}) \cap H_0^1(\Omega) | v|_T \in \mathbb{P}^1(T), T \in \mathcal{T}_h\},$$

where $\mathbb{P}^1(T)$ is the vector space of first-order polynomials defined on T . Using the notation from Sec. 3, the numerical solution $u_h \in V_h$ has to fulfill the following equation:

$$a(u_{h,\text{red}}, v_h) = L(v_h), \quad \forall v_h \in V_h. \quad (5.1)$$

A first convergence result for this discretization is provided in the next theorem.

Theorem 5.1. *Let $u_{\text{red}} \in H_0^1(\Omega) \cap H^{\frac{3}{2}-\epsilon}(\Omega)$ be the solution of (3.4) and let $u_{h,\text{red}}$ be defined by (5.1). For the discretization error $u_{\text{red}} - u_{h,\text{red}}$, we have the upper bounds*

$$\|u_{\text{red}} - u_{h,\text{red}}\|_{H^1(\Omega)} \leq C_1 h^{\frac{1}{2}-\epsilon} \|u_{\text{red}}\|_{H^{\frac{3}{2}-\epsilon}(\Omega)}$$

and

$$\|u_{\text{red}} - u_{h,\text{red}}\|_{L^2(\Omega)} \leq C_2 h^{\frac{3}{2}-\epsilon} \|u_{\text{red}}\|_{H^{\frac{3}{2}-\epsilon}(\Omega)}$$

for $0 < \epsilon \leq \frac{1}{2}$ and some constants C_1, C_2 independent of h .

Proof. It is obvious that the linear form L and the bilinear form a in (3.5) and (3.6) fulfill all the conditions for Céa's lemma (see proof of Theorem 3.1). Therefore, the H^1 -error can be bounded by an interpolation error:

$$\|u_{\text{red}} - u_{h,\text{red}}\|_{H^1(\Omega)} \leq \sqrt{\frac{C_a}{\alpha}} \|u_{\text{red}} - S_h u_{\text{red}}\|_{H^1(\Omega)}, \quad (5.2)$$

where $S_h : H^1(\Omega) \rightarrow V_h$ is a suitable interpolation operator. C_a and α denote the continuity and ellipticity constant of the bilinear form a . Choosing for S_h the Scott–Zhang operator (Theorem 4.1 in Ref. 34) and considering the regularity result in Theorem 3.1, the first estimate follows. Please note that from the proof of Theorem 3.1 it can be concluded that the constant in (5.2) is bounded, even if R_i tends to zero. Based on the first estimate, the second estimate can be shown by means of an Aubin–Nitsche argument. \square

We note that although the solution is not globally in H^2 , and thus we cannot expect $\mathcal{O}(h)$ convergence in the H^1 -norm, the solution restricted to Ω_p and Ω_f can be expected to be in H^2 . Therefore, we can apply particular techniques to improve the accuracy of the numerical approximation. In this work, we discuss two possibilities to bypass the reduced regularity of the solution by modifying the computational grid. The modification of the grid consists in adapting the grid to the interfaces ∂B_j , $j \in \{1, \dots, N\}$ such that optimal error estimates can be derived. In the literature they are referred to as δ -resolving (see Definition 3.1 in Ref. 24) and graded meshes Sec. 3.1 in Ref. 6. Other ways to handle the lower regularity employ, e.g. appropriate error norms,²⁰ or an appropriate finite element space.¹¹

A grid \mathcal{T}_h is δ -resolving with respect to an interface ∂B_j , if the boundaries of the subgrids corresponding to B_j and $\Omega \setminus B_j$ have a maximal distance of δ to the interface ∂B_j . In this work, we consider a special type of a δ -resolving grid, in which the element edges adjacent to ∂B_j form an interpolating linear spline for this interface (see Fig. 1, top). From standard interpolation theory, it is well known that in this case $\delta = \mathcal{O}(h^2)$ holds. Note that to fulfill this property, \mathcal{T}_h does not have to be refined locally.

Contrary to that, a grid that is graded with respect to ∂B_j exhibits local refinements along ∂B_j , since a graded mesh has the feature that the diameters of the elements are scaled by the distance to the interface, such that the element diameters become smaller the nearer they are located to the interface, (Sec. 2 in Ref. 2), see Fig. 1, bottom. Let us denote the minimum distance of an element T to the interfaces ∂B_j by r_T and the diameter of T by h_T . For the purpose of this work, it is sufficient to consider a particular case of the graded meshes presented in Sec. 3.1 of Ref. 6. For a characteristic mesh size h , we assume that the local element size h_T scales as $\sqrt{r_T}$ and that $h_T \approx h^2$ if T is close to ∂B_i . In other words, let $\delta > 0$ be a fixed coefficient (e.g. $\delta = \frac{1}{2}$), then we assume

$$h_T \approx \begin{cases} h\sqrt{r_T}, & \text{if } r_T > \delta h, \\ h^2, & \text{otherwise.} \end{cases} \quad (5.3)$$

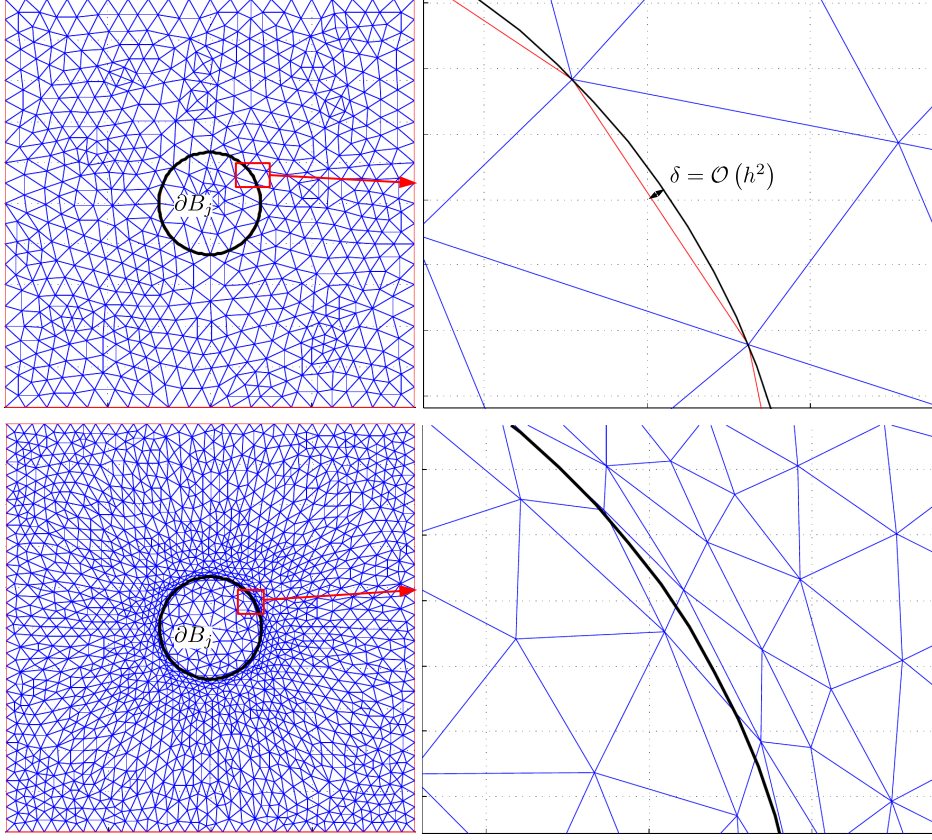


Fig. 1. Adapted meshes for a circular interface ∂B_j : δ -resolving mesh with $\delta = \mathcal{O}(h^2)$ (top), graded mesh (bottom).

In the next theorem, we show that using a δ -resolving or a graded mesh, optimal convergence rates can be recovered, provided that the corresponding solution exhibits some local smoothness.

Theorem 5.2. *Let u be the weak solution of (3.4) such that it holds: $u_{\text{red}} \in H^2(\Omega_s)$, where $\Omega_s = \Omega_p \cup \Omega_f$ (see (1.1)). By \mathcal{T}_h^δ we denote a family of δ -resolving meshes with $\delta = \mathcal{O}(h^2)$ and by \mathcal{T}_h^g we denote a family of graded meshes. Both meshes are adapted to the interfaces ∂B_j , $j \in \{1, \dots, N\}$. The corresponding finite element solutions of (5.1) are $u_{h,\text{red}}^\delta$ and $u_{h,\text{red}}^g$. On these conditions, one can prove for the discretization errors $u_{\text{red}} - u_{h,\text{red}}^k$, $k \in \{\delta, g\}$ the following optimal $H^1(\Omega)$ - and $L^2(\Omega)$ -estimates:*

$$(E1) \quad \|u_{\text{red}} - u_{h,\text{red}}^\delta\|_{H^1(\Omega)} + \frac{1}{h} \|u_{\text{red}} - u_{h,\text{red}}^\delta\|_{L^2(\Omega)} \lesssim h \|u_{\text{red}}\|_{H^2(\Omega_s)},$$

$$(E2) \quad \|u_{\text{red}} - u_{h,\text{red}}^g\|_{H^1(\Omega)} + \frac{1}{h} \|u_{\text{red}} - u_{h,\text{red}}^g\|_{L^2(\Omega)} \lesssim h^{1-\epsilon} \|u_{\text{red}}\|_{H^{\frac{3}{2}-\epsilon}(\Omega)} \\ + h \|u_{\text{red}}\|_{H^2(\Omega_s)},$$

where $0 < \epsilon \leq \frac{1}{2}$.

Proof. As in the proof of the previous theorem, the H^1 -errors for both discretizations can be bounded by an interpolation error. In the case of the δ -resolving mesh, we use a modified Cl ement operator S_{ch} presented in Definition 3.3 of Ref. 24. For this operator, one can prove the following approximation result (see Theorem 3.5 in Ref. 24):

$$\|u_{\text{red}} - S_{ch}u_{\text{red}}\|_{H^1(\Omega)}^2 \lesssim h^2 \|u_{\text{red}}\|_{H^2(\Omega_s)}^2 + \delta \|u_{\text{red}}\|_{H^2(\Omega_s)}^2. \quad (5.4)$$

Then estimate (E1) follows from the assumption $\delta = \mathcal{O}(h^2)$. For a graded mesh \mathcal{T}_h^g , we choose the Scott–Zhang operator S_{zh} from Theorem 4.1 in Ref. 34 and compute:

$$\begin{aligned} \|u_{\text{red}} - S_{zh}u_{\text{red}}\|_{H^1(\Omega)}^2 &= \sum_{T \in \mathcal{T}_h^g} \|u_{\text{red}} - S_{zh}u_{\text{red}}\|_{H^1(T)}^2 \\ &= \sum_{\substack{T \in \mathcal{T}_h^g \\ r_T \leq \delta h}} \|u_{\text{red}} - S_{zh}u_{\text{red}}\|_{H^1(T)}^2 \\ &\quad + \sum_{\substack{T \in \mathcal{T}_h^g \\ r_T > \delta h}} \|u_{\text{red}} - S_{zh}u_{\text{red}}\|_{H^1(T)}^2. \end{aligned}$$

By Theorem 3.1 for the elements of the first summand we have:

$$\|u_{\text{red}} - S_{zh}u_{\text{red}}\|_{H^1(T)}^2 \lesssim h_T^{1-2\epsilon} \|u_{\text{red}}\|_{H^{\frac{3}{2}-\epsilon}(\omega_T)}^2,$$

where ω_T is a patch of elements around T . For $0 < \epsilon \leq \frac{1}{2}$ and using (5.3), we have:

$$\sum_{\substack{T \in \mathcal{T}_h^g \\ r_T \leq \delta h}} \|u_{\text{red}} - S_{zh}u_{\text{red}}\|_{H^1(T)}^2 \lesssim h^{2-4\epsilon} \|u_{\text{red}}\|_{H^{\frac{3}{2}-\epsilon}(\Omega)}^2. \quad (5.5)$$

Using $u_{\text{red}} \in H^2(\Omega_s)$ and the approximation properties of S_{zh} , for the second summand we have:

$$\sum_{\substack{T \in \mathcal{T}_h^g \\ r_T > \delta h}} \|u_{\text{red}} - S_{zh}u_{\text{red}}\|_{H^1(T)}^2 \lesssim h^2 \|u_{\text{red}}\|_{H^2(\Omega_s)}^2. \quad (5.6)$$

Combining (5.5) and (5.6), we obtain the H^1 -estimate. The L^2 -estimates follow from an Aubin–Nitsche argument. \square

While for the 2D-0D problem the use of interface fitting or graded meshes is computational still feasible, the computational effort for the construction of such meshes can drastically increase for real complex 3D-1D structures.^{27,28,30,35} In these cases, the proposed model reduction approach gives the choice between using a uniform mesh and accepting sub-optimal convergence rate or defining a problem fitted mesh. In this case, the 3D-1D approach still features significant advantages with respect to the full 3D discretization of the inclusions. More precisely, the computational cost for solving the problem defined on the inclusion is drastically reduced (especially in the 3D-1D case). Moreover, the proposed scheme does not require

any point by point coherence of the computational meshes of the bulk and the inclusions, ensuring greater flexibility for the construction of the bulk mesh. In particular, this property is a significant advantage if stochastic components in the geometrical layout of the network have to be taken into account. Finally, the apparent analogies of the proposed methodology with the method of Green's functions for the solution of PDEs open the way for the definition of non-polynomial enrichments of the approximation space that would guarantee optimal convergence rates on quasi-uniform meshes.

6. Numerical Experiments

The objective of this section is to support by means of numerical evidence of the theoretical results of Secs. 4 and 5. In the first subsection, we show to what extent the solutions of problem (3.1) and of the simplified model (3.3) differ. The second subsection contains several tests addressing the convergence results in Theorems 5.1 and 5.2.

6.1. Investigation of the modeling error

In this subsection, we analyze numerically the modeling error in (4.2). Let us consider a single source term, that is, we set $N = 1$ in (1.3). We denote with u_{ref} and u_{red} the analytical solutions to problem (3.1) and (3.3), respectively. In the general case, these solutions are not known *a priori*. Therefore, we verify (4.2) using their linear finite element approximations $u_{h,\text{ref}}$ and $u_{h,\text{red}}$, respectively, since the numerical solutions converge to the corresponding analytical solutions as the mesh size goes to zero. We define the reduced problem (3.3) on the domain $\Omega = (-1, 1)^2$, while the full-dimensional problem (3.1) is posed on $\Omega_p = \Omega \setminus B_1$, where the only circular inclusion B_1 is a ball of radius R with center in $(0.3, 0.4)$. In many applications, the radius of the inclusion is the most relevant parameter and with estimate (4.2) we have proved that the error introduced adopting the reduced model tends to zero as the radius of the inclusion becomes smaller. Therefore, in this test, we analyze the influence of the size of the inclusion, that is, we vary its radius R , while keeping the other parameters constant. In order to verify the dependency of the modeling error on the radius R of the inclusion, we take $R \in \{0.1, 0.05, 0.025, 0.0125, 0.00625, 0.003125\}$, while we set $\kappa = U = 1$ constant for all simulations. As the source term, we choose the function

$$\mathcal{F}(x, y) = \sin(9x) + \sin(13y) + x + y, \quad \text{for } (x, y) \in \Omega.$$

According to Theorem 5.1 and standard convergence results, we can bound the modeling error by:

$$\begin{aligned} \|u_{\text{ref}} - u_{\text{red}}\|_{H^1(\Omega_p)} &\leq \|u_{\text{ref}} - u_{h,\text{ref}}\|_{H^1(\Omega_p)} + \|u_{\text{red}} - u_{h,\text{red}}\|_{H^1(\Omega_p)} \\ &\quad + \|u_{h,\text{ref}} - u_{h,\text{red}}\|_{H^1(\Omega_p)} \\ &\lesssim \mathcal{O}(h^{\frac{1}{2}}) + \|u_{h,\text{ref}} - u_{h,\text{red}}\|_{H^1(\Omega_p)}. \end{aligned}$$

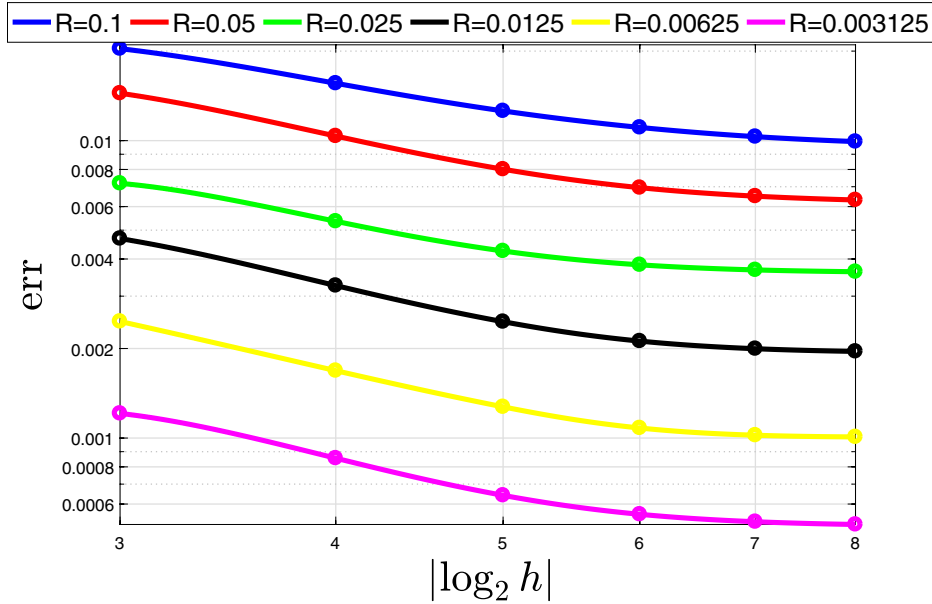


Fig. 2. The numerical modeling error is calculated for different values of the mesh characteristic size ($h = 2^{-i}$ for $i = 3, \dots, 8$) and for different radii of the ball B_1 (each line shown with different colors). For each radius the modeling error values are interpolated using splines. We observe that as the mesh size h tends to zero, the error converges to a fixed value, which is the actual modeling error.

As the mesh size h tends to zero, we may assume that the modeling error between numerical solutions converges to the actual modeling error, as Fig. 2 suggests. As an error measure, we employ the numerical modeling error defined by:

$$\text{err} = \|u_{h,\text{ref}} - u_{h,\text{red}}\|_{H^1(\Omega_p)}.$$

Furthermore, we define an error functional to show the experimental order of convergence by

$$\text{Rate} = \frac{\log(\text{err}(R_1)/\text{err}(R_2))}{\log(R_1/R_2)},$$

where $\text{err}(R)$ is the numerical modeling error for the radius R . In Table 1, the modeling error, computed at the finest level of the δ -resolving mesh, is provided for different radii together with the rate of convergence with respect to the radius R of the inclusion. We observe that the modeling error decays quasi-linearly as R , which is in good agreement with our estimate (4.2).

6.2. Convergence tests

The objective of this section is to illustrate the convergence results of Theorems 5.1 and 5.2 by means of numerical experiments based on test cases where the analytical solution is explicitly available. For our first convergence test, we consider a single source term, i.e. we set in (1.3) $N = 1$. The ball B_1 has the radius $R = 0.25$ and the center $x_1 = (0, 0)$. As a computational domain, we choose the square:

Table 1. The numerical modeling error is shown for different radii and $\kappa = U = 1$. The convergence rate is reported in the last column.

R	err	Rate
0.1	$9.92770e - 03$	/
0.05	$6.31752e - 03$	0.65
0.025	$3.62451e - 03$	0.80
0.0125	$1.95587e - 03$	0.89
0.00625	$1.00884e - 03$	0.96
0.003125	$5.12174e - 04$	0.98

$\Omega = (-1, 1)^2 \subset \mathbb{R}^2$. The remaining parameters of the problem are given by $\kappa_1 = 0.1$ and $U_1 = 1$. Setting $\mathcal{F} \equiv 0$ and appropriate Dirichlet boundary conditions, the exact solution of this problem is given by⁸:

$$u_{e,1}(x) = \begin{cases} U_1 \frac{\kappa_1}{1 + \kappa_1} \left(1 - R \ln \left(\frac{r}{R}(x) \right) \right), & r(x) > R, \\ U_1 \frac{\kappa_1}{1 + \kappa_1}, & r(x) \leq R, \end{cases}$$

where $r(x)$ is the Euclidean distance from an arbitrary point $x \in \Omega$ to the center of the ball B_1 :

$$r(x) = \|x - x_1\|_2. \quad (6.1)$$

The numerical solution $u_{h,1}$ is defined by (5.1), and the numerical discretization error $e_{h,1}$ is given as follows: $e_{h,1} = u_{e,1} - u_{h,1}$. For the triangulation of Ω three different types of meshes are used: A uniform mesh, a δ -resolving mesh with $\delta = \mathcal{O}(h^2)$ and a graded mesh, defined by (5.3). The second refinement levels of these grid types are depicted in Fig. 3. Tables 2 and 3 show the discretization errors $e_{h,1}$ with respect to the L^2 - and the H^1 -norm. Considering the convergence rates in both tables it can be seen that the theoretical convergence results in Theorems 5.1 and 5.2 are confirmed, since it holds $u_{e,1} \in H^2(\Omega_s)$.

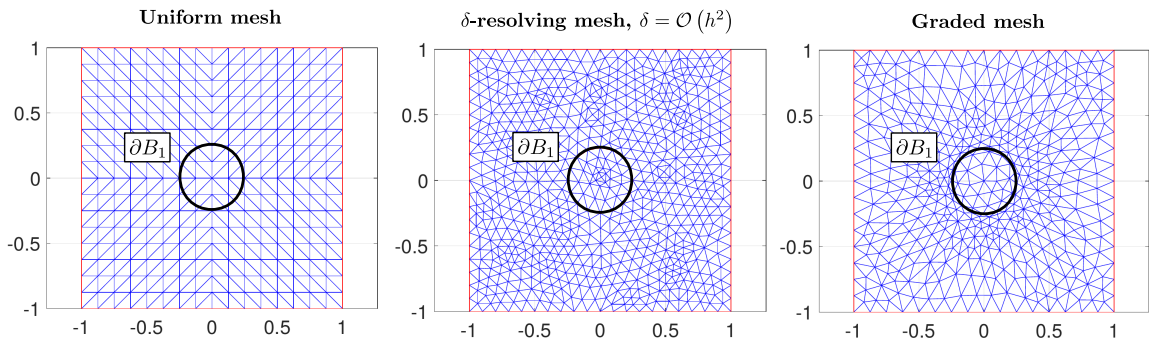


Fig. 3. Three different types of meshes are used for the first convergence test (single point source term). left: Uniform mesh (521 elements), middle: δ -resolving mesh, $\delta = \mathcal{O}(h^2)$ (1368 elements), right: Graded mesh (870 elements).

Table 2. L^2 -norms of $e_{h,1}$ and convergence rates for three different meshes (uniform, δ -resolving, graded). In the last line of the table the theoretical convergence rates are listed.

Level	Uniform mesh	Rate	δ -resolving mesh	Rate	Graded mesh	Rate
1	$8.506954e - 03$	/	$8.844852e - 04$	/	$1.154294e - 03$	/
2	$2.717929e - 03$	1.65	$2.272761e - 04$	1.96	$2.517585e - 04$	2.20
3	$8.675497e - 04$	1.65	$4.925913e - 05$	2.21	$7.779338e - 05$	1.69
4	$3.011329e - 04$	1.53	$1.452474e - 05$	1.76	$2.061325e - 05$	1.92
5	$1.041544e - 04$	1.53	$3.649972e - 06$	1.99	$4.491752e - 05$	2.20
	expected	1.50	expected	2.00	expected	2.00

 Table 3. H^1 -norms of $e_{h,1}$ and convergence rates for three different meshes (uniform, δ -resolving, graded). In the last line of the table the theoretical convergence rates are listed.

Level	Uniform mesh	Rate	δ -resolving mesh	Rate	Graded mesh	Rate
1	$6.074554e - 02$	/	$2.463609e - 02$	/	$2.826352e - 02$	/
2	$3.995154e - 02$	0.60	$1.132668e - 02$	1.12	$1.482623e - 02$	0.93
3	$2.995280e - 02$	0.42	$5.583932e - 03$	1.02	$9.268436e - 03$	0.68
4	$2.047021e - 02$	0.55	$2.772943e - 03$	1.01	$4.954802e - 03$	0.90
5	$1.460174e - 02$	0.49	$1.381250e - 03$	1.01	$2.162039e - 03$	1.20
	expected	0.50	expected	1.00	expected	1.00

As a next step we want to study problem (1.3) with several circular inclusions B_i for $i = 1, \dots, N$ ($N > 1$). For this purpose, a new analytical solution $u_{e,2}$ is determined. Analogously to (6.1), the distance between the centers of the balls x_i and an arbitrary point $x \in \Omega$ is given by $r_i(x) = \|x - x_i\|_2$, $i \in \{1, \dots, N\}$. Using this notation we define the solution $u_{e,2}$ as a linear combination:

$$u_{e,2}(x) = \begin{cases} \sum_{i=1}^N \alpha_i \left(1 - R_i \log \frac{r_i}{R_i} \right), & x \notin \bigcup_{i=1}^N B_i, \\ G_i(x), & x \in B_i, \end{cases}$$

where $\alpha_i \in \mathbb{R}$ and $G_i(x)$ is a harmonic function in B_i . Then it holds:

$$-\Delta u_{e,2} = \sum_{i=1}^N \alpha_i \delta_{\partial B_i}. \quad (6.2)$$

A comparison of the right-hand sides in (6.2) and (1.3) yields the following equations for the coefficients α_i :

$$\alpha_i = \kappa_i (U_i - \bar{u}_{e,2}^{(i)}), \quad i \in \{1, \dots, N\}.$$

In order to compute the average $\bar{u}_{e,2}^{(i)}$, we use the fact that the functions

$$u_j = 1 - R_j \log \frac{r_j}{R_j}, \quad j \in \{1, \dots, N\} \setminus \{i\}$$

are harmonic in B_i . By the mean-value formula for harmonic functions (see Chap. 2.2, Theorem 2 in Ref. 9), we have:

$$\bar{u}_j^{(i)} = 1 - R_j \log \frac{r_{ij}}{R_j}, \quad r_{ij} = \|x_j - x_i\|_2, \quad i \neq j,$$

resulting in the following expression for $\bar{u}_{e,2}^{(i)}$:

$$\bar{u}_{e,2}^{(i)} = \alpha_i + \sum_{j \neq i} \alpha_j \bar{u}_j^{(i)}.$$

Now, the coefficient vector $\alpha = (\alpha_1, \dots, \alpha_N)^T$ can be determined by a system of equations:

$$A \cdot \alpha = b,$$

where the matrix $A \in \mathbb{R}^{N \times N}$ and the right-hand side $b \in \mathbb{R}^N$ are given by:

$$A_{ij} = (1 + \kappa_i) \delta_{ij} + \kappa_i \bar{u}_j^{(i)} (1 - \delta_{ij}) \quad \text{and} \quad b_i = \kappa_i U_i, \quad i, j \in \{1, \dots, N\}.$$

It remains to determine the functions G_i on B_i . An appropriate expression for these functions is given by the following linear combination:

$$G_i = \alpha_i + \sum_{j \neq i} \alpha_j \left(1 - R_j \log \frac{r_j}{R_j} \right),$$

since these functions are harmonic and represent a continuous extension of $u_{e,2}|_{\Omega \setminus \bigcup_{i=1}^N B_i}$.

For the numerical simulations, we again consider $\Omega = (-1, 1)^2$ and five source terms ($N = 5$, Fig. 4). As in the case $N = 1$ the boundary conditions are adjusted such that $u_{e,2}$ is the exact solution of problem (1.3). Table 4 contains the remaining parameters used for the numerical simulations. The discretization errors in the L^2 - and the H^1 -norm summarized in Table 5 are based on a uniform triangulation of Ω (see e.g. Fig. 3, left). We observe that the discretization scheme converges as predicted by Theorem 5.1.

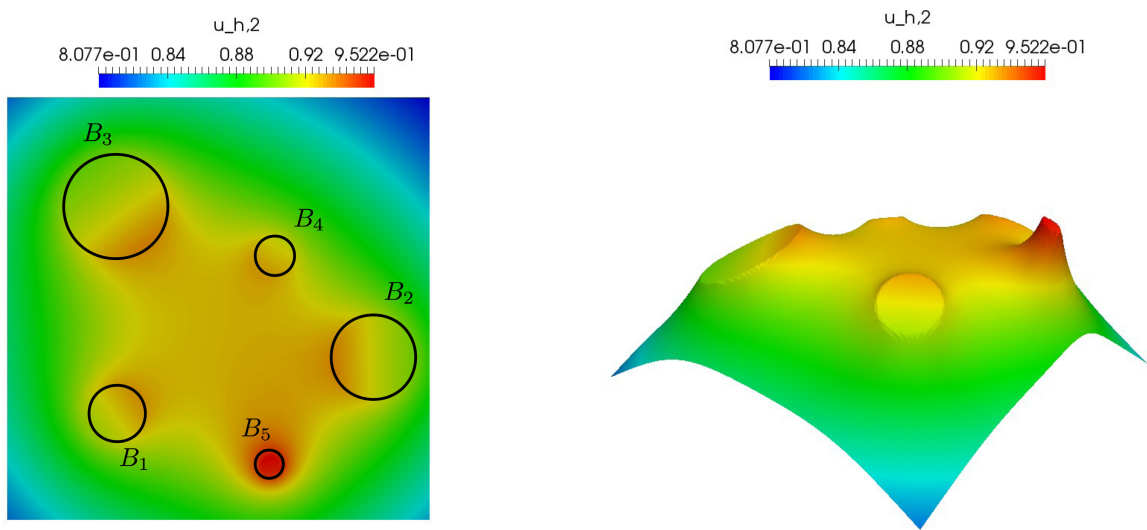


Fig. 4. (Color online) Location of the balls B_1, \dots, B_5 in the computational domain $\Omega = (-1, 1)^2$ (left), Three-dimensional graph of the numerical solution $u_{h,2}$ based on the parameters in Table 4 (right).

Table 4. Parameter set used for problem (1.3) with $N = 5$ source terms.

	x_i	R_i	U_i	κ_i
B_1	$(-0.50, 0.50)$	0.15	2.30	0.12
B_2	$(0.75, -0.25)$	0.20	2.50	0.10
B_3	$(-0.50, 0.50)$	0.25	2.80	0.09
B_4	$(0.25, 0.25)$	0.10	2.50	0.08
B_5	$(0.25, -0.75)$	0.05	3.00	0.25

 Table 5. L^2 - and H^1 -norms and of $e_{h,2}$. In the last line of the table the theoretical convergence rates are listed.

Level	L^2 -error	Rate	H^1 -error	Rate
1	$2.669615e - 02$	/	$1.884496e - 01$	/
2	$8.892418e - 03$	1.59	$1.749503e - 01$	0.11
3	$3.855905e - 03$	1.21	$1.177106e - 01$	0.57
4	$1.279445e - 03$	1.59	$8.816140e - 02$	0.42
5	$4.521436e - 04$	1.50	$6.029469e - 02$	0.55
6	$1.537090e - 04$	1.56	$4.283918e - 02$	0.50
	expected	1.50	expected	0.50

7. A 3D Problem Coupled with 1D Inclusions with Application to Microcirculation

We present a prototype model for stationary flow in a permeable biological tissue perfused by a network of capillaries. Although flow in the capillary network is better described by a mixed type model addressing velocity and pressure simultaneously and transport of chemical species is often unsteady, we consider here steady coupled elliptic problems. The domain Ω where the model is composed of two parts, Ω_p and Ω_f , denoting the interstitial volume and the capillaries, respectively. We assume that the capillaries can be described as cylindrical vessels and Λ denotes their center line. We decompose the network Λ into individual branches Λ_i . Branches are parametrized by the arc length s_i ; a tangent unit vector $\boldsymbol{\lambda}_i$ is also defined over each branch, determining in this way an arbitrary branch orientation. The capillary radius R_i , is for simplicity considered to be constant along each branch of the network. In particular, the domain Ω_f can be split into cylindrical branches Ω_i defined as follows:

$$\Omega_i = \{\mathbf{x} \in \mathbb{R}^3; \mathbf{x} = \mathbf{s} + \mathbf{r}\}, \quad \mathbf{s} \in \Lambda_i = \mathcal{M}_i(\Lambda' \subset \mathbb{R}^1),$$

$$\mathbf{r} \in \mathcal{D}_{\Lambda_i}(R_i) = \{r\mathbf{n}_{\Lambda_i}; r \in (0, R_i)\},$$

where \mathcal{M}_i is a mapping from a reference domain Λ' to the manifold $\Lambda_i \subset \mathbb{R}^3$ and \mathbf{n}_{Λ_i} denotes a unit normal vector with respect to Λ_i . We denote with Γ_i the lateral

surface of Ω_i . Using this notation, problem (1.2) becomes,

$$\begin{cases} -\Delta u_p = 0 & \text{in } \Omega_p, \\ -\Delta u_f = 0 & \text{in } \Omega_f, \\ -\nabla u_p \cdot \mathbf{n}_p = \kappa_i(u_p - u_f) & \text{on } \Gamma_i, \\ -\nabla u_f \cdot \mathbf{n}_f = \kappa_i(u_f - u_p) & \text{on } \Gamma_i, \\ u_p = 0 & \text{on } \partial\Omega_p \setminus \bigcup_{i=1}^N \Gamma_i, \\ u_f = g & \text{on } \partial\Omega_f \setminus \bigcup_{i=1}^N \Gamma_i, \end{cases}$$

where g denotes a Dirichlet boundary condition imposed at the endpoints of the network. The problem in Ω_f is a prototype of flow or mass transport problem in a network of cylindrical channels, surrounded by the domain Ω_p where another flow and transport problem is defined. It is assumed that the interface between these regions is permeable, namely it is crossed by a normal flux proportional to $\kappa_i(u_p - u_f)$.

Applying the model reduction technique presented in Sec. 3, the equations defined on the network of inclusions Ω_f can be restricted to the one-dimensional network Λ . Differentiation over the branches is defined using the tangent unit vector as $\partial_{s_i} w = \nabla w \cdot \boldsymbol{\lambda}_i$ on Λ_i , i.e. ∂_{s_i} represents the projection of ∇ along $\boldsymbol{\lambda}_i$. As a result, the 3D-1D counterpart of problem (3.4) becomes

$$\begin{cases} a(u, v) + b_\Lambda(\bar{u}, \bar{v}) = b_\Lambda(U, \bar{v}) & \forall v \in H_0^1(\Omega), \\ A(U, V) + b_\Lambda(U, V) = b_\Lambda(\bar{u}, V) + \mathcal{F}(V) & \forall V \in H_0^1(\Lambda), \end{cases} \quad (7.1)$$

where $U, V \in H_0^1(\Lambda)$ denote trial and test functions relative to the reduced problem, with the following bilinear forms:

$$a(w, v) = (\nabla w, \nabla v)_\Omega, \quad A(w, v) = \sum_{i=1}^N (\partial_{s_i} w, \partial_{s_i} v)_{\Lambda_i}, \quad b_\Lambda(w, v) = \sum_{i=1}^N \kappa_i(w, v)_{\Lambda_i}.$$

The right-hand side $\mathcal{F}(V)$ takes into account the boundary conditions on the network endpoints, after applying a suitable lifting. A central role in Eq. (7.1) is played by the restriction operator $\bar{(\cdot)}$ that is defined as:

$$\bar{w}^{(i)}(\mathbf{s}) = \frac{1}{2\pi R_i} \int_0^{2\pi} w(\Lambda_i(\mathbf{s}) + R_i \mathbf{n}_{\Lambda_i}(\mathbf{s}, \theta)) R_i d\theta.$$

The vector $\mathbf{n}_{\Lambda_i}(\mathbf{s}, \theta)$ indicates a normal vector perpendicular to $\boldsymbol{\lambda}_i(\mathbf{s})$ and depending on an angle θ , such that the set $\{\mathbf{n}_{\Lambda_i}(\mathbf{s}, \theta) \mid \theta \in [0, 2\pi)\}$ describes a unit circle around $\Lambda_i(\mathbf{s})$ and perpendicular to $\boldsymbol{\lambda}_i(\mathbf{s})$. Taking these definitions into account, it becomes obvious that $\bar{w}^{(i)}$ represents an average value of w with respect to a circle of radius R_i around $\Lambda_i(\mathbf{s})$ and perpendicular to $\boldsymbol{\lambda}_i(\mathbf{s})$.

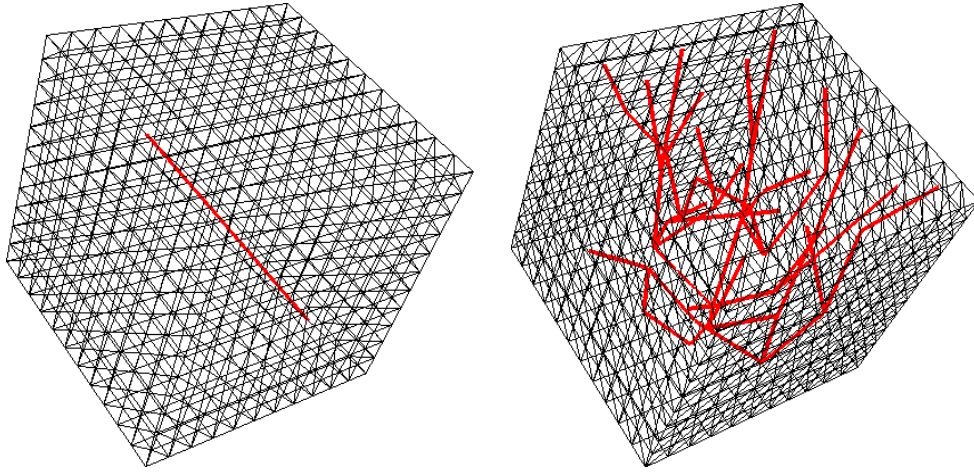


Fig. 5. Visualization of the domains Ω and Λ used in the idealized simulations of microcirculation. The computational mesh of Ω is also shown. We consider two distinct test cases: on the left the network consist of one single segment; on the right the network is a graph with 22 branches.

We solve problem (7.1) in the two test cases shown in Fig. 5. In all cases, we enforce the value $u_f = g = 1$ at the inflow (a single point on one face of the cube) and $u_f = g = 0$ at one or several outflow points (that are visible on the opposite face of the cube in Fig. 5).

The results of the simulations are depicted in Fig. 6 in the left and right panels, respectively. The test case of the single segment confirms the expected behavior of the model. The field u diffuses radially from the line source. The effect of the variation of U on the line source is also visible. The second test case shows the ability of the method and of the corresponding finite element solver to handle more complex configurations. In this case, the network consists of a unit cube $\Omega = (0, 1)^3$ that embeds an idealized branching network of 22 branches, visualized in red. For simplicity, the capillary radius and the parameter κ are kept constant for each

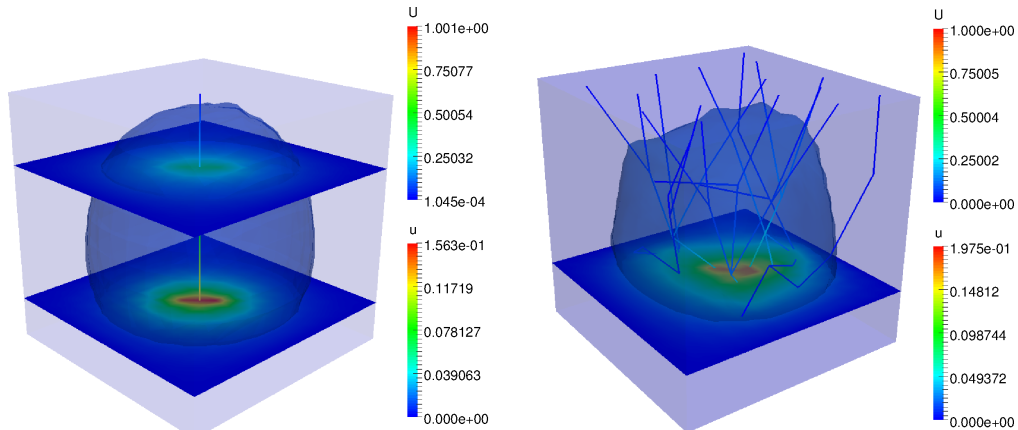


Fig. 6. (Color online) Visualization of the numerical solutions U on Λ and u on Ω of problem (7.1) for the test cases of Fig. 5. The contour plots correspond to the solution values $u = 0.02$ (left) and $u = 0.01$ (right).

branch and set to $R = 0.01$ and $\kappa = 0.1$. As a result, the solution u_f is expected to vary along Λ as shown in Fig. 6. The solution in Ω behaves correspondingly, as the solution of a Poisson equation with a constant concentrated source distributed on Λ .

8. Conclusion

Thanks to some emerging applications, such as the simulation of complex microvascular networks^{3,4,12,27,28} or the computational study of plant roots,³² the numerical approximation of problems governed by partial differential equations featuring small active inclusions, i.e. inclusions that actively interact with the surrounding environment, has recently attracted the attention of researchers in applied mathematics.^{5–7,20} From the mathematical point of view, the problem consists of coupling partial differential equations on embedded manifolds with a dimensionality gap. The analysis and approximation of such problems is not completely established yet.

We believe that this work contains some significant contributions in this specific area. More precisely, we have proposed a new problem formulation, different from the one previously introduced by D’Angelo,^{5–7} that features the following advantages: (i) the new problem formulation naturally arises from the full three-dimensional description of the problem with inclusions, upon application of well defined model reduction hypotheses; (ii) it allows us to analyze the existence of solutions in the framework of Lax–Milgram Lemma; (iii) owing to (i), it is possible to provide upper bounds for the modeling error related to the model reduction strategy and to explicitly characterize the dependence of the model error from the parameters of the problem, such as the size of the inclusions; (iv) it allows us to study the approximation properties of the finite element method exploiting the classical Céa’s approach. Combining this result with non-standard interpolation properties of functions with low regularity, we were able to prove error estimates for the proposed method in the case of uniform, δ -resolving and graded meshes. The extension of this approach to more advanced models, such as problems in mixed form²⁹ or time-dependent problems is under investigation and will be presented in forthcoming studies.

Acknowledgment

This work was partially supported by the Cluster of Excellence in Simulation Technology (EXC 310/2), by the DFG Grant (WO/671 11-1) and by the (Italian) National Group for Scientific Computing, INDAM-GNCS.

References

1. F. Andreu, J. Mazón and J. Rossi, The best constant for the sobolev trace embedding from $W^{1,1}(\Omega)$ into $L^1(\partial\Omega)$, *Nonlinear Anal.: Theory, Methods Appl.* **59** (2004) 1125–1145.

2. T. Apel, O. Benedix, D. Sirch and B. Vexler, *A priori* mesh grading for an elliptic problem with dirac right-hand side, *SIAM J. Numer. Anal.* **49** (2011) 992–1005.
3. L. Cattaneo and P. Zunino, A computational model of drug delivery through micro-circulation to compare different tumor treatments, *Int. J. Numer. Methods Biomed. Eng.* **30** (2014) 1347–1371.
4. L. Cattaneo and P. Zunino, Computational models for fluid exchange between micro-circulation and tissue interstitium, *Netw. Heterog. Media* **9** (2014) 135–159.
5. C. D’Angelo, Multi scale modelling of metabolism and transport phenomena in living tissues, PhD Thesis. EPFL, Lausanne (2007).
6. C. D’Angelo, Finite element approximation of elliptic problems with dirac measure terms in weighted spaces: Applications to one-and three-dimensional coupled problems, *SIAM J. Numer. Anal.* **50** (2012) 194–215.
7. C. D’Angelo and A. Quarteroni, On the coupling of 1d and 3d diffusion-reaction equations: Application to tissue perfusion problems, *Math. Models Methods Appl. Sci.* **18** (2008) 1481–1504.
8. B. Engquist, A. Tornberg and R. Tsai, Discretization of dirac delta functions in level set methods, *J. Comput. Phys.* **207** (2005) 28–51.
9. L. Evans, *Partial Differential Equations*, Graduate Studies in Mathematics, Vol. 19 (American Mathematical Society, 1998).
10. L. Formaggia, A. Fumagalli, A. Scotti and P. Ruffo, A reduced model for darcy’s problem in networks of fractures, *ESAIM: Math. Model. Numer. Anal.* **48** (2014) 1089–1116.
11. S. Frei and T. Richter, A locally modified parametric finite element method for interface problems, *SIAM J. Numer. Anal.* **52** (2014) 2315–2334.
12. H. Frieboes, M. Wu, J. Lowengrub, P. Decuzzi and V. Cristini, A computational model for predicting nanoparticle accumulation in tumor vasculature, *PLoS ONE* **8** (2013) e56876.
13. D. Gilbarg and N. Trudinger, *Elliptic Partial Differential Equations of Second Order*, Springer Science & Business Media, Vol. 224 (Springer, 2001).
14. V. Girault, K. Kumar and M. F. Wheeler, Convergence of iterative coupling of geomechanics with flow in a fractured poroelastic medium, *Comput. Geosci.* **20** (2016) 997–1011.
15. W. Gong, G. Wang and N. Yan, Approximations of elliptic optimal control problems with controls acting on a lower dimensional manifold, *SIAM J. Control Optim.* **52** (2014) 2008–2035.
16. C. Horgan, Eigenvalue estimates and the trace theorem, *J. Math. Anal. Appl.* **69** (1979) 231–242.
17. J. Jaffré and J. Roberts, Modeling flow in porous media with fractures; discrete fracture models with matrix-fracture exchange, *Numer. Anal. Appl.* **5** (2012) 162–167.
18. T. Köppl, R. Helmig and B. Wohlmuth, A multi-scale model for mass transport in arteries and tissue, *Lect. Notes Comput. Sci. Eng.* **105** (2015) 197–213.
19. T. Köppl, E. Vidotto and B. Wohlmuth, A local error estimate for the poisson equation with a line source term, in *Numerical Mathematics and Advanced Applications ENUMATH 2015* (Springer, 2016), pp. 421–429.
20. T. Köppl and B. Wohlmuth, Optimal *a priori* error estimates for an elliptic problem with dirac right-hand side, *SIAM J. Numer. Anal.* **52** (2014) 1753–1769.
21. T. Köppl, B. Wohlmuth and R. Helmig, Reduced one-dimensional modeling and numerical simulation for mass transport in fluids, *Int. J. Numer. Methods Fluids* **72** (2013) 135–156.

22. M. Kuchta, M. Nordaas, J. Verschaeve, M. Mortensen and K. Mardal, Preconditioners for saddle point systems with trace constraints coupling 2d and 1d domains, *SIAM J. Sci. Comput.* **38** (2016) B962–B987.
23. J. Kuttler and V. Sigillito, An inequality for a stekloff eigenvalue by the method of defect, *Proc. Amer. Math. Soc.* **20** (1969) 357–360.
24. J. Li, J. Melenk, B. Wohlmuth and J. Zou, Optimal *a priori* estimates for higher order finite elements for elliptic interface problems, *Appl. Numer. Math.* **60** (2010) 19–37.
25. P. Macklin, S. McDougall, A. Anderson, M. Chaplain, V. Cristini and J. Lowengrub, Multiscale modeling and nonlinear simulation of vascular tumour growth, *J. Math. Biol.* **58** (2009) 765–798.
26. V. Martin, J. Jaffré and J. Roberts, Modeling fractures and barriers as interfaces for flow in porous media, *SIAM J. Sci. Comput.* **26** (2005) 1667–1691.
27. M. Nabil, P. Decuzzi and P. Zunino, Modeling mass and heat transfer in nano-based cancer hyperthermia, *Roy. Soc. Open Sci.* **2** (2015) 150447.
28. M. Nabil and P. Zunino, A computational study of cancer hyperthermia based on vascular magnetic nanoconstructs, *Roy. Soc. Open Sci.* **3** (2016) 160287.
29. D. Notaro, L. Cattaneo, L. Formaggia, A. Scotti and P. Zunino, *A Mixed Finite Element Method for Modeling the Fluid Exchange Between Microcirculation and Tissue Interstitium* (Springer International Publishing, 2016), pp. 3–25.
30. J. Reichold, M. Stampanoni, A. L. Keller, A. Buck, P. Jenny and B. Weber, Vascular graph model to simulate the cerebral blood flow in realistic vascular networks, *J. Cerebral Blood Flow Metabol.* **29** (2009) 1429–1443.
31. S. Sauter and R. Warnke, Extension operators and approximation on domains containing small geometric details, *East West J. Numer. Math.* **7** (1999) 61–77.
32. N. Schröder, M. Javaux, J. Vanderborght, B. Steffen and H. Vereecken, Effect of root water and solute uptake on apparent soil dispersivity: A simulation study, *Vadose Zone J.* **11** (2012).
33. N. Schwenck, B. Flemisch, R. Helmig and B. Wohlmuth, Dimensionally reduced flow models in fractured porous media: Crossings and boundaries, *Comput. Geosci.* **19** (2015) 1219–1230.
34. L. Scott and S. Zhang, Finite element interpolation of nonsmooth functions satisfying boundary conditions, *Math. Comput.* **54** (1990) 483–493.
35. T. Secomb, R. Hsu, N. B. Beamer and B. M. Coull, Theoretical simulation of oxygen transport to brain by networks of microvessels: Effects of oxygen supply and demand on tissue hypoxia, *Microcirculation* **7** (2000) 237–247.
36. T. Secomb, R. Hsu, E. Park and M. Dewhirst, Green’s function methods for analysis of oxygen delivery to tissue by microvascular networks, *Ann. Biomed. Eng.* **32** (2004) 1519–1529.
37. O. Steinbach, *Numerical Approximation Methods for Elliptic Boundary Value Problems: Finite and Boundary Elements*, Springer Science & Business Media (Springer, 2007).
38. K. H. Støverud, M. Darcis, R. Helmig and S. M. Hassanizadeh, Modeling concentration distribution and deformation during convection-enhanced drug delivery into brain tissue, *Transp. Porous Media* **92** (2012) 119–143.
39. V. Thomée, *Galerkin Finite Element Methods for Parabolic Problems*, 2nd edn. (Springer, 2006).

Erratum: Mathematical modeling, analysis and numerical approximation of second-order elliptic problems with inclusions

Bibliographic note: T. Köppl, E. Vidotto, B. Wohlmuth and Paolo Zunino (2018): Mathematical modeling, analysis and numerical approximation of second-order elliptic problems with inclusions. *Mathematical Models and Methods in Applied Sciences* 28(05), pages: 953-978, with courtesy of World Scientific.

There is an error in the L^2 -estimate of Theorem 5.1: Instead of

$$\|u_{\text{red}} - u_{h,\text{red}}\|_{L^2(\Omega)} \leq C_2 h^{\frac{3}{2}-\epsilon} \|u_{\text{red}}\|_{H^{\frac{3}{2}-\epsilon}(\Omega)}$$

the correct L^2 -estimate should read as follows:

$$\|u_{\text{red}} - u_{h,\text{red}}\|_{L^2(\Omega)} \leq C_2 h^{1-\epsilon} \|u_{\text{red}}\|_{H^{\frac{3}{2}-\epsilon}(\Omega)}$$

I want to thank Prof. Dr. Paolo Zunino (MOX, Politecnico Milan) for bringing this error to my attention.

7 Hybrid models for simulating blood flow in microvascular networks

Bibliographic note: The content of this chapter is based on the following original article: E. Vidotto, T. Koch, T. Köppl, R. Helmig and B. Wohlmuth (2019). Hybrid models for simulating blood flow in microvascular networks. *Multiscale Modeling & Simulation*, 17(3), 1076-1102, with courtesy of SIAM.

HYBRID MODELS FOR SIMULATING BLOOD FLOW IN MICROVASCULAR NETWORKS*

ETTORE VIDOTTO[†], TIMO KOCH[‡], TOBIAS KÖPPL[†], RAINER HELMIG[‡], AND
BARBARA WOHLMUTH[†]

Abstract. In this paper, we are concerned with the simulation of blood flow in microvascular networks and the surrounding tissue. To reduce the computational complexity of this issue, the network structures are modeled by a one-dimensional graph, whose location in space is determined by the centerlines of the three-dimensional vessels. The surrounding tissue is considered as a homogeneous porous medium. Darcy’s equation is used to simulate flow in the extra-vascular space, where the mass exchange with the blood vessels is accounted for by means of line source terms. However, this model reduction approach still causes high computational costs, particularly when larger parts of an organ have to be simulated. This observation motivates the consideration of a further model reduction step. Thereby, we homogenize the fine scale structures of the microvascular networks resulting in a new hybrid approach modeling the fine scale structures as a heterogeneous porous medium and the flow in the larger vessels by one-dimensional flow equations. Both modeling approaches are compared with respect to mass fluxes and averaged pressures. The simulations have been performed on a microvascular network that has been extracted from the cortex of a rat brain.

Key words. microcirculation, homogenization, mixed-dimension models, multiscale models, hybrid models

AMS subject classifications. 76S05, 76Z05, 92C10, 92B99

DOI. 10.1137/18M1228712

1. Introduction. Modeling of blood flow and transport at the level of microcirculation is an interesting subfield in biomedical engineering. A reliable computational model for the microcirculation of the human body would enable physicians and pharmacists to obtain better insight into the oxygen supply of cells, the waste removal from the interstitial space [21], and further important biological processes without the need to perform expensive and risky experiments [5, 7, 36]. In addition, such models open up the possibility of studying the impact of diseases like Alzheimer’s [23] and to improve medicines and therapies for cancer treatment [6, 22, 29, 30]. Well-known therapies for cancer treatment are, e.g., hyperthermia [33, 48] and the injection of therapeutic agents preventing the vascularization of cancer tissue [44]. In order to increase the efficiency of the mentioned cancer therapies, it is crucial to focus the therapeutic agents or the heat on the cancerous part of an affected organ while maintaining the rest of the tissue. In order to be able to simulate the distribution of heat and the concentration of therapeutic agents with an adequate accuracy, the hierarchical structure of the vascular system supplying the considered organ has to be taken into account.

However, even for vascular systems contained in small volumes covering just a few cubic millimeters, it is a challenging task to simulate flow in the microvascular

*Received by the editors November 26, 2018; accepted for publication (in revised form) July 19, 2019; published electronically DATE.

<https://doi.org/10.1137/18M1228712>

Funding: This work was partially supported by the Cluster of Excellence in Simulation Technology (EXC 310/2) and the DFG grant (WO/671 11-1).

[†]Lehrstuhl für Numerische Mathematik, Technical University of Munich, 85748 Garching, Germany (ettore.vidotto@ma.tum.de, koeppl@ma.tum.de, wohlmuth@ma.tum.de).

[‡]Department of Hydromechanics and Modelling of Hydrosystems, University of Stuttgart, 70569 Stuttgart, Germany (timo.koch@iws.uni-stuttgart.de, rainer.helmig@iws.uni-stuttgart.de).

networks and the interstitial space, since the flow in a complex network structure consisting of thousands of vessels [17, Chap. 1] is coupled with the flow in the surrounding tissue matrix [11, 38].

As a consequence, several model reduction techniques have been developed for simulating flow through an entire organ or parts of an organ. A widespread technique in this field is homogenization. Thereby, brain tissue and the vascular system are considered as two different continua modeled as porous media [12, 32, 41, 42], and the pressure and velocity field are computed by means of Darcy's equation [20, 24]. Using this approach, the computational effort and the data volume are significantly reduced. On the other hand, both the pressure and the velocity field can only be described in an averaged sense, neglecting the exact structure of the vascular system. As a result, the distribution of therapeutic agents or heat might not be computed with sufficient accuracy. A further challenge is to determine suitable permeability tensors for the Darcy equation reflecting the structure of the vascular trees in an averaged way. Thereby, brain tissue and the vascular system are considered as two different continua modeled as porous media [12, 32, 41, 42], and the pressure and velocity field are computed by means of Darcy's equation [20, 24, 46, 32].

Another way to decrease the computational complexity is to describe the vascular networks by means of one-dimensional (1D) flow models [9, 47, 30, 16, 39, 19], while the surrounding tissue is considered as a three-dimensional (3D) porous medium. By this, an expensive meshing of a 3D blood vessel system is avoided, and at the same time the hierarchical structure of the vascular system is maintained. However, elaborate concepts for coupling 1D flow equations with a flow equation (Darcy equation) for a 3D flow problem [8, 25, 26] have to be developed. This is done by constructing suitable source terms for both the Darcy equation in 3D and the 1D flow problems. On closer examination, one notes that the source term in 3D consists of Dirac measures concentrated on the centerline of the vessels or the corresponding vessel walls, inducing a certain roughness into the solution of the 3D Darcy equation. Due to possible singularities or kinks occurring in the solution, sufficiently fine meshes are required to obtain an accurate numerical solution.

Here, we propose a new hybrid approach which preserves the advantages of reduced order models, while preserving a sufficiently high accuracy. The idea is to model the larger vessels by 1D flow models, whereas the capillaries and tissue are considered as porous continua, as is done in the homogenization approach. We apply this hybrid modeling approach to a microvascular system filling a volume of $1.134 \text{ mm} \times 1.134 \text{ mm} \times 2.268 \text{ mm}$ (see Figure 1). This microvascular system was taken from the brain of a rat, and the corresponding data was generated by the group of Weber (University of Zurich) [40]. Within this network, one can find several penetrating arterioles and venules connecting this vascular subsystem to the macro-circulation of the rat's brain; see Figure 1. Our motivation to choose this approach is that by resolving the largest vessels in this volume, the main hierarchy of the vessel system is incorporated into the model. Moreover, using a homogenized double continuum model for the capillaries and the tissue, we have a less complex model which will certainly yield some speed-up, if several units of cubes of a few cubic millimeters are aggregated to simulate larger parts of an organ. Compared to other works [13, 34, 43] investigating hybrid approaches for microvascular systems, we consider in this work the capillaries and the tissue as two coupled porous media, i.e., a double continuum approach [14]. In addition, we discuss alternative coupling conditions between the 1D vessels and the 3D continuum for the capillaries. To validate our *hybrid 3D-1D* modeling approach, a comparison with a *fully discrete 3D-1D* model [6, 8, 9, 31, 26]

is performed.

The rest of this work is structured as follows. In section 2, we describe the data set that is used for our numerical tests. In addition, the basic modeling assumptions are discussed. The model problems and the corresponding numerical discretization methods are outlined in section 3. Section 4 contains some numerical tests and a discussion of the results obtained from both models. Finally, in section 5, we summarize the key features of our work and briefly suggest directions for future research.

2. Problem setting and main simplifications. In order to illustrate the performance of our modeling approaches, we consider the microvascular network shown in Figure 1. To obtain the data for this microvascular network, first an anaesthetized rat was perfused with phosphate buffered saline and barium sulphate. In a second step, the brain was removed and a sample from the cortex was taken. Using this sample, an X-ray tomographic microscopy of the sample was performed. Based on the resulting image, vessel midlines were extracted, and the 3D coordinates of branches, kinks as well as start and end points, were determined. We denote these points as network nodes. Furthermore, curved vessel midlines were replaced by straight edges, and to each edge a mean vessel radius was assigned. In addition to the different radii, the connectivity of network nodes was determined; i.e., it was reported which network nodes are connected with each other. At the network nodes that are adjacent to the boundaries of the extracted sample, physiologically meaningful pressure boundary conditions are provided [40].

Analyzing the given data, it turns out that the radii range from $1.6 \mu\text{m}$ to $28.2 \mu\text{m}$. Within the network some larger penetrating arterioles and venules can be identified at the top of the sample. At the bottom of the sample a larger venule and arteriole are leaving or entering the cuboid domain. The rest of the microvascular network consists of tiny capillaries. Zooming in on the original data set, we detected some dead ends of the arterioles and venules (network nodes that are not connected to the capillaries). Since we want to perform a precise comparison between the fully discrete and the hybrid modeling approaches, the edges associated with dead ends are removed from the data set such that in the resulting microvascular network all the network nodes are connected.

Further modeling assumptions that are used in the remaining sections read as follows:

- (A1) The non-Newtonian flow behavior of blood is modeled in a simplified way using an algebraic relationship.
- (A2) The density of blood is constant.
- (A3) The influence of gravity is neglected.
- (A4) The inertial effects can be neglected.
- (A5) The pulsatility can be neglected.
- (A6) The walls of the larger vessels are considered impermeable; i.e., no flow occurs across their walls.

These assumptions are motivated by the following considerations: It is well known that blood consists of blood cells as well as plasma. Blood plasma itself is a mixture of water and ions, while the blood cells can be separated into the following groups: red blood cells, white blood cells, and blood platelets [17, Chap. 1]. In particular, the red blood cells determine the flow behavior of blood significantly [15]. Moving through a microvascular network, the red blood cells have to deform more and more as the vessel diameters become smaller than the diameter of the red blood cells. This results in a varying viscosity for the individual blood vessels, and therefore this feature is

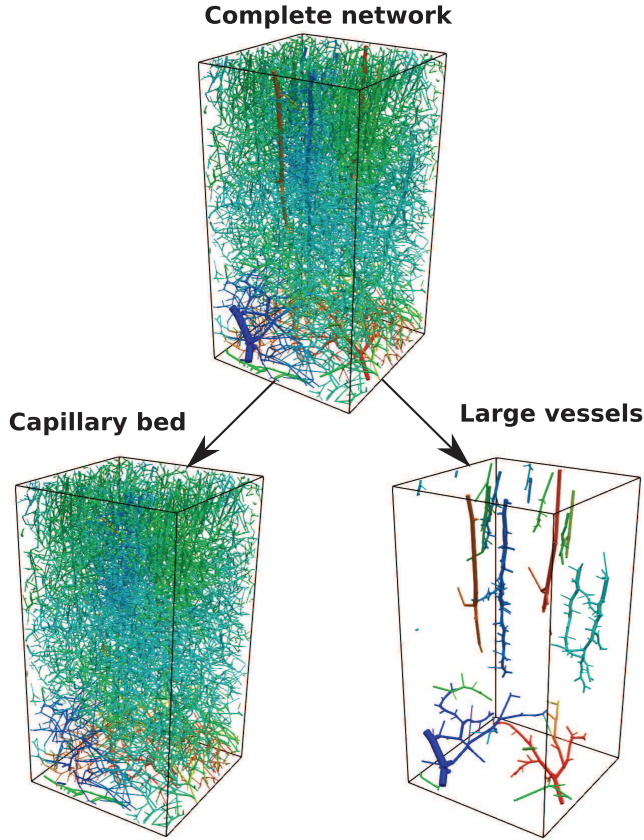


FIG. 1. A microvascular network extracted from a rat brain (top), filling a volume of $1 \text{ mm} \times 1 \text{ mm} \times 2 \text{ mm}$. A subdivision based on the vessel radius can be seen at the bottom of the figure. The network at the bottom left is the capillary bed of the microvascular network (all vessels whose radii are smaller than a given threshold, here $7 \mu\text{m}$). The motivation for such a threshold is postponed to section 4.1. At the bottom right, arterioles and venules (whose radii are larger than the given threshold) constitute the network of larger vessels.

recorded in (A1) [35]. Thereby, we adopt for an edge of diameter D the following formula for the in vivo viscosity μ_{bl} [Pa · s] [37]:

$$(2.1) \quad \mu_{\text{bl}}(D) = \mu_{\text{p}} \left(1 + (\mu_{0.45} - 1) \frac{(1 - H)^C - 1}{(1 - 0.45)^C - 1} \cdot \left(\frac{D}{D - 1.1} \right)^2 \right) \cdot \left(\frac{D}{D - 1.1} \right)^2.$$

Please note that in (2.1) the diameter D is dimensionless. The physical diameter d [μm] has to be divided by $1.0 \mu\text{m}$ to obtain D . The viscosity of the blood plasma is denoted by μ_{p} [Pa · s], and H stands for the discharge hematocrit, which is defined by the ratio between the volume of the red blood cells and the total blood volume. The apparent viscosity $\mu_{0.45}$ for a discharge hematocrit of 0.45 is calculated by

$$\mu_{0.45} = 6.0 \exp(-0.085 \cdot D) + 3.2 - 2.44 \exp(-0.06 \cdot D^{0.645}),$$

and C is a coefficient determining the influence of H on μ_{bl} :

$$C = (0.8 + \exp(-0.075 \cdot D)) \left(-1 + \frac{1}{1 + 10^{-11} D^{12}} \right) + \frac{1}{1 + 10^{-11} D^{12}}.$$

Please note that this function for the in vivo viscosity holds actually for human blood. However, we are not aware of such a function for rat blood, and therefore we assume that this function can be employed for rat blood as well. For simplicity, we assume in (A2) that blood is incompressible. Considering the total volume of the system under consideration, the quantity of fluids contained in this volume is relatively small, such that the effect of gravity can be neglected. Since the blood velocity is about 0.1 mm/s in the arterioles and venules and about 0.01 mm/s in the capillary bed in a human system [17, Table 1.7], it can be concluded that the Reynolds numbers in the whole microvascular network are significantly lower than 1.0. Therefore modeling assumption (A4) is reasonable [18]. The pulsatility of blood flow can be neglected (A5), due to the fact that the Womersley numbers in the arterioles, venules, and capillaries are much smaller than 0.1. The Womersley number is a dimensionless number relating the frequency of a pulse and the viscosity of a fluid to each other [17, Table 1.7]. The last modeling assumption (A6) is motivated by the fact that the vessel walls of capillaries consist of a thin layer of endothelial cells with gaps between them such that blood plasma, oxygen, and other substances can migrate into the interstitial space and then to the tissue cells or vice versa. Contrary to that, the vessel walls of the larger vessels (arterioles and venules) are thicker and not as permeable, since they exhibit a continuous endothelial cell layer that is surrounded by one or two concentric layers of smooth muscle cells [10], [17, Chap. 1].

3. Models and numerical methods. After describing the data set used in this work and discussing the basic modeling assumptions, we outline in this section the two modeling approaches under consideration, i.e., the fully discrete 3D–1D model and the hybrid 3D–1D model. In particular, we discuss coupling concepts between the different parts of the microvascular network and the tissue. Finally, the numerical discretization of the model equations is briefly explained.

We start by introducing some notation. The cuboid containing the microvascular network depicted in Figure 1 is denoted by Ω and given by

$$\Omega = \left\{ \mathbf{x} = (x_1, x_2, x_3)^\top \mid 0 \text{ mm} < x_1, x_2 < 1.13662 \text{ mm} \right. \\ \left. \wedge 8.75 \cdot 10^{-4} \text{ mm} < x_3 < 2.16388 \text{ mm} \right\}.$$

As has been described in section 2, we assume that the vascular system Λ under consideration has been segmented and approximated by extracting the midline of each blood vessel and approximating the midlines by straight segments $\Lambda_k \subset \Lambda$. Each segment is equipped with a constant radius value R_k for $k = 1, \dots, N$. Therefore, the entire vascular system is assumed to be given by the union of N cylinders V_k of radius R_k for $k = 1, \dots, N$. We then split the domain into two parts:

$$\Omega_v = \bigcup_{i=k}^N V_k \quad \text{and} \quad \Omega_t = \Omega \setminus \Omega_v,$$

where Ω_v represents the vascular system and Ω_t the tissue. The entire vascular system can now be described by a graph, whose edges are represented by the center lines Λ_k of each cylinder V_k for $k = 1, \dots, N$. Each segment Λ_k is parametrized by the arc length s_k , and $\boldsymbol{\lambda}_k$ is the tangent unit vector determining the orientation of the centerline of V_k . Let us denote the two endpoints of the edge Λ_k by $\mathbf{x}_{k,1}, \mathbf{x}_{k,2} \in \Omega$. With this notation at hand, each cylinder V_k can be defined as

$$V_k = \{ \mathbf{x} \in \Omega_v \mid \mathbf{x} = \mathbf{x}_{k,1} + s_k \cdot \boldsymbol{\lambda}_k + \mathbf{r}_k \},$$

where $\mathbf{x}_{k,1} + s_k \cdot \boldsymbol{\lambda}_k \in \Lambda_k = \mathcal{M}_k(\Lambda' \subset \mathbb{R}^1)$ and

$$\mathbf{r}_k \in \mathcal{D}_{\Lambda_k}(R_k) = \{r\mathbf{n}_{\Lambda_k}(s_k, \theta) : r \in [0, R_k), s_k \in (0, |\mathbf{x}_{k,2} - \mathbf{x}_{k,1}|), \theta \in [0, 2\pi)\}.$$

\mathcal{M}_k is a mapping from a reference domain Λ' to the manifold $\Lambda_k \subset \Omega$, and \mathbf{n}_{Λ_k} denotes the set of unit normal vectors with respect to Λ_k . Γ_k is the lateral surface of the branch V_k , and the union Γ corresponds approximately to the surface of the vascular system, since the cylinders V_k may not perfectly match each other: $\Gamma = \bigcup_{k=1}^N \Gamma_k$. The given blood vessel network is separated into two parts: Based on a fixed threshold R_T , we subdivide the network Λ into two subsets Λ_L , consisting of large vessels which are considered to be impermeable, and Λ_C , consisting of capillaries. Associated to this separation, we define two index sets I_L, I_C :

$$I_L := \{k \in \{1, \dots, N\} \mid R_k \geq R_T\} \quad \text{and} \quad I_C := \{k \in \{1, \dots, N\} \mid R_k < R_T\}.$$

Using these definitions, Λ_L and Λ_C can be represented as follows:

$$\Lambda_L := \bigcup_{k \in I_L} \Lambda_k \quad \text{and} \quad \Lambda_C := \bigcup_{k \in I_C} \Lambda_k.$$

The surface of the capillaries is given by $\Gamma_C := \bigcup_{k \in I_C} \Gamma_k$. Finally, to each node of the graph a pressure value is assigned. The computation of the pressure values corresponding to the interior nodes is outlined in section 3.3, while at the boundary nodes the pressure values are prescribed from the given data set (see section 2).

3.1. Fully discrete 3D–1D model. With respect to the surrounding tissue, we assume that it can be considered as a porous medium with an isotropic scalar permeability K_t [m^2] [24]. In order to model the flow in a porous medium, one can use the Darcy equation to obtain a pressure field [1, 20].

Within the 1D network Λ , we assume that the flow is described by the Hagen–Poiseuille law with a mass balance equation. Differentiation over the branches is defined using the tangent unit vector as $dw/ds_k = \nabla w \cdot \boldsymbol{\lambda}_k$ on Λ_k ; i.e., d/ds_k represents the projection of ∇ along $\boldsymbol{\lambda}_k$. The governing flow equations for the whole network Λ are obtained by summing the governing equation over the index k and introducing the global variable s . Furthermore, we assume that the mass transfer from the vessel into the tissue matrix and vice versa occurs across the membrane Γ_C of the capillaries according to Starling’s filtration law [28, 45]. Following the approach presented in [26], these exchange processes are accounted for by a Dirac measure δ_{Γ_C} in the source term of the 3D tissue problem:

$$(3.1) \quad \left\{ \begin{array}{ll} -\nabla \cdot \left(\rho_{\text{int}} \frac{K_t}{\mu_{\text{int}}} \nabla p^t \right) = L_{\text{cap}} \rho_{\text{int}} \left(p^v - \bar{p}^t - (\pi_p - \pi_{\text{int}}) \right) \delta_{\Gamma_C} & \text{in } \Omega, \\ -\frac{d}{ds} \left(\rho_{\text{bl}} \pi R^2 \frac{K_v}{\mu_{\text{bl}}} \frac{dp^v}{ds} \right) = 2\pi R L_{\text{cap}} \rho_{\text{int}} \left(\bar{p}^t - p^v + (\pi_p - \pi_{\text{int}}) \right) & \text{in } \Lambda, \\ \rho_{\text{int}} \frac{K_t}{\mu_{\text{int}}} \nabla p^t \cdot \mathbf{n} = 0 & \text{on } \partial\Omega, \\ p^v = p_D^v & \text{on } \partial\Lambda. \end{array} \right.$$

For each edge Λ_k and its lateral surface Γ_k and $f \in L^2(\Gamma_k)$, we indicate with $f\delta_{\Gamma_k}$ the linear operator in $\mathcal{C}(\Omega)$ defined by

$$\langle f\delta_{\Gamma_k}, \phi \rangle = \int_{\Lambda_k} \int_{\partial B(s_k, R_k)} f\phi \, dS \, ds_k \quad \forall \phi \in C_0^\infty(\Omega), \quad k \in I_C.$$

The symbol $\partial B(s_k, R_k)$ denotes the circle with center in $\Lambda_k(s_k)$ and perpendicular to λ_k . The variable p^v denotes the pressure in the network and p^t the pressure in the tissue. The term $\bar{p}^t(s_k)$ in (3.1) represents the average value of p^t with respect to the circle $\partial B(s_k, R_k)$:

$$(3.2) \quad \bar{p}^t(s_k) = \frac{1}{2\pi R_k} \int_0^{2\pi} p^t(\Lambda_k(s_k) + R_k \mathbf{n}_{\Lambda_k}(s_k, \theta)) R_k \, d\theta, \quad k \in I_C.$$

π_p and π_{int} represent the oncotic pressures of the plasma and the interstitial fluid, respectively. According to [27], these values are assumed to be constant. The hydraulic conductivity L_{cap} [m/(Pa · s)] of the membrane is assumed to be constant for the segments Λ_k , $k \in I_C$. The radius R [m] and the permeability K_v [m²] are defined for each segment Λ_k as

$$(3.3) \quad R|_{\Lambda_k} = R_k \text{ and } K_v|_{\Lambda_k} = \frac{R_k^2}{8}.$$

The viscosity μ_{bl} [Pa · s] of blood is computed according to (2.1), while μ_{int} [Pa · s] represents the viscosity of interstitial fluid. ρ_{int} [kg/m³] and ρ_{bl} [kg/m³] are the densities of the interstitial fluid and of blood, respectively. p_D^v [Pa] are the boundary data, obtained from the data set previously described in section 2. On the boundary of the tissue continuum $\partial\Omega \subseteq \partial\Omega_t \setminus \Gamma_C$, we set homogeneous Neumann boundary conditions. Due to the fact that we have no boundary data available, homogeneous Neumann boundary conditions have been chosen. However, if measurements or other data become available, this boundary condition can easily be replaced.

Alternative 3D–1D PDE systems simulating flow in microvascular networks can be found in [8, 9]. The difference from the presented coupling approach is that in the source term of the tissue problem, the Dirac measure is concentrated on the midlines of the vascular system. As a result, singularities along the network midlines are introduced in the 3D pressure field [25, 19]. Moreover, there are no estimates for the modeling errors arising from this type of coupling concept. In [26] we proved for a two-dimensional (2D) model problem that the coupling approach in (3.1) causes a small modeling error if the radii of the network are small compared to the considered tissue matrix. Furthermore, the pressure field in the 3D tissue matrix does not exhibit any singularities but exhibits only kinks at vessel surfaces.

3.2. Hybrid 3D–1D model. Considering the microvascular network in Figure 1, it can be seen that it consists of venules and arterioles and a large number of small capillary vessels forming a dense structure. Due to that, we consider the capillaries as a 3D porous medium, while the venules and arterioles are still considered as 1D vessel systems. This approach has the clear advantage that it does not require a high-resolution description of the microvascular network under consideration and that it preserves the hierarchy of the larger vessels. All in all, there are now two coupled 3D continua in Ω , one for the capillary bed and another one for the tissue. This means that the hybrid 3D–1D model is a *double-3D continuum* model contrary to the *fully discrete* model, which is a *single-3D continuum* model. As for the tissue, the flow

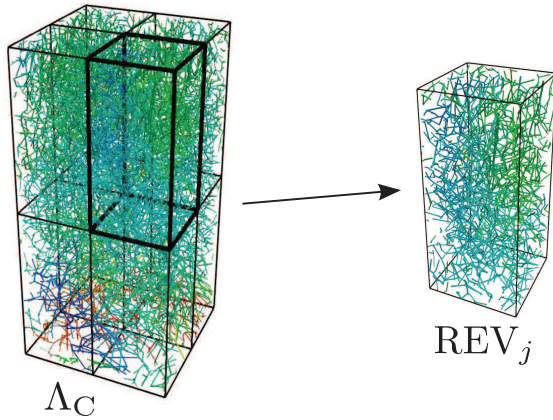


FIG. 2. Subdivision of the capillaries Λ_C into eight REVs.

in the homogenized capillaries can be described using Darcy's law, and we pose the following problem for the corresponding unknown p^{cap} :

$$(3.4) \quad \begin{cases} -\nabla \cdot \left(\rho_{\text{bl}} \frac{K_{\text{up}}}{\mu_{\text{bl}}^{\text{up}}} \nabla p^{\text{cap}} \right) = q^{\text{cap}} & \text{in } \Omega, \\ p^{\text{cap}} = p_D^{\text{cap}} & \text{on } \partial\Omega. \end{cases}$$

K_{up} is the corresponding permeability tensor, $\mu_{\text{bl}}^{\text{up}}$ is an averaged viscosity, q^{cap} indicates the source term, and p_D^{cap} denotes the Dirichlet boundary condition. These terms and parameters are described in the following.

Computing the tensor K_{up} and the averaged viscosity $\mu_{\text{bl}}^{\text{up}}$. Let us assume that the domain Ω can be decomposed into *representative elementary volumes* (REVs) [20], that is,

$$(3.5) \quad \bar{\Omega} = \bigcup_{j=1}^{N_{\text{REV}}} \overline{\text{REV}_j},$$

where N_{REV} is the total number of REVs. Furthermore, we assume that each $\text{REV}_j \subset \Omega$ is a rectangular cuboid, as depicted in Figure 2. With respect to REV_j , the viscosity $\mu_{\text{bl}}^{\text{up}}$ is defined as follows:

$$\mu_{\text{bl}}^{\text{up}}(\mathbf{x}) = \mu_{\text{bl},j}^{\text{up}} \text{ if } \mathbf{x} \in \text{REV}_j, \text{ where } \mu_{\text{bl},j}^{\text{up}} = \frac{1}{|I_{C,j}|} \sum_{k \in I_{C,j}} \mu_{\text{bl}}(2 \cdot R_k / \mu m).$$

The viscosity μ_{bl} is given by (2.1), and the set $I_{C,j}$ is defined as follows:

$$I_{C,j} = \{k \in I_C \mid \Lambda_k \cap \text{REV}_j \neq \emptyset\}.$$

Now, we determine the tensor K_{up} which represents the permeability of the homogenized capillary bed. In [12], the authors computed full permeability tensors for periodic cells based on computer-generated capillary networks, whose properties statistically match measurements in brain tissue. The off-diagonal entries were found to be on average two orders of magnitude smaller than the diagonal terms [12, Table 2]. Following this observation, we make the following simplifying assumptions for K_{up} :

(i) The permeability tensor K_{up} is constant on each REV_j :

$$K_{\text{up}}(\mathbf{x}) = K_{\text{up}}^{(j)}, \text{ if } \mathbf{x} \in \text{REV}_j.$$

(ii) The permeability tensor $K_{\text{up}}^{(j)}$ is diagonal:

$$K_{\text{up}}^{(j)} = \begin{pmatrix} k_x^{(j)} & 0 & 0 \\ 0 & k_y^{(j)} & 0 \\ 0 & 0 & k_z^{(j)} \end{pmatrix},$$

with $k_x^{(j)}, k_y^{(j)}, k_z^{(j)} > 0$.

In order to determine the components of the permeability tensor $K_{\text{up}}^{(j)}$, we apply the upscaling strategy presented in [40] which we briefly describe in the following. For simplicity, we restrict ourselves to the computation of the permeability component $k_x^{(j)}$. The other permeability components $k_y^{(j)}$ and $k_z^{(j)}$ can be computed in an analogous way. As a first step in computing this quantity, we apply a no-flow boundary condition to all the facets of the REV_j whose face normals are not aligned with the x -axis (see Figure 3). The remaining facets are denoted by $F_{\text{in},x}^{(j)}$ and $F_{\text{out},x}^{(j)}$. Between these facets a pressure gradient is applied by imposing a pressure $p_{\text{in},x}$ on $F_{\text{in},x}^{(j)}$ and a pressure $p_{\text{out},x}$ on $F_{\text{out},x}^{(j)}$, where $p_{\text{in},x} > p_{\text{out},x}$. This results in a volume flux from $F_{\text{in},x}^{(j)}$ to $F_{\text{out},x}^{(j)}$. Using the vascular graph model (VGM) described in subsection 3.3, we compute the pressure field in

$$\Lambda_{C,j} = \bigcup_{k \in I_{C,j}} \Lambda_k.$$

By means of this pressure field, the volume flux $VF_{\text{out},x}^{(j)}$ through $F_{\text{out},x}^{(j)}$ is computed as follows:

$$VF_{\text{out},x}^{(j)} = \sum_{\mathbf{x}_k \in \Lambda_{C,j} \cap F_{\text{out},x}^{(j)}} \frac{\pi R_k^2 K_v(s_k)}{\mu_{\text{bl}}} \cdot \frac{\partial p^v}{\partial s}(s_k),$$

where $\mathbf{x}_k = \Lambda_k(s_k)$ for $k \in I_{C,j}$. Based on $VF_{\text{out},x}^{(j)}$, the permeability component $k_x^{(j)}$ is approximated as follows:

$$(3.6) \quad k_x^{(j)} \approx \frac{VF_{\text{out},x}^{(j)} \cdot \mu_{\text{bl},j}^{\text{up}} \cdot L_x^{(j)}}{L_y^{(j)} \cdot L_z^{(j)} \cdot (p_{\text{in},x} - p_{\text{out},x})}.$$

$L_x^{(j)}$, $L_y^{(j)}$, and $L_z^{(j)}$ are the edge lengths of REV_j in the x -, y -, and z -directions, respectively. An open issue in this context is the choice of the REV size. In order to clarify this issue, we refer to subsection 4.2, in which the admissible size of the REVs is determined numerically.

Computing the boundary conditions $p_{\text{D}}^{\text{cap}}$. For the computation of the boundary data $p_{\text{D}}^{\text{cap}}$, we consider the REV_j that are adjacent to the boundary $\partial\Omega$, i.e., $\overline{\text{REV}_j} \cap \partial\Omega \neq \emptyset$. The six facets of an REV_j are denoted by F_{1j}, \dots, F_{6j} . For each F_{ij} with $F_{ij} \subset \partial\Omega$, we compute an averaged boundary value $p_{\text{D}}^{(ij)}$. This is done by averaging all the pressure values p_k that are assigned to the boundary nodes $\mathbf{x}_k \in \partial\Lambda_C$ and whose distance to the face F_{ij} is smaller than a small parameter $\varepsilon_d > 0$ (see Figure

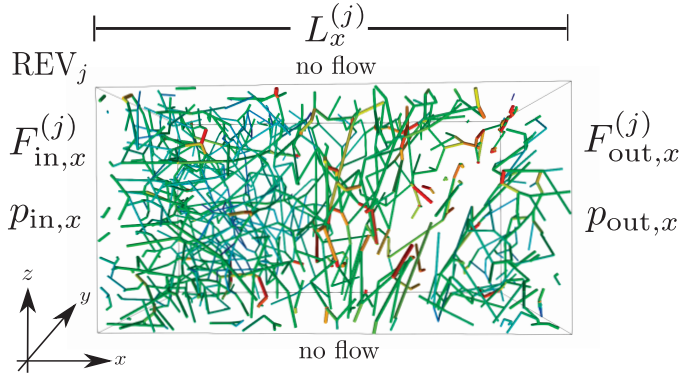


FIG. 3. Homogenization of a capillary network contained in an REV_j . On the facets $F_{in,x}^{(j)}$ and $F_{out,x}^{(j)}$ whose normals are aligned with the x -axis, we apply pressures $p_{in,x}$ and $p_{out,x}$, while on the other facets a no-flow condition is imposed. Computing the flux between $F_{in,x}^{(j)}$ and $F_{out,x}^{(j)}$, the permeability component $k_x^{(j)}$ can be estimated.

4): $\text{dist}(F_{ij}, \mathbf{x}_k) < \varepsilon_d$. For the rest of the paper, we set $\varepsilon_d = 10^{-8}$ m. Assuming that N_{ij} nodes are fulfilling these conditions, we compute the averaged pressure by an arithmetic mean:

$$p_D^{(ij)} = \frac{1}{N_{ij}} \sum_{k=1}^{N_{ij}} p_k.$$

In order to obtain a smooth function for the boundary values p_D^{cap} , we assign the pressure values $p_D^{(ij)}$ to the centers of the faces F_{ij} and construct a linear interpolant p_D^{cap} on $\partial\Omega$ based on the described setup by means of the function `interpolate` from the package PDELab of Dune [4].

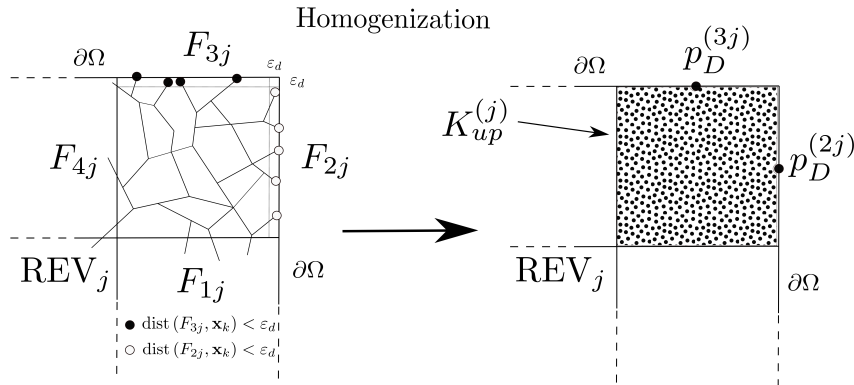


FIG. 4. The figure shows a 2D layout parallel to the x - y plane of an REV_j that is located at an edge of the domain Ω . At the top of the figure, the discrete capillary network contained in REV_j is shown, while in the bottom part of the figure, the homogenized system with the tensor $K_{up}^{(j)}$ and the averaged boundary pressures $p_D^{(2j)}$ and $p_D^{(3j)}$ can be seen.

Computing the source term q^{cap} . The source term q^{cap} in (3.4) can be split into a component q_v^{cap} accounting for the impact of the larger vessels and a component

q_t^{cap} incorporating the influence of the surrounding tissue:

$$(3.7) \quad q^{\text{cap}} = q_v^{\text{cap}} + q_t^{\text{cap}}.$$

Let \mathbf{x}_k be a node at the boundary of the subset Λ_L and in the interior of the domain Ω , i.e., $\mathbf{x}_k \in \partial\Lambda_L \cap \Omega$. Furthermore, we assume that $\mathbf{x}_k \in \Lambda_k \cap \text{REV}_j$ for an index $k \in I_L$ and an index $j \in \{1, \dots, N_{\text{REV}}\}$. This means there exists an s_k such that $\mathbf{x}_k = \Lambda_k(s_k)$. Then the flux occurring between the edge Λ_k and the capillary continuum is given by

$$(3.8) \quad \rho_{\text{bl}} \frac{\pi R_k^2 K_v(s_k)}{\mu_{\text{bl}}} \cdot \frac{\partial p^v}{\partial s}(s_k) = \alpha_v^{\text{cap}}(\Lambda_k, \text{REV}_j) \left(p_{(j)}^{\text{cap}} - p^v(s_k) \right),$$

where the factor α_v^{cap} and the averaged pressure $p_{(j)}^{\text{cap}}$ are defined as follows:

$$(3.9) \quad \alpha_v^{\text{cap}}(\Lambda_k, \text{REV}_j) = \rho_{\text{bl}} \cdot \frac{\pi R_k^2 K_v^{(j)}}{\mu_{\text{bl}}^{\text{up}} \ell_c^{(kj)}} \quad \text{and} \quad p_{(j)}^{\text{cap}} = \frac{1}{|\text{REV}_j|} \int_{\text{REV}_j} p^{\text{cap}}(x) \, dx.$$

The coefficient $K_v^{(j)}$ represents the permeability of the capillaries connected to the coupling point \mathbf{x}_k . The parameter $\ell_c^{(kj)}$ [m] indicates the average length of the blood flow paths that begin at \mathbf{x}_k and are contained in REV_j which is not known a priori and has to be estimated. Therefore, we set

$$(3.10) \quad \frac{K_v^{(j)}}{\ell_c^{(kj)}} = \alpha \frac{\overline{K_v^{(j)}}}{L_j},$$

where L_j is the smallest edge length of the REV_j , and $\overline{K_v^{(j)}}$ denotes the arithmetic average of the permeabilities (3.3) of the capillaries contained in the REV_j . A numerical study to determine the optimal value of the parameter $\alpha \in (0, 1)$ (with respect to the fluxes within the system) for the problem under consideration is postponed to subsection 4.3. Considering the right-hand side of (3.8), one has to note that the term

$$\frac{p_{(j)}^{\text{cap}} - p^v(s_k)}{\ell_c^{(kj)}}$$

represents a finite difference approximation of a pressure gradient at an outlet of the larger vessels. According to the REV concept in porous media theory [1, 20], one can assign to each REV an averaged pressure $p_{(j)}^{\text{cap}}$, which stands for the pressure field in the REV_j . The finite difference above can be considered as an approximation of the pressure gradient between an outlet of Λ_L and the homogenized capillary bed in REV_j . Using (3.8), the source term q_v^{cap} is computed for $\mathbf{x} \in \text{REV}_j$ by

$$(3.11) \quad q_v^{\text{cap}}(\mathbf{x}) = \sum_{\mathbf{x}_k \in \partial\Lambda_L \cap \text{REV}_j} \frac{\alpha_v^{\text{cap}}(\Lambda_k, \text{REV}_j)}{|\text{REV}_j|} \left(p^v(s_k) - p_{(j)}^{\text{cap}} \right),$$

such that the model is mass conservative.

Computing the source term q_t^{cap} . As in the case of the fully discrete 3D–1D model, the tissue is considered a porous structure. The main difference from the capillaries is that we assume an isotropic permeability K_t for the tissue. Furthermore, the interstitial fluid is assumed to have a constant viscosity μ_{int} . By means of Darcy's

law, the pressure p^t can be computed by

$$(3.12) \quad \begin{cases} -\nabla \cdot \left(\rho_{\text{int}} \frac{K_t}{\mu_{\text{int}}} \nabla p^t \right) = -q_t^{\text{cap}} & \text{in } \Omega, \\ \rho_{\text{int}} \frac{K_t}{\mu_{\text{int}}} \nabla p^t \cdot \mathbf{n} = 0 & \text{on } \partial\Omega. \end{cases}$$

It remains to specify the source term q_t^{cap} modeling the fluid transfer between the capillary bed and the intracellular space. For this purpose, we use as in (3.1) Starling's filtration law with respect to the vessel surface S_j that is contained in an REV $_j$:

$$S_j = \sum_{k \in I_{C,j}} \left| \tilde{\Lambda}_k \right| R_k^2 \pi,$$

where $\tilde{\Lambda}_k \subseteq \Lambda_k$ such that $\Lambda_k \cap \text{REV}_j = \tilde{\Lambda}_k$. Using this parameter, q_t^{cap} is given by

$$(3.13) \quad q_t^{\text{cap}}(\mathbf{x}) = \frac{\rho_{\text{int}} \cdot S_j \cdot L_{\text{cap}}}{|\text{REV}_j|} (p^t(\mathbf{x}) - p^{\text{cap}}(\mathbf{x}) + (\pi_p - \pi_{\text{int}})), \quad \mathbf{x} \in \text{REV}_j.$$

Summary of the equations governing the hybrid model. Summarizing all the previous considerations, the hybrid (double-continuum) 3D–3D–1D model is governed by the following equations:

- Large vessels (1D discrete network):

$$(3.14) \quad \begin{cases} -\frac{\partial}{\partial s} \left(\rho_{\text{bl}} \cdot \pi R^2 \frac{K_v}{\mu_{\text{bl}}} \frac{\partial p^v}{\partial s} \right) = 0 & \text{in } \Lambda_L, \\ p^v = p_D^v & \text{on } \partial\Lambda_L \cap \partial\Omega, \\ \text{flux term in (3.8)} & \text{on } \partial\Lambda_L \cap \Omega. \end{cases}$$

- Capillary bed (3D porous medium):

$$(3.15) \quad \begin{cases} -\nabla \cdot \left(\rho_{\text{bl}} \frac{K_{\text{up}}}{\mu_{\text{bl}}} \nabla p^{\text{cap}} \right) = q_v^{\text{cap}} + q_t^{\text{cap}} & \text{in } \Omega, \\ p^{\text{cap}} = p_D^{\text{cap}} & \text{on } \partial\Omega. \end{cases}$$

- Tissue (3D porous medium):

$$(3.16) \quad \begin{cases} -\nabla \cdot \left(\rho_{\text{int}} \frac{K_t}{\mu_{\text{int}}} \nabla p^t \right) = -q_t^{\text{cap}} & \text{in } \Omega, \\ \rho_{\text{int}} \frac{K_t}{\mu_{\text{int}}} \nabla p^t \cdot \mathbf{n} = 0 & \text{on } \partial\Omega. \end{cases}$$

The coupling term q_v^{cap} is given by (3.11) and describes the interactions between the extracted network Λ_L and the homogenized capillaries. The other coupling term q_t^{cap} is defined by (3.13) and stands for the exchange between tissue and homogenized capillaries.

3.3. Numerical discretizations. Next, we briefly describe a numerical scheme that is used to solve the model equations (3.1) and (3.14)–(3.16). The elliptic PDEs governing the flow within the tissue or the upscaled capillaries are solved numerically by means of a standard cell-centered finite volume method [20], where the numerical

fluxes across the cell surfaces are approximated by the two-point flux method. The choice of this method is motivated by its intrinsic local mass conservation, and by the fact that we can work with uniform hexahedral meshes.

For the numerical solutions of the network equations in both modeling approaches (3.1) and (3.14), we employ the VGM [14, 34, 40]. Thereby, we approximate the pressure values at the grid nodes \mathbf{x}_k discretizing the network structures. Around each grid node a control volume CV_k is placed such that the grid node is in the center of the control volume (see Figure 5). In the next step, the fluxes F_{kj} and F_k^t across the surfaces of the control volume are computed and summed up such that the sum of the fluxes is equal to zero:

$$(3.17) \quad \sum_{j \in \mathcal{N}(\mathbf{x}_k)} F_{kj} - F_k^t = 0, \quad F_{kj} = \frac{\rho_{bl} \cdot \pi R_k^4}{8\mu_{bl} |\mathbf{x}_j - \mathbf{x}_k|} \cdot (p^v(\mathbf{x}_j) - p^v(\mathbf{x}_k)),$$

where R_k is the radius of the edge linking \mathbf{x}_k and \mathbf{x}_j . $\mathcal{N}(\mathbf{x}_k)$ denotes the set of indices that share the edge Λ_k with the point \mathbf{x}_k .

When solving the fully discrete model (3.1), because the walls of the smaller vessels (capillaries) are permeable, a flux across the vessel walls has to be considered, too. This is done by computing an averaged pressure in the tissue with respect to the part of the vessel wall touching the control volume; see Figure 5. Then, this pressure value is compared to the network pressure associated with the grid node \mathbf{x}_k to determine the flux across the vessel wall:

$$F_k^t = 2\pi L_{cap} \cdot \rho_{int} \left[\sum_{j \in \mathcal{E}(\mathbf{x}_k)} R_j \int_{CV_k \cap \Lambda_j} I(p^v) - \bar{p}^t - (\pi_p - \pi_{int}) dS \right].$$

$\mathcal{E}(\mathbf{x}_k)$ is the index set for the edges containing the grid node \mathbf{x}_k . $I(p^v)$ is a linear interpolant for the pressure field p^v , whose shape on each edge is determined by the two pressure values of the edge. By this, we obtain for each grid node a mass balance equation. Summarizing these equations, we obtain a system of equations for the pressure values at the grid nodes.

The reason we consider a different discretization for the network is the treatment of bifurcations or junctions in the network. Within the VGM approach, a grid node is placed directly at a bifurcation, and the mass balance equation (3.17) can easily

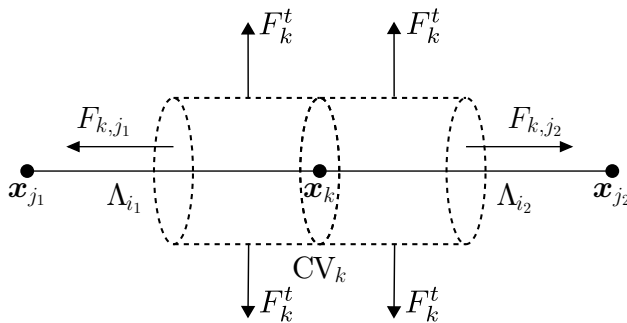


FIG. 5. Representation of the numerical fluxes through the surface of the control volume CV_k with center in \mathbf{x}_k . The point shares the edges Λ_{i_1} and Λ_{i_2} with the nodes \mathbf{x}_{j_1} and \mathbf{x}_{j_2} of the network, respectively.

be established. Applying the cell-centered finite volume method, one cannot place a degree of freedom directly at a bifurcation, and therefore the fluxes through the bifurcation point have to be computed. Since the radii of the branches and the main vessel may be different, the computation of the fluxes requires a careful computation of the numerical transmissibility coefficients in (3.17). Finally, the continuity of the pressure at a bifurcation is guaranteed using the VGM.

All in all the numerical treatment of the PDEs together with the boundary conditions, source terms, and coupling conditions yields for each model a sparse linear system of equations. Each block of the system matrix is the discrete representative of an elliptic differential operator or a coupling term, whereas the contributions of the oncotic pressures and the boundary conditions are incorporated into the right-hand side of the system of equations. For the numerical solution of the linear equation system a block AMG preconditioner is applied. The preconditioned system is then solved by a stabilized biconjugate gradient method. This solver was realized using the generic interface of the ISTL library of DUNE and its AMG implementation [2, 3].

4. Numerical tests. In this section, we test the numerical models presented in section 3 using the data set described in section 2. Thereby, by means of the fully discrete 3D–1D model (3.1), a reference solution is computed for the hybrid model (3.14)–(3.16). The results obtained by both approaches are compared with respect to mass fluxes and averaged REV pressures. The flow is driven by the boundary conditions, as described in sections 3.1 and 3.2. In particular, no-flow boundary conditions are posed for the flow in the tissue, while prescribed Dirichlet values are considered for the network (see section 2). In Table 1, the model parameters for the numerical simulations are summarized. The motivation for the choice of $R_T = 7 \mu\text{m}$ is given in subsection 4.1, while the number N_{REV} in (3.5) for the hybrid model is discussed in subsection 4.2. Subsections 4.3 and 4.4 contain the numerical results for the mass fluxes and the averaged REV pressures, respectively. Finally, in subsection 4.5, the influence of different boundary conditions is discussed.

TABLE 1
Values of the parameters used for the numerical experiments.

Discharge hematocrit	H	0.45
Tissue permeability	K_t	10^{-18} m^2
Interstitial fluid viscosity	μ_{int}	$1.3 \cdot 10^{-3} \text{ Pa} \cdot \text{s}$
Plasma viscosity	μ_p	$1.0 \cdot 10^{-3} \text{ Pa} \cdot \text{s}$
Blood density	ρ_{bl}	1030 kg/m^3
Interstitial fluid density	ρ_{int}	1000 kg/m^3
Plasma oncotic pressure	π_p	3300 Pa
Interstitial oncotic pressure	π_{int}	666 Pa
Capillary wall hydraulic conductivity	L_{cap}	$10^{-12} \text{ m}/(\text{Pa} \cdot \text{s})$
Threshold large vessels/capillaries	R_T	$7 \mu\text{m}$

4.1. Justification of the threshold R_T . In this subsection, we motivate the choice of the threshold $R_T = 7 \mu\text{m}$ that we employ to separate the larger vessels from the capillaries. Let us consider the whole vessel system Λ as depicted in Figure 1, at the top. For each segment Λ_k , we calculate the blood velocity v_k , where we set a constant pressure gradient of δp at the vertices:

$$v_k = \frac{R_k^2}{8.0\mu_{\text{bl},k}} \cdot \frac{\delta p}{|\Lambda_k|},$$

where $\mu_{bl,k}$ is the viscosity of the blood according to (2.1). The distribution of the velocities is reported in Figure 6, on the left, for the case $\delta p = 1.0$ Pa. Choosing the threshold R_T to $7.0 \mu\text{m}$, we obtain that the average velocity in the set Λ_C is approximately 60 times smaller than the average velocity in the set Λ_L . Furthermore, the set Λ_C consists of 14918 vessels, while only 337 vessels are contained in the set Λ_L . Despite the low number of larger vessels, the chosen threshold still allows us to capture the main geometry of the vessel system, as depicted in Figure 6, on the right. In fact, choosing a larger threshold such as $R_T = 18.0 \mu\text{m}$ would drastically reduce the number of larger vessels, yielding a network that provides only restricted information about the geometry of the original system. On the other hand, choosing a smaller threshold would incorporate too many vessels in the size of capillaries. Considering the morphological values listed in [13, Table 1], we can observe that the choice of our threshold is close to the lower bound of the diameter range for the arterioles. Motivated by these considerations, we fixed the threshold to $7.0 \mu\text{m}$.

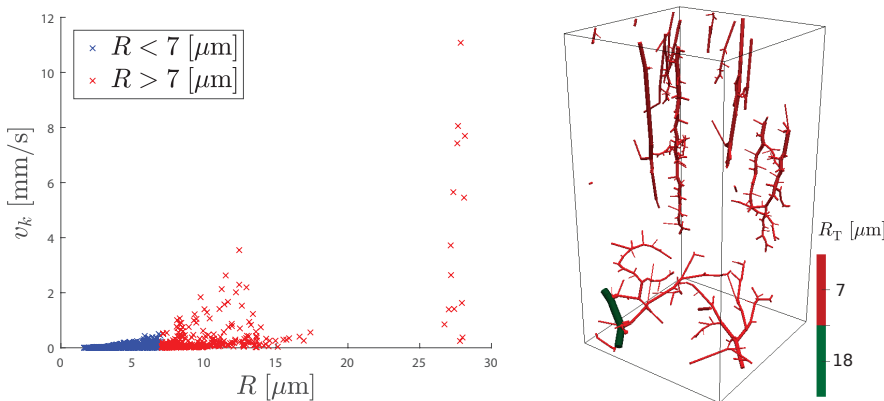


FIG. 6. On the left, the blood velocity for each vessel in the system Λ is shown, where each segment is subject to a 1.0 Pa pressure difference. Setting the threshold to $R_T = 7.0 \mu\text{m}$ yields 14918 vessels in the set Λ_C with an average velocity of 0.00714 mm/s, and 337 vessels in the set Λ_L with an average velocity of 0.41533 mm/s. On the right, the system Λ_L is depicted for the threshold $R_T = 7.0 \mu\text{m}$. The network Λ_L for the threshold $R_T = 18.0 \mu\text{m}$ is marked in green.

4.2. Homogenization of the capillary bed. In order to determine the admissible REV sizes for the approximation of the permeability tensor, we perform the following test: A single control volume, initially of size $12 \times 12 \times 24 \mu\text{m}$, is positioned in the center $(0.00056831, 0.00056831, 0.00113662)$ of the domain Ω and then enlarged in each space direction approximately by $4.0 \mu\text{m}$ in the x - and y -directions and by $8.0 \mu\text{m}$ in the z -direction. For each one of these control volumes, the values of the intrinsic permeability are determined using (3.6) and suitable adaptations for the y - and z -directions. In addition to that, we compute the *blood volume fraction*, which is defined as the ratio between the volume of the capillary network contained in the control volume under consideration and the volume of the control volume itself. The test is performed starting from the center of Ω , because this position allows for a larger margin of growth of the control volume. The numerical results confirm the expected oscillating behavior of the intrinsic permeability that typically occurs when the size of the control volume is too small (Figure 7, left). The permeabilities appear to reach stable values if the edges of the control volume are greater than approximately

500.0 μm (in the x - and y -directions). Therefore, we can assert that the control volume with half the dimensions of the domain ($568.31 \times 568.31 \times 1081.503 \mu\text{m}$) and collocated in the center of Ω can be assumed to be an REV. A further argument to support this statement can be derived considering the blood volume fraction of the capillary continuum. As depicted in Figure 7 on the right, the blood volume fraction seems to stabilize around the value 1.16% if the length of the control volume is larger than approximately 400.0 μm . However, collocating a single REV in the center of the domain with half the size of Ω is not enough, since the entire capillary network has to be homogenized. On the other hand, having a single REV covering the entire domain would mean that the heterogeneity of the capillary system is not considered. In fact, observing Figure 9 (top left), we can notice that in the upper part of the system, the capillaries are mainly aligned with the z -direction, while in the bottom part, the main directions are the x - and y -directions. These orientations are consistent with the structure of the larger vessels, as reported in Figure 1, on the bottom right. To this end, we subdivide the domain into $2 \times 2 \times 2$ control volumes, each having half the size of the domain, as the central REV from the previous test. The centers of these control volumes and their corresponding numeration are reported in Table 3. To assert that these eight control volumes are REVs as well, we observe in Figure 8 that the radii distribution of the capillaries contained in each control volume is similar to that of the central REV from the previous test. Furthermore, mean radii and standard deviations are similar as well. Supported by these observations, we can assume that the eight control volumes considered are REVs and that the permeabilities reported in Figure 9 are representative.

4.3. Comparison of the mass fluxes. A comparison between the two numerical models is provided in terms of the mass fluxes across different boundaries and interfaces. For the 1D systems in both the fully discrete network and the reduced network, the mass flux MF through a boundary node $\mathbf{x}_k = \Lambda_k(s_k) \in \partial\Lambda \cap \partial\Omega$ is computed as in (3.17).

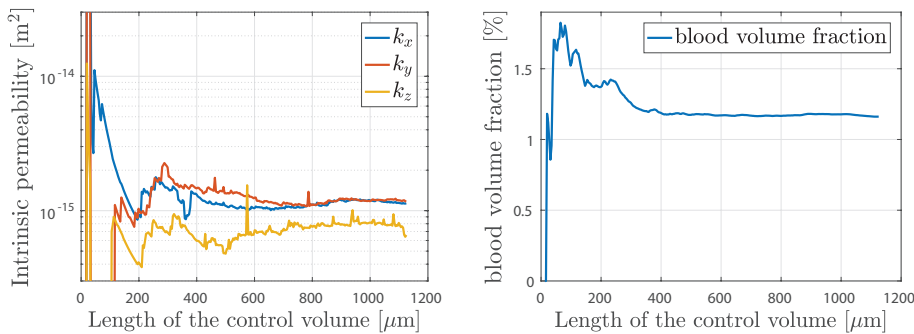


FIG. 7. On the left, the upscaled permeability is computed in the case where a single control volume is positioned in the center of the domain Ω . The dimensions of the control volume are enlarged by approximately $4 \times 4 \times 8 \mu\text{m}$ in each step until the control volume fills the entire domain Ω . The length of the control volume in the plot has to be doubled to obtain the actual size of the control volume in the z -direction. After an oscillating transition zone, each permeability stabilizes around a fixed value. On the right, the blood volume fraction of the corresponding control volume is reported.

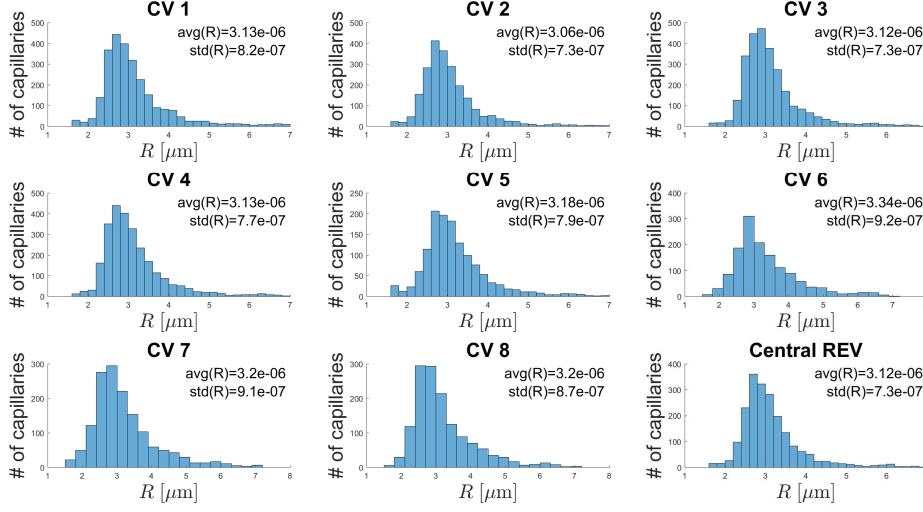


FIG. 8. Histograms of the radii distributions of the capillaries contained in each control volume. The numeration is given according to Table 3. For each CV, the mean value $\text{avg}(R)$ of the radii and the standard deviation $\text{std}(R)$ are provided. In the last histogram, the radii distribution of the capillaries contained in the REV with the same center as the domain Ω and same dimensions as the other control volumes is reported.

The inflow MF_{in} through the boundary point \mathbf{x}_k is defined as

$$MF_{\text{in}}(\mathbf{x}_k) = \begin{cases} MF(\mathbf{x}_k) & \text{if } MF(\mathbf{x}_k) > 0, \\ 0 & \text{otherwise.} \end{cases}$$

In a similar way, we can define the mass flux out of the domain:

$$MF_{\text{out}}(\mathbf{x}_k) = \begin{cases} |MF(\mathbf{x}_k)| & \text{if } MF(\mathbf{x}_k) < 0, \\ 0 & \text{otherwise.} \end{cases}$$

Having this notation at hand, we define the total inflow $MF_{LV,\text{in}}$ and outflow $MF_{LV,\text{out}}$ through the large vessels as

$$MF_{LV,\text{in}} = \sum_{\mathbf{x}_k \in \partial\Lambda_L \cap \partial\Omega} MF_{\text{in}}(\mathbf{x}_k) \quad \text{and} \quad MF_{LV,\text{out}} = \sum_{\mathbf{x}_k \in \partial\Lambda_L \cap \partial\Omega} MF_{\text{out}}(\mathbf{x}_k).$$

For the hybrid approach, the mass fluxes through the boundary $\partial\Omega$ of the capillary continuum have to be interpreted as single quantities for each boundary REV. Let us assume that the REV_j shares at least one side with the boundary of the domain, that is, $\partial\text{REV}_j \cap \partial\Omega \neq \emptyset$. In this work, we employ the following definition for the *net flux* NF with respect to the REV_j :

$$NF(\text{REV}_j) = \rho_{\text{bl}} \int_{\partial\text{REV}_j \cap \partial\Omega} \frac{K_{\text{up}}^{(j)}}{\mu_{\text{bl},j}^{(j)}} \cdot \nabla p_{(j)}^{\text{cap}} \cdot \mathbf{n} \, dS,$$

where \mathbf{n} denotes the outward unit normal vector to the boundary. Numerically, the gradient $\nabla p_{(j)}^{\text{cap}}$ is calculated by the standard two-point flux approximation for a cell-centered finite volume method. Analogously as for the 1D fluxes, we define the inflow

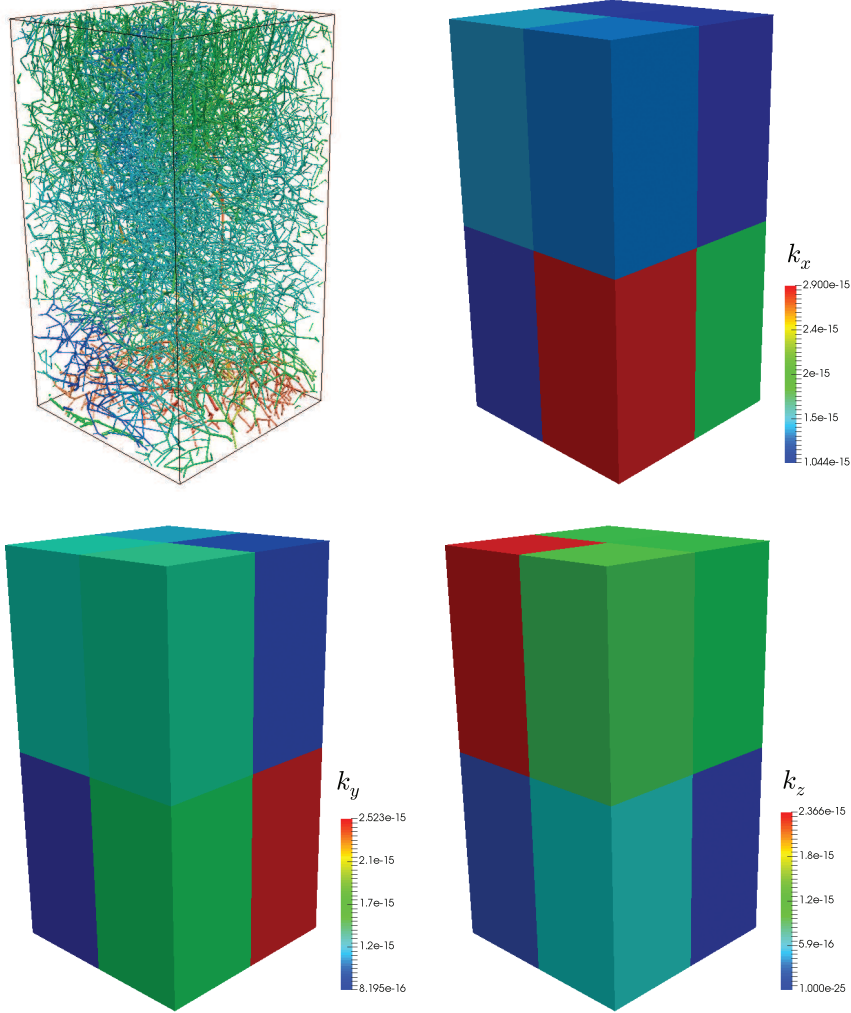


FIG. 9. Permeability tensors K_{UP} in the case of $2 \times 2 \times 2$ REV. The heterogeneous distribution of the capillaries from Figure 1 is therefore incorporated, in the sense that in the lower part of the domain, the flow occurs mainly in the xy -plane, while it is on the top in the z -direction.

NF_{in} through the REV_j as

$$(4.1) \quad NF_{\text{in}}(\text{REV}_j) = \begin{cases} NF(\text{REV}_j) & \text{if } NF(\text{REV}_j) > 0, \\ 0 & \text{otherwise,} \end{cases}$$

and the outflow as

$$(4.2) \quad NF_{\text{out}}(\text{REV}_j) = \begin{cases} |NF(\text{REV}_j)| & \text{if } NF(\text{REV}_j) < 0, \\ 0 & \text{otherwise.} \end{cases}$$

Therefore, the total net fluxes for the capillary continuum are given by

$$(4.3) \quad MF_{\text{cap,in}}^{\text{HY}} = \sum_{j=1}^{N_{\text{REV}}} NF_{\text{in}}(\text{REV}_j) \quad \text{and} \quad MF_{\text{cap,out}}^{\text{HY}} = \sum_{j=1}^{N_{\text{REV}}} NF_{\text{out}}(\text{REV}_j).$$

For a suitable comparison of the fluxes, the fluxes through the capillaries in the fully discrete method have to be averaged in the same sense as for the hybrid approach. Therefore, we can similarly define the net flux NF_{cap} for the REV_j as the sum of the fluxes through the boundary capillaries; namely,

$$NF_{\text{cap}}(\text{REV}_j) = \sum_{\mathbf{x}_k \in \partial\Lambda_{\text{C}} \cap \partial\text{REV}_j \cap \partial\Omega} MF(\mathbf{x}_k).$$

Then, the inflow $NF_{\text{cap,in}}$ and outflow $NF_{\text{cap,out}}$ through the REV_j can be defined analogously to (4.1) and (4.2). The total inflow $MF_{\text{cap,in}}^{\text{FD}}$ and outflow $MF_{\text{cap,out}}^{\text{FD}}$ through the capillaries for the fully discrete model can be defined similarly to (4.3). The mass fluxes between capillaries and tissue are denoted by $MF_{\text{cap,t}}^{\text{FD}}$ for the fully discrete model and by $MF_{\text{cap,t}}^{\text{HY}}$ for the hybrid model. Again, we compute only net fluxes for each REV following a procedure similar to that for the blood fluxes described above. In case of the hybrid model, we compute the net flux in an REV_j by

$$NF_{\text{cap,t}}^{\text{HY}}(\text{REV}_j) = \frac{\rho_{\text{int}} L_{\text{cap}} S_j}{|\text{REV}_j|} \int_{\text{REV}_j} (p^{\text{t}}(\mathbf{x}) - p^{\text{cap}}(\mathbf{x})) - (\pi_p - \pi_{\text{int}}) d\mathbf{x}.$$

Defining the net inflow flux $NF_{\text{cap,t}}^{\text{HY,in}}(\text{REV}_j)$ and outflow flux $NF_{\text{cap,t}}^{\text{HY,out}}(\text{REV}_j)$ as in the previous cases, the total inflow is given by

$$(4.4) \quad MF_{\text{cap,t}}^{\text{HY,in}} = \sum_{j=1}^{N_{\text{REV}}} NF_{\text{cap,t}}^{\text{HY,in}}(\text{REV}_j),$$

and the total outflow is calculated as the sum of the net outflows.

For the fully discrete model, we compute the net flow in REV_j as follows:

$$NF_{\text{cap,t}}^{\text{FD}}(\text{REV}_j) = \rho_{\text{int}} \cdot 2\pi L_{\text{cap}} \sum_{k \in \Lambda_{\text{C},j}} R_k \int_{\Lambda_k} (\bar{p}^{\text{t}} - p^{\text{v}}) - (\pi_p - \pi_{\text{int}}) dS.$$

As in this case of the hybrid model, the total inflow is given as in (4.4). Having these definitions at hand, we first compute the mass fluxes for the fully discrete model. Using these values, we determine the values of the parameter α in (3.10) such that the following objective functions are minimized:

$$f_1(\alpha) = \sqrt{\sum_{\beta} \sum_{\gamma} \frac{1}{2} (MF_{\beta,\gamma}^{\text{HY}} - MF_{\beta,\gamma}^{\text{FD}})^2}$$

for $\beta \in \{\text{LV}, \text{cap}\}$ and $\gamma \in \{\text{in}, \text{out}\}$, and

$$f_2(\alpha) = \sqrt{\frac{1}{2} (MF_{\text{LV,in}}^{\text{HY}} - MF_{\text{LV,in}}^{\text{FD}})^2}.$$

The results obtained with the hybrid model strongly depend on the value of α in

(3.10), as we can deduce from Figure 10, where both objective functions f_1 and f_2 are plotted with respect to the parameter α . For the objective function f_2 , it is easy to identify the minimum at $\alpha = 0.4$, while for f_1 the minimum is attained at $\alpha = 0.46$. The choice between these two values of α is made comparing the fluxes listed in Table 2, where we report the fluxes obtained on the finest level for both the fully discrete (FD) and the hybrid (HY) models (details to the mesh refinements are postponed to section 4.4). The results for the latter model are provided for $\alpha \in \{0.2, 0.4, 0.46, 0.9\}$. We can observe a good agreement between the hybrid and the fully discrete models, in particular with respect to the inflow due to the larger vessels, if $\alpha = 0.4$ is chosen. The major differences in the fluxes consist in the contributions of the homogenized capillaries. In fact, using the hybrid model, the mass fluxes into the capillary continuum and out of the capillary continuum are significantly overestimated compared to those of the fully discrete model. On the other hand, choosing $\alpha = 0.46$ yields an overall better agreement with the fully discrete model because all four fluxes are optimized at the same time, but not a single quantity is as well approximated as for $\alpha = 0.4$. Moreover, due to the fact that in a small neighborhood of the minimum, the function f_1 is relatively flat, the difference between $|f_1(0.4) - f_1(0.46)|$ is about $0.141 \mu\text{g/s}$. For completeness, we report the fluxes for $\alpha = 0.2$ and $\alpha = 0.9$ as well as show by how much these results differ from the solution of the fully discrete model. Therefore, for the rest of the paper, we proceed by comparing the fully discrete model with the hybrid model, where we fixed $\alpha = 0.4$ in (3.10).

Finally, to validate the numerical discretization of the hybrid model, we report in Figure 11 the numerical mass fluxes, where each plot of the flux is calculated with respect to the mesh refinement. It can be seen that for all the quantities reported, the curves plotted are approaching asymptotic values, as the mesh is refined. This behavior demonstrates that the mass fluxes obtained at the finest level and reported in Table 2 are representative for the hybrid model.

4.4. Comparison of the REV pressures. After comparing the mass fluxes obtained by the two modeling approaches, we proceed with the comparison of the REV pressures within the tissue and the capillary bed. For the hybrid model, the averaged pressure $p_{(j),\text{HY}}^{\text{cap}}$ in the capillaries for the REV $_j$ is given by the definition (3.9), while

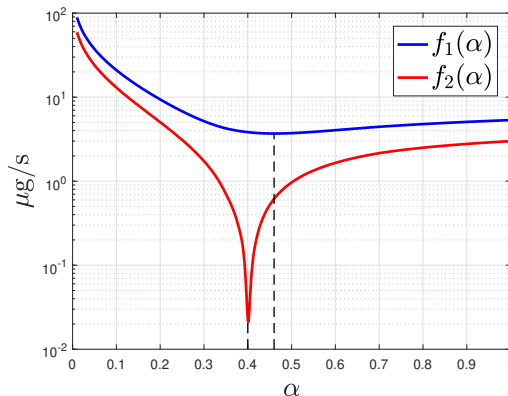


FIG. 10. Graphs of the objective functions f_1 and f_2 . For f_1 , the minimum is reached at $\alpha = 0.46$, while, for f_2 , it can be seen at first glance that the minimum is attained at $\alpha = 0.4$.

TABLE 2

Mass fluxes at the boundaries and interfaces of the vascular system. All the fluxes that are presented in this table are given in $\mu\text{g/s}$. For the hybrid method, the fluxes reported are obtained for different α .

	Large vessels		Capillary bed		Tissue
Method	$MF_{LV,in}$	$MF_{LV,out}$	$MF_{cap,in}$	$MF_{cap,out}$	$MF_{cap,t}$
FD	9.80161	10.4964	1.30573	0.61093	$2.54991 \cdot 10^{-3}$
HY $_{\alpha=0.4}$	9.79829	7.80573	2.04311	4.03567	$1.10565 \cdot 10^{-3}$
HY $_{\alpha=0.46}$	8.89951	7.14353	1.87204	3.62801	$1.04549 \cdot 10^{-3}$
HY $_{\alpha=0.2}$	16.9280	13.2730	2.86975	6.52477	$1.48711 \cdot 10^{-3}$
HY $_{\alpha=0.9}$	5.87650	4.95714	1.17063	2.08998	$0.78677 \cdot 10^{-3}$

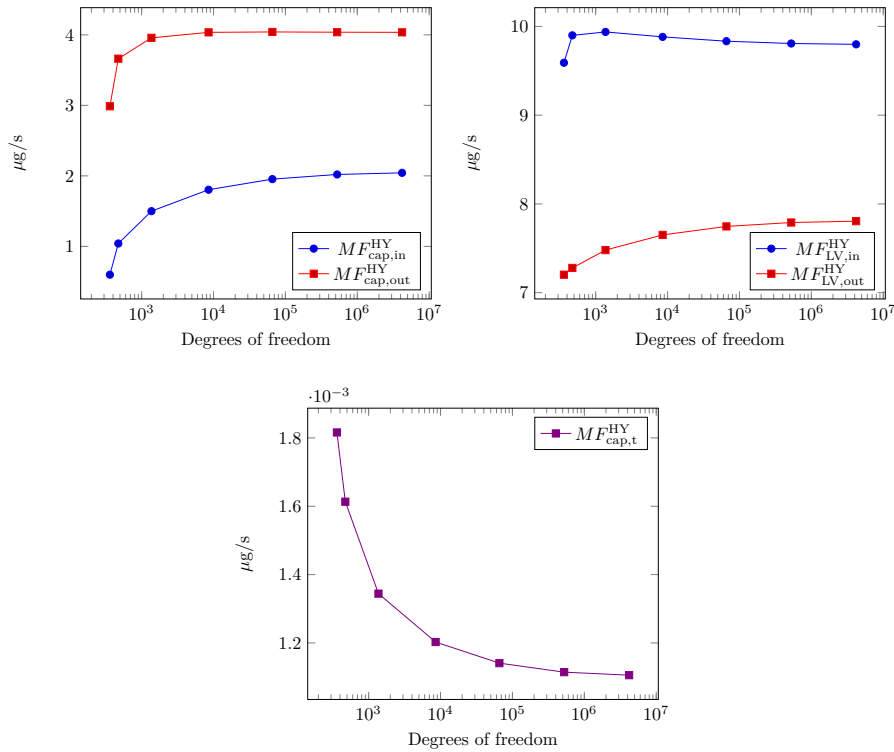


FIG. 11. Behavior of the mass fluxes for the hybrid approach with respect to the number of degrees of freedom. At the top, the fluxes at the boundaries of the capillaries and of the large vessels are reported. At the bottom, the total net flux from the capillary bed into the tissue for the hybrid approach is presented.

the average pressure in the tissue is defined as

$$(4.5) \quad p_{(j),HY}^t = \frac{1}{|\text{REV}_j|} \int_{\text{REV}_j} p^t(x) dx.$$

In case of the fully discrete model, we again use (4.5) to determine the REV pressure within the tissue and label this value by $p_{(j),FD}^t$. The REV pressure for the capillaries

with respect to an REV_{*j*} is approximated by

$$p_{(j),\text{FD}}^{\text{cap}} = \frac{1}{|\Lambda_{\text{C},j}|} \int_{\Lambda_{\text{C},j}} p^v(x) dx.$$

Furthermore, for the REV_{*j*} we define the relative pressure error E_r^{cap} in the capillaries and E_r^{t} in the tissue as

$$E_r^\beta(j) = \frac{|p_{(j),\text{HY}}^\beta - p_{(j),\text{FD}}^\beta|}{p_{(j),\text{HY}}^\beta}, \quad \beta \in \{\text{cap}, \text{t}\}.$$

The results obtained by means of the hybrid and fully discrete methods are reported for each REV in Table 3, together with the numeration in the mesh and the center of each REV. The average difference between the pressures obtained with the hybrid method and the fully discrete method is given by approximately 537.08 Pa (corresponding to 4.03 mmHg) for the capillaries, while the average difference within the tissue is given by approximately 316.27 Pa (corresponding to 2.37 mmHg). These values yield an average relative error of the pressures between the hybrid model and the fully discrete model of approximately $\overline{E_r^{\text{cap}}} = 11.37\%$ in the capillaries and of $\overline{E_r^{\text{t}}} = 13.97\%$ in the tissue.

TABLE 3
Averaged REV-pressures in the capillaries and in the tissue.

REV		$p_{(j)}^{\text{cap}}$ [Pa]			$p_{(j)}^{\text{t}}$ [Pa]		
<i>j</i>	Center [mm]	HY	FD	E_r^{cap}	HY	FD	E_r^{t}
1	(0.284, 0.284, 0.542)	5107.77	4535.61	11.20%	2400.12	1972.80	17.80%
2	(0.852, 0.284, 0.542)	5217.07	4704.37	9.83%	2465.14	2027.71	17.74%
3	(0.284, 0.852, 0.542)	5002.77	4658.86	6.87%	2325.75	1961.99	15.64%
4	(0.852, 0.852, 0.542)	5041.25	4447.64	11.77%	2392.00	1939.18	18.93%
5	(0.284, 0.284, 1.623)	4843.99	5465.34	12.83%	2156.06	2469.00	14.51%
6	(0.852, 0.284, 1.623)	5041.86	5425.96	7.62%	2295.94	2440.22	6.28%
7	(0.284, 0.852, 1.623)	3789.44	4637.19	22.37%	1847.50	2192.57	18.68%
8	(0.852, 0.852, 1.623)	4960.14	4539.09	8.49%	2178.97	2132.44	2.14%

Finally, in Table 4 we report the average relative errors $\overline{E_r^{\text{cap}}}$ and $\overline{E_r^{\text{t}}}$ of the hybrid model with mesh refinement. These errors are calculated with respect to the REV pressures obtained by the fully discrete model on the finest mesh, i.e., the values reported in Table 3 in the corresponding columns. Table 4 suggests that the errors $\overline{E_r^\beta}$ converge to a fixed value. The remaining error can be considered as the modeling error arising from the homogenization.

If we calculate the solution of the hybrid model on the mesh with $16 \times 16 \times 16$ elements in both the capillaries and tissue for a total of 8538 degrees of freedom, we obtain that the average relative errors differ by less than 1% from the average relative errors on the finest mesh. In this situation, we can assert that the modeling error dominates the discretization error, and thus the obtained pressures can be considered as representative for the hybrid model. On the other hand, the relative error for the pressure in the fully discrete model is already less than 1% on the coarsest mesh, where the elements coincide with the REV_s. However, in this case the linear system still has 12995 degrees of freedom in the network and 8 in the tissue. Therefore, compared with the fully discrete model, a smaller linear system can be solved to obtain representative values for the fluxes and pressures in the hybrid model. This

reduction in the number of degrees of freedom is expected to become more sensible if a larger system is considered.

TABLE 4

Averaged relative errors of the REV-pressures in the capillaries and in the tissue with respect to the degrees of freedom (dofs).

dofs	$\overline{E_r^{\text{cap}}}$	$\overline{E_r^t}$
362	16.20%	22.30%
474	14.15%	17.70%
1370	12.71%	15.51%
8538	11.95%	14.56%
65882	11.58%	14.17%
524634	11.42%	14.02%
4194650	11.37%	13.97%

4.5. Sensitivity analysis of α for different boundary conditions. In this section, we study the influence of the boundary conditions on the parameter α defined in (3.10). Considering the results reported in Table 2, one can conclude that the arterioles and venules significantly determine the pressure and velocity fields within the microvascular system. Therefore, we vary the pressures at the boundary of these vessels as follows. Let us denote by \overline{p}_a and \overline{p}_v the average boundary pressure of the arterioles and of the venules, respectively. For the experiment setting considered here, the difference

$$\delta = |\overline{p}_v - \overline{p}_a|$$

amounts to approximately 5000 Pa (corresponding to 37.5 mmHg). For all

$$i \in \{-10\%, \dots, -1\%, 0\%, 1\%, \dots, 10\%\},$$

we add the pressure $\frac{1}{2}\delta \cdot i$ to each boundary node corresponding to an arteriole, while at the venous boundary nodes, we subtract the same quantity. This yields a variation in the average pressure difference by the fraction i of δ . For each new network, the optimization process described in section 4.3 is conducted, and the resulting graphs of the objective functions f_1 and f_2 have the same shape as in Figure 10. Following the same strategy described above, only the optimal α for the objective function f_2 is considered and reported in Table 5.

If the average pressure difference is reduced, the optimal α is subject to relatively small variations. On the other hand, if δ becomes larger, the deviations from $\alpha = 0.4$ become larger. However, as we can observe in Figure 10, a small deviation from the optimal α yields a sensible difference in the flux $MF_{LV, \text{in}}$. Therefore, a single α cannot be determined in advance and used for other samples with different data; the calibration of α has to be repeated for every new experimental setting.

5. Concluding remarks. In this work, we have presented a hybrid model for simulating blood flow through networks at the level of microcirculation. The presented model is based on 1D flow models for the larger vessels and on homogenization techniques for the capillaries and the tissue. Thereby, the capillaries and the tissue are modeled as 3D coupled porous media resulting in a double 3D continua approach for simulating flows within both systems. In order to validate the simulation results obtained by our hybrid model, we have generated a reference solution by means of a fully discrete 3D–1D coupled model. Here, the complete vascular network is resolved

TABLE 5

Optimal α values for the cases in which the average pressure difference δ is varied by the percentage i .

i [%]	α
-10, -9 - 8 - 7, -6, -4, -3, -2	0.41
-5	0.42
-1, 0, +1	0.4
+2	0.38
+3, +4	0.39
+5, +6, +7	0.37
+8, +9, +10	0.36

by 1D flow models, and only the flow within the tissue is considered as a porous medium flow.

For the comparison criteria between the two models, we have chosen mass fluxes at the boundaries of the microvascular system and averaged pressures for each REV. If the parameter α in (3.10) is chosen appropriately, our simulation results showed that the fluxes at the inlets and outlets of the larger vessels obtained with our hybrid model coincide in a satisfactory manner with the corresponding fluxes obtained solving the fully discrete model. On the other hand, the fluxes through the capillaries are overestimated by the hybrid model. Furthermore, the net mass flux between the tissue and the capillaries is approximately 2.3 times higher for the fully discrete model than for the hybrid model. Regarding the averaged pressures for each REV, the simulations showed that the pressures obtained with the hybrid model differ, on average, by approximately 4 mmHg in the capillaries and by approximately 2.37 mmHg in the tissue from the solution of the fully discrete model. A more thorough comparison with respect to the reduction of the computational cost will be the subject of future work. For this purpose, a larger tissue sample should be examined. Additionally, we investigated the influence of different boundary conditions on the optimal parameter α . Despite the fact that α varies only slightly, the results suggest that it may be necessary to calibrate α for every experimental setting to obtain accurate approximations of the mass fluxes provided by the fully discrete model. Similarly, in [43] a parameter has to be optimized as well to model the flux between the different vessel types. These observations suggest that, in the context of hybrid models for microvasculature, different unknown parameters occur whose value is not known a priori. As a consequence, further investigations are required to improve the hybrid modeling approach. In particular, it would be of great interest to determine whether a combination of such parameters exists that can be applied to different settings and provide accurate results.

Considering other works regarding upscaling of capillary structures, such as [34], we obtained comparable results. In [34], the authors obtained permeabilities in the order of 10^{-14} m², i.e., approximately 5 times larger values than those depicted in Figure 9. However, having a closer look at the data, one can observe that in [34] the radius of the capillaries is around 3 μ m, while in our experiment the radius of the capillaries ranges between 1.6 μ m and 7 μ m, which explains the difference. Regarding the choice of the parameter R_T , the threshold 7 μ m is in good agreement with the morphological values listed in [13, Table 1].

A limitation of our hybrid model consists in the determination of the parameter α . In this paper, we employed the solution of the fully discrete model to tune the parameter α in order to optimize certain fluxes. A way to make a more independent

definition of α may involve a precise computation of the quantities $K_v^{(j)}$ and $\ell_c^{(kj)}$ in (3.9). Furthermore, a better approximation of the permeabilities of the homogenized system may be necessary, particularly if larger systems are considered. We also point out that the hybrid model we presented allows one to compute only net fluxes.

A clear advantage of the hybrid model is the fact that only mesoscale data are required to parametrize the model, whereas microscale data are necessary for fully discrete models. This holds for boundary data as well as for model parameters. Furthermore, we have provided tools to analyze homogenized models systematically that can be used to verify other upscaling strategies.

Future work in this field might be concentrated on coupling the new hybrid model for blood flow with transport models for therapeutic agents and other substances such that cancer therapies like hyperthermia can be simulated. A further interesting issue that could be studied by means of the hybrid model is enhancing existing flow models for whole organs or part of organs such that the diagnosis techniques for clinical applications can be improved.

Acknowledgments. We gratefully acknowledge the authors of [40] and, in particular, Prof. Bruno Weber and Prof. Patrick Jenny for providing the data set to the vascular network considered in this paper.

REFERENCES

- [1] J. BEAR, *Dynamics of Fluids in Porous Media*, Courier Corporation, North Chelmsford, MA, 2013.
- [2] M. BLATT AND P. BASTIAN, *The iterative solver template library*, in International Workshop on Applied Parallel Computing, Springer, New York, 2006, pp. 666–675.
- [3] M. BLATT AND P. BASTIAN, *On the generic parallelisation of iterative solvers for the finite element method*, Internat. J. Comput. Sci. Engrg., 4 (2008), pp. 56–69.
- [4] M. BLATT, A. BURCHARDT, A. DEDNER, C. ENGWER, J. FAHLKE, B. FLEMISCH, C. GERSBACHER, C. GRÄSER, F. GRUBER, C. GRÜNINGER, ET AL., *The distributed and unified numerics environment, version 2.4*, Arch. Numer. Software, 4 (2016), pp. 13–29.
- [5] D. BOAS, S. JONES, A. DEVOR, T. HUPPERT, AND A. DALE, *A vascular anatomical network model of the spatio-temporal response to brain activation*, Neuroimage, 40 (2008), pp. 1116–1129.
- [6] L. CATTANEO AND P. ZUNINO, *A computational model of drug delivery through microcirculation to compare different tumor treatments*, Internat. J. Numer. Methods Biomed. Engrg., 30 (2014), pp. 1347–1371.
- [7] C. D'ANGELO, *Multi Scale Modelling of Metabolism and Transport Phenomena in Living Tissues*, Ph.D. Thesis, EPFL, Lausanne, Switzerland, 2007.
- [8] C. D'ANGELO, *Finite element approximation of elliptic problems with Dirac measure terms in weighted spaces: Applications to one- and three-dimensional coupled problems*, SIAM J. Numer. Anal., 50 (2012), pp. 194–215, <https://doi.org/10.1137/100813853>.
- [9] C. D'ANGELO AND A. QUARTERONI, *On the coupling of 1D and 3D diffusion-reaction equations: Application to tissue perfusion problems*, Math. Models Methods Appl. Sci., 18 (2008), pp. 1481–1504.
- [10] A. DESPOPOULOS AND S. SILBERNAGL, *Color Atlas of Physiology*, Thieme, Stuttgart, Germany, 2003.
- [11] M. DEWHIRST AND T. SECOMB, *Transport of drugs from blood vessels to tumour tissue*, Nature Rev. Cancer, 17 (2017), pp. 738–750.
- [12] W. EL-BOURI AND S. PAYNE, *Multi-scale homogenization of blood flow in 3-dimensional human cerebral microvascular networks*, J. Theoret. Biol., 380 (2015), pp. 40–47.
- [13] W. EL-BOURI AND S. PAYNE, *Investigating the effects of a penetrating vessel occlusion with a multi-scale microvasculature model of the human cerebral cortex*, NeuroImage, 172 (2018), pp. 94–106.
- [14] K. ERBERTSEDER, J. REICHOLD, B. FLEMISCH, P. JENNY, AND R. HELMIG, *A coupled discrete/continuum model for describing cancer-therapeutic transport in the lung*, PLoS One, 7 (2012), e31966.

- [15] R. FAHRAEUS AND T. LINDQVIST, *The viscosity of the blood in narrow capillary tubes*, Amer. J. Physiol., 96 (1931), pp. 562–568.
- [16] L. FORMAGGIA, F. NOBILE, A. QUARTERONI, AND A. VENEZIANI, *Multiscale modelling of the circulatory system: A preliminary analysis*, Comput. Vis. Sci., 2 (1999), pp. 75–83.
- [17] L. FORMAGGIA, A. QUARTERONI, AND A. VENEZIANI, *Cardiovascular Mathematics: Modeling and Simulation of the Circulatory System*, MS&A 1, Springer-Verlag, Milan, Italy, 2009.
- [18] Y. FUNG AND B. ZWEIFACH, *Microcirculation: Mechanics of blood flow in capillaries*, Ann. Rev. Fluid Mech., 3 (1971), pp. 189–210.
- [19] I. G. GJERDE, K. KUMAR, J. M. NORDBOTTEN, AND B. WOHLMUTH, *Splitting Method for Elliptic Equations with Line Sources*, preprint, <https://arxiv.org/abs/1810.12979>, 2018.
- [20] R. HELMIG, *Multiphase Flow and Transport Processes in the Subsurface: A Contribution to the Modeling of Hydrosystems*, Springer-Verlag, New York, 1997.
- [21] K. HOLTER, B. KEHLET, A. DEVOR, T. SEJNOWSKI, A. DALE, S. OMHOLT, O. OTTERSEN, E. NAGELHUS, K.-A. MARDAL, AND K. PETERSEN, *Interstitial solute transport in 3D reconstructed neuropil occurs by diffusion rather than bulk flow*, Proc. Natl. Acad. Sci. USA, 114 (2017), pp. 9894–9899.
- [22] R. HSU AND T. W. SECOMB, *A Green’s function method for analysis of oxygen delivery to tissue by microvascular networks*, Math. Biosci., 96 (1989), pp. 61–78.
- [23] Y. ITURRIA-MEDINA, R. SOTERO, P. TOUSSAINT, J. MATEOS-PÉREZ, A. EVANS, M. WEINER, P. AISEN, R. PETERSEN, C. JACK, W. JAGUST, ET AL., *Early role of vascular dysregulation on late-onset Alzheimer’s disease based on multifactorial data-driven analysis*, Nature Commun., 7 (2016), 11934.
- [24] A. KHALED AND K. VAFAI, *The role of porous media in modeling flow and heat transfer in biological tissues*, Internat. J. Heat Mass Transfer, 46 (2003), pp. 4989–5003.
- [25] T. KÖPPL, E. VIDOTTO, AND B. WOHLMUTH, *A local error estimate for the Poisson equation with a line source term*, in Numerical Mathematics and Advanced Applications, ENUMATH 2015, Springer, New York, 2016, pp. 421–429.
- [26] T. KÖPPL, E. VIDOTTO, B. WOHLMUTH, AND P. ZUNINO, *Mathematical modeling, analysis and numerical approximation of second-order elliptic problems with inclusions*, Math. Models Methods Appl. Sci., 28 (2018), pp. 953–978.
- [27] J. LEVICK, *Capillary filtration-absorption balance reconsidered in light of dynamic extravascular factors*, Exp. Physiol., 76 (1991), pp. 825–857.
- [28] J. R. LEVICK AND C. C. MICHEL, *Microvascular fluid exchange and the revised starling principle*, Cardiovascular Res., 87 (2010), pp. 198–210.
- [29] S. MAHJOOB AND K. VAFAI, *Analytical characterization of heat transport through biological media incorporating hyperthermia treatment*, Internat. J. Heat Mass Transfer, 52 (2009), pp. 1608–1618.
- [30] M. NABIL AND P. ZUNINO, *A computational study of cancer hyperthermia based on vascular magnetic nanoconstructs*, Royal Soc. Open Sci., 3 (2016), 160287.
- [31] D. NOTARO, L. CATTANEO, L. FORMAGGIA, A. SCOTTI, AND P. ZUNINO, *A mixed finite element method for modeling the fluid exchange between microcirculation and tissue interstitium*, in Advances in Discretization Methods, Springer, New York, 2016, pp. 3–25.
- [32] R. PENTA, D. AMBROSI, AND A. QUARTERONI, *Multiscale homogenization for fluid and drug transport in vascularized malignant tissues*, Math. Models Methods Appl. Sci., 25 (2015), pp. 79–108.
- [33] A. PETRYK, A. GIUSTINI, R. GOTTESMAN, P. KAUFMAN, AND P. HOOPES, *Magnetic nanoparticle hyperthermia enhancement of cisplatin chemotherapy cancer treatment*, Internat. J. Hyperthermia, 29 (2013), pp. 845–851.
- [34] M. PEYRONNETTE, Y. DAVIT, M. QUINTARD, AND S. LORTHOIS, *Multiscale modelling of blood flow in cerebral microcirculation: Details at capillary scale control accuracy at the level of the cortex*, PLoS One, 13 (2018), e0189474.
- [35] L. POSSENTI, S. DI GREGORIO, F. M. GEROSA, G. RAIMONDI, G. CASAGRANDE, M. L. COSTANTINO, AND P. ZUNINO, *A computational model for microcirculation including Fahraeus-Lindqvist effect, plasma skimming and fluid exchange with the tissue interstitium*, Internat. J. Numer. Methods Biomed. Engrg., 35 (2019), e3165.
- [36] A. PRIES AND T. SECOMB, *Making microvascular networks work: Angiogenesis, remodeling, and pruning*, Physiology, 29 (2014), pp. 446–455.
- [37] A. PRIES, T. SECOMB, AND P. GAEHTGENS, *Biophysical aspects of blood flow in the microvasculature*, Cardiovascular Res., 32 (1996), pp. 654–667.
- [38] A. PRIES, T. SECOMB, P. GAEHTGENS, AND J. GROSS, *Blood flow in microvascular networks. Experiments and simulation*, Circulation Res., 67 (1990), pp. 826–834.
- [39] A. QUARTERONI AND L. FORMAGGIA, *Mathematical modelling and numerical simulation of*

- the cardiovascular system*, in Handbook of Numerical Analysis, Handb. Numer. Anal. 12, North-Holland, Amsterdam, 2004, pp. 3–127.
- [40] J. REICHOLD, M. STAMPANONI, A. L. KELLER, A. BUCK, P. JENNY, AND B. WEBER, *Vascular graph model to simulate the cerebral blood flow in realistic vascular networks*, J. Cerebral Blood Flow Metabolism, 29 (2009), pp. 1429–1443.
- [41] T. ROOSE AND M. SWARTZ, *Multiscale modeling of lymphatic drainage from tissues using homogenization theory*, J. Biomech., 45 (2012), pp. 107–115.
- [42] R. SHIPLEY AND S. CHAPMAN, *Multiscale modelling of fluid and drug transport in vascular tumours*, Bull. Math. Biol., 72 (2010), pp. 1464–1491.
- [43] R. SHIPLEY, A. SMITH, P. SWEENEY, A. PRIES, AND T. SECOMB, *A hybrid discrete–continuum approach for modelling microcirculatory blood flow*, Math. Med. Biol., March (2019), <https://doi.org/10.1093/imammb/dqz006>.
- [44] S. STACKER AND M. ACHEN, *Emerging roles for VEGF-D in human disease*, Biomolecules, 8 (2018), p. 1.
- [45] E. H. STARLING, *On the absorption of fluids from the connective tissue spaces*, J. Physiology, 19 (1896), pp. 312–326.
- [46] K. H. STØVERUD, M. DARCIS, R. HELMIG, AND S. M. HASSANIZADEH, *Modeling concentration distribution and deformation during convection-enhanced drug delivery into brain tissue*, Transp. Porous Media, 92 (2012), pp. 119–143.
- [47] Y. TANG AND Y. HE, *Numerical modeling of fluid and oxygen exchanges through microcirculation for the assessment of microcirculation alterations caused by type 2 diabetes*, Microvascular Res., 117 (2018), pp. 61–73.
- [48] F. WATERMAN, L. TUPCHONG, R. NERLINGER, AND J. MATTHEWS, *Blood flow in human tumors during local hyperthermia*, Internat. J. Radiation Oncology* Biol.* Phys., 20 (1991), pp. 1255–1262.

Part III

Simulation of fluid injection into porous media

The objective of the last part is the analysis of hysteresis models for injection processes of fluids into a dry porous medium. Considering measurements obtained in context of water infiltration into a dry sand column, different features can be observed, which can not be explained by standard porous media equations. First of all, one notices that despite of the fact that there are no external sources a water saturation overshoot can be seen, which is increasing as the depth within the sandcolumn increases. Furthermore, it can be observed that the overshoots have the shape of a plateau. In order to model these phenomena, the standard equations for two-phase flow in porous media are extended by an ODE containing a parameter $\tau > 0$ to simulate the generation of saturation overshoots. In literature, this equation is referred to as " τ -term". The formation of plateaus is modelled by introducing for both the drainage and the imbibition process a main curve with respect to the permeabilities and the capillary pressure. In experiments it can be seen that the transition between the two processes is governed by curves called scanning curves. Thereby, one has to note that their shapes depend on the place of their origin. In order to account for this transition behaviour, hysteresis models are used. The following two chapters are concerned with the issue how the saturation overshoots look like for a given set of parameters.

Chapter 8:

Stable propagation of saturation overshoots for two-phase flow in porous media

In the first chapter of Part III, we use two different two-phase flow models to investigate under which conditions a given saturation overshoot is stable or how it behaves when it moves through the porous medium. In case of both models it is assumed in a first step that the total velocity is constant in space and time. To enforce a constant total velocity, we simplify the two phase flow equations by means of this assumption to a fractional flow formulation. The other model is based on the standard two-phase flow equations. Here, a constant total velocity is obtained by choosing appropriate boundary conditions. Both models use cubic spline curves, in order to describe the transition between drainage and imbibition curves. By means of the Rankine-Hugoniot conditions, we estimate the speed of the drainage and imbibition fronts to obtain some insight into the behaviour of a given overshoot. The analytical results are confirmed by several numerical tests. Finally, we use the second model, to simulate further infiltration problems, neglecting the restriction that the total velocity is constant in time.

Chapter 9:

Fronts in two-phase porous media flow problems: the effects of hysteresis and dynamic capillary

In the last chapter of this thesis, we derive as in the previous chapter a fractional flow formulation of the two-phase flow model assuming again that the total velocity is constant in space and time. Contrary to Chapter 8, we consider also the τ -term to model the formation of saturation overshoots. The hysteresis model we are using is not based on cubic splines, but the scanning curves are approximated

by straight lines. This type of hysteresis model is also called "playtype" hysteresis model. In order to analyse the model, we transform the fractional flow formulation into an ODE-system consisting of two equations. For this purpose, we use a travelling wave ansatz. The resulting ODE-system is analysed by means of different mathematical tools for dynamical systems, i.e., we identify the equilibrium points of the system and decide whether they are stable or not. By this, it can be determined whether two equilibrium points can be connected by a travelling wave or a rarefied wave. The analytical results are supported by numerical simulation results.

8 Stable propagation of saturation overshoots for two-phase flow in porous media

Bibliographic note: The content of this chapter is based on the following original article: M. Schneider, T. Köppl, R. Helmig, R. Steinle and R. Hilfer (2018): Stable Propagation of Saturation Overshoots for Two-Phase Flow in Porous Media. *Transport in Porous Media*, 121(3), pages: 621-641, with courtesy of Springer Netherlands.

Stable Propagation of Saturation Overshoots for Two-Phase Flow in Porous Media

M. Schneider¹  · T. Köppl¹ · R. Helmig¹ · R. Steinle² · R. Hilfer²

Received: 21 February 2017 / Accepted: 23 November 2017 / Published online: 5 December 2017
© Springer Science+Business Media B.V., part of Springer Nature 2017

Abstract Propagation of saturation overshoots for two-phase flow of immiscible and incompressible fluids in porous media is analyzed using different computational methods. In particular, it is investigated under which conditions a given saturation overshoot remains stable while moving through a porous medium. Two standard formulations are employed in this investigation, a fractional flow formulation and a pressure–saturation formulation. Neumann boundary conditions for pressure are shown to emulate flux boundary conditions in homogeneous media. Gravity driven flows with Dirichlet boundary conditions for pressure that model infiltration into heterogeneous media with position-dependent permeability are found to exhibit pronounced saturation overshoots very similar to those seen in experiment.

Keywords Two-phase flow · Hysteresis · Overshoot · Stability

M. Schneider
martin.schneider@iws.uni-stuttgart.de

T. Köppl
tobias.koepl@iws.uni-stuttgart.de

R. Helmig
rainer.helmig@iws.uni-stuttgart.de

R. Steinle
rouven.steinle@icp.uni-stuttgart.de

R. Hilfer
hilfer@icp.uni-stuttgart.de

¹ Lehrstuhl für Hydromechanik und Hydrosystemmodellierung, Pfaffenwaldring 61, 70569 Stuttgart, Germany

² Institut für Computerphysik, Allmandring 3, 70569 Stuttgart, Germany

1 Introduction

Flow processes in porous media involving two immiscible fluids can be found in different industrial applications and subsurface hydrosystems (Dullien 1992). The movement of fluids through filter systems or the infiltration of ink into paper, for example, can be described by a two-phase flow model (Middendorf 2000). In the unsaturated part of a subsurface system, the flow behavior of the water and air phase governs the transport of contaminants such as pesticides or chemicals used within fracking processes (Boudet et al. 2014; Charbeneau 2000). Furthermore, the water uptake of root networks from the surrounding soil can be modeled by a two-phase flow system (Schröder et al. 2012).

In order to get a better understanding of two-phase flow through porous media, several experiments have been performed. Infiltration experiments on constant flux imbibition into a dry porous medium have revealed that the water saturation exhibits a non-monotone and fluctuating profile with an overshoot region (DiCarlo 2004; Kalaydjian et al. 1992; Shiozawa and Fujimaki 2004). Figure 1 shows several overshoot profiles. The profiles seem to consist of an imbibition front followed by a drainage front together forming a saturation overshoot (DiCarlo 2004; Hilfer and Steinle 2014; Kalaydjian et al. 1992; Shiozawa and Fujimaki 2004).

Initiation and propagation of saturation overshoots have been long-standing challenges (Alt and Luckhaus 1983; Alt et al. 1984; Beliaev and Hassanizadeh 2001; Briggs and Katz 1966; Cueto-Felgueroso and Juanes 2009; DiCarlo 2004, 2013; DiCarlo et al. 2012; Eliassi and Glass 2001, 2002; Glass et al. 1989; Otto 1996; Shiozawa and Fujimaki 2004; Duijn et al. 2013, 2007; Xiong 2014; Youngs 1958). Existence of saturation overshoots have been excluded mathematically within established traditional equations for two-phase flow (DiCarlo et al. 2012; Egorov et al. 2003; Eliassi and Glass 2001; Fürst et al. 2009; Duijn et al. 2007). Many non-standard physical-mathematical models have been developed to predict the formation of saturation overshoots (see Xiong (2014) for a recent review). One approach models a hold-back-pile-up effect by extending the Richards equation with additional terms (Eliassi and Glass 2002). Static as well as dynamic overshoots appear in models that take the differ-

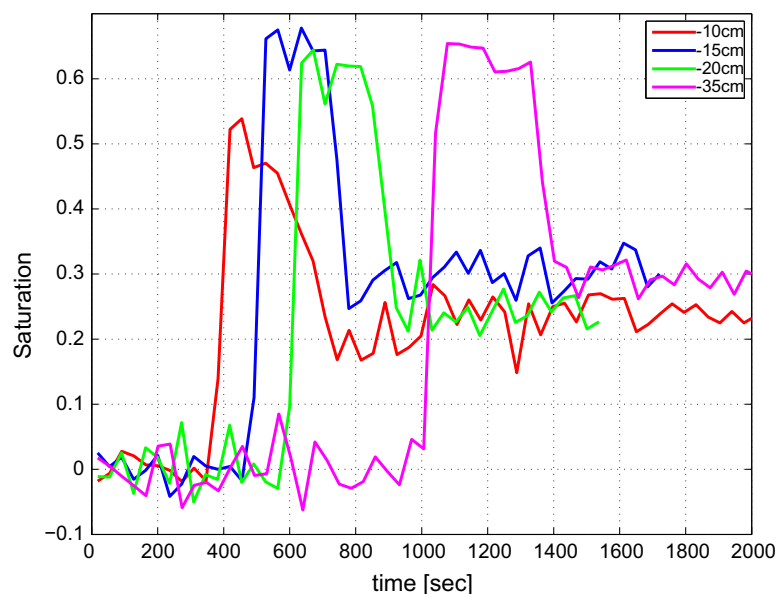


Fig. 1 Measurements of water saturations within several sand columns, during an infiltration experiment with a constant injection rate. The curves in the graph are reported at different depths and for different media. The curves seem to suggest that the water saturation curves exhibit overshoots containing a plateau (DiCarlo 2004; Fritz 2012) as predicted by traditional theory in Hilfer and Steinle (2014); Steinle and Hilfer (2016)

ence between percolating and nonpercolating fluids parts explicitly into account (Doster et al. 2010; Hilfer et al. 2012). A further widespread modeling concept utilizes dynamic extensions of the capillary pressure to enforce saturation overshoots (Koch et al. 2013; Lamacz et al. 2011; Manthey et al. 2008; Nieber et al. 2005; Rätz and Schweizer 2014; Duijn et al. 2007). Recently, it was shown that the traditional theory reproduces quantitatively the propagation of saturation overshoot (Steinle and Hilfer 2017).

In this paper, we are not interested in the formation process of a saturation overshoot. Instead we want to investigate under which conditions (initial conditions, boundary conditions, porous media parameters, etc.) a given saturation overshoot remains stable as it propagates through a homogeneous or heterogeneous porous medium. More specifically, the objective of this paper is twofold. In Hilfer and Steinle (2014); Steinle and Hilfer (2016, 2017) it was shown that a stable propagation of saturation overshoots can be observed in a traditional fractional flow simulation using flux boundary conditions. The first objective is to confirm or disprove this result for homogeneous media in a pressure–saturation formulation with pressure boundary conditions. The second objective is to extend the investigation to gravity driven infiltration with Dirichlet pressure conditions, as well as to heterogeneous porous media.

All results in this work pertain to the flow of two immiscible and incompressible fluids in a rigid porous medium. In Sect. 2, we describe the governing flow equations in two formulations, the hysteresis model, the initial and the boundary conditions. In Sect. 3 the stability analysis and the numerical methods are presented. Finally in Sect. 4 the results for homogeneous media are given in Sect. 4.1 while the results for inhomogeneous media are found in Sect. 4.2.

2 Mathematical Model

In this section, we present the standard physical-mathematical model which can be used to describe infiltration experiments with a constant injection rate q_w [m^3/s] into a porous medium. We denote the absolute permeability of the porous medium by K [m^2] and the porosity by ϕ [–]. An experimental setup that can be characterized by this parameter set is the injection of water into a sand column which has a height L [m] (see Fig. 2).

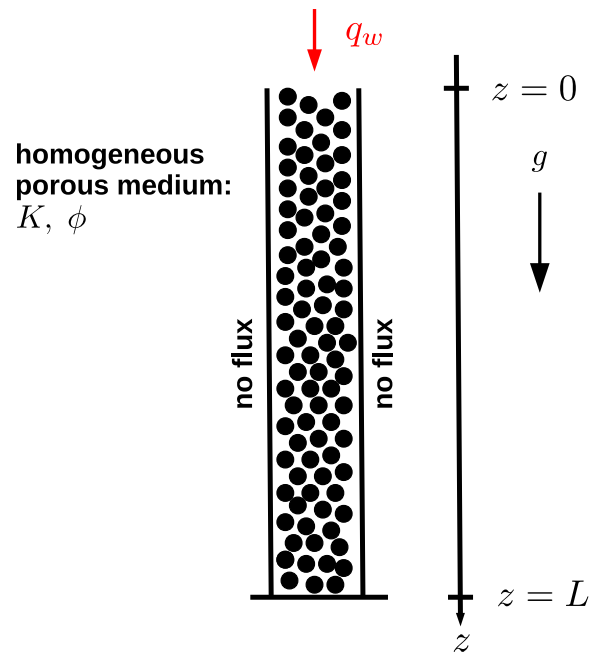
2.1 Governing Equations

For simplicity, we assume that the walls of the sand column in Fig. 2 are impermeable for the injected fluid and that the saturation profile is almost constant across the section area of the column. Under these circumstances, it is sufficient to describe the flow within the sand column by one-dimensional models. These models are defined on an interval $(0, L)$ which parameterizes the main axis of the column. Without loss of generality, it is further assumed that this axis is parallel to the direction of gravity and identical with the z -axis of a Cartesian coordinate system. It is assumed that its origin is located in the middle of the inlet of the sand column (see Fig. 2). The two-phase flow process within the porous medium consists of a wetting phase $\alpha = w$ and a non-wetting phase $\alpha = n$.

2.1.1 Pressure–Saturation Formulation

Let $z \in [0, L] \subset \mathbb{R}$ denote the position and $t \geq 0$ the time variable. The saturation $S_w(z, t)$ of the wetting phase and the pressure $p_n(z, t)$ of the non-wetting phase are chosen as primary

Fig. 2 Setup of an infiltration experiment. At the top of a column having the height L a fluid is injected, where the injection rate is constant and denoted by q_w



unknowns. If no external source or sink terms are given, the mass balance of each phase α having saturation $S_\alpha(z, t)$, velocity $v_\alpha(z, t)$ and density $\rho_\alpha(z, t)$ reads as follows (Helmig 1997; Hilfer and Steinle 2014):

$$\phi \frac{\partial (\rho_\alpha S_\alpha)}{\partial t} + \frac{\partial (\rho_\alpha v_\alpha)}{\partial z} = 0, \quad \alpha \in \{w, n\}, \quad z \in (0, L), \quad t > 0. \quad (1)$$

v_α is given by the generalized Darcy law:

$$v_\alpha = -\frac{k_{r\alpha}(S_w)}{\mu_\alpha} K \left(\frac{\partial p_\alpha}{\partial z} - \rho_\alpha g \right), \quad \alpha \in \{w, n\}, \quad (2)$$

where μ_α [Pa · s] is the viscosity. $k_{r\alpha}$ stands for the relative permeability function of each phase. By this, one can define the mobility of the phase α by:

$$\lambda_\alpha = \frac{k_{r\alpha}}{\mu_\alpha}, \quad \alpha \in \{w, n\}. \quad (3)$$

p_α [Pa] and g [m/s²] denote the pressure and the gravity constant, respectively. For simplicity, we assume that the two fluids are incompressible and set the densities to a constant value such that with $\alpha = w, n$

$$\rho_\alpha(z, t) \equiv \rho_\alpha \quad (4)$$

holds for all z and t . The system is closed by two constitutive relations. One of these relations is the saturation balance:

$$S_w + S_n = 1. \quad (5)$$

The second one describes the relation between the fluid pressures:

$$p_c(S_w(z, t)) = p_n(z, t) - p_w(z, t), \quad (6)$$

where $p_c(S_w)$ is a given capillary pressure–saturation model. Summarizing Eqs. (1)–(6), we obtain the following system of equations

$$\frac{\partial S_w}{\partial t} - \frac{\partial}{\partial z} \left(\lambda_w \frac{K}{\phi} \left(\frac{\partial p_w}{\partial z} - \rho_w g \right) \right) = 0, \quad z \in (0, L), \quad t > 0, \tag{7a}$$

$$-\frac{\partial S_w}{\partial t} - \frac{\partial}{\partial z} \left(\lambda_n \frac{K}{\phi} \left(\frac{\partial p_n}{\partial z} - \rho_n g \right) \right) = 0, \quad z \in (0, L), \quad t > 0, \tag{7b}$$

$$p_c - p_n + p_w = 0, \quad z \in (0, L), \quad t > 0, \tag{7c}$$

where the unknowns are S_w, p_w and p_n . The field S_n is then obtained from the constraint (5).

In experiments there is often a pump injecting fluid into the porous medium (as illustrated in Fig. 2). These experimental situations are usually modeled using the following fractional flow formulation.

2.1.2 Fractional Flow Formulation

The fractional flow formulation is obtained by reformulating the problem in terms of saturation $S_w(z, t)$, pressure $p_n(z, t)$, and total velocity $v(z, t)$ defined as

$$v(z, t) := v_w(z, t) + v_n(z, t) \tag{8}$$

$z \in [0, L], t \geq 0$. If $v > 0$, the fluid flows from the top to the bottom of the sand column (see Fig. 2). The unknowns v, p_n and S_w obey the coupled system

$$\frac{\partial v}{\partial z} = 0 \tag{9a}$$

$$\frac{\partial p_n}{\partial z} = \frac{\lambda_w}{\lambda_{to}} \left(\frac{\partial p_c}{\partial z} + \rho_w g \right) + \frac{\lambda_n}{\lambda_{to}} \rho_n g - \frac{v}{\lambda_{to} K} \tag{9b}$$

$$\phi \frac{\partial S_w}{\partial t} + \frac{\partial}{\partial z} \left\{ \frac{\lambda_w}{\lambda_{to}} \left[v + K \lambda_n (\rho_w - \rho_n) g + K \lambda_n \frac{\partial p_c}{\partial z} \right] \right\} = 0 \tag{9c}$$

where (4) was used and $\lambda_\alpha = \lambda_\alpha(S_w), p_c = p_c(S_w)$ with $\alpha = n, w, to$ are nonlinear functions of the water saturation. The symbol

$$\lambda_{to} = \lambda_w + \lambda_n \tag{10}$$

is the total mobility. The fractional flow function $f(S_w)$ is defined by Steinle and Hilfer (2016):

$$f(S_w) = \frac{1 + k_{rn}(S_w) \frac{\rho_w g K}{v \mu_n} \left(1 - \frac{\rho_n}{\rho_w} \right)}{1 + \frac{\mu_w}{\mu_n} \frac{k_{rn}(S_w)}{k_{rw}(S_w)}} \tag{11}$$

and depends on v . Solving (9a) and rewriting (9c) gives the system:

$$v(z, t) = v(t) \tag{12a}$$

$$\frac{\partial p_n}{\partial z} = \frac{\lambda_w}{\lambda_{to}} \left(\frac{\partial p_c(S_w)}{\partial z} + \rho_w g \right) + \frac{\lambda_n}{\lambda_{to}} \rho_n g - \frac{v(t)}{\lambda_{to} K} \tag{12b}$$

$$\frac{\partial S_w}{\partial t} + \frac{v(t)}{\phi} \frac{\partial}{\partial z} \left[f(S_w) - D(S_w) \frac{\partial S_w}{\partial z} \right] = 0 \tag{12c}$$

with $z \in [0, L]$, $t \geq 0$. The diffusion function $D(S_w)$ again depends on v . It is defined by Steinle and Hilfer (2016):

$$D(S_w) = - \frac{k_{rw}(S_w) \frac{K}{v\mu_w} p'_c(S_w)}{1 + \frac{\mu_n}{\mu_w} \frac{k_{rw}(S_w)}{k_{rn}(S_w)}} \quad (13)$$

with $p'_c = dp_c(S_w)/dS_w$. The system of equations (12) is incomplete, if $v(t)$ is considered to be unknown. When the total flux density $v(t)$ is unknown, it has to be computed as a part of the solution of (9).

The system of equations (12) is particularly useful for experiments in which a pump injects a total flux density $v(t)$ into the porous medium. In that case $v(t)$ is known and experimentally controlled. If $v(t)$ is known, then (12c) is solved for the saturation profile $S_w(z, t)$, and the result is inserted into (12b), to compute the pressure $p_n(z, t)$ by integration over z .

The pressure–saturation formulation (7) and the fractional flow formulation in (9) are equivalent. However, different primary variables and appropriate boundary conditions might be chosen. Before discussing initial and boundary conditions further, the constitutive functions and parameters need to be specified.

2.2 Modeling of Hysteresis

Following Hilfer and Steinle (2014) we consider two different relative permeability and capillary pressure functions of van Genuchten form (Luckner et al. 1989; Genuchten 1980) to account for the hysteresis between drainage and imbibition processes. A distinction between drainage and imbibition is achieved by introducing two sets of model parameters determining the shape of the corresponding functions:

$$\alpha_i, \beta_i, \gamma_i, K_{rw}^i, K_{rn}^i, S_{wr}^i, S_{nr}^i \text{ and } P_{b_i}, i \in \{im, dr\}. \quad (14)$$

$i = im$ abbreviates the term imbibition, while $i = dr$ represents the drainage process. The van Genuchten functions are given by:

$$k_{rw}^i(S_{e_i}) = K_{rw}^i \sqrt{S_{e_i}} \left[1 - \left(1 - S_{e_i}^{1/\alpha_i} \right)^{\alpha_i} \right]^2, \quad (15a)$$

$$k_{rn}^i(S_{e_i}) = K_{rn}^i \sqrt{1 - S_{e_i}} \left(1 - S_{e_i}^{1/\beta_i} \right)^{2\beta_i}, \quad (15b)$$

$$p_c^i(S_{e_i}) = P_{b_i} \left(S_{e_i}^{-1/\gamma_i} - 1 \right)^{1-\gamma_i}, \quad (15c)$$

where S_{e_i} is called effective saturation and is defined as follows:

$$S_{e_i} = \frac{S_w - S_{wr}^i}{1 - S_{wr}^i - S_{nr}^i}.$$

In the following subsection a scanning curve approach for hysteresis is outlined. The idea of this approach is to construct a cubic spline between the imbibition and drainage curve, when it is necessary to switch from drainage to imbibition or vice versa. This results in a smooth change between drainage and imbibition. For a general discussion and formulation of the presented hysteresis model, as well as a comparison with the simplistic hysteresis model used in Hilfer and Steinle (2014); Steinle and Hilfer (2016) the reader is referred to Steinle and Hilfer (2017).

2.2.1 Scanning Curve Approach

Let us consider a time interval $[t_n, t_{n+1}]$ with a duration of the stepsize $\Delta t = t_{n+1} - t_n$. The saturations for $t = t_n$ and $t = t_{n+1}$ are denoted by $S_w^{(n)}$ and $S_w^{(n+1)}$, respectively. Since we are using an implicit Euler method to integrate the pressure–saturation formulation in time, we require an iterative solver to determine the solution of the system of equations arising at every time step. The saturation produced by the k -th iteration is indicated by $S_w^{(n,k)}$. In order to decide, whether we have to define a drainage or imbibition process, we observe the sign of the time derivative in $\partial_t S_w$. Concerning the time interval $[t_n, t_{n+1}]$ this is done as follows: first of all, the time derivative is approximated by a finite difference quotient:

$$\partial_t S_w^{(n,k)}(z) \approx \frac{S_w^{(n,k)} - S_w^{(n)}}{\Delta t}, \quad z \in (0, L), \tag{16}$$

where $S_w^{(n,0)} = S_w^{(n)}$. Next we fix a parameter $\epsilon > 0$ and distinguish the cases:

- If $\partial_t S_w^{(n,k)}(z) > \epsilon$, we consider an imbibition process in $z \in (0, L)$.
- If $\partial_t S_w^{(n,k)}(z) < -\epsilon$, we consider a drainage process in $z \in (0, L)$.
- If $|\partial_t S_w^{(n,k)}(z)| \leq \epsilon$, we take for $z \in (0, L)$ over the process from the last time step and stay on the curve for drainage or imbibition, respectively.

If the process differs from the process of the last time step, a further parameter $\delta > 0$ is introduced. Using this parameter, we define the saturation $S_{w,\delta}^{(n)}$ by:

$$S_{w,\delta}^{(n)} = \begin{cases} S_w^{(n)} - \delta, & \text{if we switch from imbibition to drainage,} \\ S_w^{(n)} + \delta, & \text{if we switch from drainage to imbibition.} \end{cases}$$

Next, we compute a cubic spline G_{sc} connecting the points

$$\left(S_w^{(n)}, G_1 \left(S_w^{(n)} \right) \right) \text{ and } \left(S_{w,\delta}^{(n)}, G_2 \left(S_{w,\delta}^{(n)} \right) \right),$$

where the first derivatives of G_{sc} coincide with the first derivatives of G_1 and G_2 :

$$G'_1 \left(S_w^{(n)} \right) = G'_{sc} \left(S_w^{(n)} \right) \text{ and } G'_2 \left(S_{w,\delta}^{(n)} \right) = G'_{sc} \left(S_{w,\delta}^{(n)} \right).$$

Switching from imbibition to drainage the expressions G_1, G_2 are chosen from

$$(G_1, G_2) \in \left\{ \left(k_{rw}^{im}, k_{rw}^{dr} \right), \left(k_{rn}^{im}, k_{rn}^{dr} \right), \left(p_c^{im}, p_c^{dr} \right) \right\}$$

otherwise, we have:

$$(G_1, G_2) \in \left\{ \left(k_{rw}^{dr}, k_{rw}^{im} \right), \left(k_{rn}^{dr}, k_{rn}^{im} \right), \left(p_c^{dr}, p_c^{im} \right) \right\}.$$

The resulting splines for the relative permeabilities and the capillary pressure are denoted by k_{rw}^{sc}, k_{rn}^{sc} and p_c^{sc} . Finally, the new functions k_{rw}, k_{rn} and p_c within the iteration $k + 1$ are determined as follows: In the case of switching from imbibition to drainage it holds:

$$G \left(S_w^{(n,k+1)} \right) = \begin{cases} G_{im} \left(S_w^{(n,k+1)} \right), & \text{if } S_w^{(n,k+1)} > S_w^{(n)}, \\ G_{sc} \left(S_w^{(n,k+1)} \right), & \text{if } S_w^{(n)} > S_w^{(n,k+1)} \geq S_{w,\delta}^{(n)}, \\ G_{dr} \left(S_w^{(n,k+1)} \right), & \text{if } S_w^{(n,k+1)} < S_{w,\delta}^{(n)}, \end{cases}$$

while in the other case, we have:

$$G \left(S_w^{(n,k+1)} \right) = \begin{cases} G_{im} \left(S_w^{(n,k+1)} \right), & \text{if } S_w^{(n,k+1)} > S_{w,\delta}^{(n)}, \\ G_{sc} \left(S_w^{(n,k+1)} \right), & \text{if } S_w^{(n)} < S_w^{(n,k+1)} \leq S_{w,\delta}^{(n)}, \\ G_{dr} \left(S_w^{(n,k+1)} \right), & \text{if } S_w^{(n,k+1)} < S_w^{(n)}, \end{cases}$$

for all

$$(G, G_{sc}, G_{dr}, G_{im}) \in \left\{ \left(k_{rw}, k_{rw}^{sc}, k_{rw}^{dr}, k_{rw}^{im} \right), \left(k_{rn}, k_{rn}^{sc}, k_{rn}^{dr}, k_{rn}^{im} \right), \left(p_c, p_c^{sc}, p_c^{dr}, p_c^{im} \right) \right\}.$$

Here, we want to point out that the Newton iteration can terminate, while we are moving on a scanning curve. In this case it holds that

$$S_w^{(n+1)} \in \left[S_w^{(n)}, S_{w,\delta}^{(n)} \right] \text{ or } S_w^{(n+1)} \in \left[S_{w,\delta}^{(n)}, S_w^{(n)} \right] \quad (17)$$

and we store the parameters determining the connecting spline. For the next time step, we set $S_w^{(n+1,0)} = S_w^{(n+1)}$ and use the connecting spline to evaluate the corresponding functions until the results of the Newton iterations are not anymore contained in one of the intervals listed in (17).

Inserting Eqs. (15a)–(15c) into the formulas (11) and (13) yields pairs of functions for drainage and imbibition which are denoted by (f_{im}, D_{im}) for the imbibition process and by (f_{dr}, D_{dr}) for the drainage process.

2.3 Initial and Boundary Conditions

It remains to specify the initial and boundary conditions for the various fields as a function of $z \in [0, L]$ and $t \in [0, t_{end}]$.

2.3.1 Fractional Flow Formulation

The initial condition for the fractional flow formulation is given by

$$S_w(z, t = 0) = S_w^{out}, \quad z \in (0, L), \quad (18)$$

for the water saturation. Consequently, by virtue of (6) and (12b) the initial pressure profile obeys

$$\frac{\partial}{\partial z} p_n(z, t = 0) = \frac{g}{\lambda_{to}} \left(\lambda_w \rho_w + \lambda_n \rho_n - \frac{v}{g K} \right) \quad (19)$$

and the resulting pressure $p_n(z, 0)$ is linear in z .

The total flux density $v(t)$ is assumed to be controlled by a pump so that it is given and known. In experiments, it is usually constant so that

$$v(t) = v = \text{const} \quad (20)$$

is assumed in our simulations.

At the boundary $z = 0$, we set the following Dirichlet condition

$$S_w(z = 0, t) = \begin{cases} S_w^P, & t \leq 500 \text{ s}, \\ S_w^{in}, & t > 500 \text{ s}, \end{cases} \quad (21)$$

to generate an initial overshoot whose propagation is then monitored. As emphasized in Steinle and Hilfer (2016), the time-dependent boundary values at $z = 0$ specified above can be viewed also as an initial value problem with time-independent constant boundary value (S_w^{in} at the inlet) if one uses $t = 500$ s instead of $t = 0$ as the initial instant.

At the boundary $z = L$, the Dirichlet condition

$$S_w(z = L, t) = S_w^{out}, \quad t \in (0, t_{end}) \tag{22}$$

is used. The end of the simulation time period t_{end} has to be chosen such that the water front does not reach the boundary $z = L$, where L is the system size. As a consequence of this choice of t_{end} , the non-wetting pressure p_n obeys a Neumann condition at $z = L$ throughout $(0, t_{end})$ due to (19). The integration constant can be used to specify the pressure at the inlet.

2.3.2 Pressure–Saturation Formulation

In a pressure–saturation formulation (7), additional conditions are needed for the pressure. To emulate flux boundary conditions, (19) suggests to use Neumann conditions for the pressure. The total velocity is again fixed as in (20).

Initial conditions for pressure and saturation in the pressure–saturation formulation are

$$S_w(z, t = 0) = S_w^{out}, \quad z \in (0, L) \tag{23a}$$

$$p_n(z, t = 0) = p_{atm} + \frac{gz}{\lambda_{to}} \left(\lambda_w \rho_w + \lambda_n \rho_n - \frac{v}{gK} \right), \quad z \in (0, L). \tag{23b}$$

The pressure initial condition is not essential. However, an appropriate choice of the initial condition improves the convergence of iterative solvers, which are used in the context of an implicit time integrator.

At the inlet boundary $z = 0$ the time-dependent Dirichlet condition (21) for saturation is applied, exactly as in the fractional flow case. In addition the pressure boundary condition

$$p_n(z = 0, t) = p_{atm}, \quad t \in (0, t_{end}) \tag{24}$$

is needed.

The total velocity v is controlled through the boundary condition at the outlet. In addition to the Dirichlet condition (22) for saturation, the following Neumann condition is set at the outlet boundary $z = L$

$$\left. \frac{\partial}{\partial z} p_n(z, t) \right|_{z=L} = \frac{g}{\lambda_{to}} \left(\lambda_w \rho_w + \lambda_n \rho_n - \frac{v}{gK} \right), \quad t \in (0, t_{end}), \tag{25}$$

for p_n to emulate the flux boundary condition as suggested by (19). Note, that the Neumann condition at $z = L$ is crucial to emulate flux boundary conditions. It seems, however, somewhat artificial in view of the difficulty to imagine an experimental device for it.

3 Methods

3.1 Rankine–Hugoniot Velocity Estimates

For the analysis of the front velocities, we assume that the diffusive terms are dominated by the convective term:

$$D_i \frac{\partial S_w}{\partial z} \ll f_i, \quad i \in \{im, dr\}, \tag{26}$$

which means that (12c) can be regarded as a Buckley–Leverett-type equation. The basic idea to analyze the stability of saturation overshoots is to approximate the traveling wave profile with piecewise constant functions (Hilfer and Steinle 2014). As a consequence, the approximated profile can be considered as a superposition of two Buckley–Leverett shock fronts (Hilfer and Steinle 2014). At the imbibition and drainage discontinuities, the Rankine–Hugoniot condition (Evans 1998, Section 3.4.1) allows us to estimate the speed of imbibition and drainage front (Hilfer and Steinle 2014, Section 4.2). The stability of the overshoot region is preserved if the speeds of the imbibition and drainage front are equal. Otherwise, the overshoot region grows or shrinks.

For convenience of the reader, we recall here the formulas for the speed of the drainage front c_{dr} and the speed of the imbibition front c_{im} . Thereby, it is assumed that a given water saturation overshoot has a height of S_w^P . Let us further assume that beyond the drainage and imbibition front the saturations are given by S_w^{in} and S_w^{out} , respectively. Then c_{im} and c_{dr} can be estimated by the following formulas:

$$c_{im} = \frac{v}{\phi} \frac{f_{im}(S_w^P) - f_{im}(S_w^{out})}{S_w^P - S_w^{out}} \quad (27a)$$

$$c_{dr} = \frac{v}{\phi} \frac{f_{im}(S_w^P) - f_{dr}(S_w^{in})}{S_w^P - S_w^{in}}. \quad (27b)$$

Note that the transition from drainage to imbibition is determined by the scanning curve, which connects the primary drainage and imbibition curves. Therefore, at this transition it holds that $f_{sc}(S_w^P) = f_{im}(S_w^P)$, see Sect. 2.2.1, which justifies the use of formula (27b) to estimate the drainage front propagation speed.

3.2 Numerical Methods

The mathematical models (7) and (12c) with initial and boundary value problems are solved numerically. The numerical solution of (7) is carried out by means of the software package DuMu^x (Weishaupt et al. 2016). The abbreviation DuMu^x stands for the term DUNE for Multi-{Phase, Component, Scale, Physics, ...}. This software package is a free and open-source simulator for flow and transport processes in porous media (Flemisch et al. 2011) based on the modular PDE-toolbox DUNE (Distributed and Unified Numerics Environment, Bastian et al. 2010). The discretization method implemented in DuMu^x uses the Implicit Euler method for the time integration and a standard cell-centered Finite Volume method for the spatial discretization.

In the case of the fractional flow formulation, the open-source CFD-software OpenVFOAM (Jasak et al. 2007; Weller et al. 1998) is used. Thereby, a constant total velocity v is assumed and only Eq. (12c) is solved numerically. The implementation of the numerical solution scheme uses an explicit discretization scheme for the convection dominated part which is described by the flow function f . For the diffusive part which is described by the function D an implicit discretization scheme is considered (Hilfer and Steinle 2014, Section 5.2).

4 Numerical Simulations

In this section we achieve the objectives of the paper. The first objective is to compare the fractional flow formulation with a given constant total velocity v and Dirichlet boundary

conditions (see Sect. 2.3.1) with the pressure–saturation formulation using both Dirichlet and flux boundary conditions (see Sect. 2.3.2). In this context, we point out that for the pressure–saturation formulation, the assumption of a constant total velocity is enforced by the choice of the boundary conditions. Contrary to that, in the fractional flow formulation, a constant total velocity is directly enforced in Eq. (12c). In addition to that, the influence of the different discretization schemes, see Sect. 3.2, is analyzed. Moreover, it is of interest how the parameters have to be chosen such that a given saturation overshoot remains stable and under which conditions it is enlarged or diminished. The qualitative behavior of the drainage and imbibition front is predicted by (27). These formulas indicate the parameter dependency of the drainage and imbibition front speeds. Besides the shape of the fractional flow functions f_{im} , f_{dr} , the choice of S_w^P , S_w^{in} , S_w^{out} governs the propagation of saturation overshoots.

The second objective is to simulate gravity driven flow with pressure boundary conditions similar to an infiltration experiment. In this case the total flux density $v(t)$ is unknown and not given. Finally, the investigations are extended to heterogeneous systems with position-dependent permeability.

4.1 Fractional Flow Versus Pressure–Saturation Formulation

The parameters for our first numerical test are listed in Table 1. The parameter sets from Table 1 yield a total velocity of $v = 1.0 \times 10^{-5}$ m/s. It remains to specify the values for S_w^{in} . Therefore, we plot for

$$S_w^{in} \in \{0.44, 0.48754, 0.51\}$$

the velocities given in Eq. (27), as a function of the plateau saturation S_w^P . The corresponding results can be seen in Fig. 3. In the case of $S_w^{in} = 0.44$ the velocity of the drainage front is faster than the imbibition front. For $S_w^{in} = 0.48754$ the velocities of the drainage and imbibition front are equal and in the third case $S_w^{in} = 0.51$ the drainage front is slower than the imbibition front. Based on this analysis, we can expect that for $S_w^{in} = 0.44$ the initial overshoot is not stable and vanishes, whereas in the case of $S_w^{in} = 0.48754$ the saturation overshoot should remain stable. The third value $S_w^{in} = 0.51$ yields together with the other parameters a saturation overshoot whose plateau is enlarged.

Since we have assumed for the velocity analysis that the Buckley–Leverett limit holds, the issue arises, if the velocities in Eq. (27) represent a good estimation of the velocities produced by the given parameter set. This would be the case, if the diffusive term in (12c) is dominated by the convective term (see Eq. (26)).

The graph in the top left corner of Fig. 4 shows a typical shape of solutions for the water saturation S_w that are obtained from our models. We observe that it consists of three plateaus where S_w attains the constant values S_w^{in} , S_w^P and S_w^{out} . In these regions, the spatial derivative is equal to zero and therefore the diffusive term vanishes there (see Fig. 4, bottom left).

In between these plateaus, there are two transition zones located at the drainage and the imbibition front. Considering the difference between the fractional flow function and the diffusive term (see Fig. 4, top right), it can be seen that even in these regions the fractional flow function governs the physical behavior, despite of the fact that the absolute values for the fractional flow function f are not much larger than those of the diffusive term (see Fig. 4, bottom right). From these observations, we conclude that the velocities provided in (27) yield a useful estimate for the propagation velocities of both water saturation fronts, even though we do not consider a pure Buckley–Leverett system.

Table 1 Parameters for the first numerical experiment

Parameter	Symbol	Value	Unit
Height of the sand column	L	2.0	m
Porosity	ϕ	0.348	–
Permeability	K	2.0×10^{-10}	m ²
Density wetting phase	ρ_w	1.0×10^3	kg/m ³
Density non-wetting phase	ρ_n	1.0	kg/m ³
Viscosity wetting phase	μ_w	1.0×10^{-3}	Pa s
Viscosity non-wetting phase	μ_n	3.0×10^{-5}	Pa s
Gravity	g	9.81	m/s ²
Pressure imbibition	$P_{b_{im}}$	690	Pa
Pressure drainage	$P_{b_{dr}}$	700	Pa
Atmospheric pressure	p_{atm}	$1.0 \cdot 10^5$	Pa
Exponent, imbibition, wetting phase	α_{im}	0.6	–
Exponent, imbibition, non-wetting phase	β_{im}	1.2	–
Exponent, imbibition, capillary pressure	γ_{im}	0.9206	–
Exponent, drainage, wetting phase	α_{dr}	0.85	–
Exponent, drainage, non-wetting phase	β_{dr}	1.1	–
Exponent, drainage, capillary pressure	γ_{dr}	0.906	–
Rel. perm., imbibition, wetting phase	K_{rw}^{im}	0.6	–
Rel. perm., imbibition, non-wetting phase	K_{rn}^{im}	1.0	–
Rel. perm., drainage, wetting phase	K_{rw}^{dr}	0.6	–
Rel. perm., drainage, non-wetting phase	K_{rn}^{dr}	0.4	–
Res. sat., imbibition, wetting phase	S_{wr}^{im}	0.0	–
Res. sat., drainage, wetting phase	S_{wr}^{dr}	0.07	–
Res. sat., imbibition, non-wetting phase	S_{nr}^{im}	0.045	–
Res. sat., drainage, non-wetting phase	S_{nr}^{dr}	0.045	–
Saturation, wetting phase, plateau	S_w^P	0.7	–
Saturation, wetting phase, outlet	S_w^{out}	0.01	–
Hysteresis parameter	δ	0.01	–
Hysteresis parameter	ε	1.0×10^{-5}	–
Mesh size	Δz	5×10^{-4}	m

The parameters δ and ε that are used for the hysteresis model are also listed in Table 1. As previously mentioned, we use Newton's method to solve the nonlinear system of equations arising in each time step. Depending on the number of Newton iterations, we adapt the time step size such that the Newton solver converges. If the Newton method does not convergence, the time step size is reduced, where the maximal time step size is chosen as $\Delta t_{\max} = 1.0 \times 10^{-3}$ s.

The numerical solutions for S_w are shown in Figs. 5, 6, 7. Figure 5 corresponds to the first case with $S_w^{in} = 0.44$, whereas Figs. 6 and 7 correspond to the second and third case with $S_w^{in} = 0.48754$ and $S_w^{in} = 0.51$, respectively.

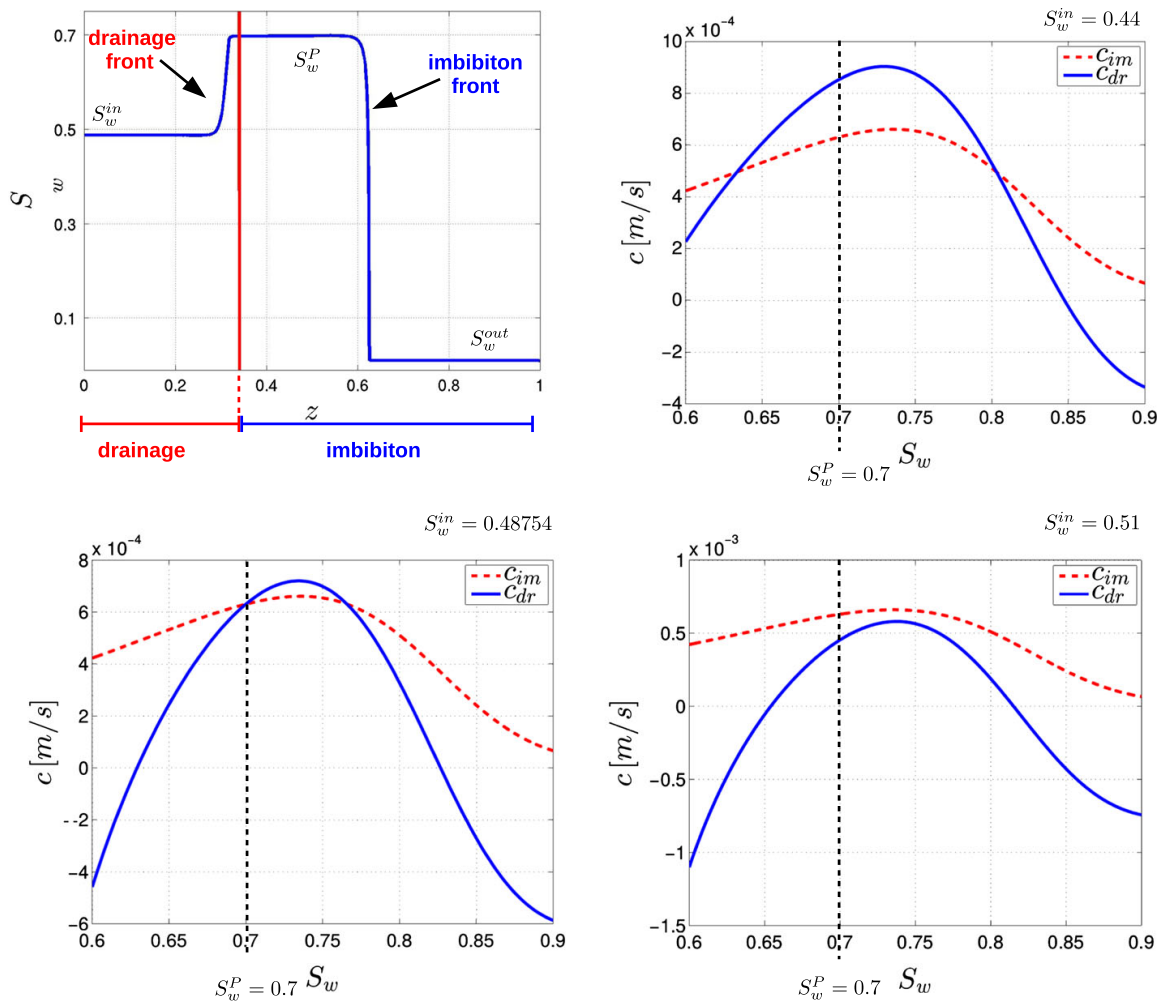


Fig. 3 Traveling wave composed of a drainage and a imbibition front (top left), propagation velocities of drainage and imbibition front for $S_w^{in} = 0.44$ (top right), $S_w^{in} = 0.48754$ (bottom left) and $S_w^{in} = 0.51$ (bottom right). It can be seen that for $S_w^P = 0.7$, the different values for S_w^{in} yield different velocities for the drainage front, while the imbibition front velocities remain the same

In the following, these results are discussed using the front velocities for $S_w^P = 0.7$, which are shown in Fig. 3. The imbibition velocity is given as $c_{im} \approx 6.3 \times 10^{-4}$ m/s, which is the same for all three cases. The drainage front velocity for case one is $c_{dr} \approx 8.53 \times 10^{-4}$ m/s. Therefore, the drainage front moves faster than the imbibition front and we observe that the initial plateau vanishes at the time point $t \approx 1917$ s. As a consequence, the saturation decreases because of diffusion, see Fig. 5 (top right). The reduction of the plateau height implies a front velocity change. Figure 3 (top right) shows that the drainage velocity decreases faster than the imbibition velocity. For plateau heights below $S_w^P \approx 0.6336$, the imbibition front propagates faster than the drainage front. This means that a second plateau is formed. As the plateau length increases, the influence of the diffusive term decreases and the niveau of the second plateau is approximately $S_w^P \approx 0.6117$. Furthermore, it can be seen in Fig. 5 that the plateau width increases with time due to the fact that $c_{im} > c_d$.

In the second scenario, S_w^{in} is chosen such that the front velocities are the same, meaning that the width of the plateau, which is approximately 0.3151 m, is constant over time. The results shown for $t = 800$ s and $t = 1500$ s in Fig. 6 confirm this thesis.

The last case exhibits an enlargement of the plateau width. Here, S_w^{in} is selected such that the imbibition front, with $c_{im} \approx 6.3 \times 10^{-4}$ m/s, moves faster than the drainage front, with

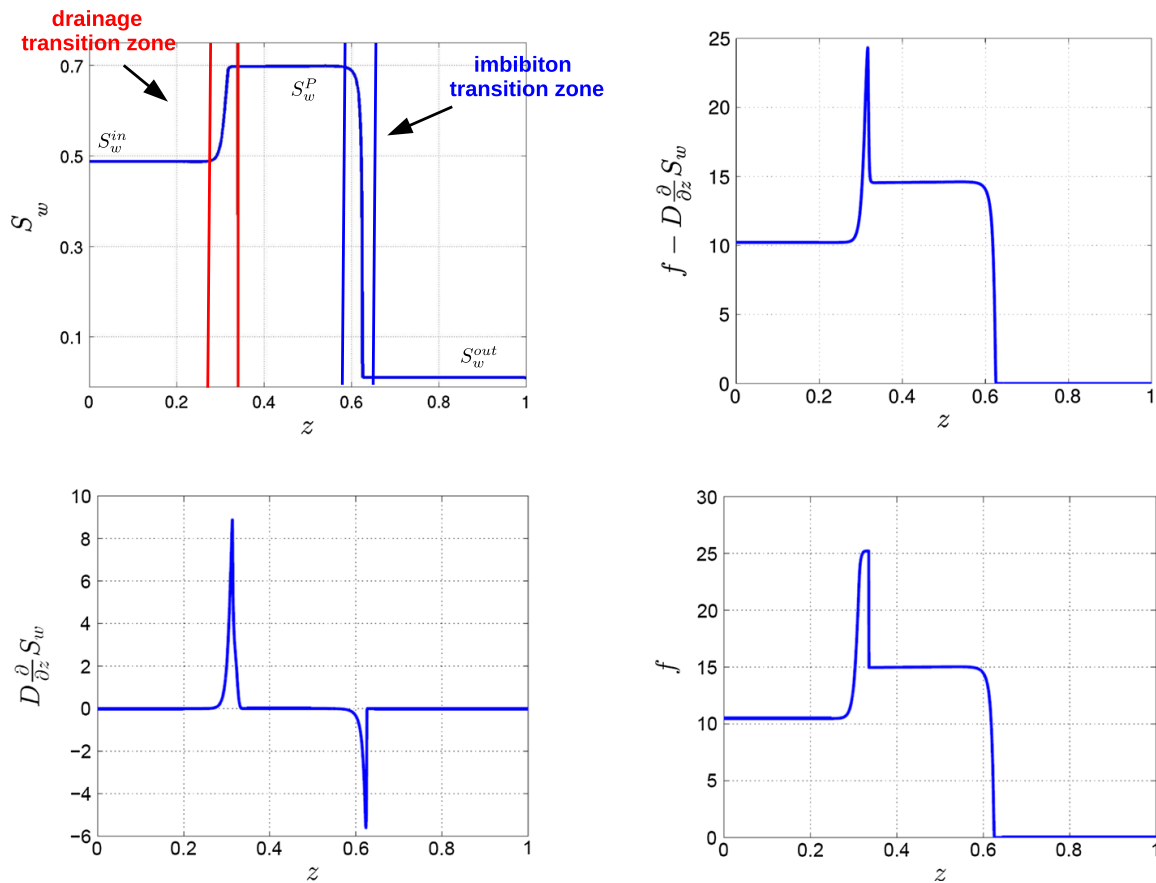


Fig. 4 Transition zones around the drainage and the imbibition zone (top left), difference between the fractional flow function and the diffusive term (top right), values of the fractional flow function f (bottom right), values of the diffusive term (bottom left)

$c_{dr} \approx 4.5 \times 10^{-4}$ m/s, see Fig. 3. The results at $t = 800$ s and $t = 1500$ s are shown in Fig. 7. The pressure–saturation formulation and the fractional flow formulation yield similar solutions, where the deviation increases with time. This is due to the fact that the fully implicit scheme applied in the DuMu^x-implementation produces more numerical diffusion than the OpenFOAM implementation. Furthermore, the total velocity v is only constant up to the nonlinear and linear solver tolerances. Therefore, the initial plateau saturation slightly decreases with time, which in turn influences the front propagation. Nevertheless the numerical results indicate that the velocity analysis assuming the Buckley–Leverett limit provides reasonable estimates.

To quantify the difference between the numerical implementations, the following discrete norm is defined:

$$e_S = \left(\sum_i \Delta z (S_{w,i}^d - S_{w,i}^f)^2 \right)^{0.5}, \tag{28}$$

where $S_{w,i}^d$ is the numerical saturation value in cell i in the OpenFOAM implementation, while $S_{w,i}^f$ denotes the value in cell i in DuMu^x. The errors e_S for the different cases are calculated for each time point shown in Figs. 5, 6, 7. They can be found in Table 2. In accordance with the graphs in the above figures, a slight error increase in time can be observed. Furthermore, it can be seen that the errors have approximately the same order of magnitude.

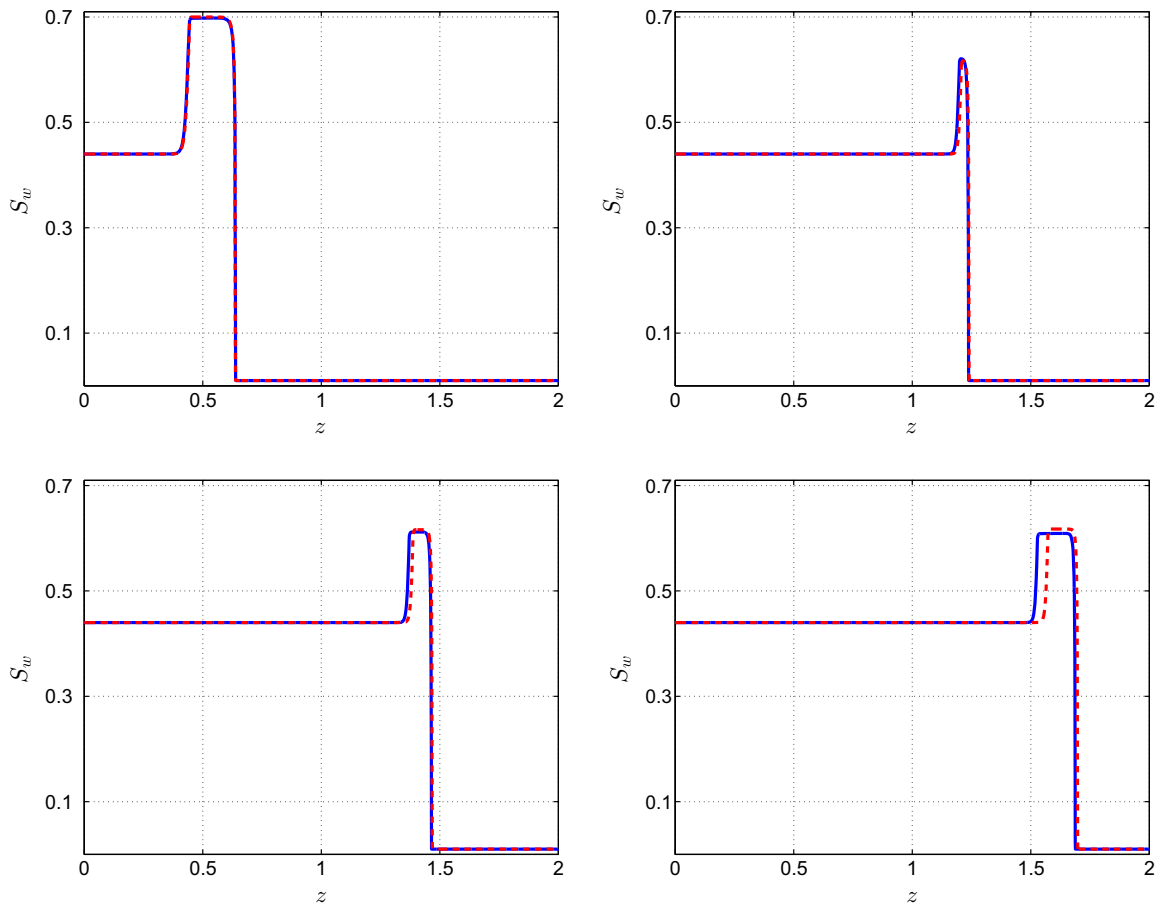


Fig. 5 Saturation profiles for the first case with $S_w^{in} = 0.44$ and $t \in \{1000 \text{ s}, 2000 \text{ s}, 2500 \text{ s}, 3000 \text{ s}\}$. The solid line represents the solution of (7), whereas the dashed line represents the solution of (12c)

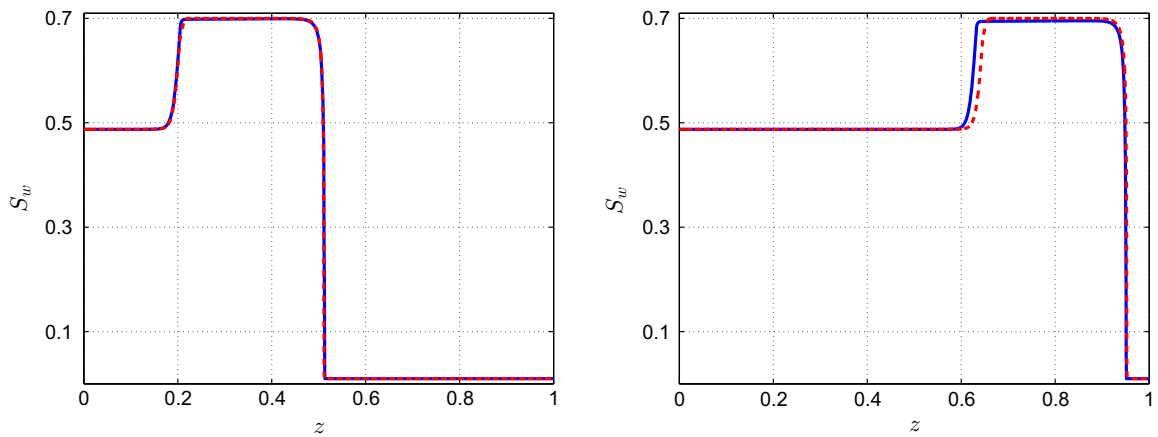


Fig. 6 Saturation profiles for the second case with $S_w^{in} = 0.48754$ and $t \in \{800 \text{ s}, 1500 \text{ s}\}$. The solid line represents the solution of (7), whereas the dashed line represents the solution of (12c)

4.2 Pressure Boundary Conditions and Heterogeneous Media

In the previous subsection, different scenarios have been simulated based on the assumption that the total velocity is constant. However, for two-phase flow this assumption is only satisfied for special cases. If Dirichlet conditions are assigned to the boundaries or if the fluids are no longer assumed to be incompressible, this assumption is violated. Here, only the fully implicit formulation is used to simulate a test problem with a non-constant total velocity. We

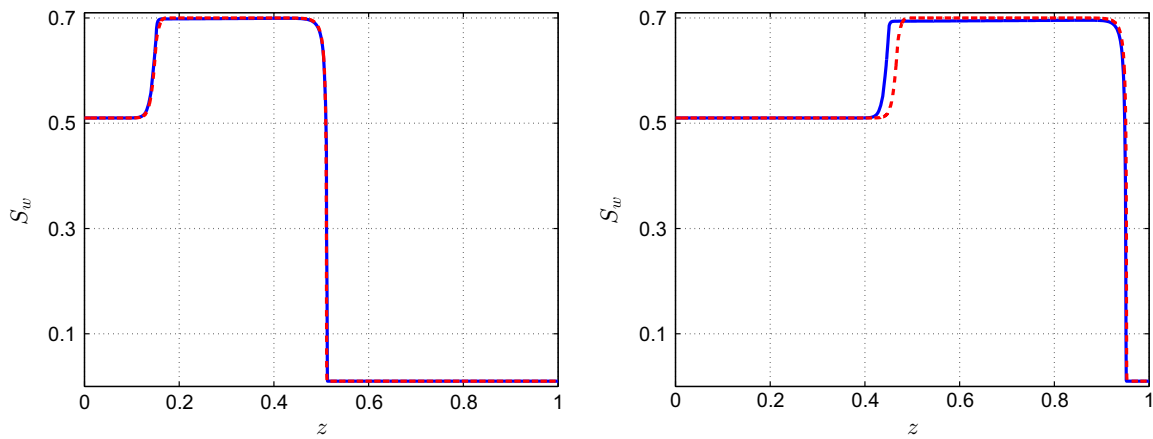
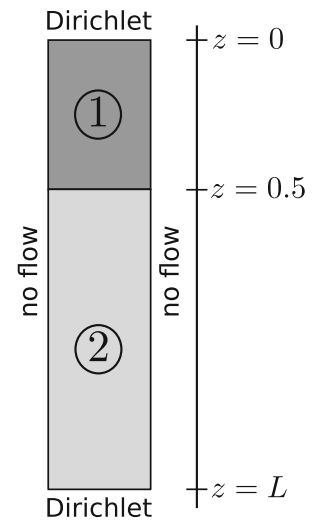


Fig. 7 Saturation profiles for the third case with $S_w^{in} = 0.51$ and $t \in \{800 \text{ s}, 1500 \text{ s}\}$. The solid line represents the solution of (7), whereas the dashed line represents the solution of (12c)

Table 2 Discrete norms e_S of the OpenFOAM and the DuMuX implementation

	Case 1				Case 2		Case 3	
Time	1000 s	2000 s	2500 s	3000 s	800 s	1500 s	800 s	1500 s
e_S	0.68e-2	1.93e-2	2.93e-2	6.12e-2	1.01e-2	2.36e-2	1.02e-2	2.55e-2

Fig. 8 Setting for the heterogeneous test problem with Dirichlet boundary conditions



consider besides a varying total velocity a heterogeneous permeability K . The setting of this test case is shown in Fig. 8, and Table 3 lists the parameters that are used for the simulation, where we list only those parameters that differ from those in Table 1.

The initial conditions are again set to

$$S_w(z, t = 0) = S_w^{out}, \quad z \in (0, L).$$

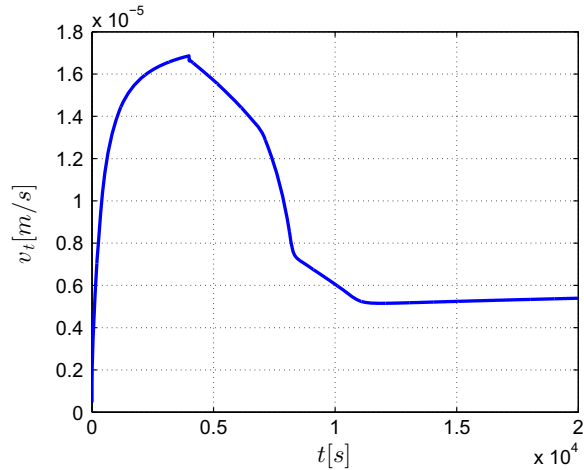
At the boundary $z = 0$, we set the following Dirichlet boundary condition:

$$S_w(z = 0, t) = \begin{cases} S_w^P, & t \leq 4000 \text{ s}, \\ S_w^{in}, & t > 4000 \text{ s}, \end{cases}$$

Table 3 Parameters for the second numerical experiment with heterogeneous permeability

Parameter	Symbol	Value	Unit
Permeability domain one	K_1	2.0×10^{-11}	m^2
Permeability domain two	K_2	4.0×10^{-11}	m^2
Hysteresis parameter	δ	0.01	–
Hysteresis parameter	ε	1.0×10^{-7}	–

Fig. 9 Averaged total velocity v plotted over time. It can be observed that v is varying significantly over time. The kink at 4000 s is caused by changing the Dirichlet boundary value for the water saturation



with $S_w^{in} = 0.4$. At $z = L$, we set $S_w(z = L, t) = S_w^{out}$. For the pressure of the non-wetting phase, we use Dirichlet conditions:

$$p_n(z = 0, t) = p_{atm}, \quad p_n(z = L, t) = p_{atm} + \rho_n g L$$

and the permeability is given by:

$$K(z) = \begin{cases} K_1, & z \geq 0.5 \text{ m,} \\ K_2, & z < 0.5 \text{ m,} \end{cases} \tag{29}$$

where K_1 and K_2 can be found in Table 3. Using for each boundary a Dirichlet condition, the assumption of a constant total velocity in space and time is no longer fulfilled. This is shown in Fig. 9, where the time evolution of the spatially averaged total velocity is depicted. Therefore, the front velocity analysis which has been used in the last section, is not valid for this test case. Nevertheless, we obtain similar solution profiles as before. In Fig. 10, the saturation profiles are shown for

$$t \in \{5000 \text{ s, } 8000 \text{ s, } 9000 \text{ s, } 10000 \text{ s, } 15000 \text{ s, } 20000 \text{ s}\}.$$

After $t = 5000$ s, the plateau width is about 0.3 m long (see Fig. 10, top left) and after $t = 7000$ s, the imbibition front has reached the heterogeneity at $z = 0.5$ m. Due to the fact that the permeability is larger in the second domain, the saturation decreases (see Fig. 10, top right). At the time point $t = 8270$ s the entire plateau has reached the second domain, where it can be seen that the height of the new plateau is decreased to $S_w^P = 0.593$. Considering all the remaining simulation results in Fig. 10, the same solution behavior as in case one from the last subsection can be observed: first, the plateau width shrinks and the saturation overshoot decreases. After that the imbibition front overtakes the drainage front, resulting in the formation of another plateau which is enlarged as time goes by. All in all, this demonstrates

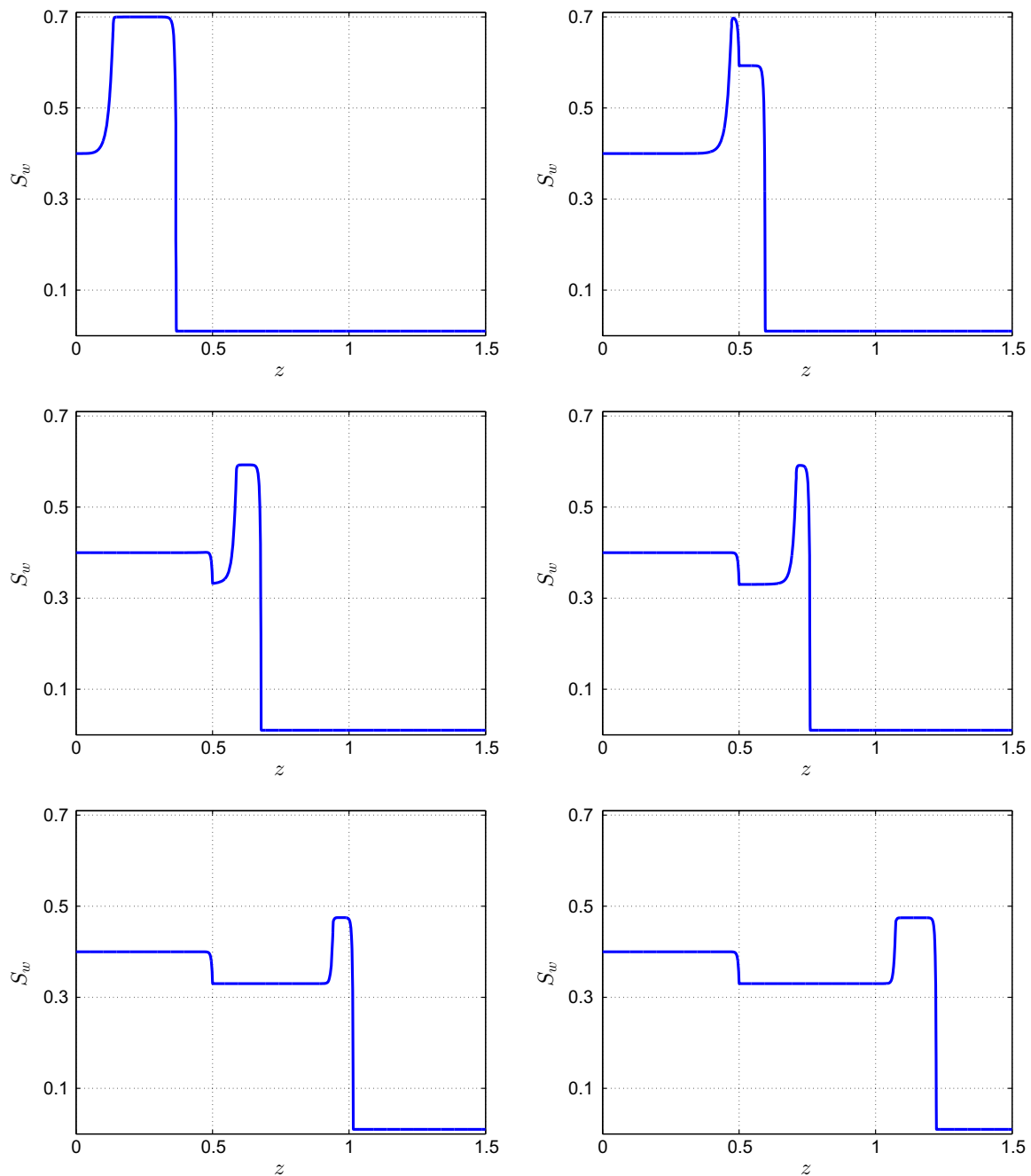


Fig. 10 Saturation profiles for a heterogeneous permeability (see Eq. (29)) and $S_w^{in} = 0.4$ for $t \in \{5000 \text{ s}, 8000 \text{ s}, 9000 \text{ s}, 10000 \text{ s}, 15000 \text{ s}, 20000 \text{ s}\}$

that the fully implicit model is capable of solving heterogeneous problems with a total velocity that is not constant.

5 Final Remarks

The long-standing experimental and theoretical problems related to existence, initiation and propagation of saturation overshoot in porous media have been controversially discussed for several decades by numerous authors (Alt and Luckhaus 1983; Alt et al. 1984; Beliaev and Hassanizadeh 2001; Briggs and Katz 1966; Cueto-Felgueroso and Juanes 2009; DiCarlo

2004, 2013; DiCarlo et al. 2012; Eliassi and Glass 2001, 2002; Glass et al. 1989; Otto 1996; Shiozawa and Fujimaki 2004; Duijn et al. 2013, 2007; Xiong 2014; Youngs 1958). In this paper, we have investigated and extended recent predictions for propagation and stability of saturation overshoots within the traditional generalized Darcy model for two-phase immiscible displacement (Hilfer and Steinle 2014). The propagation speeds of the drainage and imbibition front have been estimated using Rankine–Hugoniot conditions. For convection dominated flow, as analyzed in this paper, these estimates yield satisfactory predictions on the stability of saturation overshoots. Predictions on the stability or instability of a given overshoot have also been confirmed numerically. Finally, the numerical analysis has been extended to heterogeneous media.

Our numerical simulations show that for a constant total velocity the fractional flow formulation and the pressure–saturation formulations yield almost the same results. Furthermore, the theoretical predictions with respect to the stability of the overshoots have been confirmed by the simulation results. Finally, it has been demonstrated that saturation overshoots exist in gravity driven infiltration experiments with Dirichlet boundary conditions for pressure, as well as for heterogeneous media with position-dependent permeability.

Future work in this field may be concerned with applying this model to problems in several space dimensions. For this purpose, it is necessary to improve the efficiency of the nonlinear solvers such that larger time steps can be exerted and fewer iterations are required for the convergence of the iterative solvers.

Acknowledgements We would like to thank Mike Celia for his comments and many fruitful discussions. This work was partially supported by the Cluster of Excellence in Simulation Technology (EXC 310/2), the Internationales Graduiertenkolleg NUPUS and the Deutsche Forschungsgemeinschaft.

References

- Alt, H., Luckhaus, S.: Quasilinear elliptic–parabolic differential equations. *Math. Z.* **183**, 311 (1983)
- Alt, H., Luckhaus, S., Visintin, A.: On nonstationary flow through porous media. *Ann. Mat. Pura Appl.* **136**, 303 (1984)
- Bastian, P., Heimann, F., Marnach, S.: Generic implementation of finite element methods in the distributed and unified numerics environment (Dune). *Kybernetika* **46**(2), 294–315 (2010)
- Beliaev, A.Y., Hassanizadeh, S.M.: A theoretical model of hysteresis and dynamic effects in the capillary relation for two-phase flow in porous media. *Transp. Porous Media* **43**(3), 487–510 (2001)
- Boudet, H., Clarke, C., Bugden, D., Maibach, E., Roser-Renouf, C., Leiserowitz, A.: Fracking controversy and communication: using national survey data to understand public perceptions of hydraulic fracturing. *Energy Policy* **65**, 57–67 (2014)
- Briggs, J., Katz, D.: Drainage of water from sand in developing aquifer storage. Paper SPE1501 presented 1966 at the 41st Annual Fall Meeting of the SPE, Dallas, USA (1966)
- Charbeneau, R.: *Groundwater Hydraulics and Pollution Transport*. Prentice Hall, Upper Saddle River (2000)
- Cueto-Felgueroso, L., Juanes, R.: Stability analysis of a phase-field model of gravity-driven unsaturated flow through porous media. *Phys. Rev. E* **79**, 036301 (2009)
- DiCarlo, D.: Experimental measurements of saturation overshoot on infiltration. *Water Resour. Res.* **40**, W04215 (2004)
- DiCarlo, D.: Stability of gravity-driven multiphase flow in porous media: 40 years of advancements. *Water Resour. Res.* **49**, 4531 (2013)
- DiCarlo, D., Mirzaei, M., Aminzadeh, B., Dehghanpur, H.: Fractional flow approach to saturation overshoot. *Transp. Porous Media* **91**, 955 (2012)
- Doster, F., Zegeling, P., Hilfer, R.: Numerical solutions of a generalized theory for macroscopic capillarity. *Phys. Rev. E* **81**, 036307 (2010)
- Dullien, F.A.L.: *Porous Media—Fluid Transport and Pore Structure*. Academic Press, San Diego (1992)
- Egorov, A., Dautov, R., Nieber, J., Sheshukov, A.: Stability analysis of gravity-driven infiltrating flow. *Water Resour. Res.* **39**, 1266 (2003)

- Eliassi, M., Glass, R.: On the continuum-scale modeling of gravity-driven fingers in unsaturated porous media: The inadequacy of the Richards equation with standard monotonic constitutive relations and hysteretic equations of state. *Water Resour. Res.* **37**, 2019 (2001)
- Eliassi, M., Glass, R.J.: On the porous-continuum modeling of gravity-driven fingers in unsaturated materials: Extension of standard theory with a hold-back-pile-up effect. *Water Resour. Res.* **38**(11), 16-1–16-11 (2002)
- Evans, L.C.: *Partial Differential Equations*. Graduate studies in mathematics. American Mathematical Society, Providence (1998)
- Flemisch, B., Darcis, M., Erbertseder, K., Faigle, B., Lauser, A., Mosthaf, K., Müthing, S., Nuske, P., Tatomir, A., Wolff, M., Helmig, R.: DuMux: DUNE for multi-{phase, component, scale, physics,..} flow and transport in porous media. *Adv. Water Resour.* **34**(9), 1102–1112 (2011)
- Fritz, S.: *Experimental Investigations of Water Infiltration into Unsaturated Soil—Analysis of Dynamic Capillarity Effects*. Master's thesis, Universität Stuttgart, Department of Hydromechanics and Modelling of Hydrosystems (2012)
- Fürst, T., Vodak, R., Sir, M., Bil, M.: On the incompatibility of Richards' equation and finger-like infiltration in unsaturated homogeneous porous media. *Water Resour. Res.* **45**, W03408 (2009)
- Glass, R., Steenhuis, T., Parlange, J.: Mechanism for finger persistence in homogeneous unsaturated, porous media: theory and verification. *Soil Sci.* **148**, 60 (1989)
- Helmig, R.: *Multiphase Flow and Transport Processes in the Subsurface: A Contribution to the Modeling of Hydrosystems*. Springer, Berlin (1997)
- Hilfer, R., Doster, F., Zegeling, P.: Nonmonotone saturation profiles for hydrostatic equilibrium in homogeneous media. *Vadose Zone J.* (2012). <https://doi.org/10.2136/vzj2012.0021>
- Hilfer, R., Steinle, R.: Saturation overshoot and hysteresis for twophase flow in porous media. *Eur. Phys. J. Spec. Top.* **223**(11), 2323–2338 (2014)
- Jasak, H., Jemcov, A., Tukovic, Z.: OpenFOAM: A C++ library for complex physics simulations. In: *International Workshop on Coupled Methods in Numerical Dynamics*, vol. 1000, pp. 1–20 (2007)
- Kalaydjian, F.J.-M. et al. Dynamic capillary pressure curve for water/oil displacement in porous media: theory vs. experiment. In: *SPE Annual Technical Conference and Exhibition*. Society of Petroleum Engineers (1992)
- Koch, J., Rätz, A., Schweizer, B.: Two-phase flow equations with a dynamic capillary pressure. *Eur. J. Appl. Math.* **24**(01), 49–75 (2013)
- Lamacz, A., Rätz, A., Schweizer, B.: A well-posed hysteresis model for flows in porous media and applications to fingering effects. *Adv. Math. Sci. Appl.* **21**(01), 33–64 (2011)
- Luckner, L., Van Genuchten, M.T., Nielsen, D.R.: A consistent set of parametric models for the two-phase flow of immiscible fluids in the subsurface. *Water Resour. Res.* **25**(10), 2187–2193 (1989)
- Manthey, S., Hassanizadeh, S.M., Helmig, R., Hilfer, R.: Dimensional analysis of two-phase flow including a rate-dependent capillary pressure–saturation relationship. *Adv. Water Resour.* **31**(9), 1137–1150 (2008)
- Middendorf, J.: *Zur Beschreibung des kapillaren Flüssigkeitstransports in Papier*. Ph.D. thesis, Fakultät für Maschinenbau und Verfahrenstechnik, Technische Universität Chemnitz, Germany (2000)
- Nieber, J.L., Dautov, R.Z., Egorov, A.G., Sheshukov, A.Y.: Dynamic capillary pressure mechanism for instability in gravity-driven flows; review and extension to very dry conditions. *Transp. Porous Media* **58**(1–2), 147–172 (2005)
- Otto, F.: L^1 -contraction and uniqueness for quasilinear elliptic–parabolic equations. *J. Differ. Equ.* **131**, 20 (1996)
- Rätz, A., Schweizer, B.: Hysteresis models and gravity fingering in porous media. *ZAMM J. Appl. Math. Mech.* **94**(7–8), 645–654 (2014)
- Schröder, N., Javaux, M., Vanderborght, J., Steffen, B., Vereecken, H.: Effect of root water and solute uptake on apparent soil dispersivity: A simulation study. *Vadose Zone J.* **11**(3), 1–16 (2012)
- Shiozawa, S., Fujimaki, H.: Unexpected water content profiles under flux-limited one-dimensional downward infiltration in initially dry granular media. *Water Resour. Res.* **40**(7), W07404 (2004)
- Steinle, R., Hilfer, R.: Influence of initial conditions on propagation, growth and decay of saturation overshoot. *Transp. Porous Media* **111**(2), 369–380 (2016)
- Steinle, R., Hilfer, R.: Hysteresis in relative permeabilities suffices for propagation of saturation overshoot: A quantitative comparison with experiment. *Phys. Rev. E* **95**, 043112 (2017)
- van Duijn, C., Fan, Y., Peletier, L., Pop, I.: Travelling wave solutions for degenerate pseudo-parabolic equations modelling two-phase flow in porous media. *Nonlinear Anal. Real World Appl.* **14**, 1361–1383 (2013)
- Van Duijn, C.J., Peletier, L.A., Pop, I.S.: A new class of entropy solutions of the Buckley–Leverett equation. *SIAM J. Math. Anal.* **39**(2), 507–536 (2007)
- Van Genuchten, M.T.: A closed-form equation for predicting the hydraulic conductivity of unsaturated soils. *Soil Sci. Soc. Am. J.* **44**(5), 892–898 (1980)

- Weishaupt, K., Beck, M., Becker, B., Class, H., Fetzer, T., Flemisch, B., Futter, G., Gläser, D., Grüninger, C., Hommel, J., Kissinger, A., Koch, T., Schneider, M., Schröder, N., Schwenck, N., Seitz, G.: *Dumux 2.9.0* (2016)
- Weller, H.G., Tabor, G., Jasak, H., Fureby, C.: A tensorial approach to computational continuum mechanics using object-oriented techniques. *Comput. Phys.* **12**(6), 620–631 (1998)
- Xiong, Y.: Flow of water in porous media with saturation overshoot: a review. *J. Hydrol.* **510**, 353–362 (2014)
- Youngs, E.G.: Redistribution of moisture in porous materials after infiltration: 2. *Soil Sci.* **86**, 202–207 (1958)

9 Fronts in two-phase porous flow problems: effects of hysteresis and dynamic capillarity

Bibliographic note: The content of this chapter is based on the following original article: K. Mitra, T. Köppl, I. S. Pop, C. J. van Duijn and R. Helmig (2020). Fronts in two-phase porous media flow problems: The effects of hysteresis and dynamic capillarity. *Studies in Applied Mathematics*, 144(4), 449-492, with courtesy of Wiley.

Fronts in two-phase porous media flow problems: The effects of hysteresis and dynamic capillarity

K. Mitra¹  | T. Köppl² | I. S. Pop^{3,4} | C. J. van Duijn^{5,6} | R. Helmig⁷

¹Faculty of Mathematics, Technical University of Dortmund, Dortmund, Germany

²Department of Mathematics, University of Technology Munich, Garching bei München, Germany

³Faculty of Science, Hasselt University, Hasselt, Belgium

⁴Department of Mathematics, University of Bergen, Norway

⁵Department of Earth Sciences, University of Utrecht, Utrecht, The Netherlands

⁶Department of Mechanical Engineering, Eindhoven University of Technology, Eindhoven, The Netherlands

⁷Department of Hydromechanics and Modelling of Hydrosystems, University of Stuttgart, Stuttgart, Germany

Correspondence

K. Mitra, Faculty of Mathematics, Technical University of Dortmund, Vogelpothsweg 87, 44227 Dortmund, Germany.
Email: koondanibha.mitra@tu-dortmund.de

Funding information

Deutsche Forschungsgemeinschaft, Grant/Award Number: 327154368; Technische Universität Dortmund; Universiteit Hasselt, Grant/Award Number: BOF17BL04; Fonds Wetenschappelijk Onderzoek, Grant/Award Numbers: G051418N, G0G1316N; Darcy Center, Eindhoven University of Technology and Utrecht University; Cluster of Excellence in Simulation Technology, Grant/Award Number: (EXC 310/2); Nederlandse Organisatie voor Wetenschappelijk Onderzoek, Grant/Award Number: 14CSER016

Abstract

In this work, we study the behavior of saturation fronts for two-phase flow through a long homogeneous porous column. In particular, the model includes hysteresis and dynamic effects in the capillary pressure and hysteresis in the permeabilities. The analysis uses traveling wave approximation. Entropy solutions are derived for Riemann problems that are arising in this context. These solutions belong to a much broader class compared to the standard Oleinik solutions, where hysteresis and dynamic effects are neglected. The relevant cases are examined and the corresponding solutions are categorized. They include non-monotone profiles, multiple shocks, and self-developing stable saturation plateaus. Numerical results are presented that illustrate the mathematical analysis. Finally, we discuss the implication of our findings in the context of available experimental results.

KEYWORDS

dynamic capillarity, hysteresis, Riemann problem, traveling waves, two-phase flow

This is an open access article under the terms of the Creative Commons Attribution License, which permits use, distribution and reproduction in any medium, provided the original work is properly cited.

© 2020 The Authors. *Studies in Applied Mathematics* published by Wiley Periodicals, Inc.

1 | INTRODUCTION

Modeling of two-phase flow through the subsurface is important for many practical applications, from groundwater modeling and oil and gas recovery to CO₂ sequestration. For this purpose, the mass balance equations are used which read in the absence of source terms^{1,2} as follows:

$$\phi \frac{\partial(\rho_\alpha S_\alpha)}{\partial t} + \nabla \cdot (\rho_\alpha v_\alpha) = 0, \quad \alpha \in \{w, n\}, \quad (1)$$

where $\alpha = n$ denotes the nonwetting phase and $\alpha = w$ the wetting phase. Furthermore, ϕ is the porosity, S_α and ρ_α the saturation and density of the phases. The phase-velocities v_α are given by the Darcy's law,^{1,2}

$$v_\alpha = -\frac{k_{r\alpha}}{\mu_\alpha} K (\nabla p_\alpha - \rho_\alpha g \hat{e}_g), \quad \alpha \in \{w, n\}. \quad (2)$$

Here $K[\text{m}^2]$ is the absolute permeability of the porous medium, $\mu_\alpha[\text{Pa} \cdot \text{s}]$ the viscosity, and $k_{r\alpha}$ the relative permeability of each phase. Moreover, p_α [Pa], g [m/s^2], and \hat{e}_g stand for the phase pressure, the gravitational acceleration, and the unit vector along gravity, respectively. Observe that the system (1)-(2) is not closed as there are more unknowns than equations, that is, S_α , $k_{r\alpha}$, and p_α . Hence, one needs to take certain assumptions. Assuming incompressibility results in ρ_α being constant. Moreover, by definition

$$S_w + S_n = 1. \quad (3)$$

Commonly it is assumed that the relative permeabilities, as well as the phase pressure difference, are functions of the saturation of the wetting phase,^{1,2}

$$k_{rn} = k_{rn}(S_w), \quad k_{rw} = k_{rw}(S_w), \quad \text{and} \quad p_n - p_w = p_c(S_w). \quad (4)$$

The function $p_c : (0, 1] \rightarrow \mathbb{R}^+$ is referred to as the capillary pressure function. System (1)-(4) reduces to the hyperbolic Buckley-Leverett equation if this term is neglected, that is, $p_c \equiv 0$. The model given by (1)-(4) works well under close to equilibrium conditions and when flow reversal does not take place. However, some more general cases cannot be explained by this model.

One of the first evidences of deviation from the standard model was reported in the 1931 paper by Richards³ where he concluded that the capillary pressure term is hysteretic in nature. Capillary hysteresis refers to the phenomenon that p_c measured for a wetting phase infiltration process follows a curve, denoted here by $p_c^{(i)}(S_w)$, which differs from p_c measured for a drainage process, denoted by $p_c^{(d)}(S_w)$. If the process changes from infiltration to drainage or vice versa, then the p_c follows scanning curves that are intermediate to $p_c^{(i)}(S_w)$ and $p_c^{(d)}(S_w)$.⁴ This is shown in detail in Figure 1 (left). Since then, hysteresis has been studied experimentally,⁵⁻⁷ analytically,⁸⁻¹² and numerically.¹²⁻¹⁶ Variety of models have been proposed to incorporate the effects of hysteresis, such as independent and dependent domain models¹⁷⁻¹⁹ and interfacial area models.²⁰⁻²³ A comprehensive study of these models can be found in Ref. 24. Using thermodynamically constrained averaging theory (TCAT),^{25,26} one can eliminate hysteresis in capillary pressure altogether by introducing interfacial area and Euler characteristics as additional unknowns. A mathematical study of such models is undoubtedly interesting. However, they require additional constitutive equations. Thus, their analysis is beyond the scope of the present work. In this paper, we will use the play-type hysteresis model^{4,24} that approximates scanning curves as constant saturation lines. Such models are generally implemented

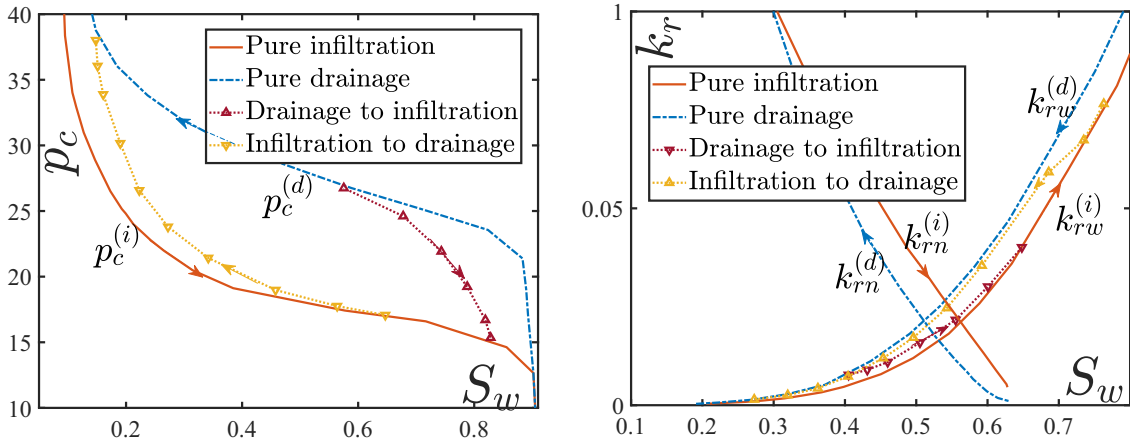


FIGURE 1 (Left) Hysteresis of capillary pressure and scanning curves. The plots drawn use data points from figs. 4 and 5 of Ref. 5. (Right) Hysteresis of relative permeabilities. Experimental data from Ref. 32 are used for the k_{rw} plots and the corresponding scanning curves. Plots for k_{rn} show data from Ref. 29. The curves are scaled in the y-direction

in classical porous media simulators. Well-posedness results for play-type hysteresis model are found in Refs. 8, 9, 11, 12, 27. It has a physical basis^{4,28} and it can be extended to depict the realistic cases accurately.²⁴ A similar hysteretic behavior is observed for the relative permeabilities too, although to a lesser extent. Hysteresis of the nonwetting phase relative permeability in the two-phase case (oil and water for example) is reported in Refs. 29-31. The wetting permeability k_{rw} also exhibits hysteresis^{6,32} but the effect is less pronounced (see Figure 1 (right)).

Another effect that cannot be explained by the standard model is the occurrences of overshoots. More precisely, in infiltration experiments through initially low saturated soils, it is observed that if the flow rate is large enough then the saturation at an interior point is larger than that on the boundary even in the absence of internal sources.³³⁻³⁵ This cannot be explained by a second-order model such as (1)-(4).³⁶⁻³⁸ Hence, based on thermodynamic considerations the dynamic capillary model was proposed in Ref. 39. Since then the dynamic capillary term has been measured experimentally^{40,41} and it was used successfully to explain overshoots.^{9,11,12,42-45} Also the well-posedness of the dynamic capillarity model has been proved⁴⁶⁻⁴⁹ and numerical methods have been investigated.⁵⁰⁻⁵⁴

In this paper, we are interested in studying how the flow behavior is influenced if one considers the nonequilibrium effects, that is, hysteresis and dynamic capillarity. For this purpose, we study the system in a one-dimensional setting. The one-dimensional case is relevant when one spatial direction is dominant; it approximates flow through viscous fingers^{12,55,56} and it can explain results from the standard experimental setting shown in Figure 2.³³⁻³⁵ In this study, the behavior of the fronts is investigated by traveling wave (TW) solutions. The TW solutions can approximate the saturation and pressure profiles in infiltration experiments through a long column, and the existence conditions of the TWs act as the entropy conditions for the corresponding hyperbolic model when the viscous terms are disregarded. For the unsaturated case ($p_n = 0$), TW solutions with dynamic effect were analyzed in Ref. 42. For the two-phase case, it was shown rigorously in Refs. 43, 44, 57 that nonmonotone TWs and nonstandard entropy solutions are existing if one includes dynamic capillarity effect. Similar analysis but for higher-order viscous terms containing spatial derivatives were performed in Refs. 58, 59. The existence of TW solutions for the unsaturated case when dynamic capillarity and capillary hysteresis are present was proved in Refs. 9, 45 and criteria for nonmonotonicity and reaching full saturation were stated. It is evidenced in Refs. 15, 60 that hysteresis can explain stable saturation plateaus but it cannot initiate them. In Refs. 10, 12, it is shown how both hysteresis and dynamic capillarity are

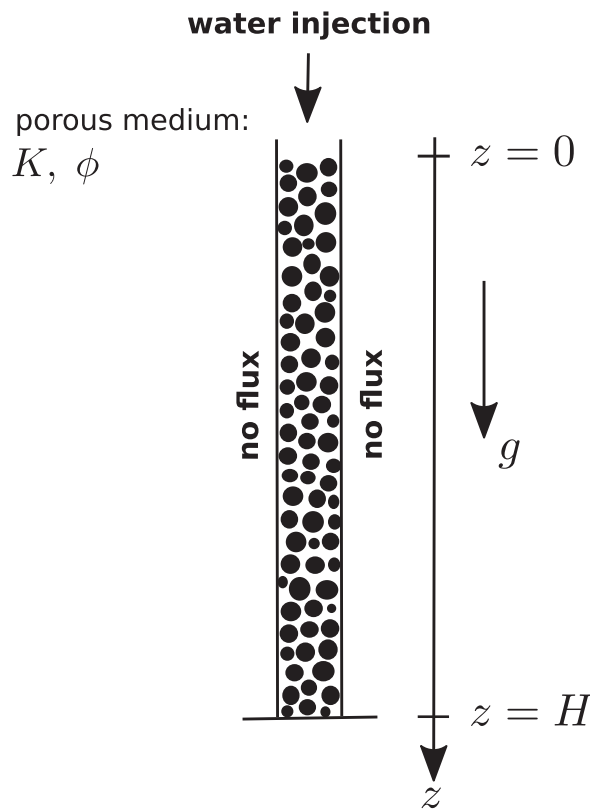


FIGURE 2 Setup of an infiltration experiment. Water is injected at a constant rate at the inlet of a column having height H . The main axis of the column is orientated along the gravity vector

required to explain the growth of viscous fingers. The entropy conditions for Buckley-Leverett equation considering hysteresis in only permeability were derived in Refs. 61-63. However, hysteresis and nonlinearities were not included in the viscous term. This is taken into consideration in Ref. 64 where the authors add a dynamic term to model permeability hysteresis, while disregarding hysteresis and dynamic effects in capillary pressure. The behavior of TW for a nonmonotone flux function in the presence of a third-order term was described in Ref. 65.

In our current work, we build upon^{9,42-45} to describe the behavior of fronts in the two-phase case when dynamic capillarity and both type of hysteresis are included. The models that are used in our analysis are introduced in Section 2. Section 3 discusses the existence of TWs when hysteresis and dynamic effects are included in the capillary pressure but not in the permeabilities. Entropy conditions are derived and they reveal that there can be nonclassical shocks. In Section 4, the analysis is extended to include hysteresis in the permeabilities. This makes self-developing stable saturation plateaus and a broader class of entropy solutions possible. Section 5 presents numerical results that support our analytical findings. Finally, we make some concluding remarks in Section 6 and compare the results with experiments.

2 | MATHEMATICAL MODEL

This section is dedicated to the formulation of a mathematical model that can be used to describe an infiltration process of a fluid into a homogeneous porous column. An example for such an infiltration process is the injection of water into a dry sand column (see Figure 2).

2.1 | Governing equations

Here we consider the one-dimensional situation where the flow problem is defined on an interval $(0, H)$. This simplification is justified by the fact that the walls of the porous column, in which the fluids are injected are impermeable and that saturation is in general almost constant across the section area of the column. The axis is pointing in the direction of gravity. The medium is assumed to be homogeneous and the fluids are incompressible. Under these constraints, (1)-(2) simplify to

$$\phi \frac{\partial S_\alpha}{\partial t} + \frac{\partial v_\alpha}{\partial z} = 0, \quad v_\alpha = -\frac{k_{r\alpha}}{\mu_\alpha} K \left(\frac{\partial p_\alpha}{\partial z} - \rho_\alpha g \right), \quad \alpha \in \{w, n\}, \quad (5)$$

where t and z are denoting the time and space variables, respectively. To further simplify the model, after summing (5) for the two phases and using (3) we observe that the total velocity

$$v(z, t) = v_w(z, t) + v_n(z, t) \quad (6)$$

is constant in space. In addition to that, we assume that v is also constant in time, which occurs, for example, if a constant influx (injection rate) is prescribed at the inlet $z = 0$. This gives

$$\frac{\partial v}{\partial t} = \frac{\partial v}{\partial z} = 0, \quad \text{or} \quad v(z, t) \equiv v \text{ for } z \in (0, H) \quad \text{and } t > 0. \quad (7)$$

From (5)-(7), one finds

$$v_w = \frac{k_{rw}}{k_{rw} + \frac{\mu_w}{\mu_n} k_{rn}} v + \frac{K}{\mu_n} \frac{k_{rw} k_{rn}}{k_{rw} + \frac{\mu_w}{\mu_n} k_{rn}} \left(\frac{\partial p_c}{\partial z} + (\rho_w - \rho_n) g \right). \quad (8)$$

At this stage, we define the fractional flow function

$$f := \frac{k_{rw}}{k_{rw} + \frac{\mu_w}{\mu_n} k_{rn}}, \quad (9)$$

and the function

$$h := \frac{k_{rw} k_{rn}}{k_{rw} + \frac{\mu_w}{\mu_n} k_{rn}} = k_{rn} f. \quad (10)$$

Substituting these relations and definitions into (5) for $\alpha = w$ yields the transport equation for the wetting phase

$$\frac{\partial S}{\partial t} + \frac{v}{\phi} \frac{\partial}{\partial z} \left[f + \frac{K(\rho_w - \rho_n)g}{v\mu_n} h + \frac{K}{v\mu_n} h \frac{\partial p}{\partial z} \right] = 0, \quad (11)$$

where we used the notation

$$S := S_w \quad \text{and} \quad p := p_n - p_w. \quad (12)$$

Note that f and h are functions of S and possibly of p , as shown below.

2.2 | Modeling hysteresis and dynamic capillarity

To incorporate hysteresis and dynamic capillarity in the model, one needs to extend capillary pressure and relative permeability given in the closure relationship (4).

2.2.1 | Capillary pressure

The following expression is used to extend the capillary pressure:

$$p \in \frac{1}{2}(p_c^{(i)}(S) + p_c^{(d)}(S)) - \frac{1}{2}(p_c^{(d)}(S) - p_c^{(i)}(S)) \cdot \text{sign}\left(\frac{\partial S}{\partial t}\right) - \tau \frac{\partial S}{\partial t}, \quad (13)$$

where $\text{sign}(\cdot)$ denotes the multivalued signum graph

$$\text{sign}(\xi) = \begin{cases} 1, & \text{for } \xi > 0, \\ [-1, 1], & \text{for } \xi = 0, \\ -1, & \text{for } \xi < 0 \end{cases} \quad (14)$$

(see Refs. 4, 11, 39). The second and third terms in the right-hand side of (13) describe, respectively, capillary hysteresis⁴ and dynamic capillarity.³⁹ Furthermore, $\tau \geq 0$ denotes the dynamic capillary coefficient. It models relaxation or damping in the capillary pressure. Although in practice τ may depend on S ,^{34,40} here we assume it to be constant. The case of nonconstant τ is considered in Refs. 9, 45. The capillary pressure functions $p_c^{(j)}$, $j \in \{i, d\}$, fulfill^{1,2,5}:

$$(P1) \quad p_c^{(j)} : (0, 1] \rightarrow [0, \infty), \quad p_c^{(j)} \in C^1((0, 1]), \quad p_c^{(j)}(1) = 0. \quad \text{Moreover,} \quad p_c^{(j)'}(S) < 0 \text{ and } p_c^{(i)}(S) < p_c^{(d)}(S) \text{ for } S \in (0, 1).$$

Here, and later in this paper, a prime denotes differentiation with respect to the argument. In the absence of dynamic effects, that is, $\tau = 0$, expression (13) implies

$$p = \begin{cases} p_c^{(i)}(S) & \text{when } \partial_t S > 0, \\ p_c^{(d)}(S) & \text{when } \partial_t S < 0. \end{cases}$$

This is precisely what is seen from water infiltration/drainage experiments.⁵ When $\frac{\partial S}{\partial t} = 0$, p is between $p_c^{(i)}(S)$ and $p_c^{(d)}(S)$. For this reason, the hysteresis described by (13) is called play-type hysteresis: that is, the scanning curves between $p_c^{(i)}(S)$ and $p_c^{(d)}(S)$ are vertical.

Before discussing the case $\tau > 0$, we introduce for convenience the sets

$$\mathcal{H}^{(i)} := \{(S, p) : S \in (0, 1], p < p_c^{(i)}(S)\}, \quad (15a)$$

$$\mathcal{H}^{(d)} := \{(S, p) : S \in (0, 1], p > p_c^{(d)}(S)\}, \quad (15b)$$

$$\mathcal{H} := \{(S, p) : S \in (0, 1], p_c^{(i)}(S) \leq p \leq p_c^{(d)}(S)\}, \quad (15c)$$

and the strip $\mathcal{W} = \mathcal{H}^{(i)} \cup \mathcal{H} \cup \mathcal{H}^{(d)} = \{0 < S \leq 1\}$. In Ref. 45, it is shown that pressure expression (13) can be written as

$$\frac{\partial S}{\partial t} = \frac{1}{\tau} \mathcal{F}(S, p) := \frac{1}{\tau} \begin{cases} p_c^{(d)}(S) - p & \text{if } (S, p) \in \mathcal{H}^{(d)}, \\ 0 & \text{if } (S, p) \in \mathcal{H}, \\ p_c^{(i)}(S) - p & \text{if } (S, p) \in \mathcal{H}^{(i)}. \end{cases} \quad (16)$$

2.2.2 | Relative permeability

To make the effect of hysteresis explicit in the relative permeabilities, we need to incorporate a dependence on both S and $\frac{\partial S}{\partial t}$. This dependence should satisfy

$$k_{r\alpha} \left(S, \frac{\partial S}{\partial t} \right) = \begin{cases} k_{r\alpha}^{(i)}(S) & \text{if } \frac{\partial S}{\partial t} > 0, \\ k_{r\alpha}^{(d)}(S) & \text{if } \frac{\partial S}{\partial t} < 0, \end{cases} \text{ for } \alpha \in \{w, n\}. \quad (17)$$

Here, $k_{r\alpha}^{(i)}, k_{r\alpha}^{(d)} : [0, 1] \rightarrow \mathbb{R}$ are the infiltration and drainage relative permeabilities obtained from experiments.^{6,29-32} In line with the experimental outcomes, we assume here for $j \in \{i, d\}$,

- (P2) $k_{rw}^{(j)} \in C^2([0, 1])$, $k_{rw}^{(j)'}(S) > 0$ for $0 < S \leq 1$, $k_{rw}^{(j)}(0) = 0$ and $k_{rw}^{(j)}$ is strictly convex. Moreover, for $0 < S < 1$, $k_{rw}^{(i)}(S) < k_{rw}^{(d)}(S)$.
- (P3) $k_{rn}^{(j)} \in C^2([0, 1])$, $k_{rn}^{(j)'}(S) < 0$ for $0 \leq S < 1$, $k_{rn}^{(j)}(1) = 0$ and $k_{rn}^{(j)}$ is strictly convex. Moreover, for $0 < S < 1$, $k_{rn}^{(d)}(S) < k_{rn}^{(i)}(S)$.

Note the reverse ordering in k_{rw} and k_{rn} when switching from infiltration to drainage. This is demonstrated experimentally in Refs. 29, 30, 32, see also Figure 1.

In Ref. 66, a play-type approach has been proposed to model $k_{r\alpha}$ where

$$k_{r\alpha} \in \frac{1}{2} (k_{r\alpha}^{(d)}(S) + k_{r\alpha}^{(i)}(S)) - \frac{1}{2} (k_{r\alpha}^{(d)}(S) - k_{r\alpha}^{(i)}(S)) \cdot \text{sign} \left(\frac{\partial S}{\partial t} \right). \quad (18)$$

However, this model is ill-posed in the unregularized case as for $\frac{\partial S}{\partial t} = 0$ the relative permeabilities are undetermined, that is, the relative permeabilities have no equation to determine them when $\frac{\partial S}{\partial t} = 0$. This is different for the capillary pressure (13) because p satisfies Equation (11) as well. With the permeabilities, we take an approach inspired by Refs. 61-63. Here, inherited from the capillary pressure, the hysteresis is of the play-type as well, but now depending on S and p , rather than on S and $\frac{\partial S}{\partial t}$. We propose the following model: for $\alpha \in \{w, n\}$

$$k_{r\alpha} = k_{r\alpha}(S, p) = \begin{cases} k_{r\alpha}^{(d)}(S) & \text{if } (S, p) \in \mathcal{H}^{(d)}, \\ \bar{k}_{r\alpha}(S, p) & \text{if } (S, p) \in \mathcal{H}, \\ k_{r\alpha}^{(i)}(S) & \text{if } (S, p) \in \mathcal{H}^{(i)}. \end{cases} \quad (19)$$

Here, $\bar{k}_{r\alpha} : \mathcal{H} \rightarrow [0, \infty)$ is a given function that satisfies

- (P4) $\bar{k}_{r\alpha} \in C^2(\mathcal{H})$ such that $k_{r\alpha} \in C(\mathcal{W})$ for $\alpha \in \{w, n\}$ and $\partial_p \bar{k}_{rw} > 0$, $\partial_p \bar{k}_{rn} < 0$ in \mathcal{H} .

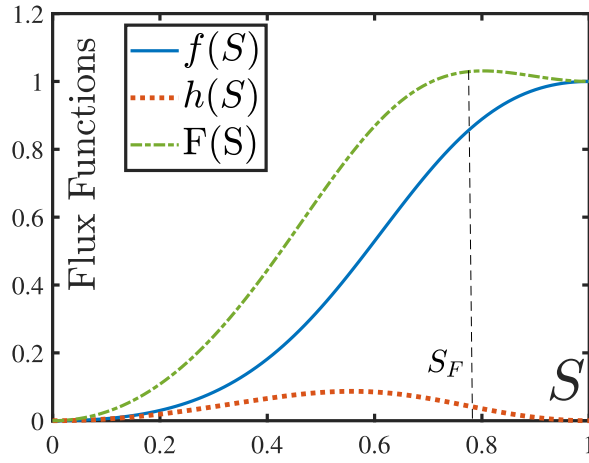


FIGURE 3 The functions $f(S)$, $h(S)$, and $F(S)$ as given in Remark 2. Here, $M = 2$ and $N_g = 4$

Observe that this implies $\bar{k}_{r\alpha}(S, p_c^{(j)}(S)) = k_{r\alpha}^{(j)}(S)$ for $j \in \{i, d\}$. For the moment we leave the choice of $\bar{k}_{r\alpha}$ unspecified except for properties (P4), as it neither influences the entropy conditions nor the critical τ values introduced afterward.

Remark 1. In the computations, one needs to specify an expression for $\bar{k}_{r\alpha}$. In Section 5, we use

$$\bar{k}_{r\alpha}(S, p) = k_{r\alpha}^{(i)}(S) + (k_{r\alpha}^{(d)}(S) - k_{r\alpha}^{(i)}(S)) \left(\frac{p - p_c^{(i)}(S)}{p_c^{(d)}(S) - p_c^{(i)}(S)} \right). \quad (20)$$

This expression is obtained by considering sign in (13) and (18) as a function that can be eliminated. With $\tau = 0$ in (13), this results in (20). Since the fraction (20) is bounded by 0 and 1 for $(S, p) \in \mathcal{H}$, we have $\lim_{S \searrow 0} k_{r\alpha}(S, p) = k_{r\alpha}^{(i)}(0) = k_{r\alpha}^{(d)}(0)$ and similar for $S \nearrow 1$.

Observe that (19) is consistent with (17) as from (16), $\frac{\partial S}{\partial t} > 0$ iff $p < p_c^{(i)}(S)$ and $\frac{\partial S}{\partial t} < 0$ iff $p > p_c^{(d)}(S)$. Moreover, the scanning curves for $k_{r\alpha}$ have constant S . Although not true in general, see, for instance, Figure 1, we restrict ourselves to play-type for both p and $k_{r\alpha}$. An extension describing nonvertical scanning curves is discussed in Ref. 24 and chapters 3,11 of Ref. 27.

Using (19) and (9),(10), the nonlinearities f and h are expressed in terms of S and p as well:

$$\zeta(S, p) = \begin{cases} \zeta^{(d)}(S) & \text{if } (S, p) \in \mathcal{H}^{(d)}, \\ \bar{\zeta}(S, p) & \text{if } (S, p) \in \mathcal{H}, \\ \zeta^{(i)}(S) & \text{if } (S, p) \in \mathcal{H}^{(i)}, \end{cases} \quad \text{for } \zeta \in \{f, h\}. \quad (21)$$

From (P2)-(P4) we deduce for f and h :

(P5) $f \in C(\mathcal{W})$, $\bar{f} \in C^2(\mathcal{H})$ and $\partial_p \bar{f} > 0$ in \mathcal{H} . For $j \in \{i, d\}$, $f^{(j)} \in C^2([0, 1])$, $f^{(j)'}(S) > 0$ for $0 < S < 1$, $f^{(j)}(0) = 0$, $f^{(j)}(1) = 1$. Moreover, for $0 < S < 1$, $f^{(i)}(S) < f^{(d)}(S)$.

(P6) $h \in C(\mathcal{W})$, $\bar{h} \in C^2(\mathcal{H})$, $h^{(j)} \in C^2([0, 1])$ and $h^{(j)}(0) = h^{(j)}(1) = 0$ for $j \in \{i, d\}$.

Observe that in general no ordering holds between $h^{(i)}$ and $h^{(d)}$. Typical curves for $f^{(j)}$ and $h^{(j)}$ are shown in Figure 3. The Equations (11), (13), and (21) are the complete set of equations for our model.

2.3 | Dimensionless formulation

Let H [m] be the characteristic length, p_r [Pa] the characteristic pressure, $t_r = \frac{\phi H}{v}$ [s] the characteristic time, and τ_r [Pa · s] the characteristic dynamic capillary constant. Inspired by the J-Leverett model,⁶⁷ we take as characteristic pressure $p_r = \sigma \sqrt{\frac{\phi}{K}}$, σ being the surface tension between the two phases. Alternatively, one could consider $p_r = (\rho_n - \rho_w)gH$ which is a more common choice for the Richards equation with gravity. Setting

$$\tilde{z} := \frac{z}{H}, \quad \tilde{t} := \frac{t}{t_r}, \quad \tilde{\psi} := \frac{\psi}{p_r}, \quad \text{and} \quad \tilde{\tau} = \frac{\tau}{\tau_r},$$

where $\psi \in \{p, p_c^{(i)}, p_c^{(d)}\}$, and defining the dimensionless numbers

$$N_g := \frac{K(\rho_w - \rho_n)g}{v\mu_n} \text{ (gravity number) and } N_c := \frac{Kp_r}{v\mu_n H} \text{ (capillary number),}$$

we obtain from (11) the dimensionless transport equation

$$\frac{\partial S}{\partial \tilde{t}} + \frac{\partial}{\partial \tilde{z}} \left(f + N_g h + N_c h \frac{\partial \tilde{p}}{\partial \tilde{z}} \right) = 0. \quad (22)$$

The closure relation (13) becomes

$$\tilde{p} \in \frac{1}{2} (\tilde{p}_c^{(i)}(S) + \tilde{p}_c^{(d)}(S)) - \frac{1}{2} (\tilde{p}_c^{(d)}(S) - \tilde{p}_c^{(i)}(S)) \cdot \text{sign} \left(\frac{\partial S}{\partial \tilde{t}} \right) - \tilde{\tau} \frac{\tau_r}{p_r t_r} \frac{\partial S}{\partial \tilde{t}}. \quad (23)$$

Now choosing $\tau_r = N_c p_r t_r = p_r^2 \frac{\phi K}{v^2 \mu_n}$, the Leverett scaling for p_r gives

$$\tau_r = \frac{\sigma^2 \phi^2}{\mu_n v^2} \text{ implying } \tilde{\tau} = \frac{\mu_n v^2}{\sigma^2 \phi^2} \tau. \quad (24)$$

This choice leaves us with a characteristic dynamic coefficient that is independent of the length scale of the problem. This is precisely the scaling used in Refs. 43, 44, 68 that is consistent with the hyperbolic limit. Realistic values of dimensional and scaled quantities are given in Ref. 69.

Dropping the $\tilde{}$ sign from the notation, we are left with the dimensionless system

$$(\mathcal{P}) \begin{cases} \frac{\partial S}{\partial t} + \frac{\partial}{\partial z} \left(F(S, p) + N_c h(S, p) \frac{\partial p}{\partial z} \right) = 0, & (25a) \\ \frac{\partial S}{\partial t} = \frac{1}{N_c \tau} \mathcal{F}(S, p), & (25b) \end{cases}$$

$$\text{where } F = f + N_g h. \quad (25c)$$

This system can be seen as a regularization of the hyperbolic Buckley-Leverett equation with gravity. Here, the regularization involves hysteresis and dynamic capillarity. Compared to the usual second-order parabolic regularization, yielding shocks that satisfy the standard Oleinik conditions,⁷⁰ different (nonparabolic) regularizations may yield shocks that violate these conditions, see, for example, Refs. 43, 71. Such shocks are called nonclassical.

One of the main issues that concerns this paper is to show the existence of nonclassical shocks originating from System (\mathcal{P}) . To this end, we proceed as in Ref. 43 and study the existence of TW

solutions of (\mathcal{P}) that connect a left state S_B to a right state S_T in the presence of both hysteresis and dynamic capillarity. TWs for the model with only dynamic capillarity are analyzed in Refs. 44, 57. For the case of unsaturated flow, that is, Richards equation with a convex flux function, existence and qualitative properties of TWs are considered in detail in Refs. 9, 42, 45.

For the purpose of TWs, we consider System (\mathcal{P}) in the domain $-\infty < z < \infty$. Then the capillary number N_c can be removed from the problem by the scaling

$$z := z/N_c \text{ and } t := t/N_c.$$

This yields the N_c independent formulation

$$(\tilde{\mathcal{P}}) \begin{cases} \frac{\partial S}{\partial t} + \frac{\partial}{\partial z} \left(F(S, p) + h(S, p) \frac{\partial p}{\partial z} \right) = 0, \\ \frac{\partial S}{\partial t} = \frac{1}{\tau} \mathcal{F}(S, p), \end{cases} \quad (26)$$

with $-\infty < z < \infty$ and $t > 0$. This is the starting point for the TW analysis.

Remark 2. Using the Brooks-Corey type expression, for example, see Ref. 72,

$$k_{rw}(S) = S^q \text{ and } k_{rn}(S) = (1 - S)^q, \quad (27)$$

with $q = 2$, the nonlinearities (9), (10), and (25c) become for no-hysteresis in permeabilities,

$$f(S) = \frac{S^2}{S^2 + M(1 - S)^2}, \quad h(S) = (1 - S)^2 f(S), \quad F(S) = S^2 \frac{(1 + N_g(1 - S)^2)}{S^2 + M(1 - S)^2},$$

where $M = \frac{\mu_w}{\mu_n}$ denotes the viscosity ratio. A plot is shown in Figure 3 for these functions. Some elementary calculations give

- (a) *Monotonicity:* If $N_g \leq M$ then $F'(S) > 0$ for all $0 < S < 1$ and if $N_g > M$ then there exists a unique $S_F \in (0, 1)$ such that $F'(S) > 0$ for all $0 < S < S_F$ and $F'(S) < 0$ for $S_F < S < 1$. Since $F(1) = 1$, clearly $F(S_F) > 1$.
- (b) *Inflection points:* $f(S)$ has only one inflection point in $(0, 1)$ whereas, $F(S)$ has at most two. To see this for $f(S)$, note that $f''(S) = P(S)Q(S)$ with $Q(S)$ being a positive function and $P(S) = M - (3M + 3)S^2 + (2M + 2)S^3$. Since $P(0) = M$, $P(1) = -1$ and $P'(S) < 0$ for $S \in (0, 1)$, the result follows.

These properties of f and F will be used when discussing the different cases of TWs.

2.4 | TW formulation

Having derived the nondimensional hysteretic two-phase flow System $(\tilde{\mathcal{P}})$, we investigate under which conditions TW solutions exist. These are solutions of the form

$$S(z, t) = S(\xi), \quad p(z, t) = p(\xi), \quad \text{with } \xi = ct - z,$$

where S and p are the wave profiles of saturation and pressure and $c \in \mathbb{R}$ the wave-speed. We seek TWs that satisfy

$$\begin{cases} \lim_{\xi \rightarrow -\infty} S(\xi) = S_B, \quad \lim_{\xi \rightarrow \infty} S(\xi) = S_T, \\ \lim_{\xi \rightarrow -\infty} p'(\xi) = \lim_{\xi \rightarrow \infty} p'(\xi) = 0, \end{cases} \quad (28)$$

where S_B corresponds to an ‘‘initial’’ saturation and S_T to the injected saturation. The choice of $p'(\pm\infty) = 0$ ensures that the diffusive flux vanishes at $\xi = \pm\infty$. Substituting (28) into (26), and integrating (26) one obtains

$$cS - (F(S, p) - h(S, p)p') = A, \quad (29a)$$

$$cS' = \frac{1}{\tau} \mathcal{F}(S, p), \quad (29b)$$

where $\xi \in \mathbb{R}$ and A is a constant of integration.

As was shown in Ref. 9 for the Richards equation, (28) and (29) do not automatically guarantee the existence of $\lim_{\xi \rightarrow \pm\infty} p(\xi)$. However, if $p(\pm\infty)$ is well-defined then (29b) and the existence of $S(\pm\infty)$ forces $\lim_{\xi \rightarrow \pm\infty} \mathcal{F}(S(\xi), p(\xi)) = 0$. Recalling that $\mathcal{F}(S, p) = 0$ iff $(S, p) \in \mathcal{H}$ we then have

$$\lim_{\xi \rightarrow -\infty} p(\xi) = p_B \in [p_c^{(i)}(S_B), p_c^{(d)}(S_B)], \quad \lim_{\xi \rightarrow \infty} p(\xi) = p_T \in [p_c^{(i)}(S_T), p_c^{(d)}(S_T)].$$

We show later that p_B , interpreted as the initial pressure, can sometimes be chosen independently, whereas, p_T , when existing, is always fixed by the choice of S_B, S_T , and p_B . Following the steps in Refs. 9, 44, 45, we obtain the Rankine-Hugoniot condition for wave-speed c , that is,

$$c = \frac{F(S_T, p_T) - F(S_B, p_B)}{S_T - S_B}. \quad (30)$$

With this, system (29) can be rewritten as a dynamical system,

$$(TW) \begin{cases} S' = \frac{1}{c\tau} \mathcal{F}(S, p), \\ p' = \mathcal{G}(S, p), \end{cases} \quad (31)$$

where

$$\mathcal{G}(S, p) := \frac{F(S, p) - \ell(S)}{h(S, p)} \quad \text{with} \quad \ell(S) := F(S_B, p_B) + c(S - S_B). \quad (32)$$

Note that when F is nonmonotone (eg, $N_g > M$ in Figure 2), the wave-speed c can be positive or negative depending on the values of S_B and S_T .

We study all possible solutions of system (TW) for $\tau > 0$. They serve as viscous profiles of admissible shocks of the limiting Buckley-Leverett equation. Existence conditions for solutions of (TW) act as admissibility/entropy conditions for the corresponding shocks.

The solutions of (TW) are investigated under two different scenarios.

A: No hysteresis in relative permeabilities, that is, $\zeta^{(i)} = \zeta^{(d)}$ for $\zeta \in \{f, h\}$. Furthermore, N_g is sufficiently small so that F satisfies properties stated for $f^{(j)}$ in (P5). For F as in Remark 2 this is satisfied if $N_g \leq M$.

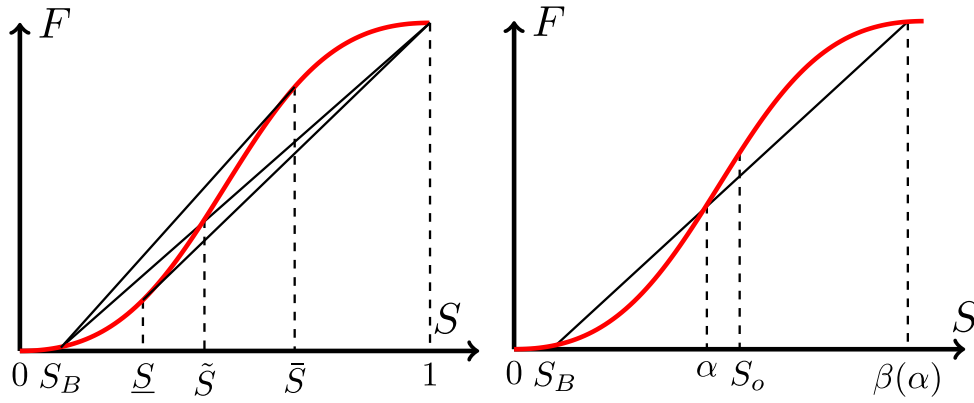


FIGURE 4 (Left) The saturations S_B , \underline{S} , \tilde{S} , and \bar{S} . Here, \underline{S} is the tangent to the $F(S)$ curve from $(1,1)$ and \bar{S} is the tangent from $(S_B, F(S_B))$. (Right) The saturation $\beta(\alpha)$ is defined by the third intersection of the line connecting $(\alpha, F(\alpha))$ and $(S_B, F(S_B))$ with F . The inflection point of F is at $S = S_o$ and $\beta(\bar{S}) = 1$

B: N_g and τ sufficiently small; relative permeabilities are hysteretic.

A third scenario where N_g is large so that F is nonmonotone is discussed briefly at the end of Section 3.

3 | NO RELATIVE PERMEABILITY HYSTERESIS AND SMALL N_g (SCENARIO A)

In the absence of relative permeability hysteresis, the functions f , h , F , and \mathcal{G} depend on S only. We explicitly state the properties of F as a result of (P5), (P6), and Remark 2.

(A1) $F \in C^2([0, 1])$, $F'(S) > 0$ for $0 < S < 1$, $F(0) = 0$, $F(1) = 1$. Moreover, a unique $S_o \in (0, 1)$ exists such that

$$F''(S_o) = 0, \quad F''(S) > 0 \text{ for } 0 < S < S_o, \text{ and } F''(S) < 0 \text{ for } S_o < S < 1.$$

3.1 | Preliminaries

For the purpose of readability, we moved the proofs of most details in Appendix A. Throughout this section, we restrict ourselves to relatively small values of S_B . Specifically, we assume

$$0 < S_B < S_o. \quad (33)$$

First let us take $S_B \leq \underline{S}$, where \underline{S} is the saturation at which $F'(\underline{S}) = \frac{1-F(\underline{S})}{1-\underline{S}}$. The convex-concave behavior of F implies $\underline{S} < S_o$. For later purpose, and with reference to Figure 4 (left), we introduce the additional saturations $S_B < \tilde{S} < \bar{S} < 1$, where \tilde{S} is the saturation at which $F(S)$ intersects the line connecting $(S_B, F(S_B))$ and $(1,1)$, and where \bar{S} is the saturation for which $F'(\bar{S}) = \frac{F(\bar{S})-F(S_B)}{\bar{S}-S_B}$. To each $\alpha \in [\tilde{S}, \bar{S}]$ corresponds a unique $\beta \in [\bar{S}, 1]$ such that $(\beta, F(\beta))$ is the third intersection point between the graph of F and the chord through $(S_B, F(S_B))$ and $(\alpha, F(\alpha))$ (see Figure 4 (right)). This

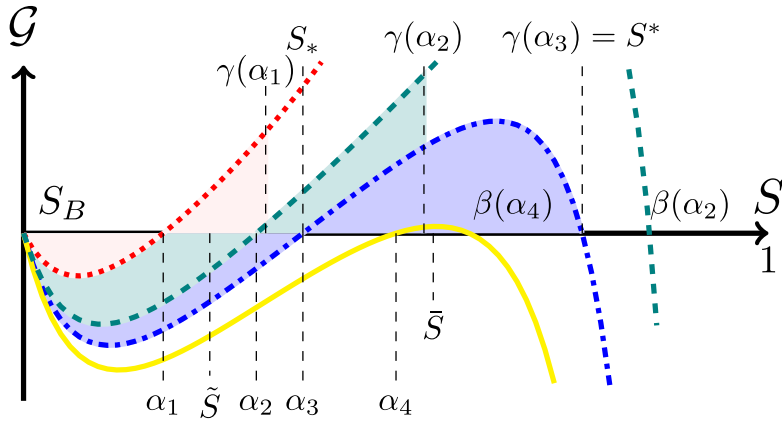


FIGURE 5 The plot of $\mathcal{G}(S; S_B, \alpha)$ for different values of α . Here, $\alpha_1 < \tilde{S} < \alpha_2 < \alpha_3 = S_* < \alpha_4 < \bar{S} < S^*$. Values of γ and β are also shown. Note that $\beta(\alpha_1)$ and $\gamma(\alpha_4)$ do not exist

defines the function

$$\begin{cases} \beta : [\tilde{S}, \bar{S}] \rightarrow [\bar{S}, 1], \beta(\bar{S}) = \bar{S}, \beta(\tilde{S}) = 1, \\ \beta(\alpha) \text{ is strictly decreasing.} \end{cases} \quad (34)$$

Later in this section, a second function $\gamma = \gamma(\alpha)$ is introduced as one of the roots of the equation

$$\int_{S_B}^{\gamma(\alpha)} \mathcal{G}(S; S_B, \alpha) dS = 0 \text{ for } S_B \leq \alpha \leq \bar{S}. \quad (35)$$

Here, $\mathcal{G}(S; S_B, \alpha)$ is the expanded notation of \mathcal{G} from (32) for the p independent case:

$$\mathcal{G}(S; S_B, \alpha) = \frac{F(S) - \ell(S; S_B, \alpha)}{h(S)} \quad \text{with} \quad \ell(S; S_B, \alpha) = F(S_B) + \frac{F(\alpha) - F(S_B)}{\alpha - S_B}(S - S_B).$$

A typical sketch of $\mathcal{G}(S; S_B, \alpha)$ for different values of α is shown in Figure 5. Note that

$$\mathcal{G}(S; S_B, \alpha) \text{ decreases with respect to } \alpha \in [S_B, \bar{S}] \text{ and} \quad (36)$$

$$\mathcal{G}(S; S_B, \alpha) \begin{cases} \left. \begin{array}{l} < 0 \text{ for } S_B < S < \alpha \\ > 0 \text{ for } S > \alpha \end{array} \right\} \text{ when } S_B < \alpha < \tilde{S}, \\ \left. \begin{array}{l} < 0 \text{ for } S_B < S < \alpha \\ > 0 \text{ for } \alpha < S < \beta(\alpha) \\ < 0 \text{ for } \beta(\alpha) < S < 1 \end{array} \right\} \text{ when } \tilde{S} < \alpha < \bar{S}. \end{cases} \quad (37)$$

Since,

$$\mathcal{G}(S; S_B, \alpha) = \begin{cases} \mathcal{O}\left(\frac{1}{k_{rn}(S)}\right) & \text{when } \alpha \neq \tilde{S}, \\ \mathcal{O}\left(\frac{1-S}{k_{rn}(S)}\right) & \text{when } \alpha = \tilde{S}, \end{cases} \quad (38)$$

as $S \nearrow 1$, we have for most practical applications

$$\mathcal{G}(S; S_B, \alpha) \text{ is nonintegrable near } S = 1 \text{ for each } S_B \leq \alpha \leq \bar{S}. \quad (39)$$

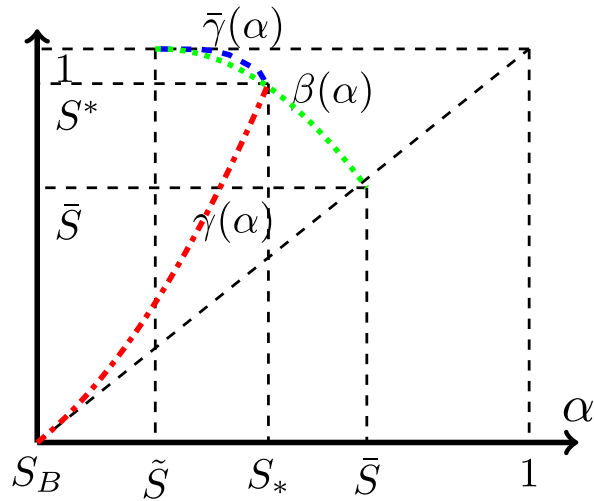


FIGURE 6 The functions β , γ , and $\bar{\gamma}$ (assuming (39)) and the definitions of S_* and S^* for $S_B < \underline{S}$

This is the case for Brooks-Corey permeabilities with $q \geq 2$ (see Remark 2).

Remark 3. We also note that in the context of this section the wave-speed (30) reduces to

$$c = \frac{F(S_T) - F(S_B)}{S_T - S_B}.$$

From assumption A1, it follows that there is a one-to-one correspondence between c and $S_T \in [S_B, \bar{S}]$. Writing $c = c(S_T)$, we have the following properties for $c(S_T)$:

$$c(S_B) = F'(S_B), \quad c(\bar{S}) = F'(\bar{S}), \quad \text{and} \quad \frac{dc}{dS_T} > 0 \text{ for } S \in [S_B, \bar{S}].$$

Returning to Equation (35), we note that $\gamma = S_B$ is the trivial solution. Properties (37) and (38) imply the existence of a second nontrivial and increasing solution $\gamma = \gamma(\alpha)$ for $\alpha \geq S_B$. It satisfies the following properties.

Proposition 1. *Assume either (39) or $S_B \in (\underline{S}, S_o)$. Let γ be the increasing (unique) solution of (35). Then it is defined in the interval $[S_B, S_*]$ where $S_* \in (\tilde{S}, \bar{S})$ is such that $\gamma(S_*) = \beta(S_*) =: S^*$. Furthermore, $\gamma(S_B) = S_B$, $\gamma(\alpha) > \alpha$ for $\alpha > S_B$ and $\gamma(\alpha) < \beta(\alpha)$ for $\alpha < S_*$ in the common domain of definition of β and γ (see Figure 6).*

Observe that, if (39) holds, then a third solution $\gamma = \bar{\gamma}$ exists for $\tilde{S} < \alpha < S_*$. It decreases in α with $\bar{\gamma}(\tilde{S}) = 1$ and $\bar{\gamma}(S_*) = S^*$. The solutions (35) and the function $\beta(\alpha)$ are sketched in Figure 6.

Remark 4. For simplicity, we assume (39) for the remaining discussion. This guarantees the existence of a (S_*, S^*) pair. The methods presented in this paper can also be applied to analyze the case when $\beta(\alpha)$ and $\gamma(\alpha)$ are not intersecting. The results are briefly discussed in Section 3.2.

Next we turn to system (TW) where, for the time being, we take

$$S_B < S_T \leq \bar{S}. \quad (40)$$

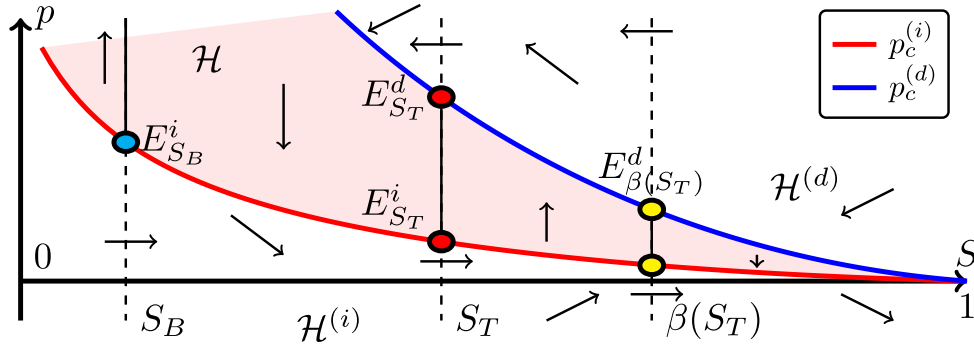


FIGURE 7 The S - p phase plane and the direction of orbits for Scenario A with $\tilde{S} \leq S_T \leq \bar{S}$. The regions \mathcal{H} , $\mathcal{H}^{(i)}$, $\mathcal{H}^{(d)}$ and the equilibrium lines are marked

Since (TW) is autonomous, it is convenient to represent solutions as orbits in the (S, p) -plane, or rather, in the strip $\{(S, p) : 0 \leq S \leq 1, p \in \mathbb{R}\}$. Moreover, orbits are same for any shift in the independent variable ξ . Therefore, we may set without loss of generality (see Refs. 9, 45),

$$S(0) = \frac{1}{2}(S_B + S_T). \quad (41)$$

Equilibrium points of (TW) that are of particular interest are

$$E_K^j \equiv (K, p_c^{(j)}(K)), \text{ where } K \in \{S_B, S_T\} \text{ and } j \in \{i, d\}.$$

If $\tilde{S} \leq S_T < \bar{S}$, a third pair exists for $K = \beta(S_T)$. The points E_K^j and the direction of the orbits are indicated in Figure 7. By the special nature of the function \mathcal{F} , we have in fact that all points of the segments $\overline{E_K^i E_K^d}$ are equilibrium points. Boundary conditions (28) are satisfied if an orbit connects the segments $\overline{E_{S_B}^i E_{S_B}^d}$ and $\overline{E_{S_T}^i E_{S_T}^d}$. As shown in Ref. 45, an orbit can leave $\overline{E_{S_B}^i E_{S_B}^d}$ only from the lowest point $E_{S_B}^i$. Then it enters region $\mathcal{H}^{(i)}$ where it moves monotonically with respect to S as a consequence of the sign in the right-hand side of Equation (31): if $p < p_c^{(i)}(S)$ we have $S' > 0$.

Due to this monotonicity, one can alternatively describe an orbit leaving $E_{S_B}^i$ as a function of the saturation as long as it belongs to $\mathcal{H}^{(i)}$. For given $\tau > 0$ and S_T satisfying (40), let $w(S) = w(S; \tau, S_T)$ denote this function. Then

$$w(S_B; \tau, S_T) = p_c^{(i)}(S_B) \quad (42a)$$

$$\text{and } w(S; \tau, S_T) < p_c^{(i)}(S) \text{ in a right neighborhood of } S_B. \quad (42b)$$

As in Refs. 9, 45, we deduce from (TW) that w should satisfy

$$w'(S; \tau, S_T) = \frac{c\tau\mathcal{G}(S; S_B, S_T)}{p_c^{(i)}(S) - w(S; \tau, S_T)} \text{ for } S > S_B. \quad (43)$$

Using techniques from,^{9,45} one can show that initial value problem (43), (42a) has a unique local solution $w(S; \tau, S_T)$ that satisfies (42b).

Remark 5. Conversely one recovers the orbit $(S(\xi), p(\xi))$ by substituting w into (31). Using (41) this gives

$$\xi = c\tau \int_{\frac{1}{2}(S_B+S_T)}^{S(\xi)} \frac{d\varrho}{p_c^{(i)}(\varrho) - w(\varrho; \tau, S_T)} d\varrho \text{ and } p(\xi) = w(S(\xi); \tau, S_T).$$

Rewriting (43) as

$$(p_c^{(i)} - w)(w - p_c^{(i)})' + (p_c^{(i)} - w)p_c^{(i)'} = c\tau \mathcal{G}(S; S_B, S_T),$$

we find recalling (P1) that

$$((p_c^{(i)} - w)^2)' = 2(p_c^{(i)} - w)p_c^{(i)'} - 2c\tau \mathcal{G}(S; S_B, S_T) \leq -2c\tau \mathcal{G}(S; S_B, S_T) \text{ in } \{w < p_c^{(i)}\}. \quad (44)$$

Integrating this inequality from S_B to S gives the lower bound

$$\left. \begin{array}{l} w(S; \tau, S_T) > p_c^{(i)}(S) - \sqrt{2c\tau \Phi(S)} \text{ in } \{w < p_c^{(i)}\}, \\ \text{where } \Phi(S) = \Phi(S; S_B, S_T) := -\int_{S_B}^S \mathcal{G}(\varrho; S_B, S_T) d\varrho. \end{array} \right\} \quad (45)$$

With S_T satisfying (40), properties (37)-(39) and Proposition 1 imply

$$\left. \begin{array}{l} \Phi(S) > 0 \text{ for } S_B < S < \gamma(S_T) \\ \Phi(S_B) = \Phi(\gamma(S_T)) = 0 \end{array} \right\} \text{ when } S_B < S_T \leq S_*, \quad (46a)$$

$$\text{and } \left. \begin{array}{l} \Phi(S) > 0 \text{ for } S_B < S < 1 \\ \lim_{S \nearrow 1} \Phi(S) = +\infty \end{array} \right\} \text{ when } S_* < S_T \leq \bar{S}. \quad (46b)$$

Observe that, depending on S_B , S_T , and τ , the interval where $w(S) < p_c^{(i)}(S)$ is either $(S_B, 1]$ if $w(S)$ and $p_c^{(i)}(S)$ do not intersect, or (S_B, S_i) with $S_i \leq 1$ in case there is an intersection at $S = S_i$. In the latter case, it follows immediately from (44) that we must have,

Proposition 2. *Suppose there exists $S_i \in (S_B, 1)$ such that $w(S) < p_c^{(i)}(S)$ for $S_B < S < S_i$ and $w(S_i) = p_c^{(i)}(S_i)$. Then $\mathcal{G}(S_i; S_B, S_T) \geq 0$.*

Hence, if the orbit exits through the capillary pressure curve $p_c^{(i)}$, it can only do so at points where $\mathcal{G} \geq 0$. From the discussion above, one defines

$$S_m(\tau, S_T) = \sup\{S \in (S_B, 1) : w(\varrho; \tau, S_T) < p_c^{(i)}(\varrho) \text{ for all } S_B < \varrho < S\}, \quad (47)$$

which is the upper limit of the interval on which w exists. Then we have

Proposition 3.

(a) *If $S_B < S_T \leq S_*$, then $S_T \leq S_m(\tau, S_T) < \gamma(S_T)$ for all $\tau > 0$;*

(b) *If $S_* < S_T \leq \bar{S}$ and $w(\beta(S_T); \tau, S_T) < p_c^{(i)}(\beta(S_T))$, then $S_m(\tau, S_T) = 1$ and $\lim_{S \nearrow 1} w(S) = -\infty$.*

In Figure 8, we sketch the behavior of $w(S; \tau, S_T)$ in $\mathcal{H}^{(i)}$. The existence of orbits as in Figure 8 (left) is a direct consequence of the behavior of the lower bound (45). Orbits as in Figure 8 (right) need

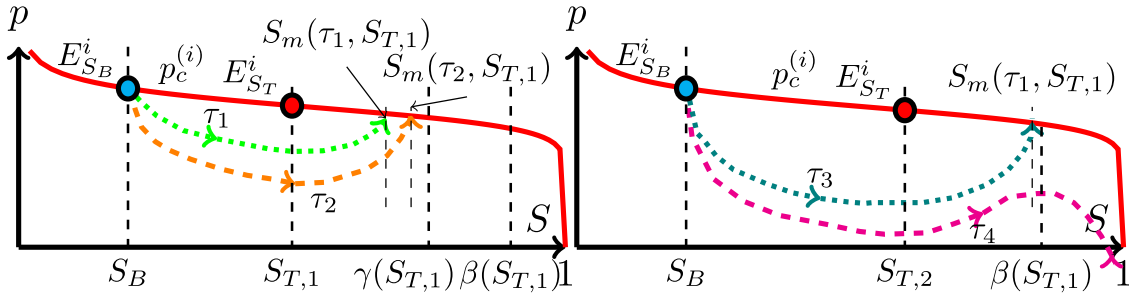


FIGURE 8 Sketch of orbits represented by $w(S; \tau, S_T)$. (Left) $S_{T,1} \in (S_B, S_*]$, $\tau_1 < \tau_2$; (Right) $S_{T,2} \in (S_*, \bar{S}]$, $\tau_3 < \tau_4$

more attention since the case $S_m(\tau, S_T) < \beta(S_T)$, represented by τ_3 , remains to be discussed. We make the behavior as sketched in Figure 8 (right) precise in a number of steps.

Next, we give a general monotonicity result.

Proposition 4 (Monotonicity).

(a) For a fixed $S_T \in (S_B, \bar{S}]$ and any pair $0 < \tau_1 < \tau_2$,

$$w(\cdot; \tau_2, S_T) < w(\cdot; \tau_1, S_T) \text{ in } \{w(\cdot; \tau_1, S_T) < p_c^{(i)}(\cdot)\}$$

and

$$S_m(\tau_1, S_T) < S_m(\tau_2, S_T) \text{ if } S_T < S_m(\tau_2, S_T) \leq \beta(S_T);$$

(b) For fixed $\tau > 0$ and any pair $S_B < S_{T,1} < S_{T,2} \leq \bar{S}$,

$$w(\cdot; \tau, S_{T,2}) < w(\cdot; \tau, S_{T,1}) \text{ in } \{w(\cdot; \tau, S_{T,1}) < p_c^{(i)}(\cdot)\}$$

and

$$S_m(\tau, S_{T,1}) < S_m(\tau, S_{T,2}) \text{ if } S_{T,2} \leq S_m(\tau, S_{T,2}) \leq \beta(S_{T,2}).$$

Remark 6. To complement Proposition 4, we further state that

$$S_m(\tau_1, S_T) = S_T \quad \text{if} \quad S_m(\tau_2, S_T) = S_T \quad \text{and} \quad S_m(\tau_2, S_T) = 1 \text{ if } S_m(\tau_1, S_T) = 1.$$

The statements follow directly from the ordering of the orbits.

So far we have shown monotonicity of the orbits in $\mathcal{H}^{(i)}$. The next results give the continuous dependence on the parameter τ and S_T . This is addressed in the following results.

Proposition 5 (Continuous dependence of w). Let $v = p_c^{(i)} - w$. In the context of Figure 4 and with Φ defined in (45), we have

$$(a) \quad 0 < v^2(S; \tau_2, S_T) - v^2(S; \tau_1, S_T) < 2c(\tau_2 - \tau_1)\Phi(S) \text{ for } S_B < S \leq S_m(\tau_1, S_T);$$

$$(b) \quad 0 < v^2(S; \tau, S_{T,2}) - v^2(S; \tau, S_{T,1}) < 2(c(S_{T,2})\Phi(S; S_B, S_{T,2}) - c(S_{T,1})\Phi(S; S_B, S_{T,1})) \quad \text{for} \\ S_B < S \leq S_m(\tau, S_{T,1});$$

Corollary 1 (Continuous dependence of S_m). Let $\tau_0 > 0$ and S_{T_0} be fixed such that $S_m(\tau_0, S_{T_0}) \leq \beta(S_{T_0})$. Then for any small $\varepsilon > 0$, there exists $\delta = \delta(\varepsilon; \tau_0, S_{T_0})$ so that $|S_m(\tau, S_T) - S_m(\tau_0, S_{T_0})| < \varepsilon$ if $\max\{|\tau - \tau_0|, |S_T - S_{T_0}|\} < \delta$ and $S_m(\tau, S_T) < \beta(S_T)$.

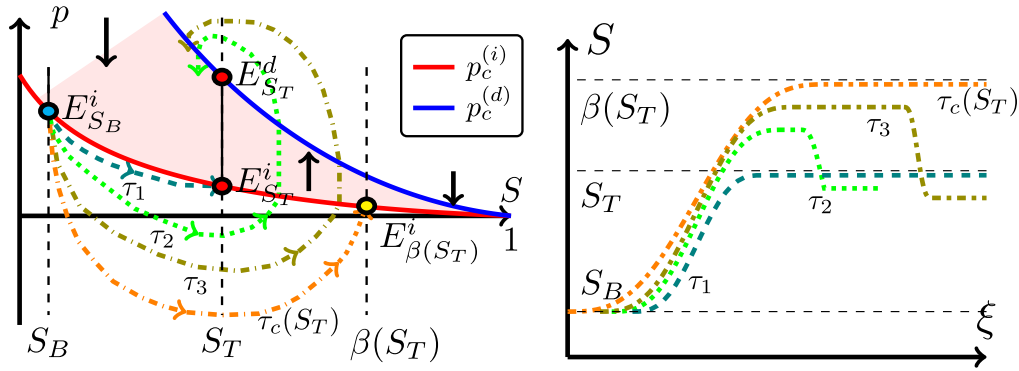


FIGURE 9 (Left) Ordering of the orbits in the S - p phase plane for $S_* < S_T < \bar{S}$ and typical values of τ : $0 < \tau_1 < \tau_2 < \tau_3 < \tau_c(S_T)$. (Right) The behavior of the orbits in the ξ - S plane for the same τ values

Now we are in a position to describe how S_m behaves for different combinations of S_T and τ .

Proposition 6. *For each $S_T \in (S_B, \bar{S}]$, there exists a $\tau_m(S_T) > 0$ such that*

$$S_m(\tau, S_T) = S_T \text{ for all } 0 < \tau \leq \tau_m(S_T) \text{ and } S_m(\tau, S_T) > S_T \text{ for all } \tau > \tau_m(S_T).$$

The proof of this result is given in proposition 2.1 of Ref. 45. For later purposes, we introduce here some definitions that are related to Proposition 6. Let $\underline{P} = \min_{S \in (S_B, \bar{S})} \{-p_c^{(i)'}(S)\} > 0$ and $m_0(S_T) = \sup_{S \in [S_B, S_T]} \mathcal{G}'(S; S_B, S_T) < \infty$, and define

$$\bar{\tau}_m = \frac{\underline{P}^2}{4cm_0(S_T)} \quad \text{and} \quad r_m = \frac{P}{2} \left[1 - \sqrt{1 - \frac{\tau}{\bar{\tau}_m}} \right]. \quad (48)$$

Then,

$$p_c^{(i)}(S) + r_m(S - S_T) < w(S; \tau, S_T) < p_c^{(i)}(S) \text{ for all } S \in (S_B, S_T) \text{ and } \tau < \bar{\tau}_m,$$

which directly gives $S_m(S_T, \tau) = S_T$. Thus, $\tau_m > 0$ is defined as

$$\tau_m(S_T) := \sup\{\tau : S_m(S_T, \tau) = S_T\} \geq \bar{\tau}_m > 0. \quad (49)$$

Finally, using [Ref. 9, proposition 4.2(b)] one concludes that $\tau_m(S_T) < \infty$.

We consider now the case $\tau > \tau_m(S_T)$. Proposition 3 guarantees that $S_m(S_T, \tau) < \gamma(S_T) \leq \beta(S_T)$ if $S_B < S_T \leq S_*$. However, for $S_T > S_*$ it is unclear whether $S_m(S_T, \tau)$ is bounded by $\beta(S_T)$ or not. We show below that a $\tau_c = \tau_c(S_T)$ exists in this case such that $S_m(S_T, \tau) \in (S_T, \beta(S_T))$ if $\tau \in (\tau_m(S_T), \tau_c(S_T))$ and $S_m(S_T, \tau_c(S_T)) = \beta(S_T)$ implying from Proposition 3 that $S_m(S_T, \tau) = 1$ for all $\tau > \tau_c(S_T)$ (see Figure 9).

Proposition 7. *We have*

(a) *For each $S_T \in (S_*, \bar{S})$, there exists a unique $\tau_c = \tau_c(S_T)$ such that*

$$S_m(\tau_c, S_T) = \beta(S_T).$$

(b) *The function $\tau_c(\cdot)$ is strictly decreasing and continuous on $[S_*, \bar{S}]$. One has $\tau_c(S_T) \rightarrow \infty$ as $S_T \searrow S_*$ and $\tau_c(\bar{S}) = \bar{\tau} = \tau_m(\bar{S}) > 0$.*

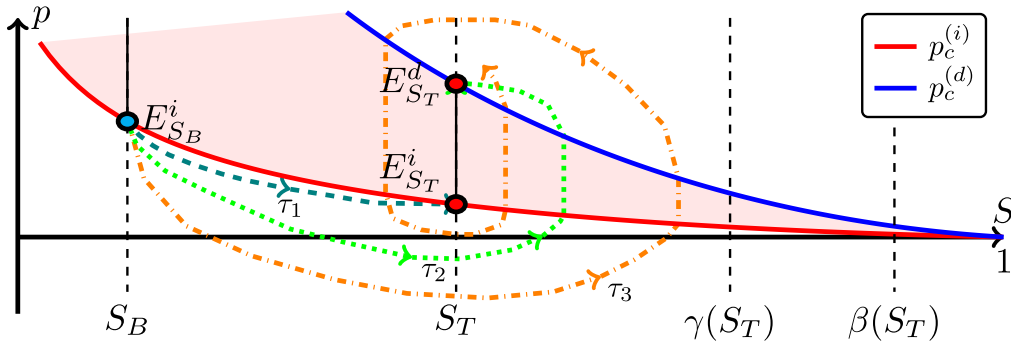


FIGURE 10 The different cases of $S_B < S_T < S_*$. The orbits are plotted for $0 < \tau_1 < \tau_i < \tau_2 < \tau_d < \tau_3$

After these preliminary statements, we are now in a position to consider the solvability of (TW) for different ranges of S_T .

3.2 | Problem (TW) with $S_B < S_T \leq \bar{S}$

We investigate the existence of an orbit connecting $(S_B, p_c^{(i)}(S_B))$ and the segment $\overline{E_{S_T}^i E_{S_T}^d}$. Defining

$$\tau_j = \frac{\left(p_c^{(j)'}(S_T)\right)^2}{4c\mathcal{G}'(S_T; S_B, S_T)} > 0, \quad j \in \{i, d\}, \quad (50)$$

the eigenvalues of the (TW) system associated with the equilibrium points $E_{S_T}^j$, $j \in \{i, d\}$ are

$$\lambda_{\pm}^j = \frac{p_c^{(j)'}(S_T)}{2c\tau} \left[1 \pm \sqrt{1 - \frac{\tau}{\tau_j}} \right] \text{ implying } \begin{cases} E_{S_T}^j \text{ is stable sink for } \tau \leq \tau_j, \\ E_{S_T}^j \text{ is stable spiral sink for } \tau > \tau_j. \end{cases}$$

This immediately gives $\tau_i \geq \tau_m$ as no monotone orbit can connect with $E_{S_T}^i$ for $\tau > \tau_i$. The general behavior of the orbits for $S_T \in (S_B, S_*]$ are stated in

Theorem 1. *Under the assumptions of Scenario A, consider S_B satisfying (33), $S_T \in (S_B, S_*]$ and $\tau_i < \tau_d$. Let (S, p) be the orbit originating from $(S_B, p_c^{(i)}(S_B))$ satisfying (TW). Then, with reference to Figure 10, as $\xi \rightarrow \infty$ one gets*

- If $0 < \tau \leq \tau_i$, then either $S \rightarrow S_T$ and $p \rightarrow p_c^{(i)}(S_T)$ monotonically with respect to ξ through $\mathcal{H}^{(i)}$ (when $\tau \leq \tau_m$) or the orbit (S, p) goes around $\overline{E_{S_T}^i E_{S_T}^d}$ finitely many times and ends up in either $E_{S_T}^i$ or $E_{S_T}^d$ (when $\tau_m < \tau \leq \tau_i$).
- If $\tau_i < \tau \leq \tau_d$, $(S, p) \rightarrow E_{S_T}^d$ after finitely many turns around $\overline{E_{S_T}^i E_{S_T}^d}$.
- If $\tau_d < \tau$, then (S, p) revolves infinitely many times around $\overline{E_{S_T}^i E_{S_T}^d}$ while approaching it and (28) is satisfied.

These statements are demonstrated by arguments from [Ref. 45, theorem 2.1 and lemmas 2.1 & 2.2]. We omit the details here. In Theorem 1, we have taken $\tau_i < \tau_d$ without loss of generality. In the $\tau_i > \tau_d$ case, the roles of the equilibrium points $E_{S_T}^i$ and $E_{S_T}^d$ are reversed. The typical behavior of the S and the p profiles with respect to ξ is given in Figure 11. Both S and p are monotone for $\tau < \tau_i$, whereas for $\tau_i < \tau < \tau_d$ they have finite number of local extrema and $p(+\infty) = p_c^{(d)}(S_T)$. For $\tau > \tau_d$,

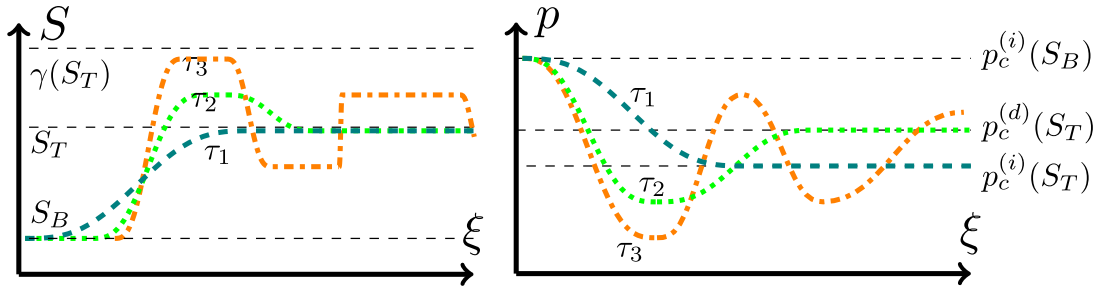


FIGURE 11 Typical behavior of $S(\xi)$ (left) and $p(\xi)$ (right) for different values of τ . Here profiles for three different τ values are plotted satisfying $0 < \tau_1 < \tau_i < \tau_2 < \tau_d < \tau_3$. The $\xi = 0$ coordinate is fixed by (41)

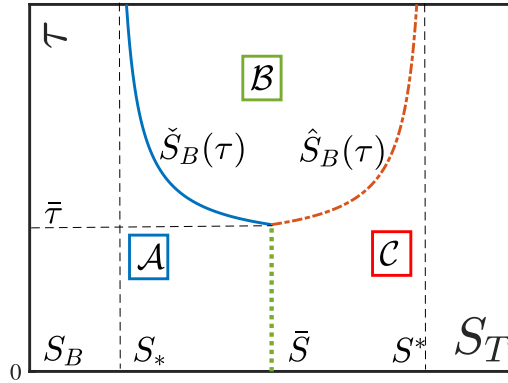


FIGURE 12 The sets \mathcal{A} , \mathcal{B} , and \mathcal{C} and the functions $\check{S}_B(\tau)$, $\hat{S}_B(\tau)$

S has infinitely many decaying local extrema, whereas p has no limit. In particular, each S maximum corresponds to a saturation overshoot. On the other hand, the oscillations in p become wider, in line with the assumption $\lim_{\xi \rightarrow \infty} p'(\xi) = 0$. In this case, the segment $\overline{E_{S_T}^i E_{S_T}^d}$ becomes an ω -limit set of the orbit.

Turning to the case, $S_T \in (S_*, \bar{S})$, we define the two functions which will be used extensively below.

Definition 1. The functions $\hat{S}_B, \check{S}_B : [0, \infty) \rightarrow (0, 1]$ are such that

$$\check{S}_B(\tau) = \begin{cases} (\tau_c)^{-1}(\tau) & \text{for } \tau > \bar{\tau}, \\ \bar{S} & \text{for } 0 \leq \tau \leq \bar{\tau}, \end{cases} \quad \text{and} \quad \hat{S}_B(\tau) = \beta(\check{S}_B(\tau)).$$

Observe that $\check{S}_B(\tau)$ is a strictly decreasing function whereas $\hat{S}_B(\tau)$ is a strictly increasing function for $\tau > \bar{\tau}$ and $\hat{S}_B(\tau) = \check{S}_B(\tau) = \bar{S}$ for $\tau \leq \bar{\tau}$. This is sketched in Figure 12. Numerically computed $\check{S}_B(\tau)$ and $\hat{S}_B(\tau)$ functions are shown in Figure 20.

Remark 7. The case when $\beta(\alpha)$ does not intersect $\gamma(\alpha)$ is treated in a similar way. However, since orbits may intersect the line segment $\{S = 1, p \leq 0\}$ in this case, a multivalued extension of $p_c^{(i)}$ at $S = 1$ needs to be introduced, see Refs. 9, 45 for further details. With this, one shows that the function $\tau_c(S_T)$ is well-defined in $[\bar{S}, \bar{S}]$. Then, a $\tau_B > 0$ exists such that $\check{S}_B(\tau_B) = \bar{S}$ and $\hat{S}_B(\tau_B) = 1$. The subsequent results remain valid if \hat{S}_B and \check{S}_B are extended by

$$\check{S}_B(\tau_B) = \bar{S} \text{ for } \tau > \tau_B, \quad \text{and} \quad \hat{S}_B(\tau) = 1 \text{ for } \tau > \tau_B.$$

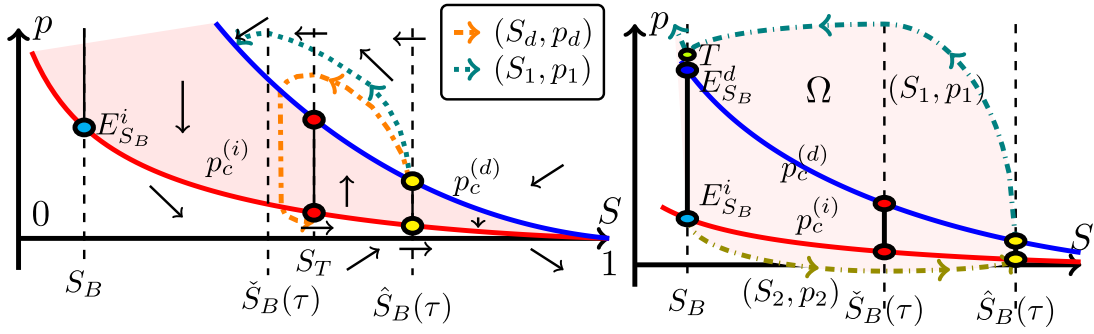


FIGURE 13 (Left) The direction of orbits for the system (31), (52) and the orbits (S_d, p_d) and (S_1, p_1) . Here the orbit (S_d, p_d) connects $E_{\hat{S}_B(\tau)}^d$ and $E_{S_T}^i$. (Right) The domain Ω used in the divergence argument for the hypothetical case where (S_1, p_1) crosses the line $S = S_B$

With this in mind, we define the following sets:

$$\begin{aligned} \mathcal{A} &= \{(S_T, \tau) : S_B < S_T < \bar{S}, \tau < \tau_c(S_T)\}, \\ \mathcal{B} &= \{(S_T, \tau) : \tau > \bar{\tau}, \check{S}_B(\tau) < S_T < \hat{S}_B(\tau)\}, \\ \mathcal{C} &= \{(S_T, \tau) : \bar{S} < S < S^*, \tau < \tau_c(\beta^{-1}(S_T))\}. \end{aligned} \quad (51)$$

Observe that if $S_T < \bar{S}$ then only regions \mathcal{A} and \mathcal{B} are relevant. With S_o defined in (A1), for $(S_T, \tau) \in \mathcal{A}$ one has

Proposition 8. For a fixed $S_B \in (0, S_o)$ and $(S_T, \tau) \in \mathcal{A}$, the orbit (S, p) entering $\mathcal{H}^{(i)}$ from $E_{S_B}^i$ behaves according to statements (a), (b), and (c) of Theorem 1.

We discuss the remaining situations, $(S_T, \tau) \in \mathcal{B}$ and $(S_T, \tau) \in \mathcal{C}$ in the next section.

3.3 | $(S_T, \tau) \notin \mathcal{A}$

Since $S_T > \check{S}_B(\tau)$, a TW cannot connect S_B and S_T . However, a different class of waves is possible when $(S_T, \tau) \in \mathcal{B}$.

Proposition 9. For a fixed $S_B \in (0, S_o)$ and $(S_T, \tau) \in \mathcal{B}$, consider the system

$$\begin{cases} S' = \frac{1}{c_d \tau} \mathcal{F}(S, p), \\ p' = \mathcal{G}(S; \hat{S}_B(\tau), S_T), \end{cases} \quad \text{with} \quad c_d = \frac{F(\hat{S}_B(\tau)) - F(S_T)}{\hat{S}_B(\tau) - S_T}. \quad (52)$$

For this system, an orbit (S_d, p_d) exists that connects $E_{\hat{S}_B(\tau)}^d$ for $\xi \rightarrow -\infty$ to $\overline{E_{S_T}^i E_{S_T}^d}$ for $\xi \rightarrow \infty$.

Proof. Upon inspection of the eigendirections for the system (52) around the equilibrium point $E_{\hat{S}_B(\tau)}^d$ one concludes that there is indeed an orbit (S_d, p_d) that connects to $E_{\hat{S}_B(\tau)}^d$ as $\xi \rightarrow -\infty$ from the set $\mathcal{H}^{(d)}$ defined in (15). Moreover, from the direction of the orbits in this case, as shown in Figure 13 (left), it is apparent that after leaving $E_{\hat{S}_B(\tau)}^d$, S_d decreases monotonically till the orbit either hits the curve $p = p_c^{(d)}(S)$ for some $S \leq S_T$ or exits $\{S > S_B\}$ through the line $S = S_B$. We prove that it is not possible for the orbit to escape through $S = S_B$. To show this, consider the orbit (S_1, p_1) that satisfies the original (TW) equations and enters $\mathcal{H}^{(d)}$ from $E_{\hat{S}_B(\tau)}^d$. We show that this orbit cannot cross the line $S = S_B$.

The divergence argument presented in Refs. 9, 42, 45 is used for this purpose. To elaborate, assume that (S_1, p_1) intersects the line $S = S_B$ at T . Consider the region Ω , enclosed by the segments $\overline{E_{S_B}^i T}$, $\overline{E_{\hat{S}_B(\tau)}^i E_{\hat{S}_B(\tau)}^d}$, the orbit (S_1, p_1) and the orbit (S_2, p_2) that satisfies (TW) and connects $E_{S_B}^i$ to $E_{\hat{S}_B(\tau)}^i$ (see Figure 13 (right)). Introducing the vector-valued function $\vec{R}(S, p) = (\frac{1}{c\tau} \mathcal{F}(S, p), \mathcal{G}(S; S_B, S_T))$ and deduces from (16),

$$\operatorname{div} \vec{R} = \frac{1}{c\tau} \frac{\partial \mathcal{F}}{\partial S}(S, p) = \frac{1}{c\tau} \begin{cases} p_c^{(i)'}(S) & \text{in } \mathcal{H}^{(i)}, \\ 0 & \text{in } \mathcal{H}, \\ p_c^{(d)'}(S) & \text{in } \mathcal{H}^{(d)}. \end{cases}$$

This gives a contradiction when the divergence theorem is applied to \vec{R} in the domain Ω : the integral of \vec{R} over $\partial\Omega$ is nonnegative whereas $\int_{\Omega} \operatorname{div} \vec{R} < 0$ from (P1) and Figure 13 (right). Hence, the orbit (S_1, p_1) intersects $p_c^{(d)}(S)$ at some $S \in (S_B, \check{S}_B(\tau)]$.

The wave-speed corresponding to the orbit (S_d, p_d) satisfies

$$c_d < \frac{F(\hat{S}_B(\tau)) - F(S_B)}{\hat{S}_B(\tau) - S_B} = c_i, \quad (53)$$

c_i being the speed of both (S_1, p_1) and (S_2, p_2) waves. Hence, by the continuity of the orbits with respect to c , as shown in Proposition 4, it is evident that (S_d, p_d) intersects $p_c^{(d)}(S)$ for some $S_d > S_B$. From here, the rest of the proof is identical to the proof of Theorem 1, and follows the arguments in [Ref. 45, theorem 2.1 and lemmas 2.1 & 2.2]. \blacksquare

The general picture is described in the following corollary:

Corollary 2. *For τ small enough, the orbit (S_d, p_d) goes monotonically to $E_{S_T}^d$. For τ large enough, (S_d, p_d) goes infinitely many times around $\overline{E_{S_T}^i E_{S_T}^d}$ while approaching it, and $\lim_{\xi \rightarrow \pm\infty} p_d'(\xi) = 0$.*

Observe that, if $(S_T, \tau) \in \mathcal{C}$ then TWs do not exist between S_T and $\hat{S}_B(\tau)$ since both are in the concave part of F with $S_T > \hat{S}_B(\tau)$. Thus we have exhausted all the possibilities of connecting S_B and S_T with Theorem 1 and Proposition 9.

3.4 | Entropy solutions to hyperbolic conservation laws

Under the conditions of Scenario A, we consider the Riemann problem

$$\frac{\partial S}{\partial t} + \frac{\partial F(S)}{\partial z} = 0 \text{ in } \mathbb{R} \times [0, \infty) \quad (54a)$$

$$\text{with } S(z, 0) = \begin{cases} S_T & \text{for } z < 0, \\ S_B & \text{for } z > 0. \end{cases} \quad (54b)$$

In the context of the viscous model discussed in this paper, we consider the Buckley-Leverett Equation (54a) as the limit of System (25) for $N_c \searrow 0$. As a consequence, we only take into account those shock solutions of (54a) that have a viscous profile in the form of a traveling wave satisfying (TW). Such shocks are called admissible because they arise as the $N_c \rightarrow 0$ limit of TWs. In this sense, the entropy

condition for shocks satisfying (54a) are equivalent to existence conditions for traveling waves satisfying (TW). This may lead to nonclassical shocks violating the well-known Oleinik entropy conditions, see, for example, Ref. 43.

Here, we assume

$$0 < S_B < S_T < 1, \quad (55)$$

which is more general compared to (33) where the additional constraint of $S_B < S_o$ was imposed. This generalization is possible since $S_B > S_o$ simply implies that the sets \mathcal{A} , \mathcal{B} are empty. Our analysis can also be applied to derive the entropy conditions for the case $S_B > S_T$, however, for simplicity we restrict our discussion to (55).

$(S_T, \tau) \in \mathcal{A}$

As in the usual Buckley-Leverett case (ie, without dynamic capillarity and hysteresis in the regularized models) the solution is given by

$$S(z, t) = \begin{cases} S_T & \text{for } z < ct, \\ S_B & \text{for } z > ct, \end{cases} \text{ where } c = \frac{F(S_T) - F(S_B)}{S_T - S_B}. \quad (56)$$

Here, the shock satisfies the classical Oleinik condition.

$(S_T, \tau) \in \mathcal{B}$

In this case, the admissible solution is composed of two shocks: an infiltration shock from S_B to $\hat{S}_B(\tau)$, followed by a drainage shock from $\hat{S}_B(\tau)$ to S_T .

$$S(z, t) = \begin{cases} S_T & \text{for } z < c_d t, \\ \hat{S}_B(\tau) & \text{for } c_d t < z < c_i t, \\ S_B & \text{for } z > c_i t, \end{cases} \text{ with } \begin{cases} c_i = \frac{F(\hat{S}_B(\tau)) - F(S_B)}{\hat{S}_B(\tau) - S_B}, \\ c_d = \frac{F(\hat{S}_B(\tau)) - F(S_T)}{\hat{S}_B(\tau) - S_T}. \end{cases} \quad (57)$$

Note that this solution is different from the Oleinik entropy solution.⁷⁰ Moreover, the shock connecting S_B and $\hat{S}_B(\tau)$ is undercompressive⁷¹ meaning that it violates the Lax entropy condition. This is because $c_i > F'(\hat{S}_B(\tau))$ for this shock. The trailing shock connecting $\hat{S}_B(\tau)$ to S_T is however classical.

$(S_T, \tau) \in \mathcal{C}$

The solution in this case violates again the Oleinik entropy condition. It consists of an infiltration shock from S_B to $\hat{S}_B(\tau)$ followed by a rarefaction wave from $\hat{S}_B(\tau)$ to S_T ,

$$S(z, t) = \begin{cases} S_T & \text{for } z < F'(S_T)t, \\ r(z/t) & \text{for } F'(S_T)t < z < F'(\hat{S}_B(\tau))t, \\ \hat{S}_B(\tau) & \text{for } F'(\hat{S}_B(\tau))t < z < c_i t, \\ S_B & \text{for } z > c_i t, \end{cases} \quad (58)$$

with $r(\cdot)$ satisfying

$$F'(r(\zeta)) = \zeta, \text{ for } F'(S_T) \leq \zeta \leq F'(\hat{S}_B(\tau)). \quad (59)$$

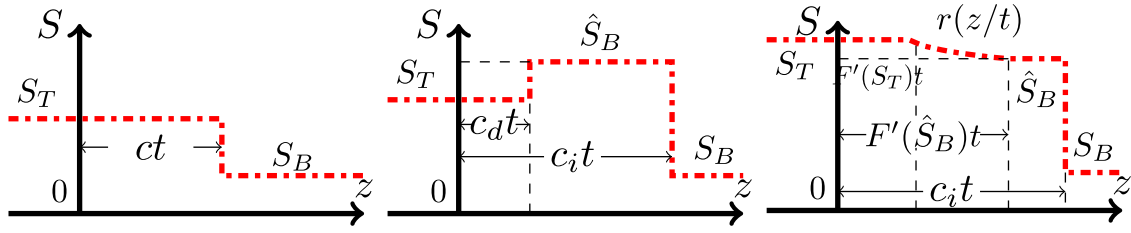


FIGURE 14 The entropy solutions for (left) $(S_T, \tau) \in \mathcal{A}$, (center) $(S_T, \tau) \in \mathcal{B}$, and (right) $(S_T, \tau) \in \mathcal{C}$. Note that the solutions in the center and the right figures include nonclassical shocks

Since F is concave for $S \in [\hat{S}_B(\tau), S_T]$, F' is monotone implying that $r(\cdot)$ is well-defined. We observe that in the last two cases the solution features a plateau-like region. This plateau appears and grows in time since the speeds of the drainage shock and of the endpoint of the rarefaction wave are lesser than the speed of the infiltration shock. Interestingly, the saturation of the plateau only depends on $p_c^{(i)}$ and not on $p_c^{(d)}$. To be more specific, although the viscous profile consisting of a TW wave connecting $E_{\hat{S}_B}^d$ and $\overline{E_{S_T}^i E_{S_T}^d}$ depends on $p_c^{(d)}$, the shock solution resulting from it, in the hyperbolic limit, does not. However, the role of the drainage curve in the entropy solutions become evident in Scenario B, which is discussed in the next section.

In the absence of hysteresis and for linear higher-order terms, which correspond to constant k and linear p_c - S dependence, in [Ref. 43, section 6] it is proved that the nonstandard entropy conditions discussed here are entropy dissipative for the entropy $U(s) = \frac{1}{2}s^2$. However, such an analysis is beyond the scope of this paper. The solution profiles for the Riemann problem are shown in Figure 14.

3.5 | Extension to the nonmonotone F case

The analysis so far can be extended to the case where N_g is large resulting in F being nonmonotone. If $S_F \in (0, 1)$ is the saturation where $F(S)$ attains its maximum (see Remark 2 and Figure 3), then the results obtained so far cover the case when S_T and S^* are below S_F . However, if $S_T > S_F$ then the TW study has to be conducted also from an S_T perspective, not only from the S_B one. In this scenario, since fronts having negative speeds and thus moving toward S_T become possible, one has to consider the functions $\hat{S}_T(\tau)$, $\check{S}_T(\tau)$ for a fixed S_T , similar to $\hat{S}_B(\tau)$, $\check{S}_B(\tau)$ from Definition 1 for fixed S_B . Due to the symmetry in the behavior of the fronts approaching S_B , respectively, S_T , some of the results obtained so far extend straightforwardly to the nonmonotone case. However, a detailed analysis is much more involved and therefore left for future research because of the following two reasons:

1. Depending on the relative positions of S_B , \hat{S}_B , S_T , and \hat{S}_T , there are many subcases to consider. In this case, up to three shocks are possible, traveling both forward and backward. Which of these shocks are admissible and how they are connected requires further analysis.
2. For a nonmonotone F , when considering the hyperbolic limit in the absence of hysteresis or dynamic effects, the entropy solutions may include rarefaction waves with endpoints moving in opposite directions, forward and backward. When capillary hysteresis is included, preliminary numerical results have provided solutions incorporating two rarefaction waves, one with endpoints traveling backward and another one with endpoints traveling forward, and a stationary shock at $z = 0$. Such solutions still need to be analyzed further.

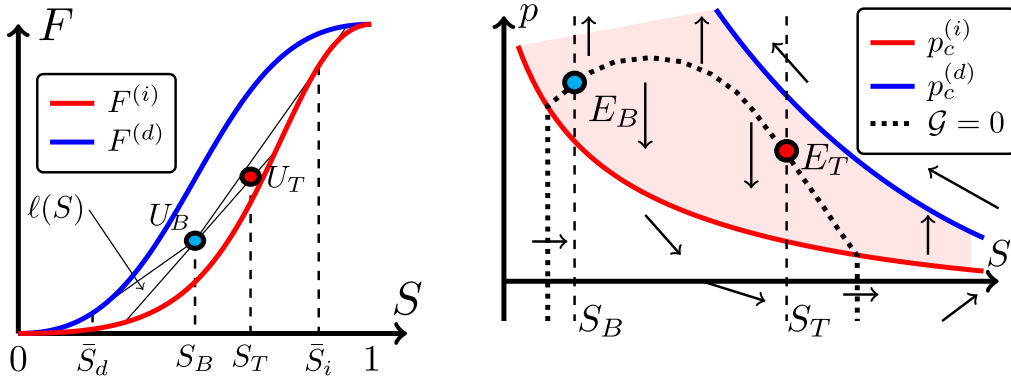


FIGURE 15 (Left) The graphs of $F^{(i)}$ and $F^{(d)}$, together with the saturations \bar{S}_i , \bar{S}_d and the points U_B , U_T . (Right) The orbit directions for Case (i) for two equilibrium points E_B and E_T . The black dotted curve represents points where $\mathcal{G}(S, p) = 0$, implying $p' = 0$

4 | HYSTERETIC RELATIVE PERMEABILITIES AND SMALL N_g (SCENARIO B)

For Scenario B, the flux function $F(S, p)$ is composed of $F^{(j)} = f^{(j)} + N_g h^{(j)}$ for $j \in \{i, d\}$ and $\bar{F} = \bar{f} + N_g \bar{h}$ such that

$$F(S, p) = \begin{cases} F^{(d)}(S) & \text{if } (S, p) \in \mathcal{H}^{(d)}, \\ \bar{F}(S, p) & \text{if } (S, p) \in \mathcal{H}, \\ F^{(i)}(S) & \text{if } (S, p) \in \mathcal{H}^{(i)}. \end{cases} \quad (60)$$

It has the following properties

(A2) $F \in C(\mathcal{W})$, $\bar{F} \in C^2(\mathcal{H})$, $\partial_p F > 0$ in \mathcal{H} and $F^{(i)}$, $F^{(d)}$ satisfy properties stated for F in A1. In addition, $F^{(d)}(S) > F^{(i)}(S)$ for $0 < S < 1$.

In this scenario, S_B can be taken in the entire interval $(0, 1)$ and p_B can be chosen independently as long as $(S_B, p_B) \in \mathcal{H}$, that is,

$$0 < S_B < 1 \quad \text{and} \quad p_B \in [p_c^{(i)}(S_B), p_c^{(d)}(S_B)]. \quad (61)$$

This is different from Scenario A where S_B is restricted to the interval $(0, S_0)$ and p_B is fixed to $p_B = p_c^{(i)}(S_B)$.

We first introduce some notation.

Definition 2. For $k \in \{B, T\}$ let $E_k = (S_k, p_k)$ and $U_k = (S_k, F(S_k, p_k))$ (see Figure 15 (left)). We define the saturations \bar{S}_j , $j \in \{i, d\}$ as the S -coordinates of the tangent points to $F^{(j)}(S)$ from U_B such that $\bar{S}_i \geq S_B$ and $\bar{S}_d \leq S_B$.

Observe that the saturations \bar{S}_j , for $j \in \{i, d\}$, are functions of U_B . The properties of $F^{(j)}$ further ensure that they are well-defined. If S_B is such that $F^{(i)''}(S_B) \leq 0$ and $p_B = p_c^{(i)}(S_B)$ then $\bar{S}_i = S_B$. Similarly if $F^{(d)''}(S_B) \geq 0$ and $p_B = p_c^{(d)}(S_B)$ then $\bar{S}_d = S_B$.

The existence of TWs is analyzed for the following two cases:

$$\text{Case (i): } S_B < S_T \leq \bar{S}_i, \quad \text{and} \quad \text{Case (ii): } \bar{S}_d \leq S_T < S_B.$$

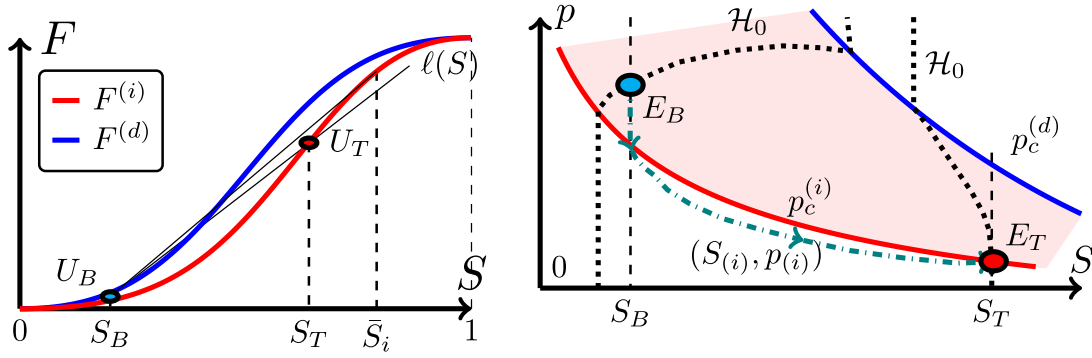


FIGURE 16 $U_B, U_T, \ell(S)$ used in Proposition 11 in the S - F plane. (Right) The S - p plane and the orbit $(S^{(i)}, p^{(i)})$ for Case (i) with $F^{(i)}(S_T) > F(S_B, p_B)$ and $\tau < \tau_i^*(S_T)$

Regarding the choice of p_T , we have the following.

Proposition 10. *Let S_B and S_T be as in Case (i) or Case (ii). Then any solution of (TW) that connects E_B and E_T can only exist if $p_T = p_c^{(i)}(S_T)$ or $p_T = p_c^{(d)}(S_T)$.*

Proof. Since E_T is an equilibrium point, $F(S_T, p_T) = 0$, which implies that $p_T \in [p_c^{(i)}(S_T), p_c^{(d)}(S_T)]$. The directions of the orbits for p_T in this interval are displayed in Figure 15 (right). We proceed by introducing the set

$$\mathcal{H}_0 = \{(S, p) : S \in (0, 1), p \in \mathbb{R} \text{ such that } \mathcal{G}(S, p) = 0\}.$$

It corresponds to the black dotted curve in Figure 15 (right). Let $\ell = \ell(S)$, defined in (32), be the line passing through U_B and U_T . If ℓ intersects $F^{(i)}$ at $S = S_H$, then the vertical half-line $\{(S_H, p) : p < p_c^{(i)}(S_H)\}$ lies in \mathcal{H}_0 due to the definition of F in (60). Concerning $F^{(d)}$, ℓ has either zero, one or two intersection points (see Figure 16 (left)). In the latter case, as before, \mathcal{H}_0 contains one or two vertical half-lines as shown in the (right) plot of Figure 16. However, this aspect plays no major role in the analysis below.

Every point in the set $\mathcal{H}_0 \cap \mathcal{H}$ is an equilibrium point. However, all points in the set $\mathcal{H}_0 \cap \text{int}(\mathcal{H})$ (the interior of \mathcal{H} being referred to as $\text{int}(\mathcal{H})$ here) are unstable and as follows from Figure 15 (right), no orbit can reach these points as $\xi \rightarrow \infty$. This eliminates all other possibilities to reach E_T as $\xi \rightarrow \infty$ except for $p_T = p_c^{(i)}(S_T)$ and $p_T = p_c^{(d)}(S_T)$. \blacksquare

We now consider the two cases separately.

4.1 | Case (i): $S_B < S_T \leq \bar{S}_i$

The main result of this section is

Proposition 11. *Assume (61) and let $S_T \in (S_B, \bar{S}_i]$, $p_T = p_c^{(i)}(S_T)$, and $F^{(i)}(S_T) > F(S_B, p_B)$. Then a $\tau_i^*(S_T) > 0$ exists such that for all $\tau < \tau_i^*(S_T)$ there is an orbit satisfying (TW) and connecting E_B to E_T .*

Proof. Consider the orbit $(S^{(i)}, p^{(i)})$ that leaves E_B vertically through the half-line $\{S = S_B, p < p_B\}$. The directions of the orbits in \mathcal{H} imply that $(S^{(i)}, p^{(i)})$ intersects $p_c^{(i)}(S)$ and enters $\mathcal{H}^{(i)}$ (the region

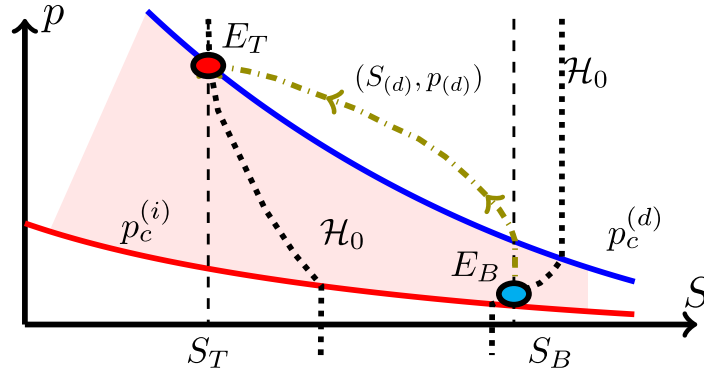


FIGURE 17 The orbit $(S_{(d)}, p_{(d)})$ for Case (ii) with $F^{(d)}(S_T) < F(S_B, p_B)$ and $\tau < \tau_d^*(S_T)$

under the graph of $p_c^{(i)}$ at some finite $\xi \in \mathbb{R}$ (see Figure 16 (right)). In $\mathcal{H}^{(i)}$, its motion is governed by the system

$$\begin{cases} S_{(i)}' = \frac{1}{c_{(i)}\tau} (p_c^{(i)}(S_{(i)}) - p_{(i)}), \\ p_{(i)}' = \mathcal{G}_i(S_{(i)}) := \mathcal{G}(S_{(i)}, p_c^{(i)}(S_{(i)})), \end{cases} \quad \text{with} \quad c_{(i)} = \frac{F^{(i)}(S_T) - F(S_B, p_B)}{S_T - S_B} > 0. \quad (62)$$

Note that $\mathcal{G}_i(S) = (F^{(i)}(S) - \ell(S))/h^{(i)}(S)$. The system (62) has exactly the same structure as (TW) described in Section 3. Defining $\tau_i^*(S_T)$ similar to τ_m in Proposition 6, the result follows directly. ■

Remark 8. Observe that the construction fails if $F^{(i)}(S_T) < F(S_B, p_B)$ which is intuitive since the overall process is not infiltration in this case. If one prescribes a flux $F = F_T$ at $\xi \rightarrow \infty$ which is less than $F(S_B, p_B)$, then Propositions 10 and 11 force the saturation at $\xi \rightarrow \infty$ to be $S_T = (F^{(d)})^{-1}(F_T) < S_B$, reducing the problem to Case (ii). However, if one fixes the saturation S_T so that $F(S_B, p_B) > F^{(i)}(S_T)$, then we get a frozen profile with a $p_T \in (p_c^{(i)}(S_T), p_c^{(d)}(S_T))$ that satisfies $F(S_T, p_T) = F(S_B, p_B)$. This is explained further in Section 5.2. We set $\tau_i^*(S_T) = \infty$ in this case.

Proposition 11 implies the following:

Corollary 3. *Under the assumptions of Proposition 11, let $S_{(i)}(\xi) = S$ for some $S \in (S_B, S_T]$ and $\xi \in \mathbb{R}$. Define $\underline{w}(S; \tau) := p_{(i)}(\xi) < p_c^{(i)}(S)$. Then $\lim_{\tau \rightarrow 0} \underline{w}(S; \tau) = p_c^{(i)}(S)$.*

Here, \underline{w} is the counterpart of w defined in Section 3 for Scenario A. The proof of Corollary 3 is based on the inequality (45) which is satisfied in this case by \underline{w} . From Corollary 3, one obtains that for Case (i), if $\tau \searrow 0$, meaning that if the dynamic capillarity is vanishing, then the orbit follows either the scanning curve, here the line segment $\{S = S_B, p_c^{(i)}(S_B) < p < p_B\}$, or the infiltration curve $p_c^{(i)}$. The result is analogous to the results for capillary hysteresis given in [Ref. 9, section 3].

4.2 | Case (ii): $\bar{S}_d \leq S_T < S_B$ and stability of plateaus

The counterpart of Proposition 11 for Case (ii) is (see also Figure 17),

Proposition 12. *Assume (61) and let $S_T \in [\bar{S}_d, S_B)$, $p_T = p_c^{(d)}(S_T)$, and $F^{(d)}(S_T) < F(S_B, p_B)$. Then a $\tau_d^*(S_T) > 0$ exists such that for all $\tau < \tau_d^*(S_T)$ there is an orbit $(S_{(d)}, p_{(d)})$ satisfying (TW) and connecting E_B to E_T . Moreover, for a fixed $S_{(d)} = S \in [S_T, S_B)$, one has $p_{(d)} \rightarrow p_c^{(d)}(S)$ as $\tau \rightarrow 0$.*

Finally, we investigate a special case related to the development of stable saturation plateaus in infiltration experiments. For $S_B \in (0, 1)$, and $S_T \in (S_B, 1)$ a stable plateau is formed when an infiltration

wave, from S_B to $S_P \in (S_T, 1)$, followed by a drainage wave, from S_P to S_T , both have the same speed resulting in the width of the plateau to remain constant. This is different from the plateaus described in (57) where the speeds of the infiltration and the drainage fronts are necessarily different. The existence of stable saturation plateaus has been widely studied experimentally^{29,33,35} and numerically.^{15,60} Although results regarding stability of the plateau are available,^{15,60} the mechanism behind its development is still not well understood. Here, we give an example where our analysis predicts that such a plateau will develop. Specifically, it occurs when $\tau > \tau_i^*(S_T)$ and a direct monotone orbit from E_B to $(S_T, p_c^{(i)}(S_T))$ is no longer possible. This is verified numerically in Section 5.2.

Proposition 13. *Assume (61) and let $S_T \in (S_B, 1)$ be such that the line ℓ through $U_B = (S_B, F(S_B, p_B))$ and $U_T = (S_T, F^{(d)}(S_T))$ in the F - S plane intersects $F^{(i)}$ at some $S = S_P \in (S_T, \bar{S}_i)$. Consider the system (TW) with the wave-speed*

$$c_P = \frac{F^{(d)}(S_T) - F(S_B, p_B)}{S_T - S_B} = \frac{F^{(i)}(S_P) - F(S_B, p_B)}{S_P - S_B} = \frac{F^{(i)}(S_P) - F^{(d)}(S_T)}{S_P - S_T}.$$

For this system, let $(S_{(i)}^P, p_{(i)}^P)$ be the orbit that passes through $\mathcal{H}^{(i)}$ and connects to the equilibrium point (S_B, p_B) as $\xi \rightarrow -\infty$, described in Proposition 11. Similarly, let $(S_{(d)}^P, p_{(d)}^P)$ be the orbit passing through $\mathcal{H}^{(d)}$ and connecting to $(S_P, p_c^{(i)}(S_P))$ as $\xi \rightarrow -\infty$, described in Proposition 12. Assume that $0 < \tau < \max\{\tau_i^*(S_P), \tau_d^*(S_T)\}$ where the $\tau_i^*(S_P)$ and the $\tau_d^*(S_T)$ values correspond to the orbits $(S_{(i)}^P, p_{(i)}^P)$ and $(S_{(d)}^P, p_{(d)}^P)$, respectively. Then, $(S_{(i)}^P, p_{(i)}^P) \rightarrow (S_P, p_c^{(i)}(S_P))$ as $\xi \rightarrow \infty$ and $(S_{(d)}^P, p_{(d)}^P) \rightarrow (S_T, p_c^{(d)}(S_T))$ as $\xi \rightarrow \infty$.

The proof follows directly from Propositions 11 and 12.

4.3 | Entropy solutions

We can now discuss the entropy solutions of the Riemann problem (54) under the assumptions of Scenario B. To be more specific, we give a selection criteria for the solutions of the system

$$\begin{cases} \frac{\partial S}{\partial t} + \frac{\partial F(S, p)}{\partial z} = 0, \\ p \in \frac{1}{2} \left(p_c^{(d)}(S) + p_c^{(i)}(S) \right) - \frac{1}{2} \left(p_c^{(d)}(S) - p_c^{(i)}(S) \right) \cdot \text{sign} \left(\frac{\partial S}{\partial t} \right), \end{cases} \quad \text{in } \mathbb{R} \times [0, \infty) \quad (63)$$

$$\text{with } S(z, 0) = \begin{cases} S_T & \text{for } z < 0, \\ S_B & \text{for } z > 0, \end{cases} \quad \text{and } p(z, 0) = p_B \text{ for } z > 0. \quad (64)$$

We view (63) as the limit of (\mathcal{P}) when the capillary effects vanish. However, hysteresis is still present in the model.

Note that τ still plays a role in determining the entropy solution despite being absent in (63). This is similar to what we saw in Section 3. However, the focus here being hysteresis in permeability and capillary pressure, for a fixed $S_B \in (0, 1)$ we take

$$0 < \tau < \min \left\{ \inf_{S_T \in (S_B, \bar{S}_i]} \tau_i^*(S_T), \inf_{S_T \in [\bar{S}_d, S_B)} \tau_d^*(S_T) \right\}. \quad (65)$$

Observe that (65) does not provide a void interval for τ . To see this, note that $\tau_i^*(S_T)$ is defined similar to τ_m in Proposition 6 and thus, it satisfies the inequality in (49), that is, it has the positive quantity $\bar{\tau}_m$

as its lower bound. Although $\bar{\tau}_m$ in Proposition 6 actually depends on S_T , one sees from (48) that the values of $\bar{\tau}_m$ are bounded away from 0 uniformly with respect to S_T . Hence, $\tau_i^*(S_T)$ is also bounded uniformly away from 0. Similar argument holds for $\tau_d^*(S_T)$.

We now consider the cases $S_T > S_B$ and $S_T < S_B$ separately.

$S_T > S_B$

If $S_T \leq \bar{S}_i$ (\bar{S}_i introduced in Definition 2) and $F^{(i)}(S_T) > F(S_B, p_B)$ then the entropy solution is a shock:

$$S(z, t) = \begin{cases} S_T & \text{for } z < c_{(i)}t, \\ S_B & \text{for } z > c_{(i)}t, \end{cases} \quad \text{with} \quad c_{(i)} = \frac{F^{(i)}(S_T) - F(S_B, p_B)}{S_T - S_B}. \quad (66)$$

For $F^{(i)}(S_T) < F(S_B, p_B)$, from Remark 8, the solution is (66) but with $c_{(i)} = 0$, that is, it is a stationary shock. However, if $S_T > \bar{S}_i$ then the solution becomes more complex, combining a rarefaction wave with a shock:

$$S(z, t) = \begin{cases} S_T & \text{for } z < F^{(i)'}(S_T)t, \\ r_{(i)}(z/t) & \text{for } F^{(i)'}(S_T)t < z < F^{(i)'}(\bar{S}_i)t, \\ \bar{S}_i & \text{for } F^{(i)'}(\bar{S}_i)t < z < c_{(i)}t, \\ S_B & \text{for } z > c_{(i)}t. \end{cases} \quad (67)$$

Here, $r_{(i)}(\cdot)$ satisfies

$$F^{(i)'}(r_{(i)}(\zeta)) = \zeta, \quad \text{for } F^{(i)'}(S_T) \leq \zeta \leq F^{(i)'}(\bar{S}_i).$$

$S_T < S_B$

If $S_T \geq \bar{S}_d$ then the entropy solution for $F(S_B, p_B) > F^{(d)}(S_T)$ is the shock

$$S(z, t) = \begin{cases} S_T & \text{for } z < c_{(d)}t, \\ S_B & \text{for } z > c_{(d)}t, \end{cases} \quad \text{with} \quad c_{(d)} = \frac{F(S_B, p_B) - F^{(d)}(S_T)}{S_B - S_T}, \quad (68)$$

and for $F(S_B, p_B) < F^{(d)}(S_T)$ it is (68) with $c_{(d)} = 0$. If $S_T < \bar{S}_d$ then the solution has a similar structure to (67), that is,

$$S(z, t) = \begin{cases} S_T & \text{for } z < F^{(d)'}(S_T)t, \\ r_{(d)}(z/t) & \text{for } F^{(d)'}(S_T)t < z < F^{(d)'}(\bar{S}_d)t, \\ \bar{S}_d & \text{for } F^{(d)'}(\bar{S}_d)t < z < c_{(d)}t, \\ S_B & \text{for } z > c_{(d)}t, \end{cases} \quad (69)$$

with the function $r_{(d)}(\cdot)$ satisfying

$$F^{(d)'}(r_{(d)}(\zeta)) = \zeta, \quad \text{for } F^{(d)'}(S_T) \leq \zeta \leq F^{(d)'}(\bar{S}_d).$$

5 | NUMERICAL RESULTS

For the numerical experiments, we solve $(\tilde{\mathcal{P}})$ (System (26)) in a domain (z_{in}, z_{out}) , where $z_{in} < 0$ and $z_{out} > 0$. As an initial condition for the saturation variable, we choose a smooth and monotone approximation of the Riemann data:

$$S(z, 0) = \begin{cases} S_T & \text{for } z < -l, \\ \frac{(S_B + S_T)}{2} + \frac{(S_T - S_B)}{4l^3} z \cdot (z^2 - 3l^2) & \text{for } -l \leq z \leq l, \\ S_B & \text{for } z > l. \end{cases} \quad (70)$$

Here, l is a smoothing parameter, S_T denotes the saturation induced by a certain injection rate and S_B is the initial saturation within the porous medium. To model the capillary pressure, a van Genuchten parameterization is considered, that is,

$$p_c^{(j)}(S) = \Lambda_j \left(S^{-\frac{1}{m_j}} - 1 \right)^{1-m_j}, \quad j \in \{i, d\}.$$

In the remainder of this section, we use the following parameter set: $\Lambda_i = 3.5$, $m_i = 0.92$, $\Lambda_d = 7$, and $m_d = 0.9$. To solve $(\tilde{\mathcal{P}})$ numerically, for $n \in \mathbb{N} \cup \{0\}$ and $t_0 = 0$, we solve within the time step

$$[t_n, t_{n+1}] \text{ of width } \Delta t_n = t_{n+1} - t_n,$$

the elliptic problem

$$-\frac{\partial}{\partial z} \left(F(S, p) + h(S, p) \frac{\partial p}{\partial z} \right) = \frac{1}{\tau} \mathcal{F}(S, p),$$

with respect to the pressure variable p . For a given S , this is a nonlinear elliptic problem and to solve it, a linear iterative scheme is employed which is referred to as the L-scheme in literature⁷³⁻⁷⁵:

$$L(p_n^i - p_n^{i-1}) - \frac{\partial}{\partial z} \left(F(S_n, p_n^{i-1}) + h(S_n, p_n^{i-1}) \frac{\partial p_n^i}{\partial z} \right) = \frac{1}{\tau} \mathcal{F}(S_n, p_n^{i-1}).$$

Here, p_n^i denotes the pressure at the i th iteration and $p_n^0 = p(z, t_n)$. On closer examination, the L-scheme corresponds to a linearization of the nonlinear problem, since for each iteration a linear equation in the unknown pressure variable p_n^i is solved. For Scenario A the parameter L is set to $L = \frac{1}{\tau}$ to ensure convergence of the L-scheme^{45,73} and for Scenario B the modified variant of the L-scheme is used^{9,75} to speed up the convergence, since in this scenario the stiffness matrix has to be recomputed in every iteration. A standard cell centered finite volume scheme is considered for discretizing the linearized elliptic problem in space. Having the pressure variable p_n and the saturation variable S_n for $t = t_n$ at hand, we update the saturation as follows:

$$S_{n+1} = S_n + \frac{\Delta t_n}{\tau} \mathcal{F}(S_n, p_n).$$

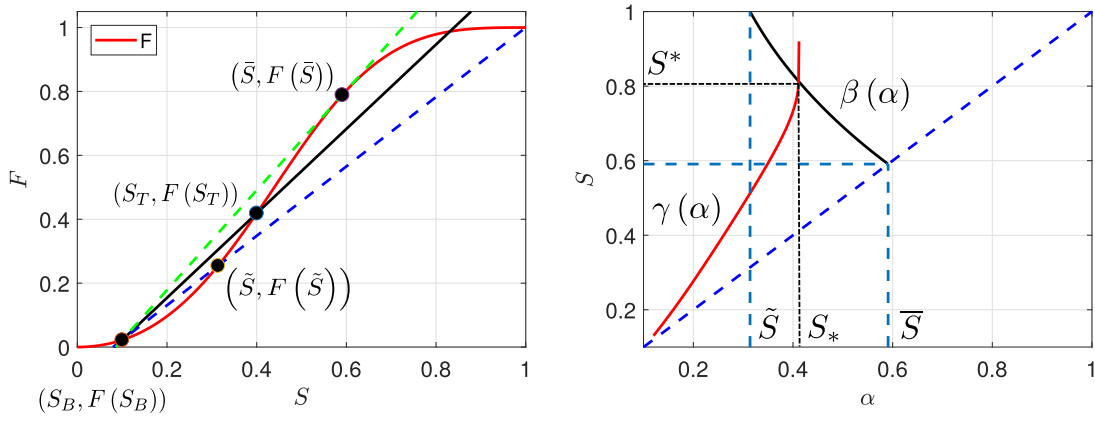


FIGURE 18 Fractional flow function F for Scenario A (left). The characteristic points \tilde{S} , \bar{S} , and S_T are shown. (Right) Curves for γ (red) and β (black) corresponding to F . The intersection point of these curves is denoted by (S_*, S^*)

5.1 | Numerical results for Scenario A

First we illustrate the theoretical findings of Scenario A. The boundary conditions with respect to the pressure variable are of Neumann type at $z = z_{in}$ and of Dirichlet type at $z = z_{out}$:

$$p'(z_{in}, t) = 0 \text{ and } p(z_{out}, t) = p_c^{(i)}(S_B) \text{ for all } t > 0. \quad (71)$$

The boundaries of the domain are given by: $z_{in} = -10$ and $z_{out} = 500$. Because we do not include hysteresis in the relative permeabilities, the flux function F depends only on S and is determined by:

$$f(S) = \frac{S^2}{S^2 + (1 - S)^2} \quad \text{and} \quad N_g = 1.$$

The numerical results presented in this subsection are related to $t = t_{end} = 300$. For the parameters of the initial condition, we take:

$$S_B = 0.1, \quad S_T = 0.4, \quad \text{and} \quad l = 1.$$

Based on these data, some of the variables and constants occurring in Section 3.1, Figures 4 and 6 are computed, that is:

$$\tilde{S} \approx 0.3138, \quad \bar{S} \approx 0.5909, \quad S_o \approx 0.4393, \quad S_* \approx 0.4111, \quad \text{and} \quad S^* \approx 0.8132. \quad (72)$$

Moreover, the curves for γ and β are determined (see Figure 18). Observe that, from our choice, $S_B < S_o$ and $S_T \in (S_B, S_*]$. Next, the characteristic τ -values for drainage and imbibition are computed. Using (50) and given parameters, we obtain:

$$\tau_i = 0.0452 \quad \text{and} \quad \tau_d = 0.2620.$$

Because the requirements listed in Theorem 1 are all fulfilled, we can compare the numerical results with the claims contained in the theorem. For this purpose, we choose τ from the following set:

$$\tau \in \{0.045, 0.25, 1.0, 2.0\},$$

and study the resulting S - p orbits. Considering Figure 19, it can be observed that for $\tau < \tau_i$ monotone

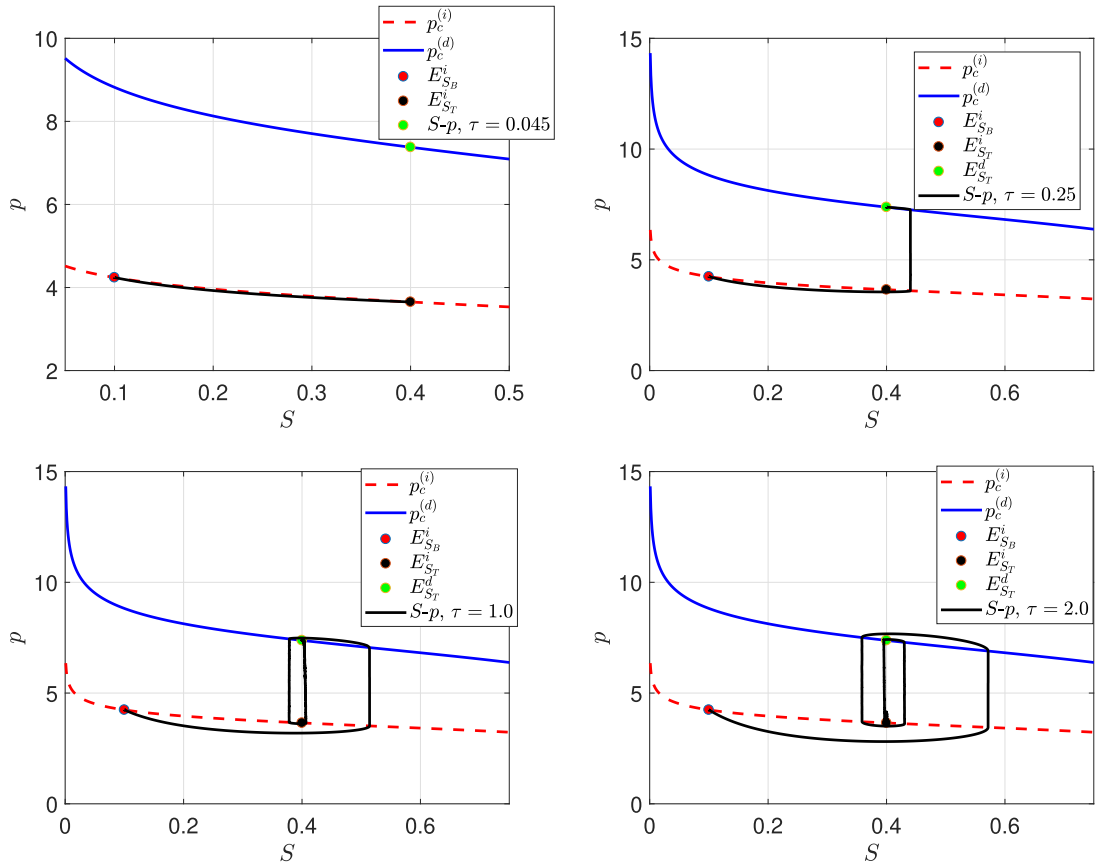


FIGURE 19 Orbits for different τ parameters in the S - p plane

saturation waves are produced by the numerical model linking $E_{S_B}^i$ and $E_{S_T}^i$. In the other cases, a saturation overshoot can be detected, where for $\tau_i < \tau < \tau_d$ the orbit ends up at the equilibrium point $E_{S_T}^d$ and for $\tau > \tau_d$ the orbits spiral around the segment $E_{S_T}^i E_{S_T}^d$. If we choose larger values of τ , the corresponding $S_m(\tau, S_T)$ value of the orbit increases. This supports the claims of Corollary 1 and Proposition 4. Similar results including variation of saturation with ξ can be found in Ref. 45.

The parameter choice considered so far, corresponds to the solution class \mathcal{A} (see (51)), whose entropy solution consists of a single shock without any saturation overshoots (see Figure 21 (top)). However, there are two further solution classes, \mathcal{B} and \mathcal{C} (see (51)), arising in the context of Scenario A, represented by entropy solutions (57) and (58). In case of solution class \mathcal{B} , the entropy solution is given by saturation plateau that is formed by an infiltration wave followed by a drainage wave. The saturation at plateau level is denoted by $\hat{S}_B(\tau)$. For solution class \mathcal{C} , the entropy solution exhibits a rarefaction wave connecting S_T with $\hat{S}_B(\tau)$, which is connected to S_B by a shock. To observe these cases numerically, we compute the $\hat{S}_B(\tau)$ and $\check{S}_B(\tau)$ curves introduced in Definition 1 (see Figure 20). In the figure, we fix $\tau = 1$ and vary S_T so that the pairs (S_T, τ) belong to one of the sets \mathcal{A} , \mathcal{B} , and \mathcal{C} . The results are shown in Figure 21 with the (left) plot showing the variation of S with z , and the (right) plot showing the profiles in the S - p phase plane. The curves corresponding to Set \mathcal{A} show a direct TW wave connecting S_B and $S_T = 0.35$. Some oscillatory behavior around S_T can be observed since τ is comparatively large, however, the existence of a single TW between S_B and S_T implies that these states are connectable by an admissible shock in the hyperbolic limit. Next, choosing $S_T = 0.55$, (S_T, τ) lies in Set \mathcal{B} , and a solution consisting of an infiltration wave followed by a drainage wave is computed in accordance with the theory. The development of the plateau is shown in Figure 22. Again, small oscillations are seen in the drainage wave part which is expected from Corollary 2 since τ is large. The resulting plateau has saturation 0.7158, whereas, the prediction from Figure 20 is $\hat{S}_B(\tau) = 0.7254$.

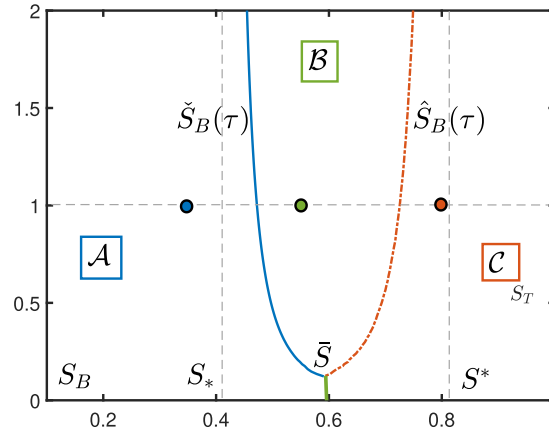


FIGURE 20 The $\hat{S}_B(\tau)$ and $\check{S}_B(\tau)$ curves computed for $S_B = 0.1$. The characteristic saturations are as in (72). The corresponding Sets \mathcal{A} , \mathcal{B} , and \mathcal{C} along with (S_T, τ) test pairs used in Figure 21 are shown

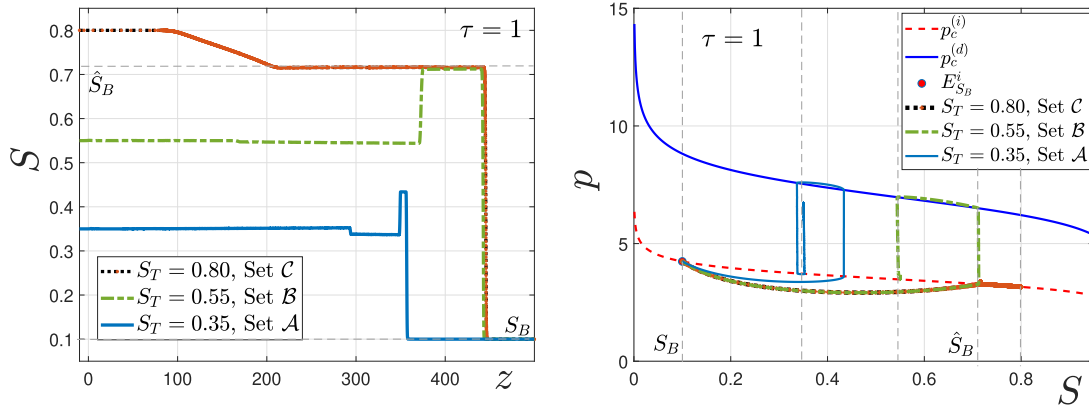


FIGURE 21 Numerical solutions corresponding to different (S_T, τ) pairs from solution classes \mathcal{A} , \mathcal{B} , and \mathcal{C} , marked in Figure 20. Here, $\tau = 1$ is fixed and S_T is chosen from $\{0.35, 0.55, 0.8\}$. The (left) plot shows the variation of S with z , whereas, the (right) plot shows p versus S . The saturation plateau for the Sets \mathcal{B} and \mathcal{C} is observed at $\hat{S}_B = 0.7158$

Finally, for $S_T = 0.8$, the pair (S_T, τ) belongs to the Set \mathcal{C} . The numerical solution exhibits a shock-like structure followed by a plateau and they coincide with the infiltration wave of Set \mathcal{B} on both plots of Figure 21. Moreover, a rarefaction wave between $\hat{S}_B(\tau)$ and S_T is detected. Thus, we conclude that the saturation profiles in Figure 21 correspond to the entropy solutions depicted in Figure 14 and the numerical results are in agreement with the theory.

5.1.1 | Stability of the TW profiles

Another important issue with regards to our discussion is the stability of the TW solutions. For the dynamic capillarity model, linearized stability of TW profiles was investigated in Refs. 76, 77 for convex flux functions. The TWs were found to be stable under small perturbations. Linear stability of the steady-state solution for the dynamic capillarity model was shown in Ref. 37. However, such a result might not hold when hysteresis is included. For example, in Ref. 38 it was shown that with hysteresis, stable planar fronts are not guaranteed. Moreover, linearized stability results might not extend to large deviations from the TW profile. Nevertheless, in our case, the stability of the TW profiles is indicated by the numerical computations. More precisely, the numerical examples are presenting the solution profiles for the partial differential equations, thus not for the TW. These numerical results are obtained

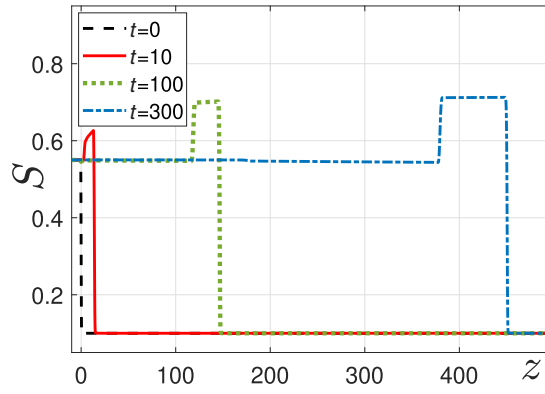


FIGURE 22 The time evolution of the solution profile for $(S_T, \tau) \in B$

by using a regularized initial data in (70). The solution quickly develops into profiles that are either an approximation of the corresponding TW if the values of S_T and S_B are states that can be connected by a TW for the chosen parameters, or it exhibits a plateau value that approximates very well the left state that can be connected by a TW to S_B . Moreover, this is obtained irrespective of the choice of the regularization parameter ℓ in the initial condition (70). Similar behavior was reported in the numerical examples of Refs. 9, 43-45. However, instability of the TWs is observed for large τ when hysteresis is included in the permeabilities. This requires further attention and we have excluded this possibility in our current analysis and computations.

5.2 | Numerical results for Scenario B

In case of Scenario B, we choose the following boundary conditions with respect to the pressure variable. As in the previous subsection, they are of Neumann type at $z = z_{in}$ and of Dirichlet type at $z = z_{out}$:

$$p'(z_{in}, t) = 0 \quad \text{and} \quad p(z_{out}, t) = p_c^{(d)}(S_B) \quad \text{for all } t > 0. \quad (73)$$

Moreover, the boundaries of the domain are given by: $z_{in} = -10$ and $z_{out} = 190$. To make matters interesting, contrary to the previous subsection, we do not start with an infiltration state for S_B , but with a drainage state. Due to the fact that we consider hysteresis both in the capillary pressure and relative permeabilities, fractional flow functions are introduced both for infiltration and for drainage. We use

$$f^{(i)}(S) = \frac{S^2}{S^2 + 3(1 - S^2)}, \quad f^{(d)}(S) = \frac{S^2}{S^2 + 2(1 - S^2)} \quad \text{with } N_g = 0,$$

and define $F^{(i)}$ and $F^{(d)}$ accordingly. We verified numerically that if $S_T > S_B$ and $F^{(i)}(S_T) < F(S_B, p_B)$ then the solution is frozen in time in the sense that $S(z, t) = S(z, 0)$ for all $t > 0$. This is what was discussed in Remark 8. To verify Propositions 11 and 12 and entropy solutions (66)-(69), we show two results: $S_B = S_{B,1} = 0.3$, $S_T = S_{T,1} = 0.95$, and $S_B = S_{B,2} = 0.95$, $S_T = S_{T,2} = 0.3$ both for $\tau = 0.02$. Let the corresponding solutions be $(S_{(i)}, p_{(i)})$ and $(S_{(d)}, p_{(d)})$. Since $S_{T,1} > \bar{S}_i$ for the first case (see Definition 2) and τ is small, from (67) it is expected that the entropy solution will have a shock from $S_{B,1}$ to \bar{S}_i , followed by a rarefaction wave from \bar{S}_i to $S_{T,1}$. This is exactly what is seen from the viscous profiles obtained numerically (see Figure 23). Similarly, for the second case, since $S_{T,2} < \bar{S}_d$ and τ is small, we see from Figure 23a viscous solution resembling a drainage shock followed by a rarefaction wave, as predicted in (69). Next, we investigate whether a stable plateau is

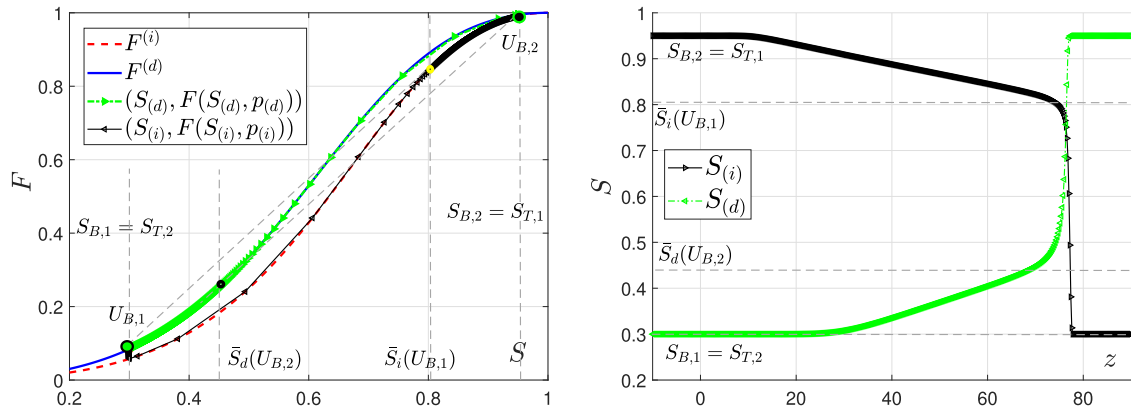


FIGURE 23 The viscous solutions for $S_{B,1} = 0.3$, $S_{T,1} = 0.95$ denoted by $(S_{(i)}, p_{(i)})$ and $S_{B,2} = 0.95$, $S_{T,2} = 0.3$ denoted by $(S_{(d)}, p_{(d)})$ with boundary conditions (73) and $\tau = 0.02$ fixed. In the (left) plot, the solutions are shown in the F - S plane and in the (right) plot the saturations are plotted as functions of z . The points $U_{B,1}$ and $U_{B,2}$ and the saturations $\bar{S}_i(U_{B,1})$ and $\bar{S}_d(U_{B,2})$, introduced in Definition 2, are marked. The results agree with the predictions of Propositions 11 and 12 and Section 4.3

formed for suitable parameter values by an infiltration wave and an ensuing drainage wave, as predicted in Proposition 13. This happens only if $\tau > \tau_i^*(S_T)$, since in this case, a monotone connection between (S_B, p_B) and $(S_T, p_c^i(S_T))$ does not exist. To this end, in the numerical experiment we have used the following parameters:

$$S_B = 0.3, \quad S_T = 0.5, \quad \text{and} \quad \tau = 0.5.$$

For a stable saturation plateau, the velocities of the infiltration wave, connecting S_B and S_P , and the drainage wave, connecting S_P and S_T , have to be equal, that is, if $c_{(i)}^P$ and $c_{(d)}^P$ are denoting the two wave-speeds, then

$$c_{(i)}^P = \frac{F^{(i)}(S_P) - F^{(d)}(S_B)}{S_P - S_B} = \frac{F^{(i)}(S_P) - F^{(d)}(S_T)}{S_P - S_T} = c_{(d)}^P,$$

where S_P stands for the saturation of the plateau. Geometrically, this equality is fulfilled, if the points

$$(S_B, F(S_B, p_B)), (S_T, F^{(d)}(S_T)) \quad \text{and} \quad (S_P, F^{(i)}(S_P))$$

are located on the same line. This is precisely the condition that the solutions $(S_{(i)}^P, p_{(i)}^P)$ and $(S_{(d)}^P, p_{(d)}^P)$ of Proposition 13 satisfy. Drawing a line through the given points for $S_B = 0.3$ and $S_T = 0.5$ (see Figure 24), we obtain that a stable plateau should be located at $S_P \approx 0.634$. As seen from Figure 24, the orbit in the S - F plane stabilizes exactly at $S_P \approx 0.634$ and all the three points line up. Considering Figure 25, we observe that the saturation plateau is in a transient state in the beginning, but it stabilizes at $S_P \approx 0.634$ for longer times, as the speeds of the infiltration and drainage waves match.

6 | FINAL REMARKS AND COMPARISON WITH EXPERIMENTS

In this work, a one-dimensional two-phase flow model has been analyzed for infiltration problems. For simplicity, we have assumed that the medium is homogeneous and a constant total velocity is prescribed at the boundary. Dynamic and hysteretic effects are included in the capillary pressure with

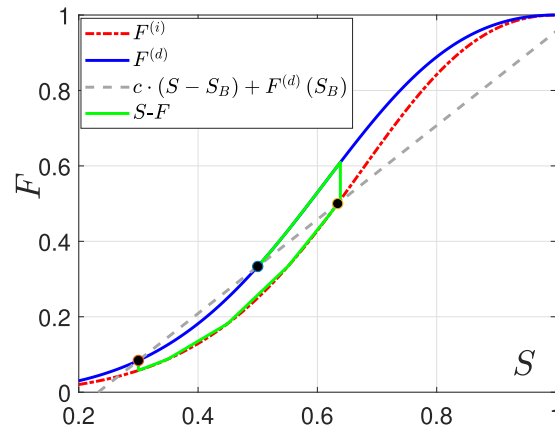


FIGURE 24 The orbit in the $S - F$ plane representing a stable saturation plateau for Scenario B. The equilibrium points for this orbit are shown on the flux curves

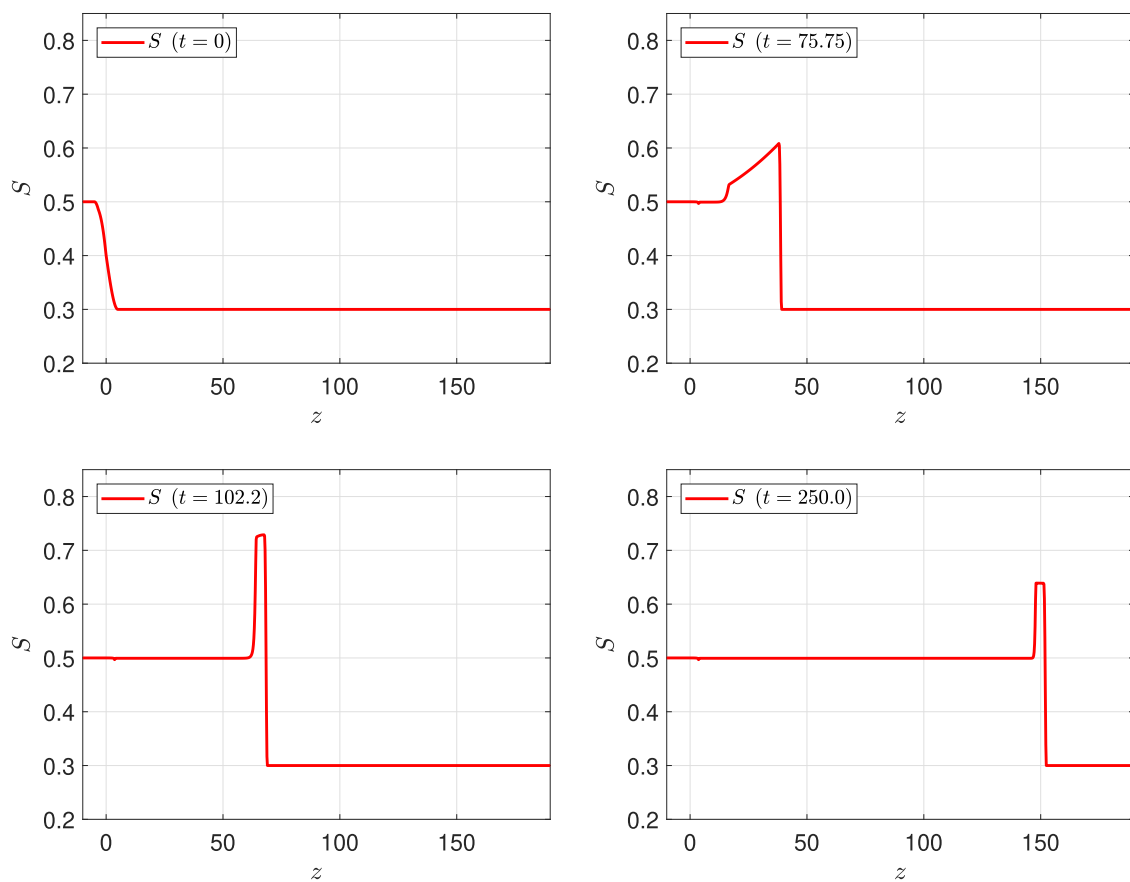


FIGURE 25 Saturation profiles for different time points. Besides the initial condition (top left) and the final saturation profile (bottom right), two intermediate profiles are shown, which have the form of a plateau. Contrary to the final saturation profile their plateaus are not stable, since the speeds of the infiltration and the drainage fronts are equal only for $S_p = 0.634$

transitions between drainage and infiltration processes being modeled by a play-type hysteresis model having vertical scanning curves. Relative permeabilities are modeled as functions of saturation and capillary pressure to make their hysteretic nature explicit.

The focus being on TWs, the system of partial differential equations is transformed into a dynamical system. This system is analyzed for two different scenarios, A and B. In Scenario A, the hysteresis appears only in the capillary pressure, and we consider a broad range of dynamic capillarity terms,

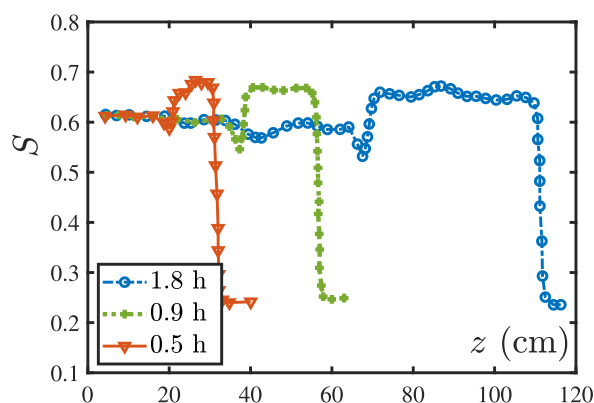


FIGURE 26 The saturation profiles for water injection experiments taken from Ref. 29. Note the presence of growing saturation plateaus

from small to large ones. In Scenario B, hysteresis is included in both the relative permeabilities and in the capillary pressure, whereas the dynamic capillary effects are kept small. For each scenario, the existence of TW solutions is studied. In particular, we show that if the dynamic capillary effects exceed a certain threshold value, the TW profiles become nonmonotonic. Such results complement the analysis in Refs. 9, 42, 45 done for the unsaturated flow case, respectively, in Refs. 43, 44 for two-phase flow but without hysteresis. From practical point of view, the present analysis provides a criterion for the occurrence of overshoots in two-phase infiltration experiments.

Based on the TW analysis, we give admissibility conditions for shock solutions to the hyperbolic limit of the system. Motivated by the hysteretic and dynamic capillarity effects, such solutions do not satisfy the classical entropy condition. This is because the standard entropy solutions to hyperbolic two-phase flow models are obtained as limits of solutions to classical two-phase flow models, thus not including hysteresis and dynamic capillarity. In particular, for the infiltration case of Scenario A, apart from the classical solutions, there can be solutions consisting of (a) an infiltration shock followed by a rarefaction wave having nonmatching speeds, or (b) an infiltration shock followed by a drainage shock resulting in a growing saturation plateau (overshoot) in between. This is similar to the results in Refs. 43, 44. In Scenario B, the entropy solutions are shown to depend also on the initial pressure. In particular, if certain parametric conditions are met, the solutions may include ones featuring a stable saturation plateau between an infiltration front and a drainage front, both traveling with the same velocity. Such solutions are obtained, for example, in Ref. 15, but only after generating the overshoot through a change in the boundary condition. All cases mentioned above have been reproduced by numerical experiments, in which a good resemblance has been observed between the TW results and the long-time behavior of the solutions to the original system of partial differential equations.

From practical point of view, we note that the present analysis can also be used to explain experimental results reported, for example, in Refs. 33, 41, 55, 66. The occurrence of saturation overshoots is predicted theoretically for high enough dynamic capillary effects, namely, of the τ value in (24). In dimensionless setting, this can be assimilated to an injection rate that is sufficiently large. This is in line with the experimental results in Ref. 33, where the development of plateau-like profiles was observed for high enough injection rates, as shown in fig. 5 of 33 and fig. 5.3 of Ref. 66. Similarly, in the water and oil case, the plateaus are seen to develop and grow in figs. 5-6, 8-9, 18 of Ref. 29 (see Figure 26). This behavior is predicted by the analysis in Section 3. Moreover, fig. 10 of 29 might be presenting the case when the saturation has developed a plateau between two fronts traveling with the same velocity, a situation that is explained by the authors by means of hysteretic effects in the flux functions. Such solutions are investigated numerically in Refs. 15, 60, where it is shown that the plateaus can persist in

time but without explaining how they are generated. The results in Section 4 partly support the conclusions there, but also explain the mechanism behind the development of such plateaus. We mention⁷⁸ in this regard, where the authors conclude that a similar mechanism must be responsible for observed stable saturation plateaus inside viscous fingers.

ACKNOWLEDGMENTS

K. Mitra is supported by TU Dortmund University, and was partly supported by the Netherlands Organisation for Scientific Research (NWO) through the CSER programme (project 14CSER016) and by Hasselt University, Belgium through the project BOF17BL04. I.S. Pop is supported by the Research Foundation-Flanders (FWO), Belgium through the Odysseus programme project G0G1316N and the project G051418N. The work of T. Köppl and R. Helmig is supported by the Cluster of Excellence in Simulation Technology (EXC 310/2) of Stuttgart University. Furthermore, C.J. van Duijn and R. Helmig acknowledge the support of the Darcy Center of Utrecht University and Eindhoven University of Technology and the support of the Deutsche Forschungsgemeinschaft (DFG, German Research Foundation), SFB 1313, Project Number 327154368.

ORCID

K. Mitra  <https://orcid.org/0000-0002-8264-5982>

REFERENCES

1. Bear J. *Hydraulics of Groundwater*. New York: McGraw-Hill International Book Co.; 1979.
2. Helmig R. *Multiphase Flow and Transport Processes in the Subsurface: A Contribution to the Modeling of Hydrosystems*. Berlin: Springer-Verlag; 1997.
3. Richards LA. Capillary conduction of liquids through porous mediums. *J Appl Phys*. 1931;1(5):318-333.
4. Beliaev A, Hassanizadeh SM. A theoretical model of hysteresis and dynamic effects in the capillary relation for two-phase flow in porous media. *Transp Porous Media*. 2001;43(3):487-510.
5. Morrow N, Harris C. Capillary equilibrium in porous materials. *Soc Pet Eng J*. 1965;5(1):15-24.
6. Poulouvasilis A. Hysteresis of pore water in granular porous bodies. *Soil Sci*. 1970;109(1):5-12.
7. Zhuang L, Bezerra Coelho CR, Hassanizadeh SM, van Genuchten MT. Analysis of the hysteretic hydraulic properties of unsaturated soil. *Vadose Zone J*. 2017;16(5):1-9.
8. Cao X, Pop IS. Two-phase porous media flows with dynamic capillary effects and hysteresis: uniqueness of weak solutions. *Comput Math Appl*. 2015;69(7):688-695. <http://www.sciencedirect.com/science/article/pii/S0898122115000620>.
9. van Duijn CJ, Mitra K, Pop IS. Travelling wave solutions for the Richards equation incorporating non-equilibrium effects in the capillarity pressure. *Nonlinear Anal Real World Appl*. 2018;41(Supplement C):232-268. <http://www.sciencedirect.com/science/article/pii/S1468121817301621>.
10. Behi-Gornostaeva EE, Mitra K, Schweizer B. Traveling wave solutions for the Richards equation with hysteresis. *IMA J Appl Math*. 2019;84(4):797-812. <https://doi.org/10.1093/imamat/hxz015>.
11. Schweizer B. The Richards equation with hysteresis and degenerate capillary pressure. *J Differ Equ*. 2012;252(10):5594-5612. <http://www.sciencedirect.com/science/article/pii/S0022039612000502>.
12. Rätz A, Schweizer B. Hysteresis models and gravity fingering in porous media. *Z Angew Math Mech*. 2014;94(7-8):645-654.
13. Zhang H, Zegeling PA. A numerical study of two-phase flow models with dynamic capillary pressure and hysteresis. *Transp Porous Media*. 2017 Jan;116(2):825-846. <https://doi.org/10.1007/s11242-016-0802-z>.
14. Papafotiou A, Sheta H, Helmig R. Numerical modeling of two-phase hysteresis combined with an interface condition for heterogeneous porous media. *Comput Geosci*. 2010;14(2):273-287.
15. Schneider M, Köppl T, Helmig R, Steinle R, Hilfer R. Stable propagation of saturation overshoots for two-phase flow in porous media. *Transp Porous Media*. 2018;121(3):621-641.

16. Brokate M, Botkin ND, Pykhteev OA. Numerical simulation for a two-phase porous medium flow problem with rate independent hysteresis. *Physica B Condense Matter*. 2012;407(9):1336-1339.
17. Philip JR. Similarity hypothesis for capillary hysteresis in porous materials. *J Geophys Res*. 1964;69(8):1553-1562.
18. Mualem Y. A conceptual model of hysteresis. *Water Resour Res*. 1974;10(3):514-520. <http://doi.org/10.1029/WR010i003p00514>.
19. Parker JC, Lenhard RJ, Koppusamy T. A parametric model for constitutive properties governing multiphase flow in porous media. *Water Resour Res*. 1987;23(4):618-624.
20. Hassanizadeh SM, Gray WG. Mechanics and thermodynamics of multiphase flow in porous media including interphase boundaries. *Adv Water Resour*. 1990;13(4):169-186. <http://www.sciencedirect.com/science/article/pii/030917089090040B>.
21. Hassanizadeh SM, Gray WG. Toward an improved description of the physics of two-phase flow. *Adv Water Resour*. 1993;16(1):53-67.
22. Pop IS, van Duijn CJ, Niessner J, Hassanizadeh SM. Horizontal redistribution of fluids in a porous medium: the role of interfacial area in modeling hysteresis. *Adv Water Resour*. 2009;32(3):383-390.
23. Niessner J, Hassanizadeh SM. A model for two-phase flow in porous media including fluid-fluid interfacial area. *Water Resour Res*. 2008;44(8), W08439, <https://doi.org/10.1029/2007WR006721>.
24. Duijn CJV, Mitra K. Hysteresis and horizontal redistribution in porous media. *Transp Porous Media*. 2018;122(2):375-399. <https://doi.org/10.1007/s11242-018-1009-2>.
25. Gray WG, Miller CT. TCAT analysis of capillary pressure in non-equilibrium, two-fluid-phase, porous medium systems. *Adv Water Resour*. 2011;34(6):770-778.
26. Miller CT, Bruning K, Talbot CL, McClure JE, Gray WG. Nonhysteretic capillary pressure in two-fluid porous medium systems: definition, evaluation, validation, and dynamics. *Water Resour Res*. 2019;55(8):6825-6849.
27. Mitra K. *Mathematical Complexities in Porous Media Flow*. Eindhoven University of Technology & Hasselt University; 2019.
28. Schweizer B. Laws for the capillary pressure in a deterministic model for fronts in porous media. *SIAM J Math Anal*. 2005;36(5):1489-1521.
29. Gladfelter RE, Gupta SP. Effect of fractional flow hysteresis on recovery of tertiary oil. *Soc Pet Eng J*. 1980;20(6):508-520.
30. Braun EM, Holland RF. Relative permeability hysteresis: Laboratory measurements and a conceptual model. *SPE Reserv Eng*. 1995;10(03):222-228.
31. Killough JE. Reservoir simulation with history-dependent saturation functions. *Soc Pet Eng J*. 1976;16(01):37-48.
32. Topp GC, Miller EE. Hysteretic moisture characteristics and hydraulic conductivities for glass-bead media. *Soil Sci Soc Am J*. 1966;30(2):156-162.
33. DiCarlo DA. Experimental measurements of saturation overshoot on infiltration. *Water Resour Res*. 2004;40(4), W04215, <https://doi.org/10.1029/2003WR002670>.
34. Bottero S, Hassanizadeh SM, Kleingeld PJ, Heimovaara TJ. Nonequilibrium capillarity effects in two-phase flow through porous media at different scales. *Water Resour Res*. 2011;47(10), W10505, <https://doi.org/10.1029/2011WR010887>.
35. Shiozawa S, Fujimaki H. Unexpected water content profiles under flux-limited one-dimensional downward infiltration in initially dry granular media. *Water Resour Res*. 2004;40(7), W07404, <https://doi.org/10.1029/2003WR002197>.
36. Egorov AG, Dautov RZ, Nieber JL, Sheshukov AY. Stability analysis of gravity-driven infiltrating flow. *Water Resour Res*. 2003;39(9), 1266, <https://doi.org/10.1029/2002WR001886>.
37. Van Duijn CJ, Pieters GJM, Raats PAC. Steady flows in unsaturated soils are stable. *Transport Porous Media*. 2004;57(2):215-244.
38. Schweizer B. Instability of gravity wetting fronts for Richards equations with hysteresis. *Interfaces Free Bound*. 2012;14(1):37-64.
39. Hassanizadeh SM, Gray WG. Thermodynamic basis of capillary pressure in porous media. *Water Resour Res*. 1993;29(10):3389-3405.
40. Camps-Roach G, O'Carroll DM, Newson TA, Sakaki T, Illangasekare TH. Experimental investigation of dynamic effects in capillary pressure: grain size dependency and upscaling. *Water Resour Res*. 2010;46(8), W08544, <https://doi.org/10.1029/2009WR008881>.

41. Kalaydjian FJM. Dynamic capillary pressure curve for water/oil displacement in porous media: theory vs. experiment. In: *SPE Annual Technical Conference and Exhibition*. Society of Petroleum Engineers; 1992.
42. Cuesta C, van Duijn CJ, Hulshof J. Infiltration in porous media with dynamic capillary pressure: travelling waves. *Eur J Appl Math*. 2000;11(4):381-397.
43. van Duijn CJ, Peletier LA, Pop IS. A new class of entropy solutions of the Buckley–Leverett equation. *SIAM J Math Anal*. 2007;39(2):507-536.
44. van Duijn CJ, Fan Y, Peletier LA, Pop IS. Travelling wave solutions for degenerate pseudo-parabolic equations modelling two-phase flow in porous media. *Nonlinear Anal Real World Appl*. 2013;14(3):1361-1383.
45. Mitra K, van Duijn CJ. Wetting fronts in unsaturated porous media: the combined case of hysteresis and dynamic capillary pressure. *Nonlinear Anal Real World Appl*. 2019;50:316-341. <http://www.sciencedirect.com/science/article/pii/S1468121818306254>.
46. Cao X, Pop IS. Degenerate two-phase porous media flow model with dynamic capillarity. *J Differ Equ*. 2016;260(3):2418-2456.
47. Cao X, Pop IS. Uniqueness of weak solutions for a pseudo-parabolic equation modeling two phase flow in porous media. *Appl Math Lett*. 2015;46:25-30.
48. Mikelić A. A global existence result for the equations describing unsaturated flow in porous media with dynamic capillary pressure. *J Differ Equ*. 2010;248(6):1561-1577.
49. Böhm M, Showalter RE. Diffusion in fissured media. *SIAM J Math Anal*. 1985;16(3):500-509.
50. Karpinski S, Pop IS. Analysis of an interior penalty discontinuous Galerkin scheme for two phase flow in porous media with dynamic capillary effects. *Numer Math*. 2017;136(1):249-286.
51. Cao X, Nemađjeu SF, Pop IS. Convergence of an MPFA finite volume scheme for a two-phase porous media flow model with dynamic capillarity. *IMA J Numer Anal*. 2018;39(1):512-544.
52. Karpinski S, Pop IS, Radu FA. Analysis of a linearization scheme for an interior penalty discontinuous Galerkin method for two-phase flow in porous media with dynamic capillarity effects. *Int J Numer Methods Eng*. 2017;112(6):553-577.
53. Cao X, Mitra K. Error estimates for a mixed finite element discretization of a two-phase porous media flow model with dynamic capillarity. *J Comput Appl Math*. 2019;353:164-178. <http://www.sciencedirect.com/science/article/pii/S0377042718307532>.
54. Ewing RE. Time-stepping Galerkin methods for nonlinear Sobolev partial differential equations. *SIAM J Numer Anal*. 1978;15(6):1125-1150.
55. Glass RJ, Steenhuis TS, Parlange JY. Mechanism for finger persistence in homogeneous, unsaturated, porous media: theory and verification. *Soil Sci*. 1989;148(1):60-70.
56. Rezaeezhad F, Vogel HJ, Roth K. Experimental study of fingered flow through initially dry sand. *Hydrol Earth System Sci Discuss*. 2006;3(4):2595-2620.
57. Spayd K, Shearer M. The Buckley–Leverett equation with dynamic capillary pressure. *SIAM J Appl Math*. 2011;71(4):1088-1108.
58. Bedjaoui N, LeFloch PG. Diffusive–dispersive traveling waves and kinetic relations: part I: nonconvex hyperbolic conservation laws. *J Differ Equ*. 2002;178(2):574-607.
59. El GA, Hofer MA, Shearer M. Dispersive and diffusive-dispersive shock waves for nonconvex conservation laws. *SIAM Rev*. 2017;59(1):3-61.
60. Hilfer R, Steinle R. Saturation overshoot and hysteresis for twophase flow in porous media. *Eur Phys J Spec Top*. 2014;223(11):2323-2338.
61. Plohr B, Marchesin D, Bedrikovetsky P, Krause P. Modeling hysteresis in porous media flow via relaxation. *Comput Geosci*. 2001;5(3):225-256.
62. Schaerer CE, Marchesin D, Sarkis M, Bedrikovetsky P. Permeability hysteresis in gravity counterflow segregation. *SIAM J Appl Math*. 2006;66(5):1512-1532.
63. Bedrikovetsky P, Marchesin D, Ballin PR. Mathematical model for immiscible displacement honouring hysteresis. In: *SPE Latin America/Caribbean Petroleum Engineering Conference*. Society of Petroleum Engineers; 1996.
64. Abreu E, Bustos A, Ferraz P, Lambert W. A relaxation projection analytical-numerical approach in hysteretic two-phase flows in porous media. *J Sci Comput*. 2019;79(3):1936-1980.
65. Shearer M, Spayd KR, Swanson ER. Traveling waves for conservation laws with cubic nonlinearity and BBM type dispersion. *J Differ Equ*. 2015;259(7):3216-3232.

66. Zhuang L. *Advanced Theories of Water Redistribution and Infiltration in Porous Media: Experimental Studies and Modeling*. University of Utrecht, Dept. of Earth Sciences; 2017.
67. Leverett MC. Capillary behavior in porous solids. *Trans AIME*. 1941;142(1):152-169.
68. Graf M, Kunzinger M, Mitrovic D, Vujadinovic D. A vanishing dynamic capillarity limit equation with discontinuous flux. arXiv preprint arXiv:180502723; 2018.
69. Manthey S, Hassanzadeh SM, Helmig R, Hilfer R. Dimensional analysis of two-phase flow including a rate-dependent capillary pressure–saturation relationship. *Adv Water Resour*. 2008;31(9):1137-1150.
70. Oleinik OA. Discontinuous solutions of non-linear differential equations. *Uspekhi Mate Nauk*. 1957;12(3):3-73.
71. LeFloch PG. *Hyperbolic Systems of Conservation Laws: The Theory of Classical and Nonclassical Shock Waves*. Springer Science & Business Media; Basel 2002.
72. Brooks RH, Corey AT. Properties of porous media affecting fluid flow. *J Irrig Drain Div*. 1966;92(2):61-90.
73. Pop IS, Radu FA, Knabner P. Mixed finite elements for the Richards equation: linearization procedure. *J Comput Appl Math*. 2004;168(1):365-373.
74. List F, Radu FA. A study on iterative methods for solving Richards' equation. *Comput Geosci*. 2016;20(2):341-353.
75. Mitra K, Pop IS. A modified L-scheme to solve nonlinear diffusion problems. *Comput Math Appl*. 2019;77(6):1722-1738. <http://www.sciencedirect.com/science/article/pii/S0898122118305546>.
76. Cuesta C, Hulshof J. A model problem for groundwater flow with dynamic capillary pressure: stability of travelling waves. *Nonlinear Anal Theory Methods Appl*. 2003;52(4):1199-1218.
77. Nieber JL, Dautov RZ, Egorov AG, Sheshukov AY. Dynamic capillary pressure mechanism for instability in gravity-driven flows, review and extension to very dry conditions. *Transport Porous Media*. 2005; 58(1-2): 147-172.
78. Kacimov AR, Yakimov ND. Nonmonotonic moisture profile as a solution of Richards' equation for soils with conductivity hysteresis. *Adv Water Resour*. 1998;21(8):691-696.

How to cite this article: Mitra K, Köppl T, Pop IS, van Duijn CJ, Helmig R. Fronts in two-phase porous media flow problems: The effects of hysteresis and dynamic capillarity. *Stud Appl Math*. 2020;1–44. <https://doi.org/10.1111/sapm.12304>

APPENDIX A: PROOFS OF SOME RESULTS GIVEN IN SECTION 3.1

Proof of Proposition 1. The property that $\gamma(\alpha)$ increases follows directly from (36). Moreover, $\gamma(\alpha) > \alpha$ for $\alpha > S_B$, since $\int_{S_B}^{\alpha} \mathcal{G}(S; S_B, \alpha) dS < 0$ in this case (see (37)). Observe that, if (39) is satisfied then $\gamma(\tilde{S}) < 1$. This shows the existence of $\gamma(\alpha)$ in a right neighborhood of $S = \tilde{S}$. The solution in this case exists up to $\alpha = S_* \in (\tilde{S}, \bar{S})$ where $\gamma(\alpha)$ and $\beta(\alpha)$ intersect: $\gamma(S_*) = \beta(S_*) =: S^*$.

For $S_B \in (\underline{S}, S_o)$, $\beta(\alpha)$ and $\gamma(\alpha)$ can similarly be defined, although the domain where $\beta(\alpha)$ is defined is different. In this case, the intersection of $\beta(\alpha)$ and the second solution $\gamma(\alpha)$ is guaranteed irrespective of (39) since $\int_{S_B}^{\bar{S}} \mathcal{G}(S; S_B, \bar{S}) dS < 0$ and $\int_{S_B}^1 \mathcal{G}(S; S_B, 1) dS > 0$. This is because $\mathcal{G}(S; S_B, \bar{S}) < 0$ for $S_B < S < \bar{S}$ and $\mathcal{G}(S; S_B, 1) > 0$ for $S_B < S < 1$. ■

Proof of Proposition 3.

(a) The lower bound follows from Proposition 2. To show the upper bound, observe that if $S_m(\tau, S_T) \geq \gamma(S_T)$, then $w(\gamma(S_T)) \leq p_c^{(i)}(\gamma(S_T))$. This directly contradicts the strict inequality in (45) since $\Phi(\gamma(S_T)) = 0$.

(b) Since $\mathcal{G}(\cdot; S_B, S_T) < 0$ in $(\beta(S_T), 1)$, Proposition 2 and (45), (46a) imply $S_m(\tau, S_T) = 1$. Since (45) holds for all $S < 1$ and since $w' < 0$ in a left neighborhood of $S = 1$, let us suppose that $\lim_{S \nearrow 1} w(S; \tau, S_T) = -L$ ($L > 0$). Then Equation (43) and property (39) give $w' \notin L^1$ near $S = 1$, contradicting the boundedness of w . ■

Proof of Proposition 4. We argue as in Refs. 43,44. The key idea is to introduce the function

$$u = \frac{(p_c^{(i)} - w)}{\sqrt{d}} \text{ with } d = c(S_T)\tau. \quad (\text{A1})$$

Using (43) one obtains for u the equation

$$u'(S; \tau, S_T) = \frac{1}{\sqrt{d}} p_c^{(i)'}(S) - \frac{\mathcal{G}(S; S_B, S_T)}{u(S; \tau, S_T)}. \quad (\text{A2})$$

Clearly, $u|_{S_B} = 0$ and $u > 0$ in a right neighborhood of S_B . Since $\mathcal{G}|_{S_B} = 0$ as well, one finds from (A2) and the sign of u

$$u'(S_B; \tau, S_T) = \frac{p_c^{(i)'}(S_B)}{2} \left[\sqrt{\frac{1}{d} - 4 \frac{\mathcal{G}'(S_B; S_B, S_T)}{(p_c^{(i)'}(S_B))^2}} - \frac{1}{\sqrt{d}} \right] > 0$$

since $\mathcal{G}'(S_B; S_B, S_T) < 0$. Using (36), Remark 3 and some elementary algebra

$$u'(S_B; \tau_1, S_T) < u'(S_B; \tau_2, S_T) \quad \text{in case (a)}, \quad (\text{A3a})$$

$$u'(S_B; \tau, S_{T,1}) < u'(S_B; \tau, S_{T,2}) \quad \text{in case (b)}. \quad (\text{A3b})$$

(a) From (A3a), $u_1(\cdot) := u(\cdot; \tau_1, S_T) < u(\cdot; \tau_2, S_T) =: u_2(\cdot)$ in a right neighborhood of S_B . We claim that u_1 and u_2 do not intersect in $\{u_1 > 0\}$. Suppose, to the contrary, there exists $S_i > S_B$ such that $u_1(S) < u_2(S)$ for $S_B < S < S_i$ and $u_1(S_i) = u_2(S_i)$. Thus $u_1'(S_i) \geq u_2'(S_i)$. Evaluating (A2) at S_i gives

$$u_1'(S_i) = \frac{p_c^{(i)'}(S_i)}{\sqrt{d_1}} - \frac{\mathcal{G}(S_i; S_B, S_{T,1})}{u_1(S_i)} < \frac{p_c^{(i)'}(S_i)}{\sqrt{d_2}} - \frac{\mathcal{G}(S_i; S_B, S_{T,2})}{u_2(S_i)} = u_2'(S_i),$$

a contradiction. If $S_T < S_m(\tau_2, S_T) \leq \beta(S_T)$, the u -monotonicity gives $S_m(\tau_1, S_T) \leq S_m(\tau_2, S_T)$. We rule out the equality by contradiction. Suppose $S_m(\tau_1, S_T) = S_m(\tau_2, S_T) =: S_m$. Then

$$u_1 < u_2 \text{ in } (S_B, S_m).$$

Integrating Equation (A2) from S_T to S_m gives

$$u_2(S_T) - u_1(S_T) = (p_c^{(i)}(S_T) - p_c^{(i)}(S_m)) \left(\frac{1}{\sqrt{d_2}} - \frac{1}{\sqrt{d_1}} \right) + \int_{S_T}^{S_m} \mathcal{G} \left(\frac{1}{u_2} - \frac{1}{u_1} \right). \quad (\text{A4})$$

Since $\mathcal{G} > 0$ in (S_T, S_m) for $S_T < S_m \leq \beta(S_T)$, the term in the right of (A4) is negative, yielding a contradiction.

(b) Using (36), this part is demonstrated along the same lines. Details are omitted. ■

Proof of Proposition 5. As seen from (A2), v satisfies the equation

$$(v^2)' = 2vp_c^{(i)'} - 2c\tau\mathcal{G} \text{ in } \{v > 0\}.$$

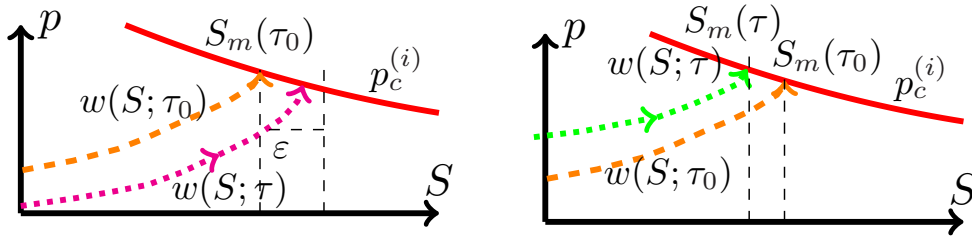


FIGURE A1 Behavior of w close to S_m : (left) $\tau > \tau_0$ and (right) $\tau < \tau_0$

Integrating this equation and using Proposition 4 and Φ from (45) gives the desired inequalities. ■

Proof of Corollary 1. We only demonstrate continuity with respect to τ . The proof of continuity with respect to S_T follows the same arguments. We therefore take $S_T = S_{T_0}$ and drop its dependence from the notation for simplicity. Consider first $\tau > \tau_0$ and $S_{T_0} < \beta(S_{T_0})$. Recalling $v(S_m(\tau_0); \tau_0) = 0$, Proposition 5 gives

$$0 < v(S_m(\tau_0); \tau) < \sqrt{2c(\tau - \tau_0)\Phi(S_m(\tau_0))},$$

where $\Phi(S_m(\tau_0)) > 0$ by (46) and Proposition 3. For any given (small) $\varepsilon > 0$ and with reference to Figure A1 choosing $\delta < \frac{p_c^{(i)}(S_m(\tau_0)) - p_c^{(i)}(S_m(\tau_0) + \varepsilon)}{2c\Phi(S_m(\tau_0))}$ we have

$$w(S_m(\tau_0), \tau) > p_c^{(i)}(S_m(\tau) + \varepsilon) \text{ for all } \tau - \tau_0 < \delta.$$

Since $w' > 0$, this implies the continuity of $\tau > \tau_0$.

Next let $\tau < \tau_0$ and $S_{T_0} \leq \beta(S_{T_0})$. Now we have from Proposition 5

$$0 < v(S_m(\tau); \tau_0) < \sqrt{2c(\tau_0 - \tau)\Phi(S_m(\tau))}. \quad (\text{A5})$$

Since $v(\cdot, \tau_0) \in C([S_B, S_m(\tau_0)])$, $v(S_m(\tau_0), \tau_0) = 0$ and $v(\cdot, \tau_0) > 0$ in $(S_B, S_m(\tau_0))$, the continuity of S_m follows directly from (A5). ■

Proof of Proposition 7.

(a) Suppose no $\tau_c(S_T)$ exists such that $S_m(\tau_c, S_T) = \beta(S_T)$, meaning $S_m(\tau, S_T) < \beta(S_T)$ for all $\tau > 0$. From [Ref. 9, proposition 4.2(b)] we have that

$$w(S; \tau, S_T) \rightarrow -\infty \text{ as } \tau \rightarrow \infty \text{ for all } S \in (S_B, S_T].$$

This implies that for large enough τ , a $S_1 \in [S_T, \beta(S_T)]$ exists for which $w(S_1) = 0$. From (43), it is evident that $w(S_T) \leq w(S)$, in particular $w(S_T) < w(S_1) = 0$. Moreover, (45) gives the lower bound $w(S) \geq w(S_T) \geq p_c^{(i)}(S_T) - \sqrt{2c\tau\Phi(S_T)} \geq -\sqrt{2c\tau\Phi(S_T)}$ for all $S \in [S_B, S_m(\tau, S_T)]$. Multiplying both sides of (A2) by u , integrating from S_B to S_1 and using the above inequality we get

$$\begin{aligned} -\frac{1}{2}p_c^{(i)2}(S_B) &= \int_{S_B}^{S_1} (c\tau\mathcal{G}(S; S_B, S_T) + p_c^{(i)'}(S)w(S; c, \tau))dS \\ &\leq -c\tau\Phi(S_1) + (p_c^{(i)}(S_B) - p_c^{(i)}(S_1))\sqrt{2c\tau\Phi(S_T)}. \end{aligned}$$

Since $\Phi(S_1) > 0$ (as stated in (46b)), this leads to a contradiction for $\tau \rightarrow \infty$. Hence, $S_m(\tau, S_T) = \beta(S_T)$ for some $\tau > 0$. The uniqueness follows from Proposition 4.

(b) The monotonicity and continuity follows from Propositions 4 and 5 and Corollary 1. To show the limit for $S_T \searrow S_*$, assume that $\lim_{S_T \searrow S_*} \tau_c(S_T) = \tau_\infty < \infty$. Let then $\tau > \tau_\infty$. Proposition 3 implies that $S_m(\tau, S_*) < \beta(S_*)$. Choose an $S_T > S_*$ such that $\beta(S_T) \geq S_m(\tau, S_*)$. Since $\tau > \tau_c(S_T)$, we get that $w(S_m(\tau, S_*); \tau, S_T) \leq w(\beta(S_T); \tau, S_T) \leq p_c^{(i)}(\beta(S_T))$, implying $w(S_m(\tau, S_*); \tau, S_*) - w(S_m(\tau, S_*); \tau, S_T) \geq p_c^{(i)}(S_m(\tau, S_*)) - p_c^{(i)}(\beta(S_T))$. This gives a contradiction when $S_T \searrow S_*$ since the right-hand side goes to $p_c^{(i)}(S_m(\tau, S_*)) - p_c^{(i)}(\beta(S_*)) > 0$, whereas the left-hand side converges to 0 from Corollary 1.

The existence of a $\bar{\tau} > 0$ is a consequence of the continuity of τ_c with $\bar{\tau} = \tau_m(\bar{S}) \geq \bar{\tau}_m(\bar{S})$ following from Proposition 6.

■

10 Concluding remarks and outlook

In this habilitation thesis we have investigated how model reduction techniques can be used to simulate complex flow processes in an efficient way. This has been exemplified by means of the following flow processes: Blood flow in large arteries and microvascular networks, oil transport in pipelines and injection of fluids into porous media. The model reduction techniques which have been considered comprise dimension reduction, data based learning and homogenisation techniques. In different chapters of the submitted work, the resulting modelling approaches have been analysed mathematically (see Chapters 5, 6 and 9). The other chapters are concerned with the computational analysis of model reduction techniques or their application to a certain problem setting (see Chapters 2, 3, 4, 7 and 8). All these chapters have a dedicated conclusion. In the final chapter these conclusions are summarised and put into context of this thesis. Furthermore, several aspects of future research are discussed.

Part I is focused on simplified models in context with blood flow in networks of large arteries and oil pipelines. The first chapter of this part contains a mathematical model, which can be used to simulate the influence of a peripheral arterial stenosis on blood supply of distal tissue. Furthermore, two mechanisms that help to restore the reduced blood flow, i.e., metabolic regulation and arteriogenesis have been modelled. As model reduction techniques we have used dimensionally reduced differential equations and algebraic coupling equations. Our simulation results show that reduced blood supply caused by a severe stenosis can only be recovered if these compensation mechanisms are combined and a sufficient number of collateral vessels is given. Balancing the missing blood supply caused by a stenosis of lower degree it is sufficient to take only metabolic regulation into consideration. The existing model could be enhanced by incorporating further compensation mechanisms, e.g., angiogenesis or an advanced model for arteriogenesis.

The following Chapter 3 is closely related to the first chapter of Part I. As the title suggests, it is concerned with the same issue from biomedical engineering. However, contrary to Chapter 2, we do not incorporate compensation mechanisms. In this chapter, we are focused on the numerical effort arising when the stenosis degree is varied many times as it has been done in the previous chapter. For this purpose a surrogate model depending on the stenosis degree is designed having the form of a linear combination of kernel functions like Gaussian kernel functions. Using simulation data produced by a dimensionally reduced blood flow model, the coefficients of the corresponding linear combinations as well as parameters determining the kernel functions are computed based on a Greedy algorithm. It has been shown that the error between the surrogate kernel model and the exact simulation data is decreasing as an increasing amount of simulation data is used to design the surrogate model. Moreover, the surrogate kernel model has been used to solve a parameter estimation problem. Thereby, the degree of stenosis has been estimated for a given pressure or flow rate curve in the vicinity of the stenosis. Future work related to the simplified blood flow model may be concerned with simulating the whole circulation based on a closed loop model. This means that besides the left ventricle also the remaining chambers of the heart as well as the pulmonary circulation and the venous part of the systemic circulation would

have to be modelled. A further aspect that could be investigated would be to apply besides the kernel based methods also a Reduced Basis method to the parameterised stenosis problem and compare the performance of both methods. In particular, the cost function for the parameter estimation problem should be improved such that the estimates for low stenosis degrees are more accurate.

In Chapter 4 the modelling technique that has been used to simulate blood flow in the first two papers is adapted to simulate oil transport in a pipeline. As the one-dimensional flow equations for single arteries, the flow equations for oil in a single pipeline are one-dimensional (1D models) in space and have the form of a hyperbolic system of equations. The difference between the two flow models is that the flow model for the oil pipeline can be linearised, since the interaction between the tube walls and the flow are neglectable. Pumps and security systems are simulated by systems of ODEs (0D models). At the places where the pumps and the security systems are located, the main pipeline is decomposed. In order to couple the different pipeline parts again, the ODE-systems yield for each time point boundary values at the new interfaces. This is the same technique used for the simulation of a stenosis. All in all, both the pipeline system and networks of large arteries can be governed by means of 1D-0D coupled models. For the numerical discretisation, a discontinuous Galerkin method (DG-method) and the method of characteristics (MOC) have been used, where the MOC proved to be as accurate as the DG-method, but much more efficient as the DG-method. Our numerical simulations reveal that a pressure shock wave, which is initiated by the stoppage of a pump, can be significantly damped by a security system and a rupture of the pipeline can be prevented. Moreover, it has been possible to reproduce field measurements taken upstream and downstream of a pump, demonstrating the efficiency of the model. Further work could be focused on further validating the dimensionally reduced model, e.g., by comparing the simplified model with full-dimensional (3D) models. Concerning the discretisation methods, one could design a stable time integrator for the DG-method with a less restrictive CFL-condition. Besides, a more sophisticated limiter method for the DG-discretisation in space should be considered. Concerning modelling aspects, more advanced relief systems should be investigated.

The main focus of Part II is on modelling and simulation of blood flow in microvascular networks and the surrounding tissue. In order to decrease the complexity of this issue the blood vessel network is approximated by a 1D graph-like structure, while the tissue has been considered as a homogeneous porous medium. As flow models a 1D Poiseuille flow model for the vascular network and a standard Darcy equation for the tissue flow have been chosen. Both flow models are coupled by their source terms, where the 1D model appears as a Dirac measure within the source term of the 3D Darcy equation. This results in a 3D-1D coupled flow model for the considered issue.

Related to the 3D Darcy equation with a 1D Dirac source term one can define a mathematical model problem, which can be used to study the convergence behaviour of standard finite element methods. In Chapter 5 the Poisson equation with a line source term is investigated. Since the pressure in the 3D tissue matrix is only of interest in regions that are not covered by the vascular system, we have studied in this chapter the local convergence behaviour of a standard finite element discretisation based on quasi-uniform meshes. For this purpose, we cut out a cylinder around the line, which can be considered as a blood vessel. On the remainder of the domain we study the local convergence behaviour of the finite element method. It can be proved that even if a quasi-uniform mesh is used a linear finite element method exhibits an optimal convergence behaviour. Our numerical tests confirm the optimal convergence rate after a preasymptotic range, which ends if the meshsize is in

the size of the radius of the cylinder.

The fact that the preasymptotic range ends if the meshsize is in the range of the radii of the blood vessels is not satisfactory. Since in microvascular systems these vessels are typically very small compared to the computational domain, a very fine mesh is required to resolve the steep gradients and to guarantee optimal convergence. Moreover the pressure field in the tissue matrix exhibits singularities along the mid axes of the blood vessels, which can not be observed in reality. These features motivate the development of a new coupling concept. In Chapter 6 we have investigated an elliptic model problem that is related to a coupling concept projecting the 1D model not on the midaxes of the vessels but on their vessel walls, because the actual exchange between the vascular system and the tissue occurs there. The new coupling concept exhibits some advantages compared to the standard coupling approach [28, 29, 30]. One of these advantages is that the new problem formulation naturally arises from the full 3D description of the problem with inclusions, using well-founded model reduction hypotheses. Hence, it is possible to provide upper bounds for the modelling error related to the model reduction strategy and to characterise the dependence of the model error from the parameters of the problem explicitly, such as the radius of a blood vessel. Furthermore, it is possible to analyse the existence of solutions by means of the Lax-Milgram lemma. Finally, we have studied the approximation properties of the finite element method exploiting Céa's classical approach. Combining this result with non-standard interpolation properties of functions with low regularity, we have been able to prove error estimates for the proposed method in case of uniform and adapted meshes. Future work in this field might be concerned with the extension of this approach to more advanced models, such as problems in mixed form [100] or transient problems.

Despite of the fact that the new coupling approach from Chapter 6 has several advantages compared to other coupling approaches, it is still unfeasible to simulate larger parts of an organ. One reason for this is that even in small organic volumes covering just a few cubic millimeters, it is a challenging task to simulate flow in the microvascular networks and the interstitial space, since they consist of thousands of vessels [56, Chap. 1]. In addition to that it can happen that due to image segmentation errors small capillaries can not be reconstructed with a sufficient accuracy. As a consequence we just model flow in the larger vessels of a microvascular network by 1D Poiseuille flow models. The fine scale vessels are homogenised and converted into a porous medium coupled with the porous tissue matrix, which yields a double continuum flow model. Since we use a 1D flow model and a double continuum flow model, we refer to this model as "hybrid model". In order to validate the simulation results obtained by our hybrid model, we have generated a reference solution by means of the 3D-1D coupled model. Choosing the modelling parameters appropriately, our simulation results reveal that the mass fluxes at the boundaries of the larger vessels obtained with our hybrid model coincide in a satisfactory manner with the corresponding fluxes obtained solving the 3D-1D model. On the other hand, the mass fluxes with respect to the capillaries are overestimated by the hybrid model. Moreover, the net mass flux between the tissue and the capillaries is approximately 2.3 times higher for the 3D-1D model than for the hybrid model. Regarding the averaged pressures for each REV, the simulations suggest that the pressures obtained with the hybrid model differ, in average, by approximately 4 mmHg in the capillaries and by approximately 2.37 mmHg in the tissue from the solution of the fully-discrete model. However, we are able to show that a smaller linear system can be obtained compared to the 3D-1D model. In particular, we have shown that pressure values are representative for the model, in the sense that the discretisation error is negligible with respect to the modelling error. A more thorough comparison with

respect to the reduction of the computational costs would be subject of future work. For this purpose, a larger tissue sample should be considered. Finally, it would be of great interest to determine, whether a combination of modelling parameters exists that can be applied to different settings. As the authors of [128], we observe that in context of hybrid models for microvasculature different unknown parameters occur, whose values are not known a priori.

Part III is concerned with two-phase flow models for injection of fluids into dry porous media. In particular, it is investigated how the propagation and generation of saturation overshoots with respect to the fluid phase can be modelled and simulated [6, 7, 16, 20, 27, 34, 35, 36, 44, 45, 61, 104, 127, 139, 141, 152, 154]. For this purpose we have considered in a first step (Chapter 8) a two-phase flow problem with time dependent boundary conditions at the injection interface creating an artificial saturation overshoot. By means of two different flow models it is simulated how this artificial saturation overshoot propagates through the dry porous medium. Thereby, it is assumed that the total velocity of the two-phase flow system is constant. The change between drainage and imbibition processes is incorporated using hysteresis models [131, 132]. In addition to that, we estimate the propagation speed of the drainage and saturation fronts marking the overshoot. This is done considering Rankine-Hugoniot conditions. It can be observed that the theoretical and numerical results coincide with respect to the qualitative behaviour of the saturation overshoot. Future work in this context might be concerned with applying this model to problems in several space dimensions. Therefore, it would be necessary to improve the efficiency of the non-linear solvers such that larger time steps can be exerted and fewer iterations are required for the convergence of the iterative solvers.

In the final chapter of this part, we enhance the analysis of the previous chapter. Furthermore, the formation of saturation overshoots is not enforced by a boundary condition. Instead a further ODE is added to the two-phase flow model from the previous chapter [71, 26, 96, 114, 123, 141, 139, 140] such that non-monotone saturation profiles can be simulated. This ODE contains a parameter τ controlling the size of the overshoot. Our mathematical analysis is based on transforming the PDE system into a system of ODEs by means of the travelling wave approach. Thereby, we remove the space and time variables of the system by introducing a new coordinate and integrating the transformed equations on both sides with respect to this new coordinate. By means of this analysis, we have determined, how τ has to be chosen such that a saturation overshoot can be seen. Finally, we have provided accurate estimates for the velocities of the drainage and imbibition fronts such that the behaviour of overshoots can be determined more precisely. Our theoretical findings have been confirmed by several numerical tests. Further work could be concerned with analysing the same type of two-phase flow models which are not based on the assumption that the total velocity of the two-phase flow system is constant in space and time.

Concluding the submitted thesis, we note that the main focus of this work is fundamental research for reducing the computational complexity arising in the context of interesting application areas like physiology, energy storage systems and pipeline engineering. We have demonstrated that dimensionally reduced models, data based surrogate models and homogenised models can be used to produce applicable results. However, further effort has to be put into this type of research so that it is useable for complex issues in application fields like medicine or energy industry. One important aspect would be to combine the blood flow models for the macroscaled blood vessel networks and microcirculation. For this purpose, 1D Navier-Stokes equations could be used for the macroscaled blood vessel networks and

hybrid models for the capillary bed. A robust and meaningful model comprising both scales, would enable physiologists to study the distribution of a certain drug that is typically injected into a larger vein and then transported through the whole cardiovascular system. Thereby, it is important to determine the injected concentration, since many drugs have only an effect, if their concentration in blood or in tissue exceeds a certain threshold. Using a computer model the amount of drugs that is injected can be optimised such that the concentration is sufficiently high but that on the other hand no drugs are wasted and side effects can be kept to a minimum. The models for injection processes, which have been analysed in the last part of this thesis, have to be extended such that they can handle multi-phase flow and multi-component transport as well as heat transport. This is important to be able to simulate an injection of fuels into an energy storage device. Fuel itself is typically not a homogeneous fluid, but it consists of several components. Moreover, the injection of fuel or hot water into energy storage systems involve that different components can change their phase. If in a heat storage system, salts like sodium acetate are heated in their solid state, they become liquid. Finally, robust and efficient numerical methods have to be tested or newly developed such that not only 1D models, but also 3D models can be treated in an efficient way.

Bibliography

- [1] S. Acosta, C. Puelz, B. Riviere, Daniel J., and C. Rusin. Numerical method of characteristics for one-dimensional blood flow. *Journal of Computational Physics*, 294:96–109, 2015.
- [2] A. Adamkowski and M. Lewandowski. Experimental examination of unsteady friction models for transient pipe flow simulation. *Journal of Fluids Eng.*, 128(6):1351–1363, 2006.
- [3] J. Alastruey, S. Moore, K. Parker, T. David, J. Peiró, and S. Sherwin. Reduced modelling of blood flow in the cerebral circulation: Coupling 1-d, 0-d and cerebral auto-regulation models. *International journal for numerical methods in fluids*, 56(8):1061–1067, 2008.
- [4] J. Alastruey, K. Parker, J. Peiró, S. Byrd, and S. Sherwin. Modelling the circle of willis to assess the effects of anatomical variations and occlusions on cerebral flows. *Journal of biomechanics*, 40(8):1794–1805, 2007.
- [5] J. Alastruey, K. Parker, J. Peiró, and S. Sherwin. Lumped parameter outflow models for 1-d blood flow simulations: effect on pulse waves and parameter estimation. *Communications in Computational Physics*, 4(2):317–336, 2008.
- [6] H. Alt and S. Luckhaus. Quasilinear elliptic-parabolic differential equations. *Mathematische Zeitschrift*, 183(3):311–341, 1983.
- [7] H. Alt, S. Luckhaus, and A. Visintin. On nonstationary flow through porous media. *Annali di Matematica Pura ed Applicata*, 136(1):303–316, 1984.
- [8] T. Apel, O. Benedix, D. Sirch, and B. Vexler. A priori mesh grading for an elliptic problem with dirac right-hand side. *SIAM Journal on Numerical Analysis*, 49(3):992–1005, 2011.
- [9] N. Arbuzov and M. et. al Lurie. Protection of oil-loading tanker terminals from damages occurring due to hydraulic shock waves (based on existing russian terminals examples). In *21st World Petroleum Congress*. World Petroleum Congress, 2014.
- [10] A. Bahadori. *Oil and gas pipelines and piping systems: design, construction, management, and inspection*. Gulf Professional Publishing, 2016.
- [11] A. Barnard, W. Hunt, W. Timlake, and E. Varley. A theory of fluid flow in compliant tubes. *Biophysical Journal*, 6(6):717–724, 1966.
- [12] P. Bastian, F. Heimann, and S. Marnach. Generic implementation of finite element methods in the Distributed and Unified Numerics Environment (Dune). *Kybernetika*, 46(2):294–315, 2010.
- [13] J. Bear. *Hydraulics of groundwater*. McGraw-Hill International Book Co., 1979.

- [14] J. Bear. *Dynamics of fluids in porous media*. Courier Corporation, 2013.
- [15] B. Becker, B. Guo, B. Flemisch, and R. Helmig. Developing a coupled numerical model for underground gas storage, 5 2015. date=05.05.2015, IWS2ID=4432.
- [16] A.Y. Beliaev and S.M. Hassanizadeh. A theoretical model of hysteresis and dynamic effects in the capillary relation for two-phase flow in porous media. *Transport in Porous Media*, 43(3):487–510, 2001.
- [17] G. Bertotti. *Hysteresis in magnetism: for physicists, materials scientists, and engineers*. Academic press, 1998.
- [18] S. Boyaval, C. Le Bris, T. Lelievre, Y. Maday, N. Nguyen, and A. Patera. Reduced basis techniques for stochastic problems. *Archives of Computational methods in Engineering*, 17(4):435–454, 2010.
- [19] D. Braess. *Finite elements: Theory, fast solvers, and applications in solid mechanics*. Cambridge University Press, 2007.
- [20] J. Briggs, D. Katz, et al. Drainage of water from sand in developing aquifer storage. In *Fall Meeting of the Society of Petroleum Engineers of AIME*. Society of Petroleum Engineers, 1966.
- [21] G. Camps-Roach, D. O’Carroll, T. Newson, T. Sakaki, and T. Illangasekare. Experimental investigation of dynamic effects in capillary pressure: Grain size dependency and upscaling. *Water Resources Research*, 46(8), 2010.
- [22] S. Čanić and E. Kim. Mathematical analysis of the quasilinear effects in a hyperbolic model blood flow through compliant axi-symmetric vessels. *Mathematical Methods in the Applied Sciences*, 26(14):1161–1186, 2003.
- [23] X. Cao and S. Pop. Two-phase porous media flows with dynamic capillary effects and hysteresis: uniqueness of weak solutions. *Computers & Mathematics with Applications*, 69(7):688–695, 2015.
- [24] M. Carvalho, A. Oliveira, E. Azevedo, and A. Bastos-Leite. Intracranial arterial stenosis. *Journal of Stroke and Cerebrovascular Diseases*, 23(4):599–609, 2014.
- [25] P. Chen, A. Quarteroni, and G. Rozza. Simulation-based uncertainty quantification of human arterial network hemodynamics. *International journal for numerical methods in biomedical engineering*, 29(6):698–721, 2013.
- [26] C. Cuesta, C. van Duijn, and J. Hulshof. Infiltration in porous media with dynamic capillary pressure: travelling waves. *European Journal of Applied Mathematics*, 11(4):381–397, 2000.
- [27] L. Cueto-Felgueroso and R. Juanes. Stability analysis of a phase-field model of gravity-driven unsaturated flow through porous media. *Physical Review E*, 79(3):036301, 2009.
- [28] C. D’Angelo. Multiscale modelling of metabolism and transport phenomena in living tissues. Technical report, EPFL, 2007.

- [29] C. D’Angelo. Finite element approximation of elliptic problems with dirac measure terms in weighted spaces: applications to one-and three-dimensional coupled problems. *SIAM Journal on Numerical Analysis*, 50(1):194–215, 2012.
- [30] C. D’Angelo and A. Quarteroni. On the coupling of 1d and 3d diffusion-reaction equations: application to tissue perfusion problems. *Mathematical Models and Methods in Applied Sciences*, 18(08):1481–1504, 2008.
- [31] S. De Marchi, R. Schaback, and H. Wendland. Near-optimal data-independent point locations for radial basis function interpolation. *Adv. Comput. Math.*, 23(3):317–330, 2005.
- [32] A. Despopoulos and S. Silbernagl. *Color atlas of physiology*. Thieme, 2003.
- [33] K. DeVault, P. Gremaud, V. Novak, M. Olufsen, G. Vernieres, and P. Zhao. Blood flow in the circle of willis: modeling and calibration. *Multiscale Modeling & Simulation*, 7(2):888–909, 2008.
- [34] D. DiCarlo. Experimental measurements of saturation overshoot on infiltration. *Water Resources Research*, 40(4), 2004.
- [35] D. DiCarlo. Stability of gravity-driven multiphase flow in porous media: 40 years of advancements. *Water Resources Research*, 49(8):4531–4544, 2013.
- [36] D. DiCarlo, M. Mirzaei, B. Aminzadeh, and H. Dehghanpour. Fractional flow approach to saturation overshoot. *Transport in porous media*, 91(3):955–971, 2012.
- [37] D. Drzisga, T. Köppl, U. Pohl, R. Helmig, and B. Wohlmuth. Numerical modeling of compensation mechanisms for peripheral arterial stenoses. *Computers in biology and medicine*, 70:190–201, 2016.
- [38] C.J. van Duijn and K. Mitra. Hysteresis and horizontal redistribution in porous media. *Transport in Porous Media*, 122(2):375–399, Mar 2018.
- [39] F. Dullien. *Porous media: fluid transport and pore structure*. Academic press, 2012.
- [40] A. Egorov, R. Dautov, J. Nieber, and A. Sheshukov. Stability analysis of gravity-driven infiltrating flow. *Water resources research*, 39(9), 2003.
- [41] W. El-Bouri and S. Payne. Multi-scale homogenization of blood flow in 3-dimensional human cerebral microvascular networks. *Journal of theoretical biology*, 380:40–47, 2015.
- [42] W. El-Bouri and S. Payne. Investigating the effects of a penetrating vessel occlusion with a multi-scale microvasculature model of the human cerebral cortex. *NeuroImage*, 172:94–106, 2018.
- [43] A. Elansary. Waterhammer protection for the toshka pumping system. In *Building Partnerships*. ASCE, 2000.
- [44] M. Eliassi and R. Glass. On the continuum-scale modeling of gravity-driven fingers in unsaturated porous media: The inadequacy of the richards equation with standard monotonic constitutive relations and hysteretic equations of state. *Water Resources Research*, 37(8):2019–2035, 2001.

- [45] M. Eliassi and R.J. Glass. On the porous-continuum modeling of gravity-driven fingers in unsaturated materials: Extension of standard theory with a hold-back-pile-up effect. *Water Resources Research*, 38(11), 2002.
- [46] L.C. Evans. *Partial Differential Equations*. Graduate studies in mathematics. American Mathematical Society, 1998.
- [47] R. Eyres, A. Champneys, and N. Lieven. Modelling and dynamic response of a damper with relief valve. *Nonlinear Dynamics*, 40(2):119–147, 2005.
- [48] G. Fasshauer and M. McCourt. *Kernel-Based Approximation Methods Using MATLAB*, volume 19 of *Interdisciplinary Mathematical Sciences*. World Scientific Publishing Co. Pte. Ltd., Hackensack, NJ, 2015.
- [49] J. A. Fay. *Introduction to fluid mechanics*. MIT press, 1994.
- [50] M. Fernández, V. Milisic, and A. Quarteroni. Analysis of a geometrical multiscale blood flow model based on the coupling of odes and hyperbolic pdes. *Multiscale Modeling & Simulation*, 4(1):215–236, 2005.
- [51] J. Ferziger and M. Peric. *Computational methods for fluid dynamics*. Springer Science & Business Media, 2012.
- [52] B. Flemisch, M. Darcis, K. Erbertseder, B. Faigle, A. Lauser, K. Mosthaf, S. Müthing, P. Nuske, A. Tatomir, M. Wolff, and R. Helmig. DuMux: DUNE for multi-{phase, component, scale, physics, ...} flow and transport in porous media. *Advances in Water Resources*, 34(9):1102–1112, 2011.
- [53] L. Formaggia, D. Lamponi, and A. Quarteroni. One-dimensional models for blood flow in arteries. *Journal of engineering mathematics*, 47(3-4):251–276, 2003.
- [54] L. Formaggia, D. Lamponi, M. Tuveri, and A. Veneziani. Numerical modeling of 1d arterial networks coupled with a lumped parameters description of the heart. *Computer Methods in Biomechanics and Biomedical Engineering*, 9(5):273–288, 2006.
- [55] L. Formaggia, F. Nobile, and A. Quarteroni. A one dimensional model for blood flow: application to vascular prosthesis. In *Mathematical modeling and numerical simulation in continuum mechanics*, pages 137–153. Springer, 2002.
- [56] L. Formaggia, A. Quarteroni, and A. Veneziani. *Cardiovascular Mathematics: Modeling and simulation of the circulatory system*, volume 1. Springer Science & Business Media, 2010.
- [57] S. Fritz. Experimental Investigations of Water Infiltration into Unsaturated Soil - Analysis of Dynamic Capillarity Effects. Master’s thesis, Universität Stuttgart, Department of Hydromechanics and Modelling of Hydrosystems, 2012.
- [58] S. et. al. Genic. A review of explicit approximations of colebrook’s equation. *FME Transactions*, 39(2):67–71, 2011.
- [59] A. Ghodhbani and E. Taïeb. A four-equation friction model for water hammer calculation in quasi-rigid pipelines. *Int. J. of Pressure Vessels and Piping*, 151:54–62, 2017.

- [60] I. Gjerde, K. Kumar, J. Nordbotten, and B. Wohlmuth. Splitting method for elliptic equations with line sources. *ESAIM: Mathematical Modelling and Numerical Analysis*, 53(5):1715–1739, 2019.
- [61] R. Glass, T. Steenhuis, and J. Parlange. Mechanism for finger persistence in homogeneous, unsaturated, porous media: Theory and verification. *Soil Sci*, 148(1):60–70, 1989.
- [62] W. Gong, G. Wang, and N. Yan. Approximations of elliptic optimal control problems with controls acting on a lower dimensional manifold. *SIAM Journal on Control and Optimization*, 52(3):2008–2035, 2014.
- [63] S. Gottlieb and C. Shu. Total Variation Diminishing Runge-Kutta schemes. *Math. Comp.*, 67:73–85, 1998.
- [64] Brian H Grimard, Jan M Larson, et al. Aortic stenosis: diagnosis and treatment. *Am Fam Physician*, 78(6):717–724, 2008.
- [65] F. Haakh and H. Horlacher. Planung, bau und betrieb von fernwasserleitungen. *Rohrleitungen*, pages 1–27, 2016.
- [66] B. Haasdonk. *Transformation Knowledge in Pattern Analysis with Kernel Methods*. PhD thesis, PhD thesis, Albert-Ludwigs-Universität Freiburg, 2005.
- [67] B. Haasdonk. Reduced basis methods for parametrized PDEs – a tutorial introduction for stationary and instationary problems. In M. Ohlberger P. Benner, A. Cohen and K. Willcox, editors, *Model Reduction and Approximation: Theory and Algorithms*. SIAM, Philadelphia, 2017.
- [68] B. Haasdonk and H. Burkhardt. Invariant kernel functions for pattern analysis and machine learning. *Machine learning*, 68(1):35–61, 2007.
- [69] B. Haasdonk and G. Santin. Greedy kernel approximation for sparse surrogate modelling. In *Proceedings of the KoMSO Challenge Workshop on Reduced-Order Modeling for Simulation and Optimization*, 2017.
- [70] W. Hackbusch. *Elliptic differential equations: theory and numerical treatment*, volume 18. Springer, 2017.
- [71] M. Hassanizadeh and G. Gray. Thermodynamic basis of capillary pressure in porous media. *Water resources research*, 29(10):3389–3405, 1993.
- [72] T. Hatcher and J. Vasconcelos. Peak pressure surges and pressure damping following sudden air pocket compression. *Journal of Hydraulic Engineering*, 143(4):04016094, 2017.
- [73] R. Helmig. *Multiphase flow and transport processes in the subsurface: a contribution to the modeling of hydrosystems*. Springer-Verlag, 1997.
- [74] R. Hilfer and R. Steinle. Saturation overshoot and hysteresis for twophase flow in porous media. *The European Physical Journal Special Topics*, 223(11):2323–2338, 2014.

- [75] T. Hughes and J. Lubliner. On the one-dimensional theory of blood flow in the larger vessels. *Mathematical Biosciences*, 18(1-2):161–170, 1973.
- [76] Jinsheng Huo. Surge protections for a major raw water pump and pipeline system. In *World Environmental and Water Resources Congress*. ASCE, 2011.
- [77] IEC. Industrial-process control valves - part 1: Control valve terminology and general considerations. IEC 60534-1:2005, Int. Electrotech. Commission, Geneva, Switzerland, 2005.
- [78] C. Jan, C. Chang, J. Lai, and W. Guo et. al. Characteristics of hydraulic shock waves in an inclined chute contraction-numerical simulations. *J. of Mech.*, 25(1):75–84, 2009.
- [79] H. Jasak, A. Jemcov, and Z. Tukovic. OpenFOAM: A C++ library for complex physics simulations. In *International Workshop on Coupled Methods in Numerical Dynamics*, volume 1000, pages 1–20, 2007.
- [80] L. John, P. Pustějovská, and O. Steinbach. On the influence of the wall shear stress vector form on hemodynamic indicators. *Computing and Visualization in Science*, 18(4-5):113–122, 2017.
- [81] F.J-M. Kalaydjian et al. Dynamic capillary pressure curve for water/oil displacement in porous media: Theory vs. experiment. In *SPE Annual Technical Conference and Exhibition*. Society of Petroleum Engineers, 1992.
- [82] T. Koch, K. Heck, N. Schröder, H. Class, and R. Helmig. A new simulation framework for soil–root interaction, evaporation, root growth, and solute transport. *Vadose Zone Journal*, 17(1), 2018.
- [83] T. Köppl. *Multi-scale modeling of flow and transport processes in arterial networks and tissue*. PhD thesis, Technische Universität München, 2015.
- [84] T. Köppl, R. Helmig, and B. Wohlmuth. A multi-scale model for mass transport in arteries and tissue. In *Recent Trends in Computational Engineering-CE2014*, pages 197–213. Springer, 2015.
- [85] T. Köppl, M. Schneider, U. Pohl, and B. Wohlmuth. The influence of an unilateral carotid artery stenosis on brain oxygenation. *Medical engineering & physics*, 36(7):905–914, 2014.
- [86] T. Köppl and B. Wohlmuth. Optimal a priori error estimates for an elliptic problem with dirac right-hand side. *SIAM Journal on Numerical Analysis*, 52(4):1753–1769, 2014.
- [87] T. Köppl, B. Wohlmuth, and R. Helmig. Reduced one-dimensional modelling and numerical simulation for mass transport in fluids. *International Journal for Numerical Methods in Fluids*, 72(2):135–156, 2013.
- [88] L. Krivodonova. Limiters for high-order discontinuous galerkin methods. *Journal of Computational Physics*, 226(1):879–896, 2007.

- [89] J Rodney Levick and C Charles Michel. Microvascular fluid exchange and the revised starling principle. *Cardiovascular research*, 87(2):198–210, 2010.
- [90] J. Li, J. Melenk, B. Wohlmuth, and J. Zou. Optimal a priori estimates for higher order finite elements for elliptic interface problems. *Applied numerical mathematics*, 60(1-2):19–37, 2010.
- [91] F. Liang and L. Hao. A closed-loop lumped parameter computational model for human cardiovascular system. *JSME International Journal Series C Mechanical Systems, Machine Elements and Manufacturing*, 48(4):484–493, 2005.
- [92] F. Liang, S. Takagi, R. Himeno, and H. Liu. Multi-scale modeling of the human cardiovascular system with applications to aortic valvular and arterial stenoses. *Medical & biological engineering & computing*, 47(7):743–755, 2009.
- [93] M. Lurie. *Modeling of Oil Product and Gas Pipeline Transport*. Wiley Online Library, 2008.
- [94] S. Mahjoob and K. Vafai. Analytical characterization of heat transport through biological media incorporating hyperthermia treatment. *International Journal of Heat and Mass Transfer*, 52(5-6):1608–1618, 2009.
- [95] A. Manzoni, A. Quarteroni, and G. Rozza. Model reduction techniques for fast blood flow simulation in parametrized geometries. *International Journal for Numerical Methods in Biomedical Engineering*, 28(6-7):604–625, 2012.
- [96] K. Mitra and C. van Duijn. Wetting fronts in unsaturated porous media: the combined case of hysteresis and dynamic capillary pressure. *Nonlinear Analysis: Real World Applications*, 2018.
- [97] N. Morrow, C. Harris, et al. Capillary equilibrium in porous materials. *Society of Petroleum Engineers Journal*, 5(01):15–24, 1965.
- [98] J. Mynard and J. Smolich. One-dimensional haemodynamic modeling and wave dynamics in the entire adult circulation. *Annals of Biomedical Engineering*, 43(6):1443–1460, 2015.
- [99] M. Nabil, P. Decuzzi, and P. Zunino. Modelling mass and heat transfer in nano-based cancer hyperthermia. *Royal Society open science*, 2(10):150447, 2015.
- [100] D. Notaro, L. Cattaneo, L. Formaggia, A. Scotti, and P. Zunino. A mixed finite element method for modeling the fluid exchange between microcirculation and tissue interstitium. In *Advances in Discretization Methods*, pages 3–25. Springer, 2016.
- [101] M. Olufsen. Structured tree outflow condition for blood flow in larger systemic arteries. *American Journal of Physiology-Heart and Circulatory Physiology*, 276(1):H257–H268, 1999.
- [102] M. Olufsen and A. Nadim. On deriving lumped models for blood flow and pressure in the systemic arteries. *Math Biosci Eng*, 1(1):61–80, 2004.
- [103] J. Ottesen, M. Olufsen, and J. Larsen. *Applied mathematical models in human physiology*. SIAM, 2004.

- [104] F. Otto. L1-contraction and uniqueness for quasilinear elliptic–parabolic equations. *Journal of differential equations*, 131(1):20–38, 1996.
- [105] M. Peyrounette, Y. Davit, M. Quintard, and S. Lorthois. Multiscale modelling of blood flow in cerebral microcirculation: Details at capillary scale control accuracy at the level of the cortex. *PloS one*, 13(1):e0189474, 2018.
- [106] C. Pozrikidis. Axisymmetric motion of a file of red blood cells through capillaries. *Physics of fluids*, 17(3):031503, 2005.
- [107] A. Pries, T. Secomb, and P. Gaehtgens. Biophysical aspects of blood flow in the microvasculature. *Cardiovascular research*, 32(4):654–667, 1996.
- [108] A. Pries, T. Secomb, P. Gaehtgens, and J. Gross. Blood flow in microvascular networks. experiments and simulation. *Circulation research*, 67(4):826–834, 1990.
- [109] A. Quarteroni and L. Formaggia. Mathematical modelling and numerical simulation of the cardiovascular system. *Handbook of Numerical Analysis*, 12:3–127, 2004.
- [110] A. Quarteroni, A. Manzoni, and F. Negri. *Reduced basis methods for partial differential equations: an introduction*, volume 92. Springer, 2015.
- [111] A. Quarteroni and G. Rozza. Optimal control and shape optimization of aorto-coronary bypass anastomoses. *Mathematical Models and Methods in Applied Sciences*, 13(12):1801–1823, 2003.
- [112] A. Quarteroni and G. Rozza. *Reduced order methods for modeling and computational reduction*, volume 9. Springer, 2014.
- [113] A. Quarteroni, R. Sacco, and F. Saleri. *Numerical mathematics*, volume 37. Springer Science & Business Media, 2010.
- [114] A. Rätz and B. Schweizer. Hysteresis models and gravity fingering in porous media. *ZAMM-Journal of Applied Mathematics and Mechanics*, 94(7-8):645–654, 2014.
- [115] J. Reichold, M. Stampanoni, A. Keller, A. Buck, P. Jenny, and B. Weber. Vascular graph model to simulate the cerebral blood flow in realistic vascular networks. *Journal of Cerebral Blood Flow & Metabolism*, 29(8):1429–1443, 2009.
- [116] R. Schaback and H. Wendland. Adaptive greedy techniques for approximate solution of large RBF systems. *Numer. Algorithms*, 24(3):239–254, 2000.
- [117] W. Schaper, J. Piek, R. Munoz-Chapuli, C. Wolf, W. Ito, et al. Collateral circulation of the heart. *Angiogenesis and Cardiovascular Disease*, pages 159–198, 1999.
- [118] A. Schatz and L. Wahlbin. Interior maximum norm estimates for finite element methods. *Mathematics of Computation*, 31(138):414–442, 1977.
- [119] B. Schölkopf and A.J. Smola. *Learning with Kernels*. MIT Press, Cambridge, 2002.
- [120] D. Scholz, T. Ziegelhoeffer, A. Helisch, S. Wagner, C. Friedrich, T. Podzuweit, and W. Schaper. Contribution of arteriogenesis and angiogenesis to postocclusive hindlimb perfusion in mice. *Journal of molecular and cellular cardiology*, 34(7):775–787, 2002.

- [121] B. Schweizer. Laws for the capillary pressure in a deterministic model for fronts in porous media. *SIAM journal on mathematical analysis*, 36(5):1489–1521, 2005.
- [122] B. Schweizer. Instability of gravity wetting fronts for richards equations with hysteresis. *Interfaces and Free Boundaries*, 14(1):37–65, 2012.
- [123] B. Schweizer. The richards equation with hysteresis and degenerate capillary pressure. *Journal of Differential Equations*, 252(10):5594–5612, 2012.
- [124] B. Seeley and D. Young. Effect of geometry on pressure losses across models of arterial stenoses. *Journal of biomechanics*, 9(7):447–448, 1976.
- [125] G. Seitz, R. Helmig, and H. Class. Numerical model of a $\text{Ca(OH)}_2 / \text{CaO}$ thermochemical heat storage reactor, 5 2017. IWS2ID=4459.
- [126] S. Sherwin, L. Formaggia, J. Peiro, and V. Franke. Computational modelling of 1d blood flow with variable mechanical properties and its application to the simulation of wave propagation in the human arterial system. *International Journal for Numerical Methods in Fluids*, 43(6-7):673–700, 2003.
- [127] S. Shiozawa and H. Fujimaki. Unexpected water content profiles under flux-limited one-dimensional downward infiltration in initially dry granular media. *Water Resources Research*, 40(7), 2004.
- [128] R. Shipley, A. Smith, P. Sweeney, A. Pries, and T. Secomb. A hybrid discrete-continuum approach for modelling microcirculatory blood flow. *Mathematical medicine and biology: a journal of the IMA*, 2019.
- [129] N. Smith, A. Pullan, and P. Hunter. An anatomically based model of transient coronary blood flow in the heart. *SIAM Journal on Applied mathematics*, 62(3):990–1018, 2002.
- [130] E. H. Starling. On the absorption of fluids from the connective tissue spaces. *The Journal of physiology*, 19(4):312–326, 1896.
- [131] R. Steinle and R. Hilfer. Influence of Initial Conditions on Propagation, Growth and Decay of Saturation Overshoot. *Transport in Porous Media*, 111(2):369–380, 2016.
- [132] R. Steinle and R. Hilfer. Hysteresis in relative permeabilities suffices for propagation of saturation overshoot: A quantitative comparison with experiment. *Physical Review E*, 95:043112, 2017.
- [133] D. Stephenson. Simple guide for design of air vessels for water hammer protection of pumping lines. *Journal of Hydraulic Engineering*, 128(8):792–797, 2002.
- [134] N. Stergiopoulos, D. Young, and T. Rogge. Computer simulation of arterial flow with applications to arterial and aortic stenoses. *Journal of biomechanics*, 25(12):1477–1488, 1992.
- [135] V. Temlyakov. Greedy approximation. *Acta Numer.*, 17:235–409, 2008.
- [136] E. Toro. Brain venous haemodynamics, neurological diseases and mathematical modelling. a review. *Applied Mathematics and Computation*, 272:542–579, 2016.

- [137] P. Tran. Pressure transients caused by tilting-disk check-valve closure. *Journal of Hydraulic Engineering*, 141(3):04014081, 2015.
- [138] D. Valdez-Jasso, M. Haider, H. Banks, D. Santana, Y. Germán, R. Armentano, and M. Olufsen. Analysis of viscoelastic wall properties in ovine arteries. *IEEE Transactions on Biomedical Engineering*, 56(2):210–219, 2009.
- [139] C. Van Duijn, Y. Fan, L. Peletier, and I. Pop. Travelling wave solutions for degenerate pseudo-parabolic equations modelling two-phase flow in porous media. *Nonlinear Analysis: Real World Applications*, 14(3):1361–1383, 2013.
- [140] C. van Duijn, K. Mitra, and S. Pop. Travelling wave solutions for the richards equation incorporating non-equilibrium effects in the capillarity pressure. *Nonlinear Analysis: Real World Applications*, 41:232–268, 2018.
- [141] C. Van Duijn, A. Peletier, and S. Pop. A new class of entropy solutions of the buckley-leverett equation. *SIAM Journal on Mathematical Analysis*, 39(2):507–536, 2007.
- [142] C. Van Duijn, G. Pieters, and P. Raats. Steady flows in unsaturated soils are stable. *Transport in Porous Media*, 57(2):215–244, 2004.
- [143] C. Wang and J. Yang. Water hammer simulation using explicit-implicit coupling methods. *Journal of Hydraulic Engineering*, 141(4):04014086, 2015.
- [144] K. Weishaupt, M. Beck, B. Becker, H. Class, T. Fetzer, B. Flemisch, G. Futter, D. Gläser, C. Grüninger, J. Hommel, A. Kissinger, T. Koch, M. Schneider, N. Schröder, N. Schwenck, and G. Seitz. Dumux 2.9.0, mar 2016.
- [145] K. Weishaupt, V. Joekar-Niasar, and R. Helmig. An efficient coupling of free flow and porous media flow using the pore-network modeling approach. *Journal of Computational Physics*, 1, 2019.
- [146] H. Weller, G. Tabor, H. Jasak, and C. Fureby. A tensorial approach to computational continuum mechanics using object-oriented techniques. *Computers in Physics*, 12(6):620–631, 1998.
- [147] H. Wendland. Piecewise polynomial, positive definite and compactly supported radial functions of minimal degree. *Adv. Comput. Math.*, 4(1):389–396, 1995.
- [148] H. Wendland. *Scattered Data Approximation*, volume 17 of *Cambridge Monographs on Applied and Computational Mathematics*. Cambridge University Press, Cambridge, 2005.
- [149] D. Wirtz and B. Haasdonk. A vectorial kernel orthogonal greedy algorithm. *Dolomites Res. Notes Approx.*, 6:83–100, 2013. Proceedings of DWCAA12.
- [150] D. Wirtz, N. Karajan, and B. Haasdonk. Surrogate modeling of multiscale models using kernel methods. *International Journal for Numerical Methods in Engineering*, 101(1):1–28, 2015.

- [151] D. Wu, S. Yang, P. Wu, and L. Wang. MOC-CFD coupled approach for the analysis of the fluid dynamic interaction between water hammer and pump. *Journal of Hydraulic Engineering*, 141(6):06015003, 2015.
- [152] Y. Xiong. Flow of water in porous media with saturation overshoot: A review. *Journal of Hydrology*, 510:353–362, 2014.
- [153] D. Young and F. Tsai. Flow characteristics in models of arterial stenoses—ii. unsteady flow. *Journal of biomechanics*, 6(5):547–559, 1973.
- [154] E. Youngs. Redistribution of moisture in porous materials after infiltration: 2. *Soil Science*, 86(4):202–207, 1958.
- [155] L. Zhuang, R. Bezerra Coelho, M. Hassanizadeh, and T. van Genuchten. Analysis of the hysteretic hydraulic properties of unsaturated soil. *Vadose Zone Journal*, 16(5), 2017.